Universität Paderborn
Fakultät für Naturwissenschaften

Base Metal Iron(II)-Cobalt(III) Dyads for Photocatalytic Hydrogen Evolution

Dissertation

vorgelegt von

MARINA HUBER-GEDERT

Zur Erlangung des akademischen Grades
Doktor der Naturwissenschaften (Dr. rer. nat.)
im Department Chemie

Paderborn 2022

Promotionskommission

Prof. Dr. Sabine Fechner	Vorsitz
Prof. Dr. Matthias Bauer	Erstgutachter
Privatdozent Dr. Hans Egold	Zweitgutachter
Prof. Dr. Thomas D. Kühne	

Universität Paderborn
Fakultät für Naturwissenschaften
Chemie

Eidesstattliche Erklärung

Hiermit versichere ich, die vorliegende Arbeit selbständig angefertigt und keine anderen als die von mir angegebenen Hilfsmittel verwendet zu haben. Wörtliche und sinngemäße Zitate wurden als solche gekennzeichnet und die Genehmigungen zur Veröffentlichung der urheberrechtlich geschützten Publikationen wurden eingeholt. Fremdleistungen wurden gekennzeichnet.

Paderborn, 19. September 2022

.....
Marina Huber-Gedert

Wir erben die Erde nicht von unseren Vorfahren,
wir leihen sie von unseren Kindern.
— ***Indianer Spruch***

Abstract

Balancing climate change and rising energy demand is a key challenge for our generation. Carbon-free produced energy carriers, such as green hydrogen, are needed for a sustainable future. Photocatalytic proton reduction is one possibility to produce hydrogen. Preferably, noble metals are avoided. In this work, iron was used as photosensitizer and cobalt as catalyst.

Based on two terpyridine-based ligands and two carbene-based ligands, homoleptic and heteroleptic iron photosensitizers were synthesized. They were thoroughly characterized by X-ray diffraction, NMR spectroscopy, ESI mass spectrometry, elemental analysis, UV-Vis spectroscopy and cyclic voltammetry. The combination of different ligands results in the variation of the carbene count, modulating the physical properties of the obtained complexes. Blue-shifts of absorption bands and an extension of ^{3}MLCT lifetime occured for systems containg more carbene functionalities. The observed transitions were explained by TDDFT, dividing the absorption spectra into ligand-based π-π^* transitions below 350 nm and MLCT transitions above 350 nm. Also, the tuning of bridging ligand backbone by acetylene and phenyl-acetylene linkers led to better absorption properties and a ^{3}MLCT lifetime extension by a factor of 2. Due to the free coordination site at the terminal pyridine functionality in some complexes, sensitivity towards protonation was investigated. The partially reversible bulk metal oxidation was evaluated by spectroelectrochemistry.

Multimetal complexes, as assemblies of photosensitizer and catalyst in one molecule, were obtained by coordinating the respective photosensitizer with one or two cobaloxime moieties, resulting in dyads and triads, respectively. They showed better absorption properties and equal or extended lifetimes as confirmed by TA. Multimetal complex stability was studied by NMR. Dissociation took place at concentrations below $5{\cdot}10^{-4}$ mol/L. A complicated dissociation behaviour was found for the triad, where three different species were involved. Sensitivity towards protonation was lower in case of multimetal complexes because the pyridine functionality was coordinated by the cobaloxime moiety, but could be partially protonated upon cobaloxime dissociation.

One dyad was tested in photocatalytic proton reduction reactions, with photostability previously confirmed by NMR. The one-component system was twofold more active relative to the multi-component system composed of the corresponding photosensitizer and cobaloxime. It was explained by transient optical absorption spectroscopy and ultrafast two-colour X-ray emission spectroscopy (2C-XES), which showed the occurence of a charge transfer from iron to cobalt.

Kurzzusammenfassung

Der Klimawandel und der gleichzeitig steigende Energiebedarf stellen eine zentrale Herausforderung für unsere Generation dar. Für eine nachhaltige Zukunft werden emissionsfreie Energieträger, wie Wasserstoff, benötigt. Die photokatalytische Protonenreduktion ist eine Möglichkeit, Wasserstoff zu erzeugen. Vorzugsweise werden dabei Edelmetalle vermieden. In dieser Arbeit wurden Eisen als Photosensibilisator und Kobalt als Katalysator verwendet.

Unter Verwendung von zwei terpyridinbasierten und zwei carbenbasierten Liganden wurden homoleptische und heteroleptische Eisen-Photosensibilisatoren synthetisiert. Sie wurden durch Einkristalldiffraktometrie, NMR- und UV-Vis-Spektroskopie, ESI-Massenspektrometrie, Elementaranalyse und zyklische Voltammetrie eingehend charakterisiert. Durch Variation der Carbenanzahl wurden die physikalischen Eigenschaften der erhaltenen Komplexe moduliert. Blauverschiebungen der Absorptionsbanden und eine Verlängerung der ^{3}MLCT-Lebensdauer traten bei Systemen mit Carbenfunktionen auf. Die beobachteten Übergänge wurden durch TDDFT-Rechnungen erklärt, wobei die Absorptionsspektren in ligandenbasierte π-π^*-Übergänge unterhalb von 350 nm und MLCT-Übergänge oberhalb von 350 nm unterteilt wurden. Auch die Optimierung des verbrückenden Ligandenrückgrats durch Acetylen- und Phenylacetylen-Linker führte zu besseren Absorptionseigenschaften und einer Verdopplung der MLCT-Lebensdauer. Die Protonierung der freien Koordinationsstelle am terminalen Pyridin wurde in einigen Komplexen untersucht. Die teilweise reversible Oxidation des Metalls in Lösung wurde durch Spektroelektrochemie gezeigt.

In Dyaden bzw. Triaden wurden Photosensibilisator und Katalysator in einem Molekül verbunden. Sie zeigten bessere Absorptionseigenschaften und vergleichbare oder verlängerte Lebensdauern, welche durch TA bestätigt wurden. Die Stabilität der Dyaden und der Triade wurde mittels NMR untersucht. Bei Konzentrationen unter $5{\cdot}10^{-4}$ mol/L fand Dissoziation statt. Für die Triade wurde ein komplexes Dissoziationsverhalten festgestellt, an dem drei verschiedene Spezies beteiligt waren. Die Empfindlichkeit gegenüber Protonierung war bei den Multimetallkomplexen geringer, da die Pyridinfunktionalität durch Kobalt koordiniert wurde.

Eine Dyade wurde in der photokatalytischen Protonenreduktion getestet, wobei die Photostabilität zuvor durch NMR bestätigt wurde. Das Einkomponentensystem war im Vergleich zum Mehrkomponentensystem, bestehend aus dem entsprechenden Photosensibilisator und Cobaloxim, doppelt so aktiv. Dies wurde durch TA und ultraschnelle Zweifarb-Röntgenemissionsspektroskopie (2C-XES) erklärt. Durch 2C-XES konnte das Auftreten eines Ladungstransfers von Eisen zu Kobalt aufgezeigt werden.

Danksagung

Viele Personen haben mich während des Studiums und der Doktorarbeit begleitet. Mein Dank gilt allen, die mit Gesprächen, Austausch und gemeinsamen Erfahrungen diese Zeit schöner gestaltet haben.

Prof. Dr. Matthias Bauer möchte ich für die Möglichkeit in seinem Arbeitskreis zu promovieren danken. Durch den wissenschaftlichen Austausch und durch herausfordernde spektroskopische Methoden wurde meine Promotion zu einer spannenden Forschungsreise.

Mein Dank gilt auch Herrn PD Dr. Hans Egold für das Zweitgutachten. Darüber hinaus möchte ich mich für wertvolle Hilfestellungen bei der Auswertung von NMR-Spektren bedanken. Ich möchte auch Herrn Prof. Dr. Thomas D. Kühne und Frau Prof. Dr. Fechner für die Übernahme des 3.Prüfers und des Vorsitzes danken.

Ohne die Unterstützung von Mitarbeitenden aus der Zentralen Analytik und weiterer Abteilungen wäre diese Arbeit nicht möglich gewesen, daher bedanke ich mich bei: Dr. Roland Schoch für die Analyse der kristallographischen Daten, Dr. Adam Neuba und Christiane Gloger für die massenspektrometrischen und (spektro-)elektrochemischen Messungen, sowie für Elementaranalysen. Karin Stolte möchte ich für die unzähligen NMR-Messungen danken. Dr. Michał Nowakowski gilt mein besonderer Dank für den häufigen Austausch zur Röntgenspektroskopie, sowie für Messung und Auswertung von zeitaufgelösten röntgenspektroskopischen Daten am European XFEL. Dr. Hossam Elgabarty aus dem Arbeitskreis von Prof. Dr. Thomas D. Kühne möchte ich für die Hilfsbereitschaft bei DFT-Rechnungen und die Bereitstellung von weiterführenden quantenmechanischen Ergebnissen danken. Außerdem danke ich Dr. Patrick Müller für die Einführung in ORCA.

Diese Arbeit wurde auch durch Kooperationen mit anderen Arbeitskreisen geprägt. Ich möchte mich bei dem Arbeitskreis von Prof. Dr. Wojciech Gawelda (Adam Mickiewicz University Poznań), im Besonderen Dr. Natalia Lindner und Dr. Ahmet Kertmen, und bei dem Arbeitskreis von Prof. Dr. Stefan Haacke (University of Strasbourg), im Besonderen Dr. Bogdan Marekha, für die Messung und Auswertung von transienten Absorptionsmessungen bedanken.

Dem Fond der chemischen Industrie des Verbandes der Chemischen Industrie e.V. und der Studienstiftung des deutschen Volkes gilt mein Dank für die finanzielle Unterstützung während meiner Promotion.

Im Laufe der Promotion durfte ich zwei engagierte Studierende das präparative Arbeiten näherbringen und erhielt gleichzeitig deren Unterstützung bei den synthetischen Arbeiten. Mein Dank gilt Dominik Baier und im Besonderen Lennart Schmitz, der zusätzlich im Rahmen seiner Bachelorarbeit zum Gelingen dieser Arbeit beigetragen hat.

Meine Forschungsreise wäre nur halb so schön gewesen ohne meine Arbeitskolleg*innen. Danke für die aufmunternden Worte und den zahlreichen Austausch im L-Raum, bei Dienstreisen und abendlichen Aktivitäten. Ganz besonders möchte ich Dr. Philipp Dierks und Lennart Schmitz vom Herzen danken für eine unvergessliche Zeit in unserem Labor. Die Freitagsplaylist wird mir stets in guter Erinnerung bleiben.

Meiner Familie und meinen Freunden gebührt mein größter Dank. Dank ihres Rückhalts und ihrer Motivation konnte ich mich durch die schwere Zeiten der Promotion kämpfen und auch Zeiten fernab der Chemie genießen. Meinem Mann Alexander Gedert danke ich für das bedingungslose Verständnis und seine ausdauernde Unterstützung. Zuletzt möchte ich meinem Sohn Nicolas Gedert danken, der mir tatkräftig bei dem Erstellen dieser Arbeit geholfen hat und mich auch zu erholsamen Spielpausen ermunterte.

List of Beamtimes

European Synchrotron Radiation Facility (ESRF)

- BM26a July 08-12 2018

Spring-8 Angstrom Compact Free-Electron Laser (SACLA)

- BL3EH2 July 05-08 2019

European X-Ray Free-Electron Laser (XFEL)

- FXE September 11-16 2019

List of Publications

Publications

1. M. Huber-Gedert, M. Nowakowski, A. Kertmen, L. Burkhardt, N. Lindner, R. Schoch, R. Herbst-Irmer, A. Neuba, L. Schmitz, T.-K. Choi, J. Kubicki, W. Gawelda, M. Bauer, Fundamental Characterization, Photophysics and Photocatalysis of a Base Metal Iron(II)-Cobalt(III) Dyad, *Chem. Eur. J.*, **2021**, 27, 9905-9918.

2. M. Nowakowski, M. Huber-Gedert, H. Elgabarty, J. Kubicki, A. Kertem, N. Lindner, D. Khakhulin, F. Lima, T.-K. Choi, M. Biednov, N. Piergies, P. Zalden, K. Kubicek, A. Rodriguez-Fernandez, M. Alaraby Salem, T. Kühne, W. Gawelda, M. Bauer, Ultrafast two-colour X-ray emission spectroscopy reveals excited state landscape in a base metal dyad, *manuscript submitted.*

3. M. Huber-Gedert, B. Marekha, L. Schmitz, M. Nowakowski, R. Schoch, A. Neuba, S. Haacke, M. Bauer, Tuning the excited state properties of iron(II)-cobalt(III) dyads by varying the bridging ligand, *manuscript in preparation.*

Talks

1. M. Huber-Gedert, M. Bauer: Diametral-koordinierende Liganden für bimetallische Photokatalysatoren, 3. Ligandendesign-Workshop Köln, July 22, 2019.

2. M. Huber-Gedert, M. Bauer: Eisen-Cobalt-Dyaden zur photokatalytischen Darstellung von Wasserstoff, Regionales FCI-Stipendiaten-Treffen Göttingen, February 14, 2020.

3. M. Huber-Gedert, M. Bauer: Noble Metal-Free Photocatalytic Hydrogen Evolution Using Iron(II)-Cobalt(III) Dyads, 16. Koordinationschemie-Treffen Freiburg, March 01-03, 2020.

Posters

1. M. Huber-Gedert, M. Bauer: Noble Metal-Free Iron-Cobalt-Dyads for Photocatalytic Water Reduction, 14. Koordinationschemie-Treffen Heidelberg, March 11-13, 2018.

2. M. Huber-Gedert, M. Bauer: Noble Metal-Free Iron-Cobalt-Dyads for Photocatalytic Water Splitting, 21. JCF Frühjahrssymposium Bremen, March 20-23, 2019.

3. M. Huber-Gedert, M. Bauer: Spectroscopic Insights into Iron-Cobalt-Dyads for Photocatalytic Water Splitting, MPI Summerschool Gelsenkirchen, September 29 - October 04, 2019.

4. M. Huber-Gedert, M. Bauer: A Base Metal Iron(II)-Cobalt(III) Dyad for Photocatalytic Hydrogen Evolution, 2. Catalight Young Scientist Symposium, September 21-30, 2021.

Contents

Abstract iii

Kurzzusammenfassung v

Danksagung vii

List of Beamtimes xi

List of Publications xiii

Abbreviations xxi

Investigated Ligands xxv

Investigated Complexes xxvii

1 Introduction 1

1.1 Motivation . . . 1

1.2 Thesis Structure . . . 2

2 Background 3

2.1 Climate Change and Global Warming . . . 3

2.2 Hydrogen Production . . . 4

2.3 Homogenous Photocatalytic Water Splitting . . . 10

2.4 Photosensitizer . . . 12

2.4.1 Photophysics of iron and ruthenium d^6 complexes . . . 12

2.4.2 Strategies for MLCT lifetime elongation in iron d^6 complexes . 13

2.5 Catalyst . . . 19

2.5.1 Cobalt . . . 19

2.6 Dyads . . . 22

2.6.1 Hybrid dyads with Ru and Ir photosensitizers . . . 22

2.6.2 Noble-metal-free photosensitizers attached to cobaloxime . . . 24

2.7 Objectives . . . 26

3 Ligand Design 29

3.1 Terpyridine-based ligands . . . 29

3.2 Carbene-based ligands . . . 30

3.2.1 Synthetic Strategy . . . 30

4 Iron Complexes **39**
4.1 Homoleptic Complex Synthesis . . . 39
4.1.1 Terpyridine-based complexes . . . 39
4.1.2 Carbene-based complexes . . . 39
4.2 Heteroleptic Complex Synthesis . . . 42
4.2.1 Terpyridine-based complexes . . . 42
4.2.2 Carbene-based complex . . . 43
4.3 Characterization and Properties . . . 44
4.3.1 Crystal structures . . . 44
4.3.2 UV-Vis Spectroscopy . . . 49
4.3.3 Protonation of photosensitizer . . . 55
4.3.4 Cyclic Voltammetry . . . 58
4.3.5 Spectroelectrochemistry . . . 61
4.3.6 Chapter summary . . . 64

5 Multimetal Complexes **65**
5.1 Dyad Complex Synthesis . . . 65
5.2 Triad Complex Synthesis . . . 66
5.3 Characterization and Properties . . . 67
5.3.1 Crystal structures . . . 67
5.3.2 Dissociation study by NMR Spectroscopy . . . 70
5.3.3 UV-Vis Spectroscopy . . . 75
5.3.4 Cyclic Voltammetry . . . 86
5.3.5 Spectroelectrochemistry . . . 89
5.3.6 Transient optical absorption spectroscopy . . . 93
5.3.7 Chapter summary . . . 100

6 Photocatalytic Hydrogen Production **101**
6.1 Photocatalytic Measurement . . . 101
6.2 Spectroscopic Explanation . . . 105
6.2.1 Time-resolved Spectroscopy . . . 105
6.2.2 Chapter summary . . . 112

7 Summary and Outlook **113**

8 Experimental Part **119**
8.1 General laboratory information . . . 119
8.2 Analytic and spectroscopic methods . . . 119
8.3 Ligand synthesis . . . 123
8.4 Complex synthesis . . . 138

Bibliography **146**

9 Spectra **163**

9.1 Spectra of ligands 163

9.2 Spectra of complexes 196

10 Crystallographic data **215**

11 Computational chemistry **223**

12 Cyclic voltammograms **249**

List of Figures **263**

List of Tables **268**

Abbreviations

abbreviation	explanation
AWE	Alkaline water electrolysis
BL	Bridging ligand
BODIPY	Boron dipyrromethene
CAT	Catalyst
CCS	Carbon capture and storage
CV	Cyclic voltammogram/voltammetry
DCM	Dichlormethane
DFT	Density functional theory
DIPA	Diisopropylamine
dmgH	Dimethylglyoxime
DSSC	Dye-sensitized solar cell
ESA	Excited state absorption
ET	Electron transfer
EXAFS	Extended X-Ray absorption fine structure
FEL	Free electron laser
GA	Global analysis
GS	Ground state
GSB	Ground state bleach
HER	Hydrogen evolution reaction
HOMO	Highest occupied molecular orbital
IC	Internal Conversion
IPCC	Intergovernmental panel on climate change
IRF	Instrument response function
ISC	Intersystem crossing
LMCT	Ligand-to-metal charge transfer
LUMO	Lowest occupied molecular orbital
LS	Low-spin
MeCN	Acetonitrile
MC	Metal-centered
MIC	Mesoionic carbenes
MLCT	Metal-to-ligand charge transfer
MMCT	Metal-to-Metal charge transfer
MO	Molecular orbital
NHC	N-Heterocyclic carbene
NMR	Nuclear magnetic resonance
OER	Oxygen evolution reaction
PEM	Proton exchange membrane

abbreviation	explanation
ppm	Parts per million
PS	Photosensitizer
ROI	Regions of interest
SOEC	Solid oxide electrolysis cells
SP	1,1'-(pyridine-2,6-diyl)bis(3-(2,6-diisopropylphenyl)-1H-imidazol-3-ium) bromide
SR	Sacrificial reductant
STH	Solar-to-hydrogen
SVD	single value decomposition
TD-DFT	Time dependent density functional theory
THF	Tetrahydrofurane
TEA	Triethylamine
TEOA	Triethanolamine
TON	Turn over number
XES	X-ray emission spectroscopy
2C-XES	Two-colour X-ray emission spectroscopy

Investigated Ligands

L1

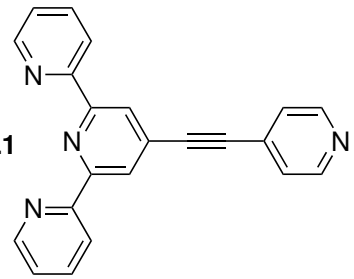

L2

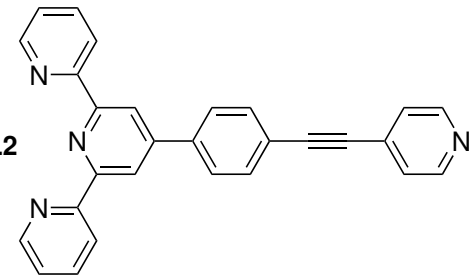

L3

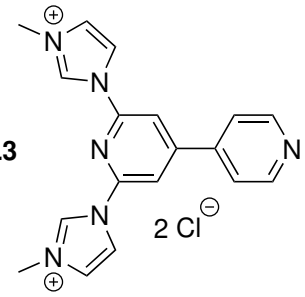

L4

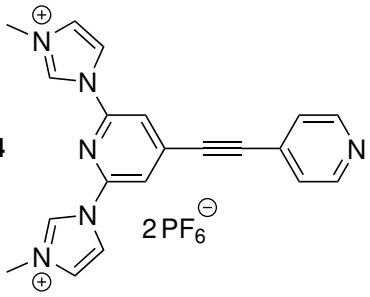

L5

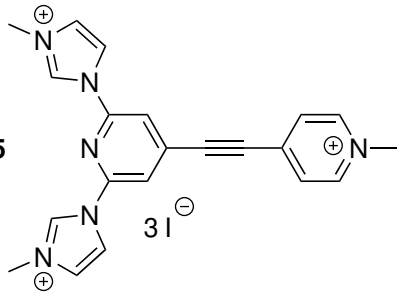

L6

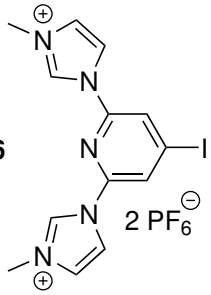

Fe1$_{homo}$

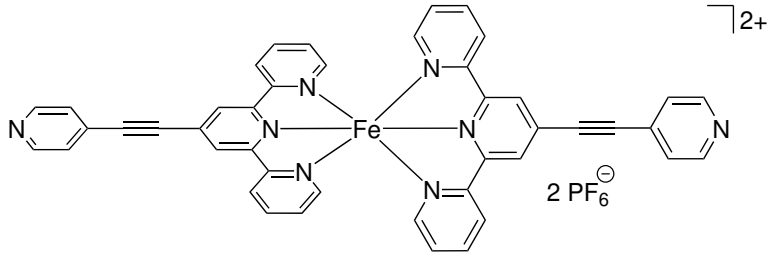

Fe1

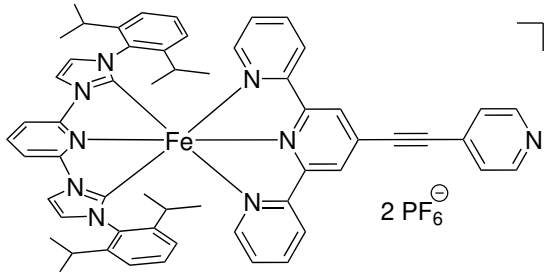

Dy1

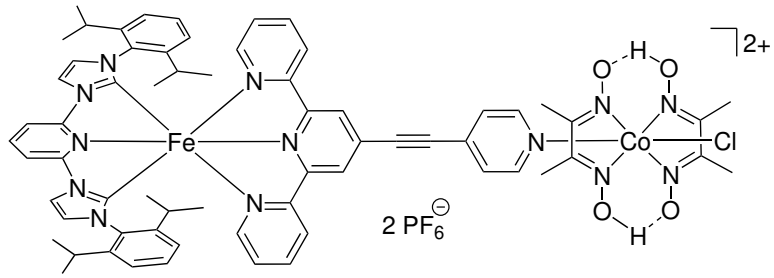

Fe2$_{homo}$

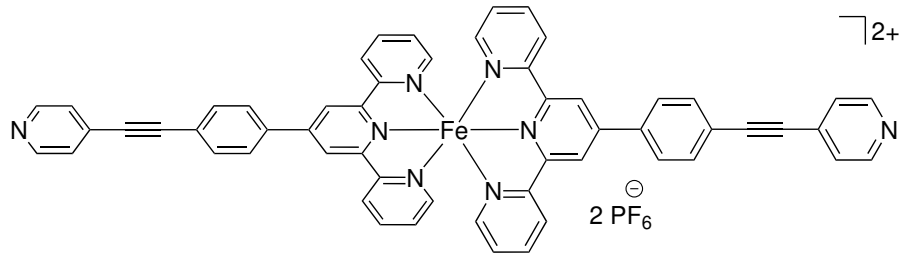

Fe2

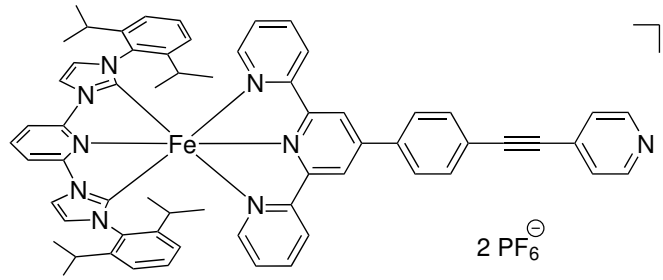

Dy2

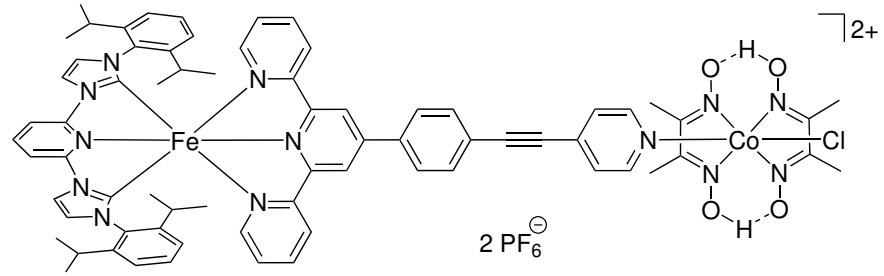

Fe3$_{homo}$

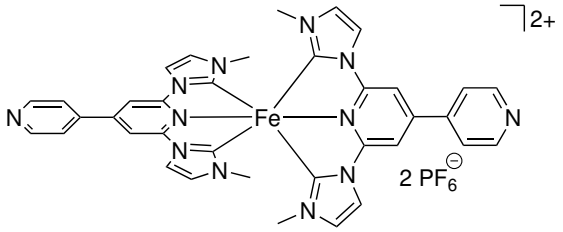

Tri3

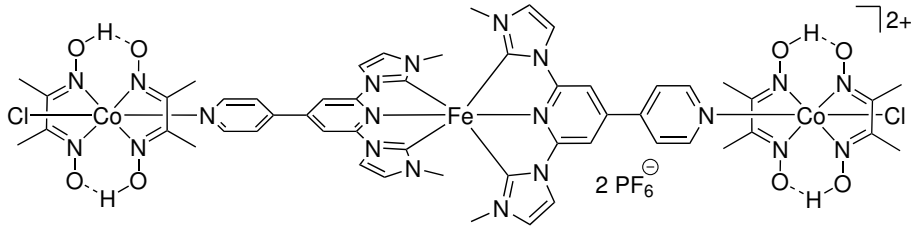

Fe3

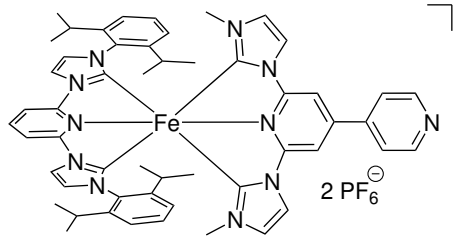

Dy3

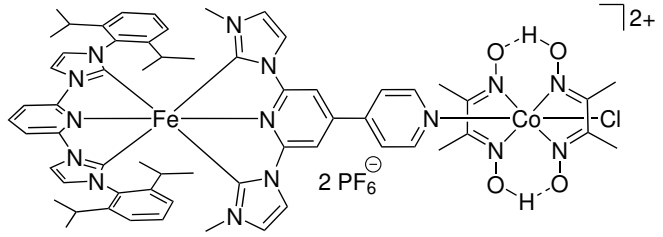

Fe6$_{homo}$

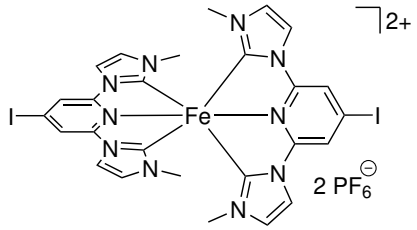

1.1 Motivation

The global energy demand is rising. In parallel, we must reduce carbon dioxide emissions in order to prevent global warming above 1.5 degrees. Otherwise, the risk to human societies, animals, and ecosystems of being threatened by weather extremes and their associated consequences increases dramatically. How can we meet the challenges of climate change?

Using carbon emission-free energy sources can reduce carbon dioxide emissions and thus global warming. One promising energy carrier is hydrogen. Its combustion is carbon-free since its use as fuel does only produce water. However, today the largest amount of hydrogen is produced by steam reforming, which is based on fossil fuels. Within this process carbon dioxide is released. It is therefore necessary to develop technologies, which generate renewable fuels. Processing of biomass or water splitting are green technologies for hydrogen production. Water splitting by electrolysis of water is a well-known technology. However, it is mandatory that the electricity in the water splitting comes from renewable enery sources such as wind or solar. Only then the water electrolysis is carbon-free. But why is the detour taken via electricity generation?

Instead, it is possible to use solar energy directly by splitting water photocatalytically. Here, a homogenous system is irradiated by solar light and the photoactive compounds in the reaction medium produce oxygen and hydrogen. Due to the complexity of both side reactions water oxidation and water reduction are often investigated separetely. In this thesis photoactive compounds are synthesized for the water reduction reaction. Usually, noble metals are applied. However, due to their low availability and high costs, base metals are great alternatives. They can be used as photosensitizer or catalyst. This work is motivated by improving the photophysical properties of iron complexes applied as photosensitizers in photocatalytic applications. It is realized by ligand modification and heterometallic coordination.

1.2 Thesis Structure

The climate change and the need for sustainable production of the carbon-free energy carrier hydrogen are the topics of chapter 1 and 2.1. Several technologies for hydrogen production are presented with a focus on photocatalytic hydrogen production. The properties of the photocatalytic system and recent advances are discussed. Chapter 2 is finished by disclosing this thesis' objectives. The ligand design is the topic of chapter 3. The synthesis and the characterization of iron complexes is described in chapter 4. Chapter 5 deals with the synthesis and the characterization of mutimetal complexes, namely dyads and one triad. The photocatalytic hydrogen production by a multi-component system and a prototype dyad is presented in chapter 6. The catalytic activity is explained by time-resolved spectroscopy and quantum mechanical calculations. The thesis results are summarized in chapter 7 along with an outlook for future work. A detailed description of the experimental work, spectroscopic and computational methods are found in chapter 8 and the appendix.

2.1 Climate Change and Global Warming

Five years ago the global warming induced by humans has reached about 1°C. This warming is compared to the pre-industrial levels between 1850-1900. Although many countries have agreed under the 2015 Paris Agreement to reduce greenhouse gas emssions to limit the global warming to 1.5°C the current warming rate predicts that by 2040 the human-induced global warming will reach 1.5°C.[1] In Figure 2.1 the global temperature change relative to the pre-industrial levels are presented from 1950 till 2017. Additionally, the predicted development of the global temperature for the 1.5°C pathway is shown for 2018 till 2100. The figure clearly highlights the human-induced warming since 1970. Moreover, the current warming rate indicates that the 1.5°C global warming will be exceeded and there will be an overshoot before the global temperature change can be again reduced to 1.5°C. It is obvious that a drastic reduction of greenhouse gas emission and the removal of carbon dioxide are necessary. The sixth assessment report from 2022 by

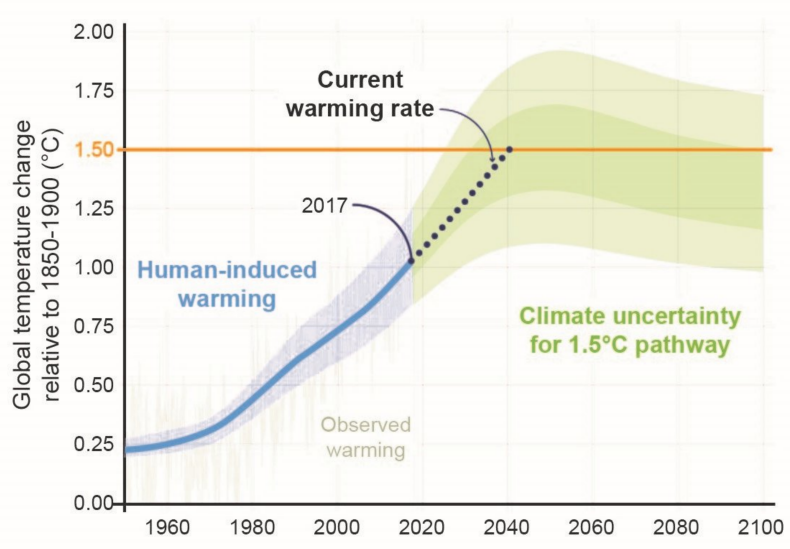

Figure 2.1: Global temperature change relative to pre-industrial levels from 1850-1900. The 1.5°C global warming prediction is indicated till 2100. Adapted from[1].

the intergovernmental panel on climate change (IPCC) highlights the impacts, which human-induced climate change has and will have on ecosystems and human systems, and discusses the vulnerability of these systems and their ability to adapt.[2] One example is the ocean warming and the ocean acidification, which endanger not only the marine biodiversity in the sea but also adversely impact the food production from aquaculture and fisheries leading to food insecurity for many parts of Africa, Asia, Central and South America. An increase of floods and droughts depending

on the regions will impact the water security and the health of many people. These risks are projected to be even greater for a global warming above 1.5°C. The report also states that reaching 1.5°C soon would lead to an increase in climate hazards and will endanger the ecosystems and humans unavoidably. It also clarifies that a limitation close to 1.5°C could reduce the predicted damages to the nature and the people depending on their vulnerability and adaption to the climate change. However, the predicted trends are highly impacted by the past development and the emission of greenhouse gases. Therefore, technical and financial efforts are needed to limit the global warming to 1.5°C.
One possibility is using renewable energies such as solar or wind energy, which produce no carbon dioxide emission. In this regard, solar energy can be utilized not only in solar plants to produce electricity but it can be used to directly produce molecular hydrogen in photocatalytic water splitting. Hydrogen can be further used as educt in the chemical industry or as mobile energy carrier in the transportation sector. Different ways to produce hydrogen will be presented in the following.

2.2 Hydrogen Production

The advantage of hydrogen is that its usage in a fuel cell leads to water as only byproduct. This means using hydrogen as energy carrier for industrial applications or to fuel vehicles can be a carbon-free and renewable option depending on the way it is produced. Depending on the raw material which are converted to hydrogen the processes can be divided into conventional and renewable technologies (Figure 2.2).[3]

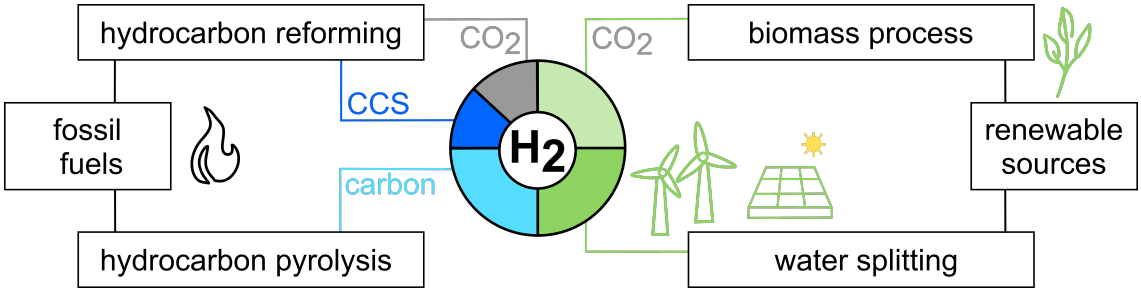

Figure 2.2: Conventional and renewable processes for hydrogen production.[3] Depending on the used technology the produced hydrogen is labelled as blue, turquoise, grey or green.

On the one hand, fossil fuels are converted into carbon dioxide or carbon in hydrocarbon reforming and hydrocarbon pyrolysis, respectively. The produced hydrogen is termed grey when CO_2 is released without further action. When CO_2 emissions are captured and stored by carbon capture and storage technology (CCS) the hydrogen is labelled as blue. Carbon is the byproduct in the hydrocarbon pyrolysis and so the

hydrogen is called turquoise H_2.
On the other hand, renewable sources allow carbon-free production of green hydrogen by water splitting which can be further divided into electrolysis, thermolysis and photolysis. In case of electrolysis, it is important that the electricity comes from wind or solar energy to stay carbon-free.
Another technology with a variety of methods covers the utilization of biomass. One has to emphasize that these processes are not completely carbon-free since CO_2 is released during the biological or thermochemical reaction of the carbon-rich plant or animal materials for some methods. However, the emission is equal to the amount which was absorbed by the organisms during their lives. In a wider sense, hydrogen produced by this technology can be called green.

One conventional methods is hydrocarbon pyrolysis. In this process a hydrocarbon is thermally decomposed. The following reaction describes the general process:

$$C_{\mathrm{n}}H_{\mathrm{m}} \rightarrow nC + \frac{1}{2}mH_2. \tag{2.1}$$

Typically, methane is pyrolyzed under water-free and oxygen-free conditions at 980°C. It is also known as cracking of methane and leads to the following equation

$$CH_4 \rightarrow C + 2H_2. \tag{2.2}$$

To produce one mole of hydrogen 37.6 kJ are required.
In the steam reforming method methane, natural gas, naphtha or light hydrocarbons up to pentane are converted by steam and a nickel-based reforming catalyst to hydrogen and carbon dioxide. The reforming process is performed at high temperatures and high pressure (3.5 MPa). It involves three steps which are described by the reforming process

$$C_{\mathrm{n}}H_{\mathrm{m}} + nH_2O \rightarrow nCO + (n + \frac{1}{2}m)H_2 \tag{2.3}$$

followed by the water-gas shift, which produces more hydrogen

$$CO + H_2O \rightarrow CO_2 + H_2 \tag{2.4}$$

and ended by the methanation reaction

$$CO + 3H_2 \rightarrow CH_4 + H_2O. \tag{2.5}$$

Large-scale hydrogen production by steam reforming uses methane as hydrocarbon source and has an efficency of 74-85 %.[3] The steam methane reforming requires

63.3kJ/mol per H_2, which is more energy-demanding compare to the methane pyrolysis. The disdavantage is also the emission of carbon dioxide. Although, efforts are made to remove the CO_2 by CCS e.g. injection in geological reservoirs or the ocean, fixation in the form of minerals or utilization carbon dioxide for industrial application, still fossil fuels are utilized as raw materials.[4]
With only 20 years left according to the global warming scenario shown in Figure 2.1, carbon-free technologies are necessary. Therefore, technologies utilizing only renewable sources should be the focus of research interest.
Biomass offers the opportunity to recycle organic waste materials. Thermochemical processes such as pyrolysis and gasification lead finally to steam reforming and water-gas shift reaction. The difference is the source of the raw material. While in the conventional steam reforming technology methane comes from fossil fuels, here gaseous products, CH_4 and CO, are produced during the biomass conversion. For this the organic materials are heated to 380-530°C at 0.1-0.5 MPa under oxygen-free conditions. The effectiveness of this method highly depends on the used catalyst, the type of feedstock, the temperature and the duration. The biomass gasification produces syngas which can be further converted according to Equation 2.4 and 2.5. High temperatures (500-1400°C) and pressure up to 33 bar are necessary. Compared to biomass pyrolysis, gasification performs better and reaches a thermal-to-hydrogen efficiency up to 52%. Nevertheless, there is not enough organic waste material to meet the needs of large hydrogen-consuming sectors such as transportation or chemical industry.
Overall, thermochemical processes yield more hydrogen and are much faster compared to the biological prcoesses. Yet, biological methods can be operated at ambient pressure and temperature using water to feed bacteria or algae. Their hydrogenase or nitrogenase enzyme systems directly produce hydrogen. Fermentation of organic waste material preferable rich in glucose transforms the carbohydrates into organic acids and further to hydrogen after bio-processing step. As stated above, the drawback of utilizing biomass is the emission of carbon dioxide except in bio-photolysis which consumes CO_2 during the photosynthesis. Hence, it is advisible to produce hydrogen by water splitting, focusing on renewable and carbon-free technologies.
Splitting water by thermolysis requires high temperatures to decompose H_2O into hydrogen and oxygen according to

$$2H_2O \rightarrow O_2 + 2H_2. \qquad 2.6$$

Temperatures about to 2500°C are necessary. The application of copper and magnesia chlorides in a thermochemical cycle process can reduce the temperature to 400-550°C. The remaining heat is provided by solar collectors to operate under carbon-free conditions.[5] Regarding the infrastructure, the availability and the cost of chemicals

as well as the material separation the H_2 production costs are about 8$/kg which is four times higher compared to the steam methane reforming ($\sim$ 2$/kg).[3]

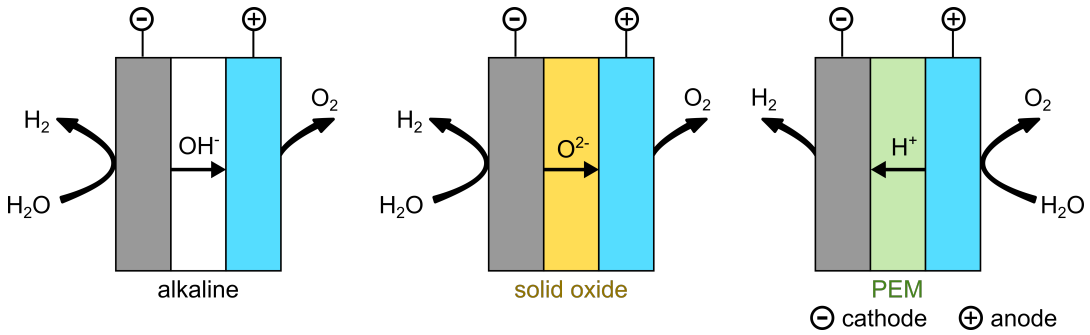

Figure 2.3: Comparison of AW electrolysis, SOEC and PEM electrolysis. Used membranes transmit hydroxide ions OH^-, oxygen ions O^{2-} or protons H^+.

Electrolysis of water is a well-known method with effiencies from 40-60 % today and was first observed by Troostwijk and Diemann in 1789.[3,6] The main technologies are the alkaline water electrolysis (AWE), the proton exchange membrane (PEM) water electrolysis and solid oxide electrolysis cells (SOEC).[7,8] Splitting water into its elements is an endothermic reaction and needs a lot of energy such as high temperatures in thermolysis or electric energy for electrolysis. To gain green hydrogen, electricity produced by renewable energies is the only option.
For AWE an alkaline solution of KOH (20-30%) is used. The cathodic and anodic electrolyte chambers are separated by a porous membrane, hindering the mixing of evolving hydrogen and oxygen. The operating temperature is 30-80°C. On the cathodic side water reacts to hydroxide ions and molecular hydrogen described by

$$2H_2O + 2e^- \rightarrow 2OH^- + H_2. \tag{2.7}$$

The hydroxide ions diffuse through the membrane and are oxidized at the anode, forming oxygen according to this equation

$$4OH^- \rightarrow O_2 + 2H_2O + 4e^-. \tag{2.8}$$

Nickel materials are used for the electrodes.[8]
With SOEC, hydrogen is produced at high pressure and elevated temperatures (500-850°C). However, it is termed to be more efficient in converting electricity into chemical energy, which is stored in hydrogen.[9] In contrast to AWE, steam is used as water source. At the cathode, oxygen ions O^{2-} and hydrogen are formed[10]:

$$H_2O + 2e^- \rightarrow H_2 + O^{2-}. \tag{2.9}$$

As shown in Figure 2.3 (middle), the oxygen ions diffuse through the dense electrolyte to the anode forming oxygen. The following equation describes the reaction.

$$O^{2-} \rightarrow O_2 + 4e^- . \qquad 2.10$$

PEM water electrolysis operates at low temperatures (20-80°C). The characteristic feature of this technology is the proton exchange membrane consisting of a polymer electrolyte e.g. sulfonated polystyrene. The half reactions differ from the AWE process. According to Figure 2.3 (right) water is introduced to the anodic chamber where it reacts to protons and oxygen described by

$$2H_2O \rightarrow O_2 + 4H^+ + 4e^- . \qquad 2.11$$

Then protons are transferred through the membrane and are reduced to H_2 at the cathode according to

$$4H^+ + 4e^- \rightarrow 2H_2 . \qquad 2.12$$

Pt and IrO_2 materials are used for the electrodes. With the help of solar cells photovoltaic-driven water splitting offers the oppurtunity to become independent from an external power supply. Here, a Si, $CuIn_xGa_{1-x}Se_2$ (CIGS) or perovskite solar cell is combined with a water splitting system. Often several cells are connected in series to achieve adequate efficiency.[7]

Solar energy is also necessary for photo-electrolysis. This method utilizes photocatalysts capable of absorbing visible light and subsequently splitting water. In the heterogenous approach the photocatalyst is immobilized on the electrode while in the homogenous approach the photocatalyst is dissolved in the water splitting system. In section 2.3 the latter is presented in detail. Now, the heterogenous set-up is described. Similarly to the reactions which take place in the PEM electrolysis the first reaction step is the oxidation of water into oxygen and protons according to Eq.2.11. The only difference is that in the light-absorbing semiconducting electrode an electron-hole pair is generated upon irradiation.[3,11] While the hole interacts with water the electron flows through an external circuit to the cathode. There, the protons are reduced to hydrogen. The cathode material is usually platinium-based while the set-up of the anode can vary a lot.[7] Tandem systems combing sensitizing materials with photoanodes are of great interest. For example, a Fe_2O_2 photoanode combined with an organic-inorganic $CH_3NH_3PbI_3$ perovskite solar cell exhibits a solar-to-hydrogen (STH) efficiency of 2.4% in light-induced water splitting as shown by Mathews *et al.*.[12] STH efficiency can be even increased up to 3.1% when a WO_3 photoanode is connected with a dye-sensitized solar cell (DSSC).[13]

To conclude, water splitting can be either performed via electrolysis, thermolysis or photolysis using only renewable energy sources. The photolysis is often studied in an

heterogenous approach using photoanodes for the oxygen evolution reaction (OER) and platinium electrodes for hydrogen evolution reaction (HER). In the following section the light-induced homogenous catalysis of water into its elements is presented.

2.3 Homogenous Photocatalytic Water Splitting

Homogenous catalysis means that the catalyst is in the same physical state as the reaction medium. In case of photocatalytic water splitting performed in solution, this means that all applied substances are soluble in the solvent mixture. Overall water splitting requires both OER and HER. However, this works focuses only on the water reduction to produce hydrogen. Contrary to the electrochemical approach by using a Pt wire, more sophisticated research is needed to find an efficient system for HER.

The photocatalytic water or proton reduction requires several compounds with distinct functions.[14,15] 1) The photosensitizer (PS), an organic or organometallic chromophore, absorbs the light in the visible region of the sunlight and electrons are excited within the molecule. 2) The catalyst (CAT) receives these excited electrons and reduces water or protons to hydrogen. 3) A transfer agent e.g. Eu^{3+}, V^{3+}, $Rh(bpy)_3{}^{3+}$ (bpy = 2,2'-bipyridine) or methylviologen MV^{2+} can be applied to mediate between the photosensitizer and the catalyst.[16,17] It works as an electron relay (R). In the overall water splitting electrons come from the water oxidation. Since only the half reaction of HER is studied, an electron donor or sacrificial reductant (SR), respectively, is needed. Typically, amines e.g. triethylamine (TEA) or triethanolamine (TEOA) are used. One of the first model systems published in 1979 by Lehn *et al.* is based on $Ru(bpy)_3{}^{3+}$, $Rh(bpy)_3{}^{3+}$, TEOA, K_2PtCl_4.[18] While TEOA is consumed, the photosensitizer, the electron relay and the catalyst catalytically produce hydrogen.

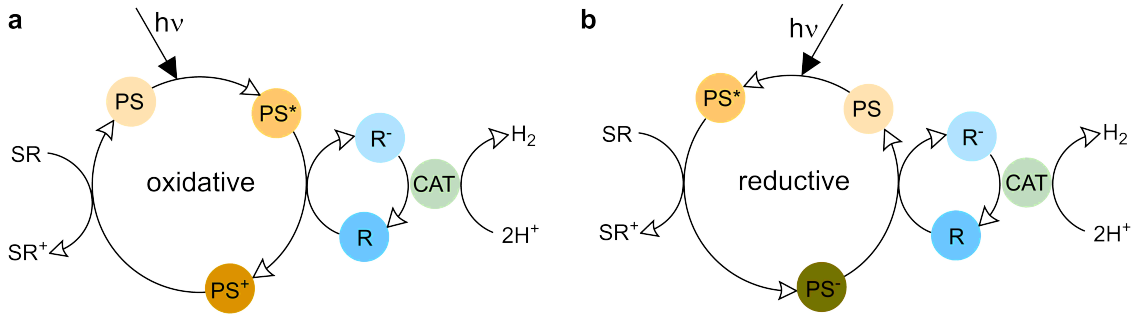

Figure 2.4: Redox catalytic cycle a) oxidative quenching mechanism, b) reductive quenching mechanism.

The reaction meachnism can be either reductive or oxidative. In Figure 2.4 both mechanisms are presented. In the oxidative mechanism **a** the photosensitzer PS is first excited to PS^*. Through interaction with the relay R, it is oxidized to PS^+. Reduced R^- transfers the electron to the catalyst so that hydrogen is generated by proton reduction reaction. PS^+ is reduced by SR. In the reductive mechanism **b**

after excitation PS^* is reduced by SR to PS^-. In the following PS^- transfers the electron to R and is oxidized to PS. The right part of the mechanism is equal to the oxidative mechanism.
The photocatalytic water reduction system can be further characterized by a multi- or one-component set-up. In the first case, PS and CAT are separate molecules and they have to meet in solution via diffusion. By connecting PS and CAT via a bridging ligand (BL) a one-component system is obtained. This generated bimetallic assembly is also called dyad. Schematic representations of both systems are shown in Figure 2.5. In the multi-component system the excited PS^* has to be long-lived

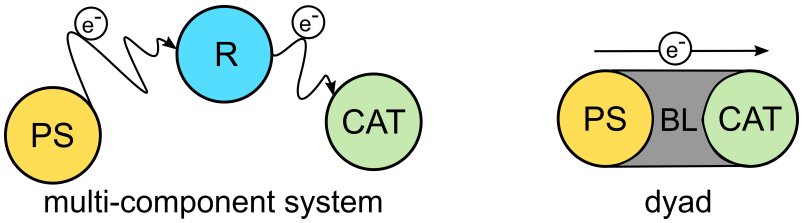

Figure 2.5: Diffusive electron transfer in multi-component system and directional transfer in a dyad.

to meet R or directly CAT within the diffusion process. The advantage of the dyad is the directional transfer between PS and CAT, making shorter lifetimes viable. However, at the same time this can also be a weakness because fast back electron transfer can be facilitated in such systems. By tuning the properties of the bridging ligand, dyads are expected to yield superior activity in photocatalysis compared to multi-component systems.[19] In this regard, several requirements can be imposed on BL. 1) Electron transfer (ET) between PS and CAT should be possible without reduction of the bridging ligand. Otherwise, it would be an electron sink.
2) Depending on the oxidative or reductive quenching mechanism BL has to stabilize several oxidation state changes at PS and CAT. 3) The bridge should be photostable under irradiation.
Numerous noble metals have been applied as photosensitizers and catalysts. Their properties for photocatalytic proton reduction will be discussed in the following sections 2.4 and 2.5. The focus will be on iron photosensitizers and cobalt catalysts as abundant and sustainable alternatives for ruthenium[16,20–22] and iridium[23–27] photosensitizers and platinum[28–30] catalysts.

2.4 Photosensitizer

In photocatalytic applications the photosensitizer plays a key role. For that, it has to provide certain properties which are necessary to drive the proton reduction process by solar irradiation. First, PS needs reversible redox properties to undergo several catalytic cycles. In this context, it has to perform several oxididation state changes without decomposition. Second, future large-scale applications need to be active within the visible light regime. In contrast, many photoelectrolysis technologies are UV-driven.[31,32] Improvements were achieved by coupling chromophores and photoelectrodes in tandem system as discussed above. However, taking advantage of the whole solar spectrum would be desirable since about 50% of the solar spectrum is infrared light. Succesful photosensitizer design does not only take into account the absorption of visible light, but extends it into the infrared region. Additionally, a high absorption coefficient is advantageous. Third, upon irradiation of PS an electron is excited from the ground state to a metal-to-ligand charge-transfer (MLCT) state. Formally, the metal is oxidized while the ligand framework is reduced. This excited MLCT state is crucial for the catalytical activity of the system. Preferably, it is long-lived. The elongation of the MLCT state in iron PS has been the focus of research interest for several decades now. The comparison of iron and its heavier transition-metal congener ruthenium will shed light on the photophysics of both and is the starting point for a detailed discussion on strategies to improve the MLCT lifetime of iron photosensitizers as presented below.

2.4.1 Photophysics of iron and ruthenium d^6 complexes

Since Lehn and coworkers have applied the ruthenium photosensitizer tris(2,2'-bipyridine)-ruthenium(II) $Ru(bpy)_3^{2+}$ in the 70s,[18] its derivatives were applied in many DSSCs[33,34] due to its catalytically-active ^{3}MLCT states with liftimes in the nanosecond regime (850-1100 ns).[35] In contrast, the lighter homologue tris(2,2'-bipyridine)iron(II) $Fe(bpy)_3^{2+}$ exhibts only an extremely short-lived ^{3}MLCT state of $\sim$50 fs.[36] This can be explained by a potential energy diagram which indicates the key electronic states of octahedral $Ru(bpy)_3^{2+}$ and $Fe(bpy)_3^{2+}$. Energetic states as a function of the ruthenium ligand Ru-L bond length are illustrated in Figure 2.6 (left). After excitation into the ^{1}MLCT fast intersystem crossing (ISC) into the ^{3}MLCT occurs. This state is phosphorescent even at room temperature with a lifetime of 850 ns. At 77 K the lifetime of the ^{3}MLCT is 5 μs. Two additional pathways deactivate the triplet state. That are a non-radiative process equal to a direct relaxation into the ^{1}GS and an internal conversion (IC) into the MC manifold. Since the ^{3}MC lies energetically higher than the ^{3}MLCT state this relaxation has to be thermally activated to overcome the energy barrier. Simulatenously, the Ru-L

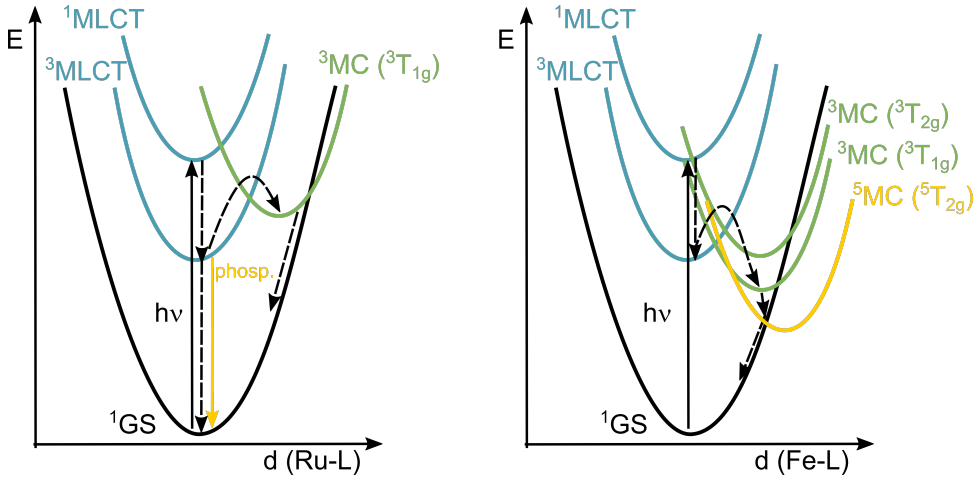

Figure 2.6: Schematic potential energy surface diagram for Ru(bpy)$_3^{2+}$ (left) and Fe(bpy)$_3^{2+}$ (right), dashed arrows indicate non-radiative decays, phosph.= phosphorescent relaxation.

bonds are elongated which can be explained by the population of σ-antibonding eg* orbitals leading to mitigation of the metal-ligand bonds. Finally, the deactivation of ^{3}MC state occurs at the intersection of the ^{3}MC and ^{1}GS potential energy surfaces back to the ground state. In case of iron, the energetic order of ^{3}MLCT/MC states is inverted causing the reduced ^{3}MLCT lifetime in d^6 iron polypyridyl complexes. This is due to the weaker ligand field splitting of iron resulting in lower-lying eg* orbitals compared to the ligand π^*-orbitals. Upon irradition and ISC into the ^{3}MLCT state almost no energy is needed to relaxe into the MC manifold due to its low energetic level. After relaxing into the lowest-energy distorted state, the ^{5}MC state, the system undergoes non-radiative decay into the ^{1}GS.[37,38]
Due to the weak ligand field splitting of iron and the resulting consequences, several research groups have be engaged in finding strategies to elongate the ^{3}MLCT for photocatalytic applications. These strategies will be discussed in the following.

2.4.2 Strategies for MLCT lifetime elongation in iron d^6 complexes

According to the potential energy surface diagram, several adjustments are possible to invert the ^{3}MLCT and $^{3/5}$MC energies similarly to the situation in ruthenium. Metal-centered states have to be destabilized and/or the MLCT state has to be stabilized. The first goal can be realized by improved octahedral geometry or introduction of stronger σ-donating ligands to increase the ligand field splitting. The second goal can be achieved by better π-acceptor ligands or an increase electron delocalization. In this regard, the improvement of iron photosensitizer lifetimes was successfully proven by different work groups and summarized by several reviews.[36,39–41] By using selected examples these strategies will be presented in the following section.

Coordination geometry

Optimized octahedral geometry can be realized by tris(bidentate) configuration. Here, the bidentate ligands are more flexible to coordinate the metal in an octahedron. Distortion from the ideal *trans* angle of 180° leads to weaker metal-ligand orbital overlap and consequently to a weaker ligand field. This fundamental principle is explained by three examples. First, with $Ru(bpy)_3^{2+}$ and $Ru(tpy)_2^{2+}$ (tpy = 2,2':6',2"-terpyridine) a comprehensive couple is presented, having a greater angular strain in $Ru(tpy)_2^{2+}$. Therefore, the latter exhibits a weaker ligand field leading to a faster deactivation of ^{3}MLCT state (τ = 0.25 ns) compared to the former (τ = 850 ns).[37,42] Excited state lifetimes for polypyridyl iron(II) complexes together with the molecular structure are shown in Figure 2.7. Excited state dynamics of $Fe(tpy)_2^{2+}$ revealed a MLCT lifetime of τ = 0.145 ps and a MC lifetime of τ = 4 ns.[43] In comparison to $Fe(tpy)_2^{2+}$'s *trans*-angle of 161.0-178.7°, **C1** exhibit a bite angle of 178.3°.[44] Surprisingly, this close to perfect octahedral geometry together with an increased ligand field splitting in **C1** does not improve the excited state properties of the iron(II) complex. Instead, the MC lifetime is reduced to 280 ps because of a reduced reorganization energy for the ^{5}MC to ^{1}GS relaxation or an enhanced electronic coupling between these states as described by the authors.[44] In complex **C2**, the terpyridine framework is extended by a phenyl unit resulting

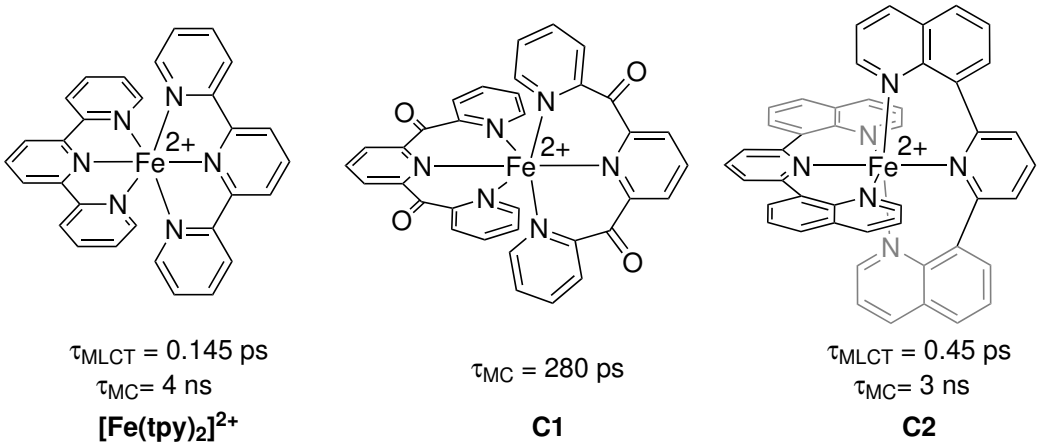

Figure 2.7: Molecular structure and excited state lifetimes of $\mathbf{Fe(tpy)_2^{2+}}$[43], **C1**[44] and **C2**[45].

in a slightly improved octahedral geometry with a *trans*-angle of 178.4° by two 2,6-diquinolylpyridine ligands. **C2** has a three times longer ^{3}MLCT lifetime than $\mathbf{Fe(tpy)_2^{2+}}$, while the MC lifetime is reduced to 3 ns. The rigidity of the ligand scaffold shows a positive impact on the excitation landscape.[45]
In the next sections the application of strong σ-donor ligands in form of carbene ligands is presented.

σ-donating N-heterocyclic carbene ligands and backbone modification

A new ligand design was introduced in the iron PS research in 2013 by Liu *et al.*[43] In Figure 2.8 selected examples are depicted. The parent compound **C3** with *N*-heterocyclic carbene (NHC) funtionalization has a triplet lifetime of 9 ps.[43] The tridenate ligand can be described regarding its binding atoms as C^N^C ligand. Although the bite angle is significantly reduced to 158.0°, the worse coordination geometry is compensated for by the introduction of strong σ-donating NHC ligands. Due to the improved ligand field splitting the MC states are destabilized according to the strong interaction of the σ-ligand orbitals with the e_g orbitals. In addition, the π-acceptability of NHCs is very low.[40] In total, an increased barrier for the relaxation from the MLCT to the MC manifold is imposed, retarding the deactivation of the ^{3}MLCT. This effect is also visible by a blue-shift of the UV-Vis absorption with a maximum at 457 nm compared to $\mathbf{Fe(tpy)_2^{2+}}$ around 550 nm.[46] The extension of

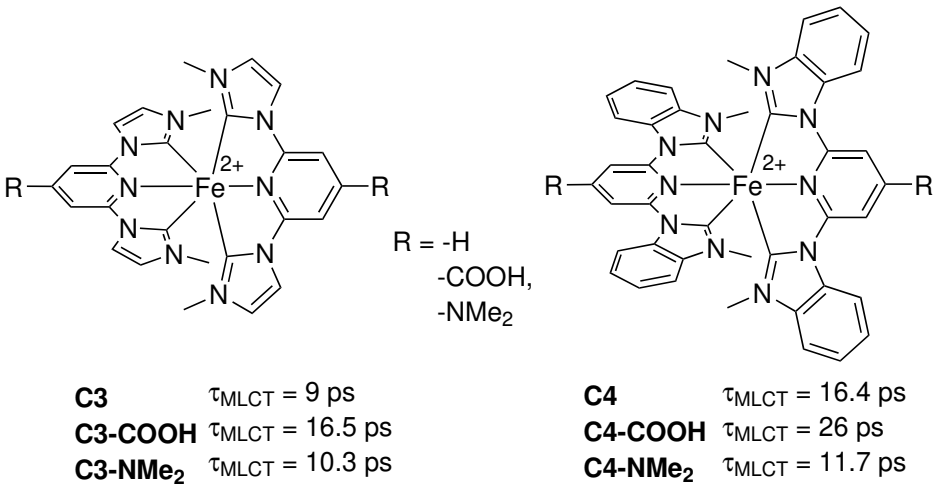

Figure 2.8: Molecular structure and excited state lifetimes of **C3**, **C3-COOH**, **C3-NMe$_2$** and **C4**, **C4-COOH**, **C4-NMe$_2$**.[40,47].

the π-system in the ligand scaffold by benzimidazolylidene instead of imidazolylidene as shown in **C4** increases the MLCT lifetime (16.4 ps) due to the stabilization of the ligand-centered LUMO levels and metal-centered HOMO levels each to different extent.[48] Simulatenously, the absorption is blue-shifted (λ_{max} (C4) = 440 nm) which is less favourable for a photocatalytic application. The hypsochromic shift is explained by the better electron-accepting property of the new ligand.
Gros *et al.* achieved further increase of ^{3}MLCT lifetime by modification of the C^N^C ligand backbone. Introduction of carboxyl groups resulted in **C3-COOH** with 16.5 ps and **C4-COOH** with record lifetime of 26 ps at the time of publication. Due to the electron-withdrawing character of the carboxyl groups the MLCT state is stabilized. Moreover, with COOH-backbone functionalization the absorption is red-shifted and sensitization of TiO_2 photoanodes is possible.[49] Another strategy

utilized amine functionalization. It was found that destabilization of the ligand-centered π levels is disadvantegeous for the ^{3}MLCT lifetime in benzimidazolylidene iron(II) complexes as shown by **C4-NMe$_2$**. Here, the lifetime is reduced to 11.7 ps. For the imidazolylidene counterpart introduction of amines has a positive impact leading to 10.3 ps for **C3-NMe$_2$** compared to the parent compound.[47]
In the multichromophoric approach the iron photosensitizer is functionalized with a chromophore in 4-position of the central pyridine ring of the C^N^C scaffold. This has two advantages. On the one hand, π-extension is achieved which is again beneficial for lowering the MLCT state. On the other hand, the interaction with the long-lived triplet state of the organic chromophore offers the opportunity to use this state as a reservoir. Ideally, the ^{3}MLCT is populated from the organic triplet state.[50]
The benefits of the multichromophoric approach was further supported by theoretical calculations by Monari *et al.*.[51] They suggested **C5** as promising candidate exhibiting dual absorption extended into the infrared region. They identified a positive effect from the acetylene bridge on the absorption properties due to better π-delocalization. The resulting low-lying π^* ligand orbitals over the chromophore are expected to enhance the lifetime of the photosensitizer or even act as reservoir. Experimentally, Dierks *et al.* have investigated the anthracenyl-functionalised **C6**. Unfortunately, a

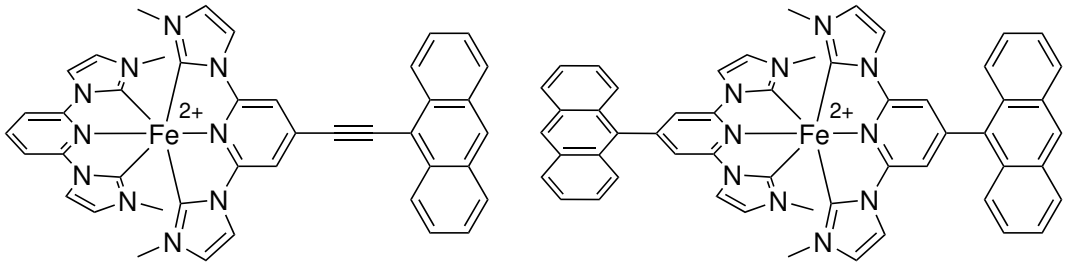

C5 **C6** τ_{MLCT} = 13.4 ps

Figure 2.9: Molecular structure of **C5**[51] and **C6**[52].Excited state lifetimes of **C6**.

reservoir effect was not present in **C6**. Instead, an antenna effect from the singlet chromophoric excited state to the ^{1}MLCT was identified. Finally, stabilization of the MLCT levels by the π-extension resulted in a lifetime of 13.4 ps. Further backbone modification has been studied by Zimmer *et al.*.[53] Here, a C^N^C ligand is combined with a N^N^N ligand. Contrary to the previous examples, the carbene count is reduced from four carbenes to two carbenes. It is expected that the lifetime of **C7** is reduced compared to the parent complex **C3** due to a weaker ligand field splitting. This was nicely shown by our working group on several iron(II) complexes with different combinations of carbene und pyridyl functionalities.[54] Indeed, **C7** exhibits a MLCT lifetime of only 1.1 ps. Yet, it is still 10 times higher than in $Fe(tpy)_2^{2+}$. Since the lifetime is very short a second metal for MLCT stabilization is attached to the iron PS leading to **C7-Co**. The photophysics of the PS are slightly improved by

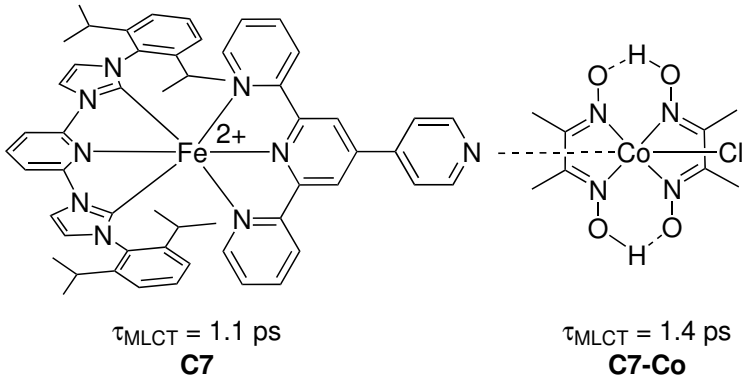

Figure 2.10: Molecular structure and excited state lifetimes of **C7** and **C7-Co**.[53]

27% yielding 1.4 ps. Moreover, this bimetallic assembly is the first Fe-Co dyad and it is the starting point for the subsequent study on Fe-Co dyads presented in this work.

Mesoionic carbenes for iron d^6 complexes

As mentioned above, the carbene count has an impressive impact on the photophysics of iron(II) complexes. In addition, mesoionic carbenes (MIC) are great alternatives for NHC as there are stronger σ-donors and better π-acceptors due to lower-lying π^* orbital levels compared to NHCs.[55] Liu *et al.* synthesized a tris(bidentate) iron(II) complex **C8** by combining two btz ligands (btz = 4,4'-bis(1,2,3-triazol- 5-ylidene) and a bpy ligand as shown in Figure 2.11 (left). Here, an improved coordination

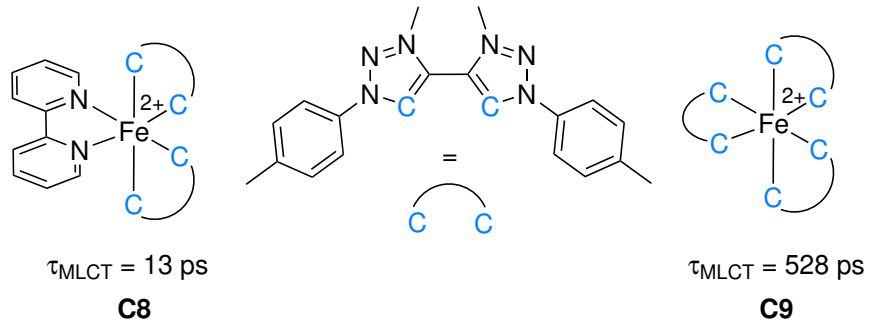

Figure 2.11: Molecular structure and excited state lifetimes of **C8** and **C9**.[55,56]

geometry results in bite angles between 172.6-178.1° and stronger σ-donating carbene ligands result in an elongated MLCT lifetime of 13 ps compared to **C3** (158°, 9 ps). Moreoever, the relaxation is retarded in **C8** due to a significant structural distortion of the ^{3}MC state. Apparently, other complex design strategies are preferable in terms of elongating the excited state lifetime as discussed above. However, the strength of MICs is surprising when three btz ligands are combined. Because of six carbene moieties the hexa-carbene complex **C9** is very electron-rich and therefore easily to oxidize. Therefore, first attempts to synthesize it resulted in the Fe^{III} d^5 analogue.

Photophysics of iron d^5 systems is out of the scope of this chapter but interesting photophysical properties e.g. photoluminescence involving ^{2}LMCT states as well as application in charge transfer processes are found in these compounds.[57–59] Focusing on the Fe^{II} complex **C9**, it has an impressive elongated ^{3}MLCT lifetime of 528 ps. Also, further distortion of the reaction coordinate along the MC manifold compared to **C8** improves the MLCT lifetime due to a stronger ligand field. Additionally, the low potential of the redox couple $Fe^{II/III}$ in **C9** offers the great opportunity to utilize it as photoreductant.

Several strategies have been presented in this section. Stabilization of MLCT states has been a key approach realized through backbone modification and π-extension. Great progress has been made in destabilization of MC states through strong σ-donating NHC and MIC ligands and optimization of coordination geometry. Often the combination of several strategies led to remarkable developments in the field of iron photosensitzers.

2.5 Catalyst

In the photocatalytic proton reduction set-up a potent photosensitizer is very important. In parallel, an active catalyst is just as important. Noble metals especially platinum have been applied in many studies as catalyst.[28–30] In contrast, iron and cobalt have received great interest in the past as more-abundant and environmental-friendly alternatives.[60–64] In the following section, the focus will be on cobalt. Selected examples will be presented and the catalytic mechanism of the HER is explained on the basis of cobaloxime.

2.5.1 Cobalt

Cobalt-based catalysts in HER can be utilized either electrochemically or photochemically.[65,66] Since the focus of this work is the photocatalytic hydrogen production, examples for cobalt electrocatalysts are excluded. Information can be found in comprehensive reviews.[65–68]

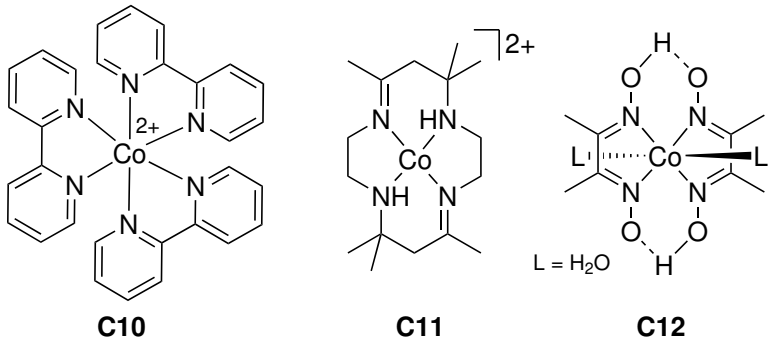

C10 **C11** **C12**

Figure 2.12: Molecular structures of cobalt catalysts.

One of the first cobalt catalysts was $Co(bpy)_3{}^{2+}$[69,70] (**C10**) which was first used as electron relay R (Figure 2.12). After reserachers realized that the photocatalytic system was still active without the applied catalyst they understood that the cobalt species worked as catalyst and not as electron relay.[18] A typical photocatalytic system produces hydrogen with a ruthenium photosensitizer, $Co(bpy)_3{}^{2+}$ as catalyst, TEOA as SR in a 1:1 mixture of acetontrile and water.[69] Macrocyclic cobalt(I) complexes such as **C11** are also attractive candidates with a high proton reduction ability.[21] Moreover, cobaloxime complexes have been succesfully applied. Herein, cobalt is coordinated by a pseudomacrocycle build by two dimethylglyoxime (dmgH) ligands. Two axial positions can be occuppied by solvent molecules e.g water as in **C12** (*cf.* Figure 2.12). The more-stable BF_2-annulated cobaloxime **C13** has shown superior activity compared to the conventional hydrogen-bridged cobaloxime using TEA, triethylammonium tetrafluoroborate as proton source and standard ruthenium

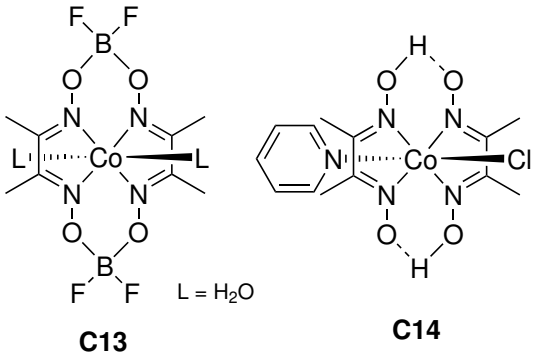

Figure 2.13: Molecular structures of cobaloxime catalysts.

photosensitizer $Ru(bpy)_3^{2+}$ in acetone.[71] This ligand motif could be applied in future research related to this work. Further studies have been focused on $Co(dmgH)_2(py)Cl$ **C14**. Eisenberg *et al.* combined **C14** succesfully with platinum chromophores. By modifying the solvent mixture or adding more SR turn-over numbers (TON) of 120 with respect to the CAT were achieved.[72,73] The versatile application of **C14** was further shown by combining it with organic chromophores.[74] This marked a major breakthrough in cobaloxime catalysis. A TON of 180 was obtained applying **C14**, the organic chromophore eosin Y and 12-fold excess of dmgH ligand in an aqueous solution of MeCN (1:1) with 5% TEOA at pH = 7. Axial ligand modification studied by Panagaiotopoulos *et al.* had a considerable impact on the catalytic activity. A zinc photosensitizer was irradiated in an aqueous solution of MeCN (1:1), 10% TEAO with different cobaloxime catalysts varied in the axial ligand (*cf.* Figure 2.14). The reference system exhibited a TON of 320 with **C14**. The TON was increased when the pyridine ligand was methylated in 4-position (TON = 443). 3-Fold increase was realized by substitution with a *N*-methylimidazole ligand (TON = 1135). A clear correlation between catalytic acitivity and basicity was found. By introducting more basic ligands the cobalt catalyst was more active.

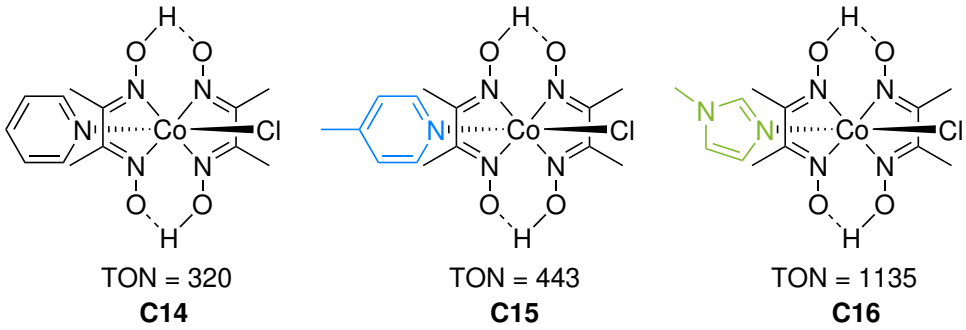

Figure 2.14: Axial modification of cobaloxime complexes.[75]

In the catalytic cycle the Co^{I} species is active. However, Co^{II} or Co^{III} complexes are often used. This means that the cobalt species has to be first reduced before it is transferred in its active state. Such induction period was suggested to be

responsible for a delayed catalytic activity.[73] After two subsequent photoinduced electron transfer steps a Co^{I} species is generated. That is the starting point for the catalytic cycle as illustrated in Figure 2.15 (top). After protonation a cobalt(III) hydride species is formed. From here on two mechanisms are possible, the homolytic or the heterolytic pathway. In the homolytic cleavage two Co^{III}-H hydride species

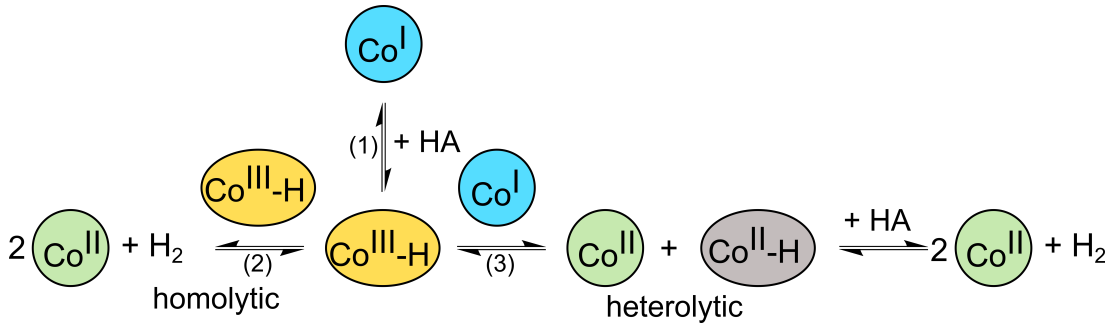

Figure 2.15: Homolytic and heterolytic mechanisms for hydrogen evolution catalyzed by cobalt catalyst.[76]

react to form molecular hydrogen and two molecules of a Co^{II} species (Figure 2.15, left). The heterolytic pathway is described by the redox reaction of Co^{III}-H hydride species with a Co^{I} species forming a Co^{II} compound and a Co^{II}-H hydride species. Subsequent protonation of the latter lead to the heterolytic production of molecular hydrogen.

Cobaloxime has proved to be a good candidate for photocatalytic application. Many research groups have applied it as catalyst in their studies. Different parameters can be adjusted to increase the catalytic activity such as the axial ligand. Inspired by noble-metal self-assemblies the idea has emerged to coordinate a photosensitizer in axial position of cobaloxime. This led to several dyads combing a noble metal PS with the cobaloxime moiety. Selected examples will be discussed in the next section.

2.6 Dyads

Heterobimetallic complexes are called dyads. There are numerous possibilities to combine two different metals in such assemblies. Dyads of noble character e.g. Ru-Pt or Ir-Pt were investigated by Sakai *et al.* and Rau *et al.*, respectively.[77–80] "Hybrid"-systems combine a noble metal PS with a base metal CAT. Examples are Ru-Co and Ir-Co. Recently, noble-metal free dyads become more attractive alternatives. Due to their abundance and their low cost, large-scale applications are possible. In the following sections selected dyads with cobaloxime scaffold are presented.

2.6.1 Hybrid dyads with Ru and Ir photosensitizers

Fihri *et al.* presented the first Ru-Co dyads in 2008.[71] The molecular structures are given in Figure 2.16. These dyads could compete with purely noble metal dyads. **C17** with 100 eq. TEA and 100 eq. Et_3NHBF_4 (proton source) in acetone gave a TON of 17 after 4h irradiation with a CdI-doped Hg light source. The BF_2-annulated analogue **C18** was even more active with a TON of 56. In **C18** the cobalt is in

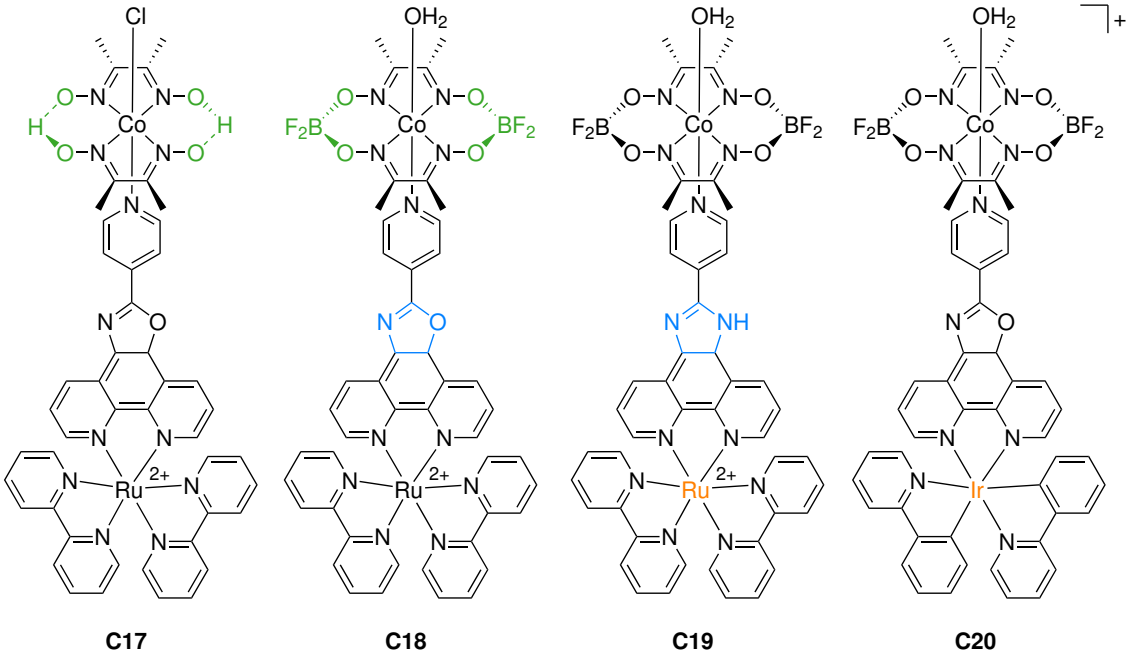

Figure 2.16: Molecular structure of Ru-Co dyads.

oxidation state +II. The Co^{II} state is more easily reducible compared to the Co(III) in **C17** resulting in a facilitated electron transfer from Ru to Co. The respective multi-component system, consisting of $[Ru(bpy)_3]Cl_2$ and $[Co(dmgH)_2(OH_2)_2]$, was less active (TON = 2). Also, an addition of free dmgH ligand was necessary to circumvent dissociation of the catalyst $[Co(dmgH)_2(OH_2)_2]$ which was not necessary

in case of the dyad. Moreover, ligand modification by using imidazole instead of oxazole in the bridging ligand improved the catalytic performance by a factor of 2 (**C19**, TON = 104). This is a great example for the high impact of rational ligand design highlighting that small changes make a huge difference. Further improvement of the dyad activity has been achieved by replacing Ru with Ir.[81] The following system afforded a TON of 140: **C20**, 300 eq. TEA/Et_3NHBF_4 in acetone during 8 h of irradiation. Comparison with the multi-component system indicated similiar activity but with lower stability over time.

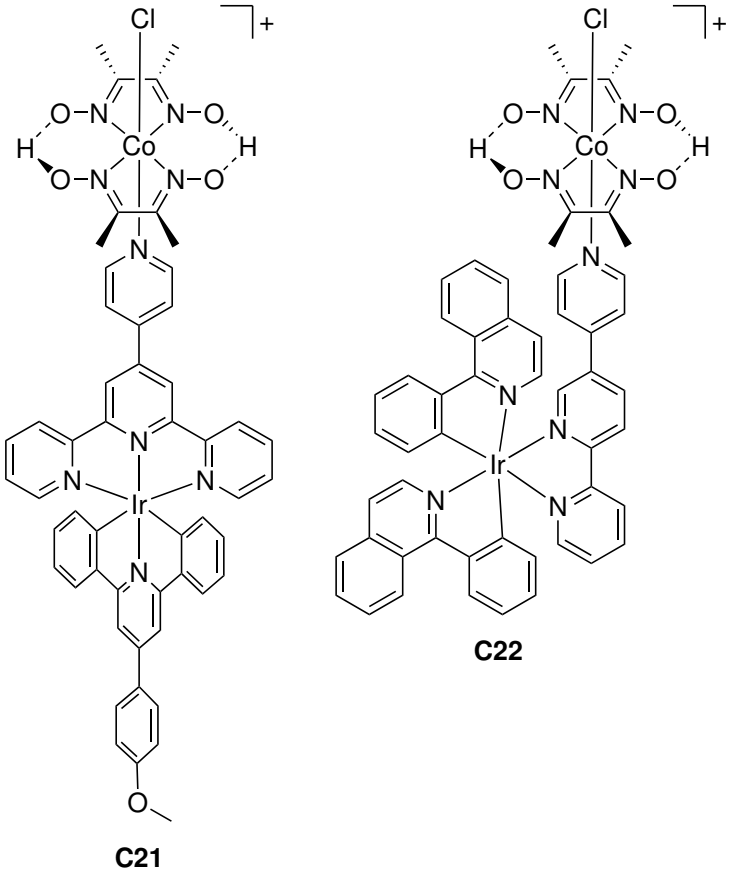

Figure 2.17: Molecular structure of Ir-Co dyads.

Elias *et al.* have designed another Ir-Co dyad with directional electron transfer upon absorption in the green or yellow.[82] **C21** shown in Figure 2.17 exhibited higher stability compared to conventional bidentate systems in photocatalytic HER with TEOA and HBF_4 in MeCN. A TON of 113 was achieved with **C21** compared to the reference system containing a tris(bidentate) Ir PS and $Co(dmgH)_2(py)Cl$ (TON = 12) under green-light irradiation (525 nm). Since the absorption was red-shifted upon cobalt coordination, hydrogen production was even detected for yellow irradiation at 595 nm while no activity was measured for the multi-component system.

A better stability and improved absorption properties compared to the multi-component system were also provided by **C22** (*cf.*Figure 2.17). In MeCN with

TEOA (0.5 M) and HBF_4 (0.05 M) the multi-component system and **C22** were studied. Under blue irradiation a TON of 180 was accomplished with the Ir-Co dyad in 2.3 h. Only a TON of 70 within 7 h was confirmed for the respective multi-component system. The hydrogen production was succesfully extendend into the red part of the solar spectrum with robust activity for 110 h in case of **C22**.

2.6.2 Noble-metal-free photosensitizers attached to cobaloxime

Further improvement of the dyad system can be realized by the substitution of the noble metal photosensitizer with a noble-metal-free PS e.g. an organic chromophore or an iron complex. In **C23** thienyl-expanded 2,6-dihalogenated boron dipyrromethene (BODIPY) with cobaloxime were combined.[83] Due to cobalt coordination the absorption spectrum was red-shifted compared to the separate PS. The dyad showed a TON of 73 in TEOA (5 Vol.-%) and $MeCN/H_2O$ (4:1) at pH = 8.5 under Xe lamp irradiation ($\lambda > 420$ nm) for 10 h. In contrast, the multi-component system exhibited only a TON of 27 after 10 h. The authors suggested that the improved performance was due to the intramolecular ET effciency causing increased reduction of the catalyst in the dyad compared to the diffusion-limited intermolecular ET. They highlighted the robustness of **C23** during the photocatalytic experiment.

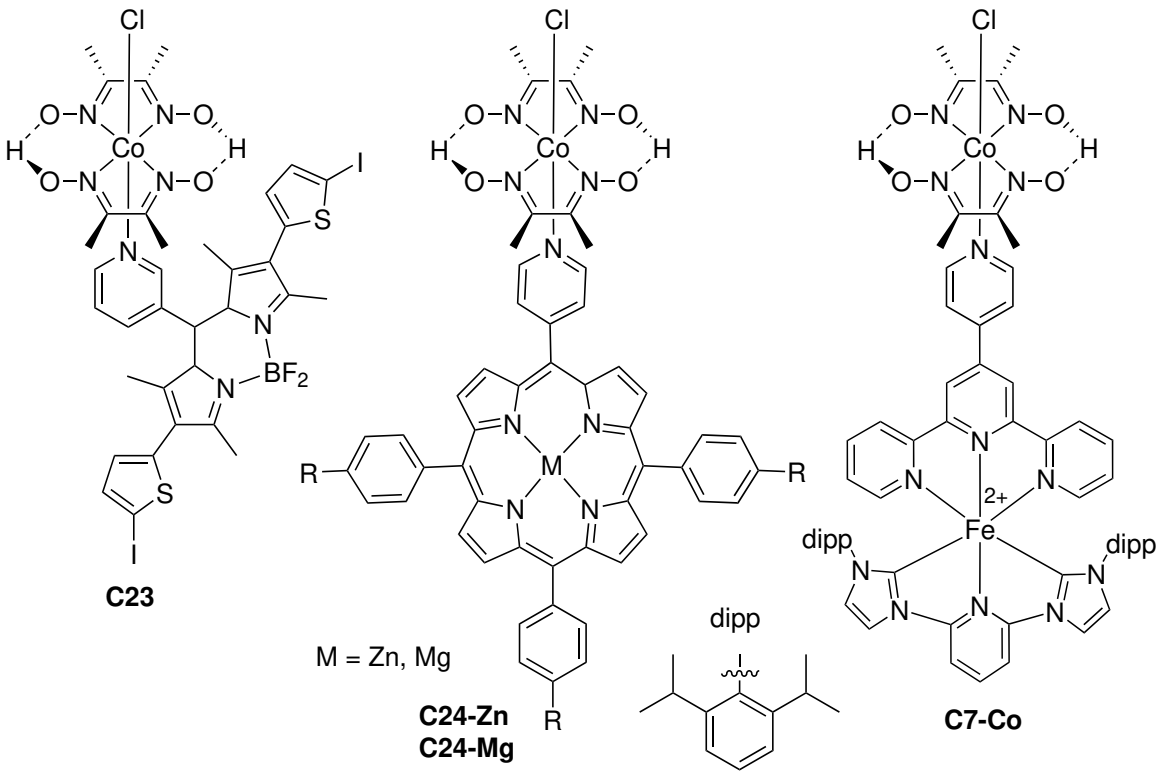

Figure 2.18: Molecular structure of noble metal-free cobaloxime dyads.[53,83,84]

The hydrogen production of **C24-Zn** and **C24-Mg** was investigated in a THF/H_2O mixture (8:2) with TEA (0.05 mol/L) as sacrifical reductant.[84] Sun *et al.* determined a TON of 22 and 3 for **C24-Zn** and **C24-Mg**, respctively. The higher hydrogen-evolving efficiency was explained by the formation of a TEA-**C24-Zn** triad which was formed due to a free axial position at Zn. An inner-sphere ET from TEA to the zinc PS was suggested, facilitated by the pre-coordination of TEA. UV-Vis titration of TEA in a solution of **C24-Mg** did not change the absorption properties hence no pre-coordination between TEA and **C24-Mg** was expected. No hydrogen production was observed for the multi-component system. Moreover, the UV-Vis spectrum of **C24-Zn** after irradiation matched the PS spectrum. This indicated dissociation of the dyad **C24-Zn** during the photocatalytic hydrogen evolution.
The Bauer group has also investigated a noble-metal-free Fe-Co dyad.[53] Although no hydrogen evolution was reported for **C7-Co**, tuning of the photophysics of the corresponding PS by cobaloxime coordination was highlighted. First, a planarization of the torsion angle between the pyridine ring of the bipyridine motif was found in the dyad compared to the PS with 37.9(2)° and 55.3(3)°, respectively. A smaller torsion angle is beneficial for a better π-orbital overlap and hence better electron conductivity. The absorption of **C7-Co** was slightly expanded to the red part of the spectrum upon cobalt coordination. A bathochromic shift of 5 nm was measured for C7-Co compared to **C7**. This was also supported by TDDFT which confirmed the stabilization of the LUMO level and therefore a smaller HOMO-LUMO gap which is manifested in a bathochromic shift of the corresponding band. The improvement of the ^{3}MLCT for this dyad was already discussed above.

2.7 Objectives

Inspired by the first Fe-Co dyad further developments in the ^{3}MLCT lifetime elongation and the study of photocatalytic activity are necessary. The improvements of iron photosensitizers and their increased ^{3}MLCT lifetime from 9 ps to 528 ps in the last decade are a great starting point for noble-metal-free dyad research. By that, the need for more sustainable technologies can be adressed. The first aim is the variation of the number of σ-donor ligands as illustrated in Figure 2.19. On the one hand, the number of NHC ligands in correlation with the destabilization of the MC states resulting into longer-lived ^{3}MLCT will be studied. On the other hand, an improvement of the directional electron transfer from the PS to the CAT due to a strong π-acceptor side via the terpyridine moiety can be tested. Also, the tuning of the absorption properties by varying the NHC and pyridine ligands is investigated. The absorption properties and the ^{3}MLCT lifetime are important for photocatalytic applications.

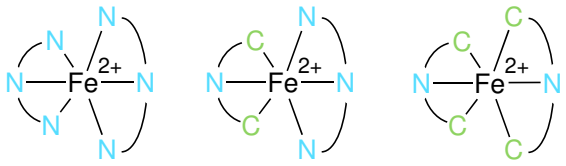

Figure 2.19: Variation of carbene count.

The second aim focuses on the bridging ligand modification. Effects of acetylene or phenyl-acetylene spacers on PS properties are studied. Here, the conductive properties of these spacers are exploited. Also, the planarization of the bridging ligand due to the introduction of the mentioned spacers is adressed. A planar ligand is desirable for good conductive properties due to better spatial π-orbital overlap.

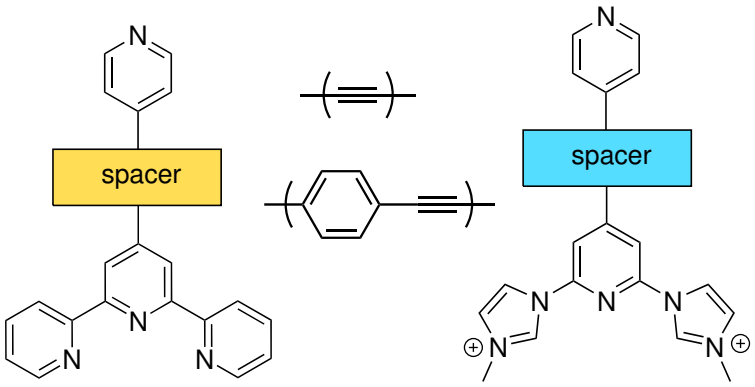

Figure 2.20: Tuning of the bridging ligands by introducing acetylene and phenyl-acetylene spacers.

The application of the proposed bridging ligands results in homoleptic and heteroleptic iron photosensitizers. In case of heteroleptic PS only one vacant coordination side remains. This can be utilized for cobaloxime coordination to synthesize iron-cobalt dyads. Homoleptic iron PS are used to synthesize iron-cobalt triads. Schematic representations of both heterobimetallic systems are shown in Figure 2.21. Both multimetal complexes are suitable to investigate the influence of the PS:CAT ratio in photocatalytic proton reduction reactions in a future work. Here, the focus is on the investigation of the catalytic activity of a dyad in comparison with the separated system. In this way, the better system can be identified.

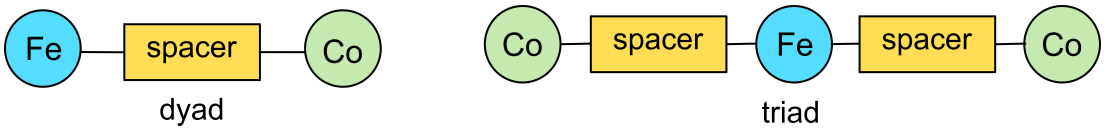

Figure 2.21: Schematic structure of multimetal complexes - dyad and triad.

In this chapter the synthesis of the bridging ligands is presented. The ligands **L1**[85] and **L2**[86] are known in literature. The synthesis routes were partially adjusted and therefore will be presented. In the case of all carbene-based ligands new synthesis routes are developed.

3.1 Terpyridine-based ligands

In this work two terpyridine-based ligands are synthesized. First, the synthesis of **L1** is described. Compound **1** is synthesized in three steps. Starting with ethyl-2-picolinate and acetone, 1,5-di(pyridin-2-yl)pentane-1,3,5-trione is formed. The twofold Claisen condensation is peformed in THF under reflux and NaH addition. The triketone reacts with ammonium acetate in ethanol to 2,6-bis(2-pyridyl)-4(1H)-pyridon in a cyclization reaction.[87] Compound **1** is obtained by adding trifluoromethanesulfonic anhydride (Tf_2O) in pyridine to the pyridon derivative. **1** and **2** reacts in a copper-catalyzed Sonogashira coupling in diisopropylamine (DIPA) at 50°C for two days (Figure 3.1).[85] $Pd(PPh_3)_4$ is used as Pd catalyst together with copper iodide as co-catalyst. PPh_3 is added as auxiliary ligand. After purification over silica with DCM and gradual increase of acetone, **L1** is obtained in 62% yield.

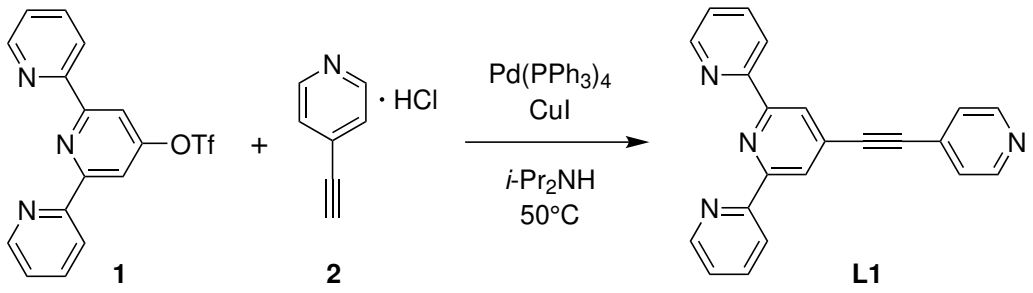

Figure 3.1: Synthesis of pyridylethinylterpyridine **L1**.

The second bridging ligand **L2** is synthesized in three steps.[88] **3** is obtained by reacting 4-bromobenzaldehyde with trimethylsilylacetylene under Sonogashira conditions and subsequent deprotection of the acetylene functionality with KOH in acetonitrile. A Kröhnke terpyridine synthesis is applied to form 4'-(4-ethinylphenyl)-2,2';6',2"-terpyridine **4**. **3**, two equivalents of 2-acetylpyridine, ammonia and NaOH react in ethanol at room temperature (Figure 3.2).[22] **4** is obtained in 36% yield after washing with ethanol and water. In the following, **4** and 4-iodopyridine are combined in a Sonogashira reaction with $Pd(PPh_3)_2Cl_2$, CuI and PPh_3. The reaction mixture is stirred in TEA at 80°C for three days.[86] After removal of solvent the crude product

is extracted with DCM. The organic phase is filtrated and washed with an aqueous KOH solution and water. Purification over silica with ethylacetate:*n*-hexane (1:1) gives **L2** in 70% yield.
The terpyridine-based ligand **L1** is synthesized according to the literature. For **L2** a modified route is chosen which increases the yield of the last reaction step from 45%[86] to 70%. It is realized by inversion of substituents of the educts. While Saha *et al.* combine 4-ethinylpyridine hydrochloride with 4'-(4-iodophenyl)-2,2';6',2"-terpyridine, in this protocol 4-iodopyrdine reacts with 4'-(4-ethinylphenyl)-2,2';6',2"-terpyridine.

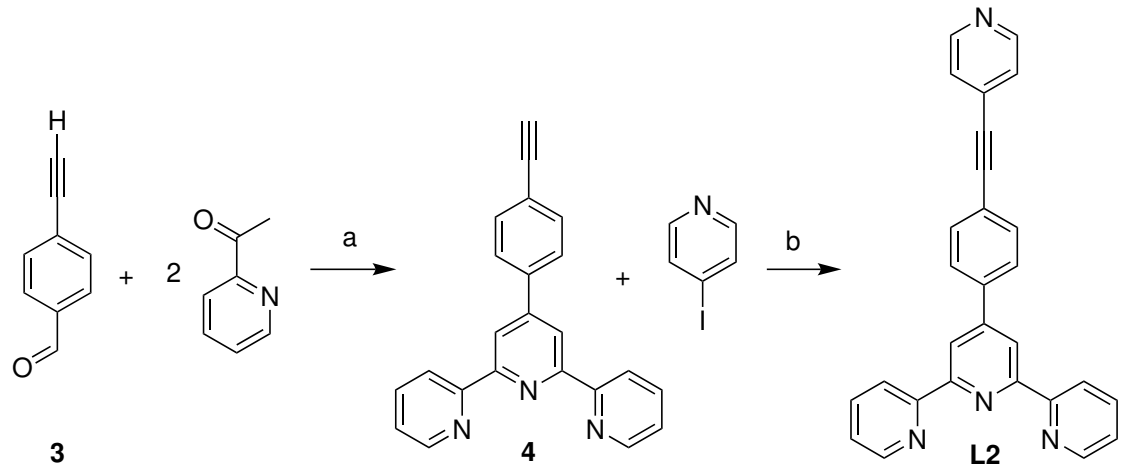

Figure 3.2: Synthesis of pyridylethinylphenylterpyridine **L2**, a) NH_3, NaOH, EtOH, RT b) $Pd(PPh_3)_2Cl_2$, CuI, PPh_3, TEA, 80°C, 3d.

3.2 Carbene-based ligands

The synthetic approach to synthesize **L3** and **L4** is inspired by literature but the ligands are synthesized for the first time. After a short presentation of the synthesis route of **L3**, different synthesis routes are discussed in detail reflecting the effort needed for the successful isolation of **L4**.

3.2.1 Synthetic Strategy

Three reaction steps are needed to obtain **L3**. **5** can be synthesized in an iridium-catalyzed C-H borylation with 2,6-dichloropyridine and bis(pinacolato)diboron.[89] In a Suzuki coupling **5** reacts with 4-bromopyridine hydrochloride (Figure 3.3). The reaction is catalyzed by $Pd(OAc)_2$ and PPh_3, which *in-situ* form the reactive species. The Suzuki reaction is performed in a 1,4-dioxane/water mixture at 110°C and he base K_2CO_3 is added. After two days water is added to the mixture and a precipitate is collected. Purification over silica with ethylacetate:cyclohexane (1:1) gives **6** in 83% yield. Five days of stirring of **6** in *N*-methylimidazole used as solvent and

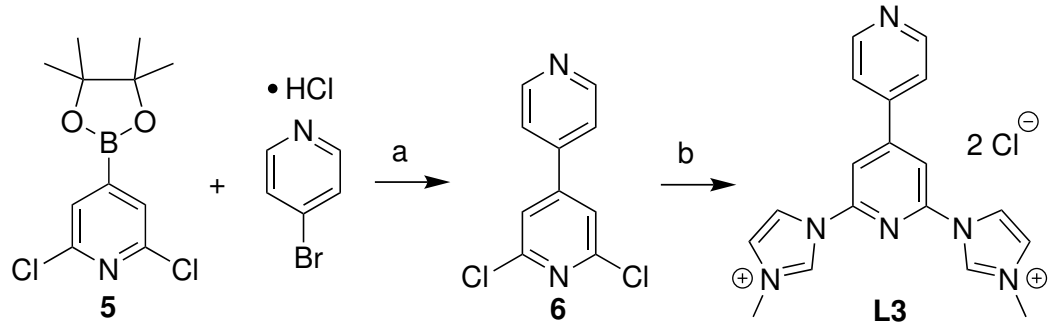

Figure 3.3: Synthesis of bipyridyl-bis-imidazolium **L3**. a) $Pd(OAc)_2$, PPh_3, K_2CO_3, 1,4-dioxane/H_2O, 110°C, 2d; b) N-methylimidazole, 150°C, 5d.

reactant at 150°C gives **L3** as raw product. It is dissolved in methanol and added dropwise into ethylacetate which causes the precipitation of the product. After purification over alumina with acetonitrile:methanol (30:1) **L3** is obtained in 38% yield.

The first attempt to synthesize **L4** starts by building the pyridine-acetylene-pyridine core of the bridging ligand (Figure 3.4). The synthesis route begins with 2,6-dichloro-4-iodopyridine which can be obtained by iodination of 2,6-dichloropyridine with *n*-BuLi and iodine.[90] **7-Cl** reacts in a Sonogashira reaction with trimethylsilyl acetylene, $Pd(PPh_3)_2Cl_2$, CuI and PPh_3. The reaction is stirred in NEt_3 for 24 hours. After removal of solvent the raw product is purified over silica with ethylacetate:*n*-hexane (1:1). TMS-protection group is removed by KOH in acetonitrile. The addition of water leads to a precipitation which is collected and dissolved in diethylether. Sublimation gives **8-Cl** in 66% yield.

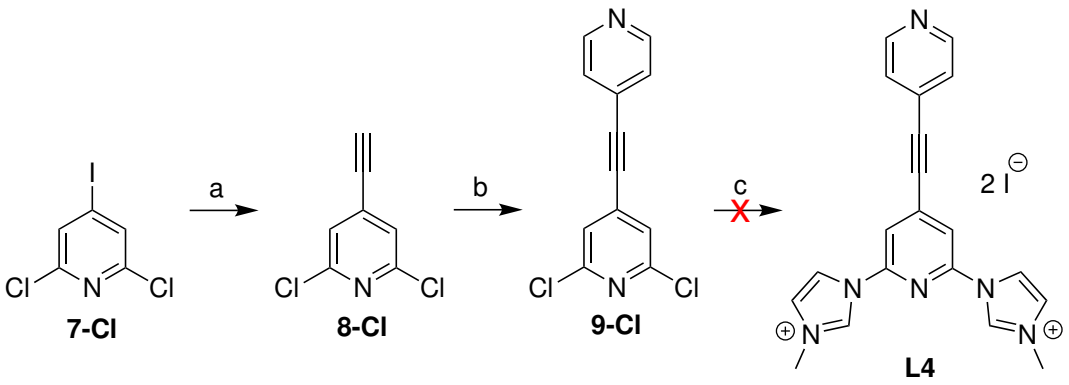

Figure 3.4: Synthesis route 1 of **L4** - part 1. a) 1) trimethylsilyl acetylene, $Pd(PPh_3)_2Cl_2$, PPh_3, CuI, NEt_3, RT, 1d, 2) KOH, MeCN; b) $Pd(PPh_3)_2Cl_2$, PPh_3, CuI, THF/NEt_3, RT, 1d; c) N-methylimidazole, 150°C or 50°C.

A second Sonogashira cross-coupling is utilized to receive **9-Cl**. The reaction conditions are identical as described in step *a* except that a solvent mixture of THF/NEt_3

(1:1) is used. Purification over silica with ethylacetate:*n*-hexane (1:1) gives the yellow product (98%). According to the synthesis parameter of **L3**, neat coupling of **9-Cl** with *N*-methylimidazole is carried out. Stirring at 150°C gives no product. Then the temperature is reduced to 50°C to avoid product decomposition. Still no product can be isolated. Therefore, an Ullman-coupling is tried (not shown) to couple two imidazole rings to the pyridine-acetylene-pyridine core. This route is not successful for **9-Cl**.

Due to lower reactivity of the chloro derivative in cross-coupling reactions the synthesis is repeated for the 2,6-dibromo analogue.[91] The preparation is shown in Figure 3.6. **7-Br** is synthesized according to Knochel *et al.* using TMPMgCl·LiCl (TMP=2,2,6,6-tetramethylpiperamide) instead of *n*-BuLi which increases the selectivity of iodination in 4-position in 2,6-dibromopyridine **10**.[92] It is dissolved in THF. TMPMgCl·LiCl and iodine are added at -40°C. After 14 h the reaction is quenched by $Na_2S_2O_3$ and the product is extracted with Et_2O and ethylacetate. Removal of solvent gives **7-Br** as white crystalline powder in 82% yield. **7-Br** reacts in a Sonogashira protocol with subsequent deprotection to **8-Br** in 64% yield. Due to bromine/iodine competition in the Sonogashira reaction two acetylene functionalities are introduced leading to 2-bromo-4,6-bis(trimethylsilyl)ethinylpyridine and 2-bromo-4,6-diethinylpyridine, respectively. This can be determine by ESI mass spectrometry (*cf.*Figure 3.5). 2-bromo-4,6-bis(trimethylsilyl)ethinylpyridine has a mol peak at 352.0378 m/z.

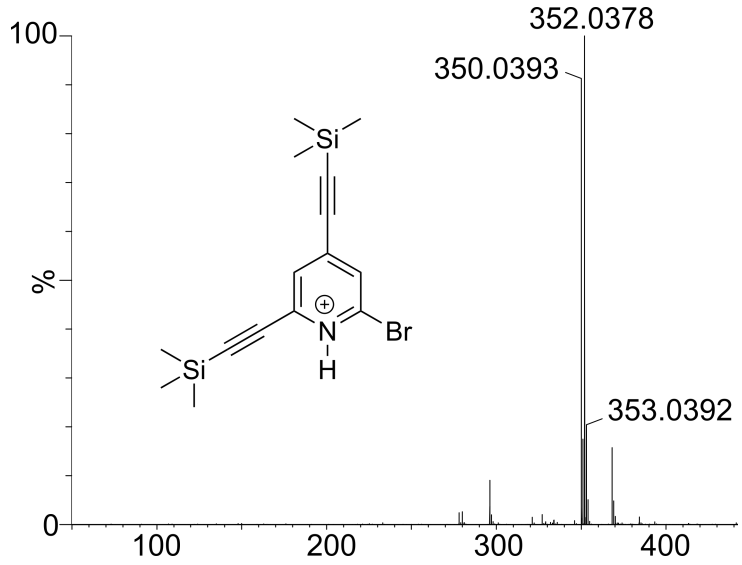

Figure 3.5: ESI mass spectrum - twofold acetylation of **7-Br**.

Twofold acetylation can be circumvented by adding **7-Br** dropwise to the solution. A second Sonogashira coupling is performed to synthesize **9-Br**. **8-Br** is added dropwise to a solution containing 4-iodopyridine, Pd-catalyst and Cu-cocatalyst at 0°C. With this method, intramolecular Sonogashira coupling of **8-Br** is again suppressed. After removal of solvent the product is purified over silica with *n*-hexane:ethylacetate

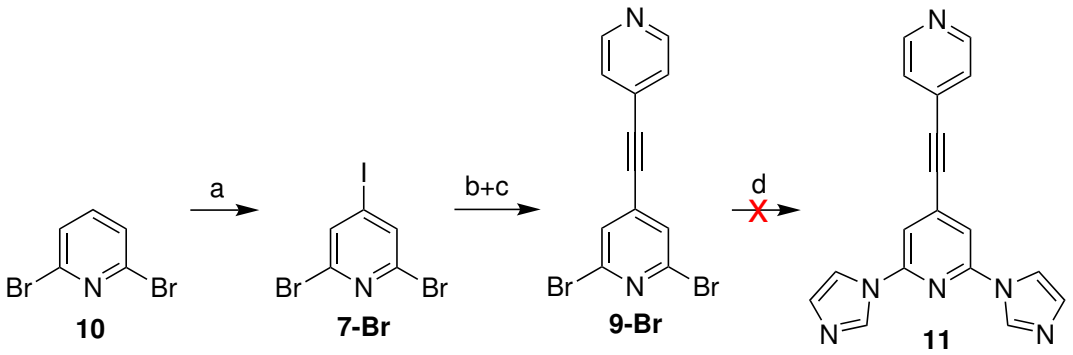

Figure 3.6: Synthesis route 1 of **L4** - part 2. a) TMPMgCl·LiCl, I_2, THF, -40°C to RT, 14h; b) 1) $Pd(PPh_3)_2Cl_2$, PPh_3, NEt_3/THF (1:1), 0°C to RT, 1d, 2) KOH, MeCN; c) 4-iodopyridine, $Pd(PPh_3)_2Cl_2$, PPh_3, DIPA/THF (4:5); d) imidazole, CuO, K_2CO_3, DMF, 100°C, 1d or imidazole, NaH, DMF, 0°C to RT, 3d.

(5:1) in 63% yield. In the following, an Ullman-type coupling is tried where imidazole is coupled to **9-Br** with CuO and K_2CO_3 in DMF. The desired product **11** can be confirmed by ESI-MS in traces. No product can be isolated after purifcation over silica with DCM:MeOH (20:1). In the following a nucleophilic aromatic substitution is carried out. NaH is added to deprotonate imidazole at 0°C in DMF. After warming to room temperature and addition of **9-Br** the reaction is stirred for three days. After work-up also here, no product could be isolated.

Since the first synthetic route is not successful the strategy is changed to first coupling the imidazole rings before the acetylene-pyridine functionality is introduced. The alternative reaction route is shown in Figure 3.7. 2,6-Dibromopyridine-4-amine **12** is the starting material. The synthesis is described elsewhere.[93] **12** reacts in a Ullman-type coupling with imidazole, K_2CO_3 and copper(II) oxide in DMF.[94] After six days at 150°C the solvent is removed and the raw product suspended in water. Filtration and washing with water gives 2,6-di(1H-imidazol-1-yl)pyridin-4-amine **13** as white powder (88%).

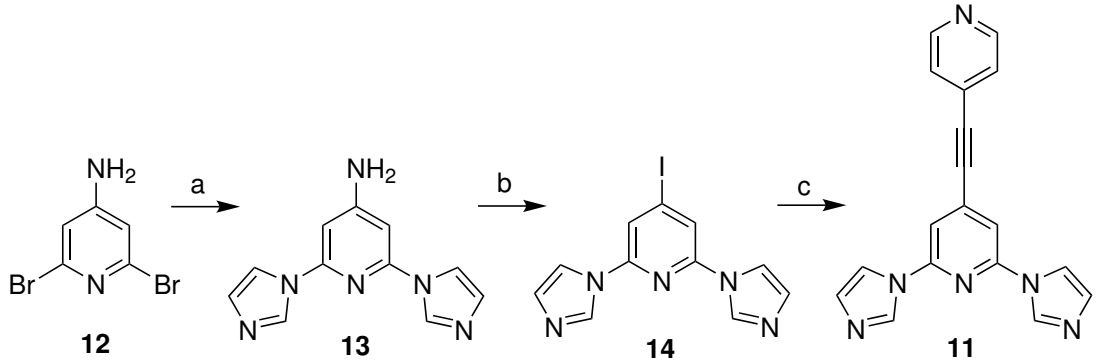

Figure 3.7: Synthesis route 2 of **L4** - part 1. a) imidazole, CuO, K_2CO_3, DMF, 150°C, 6d; b) KI, $NaNO_2$, HCl/H_2O (1:10) or H_2SO_4/H_2O (1:7); c) 4-ethinylpyridine hydrochloride, $Pd(PPh_3)_4$, CuI, DIPA/DMSO (1:1), RT, 2 weeks.

2,6-Di(1H-imidazol-1-yl)-iodopyridine **14** is synthesized in a Sandmeyer-type reaction from **13**. According to Ruben *et al.* the Sandmeyer-type reaction of related aminopyridine derivative 2,6-di-pyrazol-1-yl-pyridin-4-yl-amine to 2,6-di-pyrazol-1-yl-pyridin-4-yl-iodide can be performed in concentrated hydrochloric acid. Applying their parameters leads to a product mixture composed of iodo and chloro functionalized bisimidazole pyridine.[95] The ratio between desired iodo product to the by-product 4-chloro-2,6-di(1H-imidazol-1-yl)pyridine is 1:2 as determined by ^{1}H NMR. Figure 3.8 shows the aromatic region of a ^{1}H NMR spectrum of the iodo/chloro mixture. Two sets of proton signals are present. **14** has four proton signals. Three signals are assigned to the imidazole hydrogens at 7.14, 8.15 and 8.76 ppm (marked with orange circles), respectively. The singlet corresponding to the pyridine hydrogens is shifted to 8.23 ppm (orange square). Blue-circle marked proton signals at 7.16, 8.17 and 8.79 ppm belong to the imidazole rings in the chloro by-product. The characteristic pyridine singlet as a result of 2,4,6-substitution is high-field shifted to 8.00 ppm compared to the respective signal in **14**. Both Sandmeyer products are also confirmed by ESI mass spectrometry as shown in Figure 3.9. Therefore, the reaction procedure is adjusted to improve the ratio in favour of the iodo derivative. Instead of using concentrated hydrochloric acid, the acid is diluted. Also, the order of reactants is changed. First, KI is added to the ice-bath cooled solution, thus it is present in high concentration when $NaNO_2$ is added scopewise over two hours.

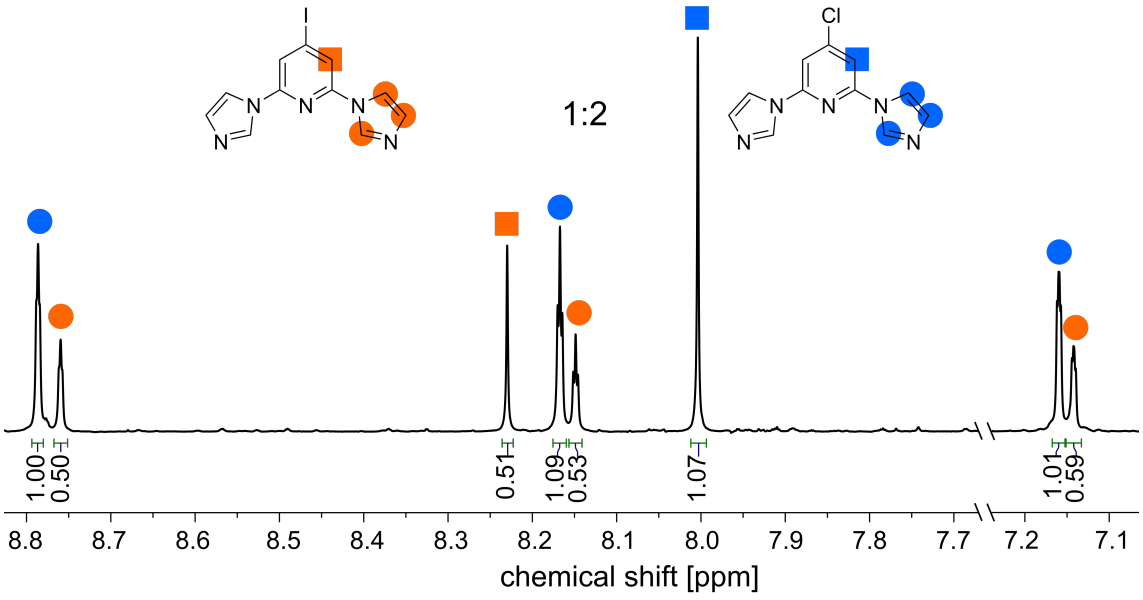

Figure 3.8: Aromatic region of ^{1}H NMR spectrum of a Sandmeyer-type reaction with concentrated hydrochloric acid. Iodo:chloro ratio is 1:2 in **14**.

With this, the ratio can be improved to 10:1 in favor of **14**. The addition of $NaHCO_3$ and Na_2SO_3 quenches the reaction and an orange precipitation is formed. The precipitate is isolated. The aqueous phase is extracted with DCM. The organic phase

and the precipitate are combined and purified over silica with acetone as eluent. Yields up to 59% related to the iodo-chloro mixture are possible.

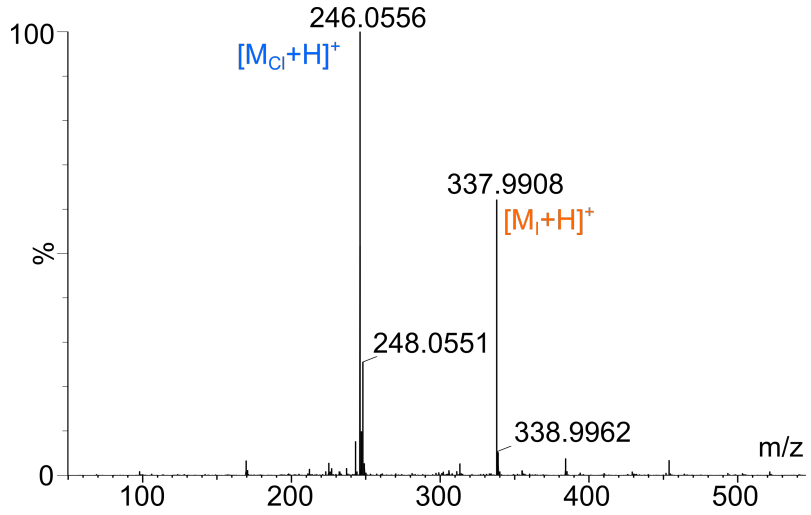

Figure 3.9: ESI mass spectrum of a Sandmeyer-type reaction with concentrated hydrochloric acid. Mass peaks of chloro and iodo derivatives $[M_{Cl}+H]^+$ and $[M_I+H]^+$ are detected.

The presence of the chloro derivative is not interfering with the following reaction step. Only the lower reactivity of chloro compared to iodo is disadvantageous in the Sonogashira reaction. A chloro-free synthetic route can be realized by using sulfuric acid instead of hydrochloric acid. The Sandmeyer-type reaction is conducted under same conditions except the exchange of HCl with H_2SO_4. The work-up is equal and gives **14** as off-white powder in 38% yield. Since chloro and iodo derivatives can be applied in a Sonogashira reaction, the reaction with higher yield is favoured.
Subsequently, **14** reacts with 4-ethinylpyridine hydrochloride, $Pd(PPh_3)_4$, CuI in DIPA/DMSO (1:1) at room temperature for two weeks. Heating gives worse results, therefore a longer reaction time is chosen. After removal of solvent, suspension in water and filtration, the raw product is purified following a HCl/NaOH protocol which is described in detail in the experimental section. **11** is obtained in 74% yield.

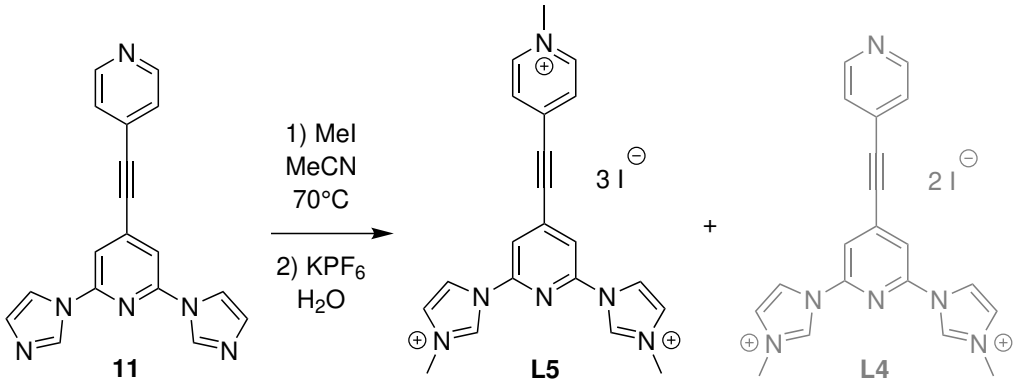

Figure 3.10: Synthesis route 2 of **L4** - part 2. Isolation of **L5** instead.

The next reaction step in the synthesis route of **L4** is the methylation of **11**. The reaction in acetonitrile and methyl iodide as methylation reagent at 70°C does not give the desired product (Figure 3.10). Instead, the terminal pyridine is also methylated in this reaction leading to **L5**.

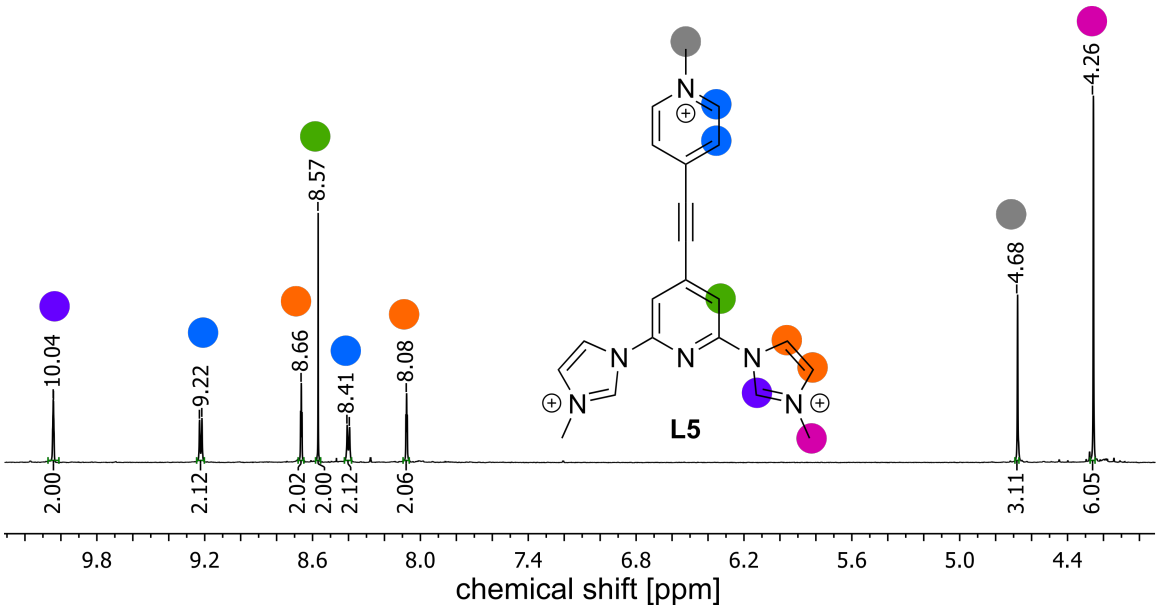

Figure 3.11: ^{1}H NMR spectrum of **L5** in DMSO-d_6.

The ^{1}H NMR spectrum of **L5** is shown in Figure 3.11. Both methyl proton signals are determined at 4.26 and 4.68 ppm (pink and grey). The integral ratio is 2:1 in accordance with the number of different methyl groups in **L5**. Terminal pyridine hydrogens are shifted to 8.41 and 9.22 ppm (blue). The 2,4,6-substituted pyridine ring exhibits one singlet at 8.57 ppm (green). Two proton signals at 8.08 and 8.66 ppm are assigned to the imidazole hydrogens in 4,5-position. Down-field shifted hydrogens at 10.04 ppm correspond to the hydrogens in the imidazole rings (purple) which are easily deprotonated to form the respective NHC ligands.

ESI mass spectrometry confirms the threefold methylation of **11** (*cf.* ESI mass spectrum in the appendix). The mol peak of **L5** is measured at 119.0602 m/z. Additionally, a second mass peak could be identified which indicates synthesis of **L4** at 171.0818 m/z. On the other hand, this mass could be also assigned to an asymmetrically methylated product where one pyridine and one imidazole ring are methylated. A more sophisticated route is chosen which protects the pyridine funtionality before the methylation is carried out. Therefore, **11** is protected as N-oxide as shown in Figure 3.12. **11** reacts with meta-chloroperoxybenzoic acid (mCPBA) and $NaHCO_3$ in DCM/H_2O (8:1) under reflux for 12 h. Removal of DCM and suspension in an aqueous $NaHCO_3$ solution lead to a precipitate which gives **15** after isolation and washing with water in 61% yield.

According to the standard methylation protocol **15** is stirred in MeCN at 80°C

and methylated with methyl iodide. To avoid monomethylation the amount of methylation reagent is increased to 10 equivalents. Methylation of the N-oxide is not observed. Removing of MeCN and excess of MeI gives **16** as orange product in 96% yield.

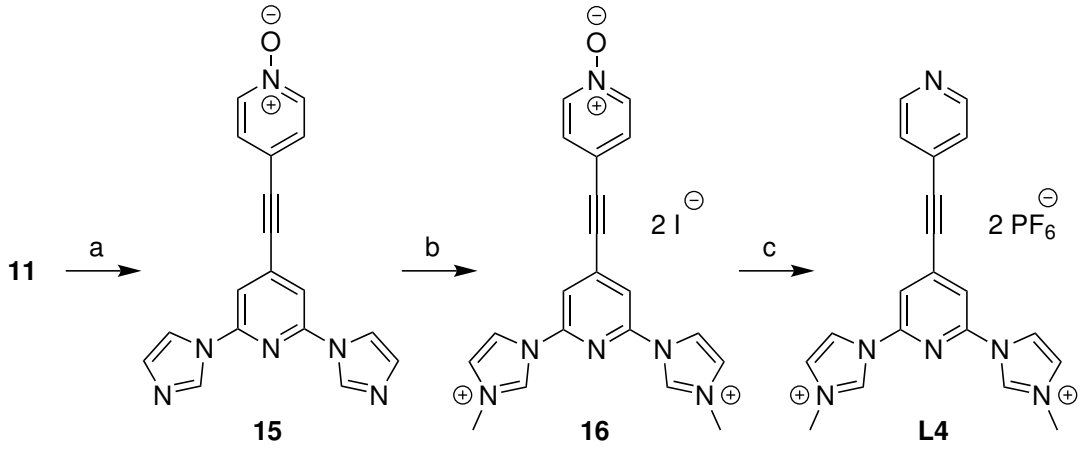

Figure 3.12: Synthesis route 2 of **L4** - part 3. a) MCPBA, $NaHCO_3$, DCM/H_2O, 40°C, 12h; b) MeI, MeCN, 80°C, 20h; c) 1) PBr_3, DCM, 50°C, 24h, 2) KPF_6, H_2O.

The selective methylation of the imidazole rings is accomplished. Deprotection of the pyridine N-oxide has to be carried out in the following. There are several methods available e.g. deoxygenation of N-oxide can be conducted with zinc and ammonium formate or with iron and acetic acid.[96,97] Both protocols are not successful in deoxygenation of **16**. Next, the deprotection with trivalent phosphorus compounds is tested. Both PBr_3 and PCl_3 are applied. **16** reacts with PCl_3 in DCM at room temperature for 3 h. After removal of DCM the crude product is dissolved in water. After filtration and neutralisation with $NaHCO_3$, an anion exchange with KPF_6 is performed. NMR investigation reveals an educt/product mixture indicating uncomplete consumption of **16**. The reaction parameters are changed to increase the NMR-yield of **L4** as shown in Table 3.1. First, the reaction time is elongated from three hours to 24 h and finally to three days (entry 1-3). Unfortunately, the NMR-yield of **L4** is not substantially improved. Second, PCl_3 is exchanged by PBr_3. First attempt at room temperature gives lower yield of 30% compared to 40% (entry 4 vs. 2). Therefore, the reaction temperature is increased to 50°C. This significantly improves the yield to 69%. Still, remaining **16** has to be remove. This can be achieved by column chromatography. Purification over alumina with MeCN/Et_2O (1:1) separates **L4** from the educt. Unfortunately, the isolated yield is only 9%. The synthesis route over seven steps has a low overall yield of only 2%.

An additional ligand can be synthesized from **14**. When **14** is obtained by the Sandmeyer-type reaction with sulfuric acid, which gives only the desired iodo product, a methylation can be conducted which gives **L6**. Complexation of this ligand gives the opportunity to study heavy-atom effect induced by iodine in the respective iron

Table 3.1: Deoxygenation of **16**.

entry	reagent	T[°C]	time	NMR-yield
1	PCl_3	20	3h	0.38
2	PCl_3	20	24h	0.40
3	PCl_3	20	3d	0.43
4	PBr_3	20	24h	0.30
5	PBr_3	50	24h	0.69

complex. First attempt to synthesize **L6** is carried out with MeI in MeCN at 70°C. This procedure gives the monomethylated product **17**. This compound could offer the opportunity to synthesize asymmetrically-substituted NHC ligands as interesting ligand class in the future.
Another reaction is tried. **14** reacts at -78°C in DCM with methyl triflate as shown in Figure 3.13 (step b). After warming to room temperature and removal of solvent anion exchange with KPF_6 is performed. **L6** is isolated as white powder in 53% yield.

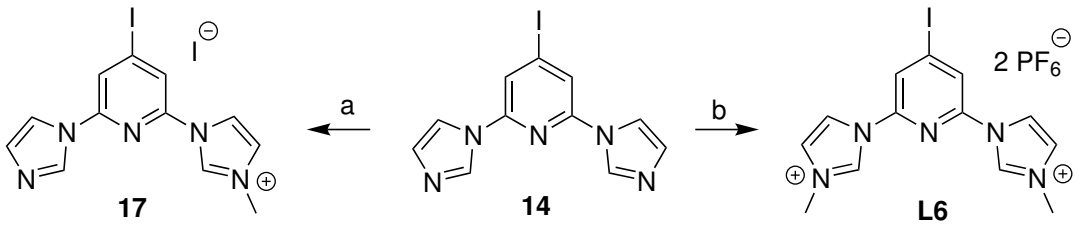

Figure 3.13: Synthesis of **L6**. a) MeI, MeCN, 70°C, 1d; b) 1) methyltriflate, DCM, -78°C, 2) KPF_6, H_2O.

Finally, five different bridging ligands are successfully synthesized. The overall yield for **L1** and **L2** are 43% and 25%, respectively. **L3** can be obtained in 30% in a three-step synthesis. After seven steps **L4** is only isolated in 2% total yield. A three-step route gives **L6** in 18% yield.

The synthesized bridging ligands can be applied in homoleptic and heteroleptic complex synthesis. Terpyridine-based bridging ligands **L1** and **L2** allow the introduction of six π-acceptor functionalities. In contrast, using **L3-L6** gives the oppourtunity to study the influnece of four carbene funtionalities on the spectroscopic properties of the respective iron complexes. The mixing of terpyridine and carbene ligands gives insight into effects on the complex properties by varying the number of carbene moieties which was also nicely shown by Zimmer *et al.*[54] A manuscript in preparation includes results of **Fe1-2**.[98] Published results of **Fe3** can be found here.[99]

4.1 Homoleptic Complex Synthesis

Synthesizing homoleptic complexes with a terminal pyridine on both sides of the iron complex offers the possbility to attach two cobaloxime moieties. With this, triads can be realized. The impact of photosensitzer to catalyst ratio can be studied in those complexes.

4.1.1 Terpyridine-based complexes

The synthesis of $\mathbf{Fe1_{homo}}$ and $\mathbf{Fe2_{homo}}$ is shown in Figure 4.1. The reactions are conducted under argon. $FeBr_2$ is added to a suspension containing the corresponding bridging ligand. In case of $\mathbf{Fe1_{homo}}$, the solution is filtrated, the solvent removed and the residue dissolved in water. Subsequent anion exchange with an aqueous solution of KPF_6 gives the homoleptic terpyridine complex as violet PF_6-salt after washing with water in 15% yield. In case of $\mathbf{Fe2_{homo}}$, dissolving in water fails due to bad solubility of the resulted complex. Instead, the MeOH solution is filtrated and concentrated. After anion exchange with KPF_6, $\mathbf{Fe2_{homo}}$ is obtained as violet powder in 21% yield.

4.1.2 Carbene-based complexes

Carbene-based complexes can not be synthesized according to the terpyridine complex protocol. The reason is the high affinity of carbene ligands to protons. Thus, the imidazolium salt has to be used as precursor ligand. The carbene is formed *in-situ* by adding a strong base e.g. potassium tert-butoxide (KO^tBu) or lithium-bis(trimethylsilyl)-amide (LiHMDS) to the solution containing the respective imidazolium salt **L3-L6**.

Figure 4.2 shows the synthesis route for $\mathbf{Fe3_{homo}}$ and $\mathbf{Fe4_{homo}}$. Both reaction are

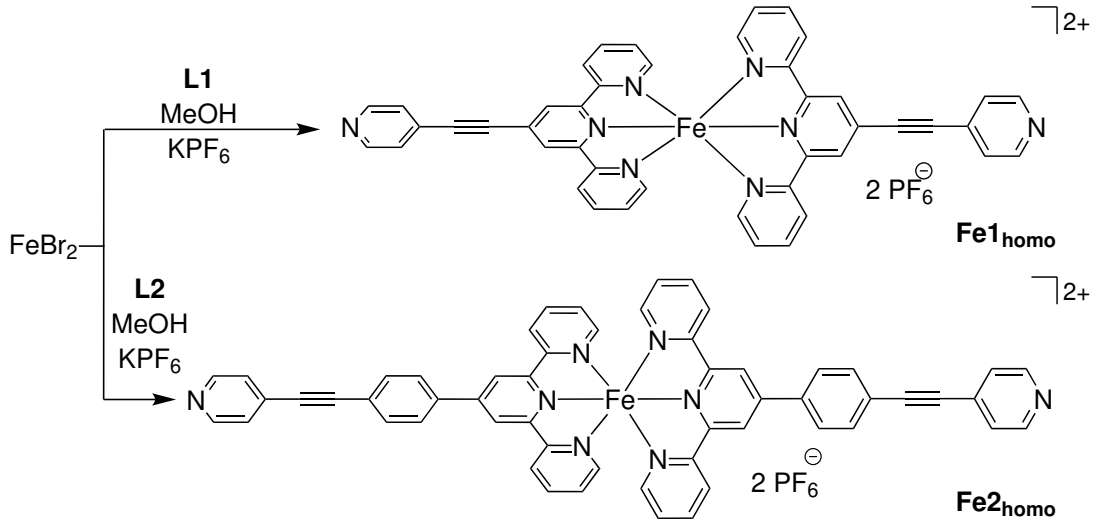

Figure 4.1: Synthesis of $\mathbf{Fe1_{homo}}$ and $\mathbf{Fe2_{homo}}$.

conducted under water- and oxygen-free conditions. **L3** is suspended in DMF. First, KO^tBu then $FeCl_2$ are added which results in a red solution. After removal of solvent, the complex is dissolved in water and an anion exchange with KPF_6 is conducted. Purification with Et_2O gives the complex in 21% yield.

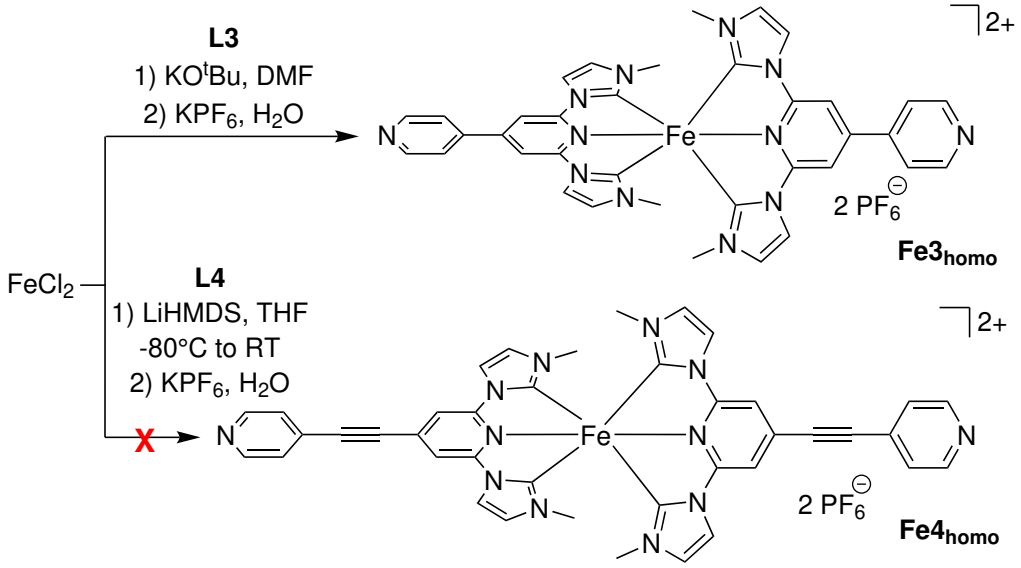

Figure 4.2: Synthesis of $\mathbf{Fe3_{homo}}$ and $\mathbf{Fe4_{homo}}$.

The synthesis of $\mathbf{Fe4_{homo}}$ with LiHMDS in dry, degassed THF is not successful. The ligand is partly isolated after the reaction. The desired complex is not obtained. There is not enough substance left to try an alternative synthesis route for $\mathbf{Fe4_{homo}}$. The other complexation methods presented in this chapter could be tested in the future.

Also, **L5** is applied in homoleptic complex synthesis. Deprotonation with LiHMDS in THF and $FeBr_2$ does not give the desired product. The reaction mixture turns brown. Also, the attempt to synthesize $\mathbf{Fe5_{homo}}$ with KO^tBu in DMF fails.

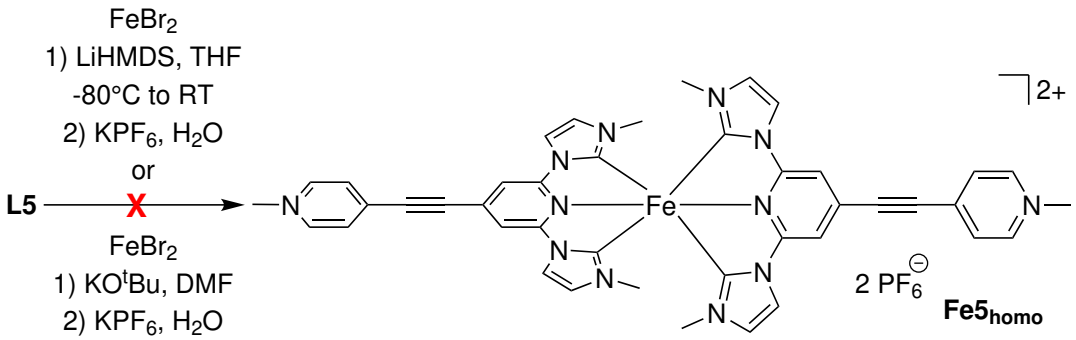

Figure 4.3: Synthesis of $\mathbf{Fe5_{homo}}$.

L6 is well suited to study the heavy-atom effect induces by the iodine. It is known that the intersystem crossing is facilitated by the heavy-atom effect.[74] This could affect the relaxation cascade in the iron photosensitizer and the lifetime of the excited states. This can be adressed in a future work. Three different synthetic procedures are tested. First, LiHMDS in THF and $FeBr_2$ as iron source are used. No color change which would indicate a complex formation is obeserved. Second, the base is exchanged. Instead of LiHMDS, KO^tBu is used. Unfortunately, this does not give the desired product. Finally, the synthetic route already successful for $Fe3_{homo}$ is applied. **L6** is dissolved in dry, degassed DMF. $FeBr_2$ and KO^tBu are added. After removal of DMF and washing with water the subsequent anion exchange with KPF_6 is conducted. The complex is obtained as orange crystals after recrystallization in $MeCN:Et_2O$.

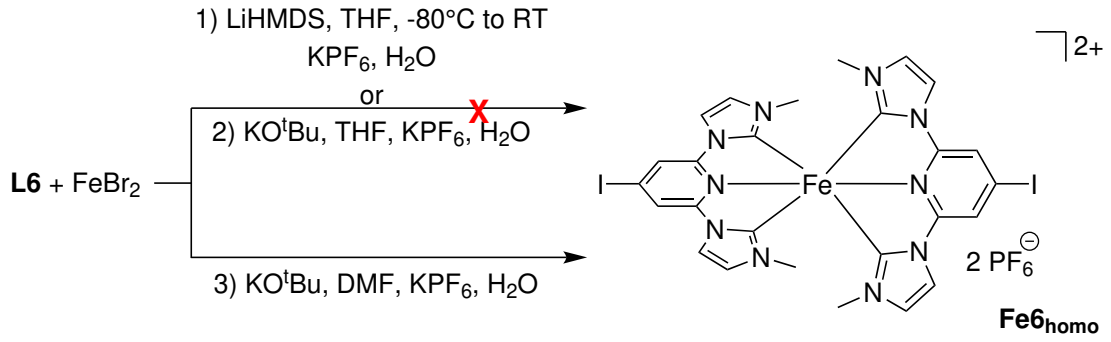

Figure 4.4: Synthesis of $\mathbf{Fe6_{homo}}$.

To conclude, only four homoleptic complexes are obtained ($\mathbf{Fe1_{homo}}$-$\mathbf{Fe3_{homo}}$, $\mathbf{Fe6_{homo}}$). The synthesis of $\mathbf{Fe4_{homo}}$ and $\mathbf{Fe5_{homo}}$ are not successful.

4.2 Heteroleptic Complex Synthesis

Synthesizing heteroleptic complexes with only one terminal pyridine offers the possbility to attach specifically one cobaloxime moiety. With this, dyads can be realized. The 1:1 ratio of photosensitzer and catalyst ratio can be studied in those complexes. For that, a special synthesis route is developed which offers the possibility to introduce subsequently two different ligands.
The first ligand **SP** (1,1'-(pyridine-2,6-diyl)bis(3-(2,6-diisopropylphenyl)-1H-imidazol-3-ium) bromide) is very bulky and shown in Figure 4.5. Due to the diisopropylphenyl ring attached to the imidazol rings the coordination of a second ligand **SP** is hindered. Additionally, the applied *in-situ* base $Fe(HMDS)_2$ is used in a 1:1 ratio. With this, no additional base is present to deprotonate a second ligand. **SP** and **Fe(HMDS$_2$)** are combined in dry, degassed THF at -80°C. After warming to room temperature a violet five-coordinated iron complex **Fe(SP)Br$_2$** is formed which is water- and air-sensitive. This parent complex is used in all heteroleptic complex synthesis. Further details are described in the following.

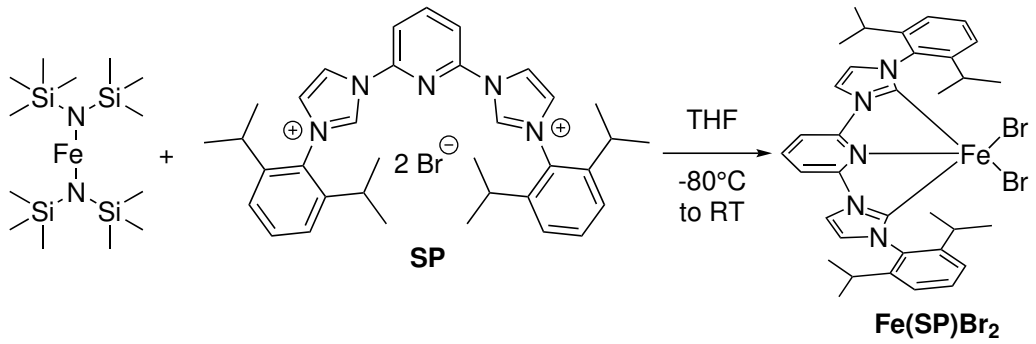

Figure 4.5: Synthesis of **Fe(SP)Br$_2$**.

4.2.1 Terpyridine-based complexes

The synthesis of **Fe1** and **Fe2** start with the formation of **Fe(SP)Br$_2$** as shown above. To this solution, the bridging ligands **L1** or **L2** are added under argon. After removal of THF, the crude product is dissolved in water. After filtration and an anion exchange with KPF_6, the iron complex is purified over alumina using MeCN:Et_2O (1:5). **Fe1** and **Fe2** are obtained in 64% and 65% yield, respectively.

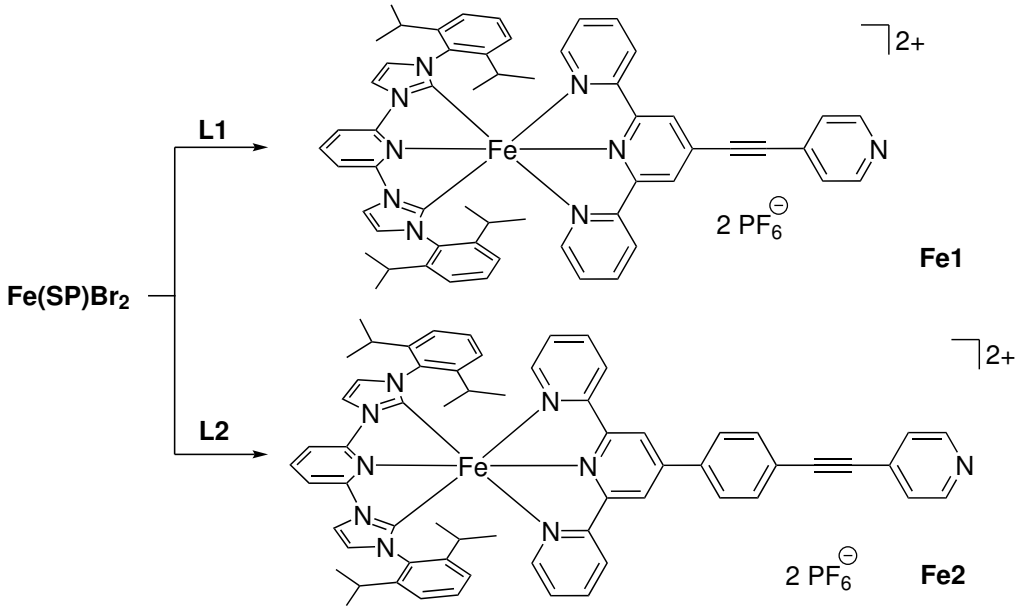

Figure 4.6: Synthesis of **Fe1** and **Fe2** in THF. Anion exchange is performed with KPF_6 in H_2O.

4.2.2 Carbene-based complex

In the heteroleptic tetra-carbene iron complex synthesis only **L3** is applied. Similar to the homoleptic carbene complex synthesis, a strong base has to be applied to obtain the free carbene. Starting with **L3** in dry, degassed THF, LiHMDS is added at -70°C. Then, the carbene solution and **Fe(SP)Br$_2$** sre combined. Removal and subsequent anion exchange with KPF_6 is performed. Purfication over alumina with MeCN/Et_2O (1:1) gives **Fe3** as orange powder in 50% yield.

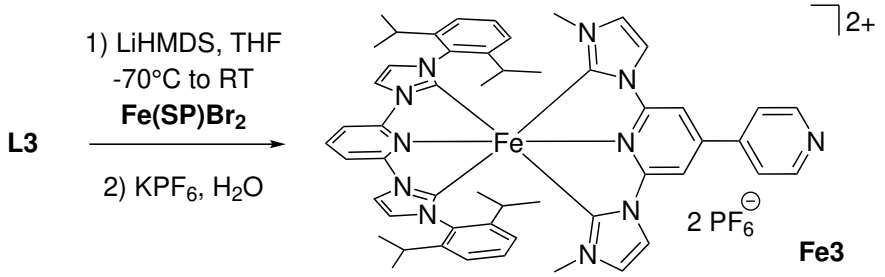

Figure 4.7: Synthesis of **Fe3**.

Homoleptic and heteroleptic iron complexes are obtained with the described synthesis routes. Characterization by single crystal diffraction for selected compounds is presented in the following chapter. Further properties of the iron complexes are accessed by UV-Vis spectroscopy combined with TDDFT and cyclic voltammetry. For the heteroleptic complexes spectroelectrochemical measurements are conducted. The excited state dynamics will be discussed together with the corresponding multimetal complexes in section 5.3.6.

4.3 Characterization and Properties

All iron photosensitizers except **Fe6$_{\mathbf{homo}}$** are characterized by single crystal diffraction. UV-Vis measurements and cyclic voltammetry give insight into the absorption properties and redox potentials of the studied compounds. Heteroleptic systems are further characterized by quantum chemical calculations (TDDFT). Additionally, molecular orbital schemes extracted from DFT depict energy levels in the respective iron complexes **Fe1**, **Fe2** and **Fe3**.

4.3.1 Crystal structures

All crystals are obtained via vapour diffusion. Acetone or acetontrile are used as solvent while Et_2O is used as anti-solvent. First, the crystallographic data of the homoleptic iron complexes are discussed. They are listed in Table 4.1 and shown in Figure 4.8. The axial Fe-N bond lengths are 1.886 Å and 1.883 Å in the terpyridine systems **Fe1$_{\mathbf{homo}}$** and **Fe2$_{\mathbf{homo}}$**, respectively. In contrast, the axial iron-nitrogen bond in the tetra-carbene system **Fe3$_{\mathbf{homo}}$** is elongated to 1.909 Å. The equatorial iron-ligand bond lengths are also shorter for **Fe1$_{\mathbf{homo}}$** and **Fe2$_{\mathbf{homo}}$**(1.983 Å and 1.977 Å), while it is 1.995 Å for **Fe3$_{\mathbf{homo}}$**. This indicates stronger bonds between iron and terpyridine ligands in comparison to carbene ligands.
As mentioned earlier, an octahedral geometry is beneficial for a large ligand-field splitting. The bond angles provide insight into octahedricity of the studied compounds. The inter-ligand bond angle between axial nitrogens and iron is between 178.4-179.2° for all three homoleptic PS. This is very close to perfect 180° angle. The equatorial bond angles between one ligand and iron are smaller. This is the important parameter which has to be optimized for an octahedral geometry.

Table 4.1: Crystallographic data of **Fe1$_{\mathbf{homo}}$**, **Fe2$_{\mathbf{homo}}$** and **Fe3$_{\mathbf{homo}}$**.

Bond lenghts [Å] and angles [°]	Fe1$_{\mathrm{homo}}$	Fe2$_{\mathrm{homo}}$	Fe3$_{\mathrm{homo}}$
Fe-C$_{\mathrm{equat.}}$			1.995(av)
Fe-N$_{\mathrm{equat.}}$	1.983(av)	1.977(av)	
Fe-N$_{\mathrm{axial}}$	1.886(av)	1.883(av)	1.909(av)
N$_{\mathrm{eq}}$-Fe-N$_{\mathrm{eq}}$	161.1(av)	161.6(av)	
C$_{\mathrm{eq}}$-Fe-C$_{\mathrm{eq}}$			158.5(av)
N$_{\mathrm{ax}}$-Fe-N$_{\mathrm{ax}}$	179.2(3)	178.41(7)	179.20(10)
torsion$_{\mathrm{triple}}$	2.3, 25.0	8.9, 6.0	
torsion$_{\mathrm{mono}}$		19.6, 25.0	24.4, 31.5

In terpyridine ligands bond angles are 161.1-161.6°. It is reduced to 158.5° for the carbene-iron-carbene bond angle in **Fe3$_{\mathbf{homo}}$**. In comparison to both bond angles, **C2** exhibits bond angles of 178.4° due the diquinolylpyridine ligands coordinating iron within a two six-membered ring.

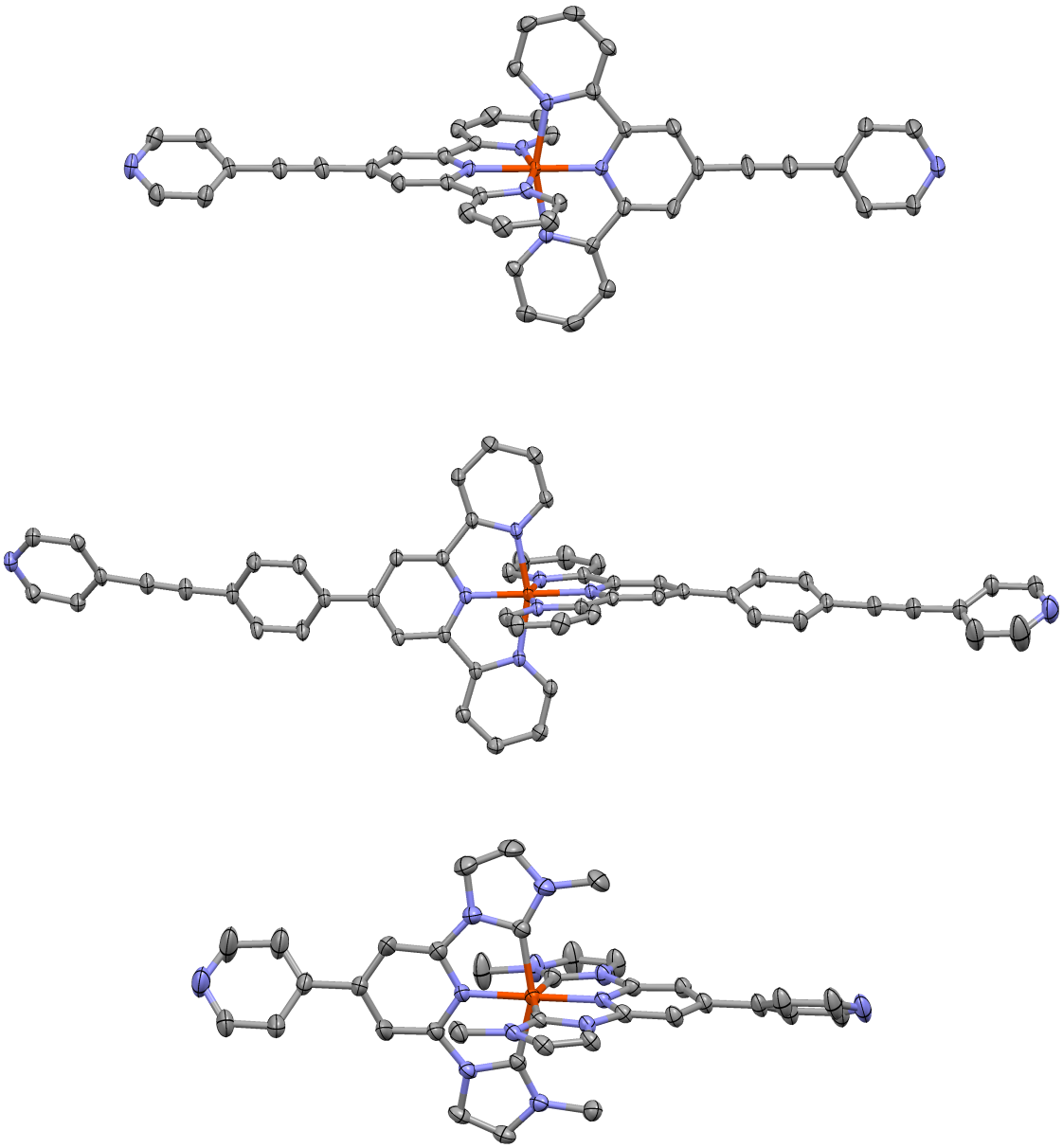

Figure 4.8: Single crystal structure of **Fe1$_{\mathbf{homo}}$** (top), **Fe2$_{\mathbf{homo}}$** (middle) and **Fe3$_{\mathbf{homo}}$** (bottom). Anisotropic displacement ellipsoids are drawn at the 50% probability level and hydrogens are omitted for clarity as well as counter ion PF_6^-.

Moreover, the influence of the spacer can be discussed on the basis of the crystal structures. The torsion angle between the two pyridine rings which are separated by a triple bond, named torsion$_{\text{triple}}$ in Table 4.1, is between 2.3-8.9° in **Fe1$_{\mathbf{homo}}$** and **Fe2$_{\mathbf{homo}}$**. In **Fe1$_{\mathbf{homo}}$** one of the torsion angles is 25.0° which could be attributed

to a packing effect in the crystal. In comparison, the torsion angle ($torsion_{mono}$) between covalently-bonded two aromatic rings, present in $\mathbf{Fe2_{homo}}$ and $\mathbf{Fe3_{homo}}$, are 19.6° and 25.0° in the former and 24.4° and 31.5° in the latter. This indicates better π-orbital overlap in ligand systems with acetylene spacer. The direct coordination of two aromatic rings either phenyl-pyridine or pyridyl-pyridine results in repulsion and increased torsion angles and therefore worse π-orbital overlap. This also has an impact on the absorption properties which will be discussed later.

Heteroleptic iron PS's are also successfully crystallized by vapour diffusion and crystallographic data are obtained. They are listed in Table 4.2 and molecular strcutures are shown in Figure 4.9. Differences in the bond length can be observed between **Fe1** and **Fe** with two carbene functionalities and **Fe3** containing four carbene functionalities. While the bulky ligand is stronger bonded in the tetra-carbene system with Fe-N_{SP} = 1.916(2) Å and Fe-C_{SP} = 1.968(av) Å, the bonds between iron and the bulky ligand **SP** are elongated in the terpyridine-bridged PS (Fe-N_{SP} = 1.924-1.925 Å and Fe-C_{SP} = 1.982-1.994 Å). On the contrary, the averaged distance between bridging ligands and iron is almost equal in all systems (Fe-BL_{av}(L1) =1.937 Å, Fe-BL_{av}(L2) =1.933 Å and Fe-BL_{av}(L3) =1.938 Å).

Table 4.2: Crystallographic data of **Fe1**, **Fe2** and **Fe3**.

Bond lenghts [Å] and angles [°]	Fe1	Fe2	Fe3
Fe-N_{SP}	1.925(8)	1.924(6)	1.916(2)
Fe-C_{SP}	1.994(av)	1.982(av)	1.968(av)
Fe-$N_{BL,axial}$	1.864(1)	1.867(4)	1.915(2)
Fe-$N_{BL,equat.}$	1.973(av)	1.966(av)	
Fe-$C_{BL,equat.}$			1.950(av)
Fe-BL_{av}	1.937	1.933	1.938
C_{SP}-Fe-C_{SP}	158.36	158.43	158.79
N_{ax}-Fe-N_{ax}	176.24	177.67	176.93
$torsion_{triple}$	84.9	20.6	
$torsion_{mono}$		45.4	43.3

The crystal structures obviously deviate from the perfect octahedron. Similar to the homoleptic tetra-NHC iron complex $\mathbf{Fe3_{homo}}$ with 158.5°, bite angles from 158.36-158.79° are found for the C-Fe-C angle in all heteroleptic complexes. Also, the inter-ligand bond angle between axial nitrogens is slightly reduced in the heteroleptic systems (N_{ax}-Fe-N_{ax} = 176.24-177.67°).
Comparison of the torsion angles in **Fe1-Fe3** supports the general influence of acetylene and phenyl spacer. Torsion angles in **Fe2** are 20.6° and 45.4° for $torsion_{triple}$ and $torsion_{mono}$, respectively. This is in agreement with the results for homoleptic PS.

However, the torsion angles between two pyridine rings spaced by an acetylene linker are slightly higher than expected. Also, in **Fe1** the outer pyrdine ring is rotated by 84.9° despite the triple bond. Most likely, packing effects induce stronger rotation of these aromatic rings. The torsion angle of 43.3° in **Fe3** is in the same range as that of **Fe2** ($\text{torsion}_{\text{mono}} = 45.4°$).

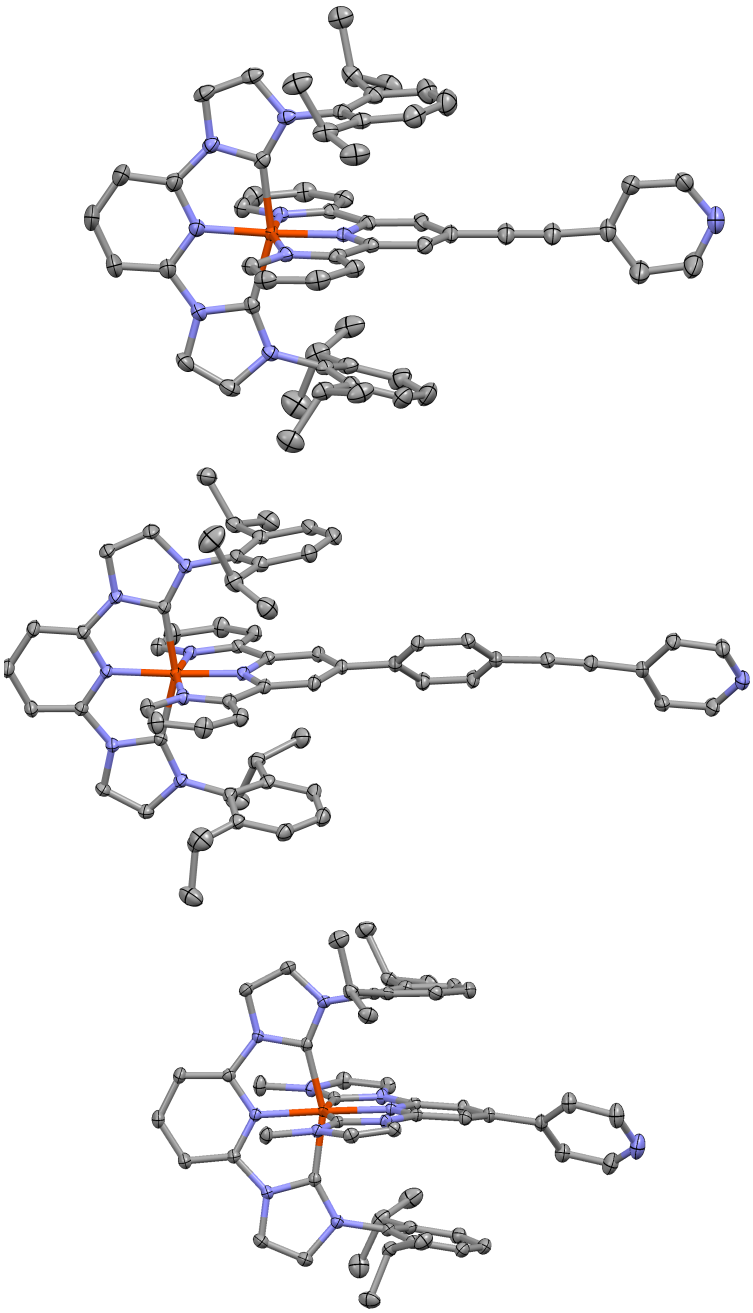

Figure 4.9: Single crystal structure of **Fe1** (top), **Fe2** (middle) and **Fe3** (bottom). Anisotropic displacement ellipsoids are drawn at the 50% probability level and hydrogens are omitted for clarity as well as counter ion PF_6^-.

Based on the crystal structure analysis the following results can be summarized. Terpyridine ligands have shorter iron-ligand bond lengths and better bite angles. Iron-carbene distances are elongated and the bite angles are only about 159°. This indicates stronger bonds in terpyridine-based complexes which can be attributed to the better π-acceptor properties of polypyridyl ligands. However, there is still room for improvement in the ligand design, which aims for better octahedrality e.g. a suitable insertion between the carbene and the pyridine ring in the C^N^C-ligand could increased the bite angle.

4.3.2 UV-Vis Spectroscopy

A working photosensitizer should have a broad absorption in the visible region of the solar spectrum. Typically, MLCT bands are in the visible range of the solar spectrum. With rational ligand design these MLCT bands can be tuned depending on the energy level of their metal-based donor orbitals and ligand-based acceptor orbitals. Applying N-donor ligands or NHC ligands has a direct impact on the absorption properties of the iron PS. The UV-Vis spectra of homoleptic and heteroleptic iron PS with different ligand motifs are presented in the following.

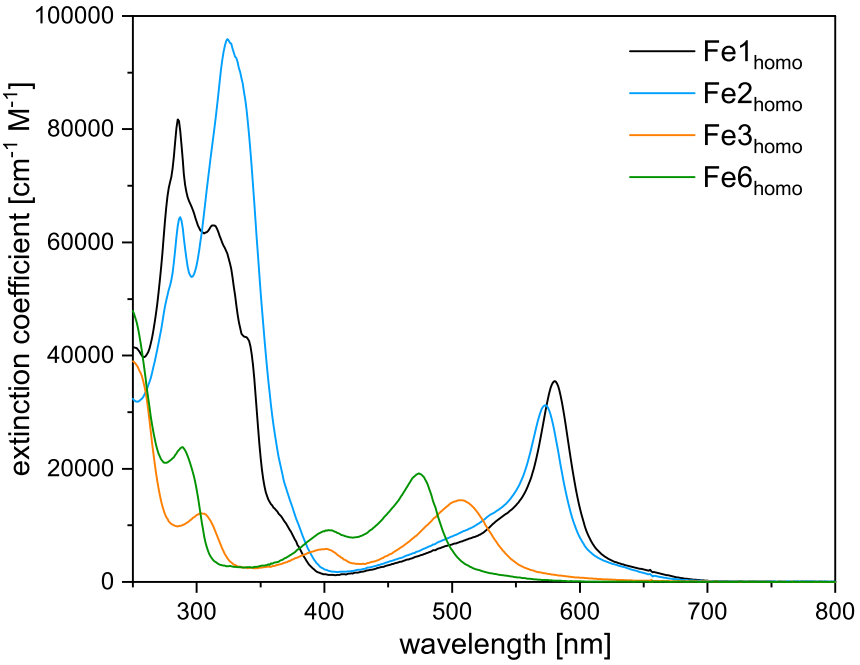

Figure 4.10: Absorption spectrum of **Fe1$_{homo}$** (black), **Fe2$_{homo}$** (blue), **Fe3$_{homo}$** (orange) and **Fe6$_{homo}$** (green).

In Figure 4.10 the absorption spectra of four homoleptic iron PS's are shown and the wavelengths of the band maxima are listed in Table 4.3. The compounds can be divided into two groups. **Fe1$_{homo}$** and **Fe2$_{homo}$** are terpyridine-based while **Fe3$_{homo}$** and **Fe6$_{homo}$** are tetra-carbene systems. For all compounds ligand-based π-π*-transitions are visible below 380 nm. Intensities of these π-π*-bands are very high in the terpyridine-coordinated iron PS because of the large aromatic system provided by **L1** and **L2**. The band at 324 nm in **Fe2$_{homo}$** is the intense one due to the introduction of a phenyl ring in the ligand backbone. Transitions above 380 nm are assigned to MLCT transitions.[100] The MLCT band of **Fe1$_{homo}$** is at 580 nm. Upon introduction of a phenyl spacer the MLCT band is blue-shifted to 573 nm in **Fe2$_{homo}$**. This is due to the energy barrier introduced by the phenyl ring because of the poor spatial overlap of π* orbitals.[101]

The carbene-based systems exhibit two distinct transitions between 390-510 nm. The

higher-energy band at 399 nm and 403 nm in **Fe3$_{\mathbf{homo}}$** and **Fe6$_{\mathbf{homo}}$**, respectively, involves most likely charge transfer from iron to the carbene moieties as in the reference complex **C3**.[102] The lower-energy bands at 506 nm (Fe3$_{\mathrm{homo}}$) and 474 nm (Fe6$_{\mathrm{homo}}$) have most likely mixed contribution from the carbene and pyridine moieties of the ligands. This is due to the different substitution in the backbone resulting in different band maxima. The red-shift $\Delta\lambda = 32$ nm in **Fe3$_{\mathbf{homo}}$** compared to **Fe6$_{\mathbf{homo}}$** indicates MLCT stabilization by π-system extension via pyridyl ring introduction. This will be further supported by TDDFT calculations conducted for the heteroleptic PS (see below).

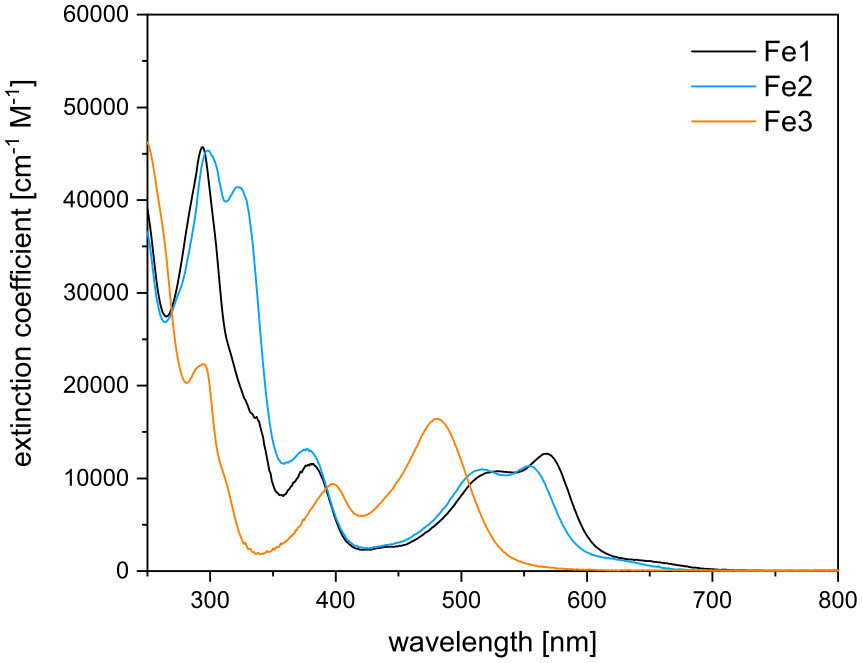

Figure 4.11: Absorption spectrum of **Fe1** (black), **Fe2** (blue) and **Fe3** (orange).

The absorption properties of heteroleptic photosensitizers are characterized by UV-Vis spectra shown in Figure 4.11. The spectra can be again divided into two band regions. Bands below 360 nm are assigned to π-π*-transitions. Extended ligand π-systems in **Fe1** and **Fe2** result into more intense bands with extinction coefficients around 45000 cm^{-1}M^{-1}. In contrast, the ligand-based transition in **Fe3** at 294 nm has only an extinction coefficient of 16800 cm^{-1}M^{-1}. Between 378-398 nm the characteristic MLCT band attributed to iron-carbene transitions in the heterolpetic systems are present. The MLCT band of **Fe3** is red-shifted about 20 nm in comparison to the terpyridine-based PS. This is reflected in the MLCT stabilization which is caused by an additional pyridine ring in **L3** while **SP** is unfunctionalized in the backbone. In contrast, the better π-acceptor ability of terpyridine ligands compared to carbene ligands results into drastically red-shifted MLCT bands at lower energies. While the MLCT band is at 481 nm in **Fe3**, MLCT transitions of **Fe1** and **Fe2** are found at 528, 568 nm and 517, 555 nm, respectively. The red-shift is between $\Delta\lambda$ = 36-87 nm.

Table 4.3: Absorption properties of homoleptic and heteroleptic iron photosensitizers.

entry	λ_{abs} [nm]($\epsilon \cdot 10^{-3}$ [$cm^{-1}M^{-1}$])		
$Fe1_{homo}$	285 (81.7), 313 (63.0), 339 (43.3)		580 (35.5)
Fe1	293 (45.7), 336 (16.7)	380 (1.16)	528 (1.08), 568 (1.27)
$Fe2_{homo}$	287 (64.4), 324 (95.9)		573 (31.2)
Fe2	299 (45.3), 322 (41.4)	378 (1.31)	517 (1.10), 555 (1.13)
$Fe3_{homo}$	303 (12.1)	399 (5.8)	506 (14.5)
Fe3	294 (16.8)	398 (6.6)	481 (11.2)
$Fe6_{homo}$	289 (23.8)	403 (9.2)	474 (19.2)

[a] Measured in MeCN at $1 \cdot 10^{-5}$ mol/L.

With UV-Vis-spectroscopy tuning of absorption properties can be quantified. In addition, theoretical calculations provide further insight into these findings. Therefore, molecular orbital schemes are extracted from single-point energy calculations. They are visualized in Figure 4.12. The energy gaps are indicated by arrows and the energy difference is given in eV and transferred to the wavelength equivalent for better comparison with the UV-Vis spectra. The average Fe 3d character is included for dπ, dπ* and dσ* orbitals in %.

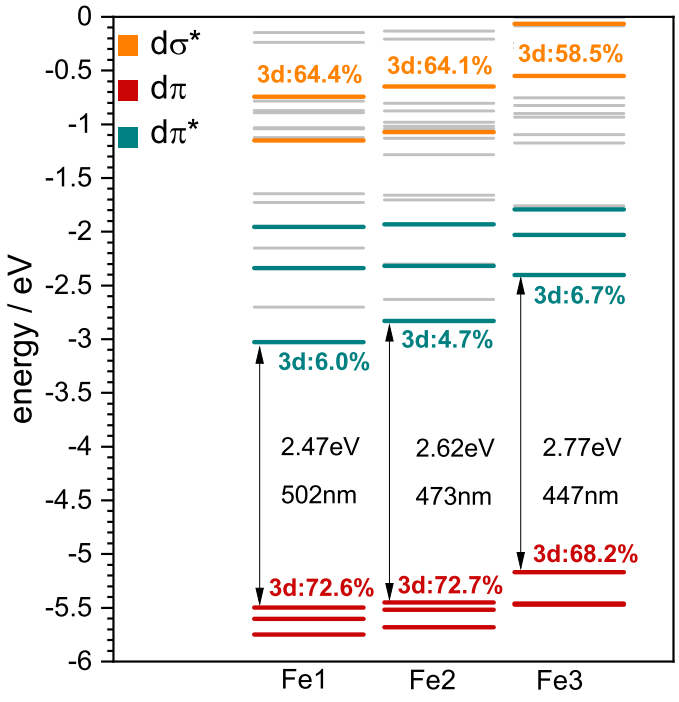

Figure 4.12: Molecular orbitals of **Fe1**, **Fe2** and **Fe3**; TPSSh, def2-TZVP(P), SMD (MeCN). HOMO-LUMO gaps are indicated (eV/nm). The average Fe 3d character is included for dπ, dπ* and dσ* orbitals in %.

The highest-occupied molecular orbital (HOMO) is mainly metal-based (Fe% 3d = 72.6%) with a reduced metal character in **Fe3** (Fe% 3d = 68.2%). This suggests a higher covalency in tetra-carbene systems compared to terpyridine systems. The

lowest-unoccupied molecular orbital (LUMO) is mainly ligand-based with only an iron 3d character between 4.7-6.7%. The blue-shift of the lowest-energy absorption is qualitatively reflected by DFT calculations. The smallest energy gap in **Fe1** at 2.47 eV is consistent with the lowest energy band being present in this PS. Accordingly, the introduction of phenyl spacer destabilize the LUMO level resulting in a blue-shift of the absorption bands which is reflected by an increased energy gap of 2.62 eV. Destabilization occurs also for **Fe3** with a HOMO-LUMO gap of 2.77 eV. Here, both HOMO and LUMO levels are destabilized, while the LUMO level in particular is energetically raised. In addition, the ligand-field splitting Δ_O can be discussed by comparison of average dπ and dσ* energies. In **Fe1** and **Fe2** a ligand-field splitting Δ_O of 4.67 eV and 4.69 eV are found, respectively. The ligand-field splitting is 5.06 eV in **Fe3** which is inline with destabilization of the MC states by the introduction of strong σ-donor ligands.

With the help of time-dependent DFT (TDDFT) the assignement of the bands can be further confirmed. Experimental and TDDFT spectra of **Fe1-3** are shown in Figure 4.13. A detailed analysis of all relevant singlet transitions are in the appendix. TPSSh-TDDFT succeeds in describing all relevant bands with partial deviation in their energy position or intensities. Experimental and computational spectra of **Fe1** are compared in Figure 4.13 (top). Band A which correlates to the lowest energy band around 570 nm results from MLCT transition from Fe(II) to the bridging ligand **L1**. Also, the band at 528 nm is described by blue-shifted transition B with MLCT character. Again, acceptor orbitals are located on **L1**. The absorption band at 380 nm can be described by band C and D. It is a result of MLCT transitions from Fe(II) to both coordinating ligands **L1** and **SP**. Band E and F cover the absorption band at 293 and the shoulder at 336 nm. They are mainly described by inter- and intraligand π-π* transitions dominated by the bridging ligand.
A similar picture is found for experimental and computational spectra of **Fe2** (Figure 4.13, middle). There are two bands A and B which can be assigned to the bands at 517 and 555 nm. Band A results from dominant MLCT transitions from iron to the bridging ligand **L2**, while transition B is characterized by MLCT transitions to both ligands. Moreover, band C reflects MLCT transition to **L2**. Also, partial π-π*-transitions are included. π-π* bands at 299 and 322 nm are confirmed by band D which is described by inter- and intraligand transitions.
All relevant bands are covered by TDDFT in **Fe3** except the ligand-based UV region due to a lower number of computed states. The absorption at 481 nm is reflected by band A. It originates from the charge transfer from iron to the bridging ligand **L3** and smaller contribution to **SP**. Band B reflecting absorption at 398 nm is dominated by MLCT transition to **SP**. This has been already proposed by comparison of experimental data (see above). Now, it is also confirmed by theoretical analysis.

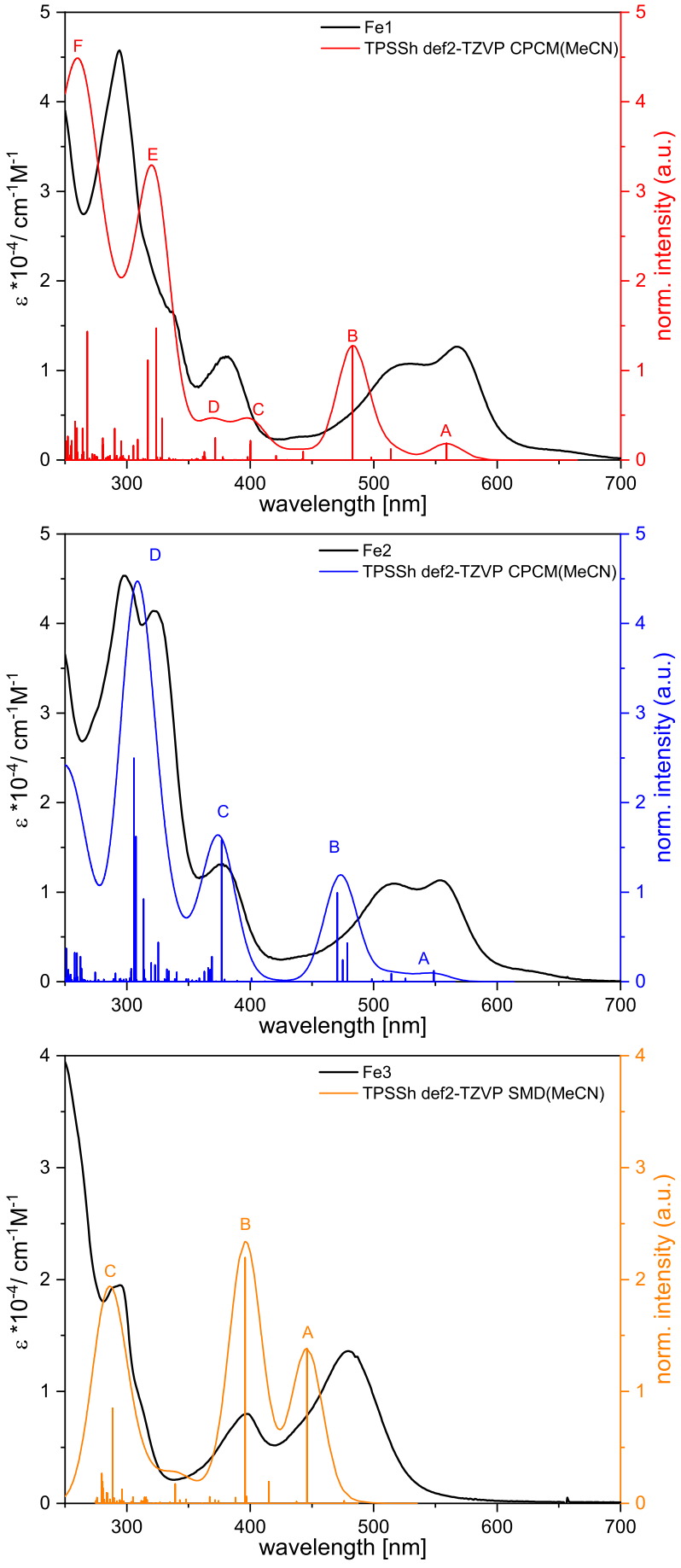

Figure 4.13: Experimental and computational spectra of **Fe1** (red), **Fe2** (blue) and **Fe3** (orange); TPSSh, def2-TZVP, SMD(MeCN) or CPCM(MeCN).

Moreover, absorption at 294 nm is best described by band C which results from inter- and intraligand π-π* transitions.
To conclude, experimental absorption properties of homoleptic and heteroleptic photosensitizers have been characterized in dependency of ligand modification such as backbone functionalization or variation of σ-donor ligands. Computed molecular orbital schemes have given insight into the energetic order of HOMO and LUMO states as well as their nature (Fe 3d character). Additionally, the observed transitions have been assessed by TDDFT. By that, the MLCT character of the lower-energy bands has been confirmed.

4.3.3 Protonation of photosensitizer

Most of the synthesized iron compounds are functionalized with one or two pyridine rings in the ligand backbone. This pyridine ring can act as proton probe. Therefore, acetonitrile solutions containing the PS are protonated with trifluoroacetic acid (TFA) and the absorption changes are followed by UV-Vis spectroscopy. In addition, unfunctionalized iron complexes are studied to compare the impact of protonation on their absorption properties. Here, $\mathbf{Fe(tpy)_2^{2+}}$ and **C3** are used. In Figure 4.14 absorption changes of $\mathbf{Fe(tpy)_2^{2+}}$, $\mathbf{Fe1_{homo}}$ and $\mathbf{Fe2_{homo}}$ are visualized.

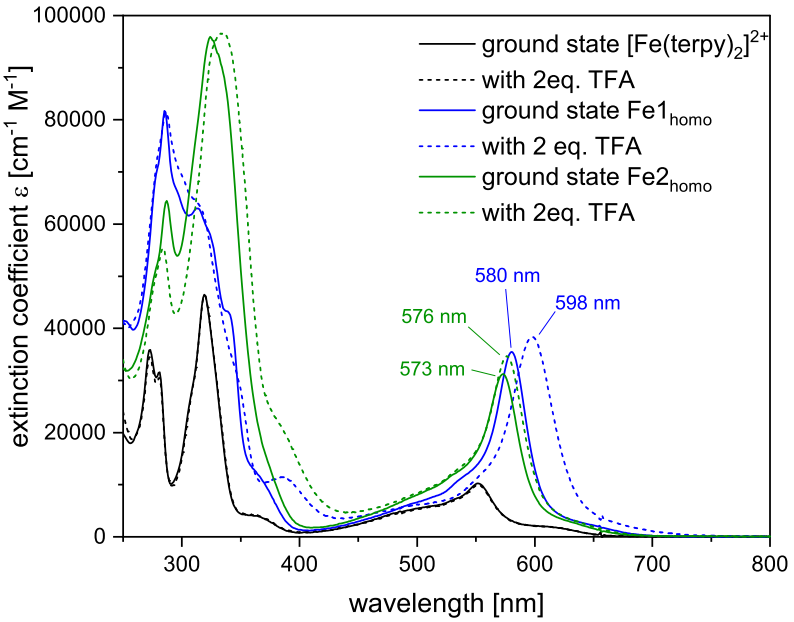

Figure 4.14: Absorption changes upon protonation of homoleptic terpyridine iron complexes $\mathbf{Fe(tpy)_2^{2+}}$, $\mathbf{Fe1_{homo}}$ and $\mathbf{Fe2_{homo}}$.

Starting with the unfunctionalized $\mathbf{Fe(tpy)_2^{2+}}$, no absorption changes are observable for this system. It is not affected by protonation. Also, changes in the dielectric constant due to acid addition are not induced. On the contrary, protonation has an effect on the absorption properties of $\mathbf{Fe1_{homo}}$ and $\mathbf{Fe2_{homo}}$. In both cases, the lowest-energy band is red-shifted upon addition of TFA. In $\mathbf{Fe1_{homo}}$ the band is shifted about 19 nm and in $\mathbf{Fe2_{homo}}$ a small shift about 3 nm is detected. This is due to the increased electron acceptability of the pyridine ring by protonation. This effect has been also investigated by Duchanois *et al.*.[46] They added TFA to a solution containing a heteroleptic iron PS with a C^N^C-ligand and a N^N^N-ligand, similar to the heteroleptic compounds **Fe1** and **Fe2**. An absorption band at 560 nm was shifted to 590 nm upon protonation.

The absorption changes of the heteroleptic terpyridine-based PS, **Fe1** and **Fe2**, are shown in Figure 4.15 together with $\mathbf{Fe6_{homo}}$. Again, the absorption properties of the unfunctionalized PS $\mathbf{Fe6_{homo}}$ are not altered by the addition of an acid. A red-shift

of $\Delta\ \lambda = 24$ nm is measured for **Fe1**. This is comparable to the literature value. In contrast, the 554 nm band in **Fe2** is only shifted by 5 nm to 559 nm. Apparently, the pyridine in the **L2** motif is less influenced by protonation which is also true for $\mathbf{Fe2_{homo}}$. Focusing on the 350-450 nm range, it can be seen that the 380 nm band decreases and a band at 419 nm evolves in **Fe1**. In **Fe2**, 378 nm band is slightly reduced and a broad shoulder appears on the red part of this band, indicating same additional feature around 419 nm as in **Fe1**. Absorption changes of tetra-carbene

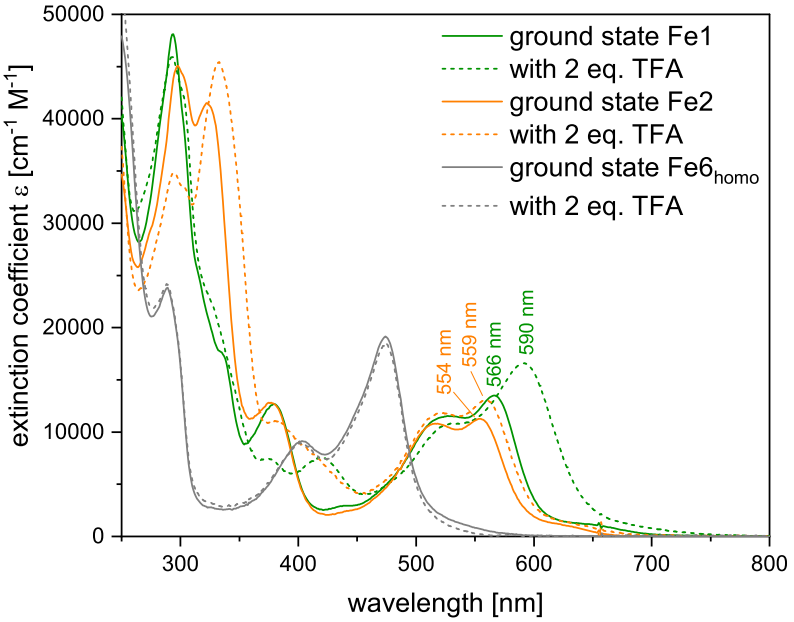

Figure 4.15: Absorption changes upon protonation of iron complexes **Fe1**, **Fe2** and $\mathbf{Fe6_{homo}}$.

iron PS upon addition of TFA are shown in Figure 4.16. Here, the influence of protonation is more pronounced. In **Fe3** a distinct red-shift from 481 nm to 551 nm is observed with $\Delta\lambda = 70$ nm. Moreoever, a third band appears at 439 nm. Most likely, the bridging ligand is involved in the corresponding MLCT transitions. Also, in $\mathbf{Fe3_{homo}}$ the lowest-energy band at 506 nm is shifted to 580 nm ($\Delta\lambda = 74$ nm). The protonated homoleptic iron complex $\mathbf{Fe3_{homo}}$ has not a new feature between 420-440 nm. Apparently, the number of pyridine functionalities is less important because the shifts of either homoleptic or heteroleptic compounds with equal bridging ligand are in the same order. A third example with **C3** confirms no effect of acid addition on pyridine-lacking systems (*cf.*Figure 4.16).

To conclude, pyridine-functionalized iron photosensitizer can be applied as proton probes. Moreover, protonation results into red-shift of absorption bands with dominating bridging ligand contribution as for example the MLCT bands in the red part of the spectrum. Thus, protonation can confirm the bridging ligand as the acceptor state in a CT transition and reveal the small contribution of the bridging ligand to the 380-400 nm band, which is in line with additional contribution of the

terminal ligand **SP**. In particular, tetra-carbene systems are more affected resulting in red-shifts of about 70 nm.
In context of photocatalytic application, proton sensitivity is also an issue since the catalysis can be operated at different pH. This suggests using acidic conditions to improve the absorption of the photosensitizers. However, the catalytic window for an active catalyst has to be kept in mind because its activity also depends on the pH as presented in section 2.5.1.

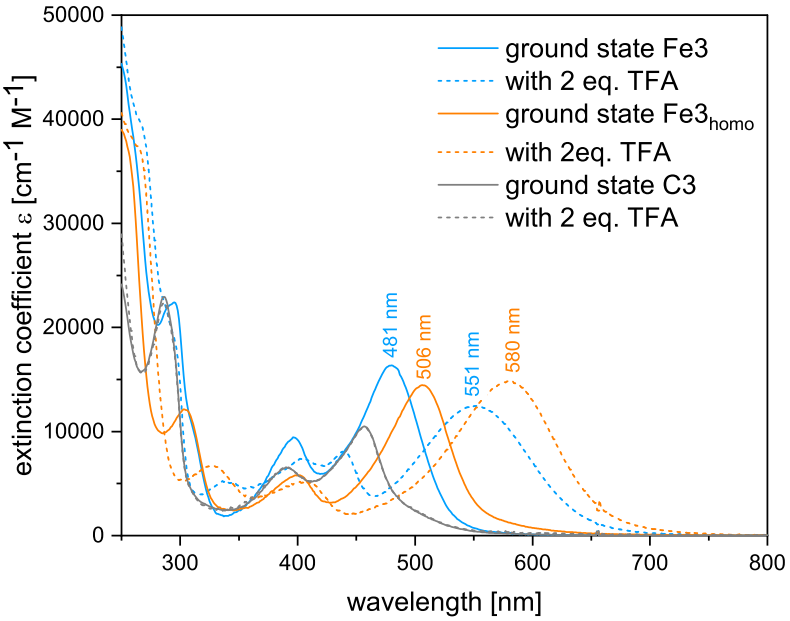

Figure 4.16: Absorption changes upon protonation of tetra-carbene iron complexes **Fe3**, **Fe3$_{\mathbf{homo}}$** and **C3**.

4.3.4 Cyclic Voltammetry

In the last section the energy levels within the iron PS have been discussed on the basis of UV-Vis and (TD)-DFT. Cyclic voltammetry is a complementary method which provides insight into the redox potentials. In turn, redox potentials are a good probe for HOMO and LUMO levels. On the anodic side, metal oxidation takes place. In this particular case, oxidation from Fe^{II} to Fe^{III} occurs. Depending on the redox potentials, the HOMO energy levels can be compared. On the cathodic side, the ligand framework is reduced. The cyclic voltammograms are shown in Figure 4.17 and Figure 4.18. The corresponding redox potentials are listed in Table 4.4. The potentials are referenced against the Fc/Fc^{+} couple.

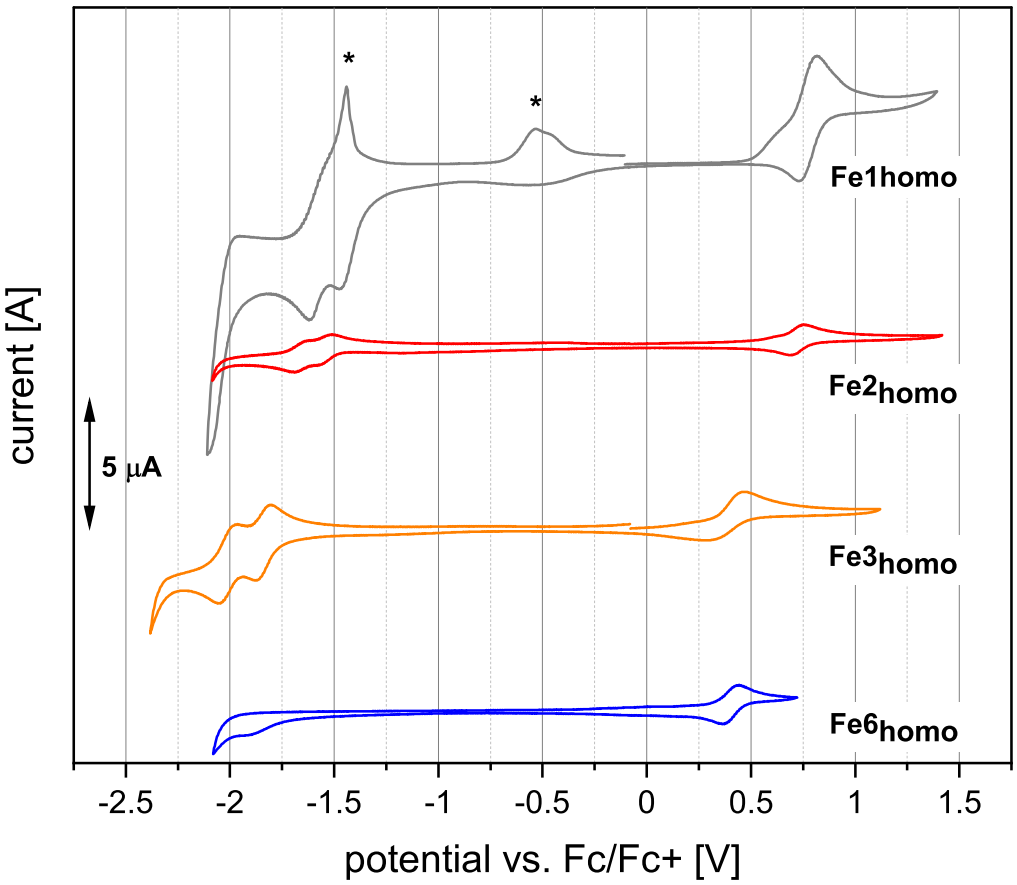

Figure 4.17: Cyclic voltammograms of homoleptic complexes **Fe1$_{homo}$**-**Fe6$_{homo}$** in MeCN ($(n$Bu$_4$N$)$(PF$_6$), 100 mV/s, 1·10^{-3} mol/L). Artifacts are marked with an asteriks.

The homoleptic complexes **Fe1$_{homo}$**, **Fe2$_{homo}$**, **Fe3$_{homo}$** and **Fe6$_{homo}$** can be divided into the terpyridine-based systems and the carbene-based systems. In the former, the redox couple of $Fe^{II/III}$ exhibits a potential of 0.78 V and 0.73 V, respectively. In contrast, redox potentials E(Fe^{II}/Fe^{III}) of **Fe3$_{homo}$** and **Fe6$_{homo}$** are 0.39 V and 0.40 V, respectively. This cathodic shift reflects the increased electron density at the iron centre, making its oxidation easier. Higher electron density is provided by the strong σ-donating NHC ligands. The ligand reduction is partially irreversible

and an energy gap can not be extracted for all homoleptic compounds. Fortunately, comparison of heteroleptic iron PS gives further insights into energetic order of HOMO and LUMO levels.

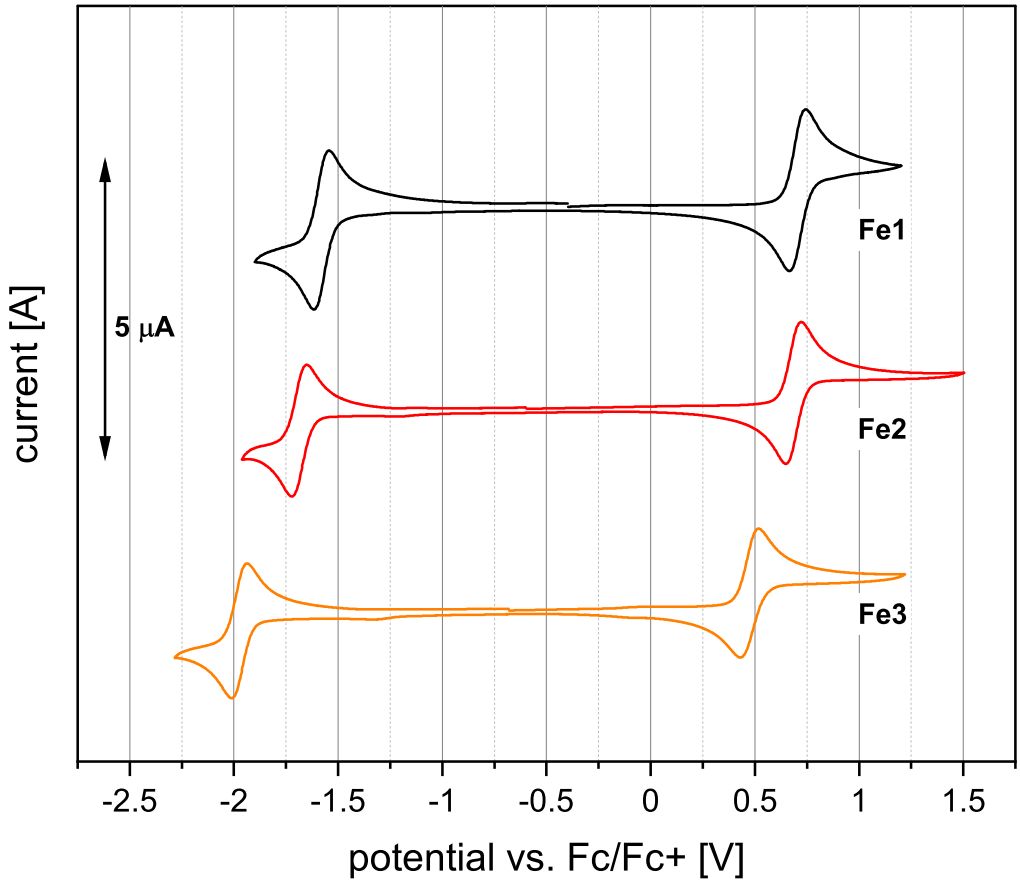

Figure 4.18: Cyclic voltammograms of heteroleptic complexes **Fe1** - **Fe3** in MeCN ($(n\mathrm{Bu_4N})(\mathrm{PF_6})$, 100 mV/s, $1{\cdot}10^{-3}$ mol/L).

First, the redox potentials of $\mathrm{Fe^{II/III}}$ decreases in the order **Fe1**>**Fe2**>**Fe3** (0.62 V, 0.58 V, 0.47 V) (*cf.* Figure 4.18). It suggests reduced π-acceptor ability or increased π-donor ability of **L2** in $\mathbf{Fe2_{homo}}$ and **Fe2** in comparison to the PS containing **L1**, resulting in a higher electron density on the metal centre. Also, the general destabilization (energy increase) of the HOMO levels, as reflected by computed molecular orbital schemes, is confirmed via cyclic voltammetry.
Second, the redox potential of **Fe3** (0.47 V) is anodically shifted relative to $\mathbf{Fe3_{homo}}$ (0.39 V). This can be explained by an improved π-accepting ability due to two coordinated pyridyl rings in the homoleptic PS which act as electron-withdrawing groups.
Third, the ligand reduction in these heteroleptic iron complexes is becoming increasingly difficult in the order **Fe1**>**Fe2**>**Fe3** (-1.67 V, -1.79 V, -1.97 V). This has been also shown by computed molecular orbital schemes in the section 4.3.2 indicating destabilization of the LUMO levels.

Table 4.4: Redox potentials of homoleptic and heteroleptic iron photosensitizers.[a]

entry	$E_{ox}(Fe^{II}/Fe^{III})$ [V]	$E_{red,1}$ [V]	$E_{red,2}$ [V]	ΔE_p [V][b]
$Fe1_{homo}$	0.78			
Fe1	0.62 (r)	-1.67 (r)		2.29
$Fe2_{homo}$	0.73 (r)	-1.53	-1.67	2.26
Fe2	0.58 (r)	-1.79 (r)		2.37
$Fe3_{homo}$	0.39	-1.83 (r)	-2.02	2.22
Fe3	0.47 (r)	-1.97 (r)		2.44
$Fe6_{homo}$	0.40	(ir)		

[a] Measured in MeCN vs. Fc/Fc^+, $1 \cdot 10^{-3}$ mol/L; [b] $\Delta E_p = E_{ox} - E_{red,1}$.

Finally, the calculated energy difference ΔE_p following equation

$$\Delta E_p = E_{ox} - E_{red,1}. \tag{4.1}$$

are increased in the following order **Fe1**<**Fe2**<**Fe3** with 2.29 V, 2.37 V and 2.44 V. This is inline with the blue-shift of the lowest-energy band in the UV-Vis spectra and the increased HOMO-LUMO gaps assessed by DFT. Thus, CV also confirms the possibility of complex modification by variation in ligand design. The following section deals with spectroelectrochemistry. It provides further insights into the redox processes and is the basis for the analysis of transient optical absorption spectra.

4.3.5 Spectroelectrochemistry

The selected heteroleptic complexes **Fe1-3** have been additionally characterized by advanced spectroscopic methods. With spectroelectrochemical measurements the nature of specific bands can be assessed. For example, upon oxidation of Fe^{II} to Fe^{III}, by applying an anodic potential, the system is transferred from d^6 to d^5. In the ground state the iron compound has distinct MLCT bands. However, upon oxidation one electron is missing so that MLCT transitions are less likely. On the contrary, due to the vacancy in the metal d-orbitals LMCT transitions become more likely. This results into absorption changes during bulk oxidation or reduction which are monitored by UV-Vis spectroscopy.

The absorption changes upon bulk oxidation of **Fe1** are shown in Figure 4.19 (top). Metal oxidation takes place at +2.2 V and results in decreasing band intensities at 380, 528 and 565 nm, while two new bands at 417 nm and 591 nm appear in spectrum A_{ox}. Actually, vanisihing of the MLCT bands would be expected. Presumably, the bulk oxidation is not complete and a geometry reorganization can be assumed. A potential of +0.5 V is applied to reduce the oxidized species (*cf.* Figure 4.19(middle)). However, no band shift is observed, only some intensity increase is detected in spectrum $A_{re\text{-}red}$. In conclusion, the bulk oxidation of **Fe1** is irreversible. Therefore, ligand reduction is assessed with a fresh solution of **Fe1**. After applying a potential of -2.3 V the absorption changes are visualized in spectrum A_{red} (*cf.* Figure 4.19(bottom)). The bands are broadened and band maxima are located at 433, 559, 652 and 760 nm. Then, the reduced species is oxidized at 0 V. Probably, the compound decomposes, resulting also in irreversible bulk reduction of **Fe1**.

The spectroelectrochemical measurements of **Fe2** show different results. Bulk oxidation at +1.3 V leads to the disappearance of the MLCT bands (516 nm, 555 nm). Instead, a broad band between 500-800 nm arises with maxima at 571 nm and 627 nm. As explained above, these changes can be explained by the removal of one electron in the d-orbitals resulting in LMCT bands.[103] Full reversibility of the systems is confirmed by re-reduction at +0.53 V. The ground state spectrum A_{gs} and the re-reduced spectrum $A_{re\text{-}red}$ match, although bands at 324 nm and 379 nm are broadenen or slightly increased (*cf.* Figure 4.20 (top)). Ligand reduction at -2.2 V causes the appearance of three new bands (426, 564 and 635 nm) while the ground state bands are vanished as shown in Figure 4.20 (bottom). The new reduced absorption spectrum A_{red} is very similar to A_{red} of **Fe1**, indicating same complex changes upon reduction. Also here, the ligand reduction is irreversible.

The optical absorption behavior of **Fe3** in the ground state A_{gs}, after bulk oxidation A_{ox} and reduction A_{red} is shown in Figure 4.21. Upon metal oxidation at +0.75 V the MLCT bands at 396 nm and 479 nm are vanished, while in parallel broad features

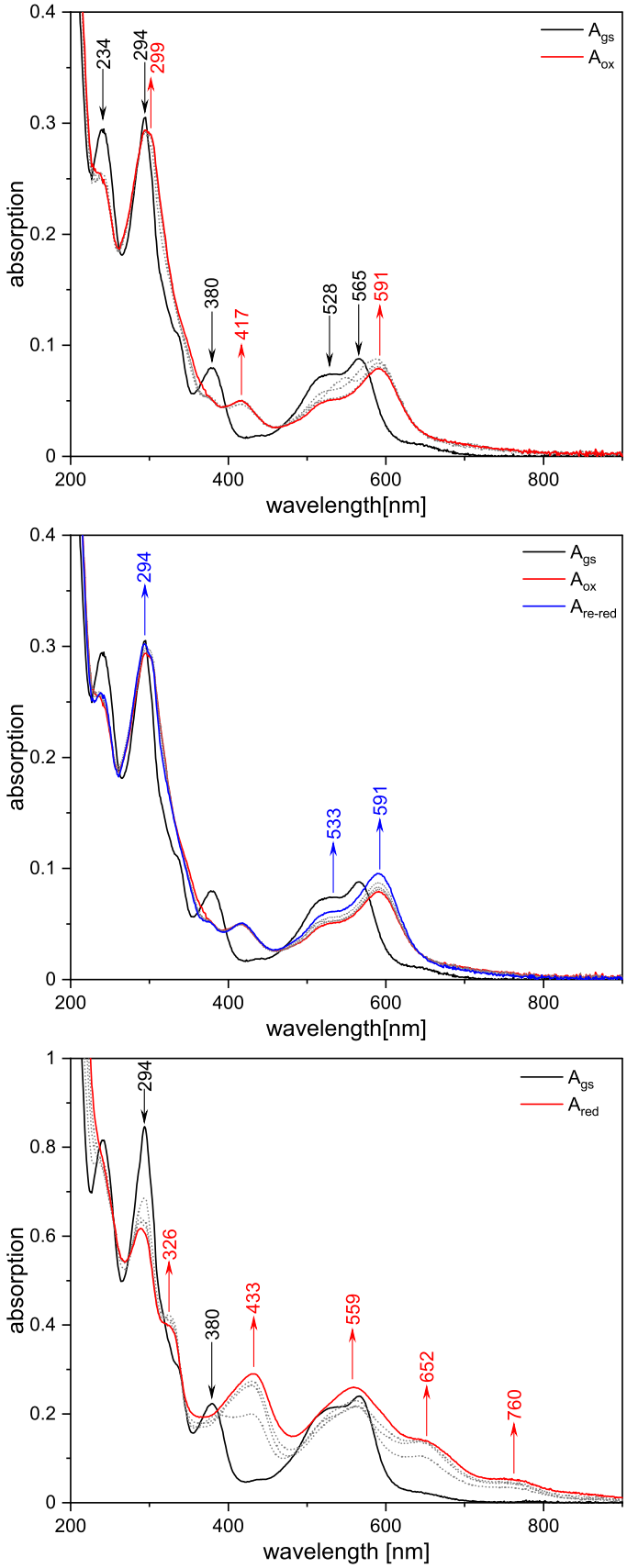

Figure 4.19: Changes in the UV-Vis spectrum of **Fe1** ($1 \cdot 10^{-4}$ mol/L) upon oxidation (A_{gs} → A_{ox} at +2.2 V (top), re-reduction at +0.53 V $A_{re\text{-}red}$ (middle), ligand-based reduction A_{red} at -2.3 V (bottom).

between 515-800 nm are detected, indicating formation of a Fe^{III} species with LMCT bands at 613 nm and 766 nm. Bulk oxidation at +0.5 V is reversible, since the re-reduced absorption spectrum $A_{re\text{-}red}$ overlaps with A_{gs}. A cathodic potential of -2.5 V does not reduce the ligand framework as can be inferred from the absence of any changes of absorption properties (*cf.* Figure 4.21, A_{red}).
Finally, with spectroelectrochemical measurements reversible metal oxidation for **Fe2** and **Fe3** are proven. Most likely, **Fe1** exhibits geometry change after oxidation making the re-reduction unsuccesful and thus, leading to irreversible oxidation of **Fe1**. All ligand reductions are irreversible in the bulk.

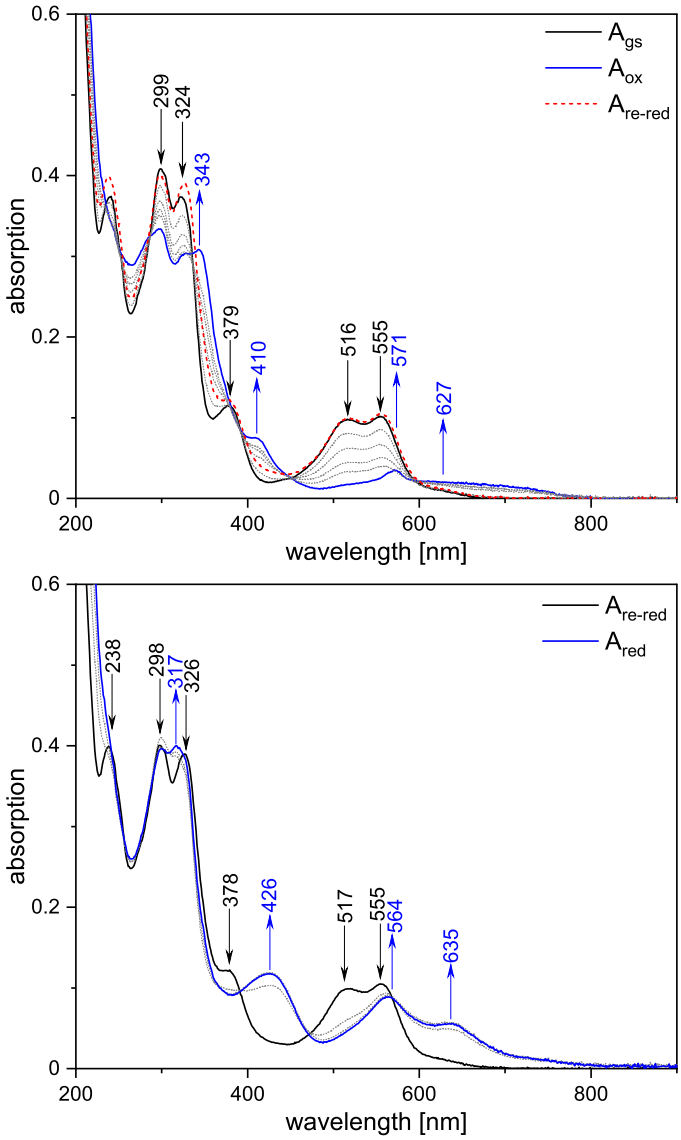

Figure 4.20: Changes in the UV-Vis spectrum of **Fe2** ($1 \cdot 10^{-4}$ mol/L) upon oxidation (A_{gs} → A_{ox} at +1.3 V and re-reduction at +0.53 V $A_{re\text{-}red}$ (top). Ligand-based reduction A_{red} occurs at -2.2 V (bottom).

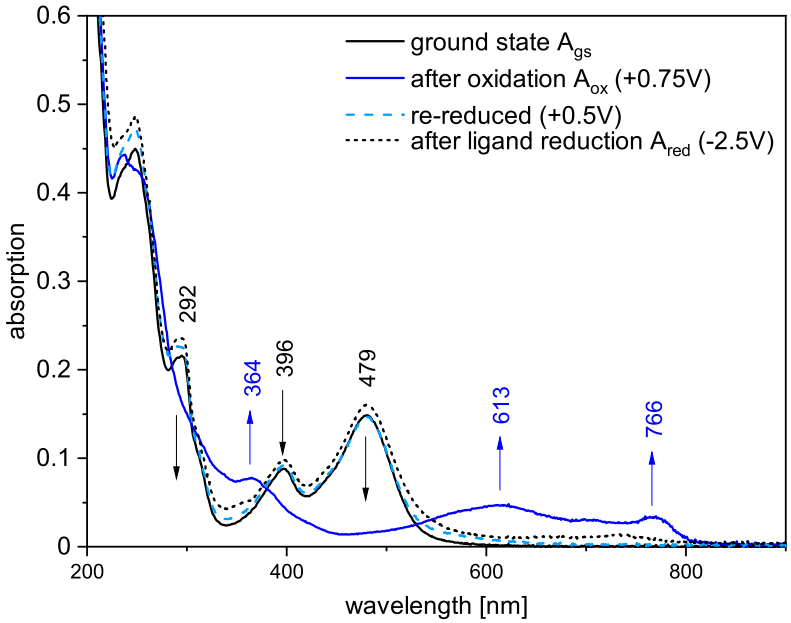

Figure 4.21: Changes in the UV-Vis spectrum of **Fe3** ($1 \cdot 10^{-4}$ mol/L) upon oxidation (A_{gs} $\rightarrow$ A_{ox} at +0.75 V, re-reduction at +0.5 V $A_{re\text{-}red}$ and ligand-based reduction A_{red} at -2.5 V. Adapted from ref.[99]

4.3.6 Chapter summary

Homoleptic and heteroleptic iron complexes have been characterized by complementary spectroscopic methods. The *trans*-angles in tetra-carbene systems is too small for a good octahedral coordination and better metal and ligand orbital overlap. Here, improvements in ligand design are necessary.

Absorption properties have been assessed by UV-Vis spectroscopy and combined with computational analysis via molecular orbital schemes and TDDFT spectra. The HOMO-LUMO gap is increased by increase of σ-donor ligands or introduction of phenyl spacer, resulting in blue-shifts of the MLCT absorption bands. MLCT stabilization is applied by protonation suggesting accurate choice of pH in photocatalytic applications.

The energy gap increase has been confirmed by cyclic voltammetry, especially in the heteroleptic PS **Fe1-3**. Moreover, spectroelectrochemical measurements show reversible metal oxidation, except for **Fe1**, and overall irreversible ligand reduction. Further modification of the physicochemical properties can be realized by the attachement of a second metal.[53,99] In the next chapter dyad and triad synthesis are presented together with the ground state characterization. Additionally, spectroscopic investigation of the multimetal complex stability assessed by NMR and UV-Vis spectroscopy is conducted, as well as further characterization by spectroelectrochemistry and transient optical absorption spectroscopy.

In multimetal complexes the properties of different metals are combined. The synthesis of suitable bridging ligands is a key aspect of proper dyad and triad synthesis (see chapter 3). The connectivity between PS and CAT is realized by the coordination of pyridine with the cobaloxime moiety. This axial monodentate coordination presents us with some challenges which will be adressed in this chapter. A manuscript in preparation includes the results of **Dy1-2**.[98] Published results of **Dy3** can be found here.[99]

5.1 Dyad Complex Synthesis

By using the presented heterolpetic iron complexes **Fe1**, **Fe2** and **Fe3**, multimetal complexes are realized. Since the iron complexes are inert under ambient conditions, there is no need to use inert conditions for dyad or triad synthesis. First, $CoCl_2 \cdot 6\ H_2O$ and dimethylglyoxime are combined in 95% EtOH and warmed to 70°C. To the brown solution **Fe1** or **Fe2** dissolved in DCM are added. Color change to violet is obeserved. After cooling to room temperature, a stream of air is passed through the solution and Et_2O is added. A formed precipation is isolated and washed with 95% EtOH, DCM and Et_2O. **Dy1** and **Dy2** are isolated as violet powders in 90% and 80% yield, respectively.

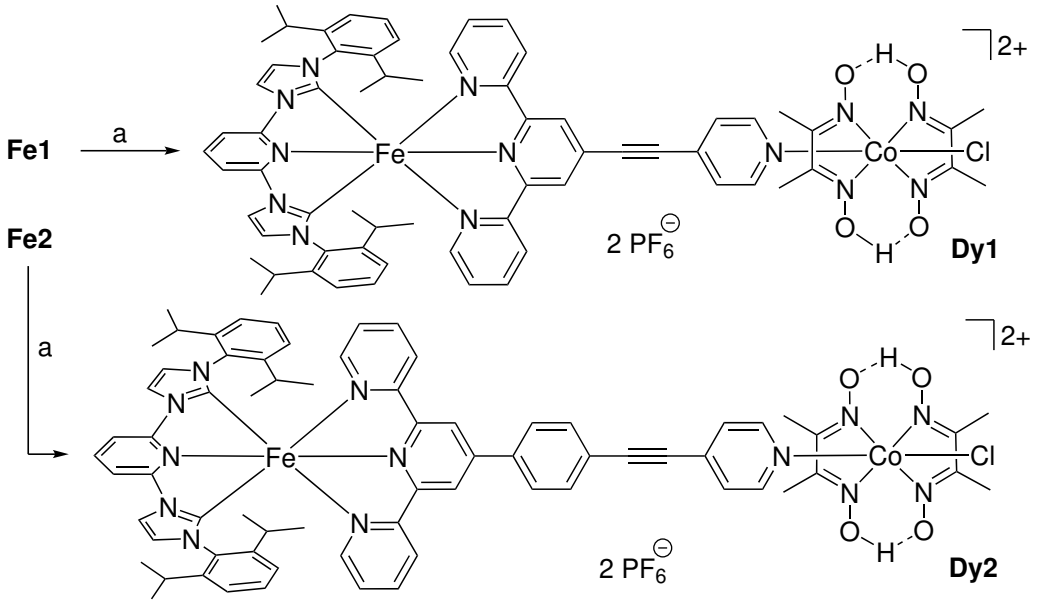

Figure 5.1: Synthesis of **Dy1** and **Dy2**. a) 1) $CoCl_2 \cdot 6\ H_2O$, dimethylglyoxime, 95% EtOH, 70°C, 2) O_2, 30min.

Following this protocol **Dy3** is synthesized accordingly. The passing of oxygen through the solution is elongated to 60 min. Isolation and subsequent washing with EtOH and Et_2O gives **Dy1** in 76% yield.[99]

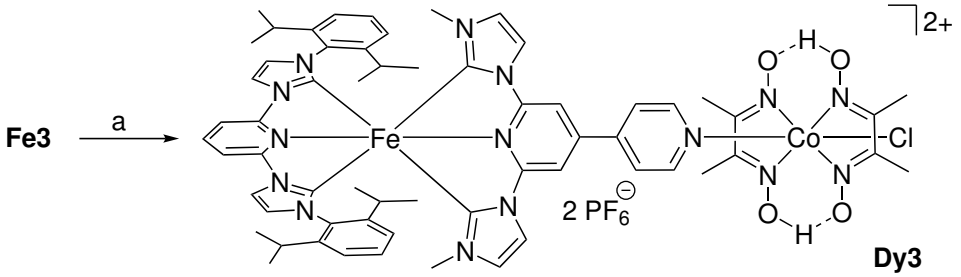

Figure 5.2: Synthesis of **Dy3**. a) 1) $CoCl_2 \cdot 6\ H_2O$, dimethylglyoxime, 95% EtOH, 70°C, 2) O_2, 60min.

5.2 Triad Complex Synthesis

Triads can be synthesized according to the presented protocol above. Using this strategy, **Tri3** is synthesized in 40% yield. Another possibility is the application of a cobalt precursor complex. Both synthesis routes are presented in Figure 5.3. $Co(dH)(dH_2)Cl_2$ is dissolved in MeOH. The addition of one equivalent NEt_3 is used to deprotonate one hydroxide functionality leading to a closed pseudo-macrocycle formed by two dmgH ligands. **L3** suspended in DCM/MeOH is added to the red solution. It turns violet. Then the solution is treated with an air stream causing oxidation of cobalt and the formation of a suspension. The violet product is isolated. Washing with Et_2O gives **Tri3** in 37% yield.

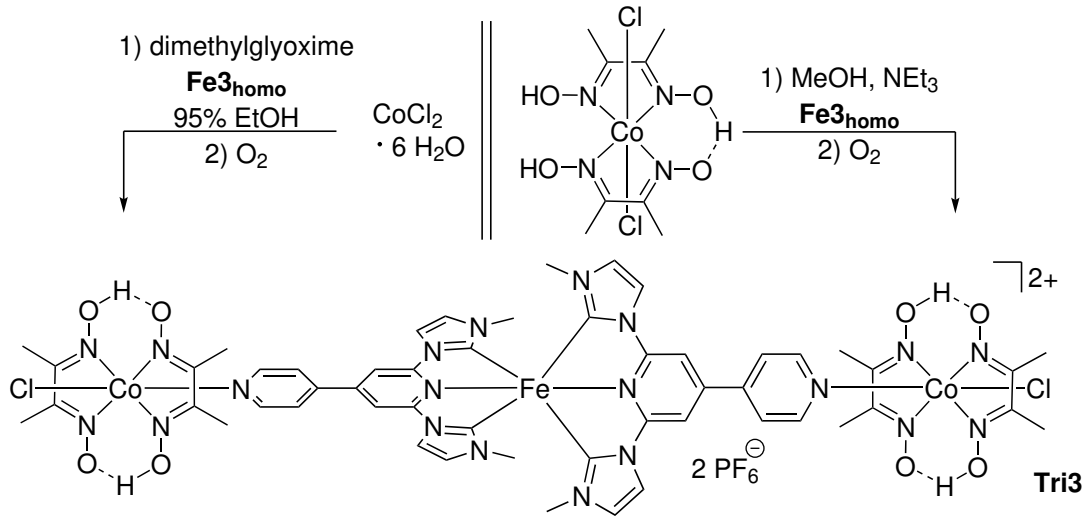

Figure 5.3: Synthesis of **Tri3**.

5.3 Characterization and Properties

The ground state characterization covers XRD, NMR spectroscopy, UV-Vis spectroscopy and CV. Due to the monodentate coordination the dyad stability has to be adressed. This is realized by NMR and UV-Vis spectroscopy. Absorption changes upon protonation are also investigated similar to the iron PS. Finally, the redox behaviour in the bulk via spectroelectrochemistry is discussed. The excited-state dynamics via transient optical absorption are investigated for the heteroleptic compounds **Fe1-3** and the corresponding dyads **Dy1-3**.

5.3.1 Crystal structures

Crystals are obtained by vapour diffusion. Acetonitrile or acetone are used as solvent and Et_2O as anti-solvent. Attempts to obtain crystals of **Dy2** and **Tri3** are not successful. The crystallographic data of **Dy1** and **Dy3** are shown in Figure 5.4 and are listed in Table 5.1.

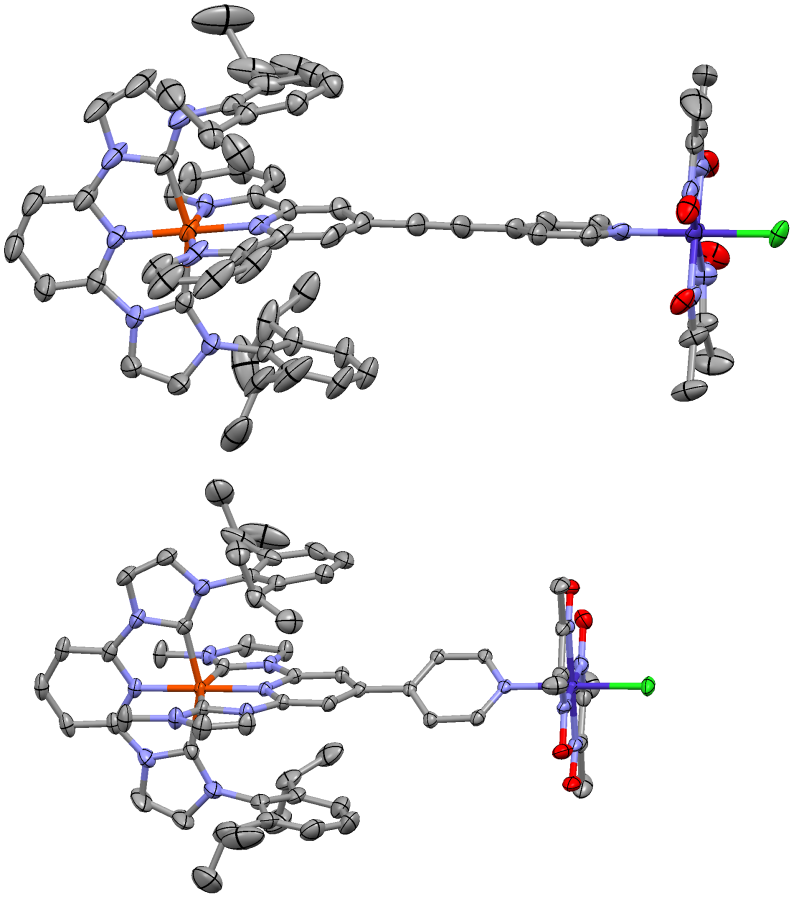

Figure 5.4: Single crystal structure of **Dy1** and **Dy3**. Anisotropic displacement ellipsoids are drawn at the 50% probability level. Hydrogens are omitted for clarity as well as counter ion PF_6^-.

In general, coordination of the PS with the cobalt moiety is confirmed by XRD. The overall coordination geometry of **Dy1** is the same as in **Fe1**. It is a distorted octahedron. The average iron-bridging ligand bond length Fe-BL_{av} of 1.933 Å suggests a stronger bond of **L1** with iron compared to 1.937 Å in **Fe3**. In addition, the intermolecular bond angle N_{ax}-Fe-N_{ax} is slightly improved in the dyad and closer to 180° (178.69°). Also, the $torsion_{triple}$ angle, which is 84.9° in **Fe1** due to packing effects, is drastically reduced to 10.1°. Here, the planarization through acetylene spacer is visible. The Co-N_{py} bond length is 1.964(1) Å. The second axial position is coordinated by the chloro ligand with a Co-Cl distance of 2.227(5) Å. Two dimethylglyoxime ligands form a pseudo-macrocycle with an averaged bond length of 1.897 Å to the cobalt.

Table 5.1: Crystallographic data of **Fe1**, **Dy1**, **Fe3** and **Dy3**.

Bond lenghts [Å] and angles [°]	Fe1	Dy1	Fe3	Dy3
Fe-N_{SP}	1.925(8)	1.934(6)	1.916(2)	1.919(2)
Fe-C_{SP}	1.994(av)	1.990(av)	1.968(av)	1.970(av)
Fe-$N_{BL,axial}$	1.864(1)	1.867(4)	1.915(2)	1.907(2)
Fe-$N_{BL,equat.}$	1.973(av)	1.966(av)		
Fe-$C_{BL,equat.}$			1.950(av)	1.953(av)
Fe-BL_{av}	1.937	1.933	1.938	1.938
C_{SP}-Fe-C_{SP}	158.36	158.68	158.79	158.45
N_{ax}-Fe-N_{ax}	176.24	178.69	176.93	179.86
$torsion_{triple}$	84.9	10.1		
$torsion_{mono}$			43.3	30.6
Co-N_{py}		1.964(1)		1.968(2)
Co-N_{dmgH}		1.897(av)		1.894(av)
Co-Cl		2.227(5)		2.2351(7)

In the following crystallographic data of **Dy3** is discussed. Upon cobalt coordination in **Dy3** the first coordination sphere around the iron center is only slightly affected. The average iron-bridging ligand bond length Fe-BL_{av} stays the same. The intramolecular angle in the terminal ligand **SP**, C_{SP}-Fe-C_{Sp}, is around 158° in both compounds, while the intermolceular bond angle N_{ax}-Fe-N_{ax} is improved to 179.86° compared to 176.93°. Regarding the torsion angle in the bpy motif, it is reduced upon cobalt attachment from 43.4°in **Fe3** to 30.6° in **Dy3**. This is either due to packing effects in the crystal or due to a better electron overlap induced by the second metal. The Co-N_{py} bond length is 1.968(2) Å. The chloro ligand is coordinated in a Co-Cl distance of 2.2351(7) Å. The averaged Co-N_{dmgH} bond length for the nitrogens in the dimethylglyoxime ligands is 1.894 Å.
Comparison between both dyads highlights equal coordination geometry around the

cobalt. However, by comparing the two different metal-nitrogen bonds it is obvious that the Co-N_{py} bond (1.964 Å and 1.968 Å) is elongated in respect to Co-N_{dmgH} (1.897 Å and 1.894 Å). This indicates a weaker bond between the pyridine nitrogen and cobalt, so possible dissociation can be expected at this position. In the following section the dyad stability is investigated via NMR.

5.3.2 Dissociation study by NMR Spectroscopy

According to the weaker cobalt-nitrogen bond connecting PS and CAT a significant risk of dyad dissociation is present in **Dy1-3**. Previous X-ray scattering studies on monodentate Ru-Co dyads have revealed dyad dissociation in coordinative solvents such as MeCN.[104,105] Usually, MeCN is the solvent of choice when physical properties of related iron PS and dyads are studied. Hence, it is important for the following spectroscopic investigations to understand the dyad stability at different concentrations. A concentrated dyad solution (10 mM, MeCN-d_3) is diluted gradually until 0.02 mM. The resulted solutions are measured via ^{1}NMR. Details of the NMR experiment are given in the appendix. In a diluted solution proton signals of PS and dyad are present. Integrals corresponding to each compound and dominant in the aromatic region are chosen for analysis and the mole fraction of the associated dyad as a function of the concentration is obtained. These dissociation curves are presented in Figure 5.5 for **Dy1** and **Dy2**.

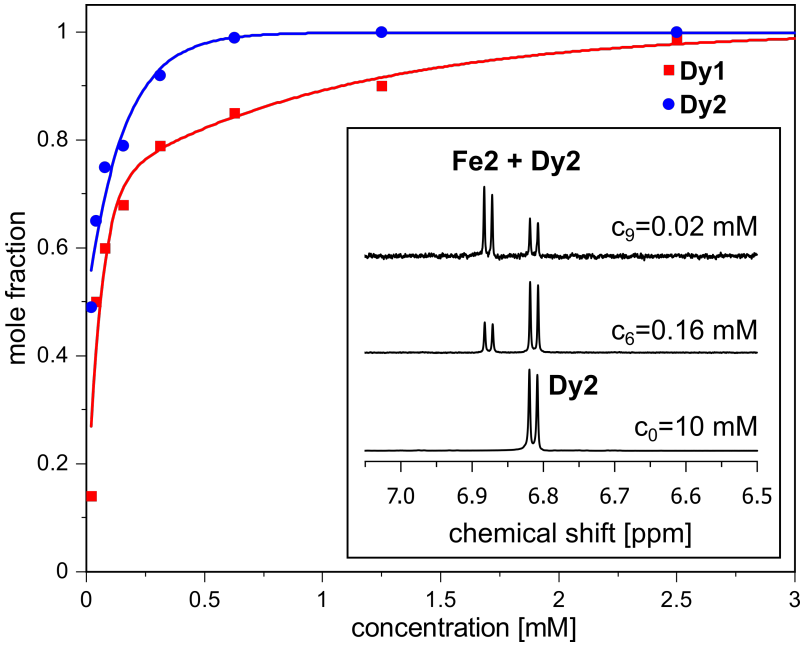

Figure 5.5: Mole fraction of **Dy1** and **Dy2** calculated from proton integral ratio following equation: $f_{dyad} = I_{dyad}/(I_{dyad}+I_{PS})$. $I_{dyad}+I_{PS}$ is proportional to the total amount of species in solution. Inset shows evolution of **Fe2** proton signal (δ = 6.80 ppm) and decrease of dyad **Dy2** signal (δ = 6.78 ppm) in diluted dyad solution.

An inset exemplifies how the dissociation of the dyad shows up in the proton NMR measurements. It shows a ^{1}NMR cut-out of the strongest signal in the spectrum. At 10 mM only the dyad proton signal is present. After dilution a second dublett evolves which corresponds to **Fe2** and is shifted more down-field (c = 0.16 mM). The dubletts correspond to the protons in the diisopropylrings of **SP** in the meta-position. Subsequent dilution up to 0.02 mM leads to dominanting PS signal and

decreasing dyad proton signal. With the dissociation curve the dyad dissociation can be discussed more quantitatively. Both dyads are stable until 3 mM. Dissociation curves until 10 mM can be found in the appendix. Comparison of the dissociation curves shows that the dissociation starts at 2.5 mM for **Dy1** and at 0.6 mM for **Dy2**. Depending on the concentration, **Dy1** dissociates earlier (steeper slope), while **Dy2** is more stable over a larger concentration window. This suggests that the bond between **Fe2** and cobaloxime moiety is stronger compared to **Dy1**. Finally, at 0.02 mM only 14% of **Dy1** and 50% of **Dy2** are intact.

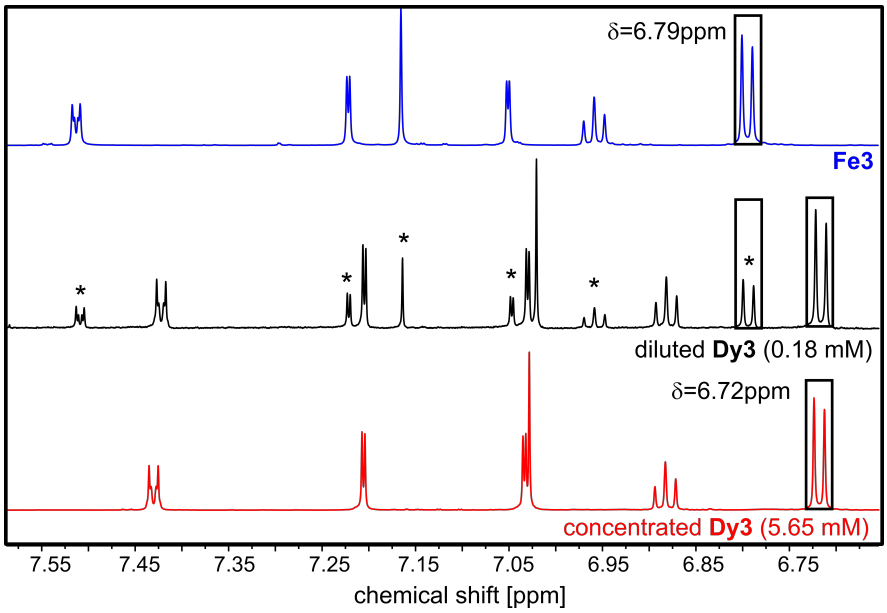

Figure 5.6: Insight into aromatic region of ^{1}H NMR of **Dy3** (concentrated=red, diluted=black) and **Fe3** (blue) in MeCN-d_3. Proton signals in diluted dyad solution originating from **Fe3** are marked with asterisks. Adapted from ref.[99].

Dissociation of **Dy3** is also evaluated by NMR. Again, ^{1}NMR spectra are shown to understand dissociation of the dyad (Figure 5.6) upon dilution. The relevant aromatic region from 7.55-6.65 ppm is chosen for discussion. NMR spectra of **Dy3** at higher (5.65 mM) and lower concentration of 0.18 mM are presented together with a NMR spectrum of **Fe3**. Details can be found in the appendix. As described above, the most intense signals, the dubletts at 6.72 ppm for **Dy3** and at 6.79 ppm for **Fe3**, are analyzed. According to the integral ratio the dissociation curve for **Dy3** is obtained (Figure 5.7). Above 5 mM the dyad is stable (> 95%). Upon dilution, PS proton signals evolve (marked with asteriks in Figure 5.6). At 0.18 mM only 18% of **Dy3** is dissociated. Further decrease of the concentration to 0.02 mM leads to a dissociation of 58%. Hence, only 42% of dyad is present in such a diluted solution.

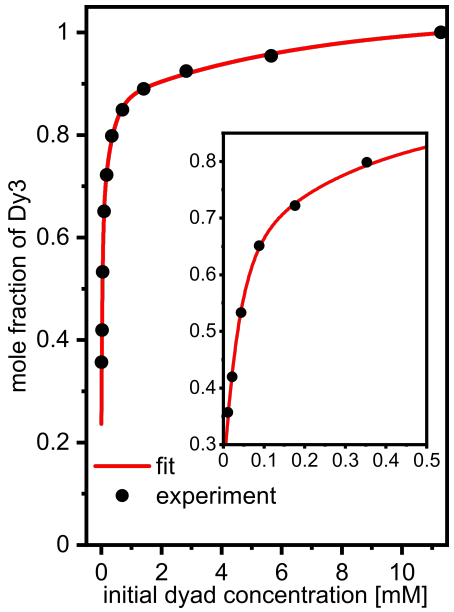

Figure 5.7: Mole fraction of dyad **Dy3** calculated from proton integral ratio (marked with squares in previous figure) following equation: $f_{dyad} = I_{dyad}/(I_{dyad}+I_{PS})$. Total amount of species in solution is proportional to $I_{dyad}+I_{PS}$. Adapted from ref.[99].

Additionally to the investigation of the dyad stability, the triad dissociation behaviour is studied. Here, dissociation of two cobaloxime moieties can happen subsequently. This means three different species are expected in the ^{1}H-NMR spectra. They are illustrated in Figure 5.8 (right).

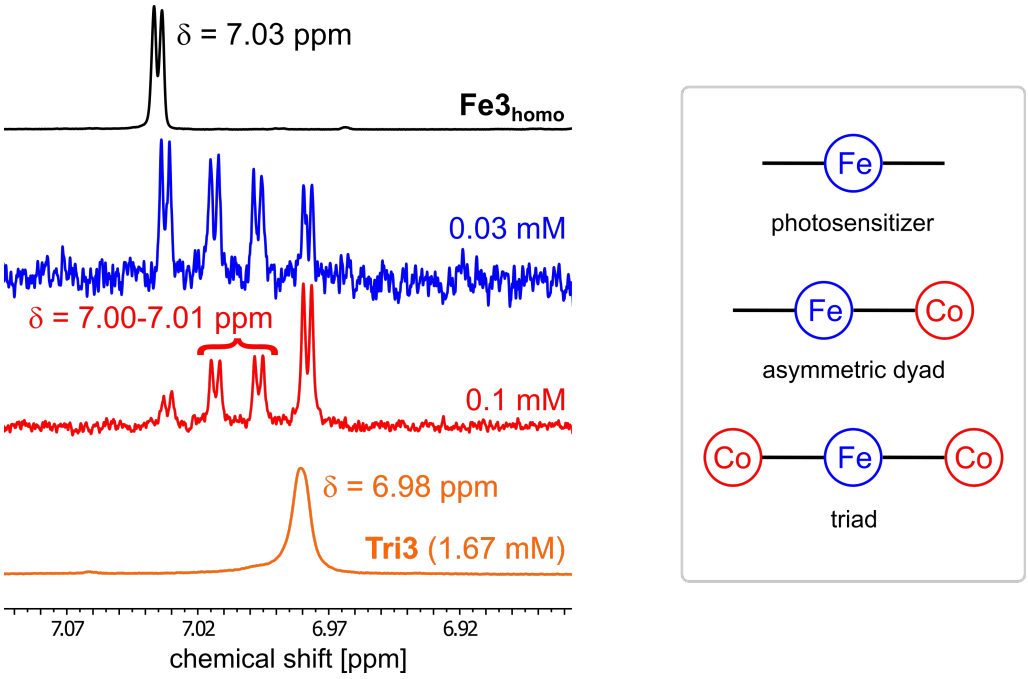

Figure 5.8: Left) Insight into aromatic region of ^{1}H NMR spectra of **Tri3** (concentrated=orange, diluted=red, blue) and $\mathbf{Fe3_{homo}}$ (black) in MeCN-d_3. Right) Schematic structures of compounds present in solution upon triad dissociation: triad, asymmetric dyad and photosensitizer.

As an example, the evolution of NMR signals of triad, asymmetric dyad and fully-dissociated **Fe3$_{\mathbf{homo}}$** between 7.07-6.92 ppm is presented in Figure 5.8 (left). The pure proton spectrum of **Fe3$_{\mathbf{homo}}$** is added for comparison. Due to a lower solubility of **Tri3** in MeCN the concentration range of the NMR study is between 0.013 mM - 1.67 mM. At high concentrations only triad signal, the corresponding imidazolylidene proton is shown here, is visible. After dilution by factor 10 three similar but down-field shifted signals evolve. Protons at 7.00 ppm and 7.01 ppm have the same intensity and are therefore assigned to the asymmetric dyad which has two different ligand sides resulting in a double set of signals. The dublett signal at 7.03 ppm is assigned to **Fe3$_{\mathbf{homo}}$**. It overlaps with the reference spectrum of pure **Fe3$_{\mathbf{homo}}$** (*cf.* Figure 5.8, black). By extracting the integrals the mole fraction f_n of each compound is calculated following this equation:

$$f_{\mathrm{n}} = I_{\mathrm{n}}/(I_{\mathrm{PS}} + I_{\mathrm{dyad}} + I_{\mathrm{triad}}), \tag{5.1}$$

with n = PS, dyad or triad. In Figure 5.9 the mole fraction f_n is plotted against the concentration. At the beginning of the dissociation experiment, at 1.67 mM and 0.84 mM, no dissociation of **Tri3** is observed. Below this concentration, at 0.42 mM, additional signals occur which are assigned to the asymmetric dyad with one cobaloxime moiety dissociated. The concentration of **Tri3** decreases while in parallel more asymmetric dyad is present. The solution at 0.1 mM contains a third component which is assigned to **Fe3$_{\mathbf{homo}}$**. The distribution is 46%, 44% and 10% for **Tri3**, asymmetric dyad and **Fe3$_{\mathbf{homo}}$**, respectively. Upon further dilution, triad dissociates linearly.

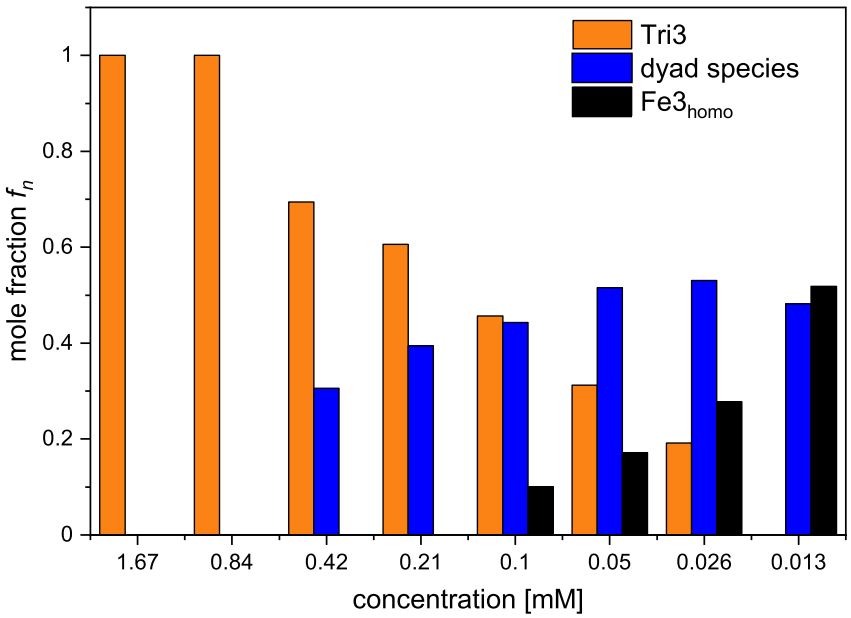

Figure 5.9: Mole fraction of the compounds **Tri3**, asymmetric dyad and **Fe3$_{\mathbf{homo}}$** present in solution upon triad dissociation.

A further increase of the asymmetric dyad is attenuated due to the strong increase of the fully-dissociated species, $\mathbf{Fe3_{homo}}$. Finally, at 0.013 M there is no triad in the solution. Instead, an almost equal distribution of the asymmetric dyad and $\mathbf{Fe3_{homo}}$ is found (48% and 52%).
To conclude, due to the monodentate coordination of PS to the cobaloxime moiety, the multimetal complexes dissociate in diluted acetonitrile solutions. This process is reversible when the concentration is increased again. The dyads are stable in the following order **Dy2**>**Dy3**>**Dy1** at very low concentrations (0.02 mM). **Tri3** is stable over a large concentration range but dissociates into asymmetric dyad and $\mathbf{Fe3_{homo}}$ to different extend depending on the concentration. Consequently, all of the following spectroscopic methods are discussed in terms of the possible dissociation of dyad/triad at setting-dependent concentrations.

5.3.3 UV-Vis Spectroscopy

The absorption properties of the multimetal complexes are as important as the photosensitizer absorption properties for photocatalytic applications. Ground-state UV-Vis spectroscopy is conducted at standard concentration of $1 \cdot 10^{-5}$ mol/L. Deduced from NMR, we know that none of the dyads and triad is completely intact. Hence, due to the dissociation behaviour of the compounds concentration-dependent UV-Vis spectra are recorded. Moreover, absorption changes upon protonation with TFA are studied by UV-Vis.

Ground-state spectroscopy

The absorption properties of the multimetal complexes are discussed in comparison to the PS counterparts. First, the terpyridine-based systems are investigated. In Figure 5.10 the UV-Vis spectra of the photosensitizers and dyads containing either **L1** or **L2** are presented. The absorption maxima and the corresponding extinction coefficients are listed in Table 5.2.

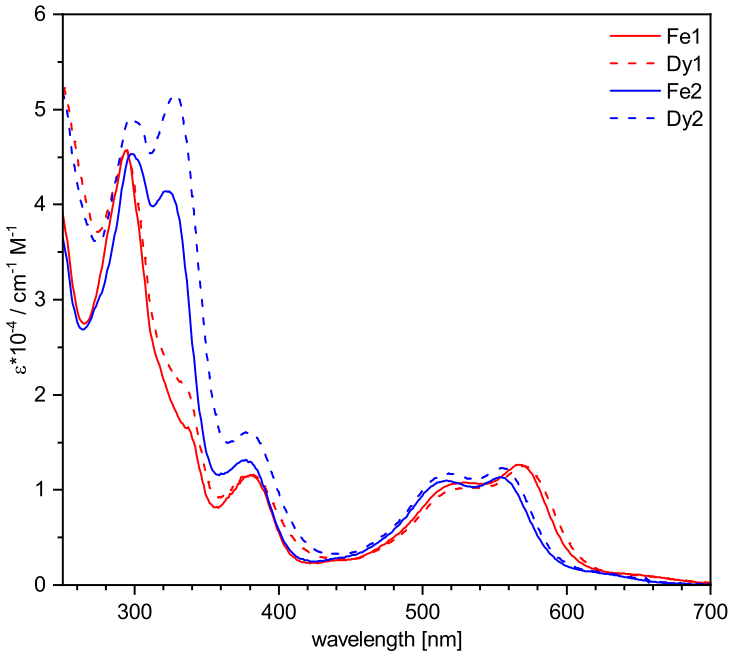

Figure 5.10: Absorption spectra of **Fe1-2** and **Dy1-2** in MeCN at $1 \cdot 10^{-5}$ mol/L.

The absorption pattern can be divided into π-π^*- transitions within the ligand manifolds and MLCT bands with contribution of either the terminal ligand **SP** or the bridging ligand, equal to the assignment for the PS in section 4.3.2. In case of **Fe1** and **Dy1**, the absorption does not change significantly. There is only a minor red-shift of the lowest-energy band from 568 nm to 570 nm. In light of the dissociation study, presumably the main species at a concentration of $1 \cdot 10^{-5}$ mol/L is the photosensitizer. Therefore, spectral differences are only slight. A second

difference is found for the shoulder at 337 nm in the part of the spectrum where π-π^*-transitions dominate. Here, the intensity of the shoulder is increased from 16,700 $cm^{-1}M^{-1}$ to 20,400 $cm^{-1}M^{-1}$.

The comparison of the UV-Vis spectra of **Fe2** and **Dy2** shows the same absorption pattern with differences in peak intensities and overall bathochromic shift of the bands of ~2 nm in the dyad. Also here, the absorption does not change significantly due to the dyad dissociation or due to very similar absorption properties of PS and dyad.

The absorption spectra of carbene-based dyad **Dy3** and triad **Tri3** are shown in Figure 5.11. The corresponding spectroscopic data are presented in Table 5.2. In **Dy3**, the absorption intensity increases for all bands. The MLCT band is broadened and red-shifted by $\Delta\lambda = 5$ nm. Additionally, a shoulder appears at 440 nm which is not present in the corresponding PS spectrum. Again, specific dyad features are difficult to identify due to the advanced dyad dissociation at such low concentration. In case of **Tri3**, the absorption is intensified most probably because of the enlarged molecule which leads to an increased number of transitions within the triad. The MLCT band intensity is increased from 14,500 $cm^{-1}M^{-1}$ to 18,300 $cm^{-1}M^{-1}$ and a significant red-shift of $\Delta\lambda = 10$ nm is detected. The MLCT band is also substantially extended until 750 nm.

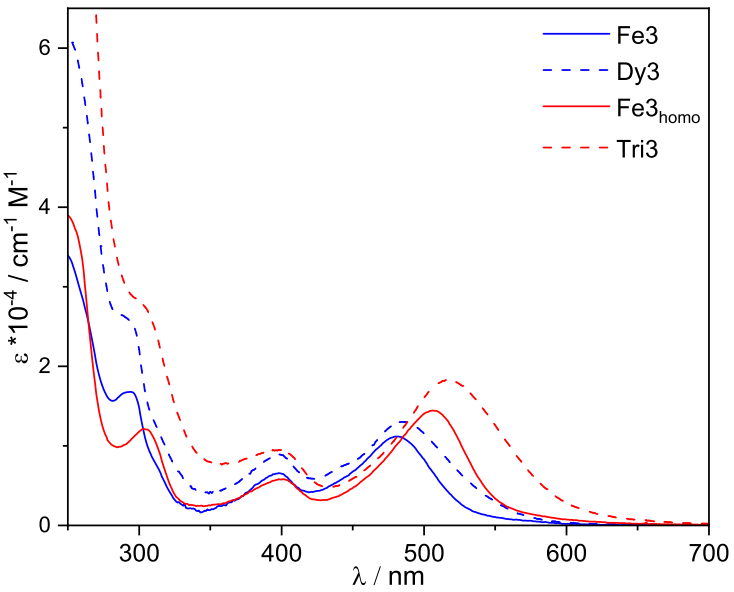

Figure 5.11: Absorption spectra of **Fe3**, $\mathbf{Fe3_{homo}}$ and **Dy3**, **Tri3** in MeCN at $1{\cdot}10^{-5}$ mol/L.

In summary, some changes between PS and the corresponding multimetal complex are identified, however the spectral changes are only manifested in small red-shifts or intensity increase. Therefore, higher concentrated solutions are investigated in a concentration-dependent UV-Vis study.

Table 5.2: Absorption properties of iron photosensitizers **Fe1-3**, **Fe3$_{homo}$** and multimetal complexes **Dy1-3** and **Tri3**.

entry	λ_{abs} [nm]($\epsilon \cdot 10^3$ [cm^{-1}M^{-1}])		
Fe1	293 (45.7), 336 (16.7)	380 (11.6)	528 (10.8), 568 (12.7)
Dy1	294 (45.9), 337 (20.4)	381 (11.8)	528 (10.2), 570 (12.5)
Fe2	299 (45.3), 322 (41.4)	378 (13.1)	517 (11.0), 555 (11.3)
Dy2	297 (49.1), 328 (51.6)	380 (16.1)	518 (11.7), 556 (12.3)
Fe3	294 (16.8)	398 (6.6)	481 (11.2)
Dy3	292 (26.0)	398 (8.9)	486 (13.0)
Fe3$_{homo}$	303 (12.1)	399 (5.8)	506 (14.5)
Tri3	303 (27.7)	398 (9.5)	516 (18.3)

[a] Measured in MeCN at $1{\cdot}10^{-5}$ mol/L.

Concentration-dependent UV-Vis spectroscopy

The samples dissolved in acetonitrile are subsequently diluted and the absorption changes are monitored by UV-Vis spectroscopy. To achieve good signal quality in a static cell (0.1 cm cuvette), only concentration up to $2.5{\cdot}10^{-4}$ mol/L can be used. The absorption properties at different concentrations are plotted for **Dy1-3**. The spectra are normalized with respect to the lowest-energy band to highlight intensity changes upon dilution from $2.5{\cdot}10^{-4}$ mol/L to 3.2 or $1.6{\cdot}10^{-5}$ mol/L (*cf.* Figure 5.12). As deduced from NMR, **Dy1**, **Dy2** and **Dy3** are relative stable at $2.5{\cdot}10^{-4}$ mol/L with 76%, 90% and 76%, respectively.
First of all, the lowest-energy band is located at 576 nm in concentrated dyad solution of **Dy1** which is more red-shifted than in the diluted standard UV-Vis spectrum. Upon dilution the band is blue-shifted to 572 nm. The ratio between the 525 nm and the 576 nm band is changed upon dilution causing an increase of 525 nm band intensity relative to the lowest-energy band. Moreover, a blue-shift of the 380 nm band is observed reflecting a destabilization of involved states upon dyad dissociation. In **Dy2** spectral changes are not significant. Bands at 519 nm and 556 nm are not shifted upon dilution. Only the 380 nm band already assigned to transitions located at the iron side is enhanced relative to the other bands.
The absorption changes of **Dy3** upon dilution from $2.5{\cdot}10^{-4}$ mol/L to $3.2{\cdot}10^{-5}$ mol/L are shown in Figure 5.12 (bottom). At a high concentration, the evolved shoulder at 440 nm in the standard UV-Vis spectrum is clearly distinguishable from the broad band around 497 nm. It flattens upon reducing the concentration. In addition, the lowest-energy band (497 nm) is shifted by 11 nm compared to the diluted spectrum with a band maximum at 486 nm and it becomes narrower. The blue-shift of this band can be followed upon dilution and highlights the stabilization of the dyad formation and the consequence of dyad dissociation.

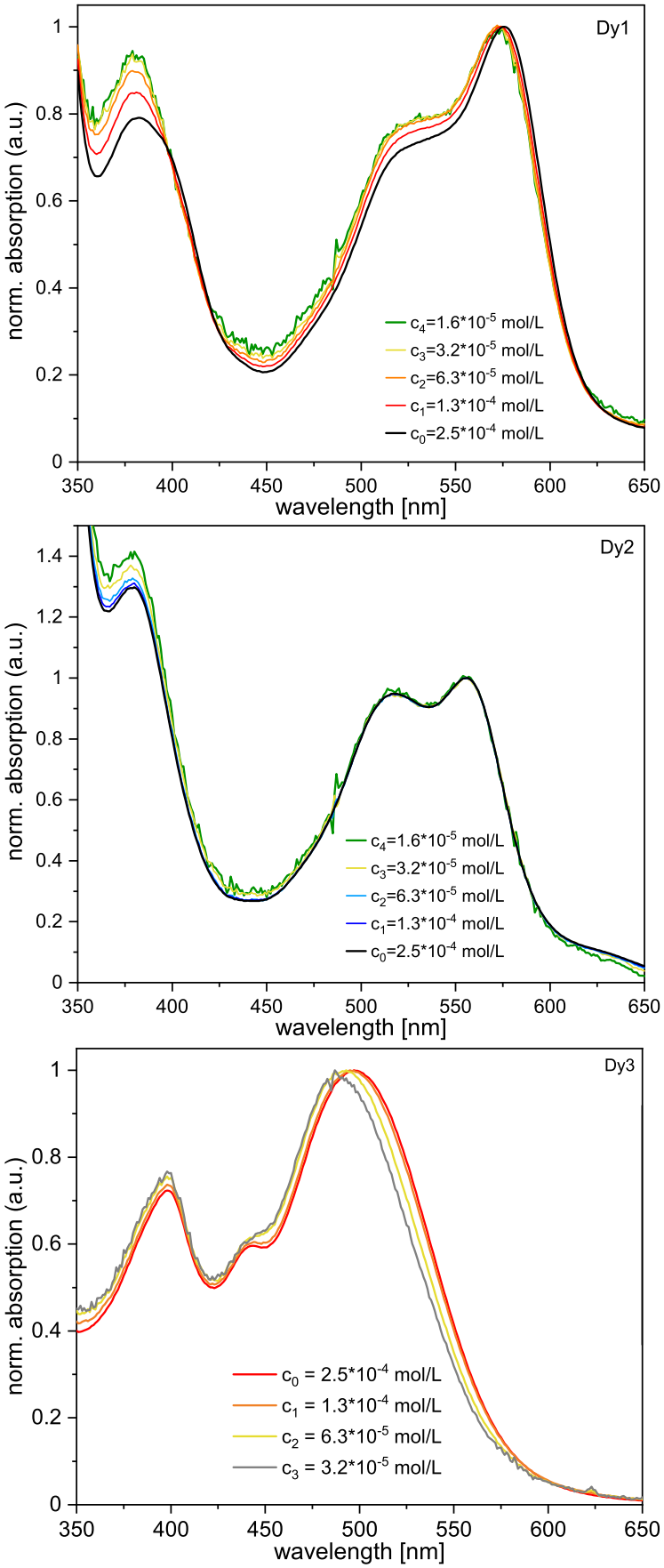

Figure 5.12: Absorption spectra of **Dy1-3** in MeCN at $2.5 \cdot 10^{-4}$ mol/L till $3.2 \cdot 10^{-5}$ mol/L or $1.6 \cdot 10^{-5}$ mol/L.

In the following, the pure dyad spectrum of **Dy3** without the PS influence is simulated. At each concentration the PS spectrum according to the mole fraction dedcued from NMR is subtracted from the dyad spectrum following equation

$$\Delta\epsilon = \epsilon_{\mathrm{Dy3}} - f_{\mathrm{n}} \cdot \epsilon_{\mathrm{Fe3}}. \qquad 5.2$$

As a result, very similar difference spectra are obtained with three main bands in the MLCT region (*cf.* Figure 5.13). While the MLCT bands at 398 nm and 440 nm are not shifted in the simulated spectra the lowest-energy band is clearly shifted to ~510 nm. The calculated difference spectra represent the absorption properties of **Dy3** without photosensitizer contribution very well. Since the spectral changes of **Dy1-2** are less pronounced, the simulated spectra are not examined.

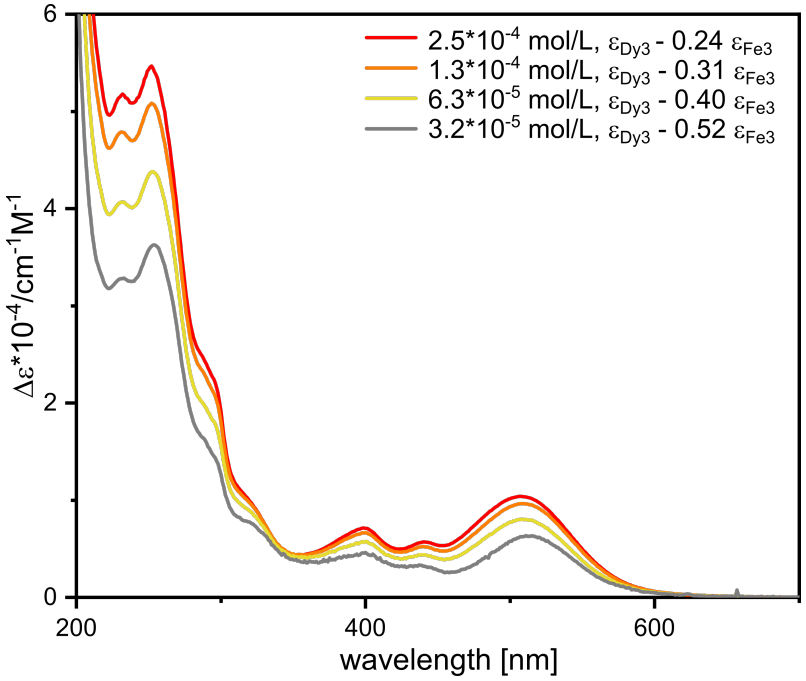

Figure 5.13: Difference absorption spectra of **Dy3** in MeCN at $2.5{\cdot}10^{-4}$ mol/L till $3.2{\cdot}10^{-5}$ mol/L simulated by calculating $\Delta\epsilon = \epsilon_{\mathrm{Dy3}}\text{-}f_n \cdot \epsilon_{\mathrm{Fe3}}$.

Protonation studied by UV-Vis spectroscopy

Regarding the dissociation behaviour of the multimetal complexes, it is interesting to investigate the spectral changes upon protonation with TFA. Since at regular UV-Vis concentration, all multimetal complexes are partially dissociated, a red-shift due to the protonation of the free pyridine functionality belonging to the PS is expected. Note, without a pyridine moiety no absorption shift occurs as shown by $\mathbf{Fe(terpy)_2}^{2+}$ and **C3**.

The absorption spectra of **Dy1-3** and **Tri3** are shown in Figure 5.14. Upon protonation of **Dy1** with TFA, below 350 nm no significant changes are observed, while

the band at 381 nm is reduced and has a shoulder around 410 nm. In addition, the 570 nm band is red-shifted to 586 nm. In **Dy2**, a π-π*-band around 295 nm is attenuated and a minor red-shift is visible.

The carbene-based multimetal complexes are more strongly affected by protonation equal to the photosensitizer counterparts (*cf.* section 4.3.3). In **Dy3**, the band around 400 nm is red-shifted ($\Delta\lambda = 4$ nm). Moreover, the lowest-energy band of **Dy3** (486 nm) is red-shifted by $\Delta\lambda = 48$ nm. Due to the red-shift from 486 nm to 534 nm the rise of a third band at 440 nm becomes visible. It is equal to the band which can be identified in higher concentrated dyad solutions (*cf.* Figure 5.12 (bottom)).

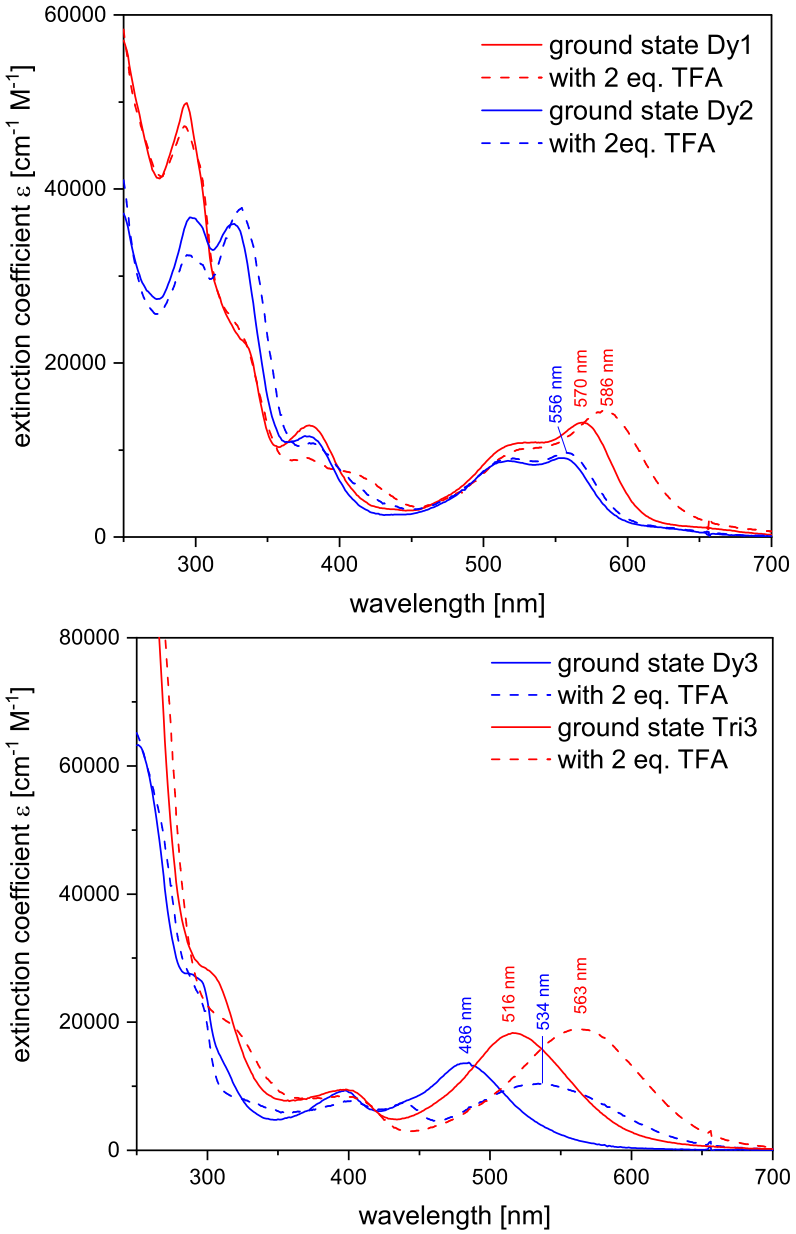

Figure 5.14: Absorption changes of **Dy1-2** (top) and **Dy3**, **Tri3** (bottom) in MeCN upon protonation with TFA.

In this context, a third band (439 nm) is also detected in the spectrum of protonated **Fe3**. Thus, protonation or cobaloxime coordination stabilizes the same states that enable additional MLCT transitions around 440 nm for **Fe3** and **Dy3**.
In **Tri3**, the shoulder around 300 nm is slightly reduced and the band around 400 nm is slightly flattened. A wavelength difference of $\Delta\lambda = 47$ nm can be found for the lowest-energy feature upon addition of the acid which results in better π-acceptor ability of the bridiging ligand.[46] Here, no band appears at 440 nm which is also true for $\mathbf{Fe3_{homo}}$ and the other homoleptic iron complexes $\mathbf{Fe1_{homo}}$, $\mathbf{Fe2_{homo}}$ and $\mathbf{Fe6_{homo}}$. This suggests that the terminal ligand **SP** might be involved in the bands at 420 or 440 nm.
To conclude, photosensitizers and multimetal complexes react differently to the addition of an acid. As a comparison, the red-shifts of the lowest-energy band are listed in Table 5.3. In each case, the absorption properties of the multimetal complexes are less affected compared to the PS. This is in agreement with the concentration-dependent NMR study which has revealed partial dissociation of the multimetal complex at low concentrations. While available photosensitizer molecules are protonated, intact dyad or triad molecules are not protonated because the pyridine moiety is coordinated by cobaloxime. Overall the concentration of free PS is lower compared to the pure PS solutions and hence the red-shift is less pronounced. Presumably, at very high concentrations no absorption changes are expected upon protonation of **Dy1-3** and **Tri3**, since dissociation does not occur.

Table 5.3: Red-shift $\Delta\lambda$ of selected complexes upon protonation.

compound	red-shift
Fe1	24 nm
Dy1	16 nm
Fe2	5 nm
Dy2	1 nm
Fe3	70 nm
Dy3	48 nm
$Fe3_{homo}$	74 nm
Tri3	47 nm

Investigation of absorption properties by theoretical calculations

As discussed above, the absorption properties of PS can be tuned by protonation or cobalt coordination. However, the dissociation of multimetal complexes at UV-Vis standard conditions poses a major challenge to measure the real signature of dyad or triad absorption. In this regard, further insights are provided by theoretical calculations. First, molecular orbital schemes of **Dy1-3** are extracted from single-point energy calculations and compared with the PS counterparts. They are visualized

in Figure 5.15. The energy gaps are indicated by arrows and the energy difference is given in eV and transferred to the wavelength equivalent for better comparison with the UV-Vis spectra. The average Fe 3d character is included for dπ, dπ* and dσ* orbitals in % and average Co 3d character for dπ and dσ* orbitals.

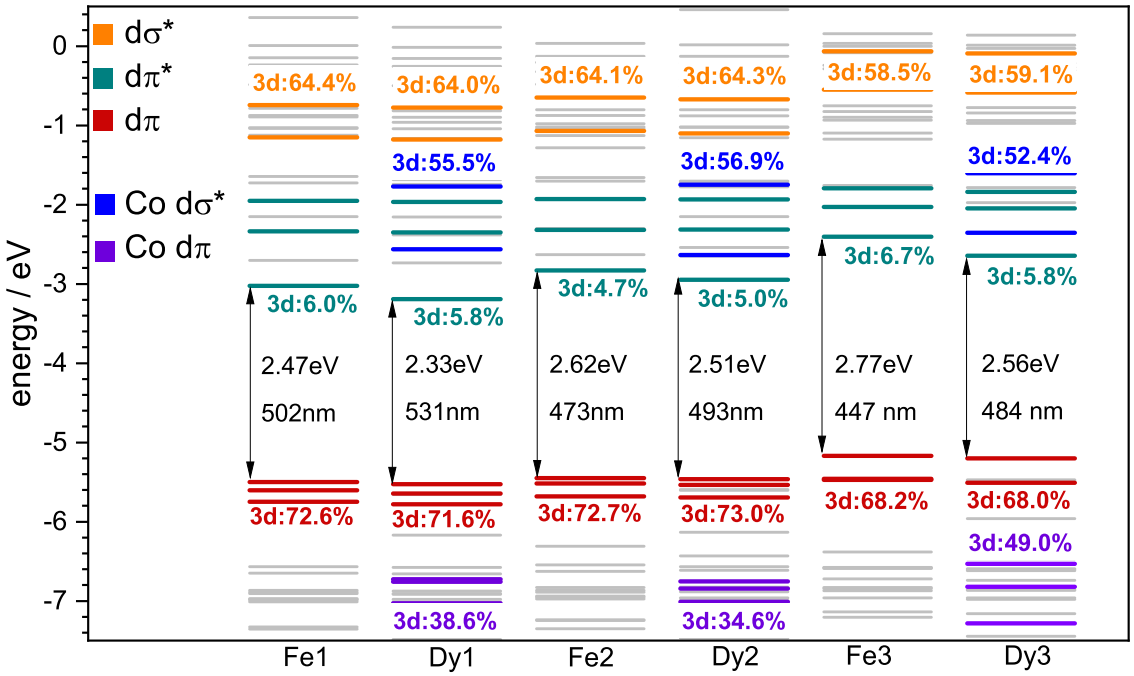

Figure 5.15: Molecular orbitals of **Fe1-3** and **Dy1-3** extracted from single point energy calculations; TPSSh, def2-TZVP(P), CPCM/SMD (MeCN). HOMO-LUMO gaps are indicated (eV/nm). The average Fe 3d and Co 3d character is included for dπ, dπ* and dσ* orbitals in %.

As with the photosensitizers, the highest-occupied molecular orbital (HOMO) is mainly metal-based ($\%Fe_{Dy1}$ = 71.6% and $\%Fe_{Dy2}$ = 73.0%) with a reduced metal character in **Dy3** ($\%Fe_{Dy3}$ = 68.0%). This indicates a higher covalency in tetra-carbene systems compared to terpyridine systems. The lowest-unoccupied molecular orbital (LUMO) is mainly ligand-based with a minor iron 3d character between 5.0-5.8%. The e_g*-like dσ*-orbitals have a %Fe of 64.0% (Dy1), 64.3% (Dy2) and 59.1% (Dy3). Three t_{2g}-like Co dπ orbitals are energetically below the iron *dπ* orbitals. Their average Co 3d character is 38.6% and 34.6% in **Dy1** and **Dy2**, respectively, suggesting a high covalency within the cobaloxime moiety. In **Dy3**, the average Co 3d character is 49.0%. The related Co dσ*-orbitals have a reduced metal character compared to the Fe dσ*-orbitals with 55.5%, 56.9% and 52.4%.
The red-shift of the lowest-energy band in the dyad spectra is qualitatively reflected by DFT calculations. Here, in the dyads the LUMO levels are stabilized resulting in smaller HOMO-LUMO gaps. As deduced from the molecular orbital scheme, the cobalt coordination affects the HOMO-LUMO energy differently. A stabilization of 0.11 eV is found for **Dy2** which translates to an expected red-shift of 20 nm.

Experimentally the absorption changes are only subtle. Upon cobalt coordination in **Dy1**, the stabilization of the LUMO levels is expressed by a reduction of 0.14 eV equal to $\Delta\lambda = 29$ nm. Again, the experimentally-detected red-shift is only 2 nm. The reduced HOMO-LUMO gap in **Dy3** suggests a red-shift of 37 nm (*cf.* Figure 5.15). In the standard UV-Vis spectrum a red-shift of 5 nm is found.
As suggested by theoretical calculations, the stabilization upon cobalt coordination is stronger than identified in the UV-Vis spectra at $1{\cdot}10^{-5}$ mol/L. Taking the concentration-dependent UV-Vis spectra into account, the terpyridine-based dyads still show a low stabilization effect upon cobalt coordination. On the contrary, the simulated spectrum of **Dy3** with a band maximum around 510 nm has a red-shift of $\Delta\lambda \approx 30$ nm, which is in good agreement with the proposed theoretical red-shift of 37 nm.
The spectral assignment of the bands is assessed by TDDFT. The experimental and TDDFT spectra of **Dy1-3** are shown in Figure 5.16. A detailed analysis of all relevant singlet transitions are in the appendix.
TPSSh-TDDFT succeeds in describing all relevant bands with partial deviation in their energetic position or intensities for **Dy1**. The experimental and computational spectra of **Dy1** are compared in Figure 5.16 (top). Band A which correlates to the lowest energy band around 570 nm results from a MLCT transition from Fe(II) to the bridging ligand **L1**. Also, the band at 528 nm is described by the blue-shifted transition B with MLCT character. The dominant acceptor orbitals are located on **L1** with spatial distribution on the iron-coordinated pyridine ring and the imidazolylidene rings or extended until the terminal pyridine ring. The absorption band at 381 nm can be described by band C, which is slightly red-shifted. Singlet transition analysis reveals transition from the cobaloxime moiety to the bridging ligand. MLCT transitions with iron involvement, which have been previously assigned to this band, are missing for band C. Donor orbitals are composed of Co dπ orbitals with 40% metal 3d character, hence these transitions can be assigned as MLCT from Co to **L1** (*cf.* appendix for details). In addition, LMCT transition from dmgH ligand framework to Co is found. In comparison, LMCT transition are also present in the reference cobaloxime, which supports this assignment.[53] Based on the TDDFT results of **Fe1**, the 381 nm band is also characterized by MLCT transitions from iron to the ligand manifold. The band at 294 and the shoulder at 335 nm are described by band D. It is dominated by inter- and intraligand π-π^* transitions within the bridging ligand **L1**.
The TDDFT and experimental spectra of **Dy2** are shown in Figure 5.16 (middle). In the red part of the spectrum only one band A covers the two main bands at 518 nm and 556 nm. The underlying transitions are very similar to the transitions A and B in **Dy1** only the energetic splitting is reduced resulting in the presences of one band A.

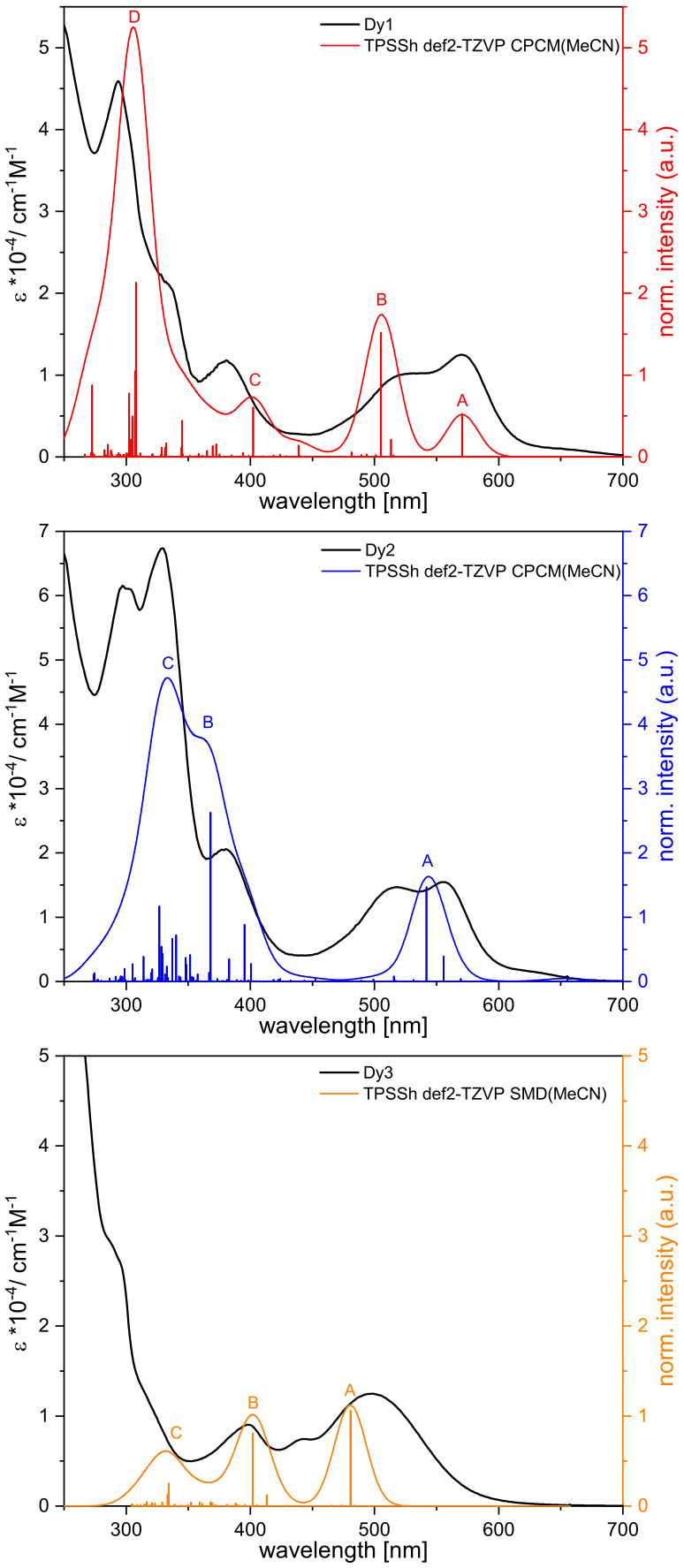

Figure 5.16: Experimental and computational spectra of **Dy1** (red), **Dy2** (blue) and **Dy3** (orange); TPSSh, def2-TZVP, SMD(MeCN) or CPCM(MeCN).

Since the other terpyridine-based PSs and dyad are well-described by TPSSh, this functional is also used for **Dy2**. In line with the assignment for **Fe2**, bands between 510-560 nm are best described by MLCT transitions from iron to **L2**. The band at 380 nm is represented by transition B, which originates from π-π* transitions within the bridging ligand. Also, the cobaloxime moiety is involved here as donor for the π-π* transition to **L1**. Furthermore, the band B is influenced by a strong singlet transition at 368 nm. It is characterized by MLCT transitions from iron to **L2** and π-π* transitions within the bridging ligand. Ligand-based π-π* transitions below 350 nm are confirmed by band C. Around 330 nm a LMCT transition theoretically occurs which is also present in **Dy1** and the reference cobaloxime. However, this result is questionable, because donor orbitals orginate from **SP** and the acceptor orbitals are located within the cobaloxime framework.
In **Dy3**, the ligand-based transitions below 300 nm are not covered within the theoretical calculations due to a lower number of computed states. The concentrated UV-Vis spectrum of **Dy3** is chosen for comparison (*cf.*Figure 5.12). TPSSh-TDDFT resolves three bands A-C, which qualitatively describe the experimental spectrum except the specific feature at 440 nm induced by cobalt coordination. The absorption around 500 nm is reflected by the blue-shifted band A. It originates from a charge transfer from iron to the bridging ligand **L3** and a smaller contribution to the cobaloxime moiety. It could be tentatively assigned as MMCT between both metals. This feature would be unique among the presented dyads. The band B reflecting the absorption at 398 nm is dominated by MLCT transition to **SP**. Again, a minor contribution (14%) is a mixture between MLCT to **L3** and to the cobaloxime moiety (MMCT). Finally, the band C covers the beginning of the intense band below 350 nm and reflects π-π^* transitions.
To conclude, the experimental absorption properties of multimetal complexes have been characterized in dependency of concentration and protonation. Computed molecular orbital schemes have given insight into the energetic order of HOMO and LUMO states as well as their nature (Fe 3d and Co 3d character). Additionally, the observed transitions have been assessed by TDDFT. By that, the MLCT character of the lower-energy bands has been confirmed. However, TPSSh-TDDFT has failed in fully describing the absorption properties of **Dy2** and **Dy3**.

5.3.4 Cyclic Voltammetry

Afer the investigation of energy levels within multimetal complexes on the basis of UV-Vis and DFT, the redox potentials of these compounds will be studied via cyclic voltammetry. The cyclic voltammograms are added in Figure 5.17. The potentials are referenced against the Fc/Fc^+ couple. The dissociation of dyads and triads is not considered because the measurements are performed at $1 \cdot 10^{-3}$ mol/L and thus all multimetal complexes are more than 90% intact. In addition to two redox events in the photosensitizer, the multimetal complexes exhibit three additional redox events originating from the cobaloxime moiety. The same redox events occur in the reference cobalt catalyst, cobaloxime **C14**. The redox potentials are added in Table 5.4. The redox event on the anodic side of the cyclic voltammogram at 0.73 V is assigned to a reversible ligand oxidation of the dmgH framework.[53] On the cathodic side, an irreversible $Co^{II/III}$ reduction occurs at -1.04 V, which leads to the dissociation of the chloro ligand.[75] Subsequently, a more cathodic potential (-1.50 V) leads to the second reduction of cobalt from Co^{II} to Co^{I}.

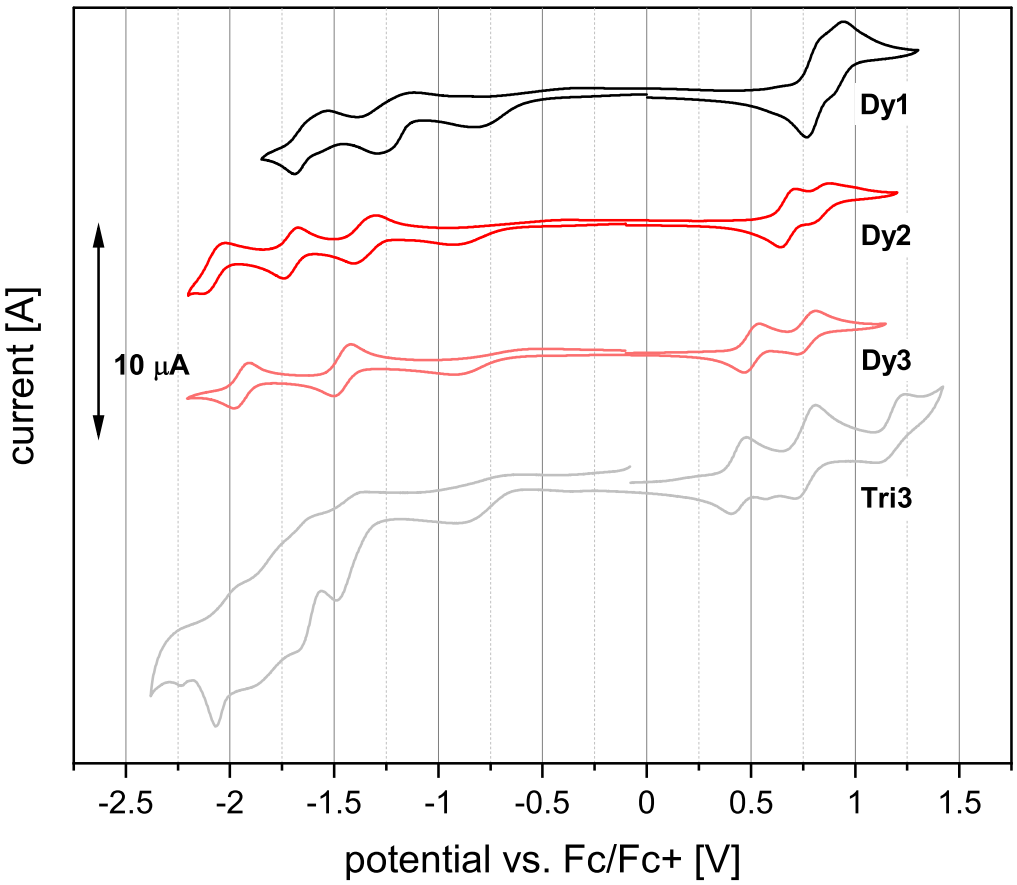

Figure 5.17: Cyclic voltammograms of multimetal complexes **Dy1** - **Dy3** and **Tri3** in MeCN ($(n\mathrm{Bu_4N})(\mathrm{PF_6})$, 100 mV/s, $1 \cdot 10^{-3}$ mol/L).

In case of **Dy1**, the ligand oxidation is anodically shifted from 0.73 V to 0.76 V compared to **C14** indicating lower electron density on the dmgH manifold. The

iron oxidation is found at 0.63 V compared to **Fe1** (0.62 V, *cf.* Table 4.4). Thus, the electron density is shifted away from iron upon dyad formation suggesting a mild effect of cobalt on the PS redox potential. The ligand reduction is cathodically shifted from -1.67 V in **Fe3** to -1.79 V. Hence, the ligand reduction is more difficult which is induced by the cobalt coordination. Consequently, the electron density on the bridging ligand is increased due to the cobaloxime bond. The energy gap is increased to 2.42 V (Δ(Fe3)=2.29 V). This is in contrast to the reduced optical band gaps extracted from UV-Vis spectroscopy upon cobalt coordination. Also, stabilization of LUMOs are not reflected by the increased energy gap.

Table 5.4: Redox potentials of iron-cobalt dyads **Dy1-3** and triad **Tri3**. Corresponding photosensitizer redox potentials in square brackets.[a]

entry	$E_{Lig,ox}$ [V]	$E_{ox}(Fe^{II/III})$ [V]	E_{red}(Co) [V]	$E_{Lig_{Fe},red}$ [V]	ΔE_p [V][a]
Dy1	0.76	0.63(r) [0.62]	-0.98(ir), -1.38	-1.79(r) [-1.67]	2.42 [2.29]
Dy2	0.74	0.57(r) [0.58]	-1.01(ir),-1.46(qr)	-1.81(r) [-1.79]	2.38 [2.37]
Dy3	0.77(r)	0.50(r) [0.47]	-0.91(ir), 1.46(qr)	-1.94(r) [-1.97]	2.44 [2.44]
Tri3	0.76 (r)	0.44(r) [0.39]	-0.87(ir)		
C14[b]	0.73 (r)		-1.04(ir), -1.50(qr)		

[a] Measured in MeCN vs. Fc/Fc^+, $1{\cdot}10^{-3}$ mol/L; [a] $\Delta E_p = E_{Fe,ox} - E_{Lig_{Fe},red}$, [b] Taken from ref.[53].

In **Dy2**, the iron oxidation is slightly cathodically shifted upon dyad formation (0.58 V to 0.57 V), indicating a destabilization of the HOMO, which is different to the **Fe1**/**Dy1** couple and contrary to the DFT results. The three redox events related to the cobaloxime moiety are located at very similar potentials compared to **C14** (0.74 V, -1.01, -1.46 V). The reversible ligand reduction occurs cathodically-shifted at -1.81 V. The energy gap ΔE_p is 2.38 V for **Dy2**.

The cyclic voltammogram of **Dy3** exhibits five redox events. On the anodic side, dmgH oxidation at 0.77 V and $Fe^{II/III}$ oxidation at 0.50 V occur. The lower Lewis basicity of **Fe3** compared to pyridine in **C14** results into lower electron density of the cobaloxime moiety. In agreement with DFT, the HOMO levels are stabilized upon cobalt formation, resulting in the anodic shift of iron oxidation. On the cathodic side, the dyad is reduced. At -0.91 V the irreversible $Co^{II/III}$ reduction is combined with the chloro ligand loss.[75] Subsequently, cobalt is further reduced to Co^{I} in a quasi-reversible event at -1.46 V.[106] The reversible ligand reduction assigned to the bipyridine motif in the **L3** framework is anodically shifted to -1.94 V ($E_{Lig_{Fe},red}$(Fe3)=-1.97 V), thus confirming the improvement of the π-accepting capability of the bridging ligand in the dyad. To summarize, the electron density are shifted from the dmgH pseudo-macro cycle and iron to **L3** and the cobalt side. The energy gap is the same for **Fe3** and **Dy3**

Due to overlapping redox events on the cathodic side in **Tri3** only the dmgH oxi-

dation, iron oxidation and first irreversible Co reduction could be quantitatively analysed. On the anodic side, dmgH oxidation occurs at 0.76 V suggesting stabilization of the dmgH π orbital energy levels. $Fe^{II/III}$ redox potential is cathodically shifted to 0.44 V leading to a stabilization of the metal-based HOMO levels in **Tri3** upon twofold coordination of cobaloxime compared to $\mathbf{Fe3_{homo}}$ (0.39). The first irreversible cobalt reduction $Co^{II/III}$ is drastically shifted from -1.04 V to -0.87 V. This indicates easier reduction of the cobalt moieties which is equal to stabilization of the cobalt-based e_g*-like dσ*-orbitals.
The iron redox potentials in most of the multimetal complexes are anodically shifted which highlights the stabilization of the iron-based HOMO energy level upon cobalt coordination. Moreover, the cobalt-based reduction is facilitated suggesting the stabilization of the cobalt-based anti-bonding energy levels and reflecting better π-accepting capability of the photosensitizer compared to the pyridine ligand in **C14**. Overall, the reduction of the HOMO-LUMO energy gap, as deduced from UV-Vis spectroscopy and DFT, is not confirmed by CV.

5.3.5 Spectroelectrochemistry

The bulk redox properties of **Dy1-3** are assessed by spectroelectrochemistry. The measurements are conducted at $1 \cdot 10^{-4}$ mol/L with expected dyad dissociation rates of 37%, 26% and 34% for **Dy1**, **Dy2** and **Dy3**, respectively. Due to very similar UV-Vis spectra of PS and dyad counterpart of **Dy1-2** (*cf.* section 5.3.3) the dyad dissociation is not adressed. In case of **Dy3**, effects of dyad dissociation are discussed.

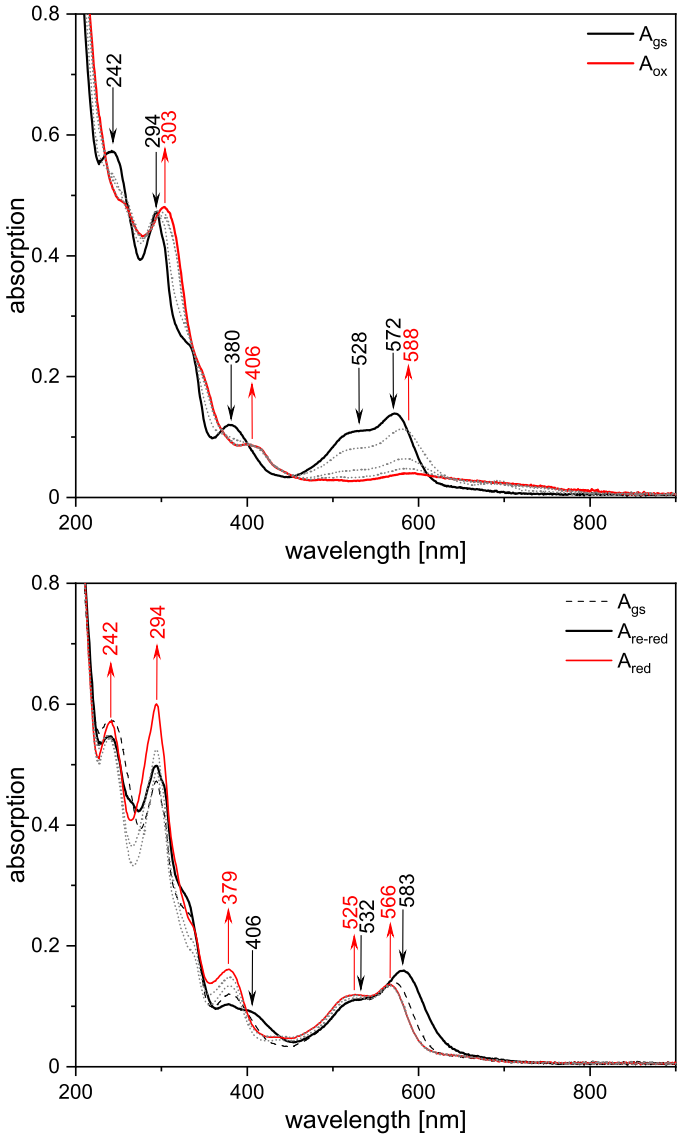

Figure 5.18: Changes in the UV-Vis spectrum of **Dy1**($1 \cdot 10^{-4}$ mol/L) upon oxidation (A_{gs} $\rightarrow$ A_{ox} at +0.9 V (top), re-reduction at +0.65 V $A_{re\text{-}red}$ and ligand-based reduction A_{red} at -1.43 V (bottom).

The spectral changes upon bulk oxidation and reduction of **Dy1** are presented in Figure 5.18. **Dy1** is oxidized in the bulk at +0.9 V. The MLCT bands at 528 nm and 572 nm are vanished and a broad signal from 500-800 nm with a maximum at 588 nm evolves, which is assigned as LMCT band in spectrum A_{ox}.[103] Applying a potential

of +0.53 V reduces the oxidized species again and the resulted absorption spectrum $A_{re\text{-}red}$ matches the ground state absorption A_{gs} partially. The lowest-energy band is shifted to 583 nm compared to 570 nm in A_{gs}. Also, the band at 379 nm is attenuated and broadened with an additional shoulder at 406 nm. In general, these spectral changes are very similar to the absorption changes upon protonation of **Dy1**. Most likely, re-reduction and protonation of **Dy1** stabilize the same states in the dyad which promote the additional absorption features. Bulk oxidation is referred to as reversible. Further ligand reduction results in A_{red} which matches A_{gs} except the increased bands at 294 nm and 379 nm. In contrast to **Fe1**, the bulk ligand reduction is not irreversible at -1.43 V. Instead, no significant spectral changes are detected at all.

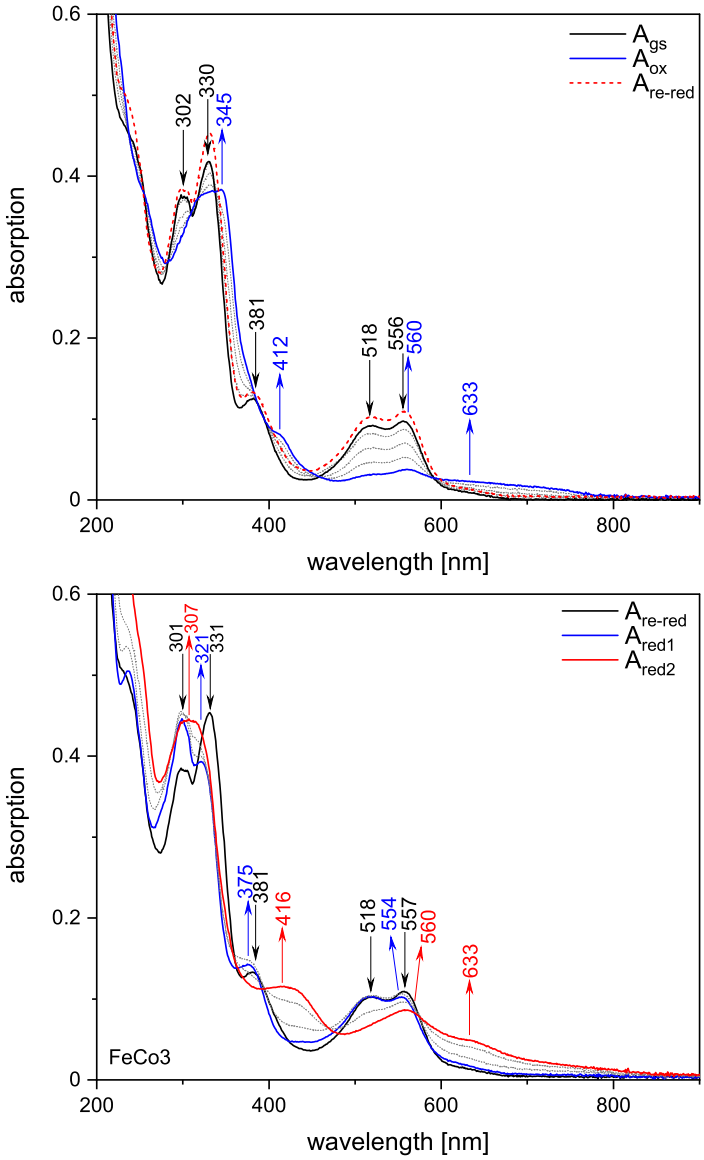

Figure 5.19: Changes in the UV-Vis spectrum of **Dy2** ($1{\cdot}10^{-4}$ mol/L) upon oxidation (A_{gs} → A_{ox} at +0.9 V and re-reduction at +0 V $A_{re\text{-}red}$ (top). Ligand-based reduction A_{red} occurs at -1.86 V (A_{red1}) and at -2.2 V (A_{red2}) (bottom).

The spectral changes upon bulk oxidation and reduction of **Dy2** are presented in Figure 5.19. The rise of LMCT bands (560 nm and 633 nm) in parallel with the decreasing MLCT bands occurs also in **Dy2** at +0.9 V. The reversibility of bulk oxidation at 0 V is confirmed by overlapping spectra of A_{gs} and $A_{re\text{-}red}$. Spectral changes upon bulk reduction at -1.86 V are shown in A_{red1}. Most notably, the ligand-based bands between 300-330 nm change their intensity. Further ligand reduction at - 2.2 V leads to the decomposition of **Dy2** as apparent from A_{red2} in Figure 5.19.

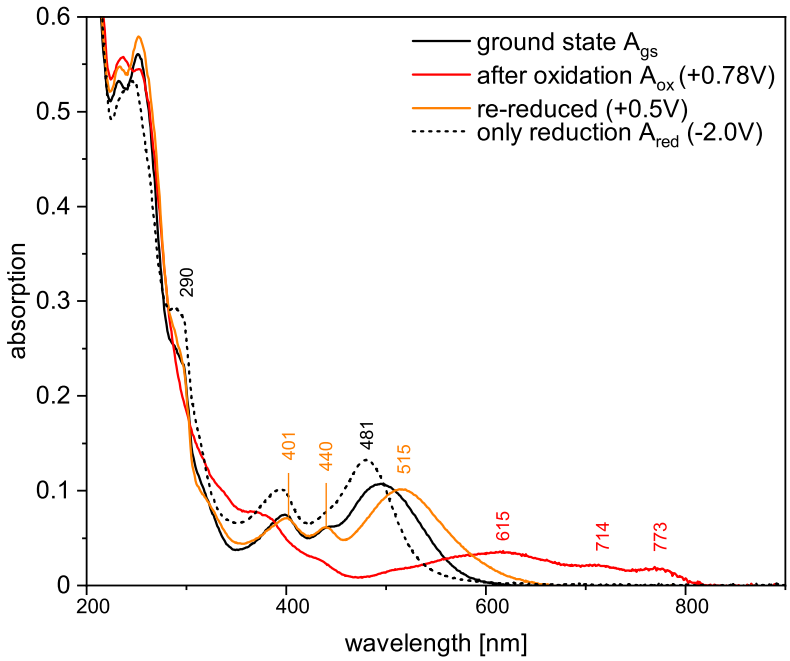

Figure 5.20: Changes in the UV-Vis spectrum of **Dy3** ($1 \cdot 10^{-4}$ mol/L) upon oxidation ($A_{gs} \rightarrow A_{ox}$ at +0.78 V, re-reduction at +0.5 V $A_{re\text{-}red}$ and ligand-based reduction A_{red} at - 2.0 V. Adapted from ref.[99]

The spectral changes upon bulk oxidation and reduction of **Dy3** are presented in Figure 5.20. Applying a potential of 0.78 V oxidizes Fe^{II} to Fe^{III} resulting in vanishing of MLCT bands at 440 and 486 nm. At the same time, characteristic broad LMCT bands appear with maxima at 615 nm, 714 nm and 773 nm as shown in A_{ox}. As deduced from CV, more than one electron can be removed at a potential of +0.78 V. Then, the oxidized species is reduced at +0.5 V. The corresponding spectrum $A_{re\text{-}red}$ features three bands above 350 nm. The bands at 401 nm and 440 nm corresponds to the bands in A_{gs}. However, the lowest-energy band is red-shifted from 486 nm to 515 nm. The strong red-shift is comparable with the absorption spectrum of **Dy3** at higher concentrations and the simulated spectrum of the dyad. Thus, the spectrum reflects a higher concentration of re-assembled dyad upon re-reduction compared to the starting conditions of the experiment before bulk oxidation with an expected dyad dissociation 34%. A fresh solution is used for the ligand reduction at -2 V. The absorption spectrum A_{red} have only two signals between 350 - 500 nm

with a lowest-energy band at 481 nm. Thus, the reduced spectrum is similar to the ground-state spectrum of **Fe3**. No reduction occurs at such cathodic potential, which is also true in **Fe3**.
Finally, with spectroelectrochemical measurements reversible metal oxidation for **Dy1-3** is proven. The ligand reduction are unsuccessful in the bulk indicating decomposition to the respective photosensitizers. Transient optial absorption data,[103] of the heteroleptic compounds **Fe1-3** and the corresponding dyads **Dy1-3** will be discussed in the following.

5.3.6 Transient optical absorption spectroscopy

Excitation after light absorption can range from tens of femtoseconds to a few nanoseconds. The investigation of ultrafast processes needs laser pulses with femtosecond duration. With ultrafast transient absorption (TA) spectroscopy photophysical and photochemical reactions can be studied.[107] Also, the lifetime of catalytically-active states of the photosensitizer is an important parameter in photocatalytic applications and affects the hydrogen evolution drastically. The measurement start with the excitation of several molecules into an excited state by a pump pulse. After a time delay of τ relative to the pump pulse a white light probe pulse is applied. Two spectra are generated, with (A_{pump}) and without the pump pulse (A_{gs}). From this spectra, a difference spectrum ΔA is calculated following

$$\Delta A = A_{\text{pump}} - A_{\text{gs}}. \tag{5.3}$$

The variation of the delay time τ gives a kinetic profile with decaying transient signal. Then, lifetimes valuable for relaxation process assignment are extracted by global analysis procedures.[107] A typical difference absorption spectrum ΔA has a region of positive residual absorption, called induced absorption, caused by absorption changes of excited molecule (excited-state absorption, ESA) or absorption of a formed photoproduct. Negative absorption, termed bleach, occurs due to the reduced population of the initial ground state by the pump pulse (ground-state bleach, GSB) or due to stimulated emission. Typically, for iron(II) complexes the strong ESA signal is assigned to a ^{3}MLCT state. MC states can not be followed by this method because these transitions are Laporte and spin-forbidden.[108] Thus, the spectroscopic signature is very weak, spectroscopic silent or overlaps with the ESA bands corresponding to the excited MLCT states.[108,109] In general, TA spectroscopy is suitable for studying the lifetime of MLCTs due to its high sensitivity to these excited states.

TA spectra of the heteroleptic complexes and the corresponding dyads are collected in cooperation with the Haacke group (**Fe1, Fe2, Dy1, Dy2**) and Gawelda group (**Fe3, Dy3**).[99] The investigation of the excited-state dynamics is conducted in acetonitrile a typical solvent to study excited-state lifetimes of iron d^6 photosensitizers. The terpyridine-based compounds have been measured at $1.5 \cdot 10^{-3}$ mol/L. To circumvent dyad dissociation the carbene-based PS and dyad have been measured at $1 \cdot 10^{-2}$ mol/L. Details of TA data analysis for **Fe3** and **Dy3** can be found here.[99]

First, the dynamics of the terpyridine-based systems are investigated. The results are based on the interpretation from B. Marekha and S. Haacke.[110] Further details can be found in the manuscript in preparation.[98] For that, a pump pulse around 550 nm is used and the probe pulse covers the spectral range from 365 - 680 nm. In Figure 5.21 the transient absorption data of **Fe1-2** and **Dy1-2** in MeCN are shown

in a 2D colormap where the probe wavelength λ_{probe} is plotted against the delay time τ. Negative signals (bleach) are shown in blue whereas positive ones (excited-state absorption) are in red. In general, all 2D colormaps are very similar in the spectral and temporal domains.

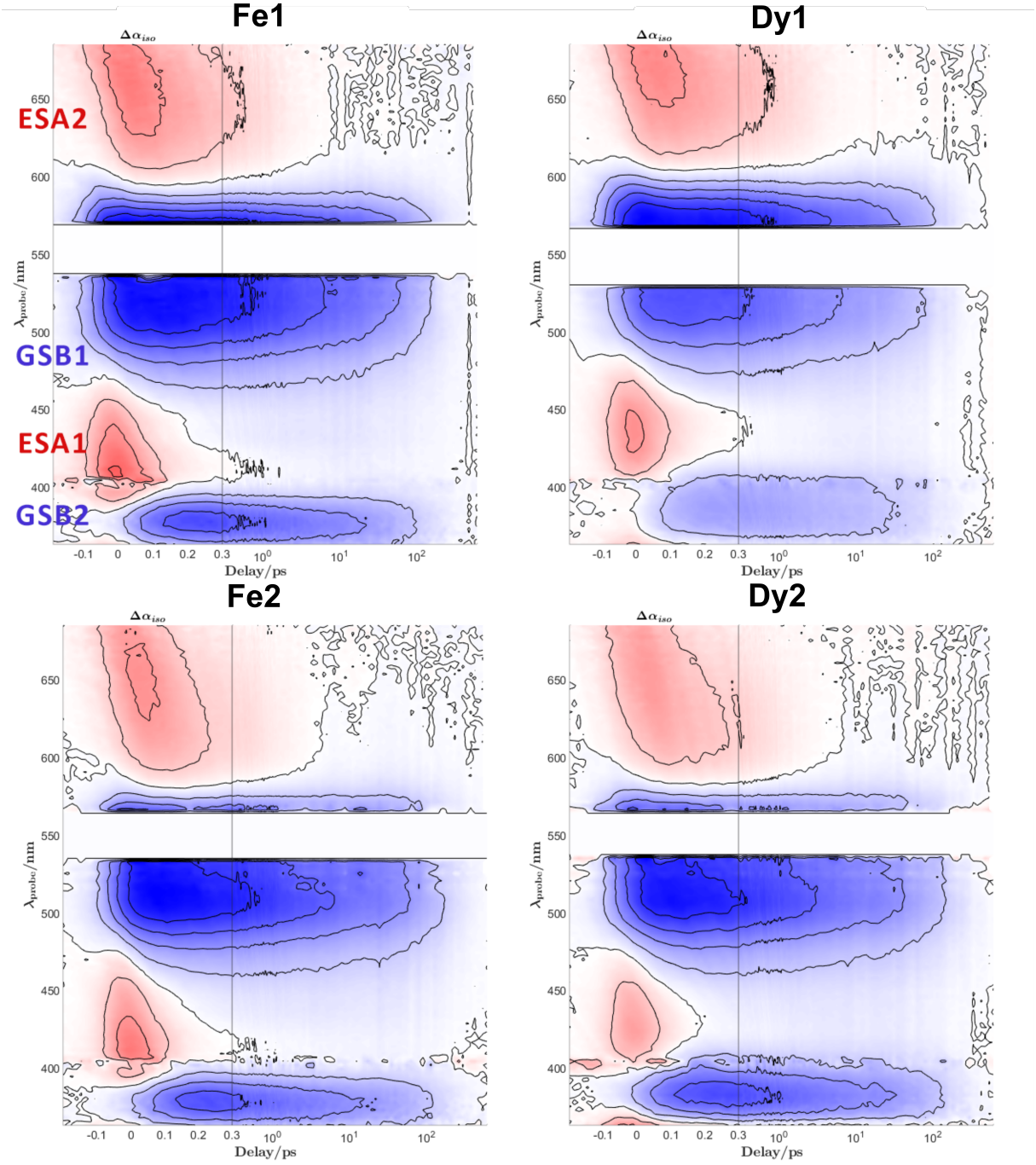

Figure 5.21: 2D colormaps of transient absorption data for **Fe1**, **Fe2**, **Dy1** and **Dy2** in MeCN. Negative signals (bleach, stimulated emission) are shown in blue whereas positive ones (excited-state, photoproduct absorption) are in red. Contour lines are drawn at 20 % intervals with respect to the strongest (abs. value) signal. Delay x-axis becomes logarithmic for delays longer than 0.3 ps. The 550 nm gap corresponds to the spectral range of pump scattering. Additional pump scattering occurs at 405 nm.

First, an ultrafast decay of an ESA signal, marked as ESA1, between 400-450 nm is found around 100-200 fs. A second ESA signal (ESA2) is present above 580 nm. It decays on the time scale of few ps. In the first few hundreds of femtoseconds it exhibits a blue-shift. A strong bleach signal (GSB1) from 470-600 nm is completely recovered on the 100 ps time scale. Around 380 nm a second bleach signal (GSB2) follows the same dynamics as GSB1.

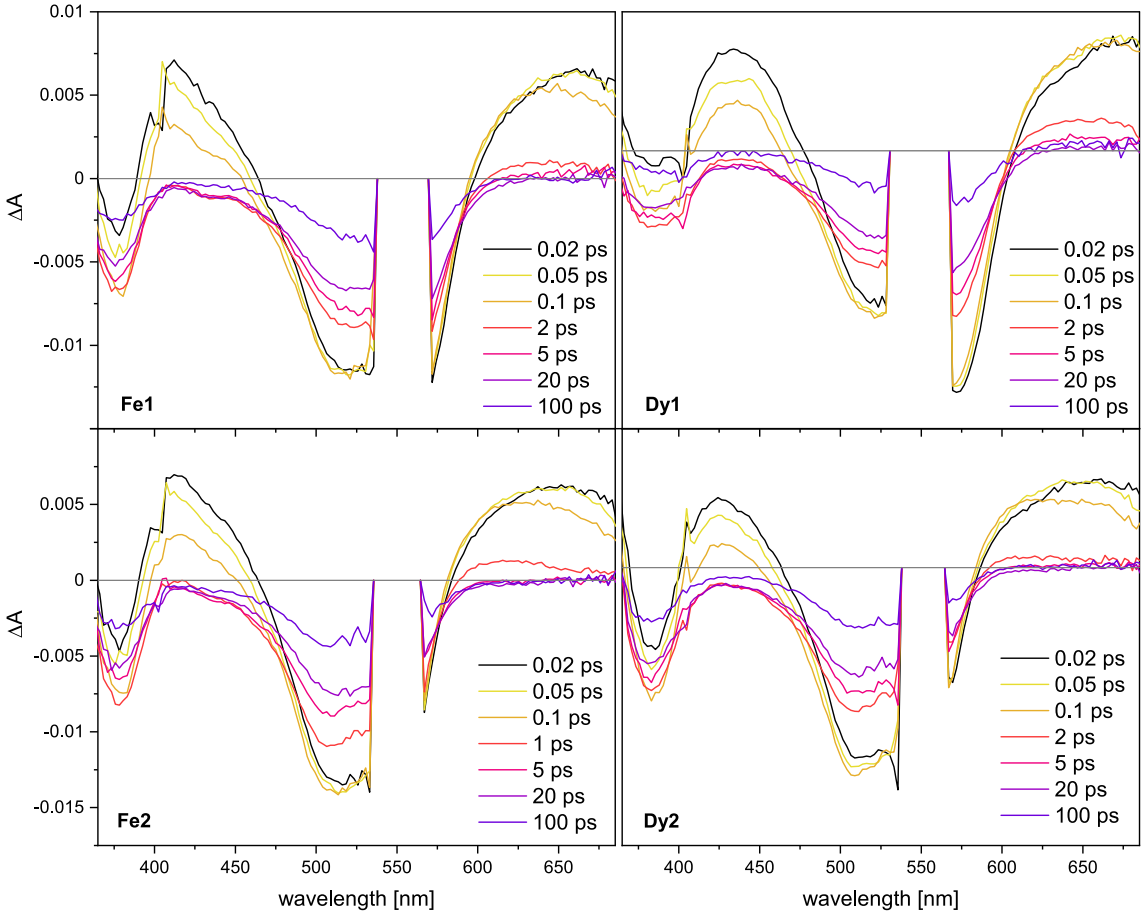

Figure 5.22: Picosecond dynamics in transient absorption spectra of **Fe1**, **Fe2**, **Dy1** and **Dy2** in MeCN. Transient signal around the pump wavelength (550 nm) was omitted due to scattering artefacts. Residual pump scattering is also present around 405 nm.

The transient spectra for different delays give further insights into the spectral dynamics of the compounds studied and are shown in Figure 5.22. The inverted ground-state absorption spectrum for each compound is added as dotted line in each panel. Significant spectral evolution is visible on the ultrafast time-scale within the first few hundreds of femtoseconds.

First, by comparing the spectral shape of the early-time transient spectra with the inverted absorption spectra, a significant spectral overlap between both GSB and ESA signals is observed. Otherwise, the inverted absorption spectrum would reflect the GSB. Due to this overlap, a delayed rise of both GSB signals (GSB1, GSB2) can be assumed. Without an overlap with the ESA signals an instantaneous rise of

bleach signal would be expected. For instant, ESA2 overcompensates the GSB above 580 nm.
Second, while the 2D colormap provides a general overview of the excited-state dynamics, the transient spectra highlight some fine details between photosensitizers and dyads. ESA1 around 400-450 nm has a qualitatively different shape in **Fe1-2** and **Dy1-2**. The transient signal decays faster for the iron complexes on the red side than on the blue side, while it decays uniformly in the transient spectra of the dyads within ~200 fs. This can be also regarded as an ultrafast blue-shift of the red-part of ESA1 accompanied with its decay.

Table 5.5: Relaxation lifetimes τ_2 and τ_3 for **Fe1-2** and **Dy1-2**.

compound	τ_2 [ps]	τ_3 [ps]
Fe1	2.0 (0.3)	140 (10)
Fe2	2.1 (0.3)	140 (20)
C7[a]	1.1 (0.12)	139 (0.12)
Dy1	2.0 (0.3)	120 (10)
Dy2	2.7 (0.2)	145 (10)
C7-Co[a]	1.4 (0.12)	118 (0.12)

Different error bars due to different set-ups. a) Adapted from[53].

Now, the transient data are analysed quantitatively. Unfortunately, global fit with four time constants (sub-100 fs, few 100s fs, few ps, ~100 ps), that is fitting the same set of time constants for all wavelengths simultaneously, does not provide satisfactory description of the data. Therefore, the data are fitted by a sum of three exponentials convolved with a Gaussian instrument-response function (fwhm = 60 fs). The advantage is that no particular kinetic scheme of the excited-state evolution is imposed on the dataset. The extracted, averaged lifetimes from fits of selected wavelengths are listen in Table 5.5 along with the error bars.
In accordance with the results, the following scheme is proposed:

$$S_0 \xrightarrow{h\nu} {}^1MLCT \xrightarrow{\tau_1} {}^3MLCT \xrightarrow{\tau_2} \begin{cases} {}^3\mathrm{MC} \xrightarrow{<<\tau_2} S_0 \\ {}^5MC \xrightarrow{\tau_3} S_0 \end{cases} \qquad 5.4$$

After excitation from the ground state S_0 to the ^{1}MLCT, a relaxation from the Franck-Condon ^{1}MLCT to a partially, vibrationally relaxed ^{3}MLCT state occurs. This happens within 80-100 fs (τ_1) for all compounds. The deactivation of the ^{3}MLCT state is assigned to the lifetime τ_2. Most importantly, tuning of the bridging ligand by acetylene or phenyl-acetylene spacer increases the ^{3}MLCT lifetime from 1.1 ps (C7) to 2.0 ps and 2.1 ps for **Fe1** and **Fe2**, respectively. Presumably, it results from a better delocalization along the bridging ligands **L1** and **L2**. Also, τ_2 is extended in the case of **Dy2** from 2.1 ps to 2.7 ps, while it remains 2.0 ps in case

of **Dy1**.

Quenching of the ^{3}MLCT occurs through lower-lying MC states. Due to partial reduction of the GSB (30%) parallel to the ESA decay, a ^{3}MC state is indicated, which is in line with iron(II) polypyridyl complexes with two carbene functionalities.[54] It retours back to the ground state faster than τ_2. The ESA2 decays almost completely at longer delay times, while the GSB1 signal is still detectable for further several tens of ps. This suggests a quintet MC state where no ESA features are present between 350-800 nm. It decays within τ_3 of 120-145 ps to S_0. The lifetime of ^{5}MC is reduced upon dyad formation in **Dy1** from 140 ps to 120 ps. This is also confirmed by the **C7/C7-Co** couple (139 ps vs. 118 ps). In case of **Dy2** a slight extension of the MC state lifetime is obtained.

The carbene-based complexes **Fe3** and **Dy3** show different excited-state dynamics related to the increased number of σ-donating ligands which causes changes of the energetic levels of MLCT and MC states, which is in agreement with the DFT calculations. The TA data are published in Ref.[99].The transient spectra with delay times τ = 0.5 -75 ps and kinetic traces of the first 5 ps for selected wavelengths are shown in Figure 5.23. The excitation wavelength is 515 nm. The dyad dissociation is circumvented by applying high-concentrated samples.

Two ESA signals and two GSB signals are identified. First, ESA below 370 nm is very similar for both compounds. In contrast, the ESA signal in the red region above 520 nm and 580 nm differs significantly for **Fe3** and **Dy3**, respectively. TA spectra of **Fe3** are dominated by GSB from 370-520 nm and by an ESA maximum at 545 nm. Focusing on the first 5 ps, one can see a temporal evolution of the ESA signal characterized by a gradual blue-shift and band narrowing. In comparison, GSB of **Dy3** is red-shifted by 30-40 which is inline with the red-shift of the absorption band in the UV-Vis spectrum of the concentrated dyad solution. In addition, it agrees with the HOMO-LUMO gap decrease of 0.17 eV in **Dy3** as predicted by DFT (see above.) The ESA signal in the dyad has a different spectral and temporal evolution compared to the PS. The amplitude of the ESA is higher and the signal is broadened. Moreover, kinetic traces around 400 nm are different for both compounds as shown in Figure 5.23 c and d. Here, the apparent GSB in **Dy3** has mixed features from ESA and GSB expressed by amplitudes above zero followed by a decay below zero. In **Fe3** the amplitude of the kinetic trace at 395 nm is below zero and clearly a GSB.

A global analysis fitting (GA) of selected kinetic traces helps to characterize the excited-state by extracting relaxation lifetimes τ and are presented in Table 5.6. Details can be found here.[99]

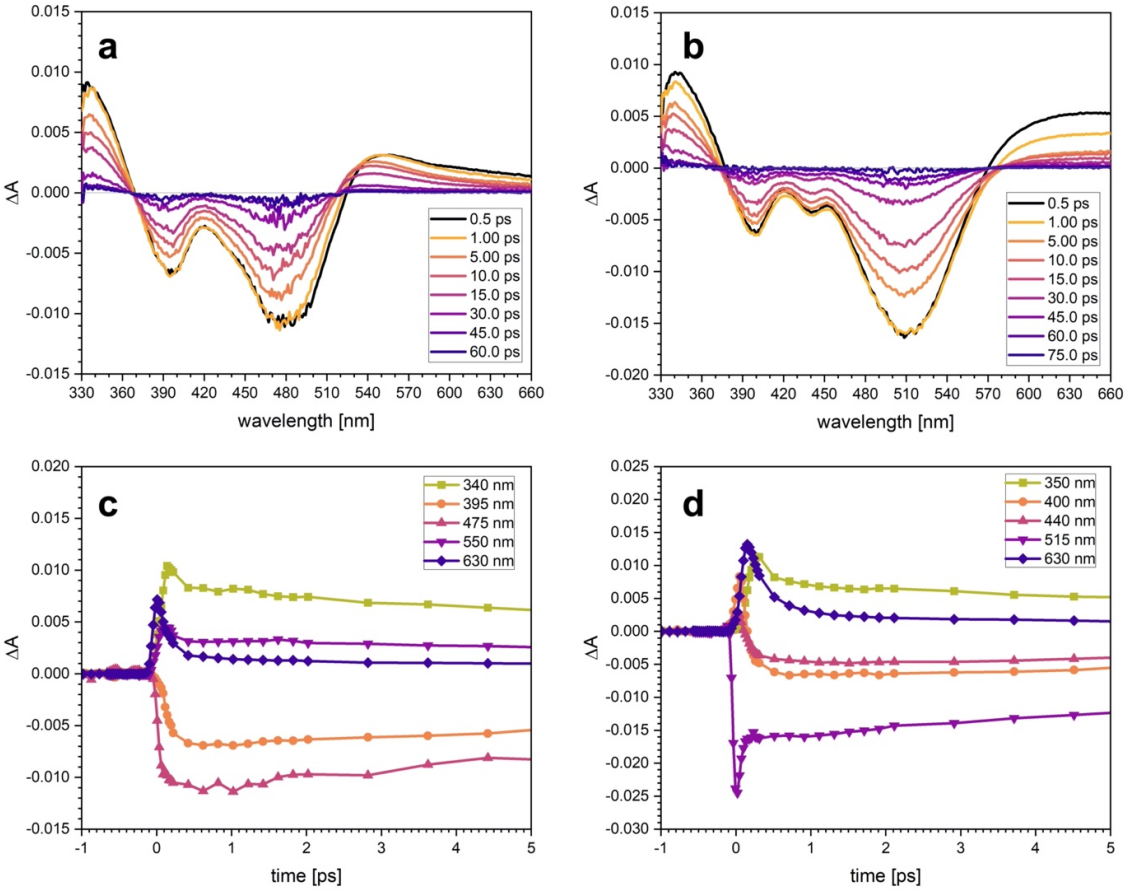

Figure 5.23: Optical TA spectra of **Fe3** (a) and **Dy3** (b) excited at 515 nm in MeCN. First 5 ps of the evolution of kinetics at selected wavelengths for **Fe3** (c) and **Dy3** (d). Adapted from ref.[99]

Three time constants are fitted with single value decomposition (SVD). In both complexes a very short component τ_1 occurs which is smaller compared to the instrument response function (IRF = 0.12 ps). Artifacts close to time-zero are included here.[111] The GA results are not effected by the very short τ_1,hence it is neglected in following discussion. The second component τ_2 of 140 fs is present in all GSB and ESA signals. The longest time constant, termed τ_4, is inline with the recovery of the ground-state signal. It is 17.1 ps in **Fe3** and 19.8 ps in **Dy3**.

Table 5.6: Kinetic data of transient spectra of **Fe1-2** and **Dy1-2**.[99]

compound	DAS, τ_1	DAS, τ_2	DAS, τ_3	DAS, τ_4
Fe3	<IRF	0.14 ps	1.7 ps	17.1 ps
Dy3	<IRF	0.14 ps	1.0 ps	19.8 ps

Regarding the qualitative discussion of the different spectral evolution of the red ESA signal in both compounds, the same nature of the excited states can be assumed. By covering the full spectral range in the following global fitting, a more reliable identification of excited-states is possible.[112] An additional component, the time

constant τ_3, is obtained and contributes to the relaxation cascade. It is 1.7 ps in **Fe3** and 1.0 ps in **Dy3**.

The obtained time constants are now assigned based on literature. Values (τ_1) typically below the temporal resolution are indicative of a hot ^{1}MLCT*.[102,113,114] This is the starting point for the explanation of the relaxation cascade characterized by TA. Two deexcitation cascades are possible and summarized in the following equations:

$$^1MLCT^* \xrightarrow{\tau_1} {}^1MLCT \xrightarrow{\tau_2} {}^3MLCT^* \xrightarrow{\tau_3} {}^3MLCT \xrightarrow{\tau_4} GS. \quad \textbf{5.5}$$

$$^1MLCT^* \xrightarrow{\tau_1} {}^3MLCT^* \xrightarrow{\tau_2} {}^3MLCT \xrightarrow{\tau_4} {}^3MC \xrightarrow{\tau_3} GS. \quad \textbf{5.6}$$

Following the first model, the hot ^{1}MLCT* decays within τ_1 into the relaxed ^{1}MLCT state. This is followed by a relaxation into a hot ^{3}MLCT* state chararcterized by τ_2. Within 1-2 ps (τ_3) ^{3}MLCT* state relaxes into a ^{3}MLCT state. On the contrary, cooling within the triplet MLCT scaffold can occur in tens of femtoseconds,[115] indicating that τ_2 would better describe the transition from ^{3}MLCT* to ^{3}MLCT state, as illustrated in model 2. A transition from ^{1}MLCT to ^{3}MLCT is excluded in both models. Based on the excited-state dynamics of **C3** and other tetra-carbene iron(II) complexes, the longest time constant τ_4 is assigned to the lifetime of the ^{3}MLCT state.[47,49,54]

Since τ_4 is assigned to a ^{3}MLCT state in model 1, the deactivation ends in the ground state without MC state contribution. This contradicts several studies on carbene-based iron complexes, in which MC states are included in the deactivation cascade.[43,55,116] In model 2, the ^{3}MLCT relaxes within τ_4 into a ^{3}MC. Time constant τ_3 is assigned to the relxation process ^{3}MC $\rightarrow$ ^{1}GS. The mixing of GSB and ESA signals and the lack of distinguishable characteristic features for the MC state make it difficult to choose one of the proposed deactivation models. Still, in light of previous studies, model 2 is more likely.

In terms of MLCT lifetime elongation, the ligand modification results in almost twofold increase of the lifetime with τ_4(Fe3) of 17.1 ps compared to 9 ps in **C3**. This is due to the MLCT stabilization by the extension of the π-system[52] and the electron-withdrawing nature of the pyridyl substituent. Further elongation is achieved by cobalt coordination (τ_4(Dy3) = 19.8 ps) which is in agreement with UV-Vis spectroscopy and DFT calculations. The same trend is confirmed in the terpyridine-based dyad **Dy2** (see above) and known dyad **C7-Co**.[53]

5.3.7 Chapter summary

Three dyads and one triad have been characterized by varius spectroscopic methods. Crystallographic data has shown similar coordination geometry around the iron center for the corresponding photosensitizers and the multimetal complexes. The dyad formation has been benefical for the planarization of bridging ligands in **Dy1** and **Dy3** as evidenced by the reduced torsion angles.
The absorption properties have been assessed by UV-Vis spectroscopy and combined with computational analysis via molecular orbital schemes and TDDFT spectra. The HOMO-LUMO gap was reduced upon dyad formation due to the stabilization of the ligand-based LUMO levels. It was confirmed by the redshift of the lowest-energy absorption bands. In the dyads the absorption changes caused by protonation were less pronounced due to the occupation of the pyrdine coordination site by cobaloxime.
In the following chapter the metal-sensitive method, ultrafast X-Ray emission spectroscopy, will help to prove the existence of a MC state, for which TA specstroscopy is not so suitable.[117]

In this chapter, photocatalytic proton reduction is tested using **Fe3** and **Dy3** as examples. In this context, the photostability of these compounds is investigated. The obtained results are explained by sophisticated spectroscopic methods such as ultrafast absorption spectroscopy and time-resolved X-ray emission spectroscopy. Computational chemistry supports the results.

6.1 Photocatalytic Measurement

As a first step of the photocatalytic experiment the photostability of the compounds has to be tested. **Fe3**, **Dy3** and **C14** are dissolved in acetontrile-d_3 and irradiated with the same xenon lamp which is also applied in the photocatalytic experiment. ^{1}H NMR spectra are recorded before irradiation, after 2.5 hours and 22 hours of irradiation. **Fe3** and **C14** do not degradate or decompose during the complete irradiation time. The corresponding ^{1}H NMR spectra can be found here.[99] In the dyad three characteristic proton signals can be identified. They correspond to the 4,4' bipyridine moiety in **L3** (*cf.* Figure 6.1). The proton signals H_A, H_B and H_C have chemical shifts of 8.34, 7.47 and 7.08 ppm, respectively. In the ^{1}H NMR spectrum of **Dy3** new proton signals evolve after irradiation of 2.5 and 22 hours which have similar coupling pattern as $H_{A\text{-}C}$. They are marked with A-C in Figure 6.1. The proton signals at δ = 8.22 ppm (A) and δ = 7.52 ppm (B) are assigned to a terminal pyridine ring similar to H_A and H_B in **Dy3**. At δ = 7.09 ppm a singlet proton signal evolves which corresponds to the aromatic singlet signal H_C. Presumably, the pyridine-cobalt coordination is weakened resulting in shifts of $H_{A\text{-}C}$ to A-C. Dissociation of the dyad can be excluded because the characteristic proton signals of **Fe3** (8.85, 7.53 and 7.18 ppm) are not found. Since all three compounds are stable under irradiation, they can be applied in photocatalytic proton reduction reactions.

The **Fe3/Dy3** couple is tested in photocatalytic proton reduction measurements. Details can be found here.[99] A standardized proton reduction set-up is used.[100] It consists of a double-walled reactor which is maintained at 25°C. A 300 W Xenon lamp with a AM1.5 global filter is applied as sun simulator. The reactor is irradiated from the side and connected via a condenser to an automatic gas burette. The condenser and the gas burette are kept at 25°C. The experiment is performed under isobar conditions, hence pressure changes upon gas production are balanced by the burette. The related volume changes due to the movement of the piston in the burette are recorded against the time. The corresponding volume-curves are temperature-

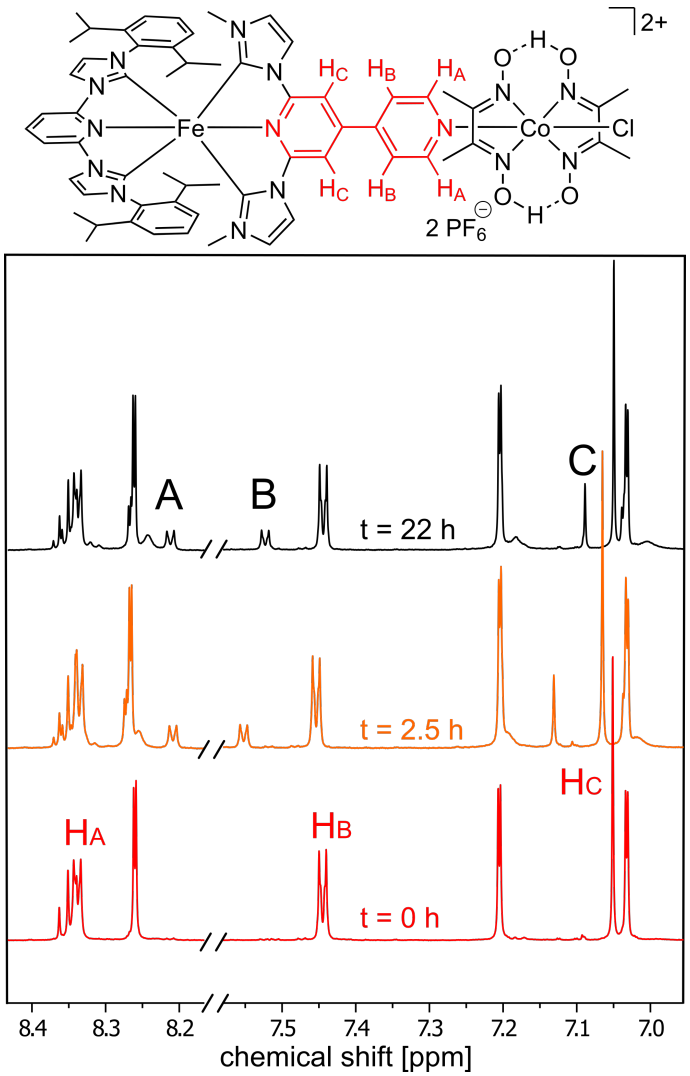

Figure 6.1: Selected aromatic regions of proton NMR spectra of **Dy3**. Before irradiation (red), after 2.5 h (orange) and 22 h of irradiation in MeCN-d_3 at $2.5 \cdot 10^{-3}$ mol/L. Adapted from ref.[99]

corrected[100] and averaged over two runs. Solvent effects are substracted. The volume change is translated to a turn-over-number (TON). Three systems are tested: **Dy3**, **Fe3** + **C14** (cobaloxime) and $[Ir(ppy)_2(bpy)]PF_6$ (termed [Ir] hereafter) + **C14** as reference system. Hence, a one-component system and a multi-component system can be compared, as well as noble-metal PS with a base metal PS. The hydrogen evolution over time is shown in Figure 6.2. The corresponding TON's are summarized in Table 6.1.

Within three hours 25 μmol hydrogen are produced by **Dy3**. This yields a TON of 10 with respect to the PS and a TON of 5 with respect to the CAT. After 45 minutes less hydrogen is produced which is noticed by decreasing hydrogen evolution rate. In comparison, the multi-component system, **Fe3** and **C14**, produces 16 μmol hydrogen after 45 minutes. A TON of 6 related to PS and a TON of 3 related to the CAT are obtained. Thus, the dyad is twofold more active than the multi-component

system. Presumably, the improved photocatalytic activity of the multimetal complex is achieved through the conductive connection between both metals. In the following sections further spectroscopic insights will shed light on the enhanced catalytic activity of **Dy3**.

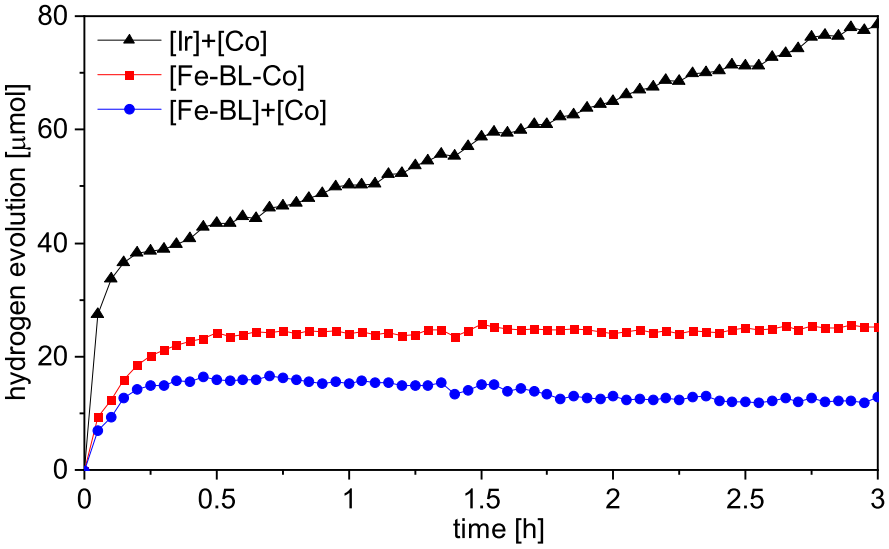

Figure 6.2: Hydrogen evolution of **Dy3** (red) and the multi-component systems **Fe3**+**C14** (blue) and **[Ir]**+**C14** (black). Reaction conditions: 0.25 mM PS/cat/dyad in MeCN/water (1:1, 20 mL, 5% TEOA) under argon. Due to temperature correction and small volume production a negative slope of the blue curve originates after a longer time period. Adapted from ref.[99]

A second multi-component system is investigated in the photocatalytic proton reduction experiment. **[Ir]** and **C14** produce 78 μmol hydrogen and are still active after three hours. A TON_{PS} of 31 and a TON_{cat} of 16 are obtained. Clearly, the system containing Ir performs best, however considering the criticality score discussed by Dierks *et al.* with a score of 66.3 for Ir and a score of 0.8 for Fe, the base metal systems are a good alternative.[39] While the activity of the noble metal-based system after three hours is only three times higher compared to **Dy3**, the higher criticality score by a factor of 82.9 for Ir does not justify the use of precious metals. Especially, because larger-scale applications are necessary to meet the challenges of global warming (*cf.* chapter 2).

Testing the reference system in our set-up reveals also the discrepancies of comparing the TON of the same system presented by other researchers. For example, a related Ir-Co dyad had a TON of 224 after irradiation for 35 h at 452 nm and the same **[Ir]**+**C14** system showed a TON_{PS} of 22 as presented by Elias *et al.*[82] They observed a decomposition of the multi-component system after 30 minutes under their conditions. In contrast, in our set-up the studied system remains active for more than three hours. In another study, Elias *et al.* obtained a TON of 16 for **[Ir]**+**C14** by irradiating at 523 nm. The system decomposed after four hours.[118] By using different

Table 6.1: Photocatalytic proton reduction of one-component system and multi-component systems with Ir/Fe as photosensitizer and Co as catalyst.

system	TON_{PS}[b]	TON_{cat}[c]	$V(H_2)$[mL]	σ[d][mL]	$n(H_2)$[e][μmol]
Dy3	10	5	0.62	0.15	25
Fe3+C14	6	3	0.39	0.03	16(0.75 h)
[**Ir**]+**C14**	31	16	1.92	-	78

a) Reaction conditions: PS, cat or dyad (5μmol) in MeCN:water (1:1, 20 mL),5% TEOA, 25°C, 3h. b) TON_{PS}=2n(H_2)/n(PS), c) TON_{cat}=n(H_2/n(cat), d) σ=standard deviation, e) Produced hydrogen n(H_2) in mol with V_m=24472 mL/mol.

set-ups or reaction conditions such as irradiation wavelength, proton/electron source or solvent mixture, it becomes difficult to compare the photocatalytic performance of different systems. Only comparison of trends within a study are possible.
The first study by Elias *et al.* revealed the improvement by a factor of 10 when applying a dyad in the photocatalytic reaction. Also, in our experiment the dyad performs twice as good as the multi-component system. Most likely, the lower improvement factor in the base metal system is related to the shorter ^{3}MLCT lifetime. [Ir] has an excited-state lifetime of 390 ns and **Fe3** only a lifetime of 17.1 ps.[23]
The results of the photocatalytic experiment indicate that a major focus must be on extending the lifetime of the excited-state. Strategics and recent progress have been presented in chapter 2. However, it is very motivating to study hydrogen evolution by base metal dyads instead of using noble metals. With this research the development of future large-scale applications is supported. The improvement of the complex design can be achieved if the working principles of the dyads are understood. Therefore, time-resolved spectroscopic methods are applied to investigate the excited-state landscape of **Fe3** and **Dy3**.

6.2 Spectroscopic Explanation

In this section two studies are combined which complementarily explain the improved photocatalytic performance of the dyad **Dy3** in comparison with the multi-component system. The TA and XES results are included the following submitted paper.[119]

6.2.1 Time-resolved Spectroscopy

Transient Optical Absorption Spectroscopy

The carbene-based compounds **Fe3** and **Dy3** are investigated again by ultrafast optical absorption spectroscopy. The concentrations of acetonitrile solutions are 10 mM. The description of the set-up is presented elsewhere.[120] The excitation wavelength is adjusted to 400 nm to match the pump pulse of the time-resolved X-ray emission measurements. Prior, a 515 nm excitation wavelength has been used for studying the excitation dynamics. The difference absorption spectra ΔA at selected delay times τ of **Dy3** are presented in Figure 6.3. The experimental UV-Vis spectrum of **Dy3** is added together with UV-Vis spectra of **Fe3** and **C14**.

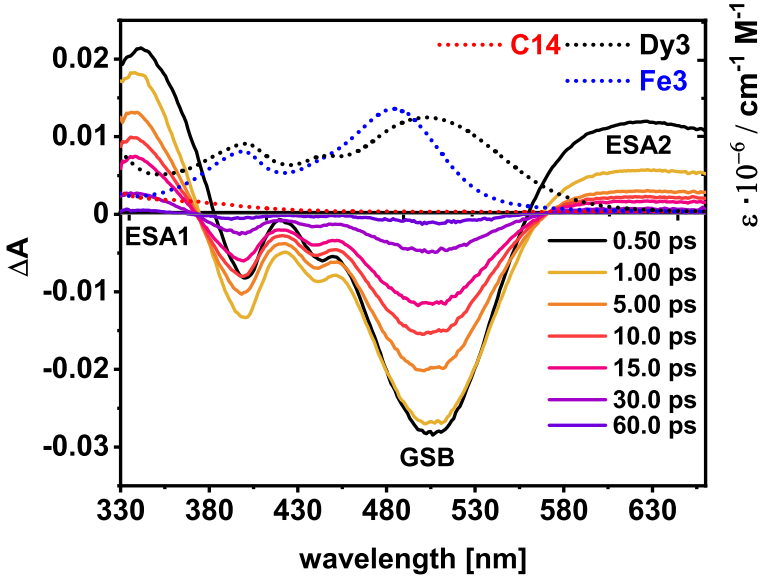

Figure 6.3: UV-Vis spectra of **Fe3**, **Dy3** and **C14** (= $Co(dmgH)_2pyCl$) combined with TA results at selected delay times.[119]

The difference spectra are dominated by an ESA1 till 370 nm and an ESA2 region above 560 nm. A large GSB region is found between 370 - 560 nm with several minima. The minima match well with the ground-state spectrum of **Dy3**. In agreement with TA analysis at 515 nm, the ESA2 is assigned to a ^{3}MLCT state. A multiexponential fit with three time constants is used for the kinetic analysis

above 560 nm. All coherent artifacts and possible ^{1}MLCT state are included by the first component (<100 fs).[121] The second component of 350 fs (τ_2) reflects thermal relaxation of a hot ^{3}MLCT* to a relaxed ^{3}MLCT state[115,122] or the intersystem-crossing (ISC) from ^{1}MLCT to ^{3}MLCT.[113,116,123,124] The first acceptor state after 400 nm excitation has been confirmed to be of ^{1}MLCT nature by excited-state TDDFT.[119] The third lifetime τ_3 = 12.8±1.2 ps is obtained as average value from several fits and assigned to the ^{3}MLCT state.[115,125–127] In comparison, the ^{3}MLCT of **Fe3** is assigned to 11.1±0.4 ps. The MLCT lifetime is elongated in **Dy3**. An involved metal-to-metal CT process in the relaxation cascade through the ^{3}MLCT state is indicated. However, TA does not provide solid proof for an iron to cobalt charge transfer. Fortunately, with X-ray emission spectroscopy the spectroscopic signature for the alteration of charge density at both metals can be investigated.

Ultrafast X-ray Emission Spectroscopy

Before we will discuss the results of the time-resolved X-ray emission spectroscopy, a short overview of the spectroscopic method is given. A X-ray pulse removes an inner-shell-electron from the 1s shell, which causes a radiative decay to fill the created vacancy. Kα and Kβ emissions occur when 2p or 3p levels are involved, respectively, as shown in Figure 6.4 (left.) Since the refilling of the 1s orbital with a 2p electron is dipole allowed the transition is very likely and thus, the XES signal is very intense. In comparison, the K$\beta_{1,3}$ emission with a smaller transition probability is about a factor 10 less intense (*cf.* Figure 6.4). Since only a small spin-orbit-coupling is present in the 3p valence shell, the K$\beta_{1,3}$ doublet is typically obtained as a single peak.[128] At lower energies relative to K$\beta_{1,3}$ a Kβ' shoulder appears. The separation between both emission signals results from the pd orbital exchange coupling and can be used as signature for spin-state assignment (high-/low-spin).[129]

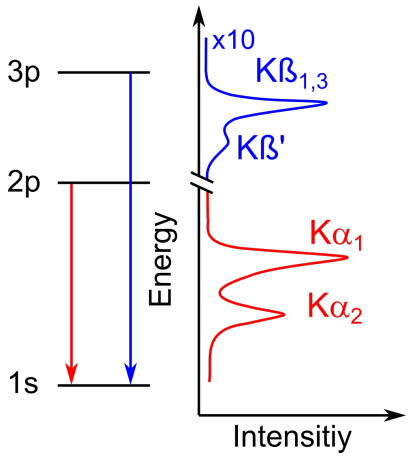

Figure 6.4: Relative intensities of K$\alpha_{1,2}$ and Kβ'/K$\beta_{1,3}$ emission lines and corresponding transitions assigned in an energy level diagram.[130]

In a time-resolved set-up, an optical pump pulse is combined with a X-ray probe pulse. Similar to the TA experiment, two different spectra are obtained, with prior excitation and without. A transient signal is calculated by subtraction of both spectra. With transient Kα emission insight about involved MC states can be obtained,[116] since the width of the XES lines correlates with the effective number of unpaired d-electrons[131] and covalency[132]. By variation of the delay time τ between pump and probe pulse kinetics are extracted. For example, ultrafast XES has been shown to provide core-sensitive details about the excitation landscape in several carbene-based iron complexes.[113,116] In the reference iron complex **C3** it was shown, that the relaxation is branched into two deactivation pathways. In the first one, a long-lived ^{3}MLCT state is involved, while in the second one, a fast transition from the hot MLCT* state to the ^{3}MC occurs with shorter lifetime.
The two-colour X-ray emission spectroscopy (2C-XES) provides unique insights into the excitation landscape of multimetal complexes especially for iron-cobalt systems. The results are presented in Ref.[119] as equal contribution from Dr. M. Nowakowski and M. Huber-Gedert. The most important information are given in this chapter. Experimental details are added in chapter 8. The data processing and analysis was done by Dr. M. Nowakowski. More information can be found here.[119]

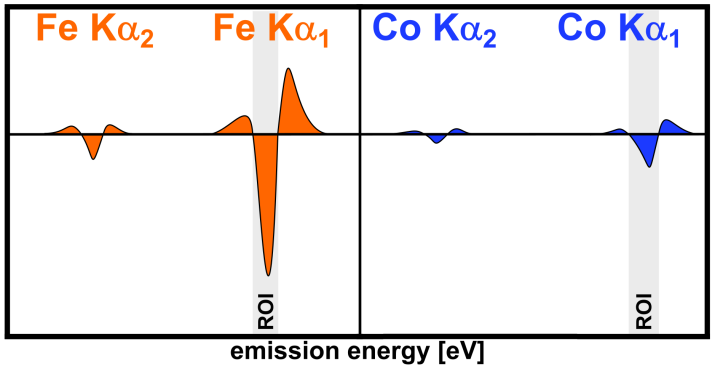

Figure 6.5: Schematic representation of the transient Kα XES signals of Fe and Co of **Dy3**. Grey area marks the region of interest (ROI) which is used to analyse the integrated areas at different delay times τ.[119]

The advantage of our time-resolved 2C-XES experiment is the simultaneous detection of both involved metals, iron and cobalt, by using a von Hamos spectrometer.[133] The potential departure of a charge from iron to cobalt can be investigated in real time by measuring the dynamics at both metals. The transient Kα lines of iron and cobalt of **Dy3** as schematic representation are shown in Figure 6.5. Iron Kα main lines of **Fe3** and cobalt Kα main lines of **C14** are measured as references. For both metals the integration regions of interest (ROIs) are marked. The integrated areas are plotted against the delay time τ resulting in transient kinetics. They are shown in Figure 6.6 with a time window from -5 ps to 15 ps. Note, the emission intensity is

lower for cobalt because the excitation wavelength is chosen to match the excitation of the MLCT band in the photosensitizer part of the dyad.

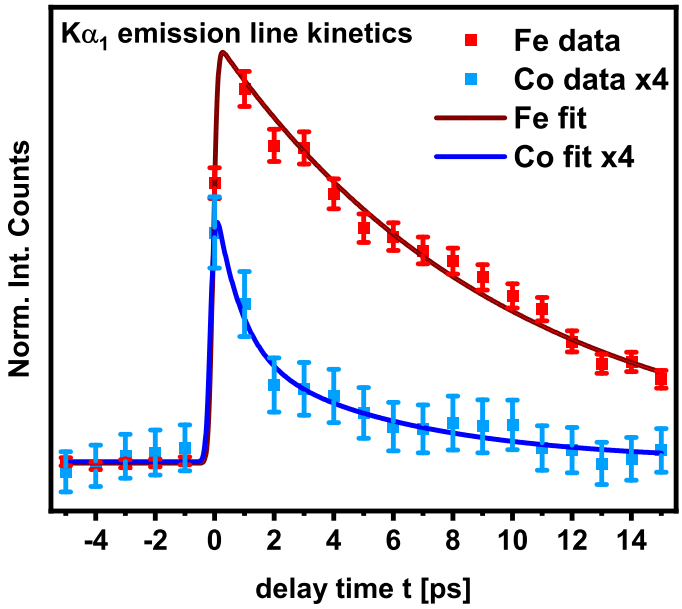

Figure 6.6: Kα_1 emission line kinetics from -5 ps to 15 ps of iron and cobalt of **Dy3**.[119]

In case of **Dy3**, three time constants are extracted from the transient kinetics. They are $\tau_{1,\mathrm{Fe}} < 0.14$ ps, $\tau_{2,\mathrm{Fe}} = 10.38(40)$ ps and $\tau_{3,\mathrm{Fe}} = 1.74(18)$ ps. The corresponding time constants of **Fe3** are $\tau_{1,\mathrm{Fe}} \sim 0.25$ ps, $\tau_{2,\mathrm{Fe}} = 8.98(27)$ ps and $\tau_{3,\mathrm{Fe}} = 1.71(35)$ ps. Most importantly, the longest time constant $\tau_{2,\mathrm{Fe}}$ in the dyad is extended. This is in good agreement with the TA results. Overall shorter fitted values in the XES experiment is attributed to the different sensitivity towards charge-transfer states compared to TA spectroscopy.

The time constant assignment is rationalized in the following. First, the XES signatures for ^{1}MLCT and ^{3}MLCT are nearly-identical because both states have one iron-localized unpaired d-electron.[134] Moreover, the coupling of the 2p core-hole and 3d electrons is weak. Therefore, intersystem crossing from the singlet to the triplet MLCT manifold cannot be followed by transient Kα XES. In contrast, changes in metal spin multiplicity, e.g. from ^{3}MLCT with local spin S_{loc} of 1/2 to ^{3}MC state ($S_{\mathrm{loc}} = 1$) are visible. The relaxation processes to the singlet ground state, where one of these states are involved as donor state, can be followed by transient XES.

Based on the TA results and previously reported values, the extracted time constants $\tau_{1,\mathrm{Fe}}$-$\tau_{3,\mathrm{Fe}}$ are assigned in both compounds as follows. Relaxation from the hot ^{3}MLCT* state to the ^{3}MC state is described by the shortest time constant $\tau_{1,\mathrm{Fe}}$ and reflects the branching behaviour which was also discussed by Tatsuno *et al.*[113] The ground state is repopulated by relaxation from the ^{3}MC state within ~ 2 ps ($\tau_{3,\mathrm{Fe}}$).[54,135] The second time constant is assigned to the relaxed ^{3}MLCT state. Involvement of the ^{3}MC state in the relaxation cascade is also confirmed by potential

energy surface calculations (*cf.* Figure 6.9).

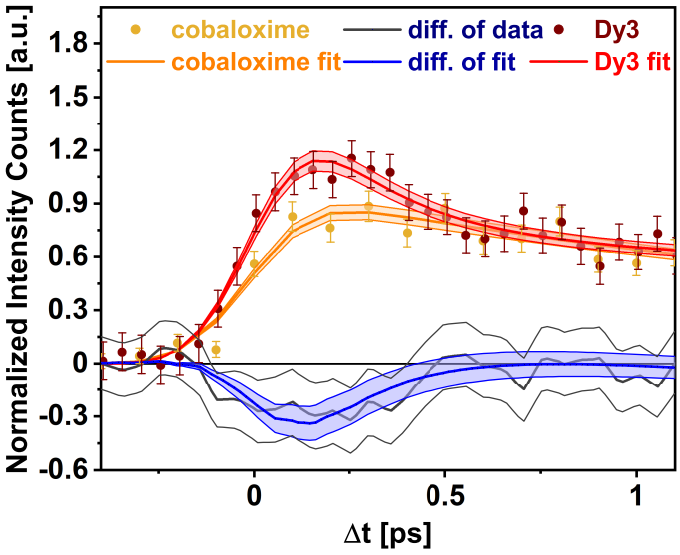

Figure 6.7: Kinetics of the cobalt Kα emission in **Dy3** and **C14** with corresponding fits. Differential signal is obtained by [C14]- [Dy3] and marked as blue lines (data+fit). Filled areas represent uncertainties.[119]

The analysis of the Co Kα emission dynamics of **Dy3** gives three time constants. $\tau_{1,\mathrm{Co}}$ = 0.25(1) ps, $\tau_{2,\mathrm{Co}}$ = 4.12(1.39) ps and $\tau_{3,\mathrm{Co}}$ ~ 23.39 ps are obtained. In the reference cobalt compound **C14** only two time constants are present with $\tau_{1,\mathrm{Co}}$ = 2.76(31) ps and $\tau_{2,\mathrm{Co}}$ = 23.39(1.82) ps. The different dynamics are also manifested in different shapes of the kinetics which are shown in Figure 6.7. They are scaled and area-normalized. In addition, the y0-values are adjusted to the fits. The early kinetics till 1 ps are compared for **Dy3** (red) and **C14** (green). Apparently, the shortest time constant in **Dy3**, $\tau_{1,\mathrm{Co}}$, induces the different shape and indicates a new excited-state pathway unique for the dyad, since such a short time constant is not present in **C14**. This is also in good agreement with the MMCT contributions in the UV-Vis spectrum of **Dy3** as assigned by TDDFT. By subtracting the kinetics of **Dy3** from **C14** a differential signal is obtained (*cf.* Figure 6.7), which reflects the MMCT signature from iron to cobalt. Apart from the real-time CT feature in the dyad, the low ps lifetimes are assigned to LMCT states in both cobalt compounds. The presence of the LMCT state in cobaloxime is reflected by the HOMO-LUMO transition composed of dmgH ligand π orbital (HOMO) and cobalt-based d-orbital (LUMO).[53] However, the direct excitation is very weak because of the low cross-section at the excitation wavelength of 400 nm as deduced from the optical absorption of **C14** (*cf.* Figure 6.3).
Consequently, the improved catalytic performance of **Dy3** results from the MMCT state, which is an unique feature of the multimetal complex compared to the system consisting of **Fe3** and **C14**. The respective excited-state with electron and hole

probabilities is visualized in Figure 6.8. The hole is located on the iron site while the electron density is distributed among the bridging ligand **L3**, **SP** and especially the cobalt dz^2-orbital.

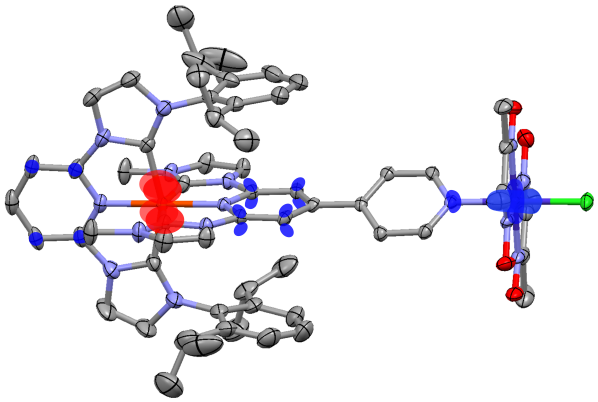

Figure 6.8: Schematic representation of holes (red) and electrons (blue) upon Fe → Co charge transfer in **Dy3**.[119]

An additional information can be extracted from the iron Kα emission signal. A coherent nuclear wavepacket signature is identified in both iron-containing systems **Fe3** and **Dy3**. The modelling describes the oscillations of **Fe3** by a single damped function with a half-period of 0.28(2) ps. For **Dy3** two contributions are found with 0.26(3) ps and 0.19(1) ps. Other systems exhibit similar oscillation half-periods.[116,136] In both compounds similar oscillations are attributed to the same origin within the photosensitizer moiety while the additional oscillation ($T_{1/2}$=0.19 ps) originates from the cobaloxime coordination. The potential energy surface calculations reveal that oscillations occur along the Fe-N distance with ^{3}MLCT*/^{3}MC equilibrium at 2.05 Å. The frequency analysis of the excited state structure of **Dy3** indicates vibrations with 175 cm^{-1} where a twisting motion of **L3** is present together with a rotational distortion and stretching of iron-nitrogen bond along the Fe-Co axis.[119] Presumably, this characteristic motions affect the MMCT because of the twisting motion of **L3** causing the modulation of π* orbital overlap. The wavepacket motions appear due to the transition from hot ^{3}MLCT* to ^{3}MC as one branching pathway. Note, such transitions can not be assessed by optical TA spectroscopy.[137]
The analysis of transient kinetics of XES has given insights into the excited state landscape of **Dy3**. In addition, the use of population analysis helps to confirm the assignment by testing different kinetic models. The population analysis gives an additional time constant of 0.22(7) ps for both compounds **Fe3** and **Dy3**. This time constant reflects the ^{1}MLCT to ^{3}MLCT transition which can not be assessed by transient XES. Moreover, TDDFT confirms the ^{1}MLCT state as first acceptor state after excitation. Also, in TA a short time constant of 350 fs has been found which is in good agreement.

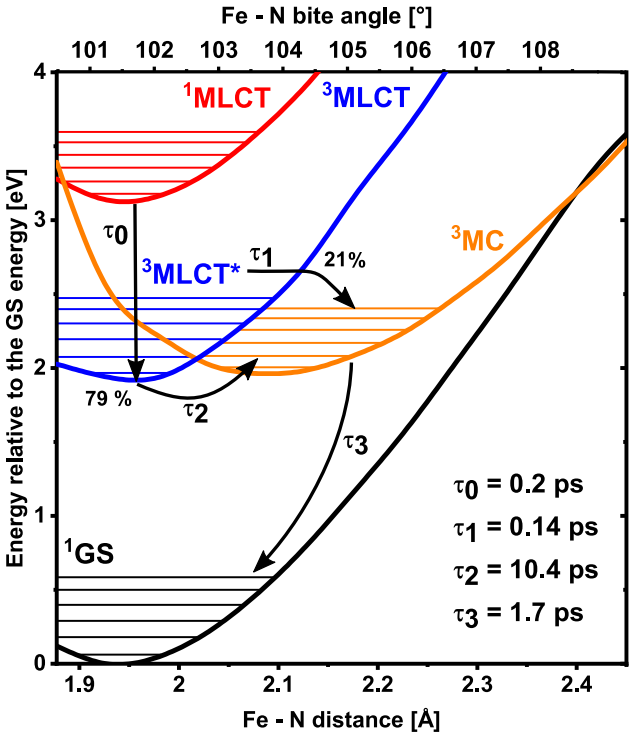

Figure 6.9: Potential energy surface of ground and excited states of **Dy3** along the Fe-N distance (low x-axis) and the Fe-N bite angle (top x-axis).[119]

The potential energy surface of **Dy3** is specified with the results from transient kinetics and population analysis and is shown in Figure 6.9. The branching, which is indicated by the wavepacket motions, is reflected in the kinetic modelling and leads to an α (79(5)%) and a β (21(5)%) channel. In case of **Fe3**, the relaxation decay branches into α and β channel with 83% and 17%, respectively. The α channel is described by the following cascade:

$$^3MLCT^* \rightarrow {}^3MLCT \rightarrow {}^3MC \tag{6.1}$$

while the β channel is characterized by the direct population of ^{3}MC from the hot ^{3}MLCT*:

$$^3MLCT^* \rightarrow {}^3MC. \tag{6.2}$$

Moreover, a MMCT deactivation channel originating from the ^{3}MLCT is obtained by kinetic fitting. The lifetime of the MMCT state is 0.25 ps. Note, also back electron transfer can occur.[138] In addition, direct excitation populates a LMCT state, similar to the reference compound **C14**. The LMCT state decays within 4.12 ps into a lower-lying state with unknown nature. Most likely, it is a MC state.[139] Subsequently, the system relaxes back to the ground state within 23-30 ps as estimated relative to cobaloxime. There, the population analysis yields a two-state decay with lifetimes of 2.78(3) ps and 24.3 ps. The ratio between direct excitation and charge transfer in the cobalt XES signal of **Dy3** is 43% and 57%, respectively.

6.2.2 Chapter summary

The photostability of **Fe3** and **Dy3** after irradiation has been confirmed by ^{1}H NMR. In a photocatalytic proton reduction set-up the dyad **Dy3** was twice as active as the multicomponent system with **Fe3** and cobaloxime. Comparison with a noble metal PS revealed the need for further ^{3}MLCT lifetime elongation to improve the catalytic activity of the base metal systems.
Ultrafast 2C-XES enables the investigation of photoinduced charge transfer processes within a base metal dyad. The direct detection of Kα XES signal of both metals with temporal self-calibration explains the improved photocatalytic performance of **Dy3** by proving the MMCT from iron to cobalt with a lifetime of 0.25 ps. An extended ^{3}MLCT lifetime and a MMCT contribution have been confirmed by ultrafast TA spectroscopy and TDDFT, respectively.

Chapter 7: Summary and Outlook

The objectives of this work were 1) the variation of the carbene count to modulate the physical properties of the iron complexes, 2) the tuning of the bridging ligand and its effect on the excited state dynamics of the iron PS, and 3) synthesis of multimetal complexes based on the homoleptic and heteroleptic iron photosensitizers. The succesfully synthesized iron and iron-cobalt compounds were thoroughly characterized by X-ray diffraction, NMR spectroscopy, ESI mass spectrometry, elemental analysis, UV-Vis spectroscopy and cyclic voltammetry. Selected compounds were further characterized by ultrafast optical absorption spectrocopy in combination with spectroelectrochemistry and TDDFT. **Dy3** was tested in photocatalytic proton reduction reactions, with photostability previously confirmed by NMR. Improved photocatalytic activity of the dyad **Dy3** relative to the multi-component system **Fe3** + **C14** was explained by transient optical absorption spectroscopy and ultrafast two-colour X-ray emission spectroscopy (2C-XES).

To modulate different absorption properties of iron photosensitizer six ligands were synthesized with N^N^N or C^N^C coordination site. The terpyridine-based ligands **L1** and **L2** are literature-known substances. However, the synthesis route of **L2** was improved in this work. After four steps **L1** was obtained in 43% overall yield. **L2** was obtained after two reaction steps and in 25% yield. Four novel carbene-based ligands were synthesized. **L3** was isolated after three steps in 30% overall yield.
Two different synthesis routes were tested for **L4**. First, the center of the bridging ligand was built by receiving 2,6-dichloro-4-(pyridin-4-ylethynyl)pyridine in two subsequent Sonogashira reactions starting from 4-iodo-2,6-dichloropyridine. Unfortunately, the substitution of the chlorines with imidazole did not work. Therefore, the central core was generated with bromine substituents. Starting with 2,6-dibromopyridine, iodination in 4-position and two carefully conducted Sonogashira reactions gave 2,6-dibromo-4-(pyridin-4-ylethynyl)pyridine, which did not react neither in a neat-coupling with *N*-methylimidazole nor in a Ullman reaction or nucleophilic aromatic substitution via NaH deprotonation.
Second synthesis route of **L4** started with 4-amino-2,6-dibromopyridine. Here, the C^N^C site was constructed before the backbone functionality was adjusted. Reaction conditions of the Sandmeyer reaction to obtain 4-iodo-2,6-di(1H-imidazol-1-yl)pyridine were improved to suppress the undesired formation of 4-chloro-2,6-di(1H-imidazol-1-yl)pyridine. The succesful Sonogashira gave the pyridine-acetylene functionalized C^N^C core, which was subsequently protected against methylation, so that only the imidazole rings were methylated. Finally, **L4** were synthesized in 2% total yield after deprotection of the terminal pyridine ring.
L5 was obtained as byproduct along the synthesis route of **L4** due to the unplanned

methylation of the terminal pyridine ring. The product of the Sandmeyer-type reaction was used to obtain **L6** after methylation. Starting from 4-amino-2,6-dibromopyridine, **L6** was isolated in 18% total yield.

The ligands were applied in homoleptic and/or heteroleptic complex synthesis. Four homoleptic photosensitizers were successfully synthesized with **L1, L2, L3** and **L6** as ligands. Three heteroleptic complexes were obtained with **L1-L3** by applying the *in-situ* base $Fe(HMDS)_2$. After formation of a five-coordinated iron precursor, the bridging ligands were added and **Fe1-3** were isolated after work-up. Crystal structures of all photosensitizers except $\mathbf{Fe6_{homo}}$ revealed larger bite angles in the terpyridine containing compounds (approx. 176°-179°), while the carbene-based C-Fe-C bite angle was about 159°. In conclusion, the octahedral geometry in the iron compounds has to be improved. The planarization after the insertion of an acetylene spacer, evidenced by a smaller torsion angle between the aromatic rings, was confirmed by crystallographic data except in **Fe1**.
With UV-Vis spectroscopy intense bands in the red part of the spectrum were detected for the terpyridine-based PS, while a blue-shift of the absorption bands was identified for the carbene-based systems. Computed molecular orbital schemes rationalized the tuning of the HOMO-LUMO gap in **Fe1-3** causing increase of the energy gap upon higher carbene count. Moreover, the observed transitions were explained by TDDFT, dividing the absorption spectra into ligand-based π-π^* transitions below 350 nm and MLCT transitions above 350 nm. In addition, CV confirmed the increasing HOMO-LUMO gap in carbene-based systems compared to terpyridine-based complexes.
The protonation of the iron photosensitizer showed no effect on systems without terminal pyridine functionality e.g. in $\mathbf{Fe6_{homo}}$ or the reference compounds $\mathbf{Fe(terpy)_2}^{2+}$ and **C3**. The lowest effect was determined for the homoleptic and heteroleptic complexes bearing **L2**, while red-shifts of about 70 nm were observed for carbene-based iron complexes **Fe3** and $\mathbf{Fe3_{homo}}$.
The reversible bulk metal oxidation in the heteroleptic compounds **Fe2** and **Fe3** were assessed by spectroelectrochemistry. In contrast, metal oxidation of **Fe1** was irreversible. It was shown that the ligand reduction was irreversible in **Fe1-3**.

Multimetal complex synthesis was straightforward. The PS were applied as pyridine derivative in a standard cobaloxime synthesis. **Dy1-3** were isolated in good yield (76-90%), while the triad **Tri3** was obtained in lower yield of 37-40%. Crystallographic data of **Dy1** and **Dy2** confirmed similar bond distances and bond angles as obtained for the PS's. Moreover, cobalt attachement resulted in smaller torsion angle and thus, better electronic overlap along the bridging ligand connecting iron and cobalt.

Due to the monodentate coordination of PS to the cobaloxime moiety, the multimetal complexes dissociated in diluted acetonitrile solutions. Hence, the dyad stability was studied. The stability can be ranked in the following order **Dy2**>**Dy3**>**Dy1** at very low concentrations (0.02 mM). **Tri3** was stable over a long concentration range but dissociated into asymmetric dyad and $\mathbf{Fe3_{homo}}$ to different extend depending on the concentration.
Upon cobalt coordination the lowest-energy bands were shifted to the red part of the spectrum. In this regard, the stabilization of the LUMO levels and thus reduction of the HOMO-LUMO gap were confirmed by DFT calculations. Since only minor absorption changes were identified for the multimetal complexes in comparison to the corresponding PS's at $1{\cdot}10^{-5}$ mol/L, higher concentrated UV-Vis spectra were recorded. In higher-concentrated solution, **Dy1** and **Dy2** showed only small red-shifts, while a shift of 11 nm was found for **Dy3**. Moreover, the removal of photosensitizer absorption in the dyad spectrum resulted in a simulated "pure" dyad spectrum, which exhibited a red-shift of 24 nm. The protonation with TFA had a similar effect on the absorption properties of the multimetal complexes as on the photosensitizers. In addition, the carbene-based complexes were more affected by protonation with significant red-shifts of 48 nm and 47 nm for **Dy3** and **Tri3**. The influence of protonation on the absorption properties was higher for the PS, since at the used concentration the multimetal complexes are only partially dissociated. Hence, full protonation of the pyridine moieties in solution was not possible due to the coordination by cobaloxime.
The stabilization of the metal-based HOMO levels was assessed by CV. The redox potentials of the iron oxidation were anodically shifted in the multimetal complexes. Unfortunately, the observed reduction of the energy gap as dedcued from UV-Vis and DFT, was not confirmed by CV. The bulk metal oxidation for **Dy1-3** was reversible. However, the ligand reduction failed indicating decomposition into the respective photosensitizers.
A ^{3}MLCT lifetime elongation upon dyad formation was proved by ultrafast transient absorption spectroscopy for **Dy2** and **Dy3**. The cobalt coordination did not have an impact on the ^{3}MLCT lifetime of **Dy1**. In addition, tuning of the bridging ligand by acetylene or phenyl-acetylene spacer improved the ^{3}MLCT lifetime in **Fe1** and **Fe2** in comparison to **C7** by a factor of 2.

Photocatalytic proton reduction was tested with the one-component system **Dy3** and the multi-component system **Fe3** and **C14**. All compounds were photostable under Xenon lamp irradiation for several hours as confirmed by NMR. The dyad was twice as active ($TON_{PS} = 10$) as the respective multi-component system ($TON_{PS} = 6$). The improved activity was explained by an extended ^{3}MLCT lifetime of the dyad via ultrafast transient absorption spectroscopy. Furthermore, time-resolved 2C-XES

revealed charge transfer from iron to cobalt in **Dy3**, which was also supported by TDDFT. The enhanced photocatalytic performance was attributed to the presence of a MMCT state in the dyad.

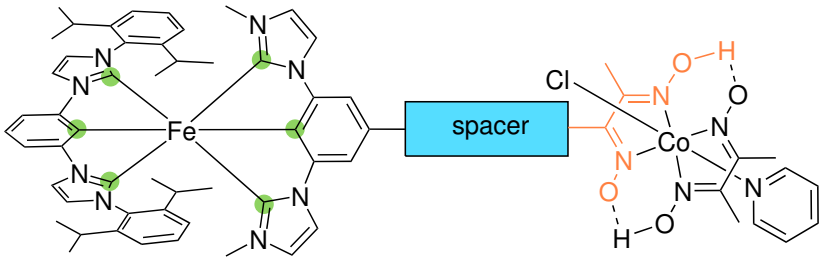

Figure 7.1: Proposed multimetal complex combing strategies deduced from this work.

In this work, the synthesis and characterization of multimetal complexes based on base metals were presented. They are promising alternatives in photocatalytic proton reduction compared to noble metals. The application of this type of systems could be less expensive and more sustainable with regard to the criticality score.[39] However, further design developments are needed to achieve better performing base metal dyads or triads. For that, 2C-XES plays a crucial role to understand excited-state processes and charge transfer dynamics on the low-ps scale. It is an important tool to disentagle the relationship between molecular design and photocatalytic behaviour. Based on the results of this work, the following outlook can be given. The ^{3}MLCT lifetime has to be extended to achieve better TON in the proton reduction experiment. First, this can be realized by increasing the number of carbene counts or using cyclometalated ligands. In Figure 7.1, one possible molecular structure is proposed. Carbene or cyclometalated ligand functionalities are highlighted in green. Fe^{III} complexes are obtained when cyclometalated ligands are applied. This results in different photophysical properties as discussed in section 2.4.2.[57–59,140] Second, as deduced from 2C-XES the deactivation has to be bypassed via the ^{3}MLCT* to ^{3}MC channel (β channel). Most likely, by stabilizing the ^{3}MLCT state the β channel contribution can be reduced, so that the population of the charge transfer from iron to cobalt is potentially increased. Third, nuclear wavepacket dynamics are involved in the population of the undesired β channel. A more rigid ligand design or replacement of the iron-nitrogen oscillation via cyclometalated coordination might hinder the vibrational motions and thus destabilize the ^{3}MC state. In addition, the tuning of the bridging ligand via acetylene or phenyl-acetylene spacer is a viable strategy to improve the MLCT lifetime (*cf.* Figure 7.1).

In this context, the multimetal complex stability has to be adressed. The monodentate nitrogen-cobalt coordination is a problem at lower concentrations in coordinative solvents. However, an arbitrary increase of the concentration does not necessarily improve the catalysis but could reduce the transmission of irradiation during the proton reduction reaction. A bidentate ligand design via the dmgH coordination site

(*cf.* Figure 7.1, orange) can drastically enhance the system's stability at suitable concentrations for photocatalytic applications.[141]

8.1 General laboratory information

Schlenk technique was applied to all cross-coupling reactions and iron complex synthesis. Multimetal complexes were synthesized under ambient conditions. Details concerning inert or anhydrous conditions can be found in the synthesis description of ligands and complexes. The solvents were dried prior to usage according to literature or taken from a solvent-drying system *MB SPS 800* from *MBraun*. Chemicals were purchased by *Sigma-Aldrich/Merck*, *abcr*, *TCI* or *Fisher Scientific*. They were used without further purification in the synthesis.

8.2 Analytic and spectroscopic methods

Column chromatography

The substances were either purified over silica or over alumina (Al_2O_3, basic/neutral). The used eluent is stated in the synthesis description. A ratio of 1:20 between substance and column material was chosen. The column was 3-4 cm in diameter. Alternatively, medium-pressure liquid chromoatography (MPLC) was applied for purification. The device Combi Flash® Rf+ was from *Teledyne ISCO*.

Nuclear magnetic resonance spectroscopy

Substances were characterized by ^{1}H, ^{13}C, ^{15}N, ^{19}F and ^{31}P NMR. Spectra were recorded either on *Bruker* Avance 500 with frequencies of 500 MHz (^{1}H) or 125 MHz (^{13}C) or on *Bruker* Ascent 700 with frequencies of 700 MHz (^{1}H), 176 MHz (^{13}C), 70.6 MHz (^{15}N), 659 MHz (^{19}F) and 283.5 MHz (^{31}P) by the team of PD Dr. Hans Egold. Deuterated solvent was specificied for each compound. Spectra were referenced against the remaining proton signal of the deuterated solvent.

Mass spectrometry

Masses of the compounds were determined using ESI and EI mass spectra by the team of Dr. Adam Neuba. The ESI measurements were performed with a quadrupole TOF mass spectrometer SYNAPT G2 from the *Waters* company. On the DFS-sector field spectrometer from the company *Themo Scientific* EI mass spectra were recorded.

Elemental Analysis

The vario MICRO Cube analyzer from *elementar* was used for the elemental analysis. Manual calibration of the analyzer was performed. With a thermal conductivity

detector the content of carbon, nitrogen and hydrogen was determined after gas chromatographic separation.

IR spectroscopy

Applying the ATR technique IR spectra were recorded on a Vertex70 by *Bruker*. Solid compounds were measured.

Single crystal X-ray diffraction

X-ray single-crystal data were recorded and analyzed by Dr. Roland Schoch, Dr. Frank Pammer or Dr. Regine Herbst-Irmer using a *Bruker* Venture D8 diffractometer with a MoK_α µ-source ($\lambda = 0.71073$ Å) and a Photon III area in detector at 120 K. Or single crystal data were collected using a *Bruker* Smart Apex II Quasar with an Incoatec Mo IµS Source ($\lambda = 0.71073$ Å) and an Apex II area detector at 100 K.

UV-Vis spectroscopy

Steady-state absoprtion spectra were recorded on a Lambda 45 double-beam UV spectrophotometer from *PerkinElmer* using 1 cm Quartz cuvettes and a concentration of $1 \cdot 10^{-5}$ mol/L. The Lambda spectrophotometer from *PerkinElmer* was used for solutions with concentration up to $2.5 \cdot 10^{-4}$ mol/L. They were measured in a 0.1 cm quartz cuvette. Spectroscopy grade acetonitrile was used for all measurements.

Electrochemistry

The measurements were conducted by Dr. Adam Neuba. An optically transparent electrochemical cell was used for spectro-electrochemical experiments with a diameter of d = 1 mm. The measurements were performed in absolute acetonitrile under argon and $(n\text{-Bu})_4NPF_6$ as supporting electrolyte. The working electrode was a platinium gauze. Oxidative or redutive potentials were applied causing spectral changes in the range of 200-1100 nm in the optical absorption which were detected by a Varian Cary 50 spectrophotometer. The PAR101 potentiostat from *Metrohm* or the Compactstat from *Ivium* were used for cyclic and square wave voltammograms. Samples were dissolved in MeCN (1 mM) with $(n\text{-Bu})_4NPF_6$ (0.1 M). The working electrode consisted of Pt (d = 1 mm) or glassy carbon (d = 2 mm). A Pt wire was used as counter electrode together with Ag/0.01 M $AgNO_3$, 0.1 M $(n\text{Bu})_4NPF_6$ in MeCN as reference electrode. After the measurements ferrocene as internal standard was added. The potentials are referenced against the Fc^+/Fc couple and analysed according to the diagnostic criteria by Randles–Sevcik equation and Nicholson.[142–145]

Transient optical absorption spectroscopy

Transient absorption spectroscopy was performed and analysed by the group of Prof. Dr. Stefan Haacke at the University of Strasbourg or by the group of Prof. Dr. Wojciech Gawelda at the Adam Mickiewicz University.
A femtosecond laser system using a Ti:Sapphire source (FemtoLasers Synergy 20) with 800 nm central wavelength was applied for **Fe1-2** and **Dy1-2**. A 20 fs temporal resolution was provided with a repetition rate of 80 MHz. By passing a Chirped Pulsed Amplification system (CPA-Amplitude Technology, Pulsar) a fundamental beam with 0.5 mJ energy and temporal resolution of 40 fs at 5 kHz was produced. A TOPAS Prime (Light Conversion) provided the 60 fs pump pulses at 550 nm. The home-built set-up was previoisly described.[146,147] Portion of the 800 nm beam was converted to the white light spectrum (460-1030 nm) in a 2 mm calcium fluoride plate. At the magic angle (54.7°) the pump and probe beams were linearly polarized (IRF $\approx$ 60 fs). Six to eigth temporal scans were averaged to achieve good S/N ratio. To remain in the linear one-photon response regime of the compounds, the pump pulse energy was adjusted to 80 nJ, resulting in a pump energy density below 1 mJ/cm^2. The samples with ~ 1.5 mM concentration in MeCN were cycled in a quartz flow-cell with 200 μm optical path length. Photobleaching was excluded due to only minor reduction of absorbance (<5%) after the experiment as deduced by UV-Vis spectroscopy. Data were processed by a home-made software (Matlab). Corrections for non-zero background signal at negative time delays, GVD of the white light, time-zero solvent response and the quartz sample cell ("coherent artefacts") were applied.[146,147]
The experimental setup for TA measurements of **Fe3** and **Dy3** was described elsewhere.[120] Optical transient absorption spectra of **Fe3** and **Dy3** were measured on a Helios spectrometer from *Ultrafast Systems* with an instrument response function (IRF) of 120 fs. The adjustment of the original commercial setup was carried out with a dichroic optical filter which was placed in front of the flow cell. This masked the residual 800 nm white light continuum. White light continuum generation in 330-720 nm was realized by a continuously moving CaF_2 crystal. Samples (10 mM, MeCN) were excited with 400 nm or 515 nm laser (2µJ) with a time window of 450 ps. The signal transmission was ensured by using a 0.12 µm flow cell with CaF_2 windows and a gear pump (1 mL/s flow) for refreshment of sample. The solvent contribution was eliminated by substracting the solvent response from the TA data.

Ultrafast X-ray emission spectroscopy

Iron and cobalt K α emission was simultaneously measured (120 fs temporal resolution) at the FXE instrument at SASE1 branch of European XFEL, Schenefeld, Germany,[148] with the help of the XFEL staff and the research group of Prof. Dr.

Wojciech Gawelda. Data were processed and analysed by Dr. Michał Nowakowski and interpreted by Dr. Michał Nowakowski and Marina Huber-Gedert. **Dy3**, **Fe3** and **C14** (10mM or 5 mM, in MeCN) were measured in a cylindrical liquid jet with 200 μm diameter, using a HPLC pump for sample recirculation. A $\approx$ 55% excitation rate was achieved by a 400 nm optical laser pulse (5.5 - 15 μJ/pulse) with 50 fs pulse length. The SASE X-ray probe beam had a central energy of 9.3 keV with 125 bunches per pulse train. The intra-train repetition rate was 0.564 MHz with a beam size of 20 μm (fwhm), pulse duration of 100 fs and ~1012 photons per pulse. An alternating pumped/unpumped train mode was realized by operating at 10 Hz repitition rate per train and at 5 Hz for the optical laser. A wavelength-dispersive 16-crystal von Hamos XES spectrometer together with a 2D charge integrating gain-switching Jungfrau 1M detctor (1024 x 1024 pixels) were used to record the fluorescence emission (Fe Kα and Co Kα with Ge(440) and Si(531) analyzer crystal reflections at 75.4° and 77°, respectively). The timing jitter was ~ 70 fs (fwhm) between the pump and probe pulse. Signal integration was done over 500 trains (= 60 s) per time point. Kinetics were recorded for three different time windows: 1) -5 ps to 15 ps with Δt = 1 ps, 2) -1.2 to 3.3 ps with Δt = 150 fs and 3) -1.0 ps to 1.5 ps with Δt = 150 fs. A good S/N ratio was achieved by individually adjusting the number of measurements.

Computational methods

The ORCA 4.0.1, 4.2.0 or 5.0.1 quantum chemistry packages were applied for all calculations.[149] The PBEh-3c method was applied for all unconstrained DFT optimizations of the investigated compounds.[150–152] Single-point or TDDFT calculations were performed using TPSSh hybrid functional and the Alrichs def2-TZVPP or def2-TZVP basis set on all atoms.[153,154] MeCN solvation was included via SMD or CPCM.[155] Correction for dispersion interaction was performed by DFT-D3 with Becke-Johnson damping scheme (D3BJ).[156–158] Singlet transitions of TDDFT spectra were broadened by Gaussian broadening with fixed FWHM of 30nm. Avogadro was used to visualized the donor and acceptor orbitals for selected transitions.
The following calculations were performed by Dr. Hossam Elgabarty from the group of Prof. Dr. Thomas Kühne. The potential energy surface including singlet and triplet states was computed based on the optimized geometry of the ground state. New states after simultaneous stretching of Fe-N distance (0.05 Å steps) and Fe-N bite angle (0.7° steps) were investigated by computing the 60 lowest-lying singlet and triplet transitions at each point. By using Mulliken population analysis the excited states were assigned as ^{1}MLCT, ^{3}MLCT and ^{3}MC state.[159,160] In the context of the wavepacket analysis, the ^{3}MC state was identified and vibrational modes were computed from the geometry-optimized structure (def2-SVP) by Gaussian 16.[161]

8.3 Ligand synthesis

4'(((Trifluoromethyl)sulfonyl)oxy)-2,2':6',2"-terpyridine 1

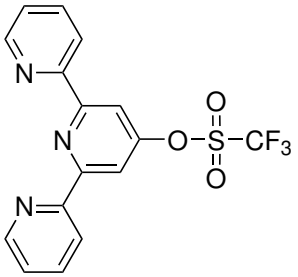

A solution of 2,6-bis(2-pyridyl)-4(1H)-pyridon (5.63 mmol, 1.74 g) in dry pyridine (20 mL) was cooled down to 0°C. Tf_2O (8.45 mmol, 1.4 mL) was added dropwise. After 30 min at 0°C the reaction was warmed to room temperature. After 20 hours cold water was added which caused formation of a precipitate. It was isolated and washed with water. Extraction with *n*-hexane or DCM gave the desired product **1** in 71% yield.[162]

^{1}H NMR (500 MHz, $CDCl_3$, ppm): δ = 8.73 (ddd, J = 4.8, 1.8, 0.9 Hz, 2H), 8.62 (dt, J = 8.0, 1.0 Hz, 2H), 8.43 (s, 2H), 7.89 (ddd, 2H), 7.39 (ddd, J = 7.5, 4.8, 1.2 Hz, 2H).
^{13}C NMR (125.7 MHz, $CDCl_3$, ppm): δ = 159.0, 158.7, 154.4, 149.6, 137.2, 124.9, 121.6, 113.3.
Elemental Analysis: calc. for $C_{16}H_{10}N_3SO_3F_3$ (%): C 50.40, H 2.64, N 11.02, S 8.41; found: C 50.13, H 2.87, N 10.93, S 8.14.

4'(Pyridn-4-ylethynyl)-2,2':6',2"-terpyridine L1

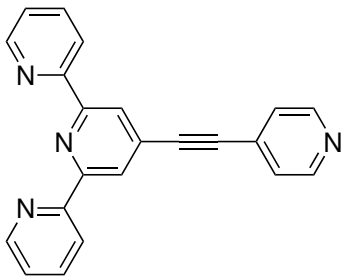

1 (2 mmol, 763 mg), 4-ethynylpyridine hydrochloride (2.6 mmol, 363 mg), $Pd(PPh_3)_4$ (0.14 mmol, 162 mg) and CuI (0.2 mmol, 38 mg) were suspended in degassed DIPA (80 mL). After two days at 50°C the solvent was removed. The raw product was

purified over silica using DCM and an increasing amount of acetone (~10%). Alternatively, basic alumina could be used. **L1** can be isolated in 62% yield.
^{1}H NMR (500 MHz, $CDCl_3$, ppm): δ = 8.73 (ddd, J = 4.8, 1.8, 0.9 Hz, 2H), 8.67 (m, J = 4.4, 1.6 Hz, 2H), 8.64 (dt, J = 8.0, 1.0 Hz, 2H), 8.62 (s, 2H), 7.89 (td, 2H), 7.45 (m, J = 4.4, 1.6 Hz, 2H), 7.38 (ddd, J = 7.5, 4.8, 1.2 Hz, 2H).
^{13}C NMR (125.7 MHz, $CDCl_3$, ppm): δ = 156.2, 155.9, 150.4, 149.7, 137.4, 132.6, 131.0, 126.1, 124.6, 123.4, 121.7, 91.9, 90.8.
ESI-MS (m/z): $[M+H]^+_{theo}$ = 335.1297, $[M+H]^+_{exp}$ = 335.1313; $[M+Na]^+_{theo}$ = 357.1116, $[M+Na]^+_{exp}$ = 357.1126.
Elemental Analysis: calc. for $C_{22}H_{14}N_4$ (%): C 79.02, H 4.22, N 16.76; found: C 79.48, H 4.56, N 16.71.

4-Ethynylbenzaldehyde 3

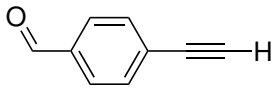

4-Bromobenzahldehyde (5 mmol, 945 mg), $Pd(PPh_3)_2Cl_2$ (0.26 mmol, 179 mg), CuI (0.25 mmol, 48 mg) and PPh_3 (0.52 mmol, 135 mg) were combined in degassed NEt_3 (25 ml). Trimethylsilylacetylene (7.5 mmol, 1 mL) was added at 60°C. After 19 hours under reflux a black suspension was filtered through silica and washed with EtOAc. Organic phase was evaporated. Purification over silica with EtOAc:*n*-hexane (1:19) gave a yellow powder which was dissolved in MeCN. KOH (5 mol/L, 15 mL) was added at 0°C. After 15 minutes the mixture was poured into water. Product was extracted with Et_2O and the organic phase was dried over Na_2SO_4. Removal of solvent and recrystallization gave **3** in good purity. Further purification over silica with ethylacetate:*n*-hexane (1:10) yielded the desired product as colourless powder (48%).[Fu.2018]
^{1}H NMR (500 MHz, $CDCl_3$, ppm): δ = 10.02 (s, 1H), 7.84 (m, 2H), 7.64 (m, 2H), 3.29 (s,1H).
^{13}C NMR (125.7 MHz, $CDCl_3$, ppm): δ = 191.5 136.1, 132.9, 129.6, 128.5, 82.8, 81.2.
Elemental Analysis: calc. for C_9H_6O (%): C 83.06, H 4.65; found: C 82.46, H 4.15.

4'(4-Ethynylphenyl)-2,2':6',2"-terpyridine 4

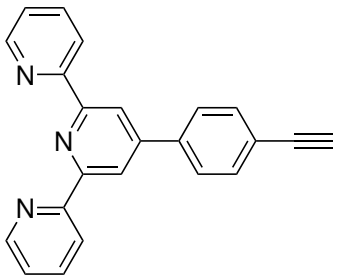

4-Ethynylbenzaldehyde **3** (2.3 mmol, 300 mg), 2-acetylpyridine (4.6 mmol, 555 mg) and NaoH (4.6 mmol, 184 mg) were combined. Concentrated ammonia solution (18.6 mL) and EtOH (36 mL) were added. The suspension was stirred for five days at room temperature and turned orange. The solid material was isolated and washed with EtOH and H_2O. The product was dissolved in EtOAc and the solvent was removed. After drying **4** was isolated as yellow powder in 36% yield.[22]

^{1}H NMR (500 MHz, $CDCl_3$, ppm): δ = 8.74 (s, 2H), 8.73 (m, 2H), 8.68 (dt, J = 7.9 Hz, 2H), 7.90-7.87 (m, 4H), 7.64 (m, J = 8.4 Hz, 2H), 7.36 (ddd, J = 7.4, 4.8, 1.2 Hz, 2H), 3.18 (s, 1H).
^{13}C NMR (125.7 MHz, $CDCl_3$, ppm): δ = 156.3, 156.3, 149.5, 149.3, 139.0, 137.0, 132.9, 127.4, 124.1, 123.0, 121.5, 118.9, 83.5, 78.6.
Elemental Analysis: calc. for $C_{23}H_{15}N_3$ (%): C 82.86, H 4.54, N 12.60; found: C 81.37, H 4.84, N 12.11.

4'(4-(Pyridin-4-ylethynyl)phenyl)-2,2':6',2"-terpyridine L2

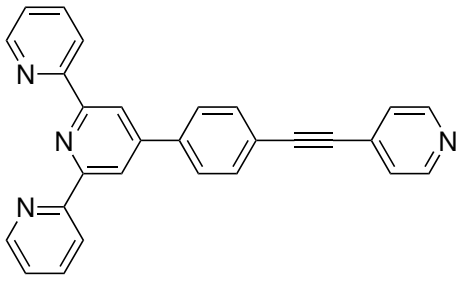

4'(4-Ethynylphenyl)-2,2':6',2"-terpyridine **4** (4.65 mmol, 1.55 g), 4-iodopyridine (5.12 mmol, 1.05g) were combined with $Pd(PPh_3)_2Cl_2$ (0.37 mmol, 261 mg), PPh_3 (0.37 mmol, 98 mg) and CuI (0.47 mmol, 89 mg). After addition of degassed NEt_3 (150 mL) the reaction was stirred for three days at 80°C. After removal of NEt_3 the residue was dissolved in DCM. Insoluable solids were filtered off. After drying over Na_2SO_4 the solvent was removed. The raw product was purified over

silica with EtOAc/*n*-hexane (1:1). **L2** was obtained as colourless powder in 70% yield.

^{1}H NMR (700 MHz, $CDCl_3$, ppm): δ = 8.77 (s, 2H), 8.74 (ddd, J = 4.7, 1.7, 0.9 Hz, 2H), 8.69 (dt, J = 7.9, 1.0 Hz, 2H), 8.63 (dd, J = 4.4, 1.6 Hz, 2H), 7.96 – 7.94 (m, 2H), 7.90 (td, J = 7.7, 1.8 Hz, 2H), 7.72 – 7.70 (m, 2H), 7.45 (dd, J = 4.4, 1.6 Hz, 2H), 7.38 (ddd, J = 7.4, 4.7, 1.2 Hz, 2H).
^{13}C NMR (176 MHz, $CDCl_3$, ppm): δ = 156.2, 156.2, 149.5, 149.4, 149.3, 139.5, 137.3, 132.7, 132.3, 127.7, 125.9, 124.2, 122.9, 121.7, 119.0, 94.4, 88.1.
ESI-MS (m/z): $[M+H]^+_{theo}$ = 411.1610, $[M+H]^+_{exp}$ = 411.1617.
Elemental Analysis: calc. for $C_{28}H_{18}N_4$ (%): C 81.93, H 4.42, N 13.65; found: C 80.90, H 5.03, N 12.52.

2,6-Dichloro-4-(4,4,5,5-tetramethyl-1,3,2-dioxaborolan-2-yl)pyridine 5

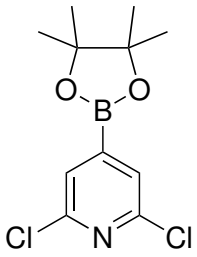

A solution of (1,5-cyclooctadiene)(methoxy)iridium(I) dimer (0.375 mmol, 249 mg), 4,4'-di-tert-butyl-2,2'-bipyridyl (0.75 mmol, 201 mg) and bis(pinacolato)diboron (25 mmol, 6.35 g) in dry, degassed MTBE (45 mL) was prepared. 2,6-Dichloropyridine (25 mmol, 3.7 g) was added. After 30 hours the solvent was removed. The raw product was purified over silica with DCM as eluent. The white crystalline powder of **5** was obtained in 97% yield.[89]

^{1}H NMR (500 MHz, $CDCl_3$, ppm): δ = 7.58 (s, 2H), 1.35 (s, 12H).
^{13}C NMR (125.7 MHz, $CDCl_3$, ppm): δ = 150.3, 127.7, 85.1, 24.7.
Elemental Analysis: calc. for $C_{11}H_{14}NO_2Cl_2B$ (%): C 48.23, H 5.15, N 5.11; found: C 48.67, H 5.48, N 5.03.

2,6-Dichloro-4,4'-bipyridine 6

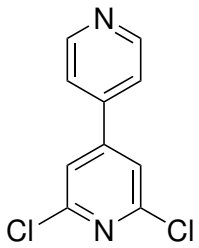

First, 2,6-Dichloro-4-(4,4,5,5-tetramethyl-1,3,2-dioxaborolan-2-yl)pyridine **5** (222 mmol, 6.03 g), 4-iodopyridine (20 mmol, 4.1 g), $Pd(OAc)_2$ (0.32 mmol, 72 mg), PPh_3 (1.6 mmol, 420 mg), K_2CO_3 (68 mmol, 9.4 g) were degassed. Second, degassed solvent mixture 1,4-dioxane/H_2O (80 ml/20 mL) was added leading to a two-phase mixture. Stirring at 110°C for two days resulted in color change to brown. The two-phase mixture was poured into water. The precipitate was collected and washed with water. The crude product was dissolved in DCM and purified over silica using EtOAc:cyclohexane (1:1). **6** was obtained in 83% yield.[163]

^{1}H NMR (500 MHz, $CDCl_3$, ppm): δ = 8.79 (m, J = 4.4, 1.7 Hz, 2H), 7.49 (s, 2H), 7.48 (m, J = 4.4, 1.7 Hz, 2H).
^{13}C NMR (125.7 MHz, $CDCl_3$, ppm): δ = 152.0, 151.5, 151.4, 143.6, 121.7, 121.2.
ESI-MS (m/z): $[M+H]^+_{theo}$ = 224.9986, $[M+H]^+_{exp}$ = 225.0024.
Elemental Analysis: calc. for $C_{10}H_6N_2Cl_2$ (%): C 53.37, H 2.69, N 12.45; found: C 52.92, H 3.24, N 12.21.

1,1'-([4,4'-Bipyridine]-2,6-diyl)bis(3-methyl-1H-imidazol-3-ium)chloride L3

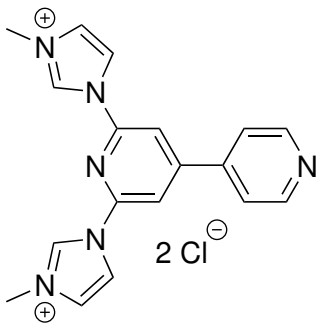

2,6-Dichloro-4,4'-bipyridine **6** (7.5 mmol, 1.69 g) and *N*-methylimidazole (75 mmol, 6 mL) were combined in a vial. After degassing the mixture was stirred for five days at 150°C. After cooling the brown solid was dissolved in MeOH and added dropwise in EtOAc. A precipitate was isolated and washed with EtOAc. The

crude product was purified over alumina using the solvent mixture MeCN/MeOH (30:1). After evaporation of solvent **L3** was obtained as beige powder in 38% yield.[164]

^{1}H NMR (500 MHz, DMSO-d_6, ppm): δ = 10.77 (s, 2H), 8.94-8.92 (m, 4H), 8.75 (s, 2H), 8.16 (m, J = 4.5, 1.6 Hz, 2H), 8.09 (t, J = 1.6 Hz, 2H), 4.06 (s, 6H).
^{13}C NMR (125.7 MHz, DMSO-d_6, ppm): δ = 152.7, 151.0, 146.2, 141.8, 136.7, 125.0, 121.6, 119.3, 111.7. 36.6.
ESI-MS (m/z): $[M]^{2+}_{theo}$ = 318.1593/2 = 159.0797, $[M]^{2+}_{exp}$ = 159.0804; $[M\text{-}H]^{+}_{theo}$ = 317.1515, $[M\text{-}H]^{+}_{exp}$ = 317.1483.
Elemental Analysis: calc. for PF_6-salt $C_{18}H_{18}N_6P_2F_{12}$ (%): C 35.54, H 2.98, N 13.82; found: C 35.37, H 3.47, N 13.71.

2,6-Dichloro-4-iodopyridine 7-Cl

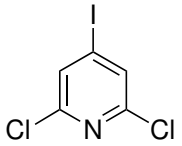

2,6-Dichloropyridine (10 mmol, 1.48 g) dissolved in THF was cooled down to -78°C. *n*-BuLi in *n*-hexane (1.6 M, 10.5 mmol, 6.6 mL) was added. After one hour iodine (20mmol, 5 g) in THF (12,5 mL) was added dropwise to the solution. After warming to room temperature over 14 hours the reaction was quenched with an aqueous sodium thiosulfate solution. The organic phase was isolated and THF was removed. Product mixture of **7**-Cl and 2,6-dichloro-3-pyridine was separated by recrystallization in EtOH. The product was isolated as white needles (50%).[90]

^{1}H NMR (500 MHz, $CDCl_3$): δ = 7.66 (s, 2H) ppm.
^{13}C NMR (125.7 MHz, $CDCl_3$): δ = 150.9, 131.6, 107.7 ppm.
Elemental Analysis: calc. for $C_5H_2NCl_2I$: C 21.93, H 0.74, N 5.11; found: C 22.20, H 1.15, N 5.49.

2,6-Dichloro-4-ethynylpyridine 8-Cl

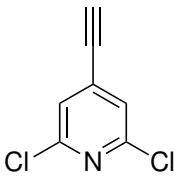

Trimethylsilylacetylene (3.1 mmol, 303 mg) and **7**-Cl (3 mmol, 822 mg) were dissolved in degassed NEt_3 (50 mL). $Pd(PPh_3)_2Cl_2$ (0.12 mmol, 84 mg), PPh_3 (0.12 mmol, 31 mg) and CuI (0.18 mmol, 34 mg) were added. After one day, the solvent was removed and the raw product was purified over silica with ethylacetate:*n*-hexane (1:1). The TMS-protected product was combined with KOH (30 mmol, 1,68 g in H_2O, 5 mL) in MeCN (18 mL) at 0°C. After 15 minutes water was added. A precipitation was collected. It was dissolved in Et_2O. After removal of solvent sublimation gave **8**-Cl as colourless crystals in 66% yield.[90]

^{1}H NMR (500 MHz, $CDCl_3$, ppm): δ = 7.32 (s, 2H), 3.42 (s, 1H).
^{13}C NMR (125.7 MHz, $CDCl_3$, ppm): δ = 151.1, 135.4, 125.4, 84.8, 78.8.
ESI-MS (m/z): $[M+H]^+_{theo}$ = 171.9721, $[M+H]^+_{exp}$ = 171.9690.
Elemental Analysis: calc. for $C_7H_3NCl_2$ (%): C 48.88, H 1.76, N 8.14; found: C 49.35, H 2.20, N 8.21.

2,6-Dichloro-4-(pyridin-4-ylethynyl)pyridine 9-Cl

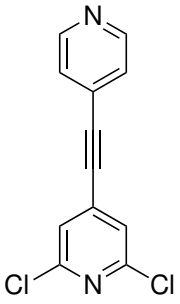

4-Iodopyridine (1.3 mmol, 258 mg), $Pd(PPh_3)_2Cl_2$ (0.04 mmol, 28 mg), PPh_3 (0.04 mmol, 10 mg) and CuI (0.05 mmol, 10 mg) were added to **8**-Cl. Dried, degassed solvent mixture NEt_3/THF (1:1, 20 mL) was used. After 14 hours a suspension was formed. After solvent removal purification over silica with ethylacetate:*n*-hexane (1:20) gave the desired product as yellow powder (98%).

^{1}H NMR (500 MHz, $CDCl_3$, ppm): δ = 8.68 (m, 2H), 7.39 (m, 2H), 7.38 (s, 2H).

^{13}C NMR (125.7 MHz, $CDCl_3$, ppm): δ = 150.9, 150.0, 135.0, 129.1, 125.5, 124.5, 92.9, 87.9.
ESI-MS (m/z): $[M+H]^+_{theo}$ = 248.9986, $[M+H]^+_{exp}$ = 248.9993.
Elemental Analysis: calc. for $C_{12}H_6N_2Cl_2$ (%): C 57.86, H 2.43, N 11.25; found: C 58.13, H 2.96, N 10.67.

2,6-Dibromo-4-iodopyridine 7-Br

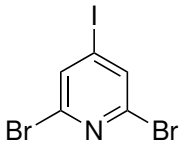

2,6-Dibromopyridine **10** (2 mmol, 484 mg) dissolved in THF (8 mL) was cooled down to -30°C. TMPMgCl·LiCl in THF/toluene (1M, 3 mL) was added dropwise. After 40 mintues iodine was added. Colour of the solution changed from yellow to red. After 14 hours and warming to room temperature the reaction was quenched with an aqueous $Na_2S_2O_3$ solution. The solution turned into a suspension. Et_2O and EtOAC were used to extract the raw product. Combined organic phases were washed with an aqueous solution of NH_4Cl and dried over Na_2SO_4. Solvents were removed and the product washed with acetone. **7**-Br was isolated in 69% yield.[92]

^{1}H NMR (500 MHz, $CDCl_3$, ppm): δ = 7.84 (s, 2H).
^{13}C NMR (125.7 MHz, $CDCl_3$, ppm): δ = 141.3, 135.8, 107.7.
Elemental Analysis: calc. for $C_5H_2NBr_2I$ (%): C 16.55, H 0.56, N 3.86; found: C 16.91, H 0.82, N 4.11.

2,6-Dibromo-4-ethynylpyridine 8-Br

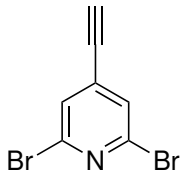

2,6-Dibromo-4-iodopyridne **7**-Br (1 mmol, 363 g) was dissolved in degassed NEt_3 (20 mL). Then $Pd(PPh_3)_2Cl_2$ (0.08 mmol, 56 mg), PPh_3 (0.08 mmol, 21 mg) and CuI (0.12 mmol, 22 mg) were added. The mixture was cooled to 0°C. Trimethylsilylacetylene (1.05 mmol, 103 mg, 0.15 mL) diluted in degassed, dry THF (20 mL) was added dropwise over one hour to avoid twofold acetylation. After complete addition the reaction was stirred for two more hours at 0°C and warmed to room temperature over night. The solvent was removed and the raw product purified over

silica. First, pure *n*-hexane was used as eluent. Then the amount of ethylacetate was gradually increased up to 1:1. The TMS-protected product was suspended in MeCN (5 mL) at 0°C. Aqueous solution of KOH (5M, 4 mL) was added. Addition of water caused the precipitation of a brown solid. It was extracted with Et_2O. Organic phase was washed with brine and solvent was removed in vacuum. Purification over silica with *n*-hexane:ethylacetate (20:1) gave **8**-Br (64%).[165]

^{1}H NMR (500 MHz, $CDCl_3$, ppm): δ = 7.50 (s, 2H), 3.41 (s, 1H).
^{13}C NMR (125.7 MHz, $CDCl_3$, ppm): δ = 141.0, 134.7, 129.3, 84.8, 78.4.
ESI-MS (m/z): $[M+H]^+_{theo}$ = 261.8690, $[M+H]^+_{exp}$ = 261.8751.
Elemental Analysis: calc. for $C_7H_3NBr_2$ (%): C 32.22, H 1.16, N 5.37; found: C 32.48, H 1.63, N 5.66.

2,6-Dibromo-4-(pyridin-4-ylethynyl)pyridine 9-Br

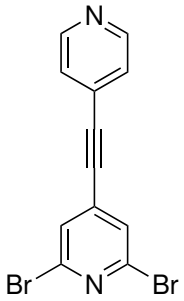

Synthesis was conducted similarly to Hübscher *et al.* with changes in the order of reagents and temperature.[90] 4-Iodopyridine (2.53 mmol, 526 mg) was dissolved in degassed DIPA (40 mL). Then $Pd(PPh_3)_2Cl_2$ (0.184 mmol, 129 mg), PPh_3 (0.184 mmol, 48 mg) and CuI (0.23 mmol, 44 mg) were added. The mixture was cooled to 0°C. 2,6-Dibromo-4-ethynylpyridine **8**-Br (2.2 mmol, 575 mg) diluted in degassed and dry THF (30 mL) was added dropwise in one hour to avoid twofold acetylation. After complete addition the reaction was stirred for two more hours at 0°C and warmed to room temperature over night. Solvent was removed. The raw product was purified over silica with *n*-hexane/EtOAc (5:1). **9**-Br was obtained in 63% yield.

^{1}H NMR (500 MHz, $CDCl_3$, ppm): δ = 8.68 (m, 2H), 7.57 (s, 2H), 7.39 (m, 2H).
^{13}C NMR (125.7 MHz, $CDCl_3$, ppm): δ = 150.3, 141.1, 134.6, 129.4, 128.8, 125.7, 93.3, 87.8.
ESI-MS (m/z): $[M+H]^+_{theo}$ = 338.8956, $[M+H]^+_{exp}$ = 338.8996.

2,6-Di(1H-imidazol-1-yl)pyridin-4-amine 13

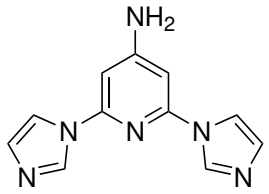

2,6-Dibromopyridine-4-amine (30 mmol, 7.56 g), imidazole (75 mmol, 5.11 g), K_2CO_3 (75 mmol, 10.37 g) and CuO (7.5 mmol, 597 mg) were degassed. Dry, degassed DMF (200 mL) was added and the mixture was stirred for six days at 150°C. After removal of DMF the residue was suspended in H_2O. The solids were isloated and dissolved in DCM/MeOH. Drying gave **13** in 88% yield.[94]

^{1}H NMR (500 MHz, DMSO-d_6, ppm): δ = 8.49 (t, J = 1.0 Hz, 2H), 7.84 (t, J = 1.3 Hz, 2H), 7.10 – 7.09 (m, 2H), 6.68 (s, 2H), 6.67 (s, 2H).
^{13}C NMR (125.7 MHz, DMSO-d_6, ppm): δ = 159.8, 149.1, 135.9, 130.5, 117.3, 95.0.
ESI-MS (m/z): $[M+H]^+_{theo}$ = 227.1045, $[M+H]^+_{exp}$ = 227.1057.

2,6-Di(1H-imidazol-1-yl)-4-iodopyridine 14

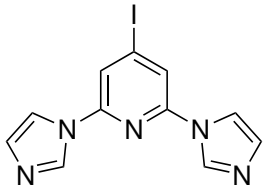

2,6-Di(1H-imidazol-1-yl)pyridin-4-amine **13** (1.9 mmol, 430 mg) was first suspended in concentrated hydrochloric acid (6 mL). Then water (34 mL) was added. KI (30.4 mmol, 5.05 g) was added while cooling with an ice-bath. After 30 minutes $NaNO_2$ (7.6 mmol, 524 mg) was added scopewise. The reaction was neutralised with $NaHCO_3$. After addition of Na_2SO_3 an orange suspension was formed. Solids were isolated. The aqueous phase was extracted with DCM. After removal of DCM and combination with the isolated solids the raw product was purified with flash clomun chromatography using acetone as eluent. **14** was obtained as off-white powder in 59% yield. I:Cl ratio was 88:12.[95] Alternative route using H_2SO_4 as acid gave the desired product in 38% yield.

^{1}H NMR (500 MHz, DMSO-d_6, ppm): δ = 8.77 (s, 2H), 8.23 (s, 2H), 8.15 (t, J = 1.3 Hz, 2H), 7.14 (s, 2H).
^{13}C NMR (125.7 MHz, DMSO-d_6, ppm): δ = 147.6, 135.8, 130.4, 118.2, 116.9,

111.9.
ESI-MS (m/z): $[M+H]^+_{theo}$ = 337.9903, $[M+H]^+_{exp}$ = 337.9908.
Elemental Analysis: calc. for $C_{11}H_8N_5I$ (%): C 39.19, H 2.39, N 20.77; found: C 39.07, H 2.43, N 20.37.

2,6-Di(1H-imidazol-1-yl)-4-(pyridin-4-ylethynyl)pyridine 11

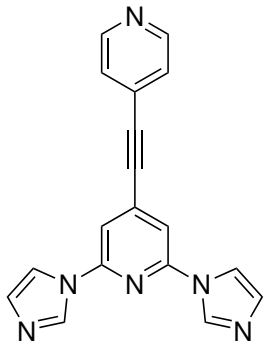

14 (6.36 mmol, 2.14 g), 4-ethynylpyridine hydrochloride (8.27 mmol, 1.15 g), $Pd(PPh_3)_4$ (0.89 mmol, 1.03 g) and CuI (1.91 mmol, 363 mg) were suspended in degassed DIPA (80 mL) and DMSO (80 mL). After twelve days, the solvent was removed under vacuum and H_2O was added. The raw product was isolated and dissolved in concentrated hydrochloric acid. Unsoluable solids were removed. The acidic solution was neutralised by aqueous NaOH (2.5 M) which caused the formation of a precipitate. It was filtered and washed with water. The product was dissolved in acetone and the solvent removed. **11** was obtained in 74% yield.

^{1}H NMR (500 MHz, DMSO-d_6, ppm): δ = 8.81 (s, 2H), 8.74 (dd, J = 4.4, 1.5 Hz, 2H), 8.20 (s, 2H), 8.05 (s, 2H), 7.62 (dd, J = 4.4, 1.6 Hz, 2H), 7.17 (s, 2H).
^{13}C NMR (125.7 MHz, DMSO-d_6, ppm): δ = 150.3, 148.1, 135.8, 135.2, 130.5, 128.6, 125.4, 116.9, 111.7, 91.7, 89.8.
ESI-MS (m/z): $[M+H]^+_{theo}$ = 313.1202, $[M+H]^+_{exp}$ = 313.1206.

1,1'-(4-((1-Methylpyridin-1-ium-4-yl)ethynyl)pyridine-2,6-diyl)bis(3-methyl-1H-imidazol-3-ium)iodide L5

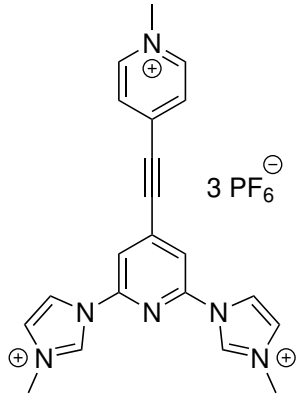

2,6-Di(1H-imidazol-1-yl)-4-(pyridin-4-ylethynyl)pyridine **11** (0.4 mmol, 125 mg) was dissolved in MeCN (5 mL). MeI (1.4 mmol, 0.08 mL) was added. The mixture was stirred at 70°C for 20h. The solvent was removed and the residue dissolved in DMSO. It was filtered and dropped into an aqueous KPF_6 solution. The precipitation was collected and washed with H_2O. After drying the product was isolated in 58% yield.

^{1}H NMR (700 MHz, acetone-d_6, ppm): δ = 10.03 (s, 2H), 9.23 (m, J = 6.6 Hz, 2H), 8.67 (t, J = 2.0 Hz, 2H), 8.57 (s, 2H), 8.40 (m, J = 6.7 Hz, 2H), 8.08 (t, J = 1.8 Hz, 2H), 4.68 (s, 3H), 4.26 (s, 6H).
^{13}C NMR (176 MHz, acetone-d_6, ppm): δ = 146.7, 146.6, 137.6, 136.7, 136.4, 130.3, 125.9, 119.9, 117.3, 95.1, 91.2, 48.9, 37.0.
ESI-MS (m/z): $[M]^{3+}_{theo}$ = 357.1828/3 = 119.0609, $[M]^{3+}_{exp}$ = 119.0602; $[M-H]^{2+}_{theo}$ = 356.1749/2 = 178.0875, $[M-H]^{+}_{exp}$ = 178.0881.
Elemental Analysis: calc. for $C_{21}H_{21}N_6P_3F_{18}$ (%): C 31.83, H 2.67, N 10.61; found: C 31.89, H 3.12, N 10.43.

4-((2,6-Di(1H-imidazol-1-yl)pyridin-4-yl)ethynyl)pyridine-1-oxide 15

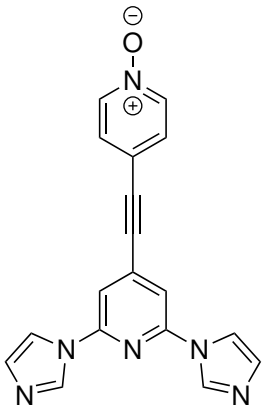

2,6-Di(1H-imidazol-1-yl)-4-(pyridin-4-ylethynyl)pyridine **11** (1.07 mmol, 334 mg) was suspended in DCM/H_2O (54 mL/7 mL) and $NaHCO_3$ (1.18 mmol, 99 mL) was added. Due to the addition of MCPBA (2.68 mmol, 462 mg) the suspension turned yellow. The reaction was stirred for 24h at 40°C. Then DCM was removed and saturated $NaHCO_3$ solution was added. The precipitate was collected and washed with water. Drying gave **15** in 61% yield.

^{1}H NMR (500 MHz, DMSO-d_6, ppm): δ = 8.80 – 8.78 (m, 2H), 8.33 – 8.30 (m, 2H), 8.17 (t, J = 1.4 Hz, 2H), 8.00 (s, 2H), 7.65 – 7.63 (m, 2H), 7.17 (dd, J = 1.4, 0.9 Hz, 2H).
^{13}C NMR (176 MHz, DMSO-d_6, ppm): δ = 148.1, 139.5, 135.8, 135.5, 130.5, 129.0, 116.9, 116.5, 111.5, 91.7, 90.5.
ESI-MS (m/z): $[M+H]^+_{theo}$ = 329.1151, $[M+H]^+_{exp}$ = 329.1163.

4-((2,6-Bis(3-methyl-1H-imidazol-3-ium-1-yl)pyridin-4-yl)ethynyl)pyridine-1-oxide iodide 16

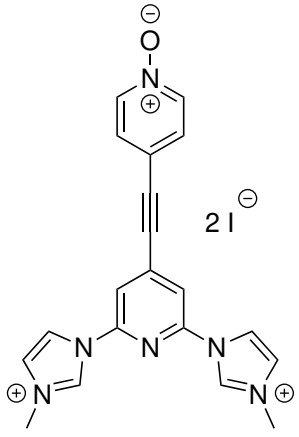

4-((2,6-Di(1H-imidazol-1-yl)pyridin-4-yl)ethynyl)pyridine-1-oxide **15** (0.65 mmol, 213 mg) and MeI (6.5 mmol, 0.4 mL) were combined in MeCN (60 mL). First, the reaction was stirred for 90 minutes at 40°C. Then, the temperature was increased to 80°C for 18h. After cooling the solvent and excess of MeI were removed. Dried product was isolated in 96%.

^{1}H NMR (500 MHz, DMSO-d_6, ppm): δ = 10.30 (s, 2H), 8.74 (t, J = 1.9 Hz, 2H), 8.45 (s, 2H), 8.37 – 8.34 (m, 2H), 8.07 (t, 2H), 7.67 – 7.64 (m, 2H), 4.03 (s, 6H).
^{13}C NMR (125.7 MHz, DMSO-d_6, ppm): δ = 145.8, 139.7, 136.7, 136.4, 129.1, 125.1, 119.1, 115.7, 115.6, 94.0, 89.2, 62.0.
ESI-MS (m/z): $[M+H]^+_{theo}$ = 358.1531/2 = 179.0767, $[M+H]^+_{exp}$ = 179.0754.

1,1'-(4-(Pyridin-4-ylethynyl)pyridine-2,6-diyl)bis(3-methyl-1H-imidazol-3-ium)hexafluorophosphate L4

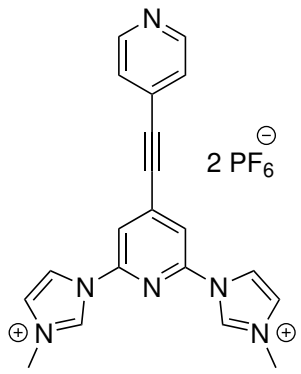

4-((2,6-Bis(3-methyl-1H-imidazol-3-ium-1-yl)pyridin-4-yl)ethynyl)pyridine-1-oxide iodide **16** (0.12 mmol, 74 mg) was suspended in dry, degassed DCM (12 mL). PBr_3 (0.77 mmol, 0.07 mL) was added. After stirring for 24h at 50°C DCM was removed in vacuo. The residue was dissolved in water and neutralised with $NaHCO_3$. After filtration the aqueous solution was dropped into an aqueous KPF_6 solution. A yellow precipitate was formed. After isolation and washing with water it was purified over alumina. The educt/product mixture was separated by using MeCN:Et_2O (1:1). **L4** was isolated in 9% yield.

^{1}H NMR (500 MHz, acetone-d_6, ppm): δ = 10.05 (s, 2H), 8.74 (dd, J = 4.4, 1.6 Hz, 2H), 8.71 (t, J = 2.0 Hz, 2H), 8.50 (s, 2H), 8.07 (t, J = 1.9 Hz, 2H), 7.58 (dd, J = 4.4, 1.6 Hz, 2H), 4.26 (s, 6H).
^{13}C NMR (125.7 MHz, acetone-d_6, ppm): δ = 150.7, 146.6, 138.2, 136.3, 128.5, 125.8, 125.6, 119.9, 116.9, 94.8, 87.9, 37.0.
ESI-MS (m/z): $[M]^{2+}_{theo}$ = 342.1593/2 = 171.0797, $[M]^{2+}_{exp}$ = 171.0818.

1,1'-(4-Iodopyridine-2,6-diyl)bis(3-methyl-1H-imidazol-3-ium) hexafluorophosphate L6

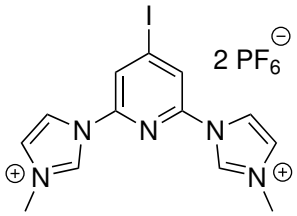

2,6-Di(1H-imidazol-1-yl)-4-iodopyridine **14** (0.3 mmol, 101 mg) was cooled down to -78°C in DCM (10 mL). Methyl triflate (0.75 mmol, 0.08 mL) was added dropwise. The reaction was stirred for three days at room temperature. A suspension was formed. The solvent was removed and DMSO was added. After filtration the DMSO solution was dropped into an aqueous solution of KPF_6. The formed precipitation was isolated and washed with water. The product **L6** was isolated as white powder in 53% yield.

^{1}H NMR (500 MHz, acetone-d_6, ppm): δ = 10.02 – 10.01 (m, 2H), 8.73 (s, 2H), 8.69 (t, J = 2.0 Hz, 2H), 8.05 – 8.04 (m, 2H), 4.24 (s, 2H).
^{13}C NMR (125.7 MHz, acetone-d_6, ppm): δ = 145.9, 136.3, 125.7, 124.1, 119.9, 111.8, 36.9.
ESI-MS (m/z): $[M]^{2+}_{theo}$ = 367.0294/2 = 183.5147, $[M]^{2+}_{exp}$ = 183.5195; $[M\text{-}H]^{+}_{theo}$ = 366.0216, $[M\text{-}H]^{+}_{exp}$ = 366.0237.

8.4 Complex synthesis

Fe1$_{homo}$

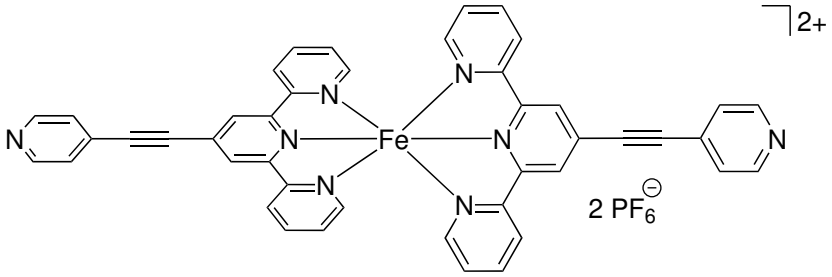

The ligand **L1** (0.5 mmol, 167 mg) and $FeBr_2$ (0.25 mmol, 54 mg) were placed in a flask containing inert gas. Degassed MeoH (20 mL) was added. After 30 minutes the solution was filtered and MeOH was removed. The violet residue was dissovled in H_2O. After filtration and addition of KPF_6 to the aqueous solution the complex precipitated. Isolation and washing with water gave **Fe1$_{homo}$** in 15% yield.

^{1}H NMR (700 MHz, CD_3CN, ppm): δ = 9.07 (s, 4H), 8.80 (dd, J = 4.2, 1.6 Hz, 4H), 8.50 – 8.48 (m, 4H), 7.94 – 7.90 (m, 4H), 7.71 (dd, J = 4.2, 1.7 Hz, 4H), 7.16 – 7.14 (m, 4H), 7.10 (ddd, J = 7.1, 5.7, 1.3 Hz, 4H).
^{13}C NMR (176 MHz, CD_3CN, ppm): δ = 160.5, 157.4, 153.4, 150.7, 139.3, 131.6, 129.3, 127.9, 125.9, 125.6, 124.4, 94.3, 89.6.
ESI-MS (m/z): $[M]^{2+}_{theo}$ = 724.1786/2 = 362.0893, $[M]^{2+}_{exp}$ = 362.0866.
Elemental Analysis: calc. for $C_{44}H_{28}N_8FeP_2F_{12}$ (%): C 52.09, H 2.78, N 11.04; found: C 51.50, H 2.89, N 10.93.

Fe1

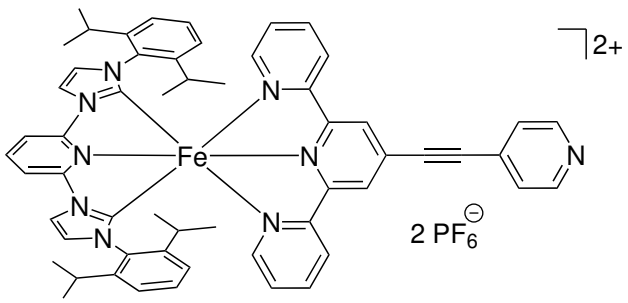

The bulky ligand 1,1'-(pyridine-2,6-diyl)bis(3-(2,6-diisopropylphenyl)-1H-imidazol-3-ium) bromide **SP** (0.2 mmol, 139 mg) was suspended in dry, degassed THF (15 mL) and cooled to -80 °C. $Fe(HMDS)_2$ (0.2 mmol, 76 mg) dissolved in THF was added

as *in-situ* base. The reaction was warmed to room temperature and turned violet. Then **L1** (0.2 mmol, 67 mg) was added. Stirring overnight and removal of THF gave the crude product. After dissolving in water and filtration, an anion exchange with KPF_6 (1.47 mmol, 270 mg) was conducted. Purification with alumina column chromatography using MeCN:Et_2O (1:5) gave **Fe1** as violet powder in moderate yield (64%).

^{1}H NMR (500 MHz, acetone-d_6, ppm): δ = 8.87 (t, 1H), 8.85 (d, J = 2.1 Hz, 2H), 8.77 (m, 2H), 8.68 (d, J = 7.6 Hz, 2H), 8.64 (d, J = 8.2 Hz, 2H), 8.34 (s, 2H), 8.14 (td, J = 7.8, 1.4 Hz, 2H), 7.64 (m, 2H), 7.59 (d, J = 2.2 Hz, 2H), 7.55 – 7.52 (m, 2H), 7.39 (ddd, J = 7.1, 5.6, 1.3 Hz, 2H), 7.30 (t, J = 7.8 Hz, 2H), 6.97 (d, J = 7.9 Hz, 4H), 0.91 (dt, J = 13.2, 6.6 Hz, 4H), 0.73 (d, J = 6.6 Hz, 12H), 0.63 (d, J = 6.6 Hz, 12H).
^{13}C NMR (76 MHz, acetone-d_6, ppm): δ = 198.3, 158.8, 157.0, 156.5, 153.4, 151.4, 145.8, 143.8, 138.2, 134.8, 132.4, 131.2, 130.3, 128.2, 127.9, 126.4, 126.2, 124.5, 123.2, 118.9, 109.7, 93.1, 90.6, 28.2, 26.8, 23.8.
ESI-MS (m/z): $[M]^{2+}_{theo}$ = 921.3930/2 = 460.6965, $[M]^{2+}_{exp}$ = 460.6991.
Elemental Analysis: calc. for $C_{57}H_{55}N_9FeP_2F_{12}$ (%): C 56.49, H 4.57, N 10.40; found: C 56.16, H 4.87, N 10.36.

Dy1

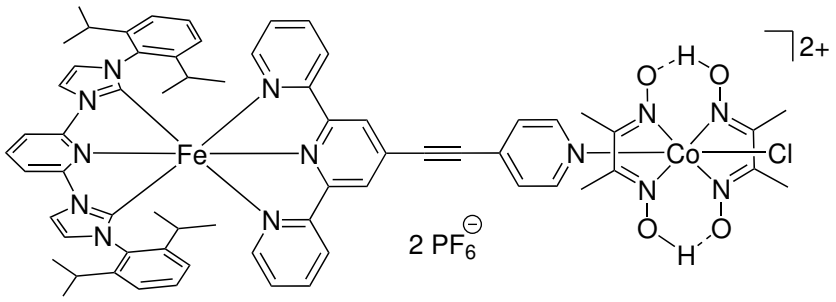

$CoCl_2$·6 H_2O (0.05 mmol, 12 mg) and dimethylglyoxime $dmgH_2$ (0.11 mmol, 13 mg) were heated to 70 °C in ethanol/water (95:5, 10 ml). **Fe1** (0.05 mmol, 61 mg) dissolved in DCM was added. The solution turned violet. After a few minutes the reaction was cooled to room temperature. Air was passed through the solution for 30 minutes which resulted into a precipitation. Addition of Et_2O enhanced the precipitation. After filtration and subsequent washing with EtOH, Et_2O and DCM **Dy1** was obtained as violet powder in 90% yield.

^{1}H NMR (700 MHz, acetone-d_6, ppm): δ = 8.88 (t, J = 8.3 Hz, 1H), 8.86 (d, J = 2.1 Hz, 2H), 8.64 (d, J = 8.3 Hz, 4H), 8.34 (m, 4H), 8.13 (dd, J = 11.1, 4.2 Hz, 2H),

7.70 (d, J = 6.6 Hz, 2H), 7.60 (d, J = 2.1 Hz, 2H), 7.54 (d, J = 5.2 Hz, 2H), 7.39 (t, J = 6.2 Hz, 2H), 7.26 (t, J = 7.8 Hz, 2H), 6.94 (d, J = 7.8 Hz, 4H), 2.44 (s, 12H), 0.93 – 0.85 (m, 4H), 0.71 (d, J = 6.6 Hz, 12H), 0.63 (d, J = 6.7 Hz, 12H).
^{13}C NMR (176 MHz, acetone-d_6, ppm): δ = 197.1, 157.9, 155.9, 155.4, 152.5, 152.4, 151.1, 144.8, 142.9, 137.3, 133.7, 133.0, 131.4, 130.2, 127.5, 127.3, 125.6, 125.3, 123.5, 122.2, 118.0, 108.8, 93.9, 90.1, 27.2, 25.8, 22.8, 12.0.
ESI-MS (m/z): $[M]^{2+}_{theo}$ = 622.6983, $[M]^{2+}_{exp}$ = 622.6917 (Signal intensity very low due to dissociation of the dyad during ESI measurement).
Elemental Analysis: calc. for $C_{65}H_{69}N_{13}FeCoClO_4P_2F_{12}$ (%): C 50.81, H 4.53, N 11.85; found: C 50.40, H 4.88, N 11.77.

Fe2$_{homo}$

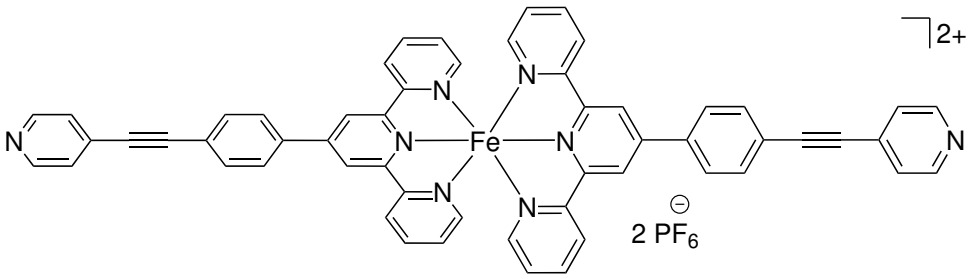

The ligand **L2** (0.5 mmol, 205 mg) and $FeBr_2$ (0.25 mmol, 54 mg) were degassed. Degassed MeoH (20 mL) was added. After 90 minutes the solution was filtered and the volume of the solution was reduced. The concentrated MeOH solution was dropped into an aqueous KPF_6 solution which caused the precipitation of the desired complex. Isolation and washing with water gave **Fe2$_{homo}$** in 21% yield.

^{1}H NMR (500 MHz, acetone-d_6, ppm): δ = 9.72 (s, 4H), 9.06 (d, J = 7.7 Hz, 4H), 8.70 (dd, J = 4.3, 1.6 Hz, 4H), 8.58 – 8.56 (m, 4H), 8.09 (td, J = 7.8, 1.4 Hz, 4H), 8.05 – 8.02 (m, 4H), 7.62 – 7.60 (m, 4H), 7.57 (dd, J = 4.3, 1.6 Hz, 4H), 7.30 – 7.26 (m, 4H).
^{13}C NMR (176 MHz, acetone-d_6, ppm): δ = 161.0, 158.6, 153.5, 150.4, 149.4, 139.2, 137.4, 133.2, 130.6, 128.4, 127.9, 125.5, 124.6, 124.4, 121.6, 92.6, 89.1.
ESI-MS (m/z): $[M]^{2+}_{theo}$ = 876.2412/2 = 438.1206, $[M]^{2+}_{exp}$ = 438.1212.
Elemental Analysis: calc. for $C_{56}H_{36}N_8FeP_2F_{12}$ (%): C 57.65, H 3.11, N 9.60; found: C 57.82, H 3.29, N 9.68.

Fe2

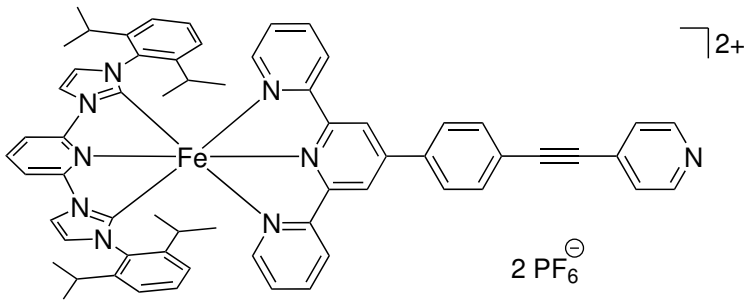

Fe2 was synthesized according to the protocol of **Fe1**. The bridging ligand **L2** (1.5 mmol, 616 mg) was used. The complex was isolated in 65% yield.

^{1}H NMR (700 MHz, CD_3CN, ppm): δ = 8.68 (dd, J = 4.2, 1.6 Hz, 2H), 8.64 (t, J = 8.3 Hz, 1H), 8.35 (d, J = 2.1 Hz, 2H), 8.28 (d, J = 7.9 Hz, 2H), 8.22 (d, J = 8.3 Hz, 2H), 7.98 (s, 2H), 7.92 – 7.88 (m, 4H), 7.79 – 7.77 (m, 2H), 7.54 (dd, J = 4.2, 1.6 Hz, 2H), 7.18 (d, J = 2.1 Hz, 2H), 7.16 (ddd, J = 7.1, 5.7, 1.2 Hz, 2H), 7.13 (dd, J = 5.6, 0.7 Hz, 2H), 7.04 (t, J = 7.8 Hz, 2H), 6.81 (d, J = 7.8 Hz, 4H), 0.80 – 0.73 (m, 4H), 0.63 (d, J = 6.5 Hz, 12H), 0.57 (d, J = 6.7 Hz, 12H).
^{13}C NMR (176 MHz, CD_3CN, ppm): δ = 207.6, 199.1, 158.5, 157.3, 156.6, 153.4, 151.2, 146.8, 145.9, 142.9, 138.8, 138.0, 134.8, 133.8, 131.8, 131.7, 131.0, 129.1, 127.7, 126.5, 125.8, 124.4, 124.4, 119.6, 118.7, 109.3, 93.6, 89.4, 31.0, 28.2, 26.7, 23.7.
ESI-MS (m/z): $[M]^{2+}_{theo} = 997.4243/2 = 498.7122$, $[M]^{2+}_{exp} = 498.7111$, $[M+H]^{3+}_{theo} = 998.4321/3 = 332.8107$, $[M+H]^{3+}_{exp} = 332.8176$.
Elemental Analysis: calc. for $C_{63}H_{59}N_9FeP_2F_{12}$ (%): C 58.75, H 4.62, N 9.79; found: C 58.81, H 5.08, N 9.80.

Dy2

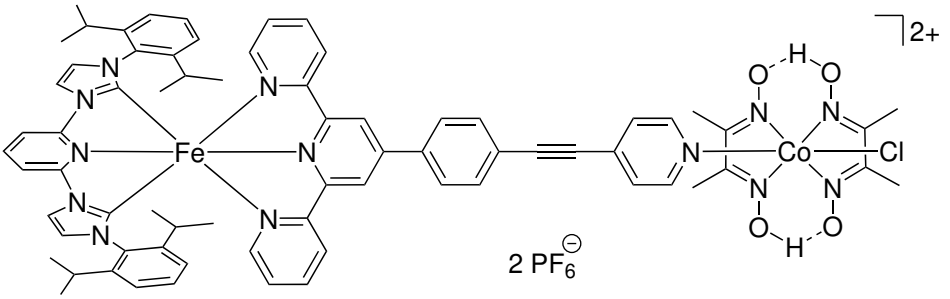

Following the protocol of **Dy1**, **Dy2** was isolated as violet powder in 80% yield.

^{1}H NMR (700 MHz, CD_3CN, ppm): δ = 8.62 (t, J = 8.3 Hz, 1H), 8.35 (d, J

= 2.1 Hz, 2H), 8.26 (d, J = 7.9 Hz, 2H), 8.21 (d, J = 8.3 Hz, 2H), 8.19 – 8.18 (m, 2H), 7.95 (s, 2H), 7.89 (td, J = 7.8, 1.4 Hz, 2H), 7.87 – 7.85 (m, 2H), 7.77 – 7.74 (m, 2H), 7.46 – 7.44 (m, 2H), 7.17 (d, J = 2.1 Hz, 2H), 7.16 – 7.13 (m, 2H), 7.11 (dd, J = 5.5, 0.6 Hz, 2H), 7.01 (t, J = 7.8 Hz, 2H), 6.79 (d, J = 7.8 Hz, 4H), 2.36 (s, 12H), 0.78 – 0.71 (m, 4H), 0.61 (d, J = 6.6 Hz, 12H), 0.56 (d, J = 6.7 Hz, 12H).
^{13}C NMR (176 MHz, CD_3CN, ppm): δ = 199.1, 158.5, 157.2, 156.6, 154.2, 153.5, 151.9, 145.9, 143.0, 139.5, 138.0, 135.2, 134.7, 134.1, 131.8, 130.9, 129.2, 128.4, 127.7, 125.8, 124.4, 123.4, 119.6, 118.8, 109.4, 98.1, 87.7, 28.1, 26.7, 23.7, 13.3.
ESI-MS (m/z): $[M]^{2+}_{theo}$ = 660.7139, $[M]^{2+}_{exp}$ = 660.7140 (Signal intensity very low due to dissociation of the dyad during ESI measurement).
Elemental Analysis: calc. for $C_{71}H_{73}N_{13}FeCoClO_4P_2F_{12}$ (%): C 52.88, H 4.56, N 11.29; found: C 53.16, H 4.90, N 11.51.

Fe3$_{homo}$

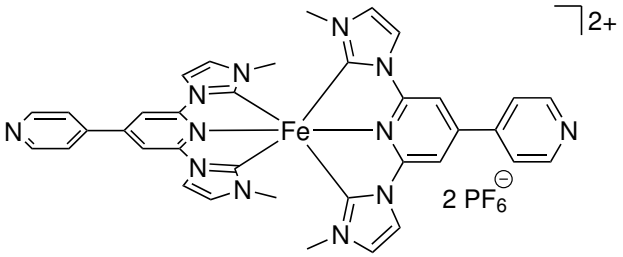

L3 (2 mmol, 779 mg) was suspended in dry, degassed DMF (50 mL). $FeCl_2$ (1 mmol, 127 mg) and potassium tert-butoxide (KO^tBu, 4 mmol, 449 mg) were added. The red solution was stirred over night. DMF was removed and the residue was dissovled in H_2O. After filtration, it was dropped into an aqueous solution of KPF_6. The product was isolated in washed with H_2O. Purification was realized by dissolving the complex in acetone and dropping into Et_2O. **Fe3$_{homo}$** was obtained as red powder in 21% yield.

^{1}H NMR (500 MHz, acetone-d_6, ppm): δ = 8.85 (d, J = 5.6 Hz, 4H), 8.65 (s, 4H), 8.57 (d, J = 1.9 Hz, 4H), 8.10 (d, J = 5.7 Hz, 4H), 7.34 (d, J = 1.9 Hz, 4H), 2.84 (s, 12H).
^{13}C NMR (125.7 MHz, acetone-d_6, ppm): δ = 201.0, 155.8, 152.0, 149.1, 144.6, 128.0, 122.4, 117.9, 104.3, 35.6.
ESI-MS (m/z): $[M]^{2+}_{theo}$ = 668.2222/2 = 334.1111, $[M+H]^{+}_{exp}$ = 344.1141.

Fe3

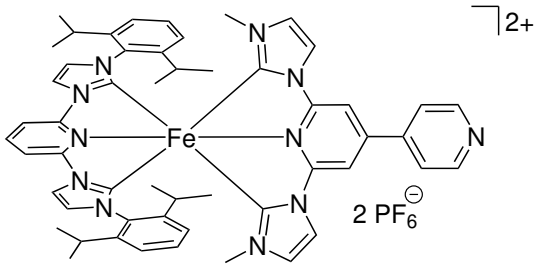

Synthesis was described by Huber-Gedert *et al.*.[99] **Fe3** was isolated in 50% yield.

^{1}H NMR (500 MHz, acetone-d_6, ppm): δ = 8.83 (m, J = 4.3, 1.7 Hz, 2H), 8.72 (d, J = 2.2 Hz, 2H), 8.55 (t, 1H), 8.45 (d, J = 2.1 Hz, 2H), 8.35 (d, J = 8.2 Hz, 2H), 7.70 (s, 2H), 7.63 (dd, J = 4.3, 1.7 Hz, 2H), 7.60 (d, J = 2.2 Hz, 2H), 7.46 (d, J = 2.1 Hz, 2H), 7.04 (t, J = 7.8 Hz, 2H), 6.88 (d, J = 7.8 Hz, 4H), 2.99 (s, 6H), 1.47 (hept, J = 6.6 Hz, 4H), 1.01 (d, J = 6.6 Hz, 12H), 0.78 (d, J = 6.7 Hz, 12H).
^{13}C NMR (125.7 MHz, acetone-d_6, ppm): δ = 201.6, 201.1, 155.0, 154.8, 151.9, 149.1, 146.1, 145.1, 140.1, 135.0, 131.7, 130.8, 127.4, 124.4, 122.5, 120.1, 117.2, 107.5, 103.3, 35.7, 28.8, 27.1, 24.4.
ESI-MS (m/z): $[M]^{2+}_{theo}$ = 903.4148/2 = 451.7072, $[M]^{2+}_{exp}$ = 451.7065.
Elemental Analysis: calc. for $C_{53}H_{57}N_{11}FeP_2F_{12}$ (%): C 53.32, H 4.81, N 12.91; found: C 52.93, H 4.94, N 12.57.

Dy3

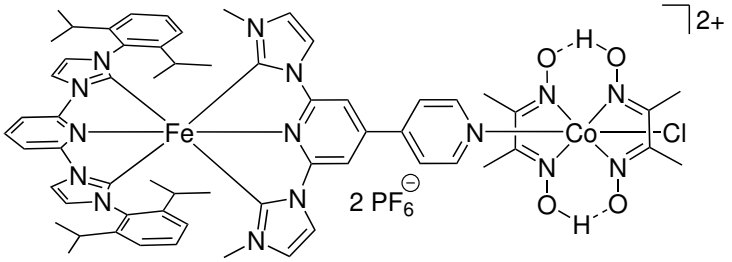

Synthesis was described by Huber-Gedert *et al.*.[99] **Dy3** was isolated in 76% yield.

^{1}H NMR (500 MHz, acetone-d_6, ppm): δ = 8.74 (d, J = 2.3 Hz, 2H), 8.60 – 8.56 (m, 1H), 8.42 (d, J = 6.8 Hz, 2H), 8.39 (d, J = 2.1 Hz, 2H), 8.36 (d, J = 8.2 Hz, 2H), 7.67 (dd, J = 5.4, 1.5 Hz, 2H), 7.62 (s, 2H), 7.59 (d, J = 2.2 Hz, 2H), 7.47 (d, J = 2.1 Hz, 2H), 6.99 – 6.95 (t, 2H), 6.85 (d, J = 7.8 Hz, 4H), 3.00 (s, 6H), 2.43 (s, 12H), 1.47 – 1.39 (m, 4H), 0.97 (d, J = 6.6 Hz, 12H), 0.75 (d, J = 6.6 Hz, 12H).

^{13}C NMR (125.7 MHz, acetone-d_6, ppm): δ = 201.0, 200.9, 154.9, 154.8, 153.4, 152.6, 148.7, 146.3, 146.1, 140.4, 134.9, 131.7, 130.7, 127.5, 125.0, 124.4, 120.1, 117.3, 107.6, 103.3, 35.8, 28.7, 27.1, 24.4, 13.0.
ESI-MS (m/z): $[M]^{2+}_{theo} = 1227.4183/2 = 613.7092$, $[M]^{2+}_{exp} = 613.7103$, $[M+PF_6]^{+}_{theo} = 1372.3825$, $[M+PF_6]^{+}_{exp} = 1372.3896$.
Elemental Analysis: calc. for $C_{61}H_{71}N_{15}FeCoO_4ClP_2F_{12}$ (%): C 48.25, H 4.71, N 13.84; found: C 47.73, H 4.97, N 13.66.

Tri3

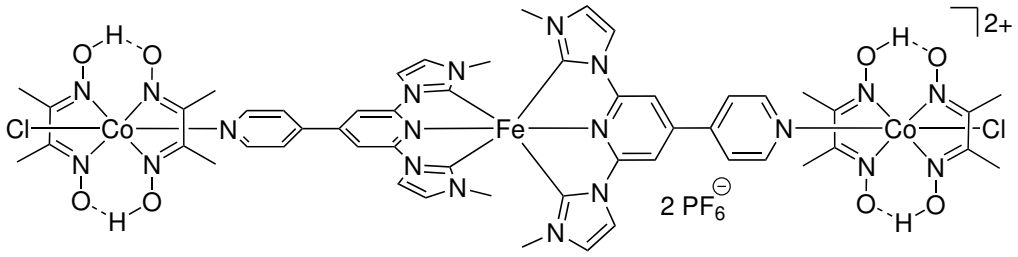

The cobalt precursor complex Co(dH)(dH_2)Cl_2 (0.05 mmol, 18 mg) was suspended in MeOH (4 mL). NEt_3 (0.05 mmol, 0.007 mL) was added and the suspension turned brown. **Fe3$_{homo}$** (0.025 mmol, 24.5 mg) suspended in MeOH (6 mL) was added and the reaction turned violet. Air was passed through for 30 minutes. Then Et_2O was added. The precipitation was collected and washed with Et_2O. **Tri3** was isolated in 37% yield.

^{1}H NMR (500 MHz, CD_3CN, ppm): δ = 8.38 (d, J = 6.8 Hz, 4H), 8.07 (d, J = 2.2 Hz, 4H), 8.03 (s, 4H), 7.91 (d, J = 6.9 Hz, 4H), 6.99 (d, J = 2.2 Hz, 4H), 2.47 (s, 12H), 2.37 (s, 24H).
^{13}C NMR (176 MHz, CD_3CN, ppm): δ = 200.2, 155.4, 154.3, 152.7, 148.1, 145.7, 128.0, 124.6, 117.7, 104.3, 35.7, 13.3.
ESI-MS (m/z): $[M]^{2+}_{theo} = 1336.2293/2 = 668.1147$, $[M]^{2+}_{exp} = 668.1162$.

Fe6$_{\mathbf{homo}}$

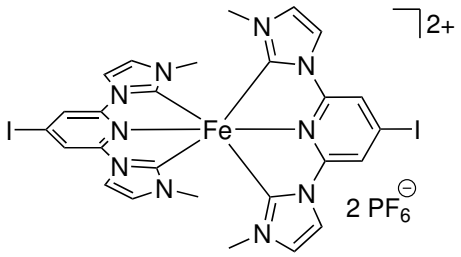

L6 (0.2mmol, 131 mg) was suspended in dry, degassed DMF (10 mL). $FeBr_2$ (0.1 mmol, 22 mg) and potassium tert-butoxide (KO^tBu, 0.5 mmol, 56 mg) were added. The orange solution was stirred for one hour. DMF was removed and the residue was washed with H_2O. It was dissolved in MeOH and dropped into an aqueous solution of KPF_6. The product was isolated in washed with H_2O. Purification was realized by recrystallization using MeCN as solvent and Et_2O as anti-solvent. **Fe6$_{\mathbf{homo}}$** was obtained as orange powder in 43% yield.

^{1}H NMR (700 MHz, CD_3CN_6, ppm): δ = 8.18 (s, 2H), 7.98 (d, J = 2.2 Hz, 2H), 7.02 (d, J = 2.2 Hz, 2H), 2.56 (s, 6H).
^{13}C NMR (176 MHz, CD_3CN, ppm): δ = 199.9, 170.9, 153.9, 127.1, 116.6, 114.8, 34.9.
ESI-MS (m/z): $[M]^{2+}_{theo}$ = 785.9624/2 = 392.9812, $[M]^{2+}_{exp}$ = 392.9823.

Bibliography

[1] M. R. Allen, O. P. Dube, W. Solecki, F. Aragon-Durand, W. Gramer and S. Humphreys, *Framing and Context. In: Global Warming of 1.5°C. An IPCC Special Report on the impacts of global warming of 1.5°C above pre-industrial levels and related global greenhouse gas emission pathways, in the context of strengthening the global response to the threat of climate change, sustainable development, and efforts to eradicate poverty*, Cambridge University Press, Cambridge, UK and New York, NY, USA, 2018, pp. 49–92.

[2] H.-O. Pörtner, D.C. Roberts, M. Tignor, E.S. Poloczanska, K. Mintenbeck, A. Alegría, M. Craig, S. Langsdorf, S. Löschke, V. Möller, A. Okem, B. Rama (eds.), *IPCC, 2022: Climate Change 2022: Impacts, Adaptation, and Vulnerability. Contribution of Working Group II to the Sixth Assessment Report of the Intergovernmental Panel on Climate Change*, Cambridge University Press. In Press, UK and New York, NY, USA, 2018.

[3] P. Nikolaidis and A. Poullikkas, 'A comparative overview of hydrogen production processes', *Renewable and Sustainable Energy Reviews*, 2017, **67**, 597–611.

[4] K. Damen, M. van Troost, A. Faaij and W. Turkenburg, 'A comparison of electricity and hydrogen production systems with CO2 capture and storage. Part A: Review and selection of promising conversion and capture technologies', *Progress in Energy and Combustion Science*, 2006, **32**, 215–246.

[5] C. E. Bamberger and D. M. Richardson, 'Hydrogen production from water by thermochemical cycles', *Cryogenics*, 1976, **16**, 197–208.

[6] S. Trasatti, 'Water electrolysis: who first?', *Journal of Electroanalytical Chemistry*, 1999, **476**, 90–91.

[7] X. Li, L. Zhao, J. Yu, X. Liu, X. Zhang, H. Liu and W. Zhou, 'Water Splitting: From Electrode to Green Energy System', *Nano-Micro Letters*, 2020, **12**, 131.

[8] S. Shiva Kumar and V. Himabindu, 'Hydrogen production by PEM water electrolysis – A review', *Materials Science for Energy Technologies*, 2019, **2**, 442–454.

[9] A. Brisse, J. Schefold and M. Zahid, 'High temperature water electrolysis in solid oxide cells', *International Journal of Hydrogen Energy*, 2008, **33**, 5375–5382.

[10] H. Xu and M. Ni, 3 - High-temperature electrolysis and co-electrolysis, in *Power to Fuel*, ed. G. Spazzafumo, Academic Press, 2021, pp. 51–73.

[11] T. Jafari, E. Moharreri, A. S. Amin, R. Miao, W. Song and S. L. Suib, 'Photocatalytic Water Splitting—The Untamed Dream: A Review of Recent Advances', *Molecules*, 2016, **21**.

[12] Gurudayal, D. Sabba, M. H. Kumar, L. H. Wong, J. Barber, M. Grätzel and N. Mathews, 'Perovskite-Hematite Tandem Cells for Efficient Overall Solar Driven Water Splitting', *Nano Lett.*, 2015, **15**, 3833–3839.

[13] Jeremie Brillet, Jun-Ho Yum, Maurin Cornuz, Takashi Hisatomi, Renata Solarska, Jan Augustynski, Michael Graetzel and Kevin Sivula, 'Highly efficient water splitting by a dual-absorber tandem cell', *Nature Photon.*, 2012, **6**, 824–828.

[14] E. S. Andreiadis, M. Chavarot-Kerlidou, M. Fontecave and V. Artero, 'Artificial Photosynthesis: From Molecular Catalysts for Light-driven Water Splitting to Photoelectrochemical Cells', *Photochemistry and Photobiology*, 2011, **87**, 946–964.

[15] M. Wang, Y. Na, M. Gorlov and L. Sun, 'Light-driven hydrogen production catalysed by transition metal complexes in homogeneous systems', *Dalton Trans.*, 2009, 6458–6467.

[16] K. Kalyanasundaram, J. Kiwi and M. Grätzel, 'Hydrogen Evolution from Water by Visible Light, a Homogeneous Three Component Test System for Redox Catalysis', *Helv. Chim. Acta*, 1978, **61**, 2720–2730.

[17] E. Amouyal, 'Photochemical production of hydrogen and oxygen from water: A review and state of the art', *Solar Energy Materials and Solar Cells*, 1995, **38**, 249–276.

[18] M. Kirch, J.-M. Lehn and J.-P. Sauvage, 'Hydrogen Generation by Visible Light Irradiation of Aqueous Solutions of Metal Complexes. An approach to the photochemical conversion and storage of solar energy', *Helv. Chim. Acta*, 1979, **62**, 1345–1384.

[19] M. Schulz, M. Karnahl, M. Schwalbe and J. G. Vos, 'The role of the bridging ligand in photocatalytic supramolecular assemblies for the reduction of protons and carbon dioxide', *Coord. Chem. Rev.*, 2012, **256**, 1682–1705.

[20] E. Deponti and M. Natali, 'Photocatalytic hydrogen evolution with ruthenium polypyridine sensitizers: unveiling the key factors to improve efficiencies', *Dalton Trans.*, 2016, **45**, 9136–9147.

[21] G. M. Brown, B. S. Brunschwig, C. Creutz, J. F. Endicott and N. Sutin, 'Homogeneous catalysis of the photoreduction of water by visible light. Mediation by a tris(2,2'-bipyridine)ruthenium(II)-cobalt(II) macrocycle system', *J. Am. Chem. Soc.*, 1979, **101**, 1298–1300.

[22] S. Chakraborty, E. H. Edwards, B. Kandemir and K. L. Bren, 'Photochemical Hydrogen Evolution from Neutral Water with a Cobalt Metallopeptide Catalyst', *Inorg. Chem.*, 2019, **58**, 16402–16410.

[23] J. I. Goldsmith, W. R. Hudson, M. S. Lowry, T. H. Anderson and S. Bernhard, 'Discovery and high-throughput screening of heteroleptic iridium complexes for photoinduced hydrogen production', *J. Am. Chem. Soc.*, 2005, **127**, 7502–7510.

[24] S. Metz and S. Bernhard, 'Robust photocatalytic water reduction with cyclometalated Ir(III) 4-vinyl-2,2'-bipyridine complexes', *Chem. Commun.*, 2010, **46**, 7551–7553.

[25] I. N. Mills, J. A. Porras and S. Bernhard, 'Judicious Design of Cationic, Cyclometalated Ir(III) Complexes for Photochemical Energy Conversion and Optoelectronics', *Acc. Chem. Res.*, 2018, **51**, 352–364.

[26] L. L. Tinker and S. Bernhard, 'Photon-driven catalytic proton reduction with a robust homoleptic iridium(III) 6-phenyl-2,2'-bipyridine complex ($\mathrm{Ir(C}NN)_2^{+}$)', *Inorg. Chem.*, 2009, **48**, 10507–10511.

[27] P. N. Curtin, L. L. Tinker, C. M. Burgess, E. D. Cline and S. Bernhard, 'Structure-activity correlations among iridium(III) photosensitizers in a robust water-reducing system', *Inorg. Chem.*, 2009, **48**, 10498–10506.

[28] K. Sakai and H. Ozawa, 'Homogeneous catalysis of platinum(II) complexes in photochemical hydrogen production from water', *Coord. Chem. Rev.*, 2007, **251**, 2753–2766.

[29] L. L. Tinker, N. D. McDaniel, P. N. Curtin, C. K. Smith, M. J. Ireland and S. Bernhard, 'Visible light induced catalytic water reduction without an electron relay', *Chem. Eur. J.*, 2007, **13**, 8726–8732.

[30] Y.-J. Yuan, J.-Y. Zhang, Z.-T. Yu, J.-Y. Feng, W.-J. Luo, J.-H. Ye and Z.-G. Zou, 'Impact of ligand modification on hydrogen photogeneration and light-harvesting applications using cyclometalated iridium complexes', *Inorg. Chem.*, 2012, **51**, 4123–4133.

[31] Y. Wang, H. Suzuki, J. Xie, O. Tomita, D. J. Martin, M. Higashi, D. Kong, R. Abe and J. Tang, 'Mimicking Natural Photosynthesis: Solar to Renewable H_2 Fuel Synthesis by Z-Scheme Water Splitting Systems', *Chem. Rev.*, 2018, **118**, 5201–5241.

[32] C. Chen, W. Ma and J. Zhao, 'Semiconductor-mediated photodegradation of pollutants under visible-light irradiation', *Chem. Soc. Rev.*, 2010, **39**, 4206–4219.

[33] A. Reynal and E. Palomares, 'Ruthenium Polypyridyl Sensitisers in Dye Solar Cells Based on Mesoporous TiO_2', *Eur. J. Inorg. Chem.*, 2011, 4509–4526.

[34] Y. Qin and Q. Peng, 'Ruthenium Sensitizers and Their Applications in Dye-Sensitized Solar Cells', *International Journal of Photoenergy*, 2012, 1–21.

[35] J. Moll, C. Wang, A. Päpcke, C. Förster, U. Resch-Genger, S. Lochbrunner and K. Heinze, 'Green-Light Activation of Push-Pull Ruthenium(II) Complexes', *Chem. Eur. J.*, 2020, **26**, 6820–6832.

[36] O. S. Wenger, 'Is Iron the New Ruthenium?', *Chem. Eur. J.*, 2019, 6043–6052.

[37] C. Förster and K. Heinze, 'Photophysics and photochemistry with Earth-abundant metals - fundamentals and concepts', *Chem. Soc. Rev.*, 2020, **49**, 1057–1070.

[38] D. M. Arias-Rotondo and J. K. McCusker, 'The photophysics of photoredox catalysis: a roadmap for catalyst design', *Chem. Soc. Rev.*, 2016, **45**, 5803–5820.

[39] P. Dierks, Y. Vukadinovic and M. Bauer, 'Photoactive iron complexes: more sustainable, but still a challenge', *Inorg. Chem. Front.*, 2022, **405**, 213129.

[40] Y. Liu, P. Persson, V. Sundström and K. Wärnmark, 'Fe N-Heterocyclic Carbene Complexes as Promising Photosensitizers', *Acc. Chem. Res.*, 2016, **49**, 1477–1485.

[41] S. Kaufhold and K. Wärnmark, 'Design and Synthesis of Photoactive Iron N-Heterocyclic Carbene Complexes', *Catalysts*, 2020, **10**, 132.

[42] Jean Pierre Sauvage, Jean Paul Collin, Jean Claude Chambron, Stephane Guillerez, Christophe Coudret, Vincenzo Balzani, Francesco Barigelletti, Luisa De Cola and and Lucia Flamigni, 'Ruthenium(II) and Osmium(II) Bis(terpyridine) Complexes in Covalently-Linked Multicomponent Systems: Synthesis, Electrochemical Behavior, Absorption Spectra, and Photochemical and Photophysical Properties', *Chem. Rev.*, 1994, **94**, 993–1019.

[43] Y. Liu, T. Harlang, S. E. Canton, P. Chábera, K. Suárez-Alcántara, A. Fleckhaus, D. A. Vithanage, E. Göransson, A. Corani, R. Lomoth, V. Sundström and K. Wärnmark, 'Towards longer-lived metal-to-ligand charge transfer states of iron(II) complexes: An N-heterocyclic carbene approach', *Chem. Commun.*, 2013, **49**, 6412–6414.

[44] L. L. Jamula, A. M. Brown, D. Guo and J. K. McCusker, 'Synthesis and Characterization of a High-Symmetry Ferrous Polypyridyl Complex: Approaching the $^5T_2/^3T_1$ Crossing Point for Fe^{II}', *Inorg. Chem.*, 2014, **53**, 15–17.

[45] M. Darari, A. Francés-Monerris, B. Marekha, A. Doudouh, E. Wenger, A. Monari, S. Haacke and P. C. Gros, 'Towards Iron(II) Complexes with Octahedral Geometry: Synthesis, Structure and Photophysical Properties', *Molecules*, 2020, **25**.

[46] T. Duchanois, T. Etienne, M. Beley, X. Assfeld, E. A. Perpète, A. Monari and P. C. Gros, 'Heteroleptic Pyridyl-Carbene Iron Complexes with Tuneable Electronic Properties', *Eur. J. Inorg. Chem.*, 2014, 3747–3753.

[47] Y. Vukadinovic, L. Burkhardt, A. Päpcke, A. Miletic, L. Fritsch, B. Altenburger, R. Schoch, A. Neuba, S. Lochbrunner and M. Bauer, 'When Donors Turn into Acceptors: Ground and Excited State Properties of Fe^{II} Complexes with Amine-Substituted Tridentate Bis-imidazole-2-ylidene Pyridine Ligands', *Inorg. Chem.*, 2020, **59**, 8762–8774.

[48] C. A. Gaggioli, G. Bistoni, G. Ciancaleoni, F. Tarantelli, L. Belpassi and P. Belanzoni, 'Modulating the Bonding Properties of N-Heterocyclic Carbenes (NHCs): A Systematic Charge-Displacement Analysis', *Chem. Eur. J.*, 2017, **23**, 7558–7569.

[49] T. Duchanois, T. Etienne, C. Cebrián, L. Liu, A. Monari, M. Beley, X. Assfeld, S. Haacke and P. C. Gros, 'An Iron-Based Photosensitizer with Extended Excited-State Lifetime: Photophysical and Photovoltaic Properties', *Eur. J. Inorg. Chem.*, 2015, 2469–2477.

[50] D. S. Tyson, J. Bialecki and F. N. Castellano, 'Ruthenium(II) complex with a notably long excited state lifetime', *Chem. Commun.*, 2000, 2355–2356.

[51] A. Francés-Monerris, P. C. Gros, M. Pastore, X. Assfeld and A. Monari, 'Photophysical properties of bichromophoric Fe(II) complexes bearing an aromatic electron acceptor', *Theor. Chem. Acc.*, 2019, **138**, 13522.

[52] P. Dierks, A. Päpcke, O. S. Bokareva, B. Altenburger, T. Reuter, K. Heinze, O. Kühn, S. Lochbrunner and M. Bauer, 'Ground- and Excited-State Properties of Iron(II) Complexes Linked to Organic Chromophores', *Inorg. Chem.*, 2020, **59**, 14746–14761.

[53] P. Zimmer, L. Burkhardt, R. Schepper, K. Zheng, D. Gosztola, A. Neuba, U. Flörke, C. Wölper, R. Schoch, W. Gawelda, S. E. Canton and M. Bauer, 'Towards Noble-Metal-Free Dyads: Ground and Excited State Tuning by a Cobalt Dimethylglyoxime Motif Connected to an Iron N-Heterocyclic Carbene Photosensitizer', *Eur. J. Inorg. Chem.*, 2018, 5203–5214.

[54] P. Zimmer, L. Burkhardt, A. Friedrich, J. Steube, A. Neuba, R. Schepper, P. Müller, U. Flörke, M. Huber, S. Lochbrunner and M. Bauer, 'The Connection between NHC Ligand Count and Photophysical Properties in Fe(II) Photosensitizers: An Experimental Study', *Inorg. Chem.*, 2018, **57**, 360–373.

[55] Y. Liu, K. S. Kjaer, L. A. Fredin, P. Chábera, T. Harlang, S. E. Canton, S. Lidin, J. Zhang, R. Lomoth, K.-E. Bergquist, P. Persson, K. Wärnmark and V. Sundström, 'A heteroleptic ferrous complex with mesoionic bis(1,2,3-triazol-5-ylidene) ligands: Taming the MLCT excited state of iron(II)', *Chem. Eur. J.*, 2015, **21**, 3628–3639.

[56] P. Chábera, K. S. Kjaer, O. Prakash, A. Honarfar, Y. Liu, L. A. Fredin, T. C. B. Harlang, S. Lidin, J. Uhlig, V. Sundström, R. Lomoth, P. Persson and K. Wärnmark, 'Fe^{II} Hexa N-Heterocyclic Carbene Complex with a 528 ps Metal-to-Ligand Charge-Transfer Excited-State Lifetime', *J. Phys. Chem. Lett.*, 2018, **9**, 459–463.

[57] P. Chábera, Y. Liu, O. Prakash, E. Thyrhaug, A. E. Nahhas, A. Honarfar, S. Essén, L. A. Fredin, T. C. B. Harlang, K. S. Kjær, K. Handrup, F. Ericson, H. Tatsuno, K. Morgan, J. Schnadt, L. Häggström, T. Ericsson, A. Sobkowiak, S. Lidin, P. Huang, S. Styring, J. Uhlig, J. Bendix, R. Lomoth, V. Sundström, P. Persson and K. Wärnmark, 'A low-spin Fe(iii) complex with 100-ps ligand-to-metal charge transfer photoluminescence', *Nature*, 2017, **543**, 695–699.

[58] K. S. Kjær, N. Kaul, O. Prakash, P. Chábera, N. W. Rosemann, A. Honarfar, O. Gordivska, L. A. Fredin, K.-E. Bergquist, L. Häggström, T. Ericsson, L. Lindh, A. Yartsev, S. Styring, P. Huang, J. Uhlig, J. Bendix, D. Strand, V. Sundström, P. Persson, R. Lomoth and K. Wärnmark, 'Luminescence and reactivity of a charge-transfer excited iron complex with nanosecond lifetime', *Science*, 2019, **363**, 249–253.

[59] N. W. Rosemann, P. Chabera, O. Prakash, S. Kaufhold, K. Wärnmark, A. Yartsev and P. Persson, 'Tracing the full bimolecular photocycle of iron(III)-carbene light-harvesters in electron donating solvents', *J. Am. Chem. Soc.*, 2020, **142**, 8565–8569.

[60] F. Gärtner, A. Boddien, E. Barsch, K. Fumino, S. Losse, H. Junge, D. Hollmann, A. Brückner, R. Ludwig and M. Beller, 'Photocatalytic hydrogen generation from water with iron carbonyl phosphine complexes: Improved water reduction catalysts and mechanistic insights', *Chem. Eur. J.*, 2011, **17**, 6425–6436.

[61] F. Gärtner, B. Sundararaju, A.-E. Surkus, A. Boddien, B. Loges, H. Junge, P. H. Dixneuf and M. Beller, 'Light-driven hydrogen generation: efficient iron-based water reduction catalysts', *Angew. Chem. Int. Ed.*, 2009, **48**, 9962–9965.

[62] J. Huo, Y.-B. Zhang, W.-Y. Zou, X. Hu, Q. Deng and D. Chen, 'Mini-review on an engineering approach towards the selection of transition metal complex-

based catalysts for photocatalytic H_2 production', *Catal. Sci. Technol.*, 2019, **9**, 2716–2727.

[63] A. J. J. Lennox, S. Fischer, M. Jurrat, S.-P. Luo, N. Rockstroh, H. Junge, R. Ludwig and M. Beller, 'Copper-Based Photosensitisers in Water Reduction: A More Efficient In Situ Formed System and Improved Mechanistic Understanding', *Chem. Eur. J.*, 2016, **22**, 1233–1238.

[64] M. J. Rose, H. B. Gray and J. R. Winkler, 'Hydrogen generation catalyzed by fluorinated diglyoxime-iron complexes at low overpotentials', *J. Am. Chem. Soc.*, 2012, **134**, 8310–8313.

[65] V. Artero, M. Chavarot-Kerlidou and M. Fontecave, 'Splitting water with cobalt', *Angew. Chem. Int. Ed.*, 2011, **50**, 7238–7266.

[66] W. T. Eckenhoff, W. R. McNamara, P. Du and R. Eisenberg, 'Cobalt complexes as artificial hydrogenases for the reductive side of water splitting', *Biochimica et biophysica acta*, 2013, **1827**, 958–973.

[67] K. E. Dalle, J. Warnan, J. J. Leung, B. Reuillard, I. S. Karmel and E. Reisner, 'Electro- and Solar-Driven Fuel Synthesis with First Row Transition Metal Complexes', *Chem. Rev.*, 2019, **119**, 2752–2875.

[68] N. Queyriaux, R. T. Jane, J. Massin, V. Artero and M. Chavarot-Kerlidou, 'Recent Developments in Hydrogen Evolving Molecular Cobalt(II)-Polypyridyl Catalysts', *Coord. Chem. Rev.*, 2015, **304-305**, 3–19.

[69] C. V. Krishnan, B. S. Brunschwig, C. Creutz and N. Sutin, 'Homogeneous catalysis of the photoreduction of water. 6. Mediation by polypyridine complexes of ruthenium(II) and cobalt(II) in alkaline media', *J. Am. Chem. Soc.*, 1985, **107**, 2005–2015.

[70] C. V. Krishnan and N. Sutin, 'Homogeneous catalysis of the photoreduction of water by visible light. 2. Mediation by a tris(2,2'-bipyridine)ruthenium(II)-cobalt(II) bipyridine system', *J. Am. Chem. Soc.*, 1981, **103**, 2141–2142.

[71] A. Fihri, V. Artero, M. Razavet, C. Baffert, W. Leibl and M. Fontecave, 'Cobaloxime-based photocatalytic devices for hydrogen production', *Angew. Chem. Int. Ed.*, 2008, **47**, 564–567.

[72] P. Du, K. Knowles and R. Eisenberg, 'A homogeneous system for the photogeneration of hydrogen from water based on a platinum(II) terpyridyl acetylide chromophore and a molecular cobalt catalyst', *J. Am. Chem. Soc.*, 2008, **130**, 12576–12577.

[73] P. Du, J. Schneider, G. Luo, W. W. Brennessel and R. Eisenberg, 'Visible light-driven hydrogen production from aqueous protons catalyzed by molecular cobaloxime catalysts', *Inorg. Chem.*, 2009, **48**, 4952–4962.

[74] T. Lazarides, T. McCormick, P. Du, G. Luo, B. Lindley and R. Eisenberg, 'Making hydrogen from water using a homogeneous system without noble metals', *J. Am. Chem. Soc.*, 2009, **131**, 9192–9194.

[75] A. Panagiotopoulos, K. Ladomenou, D. Sun, V. Artero and A. G. Coutsolelos, 'Photochemical hydrogen production and cobaloximes: The influence of the cobalt axial N-ligand on the system stability', *Dalton Trans.*, 2016, **45**, 6732–6738.

[76] S. C. Marinescu, J. R. Winkler and H. B. Gray, 'Molecular mechanisms of cobalt-catalyzed hydrogen evolution', *Proc. Natl. Acad. Sci. USA*, 2012, **109**, 15127–15131.

[77] H. Ozawa, M.-a. Haga and K. Sakai, 'A photo-hydrogen-evolving molecular device driving visible-light-induced EDTA-reduction of water into molecular hydrogen', *J. Am. Chem. Soc.*, 2006, **128**, 4926–4927.

[78] T. Kowacs, Q. Pan, P. Lang, L. O'Reilly, S. Rau, W. R. Browne, M. T. Pryce, A. Huijser and J. G. Vos, 'Supramolecular bimetallic assemblies for photocatalytic hydrogen generation from water', *Faraday Discuss.*, 2015, **185**, 143–170.

[79] B. Dietzek, W. Kiefer, J. Blumhoff, L. Böttcher, S. Rau, D. Walther, U. Uhlemann, M. Schmitt and J. Popp, 'Ultrafast excited-state excitation dynamics in a quasi-two-dimensional light-harvesting antenna based on ruthenium(II) and palladium(II) chromophores', *Chem. Eur. J.*, 2006, **12**, 5105–5115.

[80] S. Kaufhold, D. Imanbaew, C. Riehn and S. Rau, 'Rational in situ tuning of a supramolecular photocatalyst for hydrogen evolution', *Sustainable Energy Fuels*, 2017, **1**, 2066–2070.

[81] A. Fihri, V. Artero, A. Pereira and M. Fontecave, 'Efficient H_2-producing photocatalytic systems based on cyclometalated iridium- and tricarbonylrhenium-diimine photosensitizers and cobaloxime catalysts', *Dalton Trans.*, 2008, 5567–5569.

[82] A. Jacques, O. Schott, K. Robeyns, G. S. Hanan and B. Elias, 'Hydrogen Photoevolution from a Green-Absorbing Iridium(III)-Cobalt(III) Dyad', *Eur. J. Inorg. Chem.*, 2016, 1779–1783.

[83] G.-G. Luo, K. Fang, J.-H. Wu and J. Mo, 'Photocatalytic water reduction from a noble-metal-free molecular dyad based on a thienyl-expanded BODIPY photosensitizer', *Chem. Commun.*, 2015, **51**, 12361–12364.

[84] P. Zhang, M. Wang, C. Li, X. Li, J. Dong and L. Sun, 'Photochemical H_2 with noble-metal-free molecular devices comprising a porphyrin photosensitizer and a cobaloxime catalyst', *Chem. Commun.*, 2010, **46**, 8806–8808.

[85] A. Jouaiti and M. W. Hosseini, 'Design and Synthesis of New Differentiated Concurrent Mono- and Tridentate Ligands (Tectons) Based on Pyridine, Terpyridine, and Dihydrooxazole Units', *Helvetica Chimica Acta*, 2009, **92**, 2497–2506.

[86] M. L. Saha, J. W. Bats and M. Schmittel, 'Merging strong and weak coordination motifs in the integrative self-sorting of a 5-component trapezoid and scalene triangle', *Org. Biomol. Chem.*, 2013, **11**, 5592–5595.

[87] E. C. Constable and M. D. Ward, 'Synthesis and co-ordination behaviour of 6′,6″-bis(2-pyridyl)-2,2′:4,4″ : 2″,2‴-quaterpyridine; 'back-to-back' 2,2′:6′,2″-terpyridine', *J. Chem. Soc. Dalton Trans.*, 1990, **12**, 1405–1409.

[88] L. Schmitz, 'Synthese eines Brückenliganden zur Darstellung einer Eisen-Cobalt-Dyade', *Bachelorarbeit*, Universität Paderborn, 2018.

[89] S. A. Sadler, H. Tajuddin, I. A. I. Mkhalid, A. S. Batsanov, D. Albesa-Jove, M. S. Cheung, A. C. Maxwell, L. Shukla, B. Roberts, D. C. Blakemore, Z. Lin, T. B. Marder and P. G. Steel, 'Iridium-catalyzed C-H borylation of pyridines', *Org. Biomol. Chem.*, 2014, **12**, 7318–7327.

[90] J. Hübscher, W. Seichter, T. Gruber, J. Kortus and E. Weber, 'Synthesis and Structural Characterization of Ethynylene-Bridged Bisazines Featuring Various a-Substitution', *J. Heterocyclic Chem.*, 2015, **52**, 1062–1074.

[91] R. Bruckner and M. Harmata, *Organic Mechanisms*, Springer, Berlin, Heidelberg, 2010.

[92] C. J. Rohbogner, S. H. Wunderlich, G. C. Clososki and P. Knochel, 'New Mixed Li/Mg and Li/Mg/Zn Amides for the Chemoselective Metallation of Arenes and Heteroarenes', *Eur. J. Org. Chem.*, 2009, 1781–1795.

[93] D. A. Hay, F. M. Adam, G. Bish, F. Calo, R. Dixon, M. J. Fray, J. Hitchin, P. Jones, M. Paradowski, G. C. Parsons, K. J. Proctor, D. C. Pryde, N. N. Smith and T.-D. Tran, 'A flexible synthesis of C-6 and N-1 analogues of a 4-amino-1,3-dihydroimidazo[4,5-c]pyridin-2-one core', *Tetrahedron Letters*, 2011, **52**, 5728–5732.

[94] H.-M. Kim, D. Jeong, H. C. Noh, Y. K. Kang and Y. K. Chung, 'Manipulation of Absorption Maxima by Controlling Oxidation Potentials in Bis(tridentate) Ru(II) N-Heterocyclic Carbene Complexes', *Bull. Korean Chem. Soc.*, 2014, **35**, 448–456.

[95] C. Rajadurai, F. Schramm, S. Brink, O. Fuhr, M. Ghafari, R. Kruk and M. Ruben, 'Spin transition in a chainlike supramolecular iron(II) complex', *Inorg. Chem.*, 2006, **45**, 10019–10021.

[96] M. Nettekoven and C. Jenny, 'The Development of a Practical and Reliable Large-Scale Synthesis of 2,6-Diamino-4-bromopyridine', *Org. Proc. Res. Dev.*, 2003, **7**, 38–43.

[97] R. Balicki, M. Cybulski and G. Maciejewski, 'An Efficient Deoxygenation of Heteroaromatic N-Oxides Using Zinc Dust/Ammonium Formate Reagent System', *Synthetic Communications*, 2003, **33**, 4137–4141.

[98] M. Huber-Gedert, B. Marekha, L. Schmitz, M. Nowakowski, R. Schoch, A. Neuba, S. Haacke, M. Bauer, 'Tuning the excited state properties of iron(II)-cobalt(III) dyads by varying the bridging ligand', *Inorg. Chem.*, 2022, submitted.

[99] M. Huber-Gedert, M. Nowakowski, A. Kertmen, L. Burkhardt, N. Lindner, R. Schoch, R. Herbst-Irmer, A. Neuba, L. Schmitz, T.-K. Choi, J. Kubicki, W. Gawelda and M. Bauer, 'Fundamental Characterization, Photophysics and Photocatalysis of a Base Metal Iron(II)-Cobalt(III) Dyad', *Chem. Eur. J.*, 2021, **27**, 9905–9918.

[100] P. Zimmer, P. Müller, L. Burkhardt, R. Schepper, A. Neuba, J. Steube, F. Dietrich, U. Flörke, S. Mangold, M. Gerhards and M. Bauer, 'N-Heterocyclic Carbene Complexes of Iron as Photosensitizers for Light-Induced Water Reduction', *Eur. J. Inorg. Chem.*, 2017, 1504–1509.

[101] A. C. Benniston, V. Grosshenny, A. Harriman and R. Ziessel, 'Electron Delocalization in Ethynyl-Bridged Binuclear Ruthenium(II) Polypyridine Complexes', *Angew. Chem. Int. Ed.*, 1994, **33**, 1884–1885.

[102] L. Liu, T. Duchanois, T. Etienne, A. Monari, M. Beley, X. Assfeld, S. Haacke and P. C. Gros, 'A new record excited state (3)MLCT lifetime for metalorganic iron(ii) complexes', *Phys. Chem. Chem. Phys.*, 2016, **18**, 12550–12556.

[103] A. M. Brown, C. E. McCusker and J. K. McCusker, 'Spectroelectrochemical identification of charge-transfer excited states in transition metal-based polypyridyl complexes', *Dalton Trans.*, 2014, **43**, 17635–17646.

[104] K. L. Mulfort, A. Mukherjee, O. Kokhan, P. Du and D. M. Tiede, 'Structure-function analyses of solar fuels catalysts using in situ X-ray scattering', *Chem. Soc. Rev.*, 2013, **42**, 2215–2227.

[105] K. L. Mulfort and D. M. Tiede, 'Supramolecular cobaloxime assemblies for H_2 photocatalysis: An initial solution state structure-function analysis', *J. Phys. Chem. B*, 2010, **114**, 14572–14581.

[106] M. Razavet, V. Artero and M. Fontecave, 'Proton electroreduction catalyzed by cobaloximes: Functional models for hydrogenases', *Inorg. Chem.*, 2005, **44**, 4786–4795.

[107] R. Berera, R. van Grondelle and J. T. M. Kennis, 'Ultrafast transient absorption spectroscopy: principles and application to photosynthetic systems', *Photosyn. Res.*, 2009, **101**, 105–118.

[108] K. Kunnus, L. Li, C. J. Titus, S. J. Lee, M. E. Reinhard, S. Koroidov, K. S. Kjær, K. Hong, K. Ledbetter, W. B. Doriese, G. C. O'Neil, D. S. Swetz, J. N. Ullom, D. Li, K. Irwin, D. Nordlund, A. A. Cordones and K. J. Gaffney, 'Chemical control of competing electron transfer pathways in iron tetracyano-polypyridyl photosensitizers', *Chem. Sci.*, 2020, **11**, 4360–4373.

[109] A. Cannizzo, C. J. Milne, C. Consani, W. Gawelda, C. Bressler, F. van Mourik and M. Chergui, 'Light-induced spin crossover in Fe(II)-based complexes: The full photocycle unraveled by ultrafast optical and X-ray spectroscopies', *Coord. Chem. Rev.*, 2010, **254**, 2677–2686.

[110] B. Marekha and S. Haacke, unpublished.

[111] M. Lorenc, M. Ziolek, R. Naskrecki, J. Karolczak, J. Kubicki and A. Maciejewski, 'Artifacts in femtosecond transient absorption spectroscopy', *Appl. Phys. B*, 2002, **74**, 19–27.

[112] M. Darari, E. Domenichini, A. Francés-Monerris, C. Cebrián, K. Magra, M. Beley, M. Pastore, A. Monari, X. Assfeld, S. Haacke and P. C. Gros, 'Iron(ii) complexes with diazinyl-NHC ligands: impact of p-deficiency of the azine core on photophysical properties', *Dalton Trans.*, 2019, **48**, 10915–10926.

[113] H. Tatsuno et al., 'Hot Branching Dynamics in a Light-Harvesting Iron Carbene Complex Revealed by Ultrafast X-ray Emission Spectroscopy', *Angew. Chem. Int. Ed.*, 2020, **59**, 364–372.

[114] T. C. B. Harlang, Y. Liu, O. Gordivska, L. A. Fredin, C. S. Ponseca, P. Huang, P. Chábera, K. S. Kjaer, H. Mateos, J. Uhlig, R. Lomoth, R. Wallenberg, S. Styring, P. Persson, V. Sundström and K. Wärnmark, 'Iron sensitizer converts light to electrons with 92% yield', *Nat. Chem.*, 2015, **7**, 883–889.

[115] W. Gawelda, A. Cannizzo, V.-T. Pham, F. van Mourik, C. Bressler and M. Chergui, 'Ultrafast nonadiabatic dynamics of $[Fe^{II}(bpy)_3]^{2+}$ in solution', *J. Am. Chem. Soc.*, 2007, **129**, 8199–8206.

[116] K. Kunnus et al., 'Vibrational wavepacket dynamics in Fe carbene photosensitizer determined with femtosecond X-ray emission and scattering', *Nat. Commun.*, 2020, **11**, 634.

[117] M. A. Naumova, A. Kalinko, J. W. L. Wong, M. Abdellah, H. Geng, E. Domenichini, J. Meng, S. A. Gutierrez, P.-A. Mante, W. Lin, P. Zalden, A. Galler, F. Lima, K. Kubicek, M. Biednov, A. Britz, S. Checchia, V. Kabanova, M. Wulff, J. Zimara, D. Schwarzer, S. Demeshko, V. Murzin, D. Gosztola,

M. Jarenmark, J. Zhang, M. Bauer, M. L. Lawson Daku, W. Gawelda, D. Khakhulin, C. Bressler, F. Meyer, K. Zheng and S. E. Canton, 'Revealing Hot and Long-Lived Metastable Spin States in the Photoinduced Switching of Solvated Metallogrid Complexes with Femtosecond Optical and X-ray Spectroscopies', *J. Phys. Chem. Lett.*, 2020, **11**, 2133–2141.

[118] C. Lentz, O. Schott, T. Auvray, G. Hanan and B. Elias, 'Photocatalytic Hydrogen Production Using a Red-Absorbing Ir(III)-Co(III) Dyad', *Inorg. Chem.*, 2017, **56**, 10875–10881.

[119] M. Nowakowski1, M. Huber-Gedert, H. Elgabarty, J. Kubicki, A. Kertem, N. Lindner, D. Khakulin, F. Lima, T.-K. Choi, M. Biednov, N. Piergies, P. Zalden, K. Kubicek, A. Rodriguez-Fernandez, M. Alaraby Salem, T. Kühne, W. Gawelda, M. Bauer, 'Ultrafast two-colour X-ray emission spectroscopy reveals excited state landsape in a base metal dyad', *Nat. Comm.*, 2022, submitted.

[120] J. Idígoras, G. Burdziński, J. Karolczak, J. Kubicki, G. Oskam, J. A. Anta and M. Ziółek, 'The Impact of the Electrical Nature of the Metal Oxide on the Performance in Dye-Sensitized Solar Cells: New Look at Old Paradigms', *J. Phys. Chem. C*, 2015, **119**, 3931–3944.

[121] M. Lorenc, M. Ziolek, R. Naskrecki, J. Karolczak, J. Kubicki and A. Maciejewski, 'Artifacts in femtosecond transient absorption spectroscopy', *Appl. Phys. B*, 2002, **74**, 19–27.

[122] A. L. Smeigh, M. Creelman, R. A. Mathies and J. K. McCusker, 'Femtosecond time-resolved optical and Raman spectroscopy of photoinduced spin crossover: temporal resolution of low-to-high spin optical switching', *J. Am. Chem. Soc.*, 2008, **130**, 14105–14107.

[123] K. S. Kjær, T. B. Van Driel, T. C. B. Harlang, K. Kunnus, E. Biasin, K. Ledbetter, R. W. Hartsock, M. E. Reinhard, S. Koroidov, L. Li, M. G. Laursen, F. B. Hansen, P. Vester, M. Christensen, K. Haldrup, M. M. Nielsen, A. O. Dohn, M. I. Pápai, K. B. Moller, P. Chabera, Y. Liu, H. Tatsuno, C. Timm, M. Jarenmark, J. Uhlig, V. Sundstöm, K. Wärnmark, P. Persson, Z. Németh, D. S. Szemes, É. Bajnóczi, G. Vankó, R. Alonso-Mori, J. M. Glownia, S. Nelson, M. Sikorski, D. Sokaras, S. E. Canton, H. T. Lemke and K. J. Gaffney, 'Finding intersections between electronic excited state potential energy surfaces with simultaneous ultrafast X-ray scattering and spectroscopy', *Chem. Sci.*, 2019, **10**, 5749–5760.

[124] K. Kunnus, L. Li, C. J. Titus, S. J. Lee, M. E. Reinhard, S. Koroidov, K. S. Kjær, K. Hong, K. Ledbetter, W. B. Doriese, G. C. O'Neil, D. S. Swetz, J. N. Ullom, D. Li, K. Irwin, D. Nordlund, A. A. Cordones and K. J.

Gaffney, 'Chemical control of competing electron transfer pathways in iron tetracyano-polypyridyl photosensitizers', *Chem. Sci.*, 2020, **11**, 4360–4373.

[125] J. E. Monat and J. K. McCusker, 'Femtosecond Excited-State Dynamics of an Iron(II) Polypyridyl Solar Cell Sensitizer Model', *J. Am. Chem. Soc.*, 2000, **122**, 4092–4097.

[126] W. Gawelda, C. Bressler, M. Saes, M. Kaiser, A. N. Tarnovsky, D. Grolimund, S. L. Johnson, R. Abela and M. Chergui, 'Picosecond Time-Resolved X-Ray Absorption Spectroscopy of Solvated Organometallic Complexes', *Physica Scripta*, 2005, 102.

[127] D. Leshchev, T. C. B. Harlang, L. A. Fredin, D. Khakhulin, Y. Liu, E. Biasin, M. G. Laursen, G. E. Newby, K. Haldrup, M. M. Nielsen, K. Wärnmark, V. Sundström, P. Persson, K. S. Kjær and M. Wulff, 'Tracking the picosecond deactivation dynamics of a photoexcited iron carbene complex by time-resolved X-ray scattering', *Chem. Sci.*, 2018, **9**, 405–414.

[128] M. Deutsch, G. Hölzer, J. Härtwig, J. Wolf, M. Fritsch and E. Förster, 'Kα and Kβ x-ray emission spectra of copper', *Phys. Rev. A*, 1995, **51**, 283–296.

[129] K. M. Lancaster, K. D. Finkelstein and S. DeBeer, 'Kβ X-ray emission spectroscopy offers unique chemical bonding insights: revisiting the electronic structure of ferrocene', *Inorg. Chem.*, 2011, **50**, 6767–6774.

[130] P. Zimmermann, S. Peredkov, P. M. Abdala, S. DeBeer, M. Tromp, C. Müller and J. A. van Bokhoven, 'Modern X-ray spectroscopy: XAS and XES in the laboratory', *Coord. Chem. Rev.*, 2020, **423**, 213466.

[131] J. Kawai, C. Suzuki, H. Adachi, T. Konishi and Y. Gohshi, 'Charge-transfer effect on the linewidth of Fe Kα x-ray fluorescence spectra', *Phys. Rev. B*, 1994, **50**, 11347–11354.

[132] M. Lundberg, T. Kroll, S. DeBeer, U. Bergmann, S. A. Wilson, P. Glatzel, D. Nordlund, B. Hedman, K. O. Hodgson and E. I. Solomon, 'Metal-ligand covalency of iron complexes from high-resolution resonant inelastic X-ray scattering', *J. Am. Chem. Soc.*, 2013, **135**, 17121–17134.

[133] A. Kalinko, W. A. Caliebe, R. Schoch and M. Bauer, 'A von Hamos-type hard X-ray spectrometer at the PETRA III beamline P64', *J. Synchrotron Rad.*, 2020, **27**, 31–36.

[134] K. S. Kjær, K. Kunnus, T. C. B. Harlang, T. B. Van Driel, K. Ledbetter, R. W. Hartsock, M. E. Reinhard, S. Koroidov, L. Li, M. G. Laursen, E. Biasin, F. B. Hansen, P. Vester, M. Christensen, K. Haldrup, M. M. Nielsen, P. Chabera, Y. Liu, H. Tatsuno, C. Timm, J. Uhlig, V. Sundstöm, Z. Németh, D. S. Szemes, É. Bajnóczi, G. Vankó, R. Alonso-Mori, J. M. Glownia, S.

Nelson, M. Sikorski, D. Sokaras, H. T. Lemke, S. E. Canton, K. Wärnmark, P. Persson, A. A. Cordones and K. J. Gaffney, 'Solvent control of charge transfer excited state relaxation pathways in $[Fe(2,2\text{-bipyridine})(CN)_4]^{2-}$', *Phys. Chem. Chem. Phys.*, 2018, **20**, 4238–4249.

[135] L. A. Fredin, M. Pápai, E. Rozsályi, G. Vankó, K. Wärnmark, V. Sundström and P. Persson, 'Exceptional Excited-State Lifetime of an Iron(II)-N-Heterocyclic Carbene Complex Explained', *J. Phys. Chem. Lett.*, 2014, **5**, 2066–2071.

[136] H. T. Lemke, K. S. Kjær, R. Hartsock, T. B. van Driel, M. Chollet, J. M. Glownia, S. Song, D. Zhu, E. Pace, S. F. Matar, M. M. Nielsen, M. Benfatto, K. J. Gaffney, E. Collet and M. Cammarata, 'Coherent structural trapping through wave packet dispersion during photoinduced spin state switching', *Nat. Commun.*, 2017, **8**, 15342.

[137] M. Pápai, G. Vankó, T. Rozgonyi and T. J. Penfold, 'High-Efficiency Iron Photosensitizer Explained with Quantum Wavepacket Dynamics', *J. Phys. Chem. Lett.*, 2016, **7**, 2009–2014.

[138] E. Biasin, Z. W. Fox, A. Andersen, K. Ledbetter, K. S. Kjær, R. Alonso-Mori, J. M. Carlstad, M. Chollet, J. D. Gaynor, J. M. Glownia, K. Hong, T. Kroll, J. H. Lee, C. Liekhus-Schmaltz, M. Reinhard, D. Sokaras, Y. Zhang, G. Doumy, A. M. March, S. H. Southworth, S. Mukamel, K. J. Gaffney, R. W. Schoenlein, N. Govind, A. A. Cordones and M. Khalil, 'Direct observation of coherent femtosecond solvent reorganization coupled to intramolecular electron transfer', *Nat. Chem.*, 2021, **13**, 343–349.

[139] V. Singh, N. Gupta, G. N. Hargenrader, E. J. Askins, A. J. S. Valentine, G. Kumar, M. W. Mara, N. Agarwal, X. Li, L. X. Chen, A. A. Cordones and K. D. Glusac, 'Photophysics of graphene quantum dot assemblies with axially coordinated cobaloxime catalysts', *J. Chem. Phys.*, 2020, **153**, 124903.

[140] M. Bauer, J. Steube, A. Päpcke, O. Bokareva, T. Reuter, S. Demeshko, R. Schoch, S. Hohloch, F. Meyer, K. Heinze, O. Kühn and S. Lochbrunner, 'Janus-type dual emission of a Cyclometalated Iron(III) complex', *Research Square; 2020. DOI: 10.21203/rs.3.rs-64316/v1*, 2020.

[141] A. Mukherjee, O. Kokhan, J. Huang, J. Niklas, L. X. Chen, D. M. Tiede and K. L. Mulfort, 'Detection of a charge-separated catalyst precursor state in a linked photosensitizer-catalyst assembly', *Phys. Chem. Chem. Phys.*, 2013, **15**, 21070.

[142] R. S. Nicholson and I. Shain, 'Theory of Stationary Electrode Polarography. Single Scan and Cyclic Methods Applied to Reversible, Irreversible, and Kinetic Systems', *Anal. Chem.*, 1964, **36**, 706–723.

[143] J. Heinze, 'Cyclic Voltammetry—"Electrochemical Spectroscopy". New Analytical Methods(25)', *Angew. Chem.*, 1984, **23**, 831–847.

[144] J. E. B. Randles, 'A cathode ray polarograph. Part II.—The current-voltage curves', *Trans. Faraday Soc.*, 1948, **44**, 327–338.

[145] *Electroanalytical Methods: Guide to Experiments and Applications*, ed. F. Scholz, Springer, Berlin, Heidelberg, 2nd ed., 2010.

[146] T. Roland, J. Léonard, G. Hernandez Ramirez, S. Méry, O. Yurchenko, S. Ludwigs and S. Haacke, 'Sub-100 fs charge transfer in a novel donor–acceptor–donor triad organized in a smectic film', *Phys. Chem. Chem. Phys.*, 2012, **14**, 273–279.

[147] L. Liu, P. Eisenbrandt, T. Roland, M. Polkehn, P.-O. Schwartz, K. Bruchlos, B. Omiecienski, S. Ludwigs, N. Leclerc, E. Zaborova, J. Léonard, S. Méry, I. Burghardt and S. Haacke, 'Controlling charge separation and recombination by chemical design in donor–acceptor dyads', *Phys. Chem. Chem. Phys.*, 2016, **18**, 18536–18548.

[148] A. Galler, W. Gawelda, M. Biednov, C. Bomer, A. Britz, S. Brockhauser, T. K. Choi, M. Diez, P. Frankenberger, M. French, D. Görries, M. Hart, S. Hauf, D. Khakhulin, M. Knoll, T. Korsch, K. Kubicek, M. Kuster, P. Lang, F. Alves Lima, F. Otte, S. Schulz, P. Zalden and C. Bressler, 'Scientific instrument Femtosecond X-ray Experiments (FXE): instrumentation and baseline experimental capabilities', *J. Synchrotron Radiat.*, 2019, **26**, 1432–1447.

[149] F. Neese, 'Software update: the ORCA program system, version 4.0', *WIREs Computational Molecular Science*, 2018, **8**.

[150] S. Grimme, J. G. Brandenburg, C. Bannwarth and A. Hansen, 'Consistent structures and interactions by density functional theory with small atomic orbital basis sets', *J. Chem. Phys.*, 2015, **143**, 054107.

[151] J. G. Brandenburg, C. Bannwarth, A. Hansen and S. Grimme, 'B97-3c: A revised low-cost variant of the B97-D density functional method', *J. Chem. Phys.*, 2018, **148**, 064104.

[152] J. Hostaš and J. Řezáč, 'Accurate DFT-D3 Calculations in a Small Basis Set', *J. Chem. Theory Comput.*, 2017, **13**, 3575–3585.

[153] J. Tao, J. P. Perdew, V. N. Staroverov and G. E. Scuseria, 'Climbing the density functional ladder: nonempirical meta-generalized gradient approximation designed for molecules and solids', *Phys. Rev. Lett.*, 2003, **91**, 146401.

[154] F. Weigend and R. Ahlrichs, 'Balanced basis sets of split valence, triple zeta valence and quadruple zeta valence quality for H to Rn: Design and assessment of accuracy', *Phys. Chem. Chem. Phys.*, 2005, **7**, 3297–3305.

[155] B. Yang and D. G. Truhlar, 'Computational Design of an Iron Catalyst for Olefin Metathesis', *Organometallics*, 2018, **37**, 3917–3927.

[156] L. Goerigk and S. Grimme, 'A thorough benchmark of density functional methods for general main group thermochemistry, kinetics, and noncovalent interactions', *Phys. Chem. Chem. Phys.*, 2011, **13**, 6670–6688.

[157] S. Grimme, J. Antony, S. Ehrlich and H. Krieg, 'A consistent and accurate ab initio parametrization of density functional dispersion correction (DFT-D) for the 94 elements H-Pu', *J. Chem. Phys.*, 2010, **132**, 154104.

[158] S. Grimme, S. Ehrlich and L. Goerigk, 'Effect of the damping function in dispersion corrected density functional theory', *J. Comput. Chem.*, 2011, **32**, 1456–1465.

[159] Z. Liu, T. Lu and Q. Chen, 'An sp-hybridized all-carboatomic ring, cyclo[18]carbon: Bonding character, electron delocalization, and aromaticity', *Carbon*, 2020, **165**, 468–475.

[160] T. Lu and F. Chen, 'Multiwfn: a multifunctional wavefunction analyzer', *J. Comput. Chem.*, 2012, **33**, 580–592.

[161] M. e. Frisch, G. Trucks, H. Schlegel, G. Scuseria, M. Robb, J. Cheeseman, G. Scalmani, V. Barone, G. Petersson, H. Nakatsuji et al., 'Gaussian 16 Rev. C.01.', 2016.

[162] K. T. Potts and D. Konwar, 'Synthesis of 4'-vinyl-2,2': 6',2"-terpyridine', *J. Org. Chem.*, 1991, **56**, 4815–4816.

[163] T. Ohmura, Y. Morimasa and M. Suginome, 'Organocatalytic diboration involving "reductive addition" of a boron-boron sigma-bond to 4,4'-bipyridine: SuppInfo', *J. Am. Chem. Soc.*, 2015, **137**, 2852–2855.

[164] H.-J. Park and Y. K. Chung, 'Ru(II) complexes with N-heterocyclic carbene ligands or terpyridine analogues: Synthesis, characterization, and electrochemical and proton-dependent spectrometric properties', *Dalton Trans.*, 2012, **41**, 5678–5686.

[165] R. Boaretto, S. Carli, S. Caramori, C. A. Bignozzi, D. Saccone, C. Magistris, C. Barolo and G. Viscardi, 'A new ruthenium black dye design with improved optical properties for transparent dye sensitized solar devices', *Dalton Trans.*, 2017, **46**, 16390–16393.

9.1 Spectra of ligands

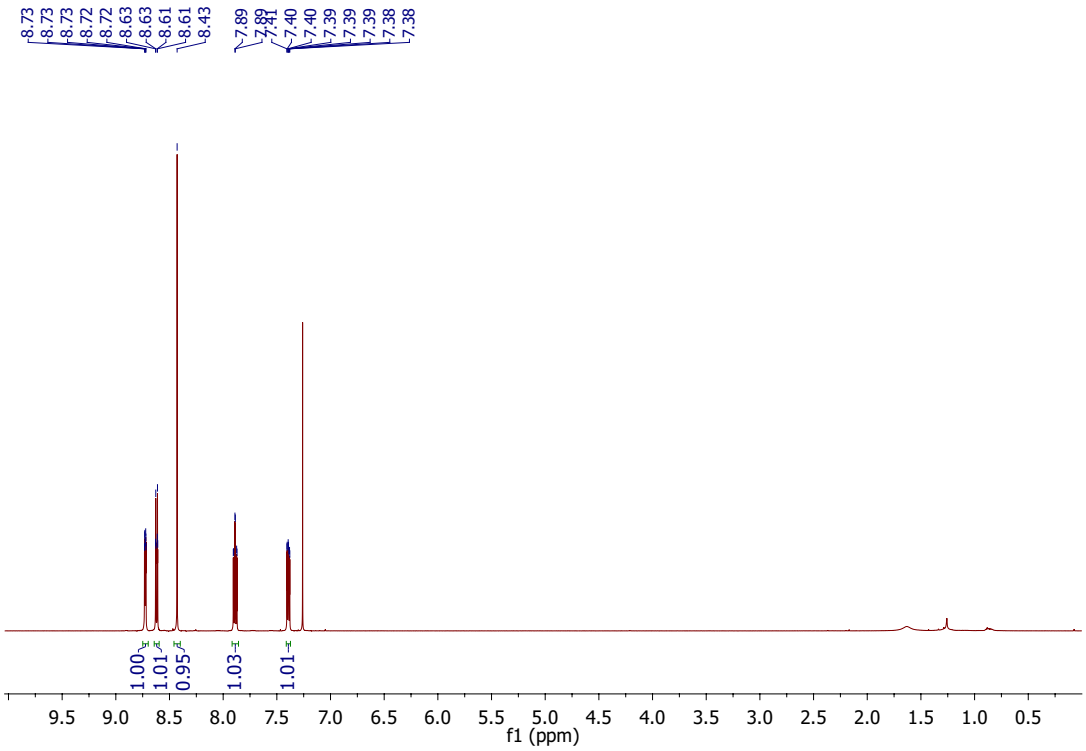

^{1}H NMR of **1** in $CDCl_3$.

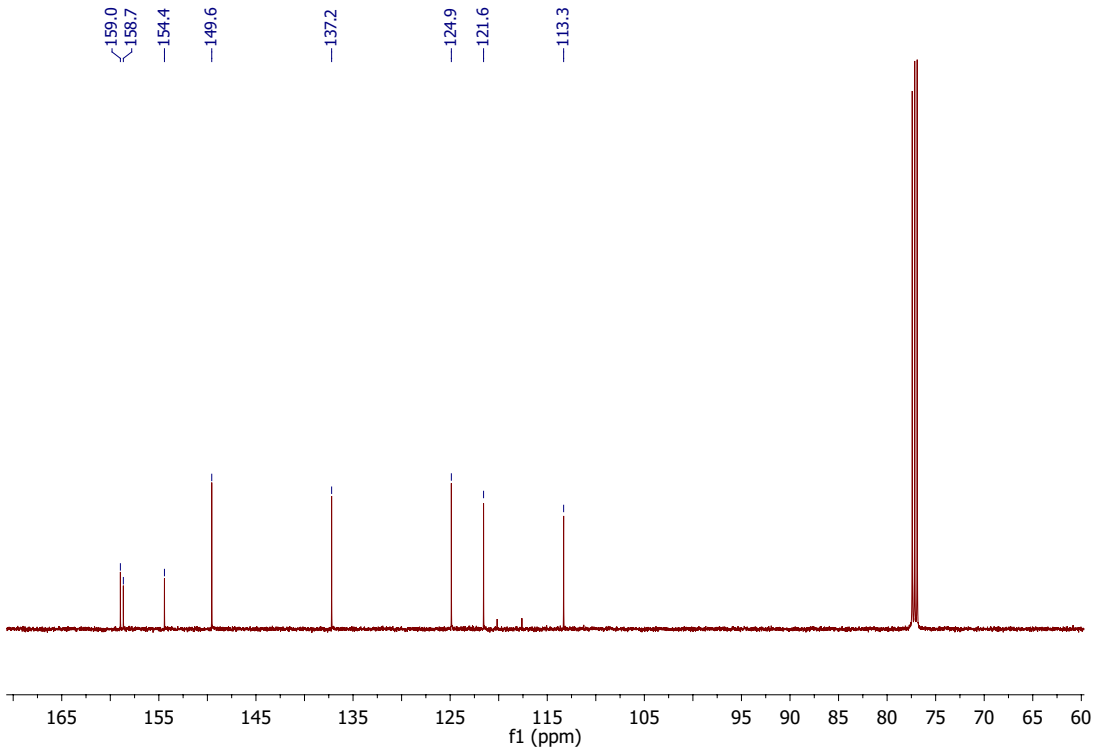

^{13}C NMR of **1** in $CDCl_3$.

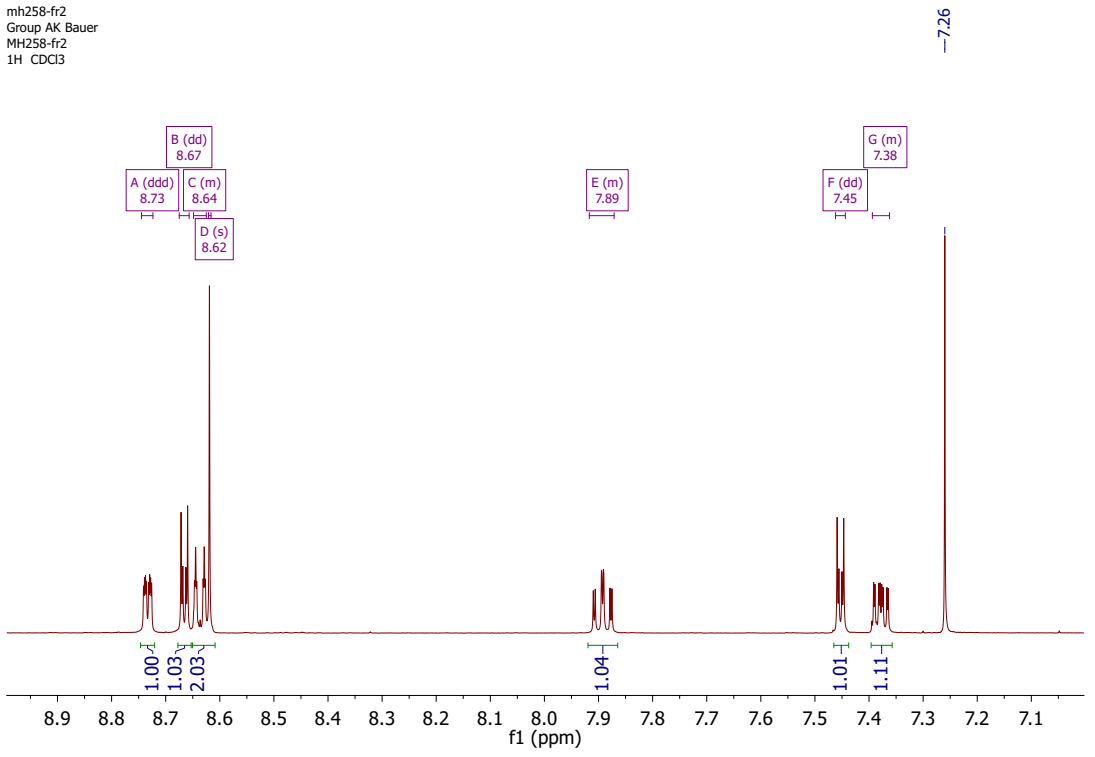

^{1}H NMR of **L1** in $CDCl_3$.

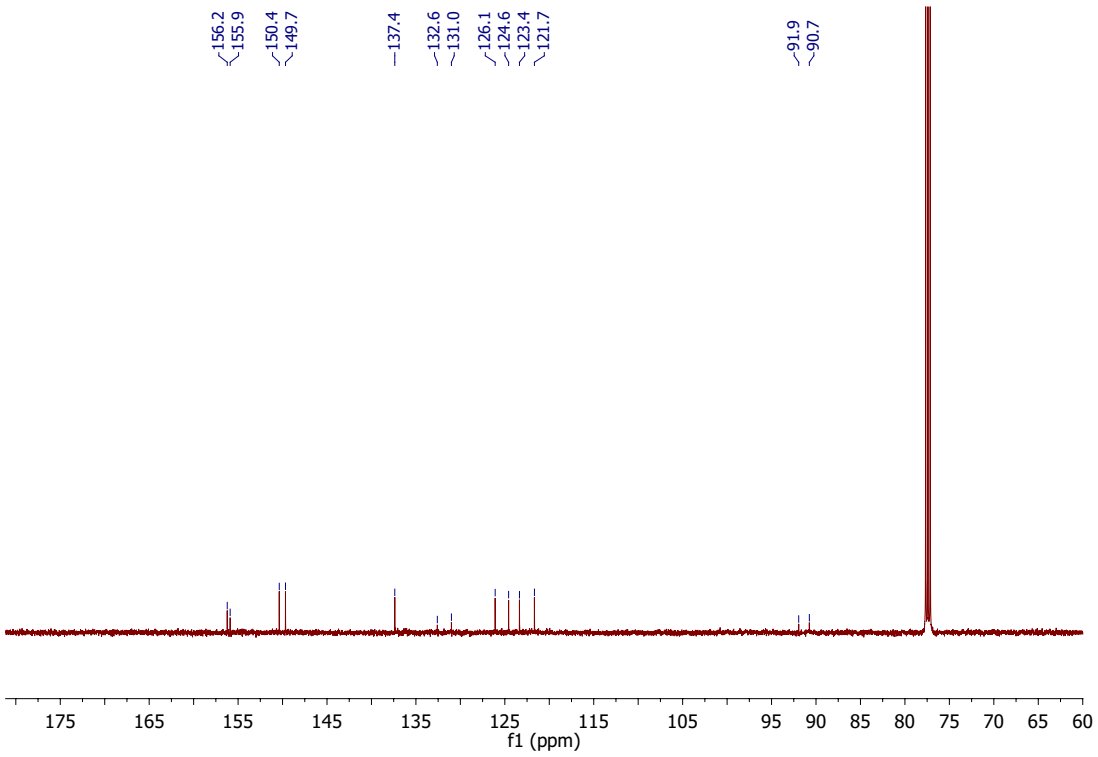

^{13}C NMR of **L1** in $CDCl_3$.

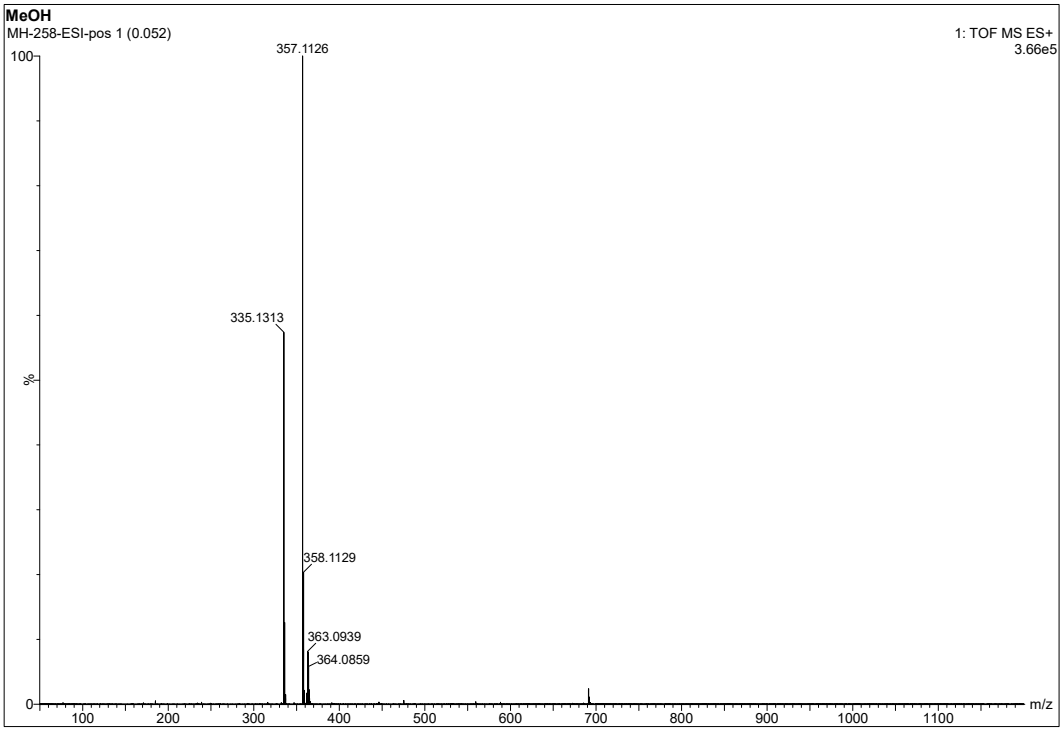

ESI-MS of **L1**.

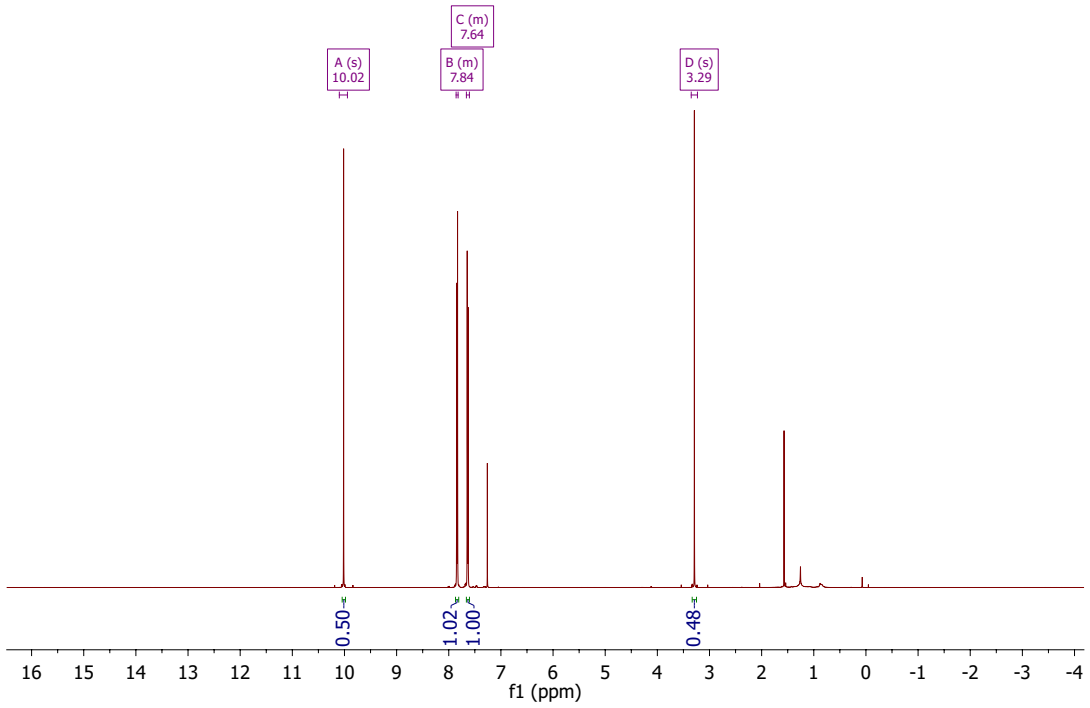

^{1}H NMR of **3** in $CDCl_3$.

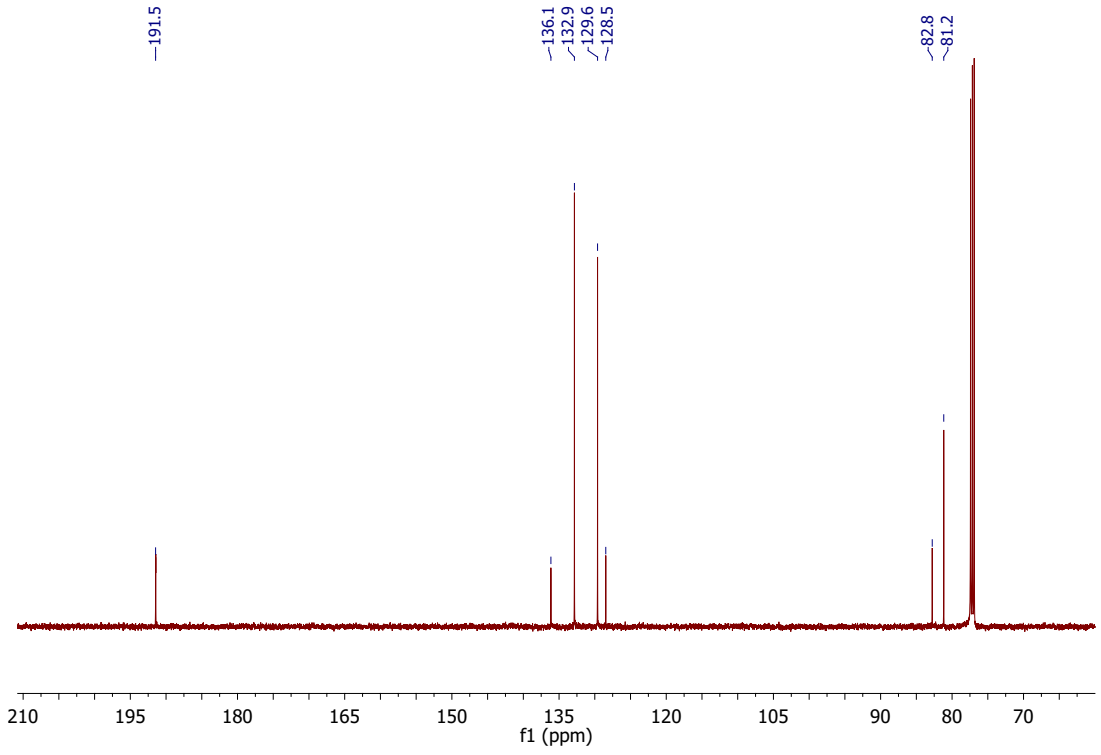

^{13}C NMR of **3** in $CDCl_3$.

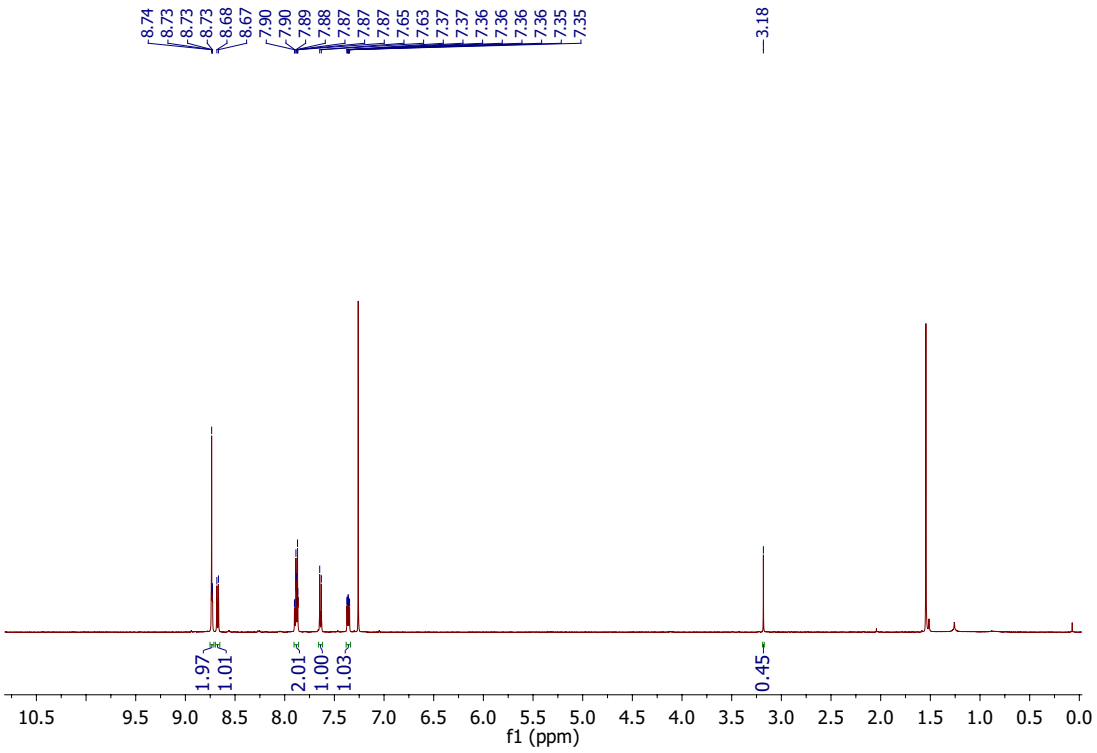

^{1}H NMR of **4** in $CDCl_3$.

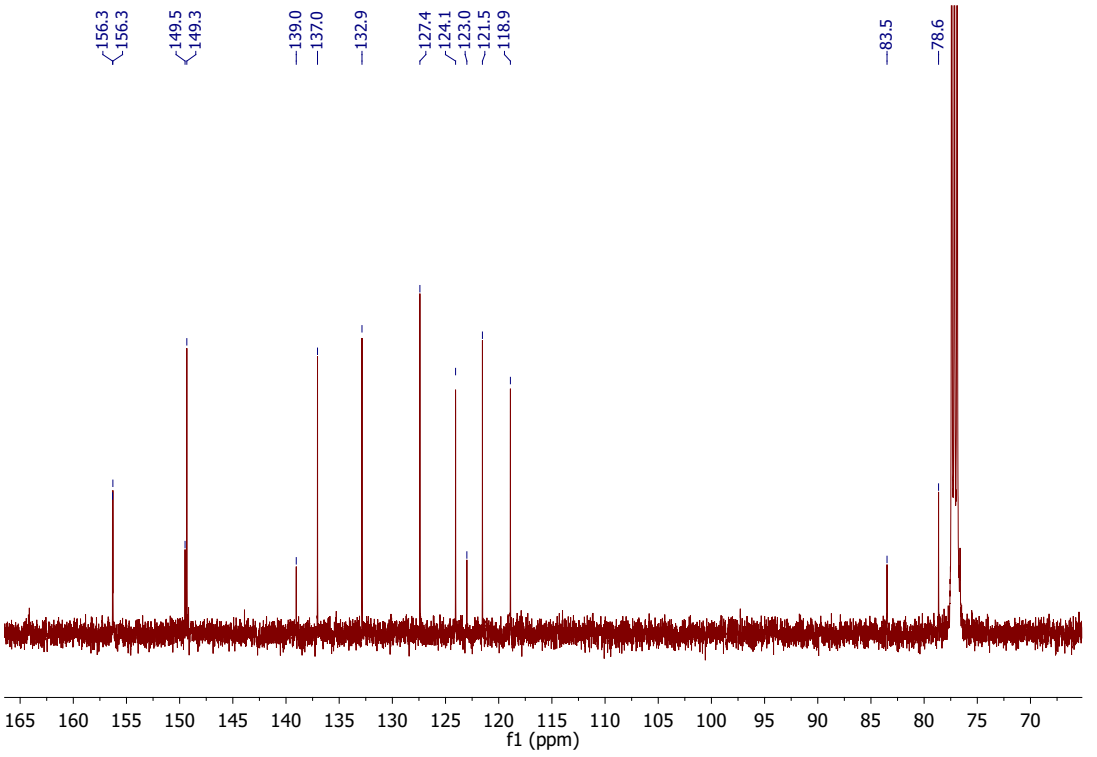

^{13}C NMR of **4** in $CDCl_3$.

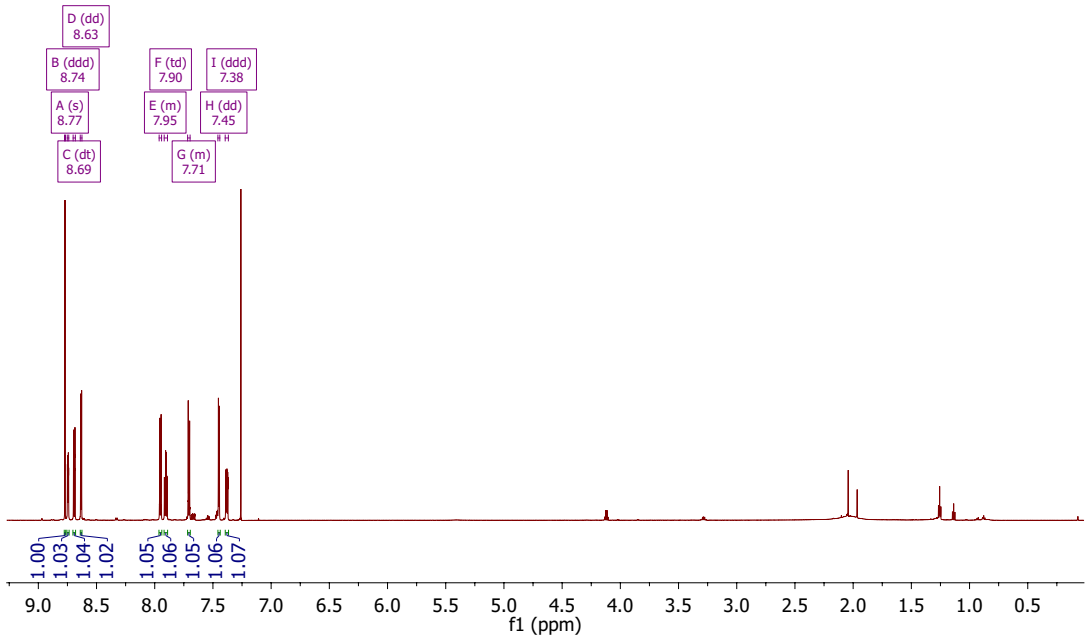

^{1}H NMR of **L2** in $CDCl_3$.

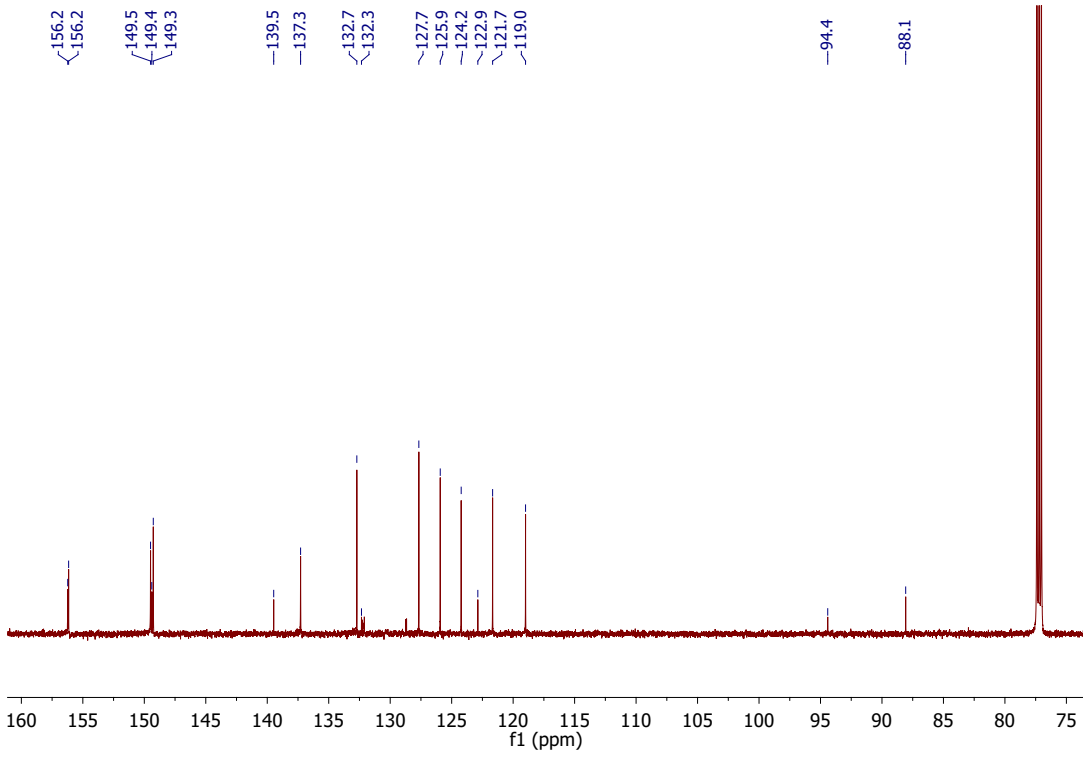

^{13}C NMR of **L2** in $CDCl_3$.

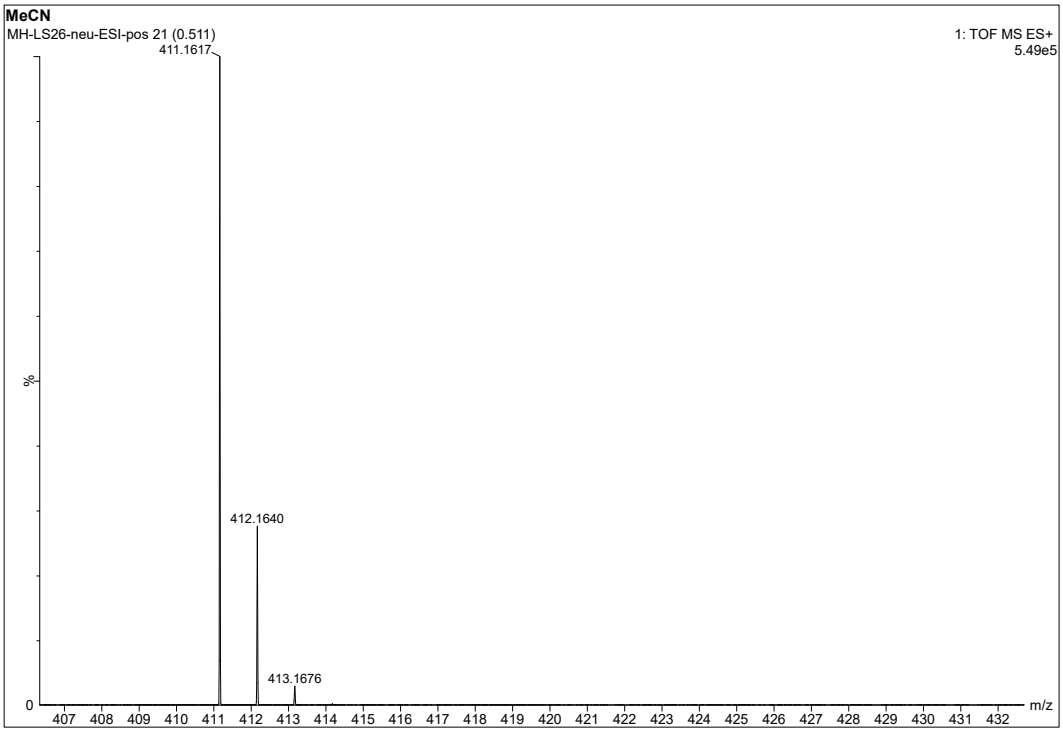

ESI-MS of **L2**.

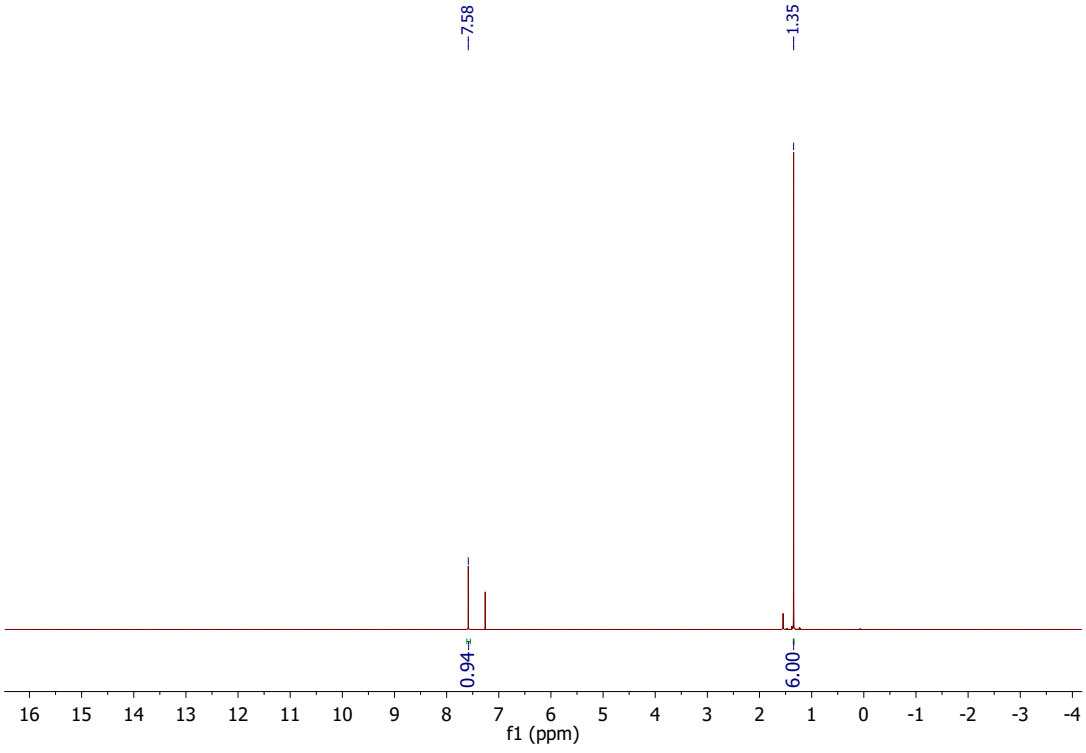

^{1}H NMR of **5** in $CDCl_3$.

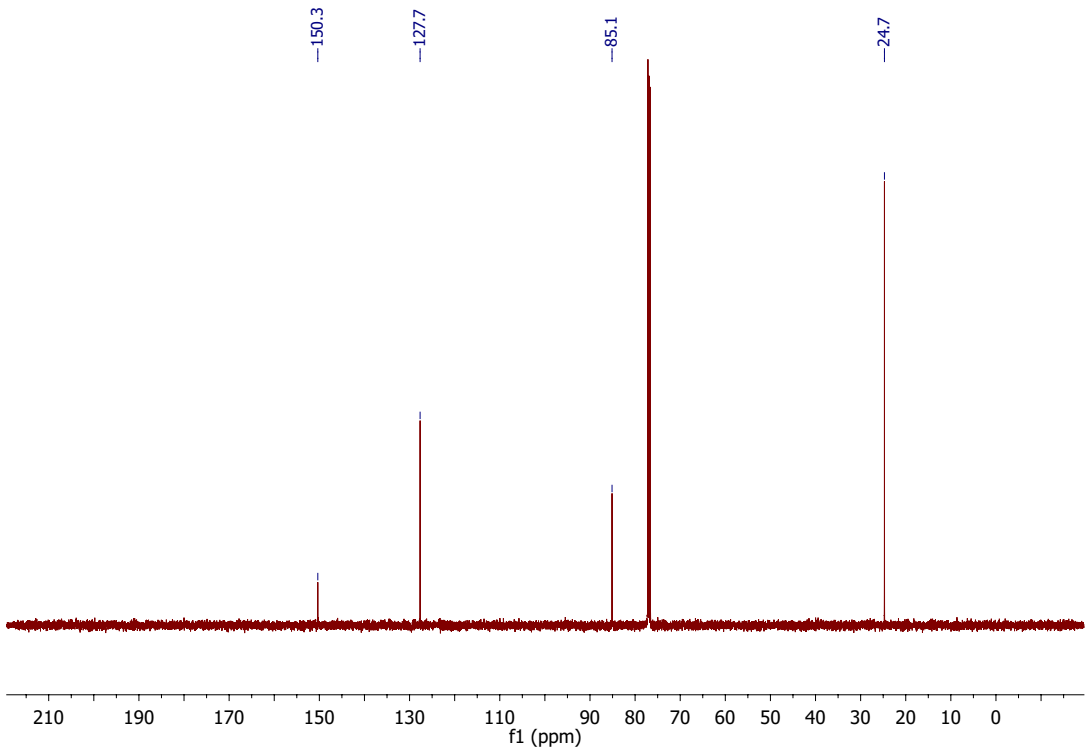

^{13}C NMR of **5** in $CDCl_3$.

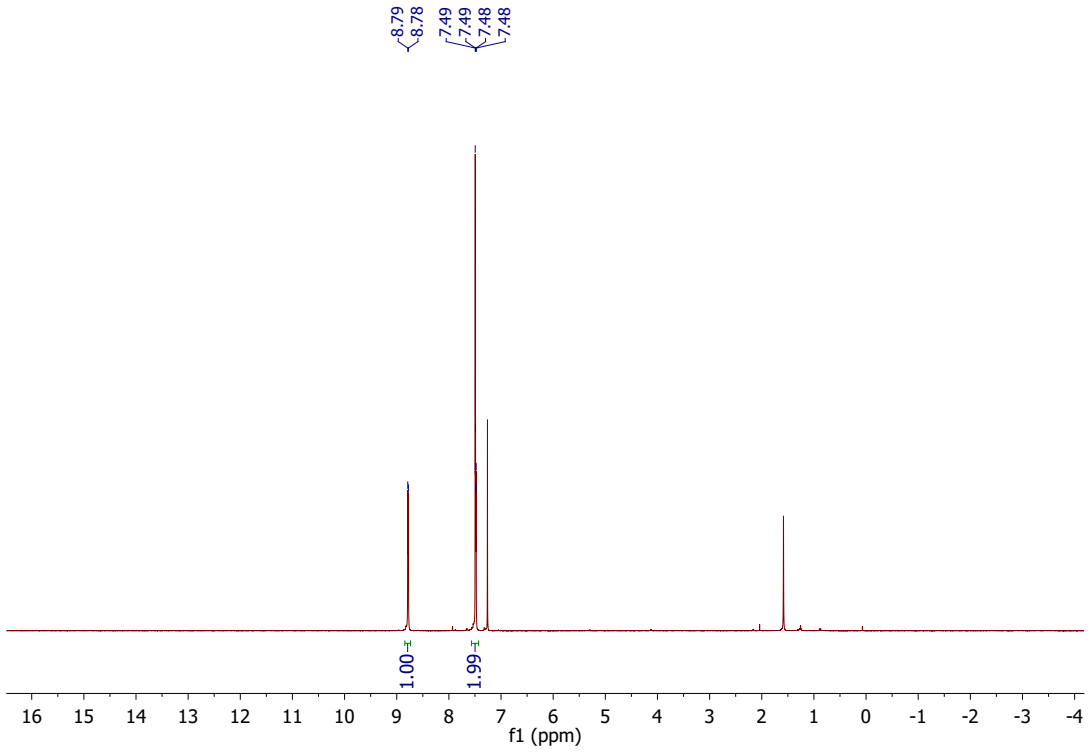

^{1}H NMR of **6** in $CDCl_3$.

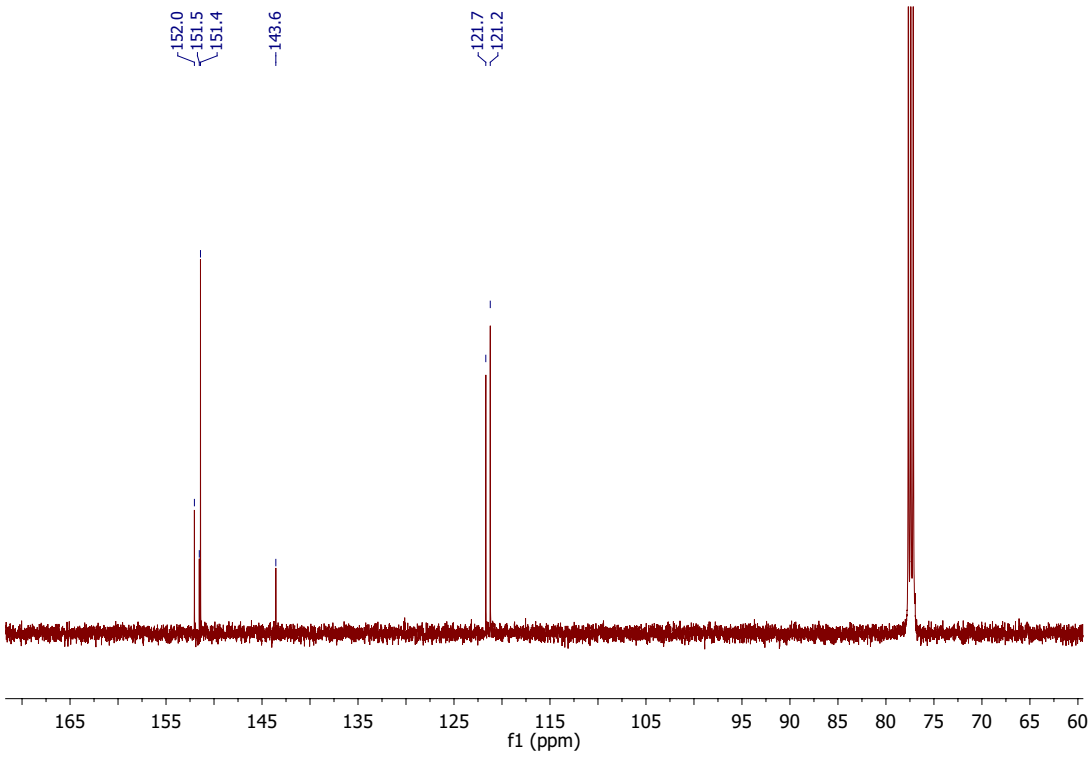

^{13}C NMR of **6** in $CDCl_3$.

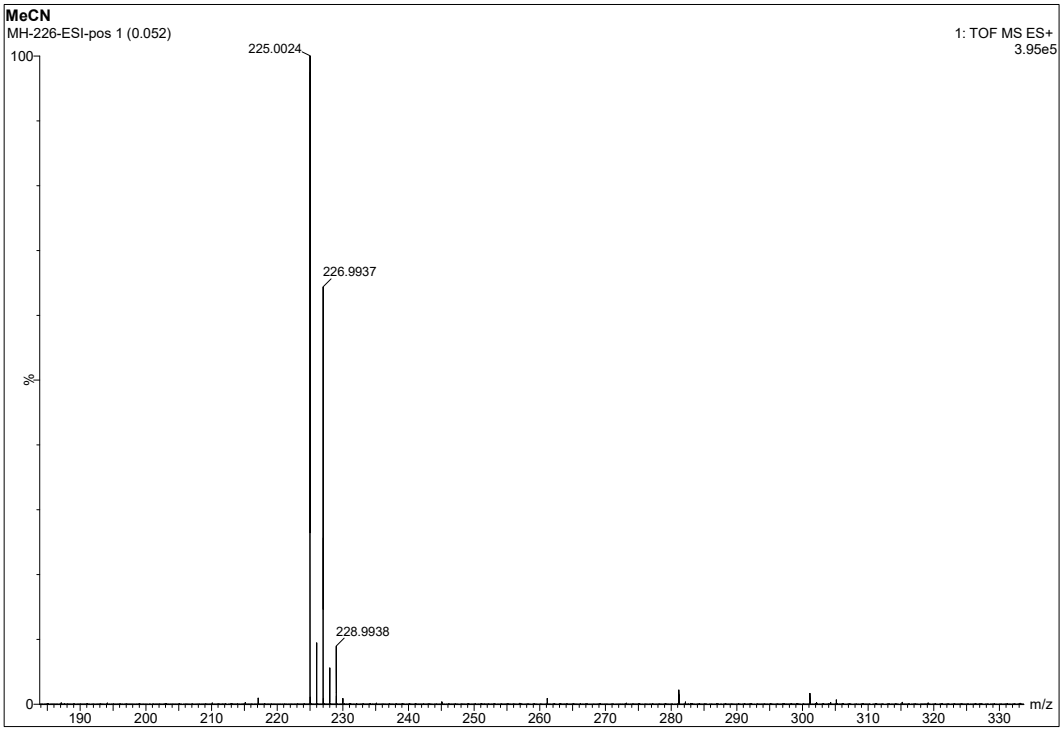

ESI-MS of **6**.

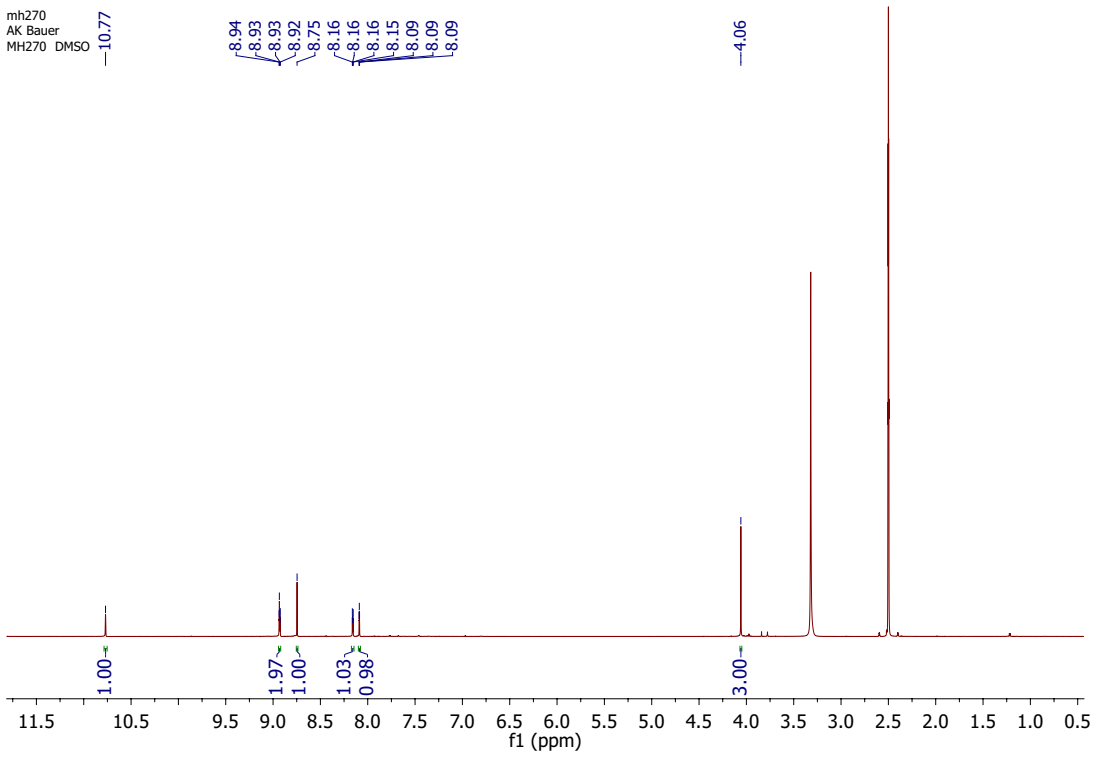

^{1}H NMR of **L3** in DMSO-d$_6$.

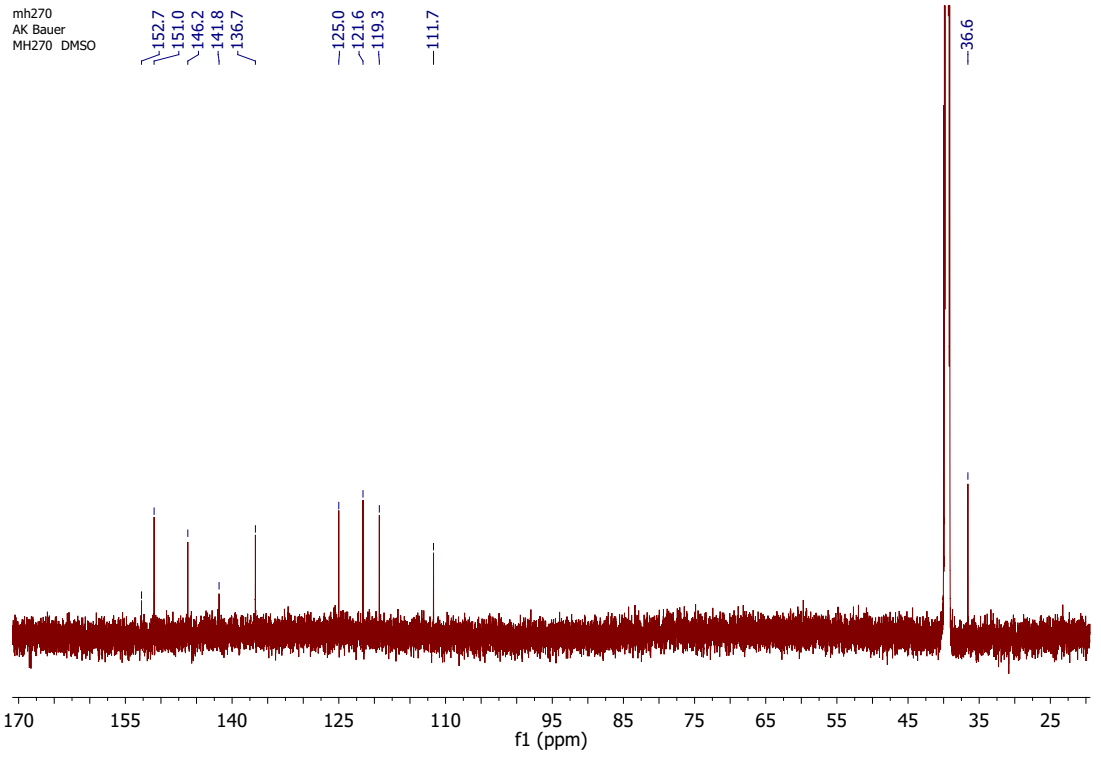

^{13}C NMR of **L3** in DMSO-d$_6$.

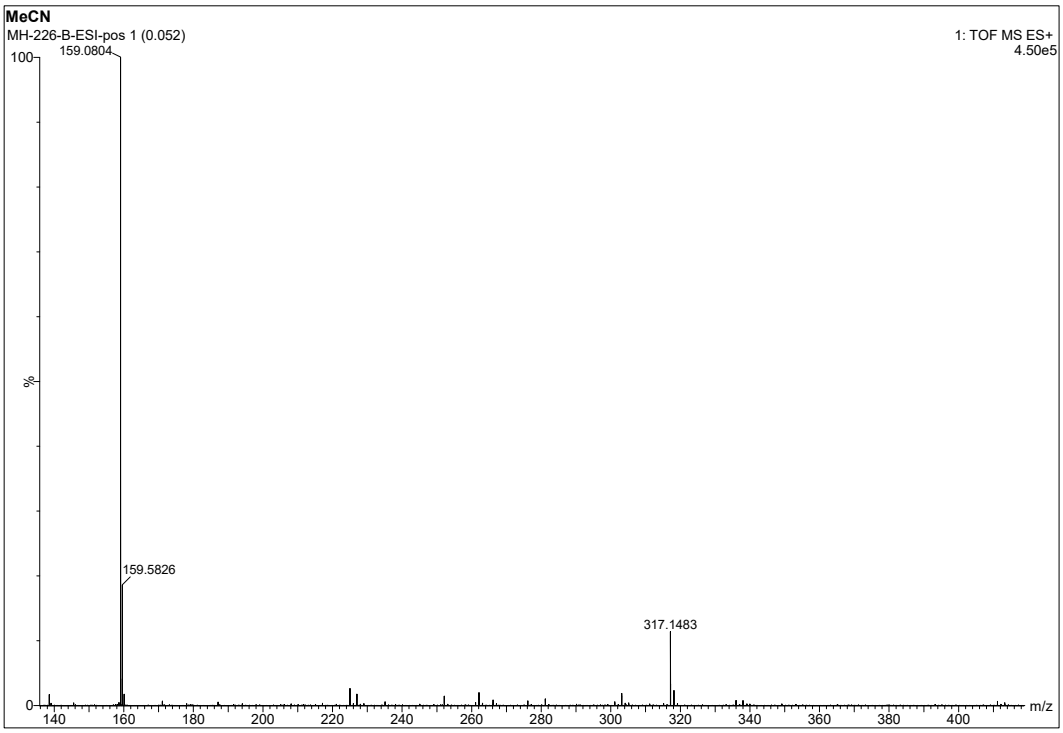
MeCN
MH-226-B-ESI-pos 1 (0.052)
1: TOF MS ES+
4.50e5
100
%
0
159.0804
159.5826
317.1483
140
160
180
200
220
240
260
280
300
320
340
360
380
400
m/z

ESI-MS of **L3**.

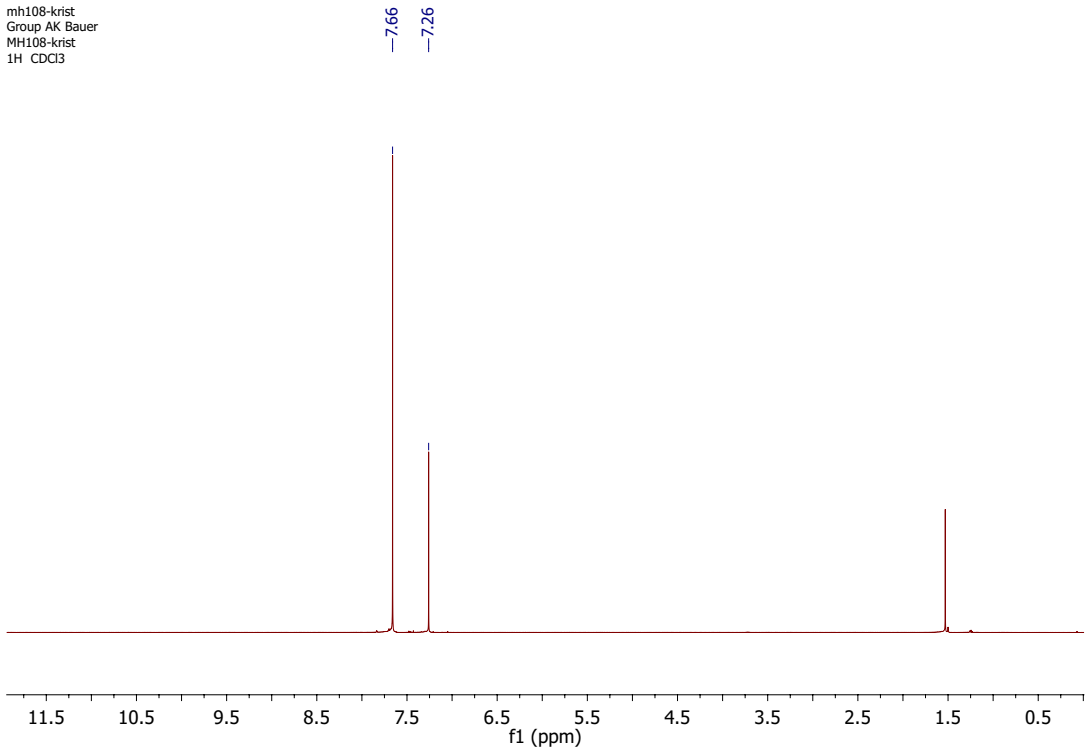

^{1}H NMR of **7**-Cl in $CDCl_3$.

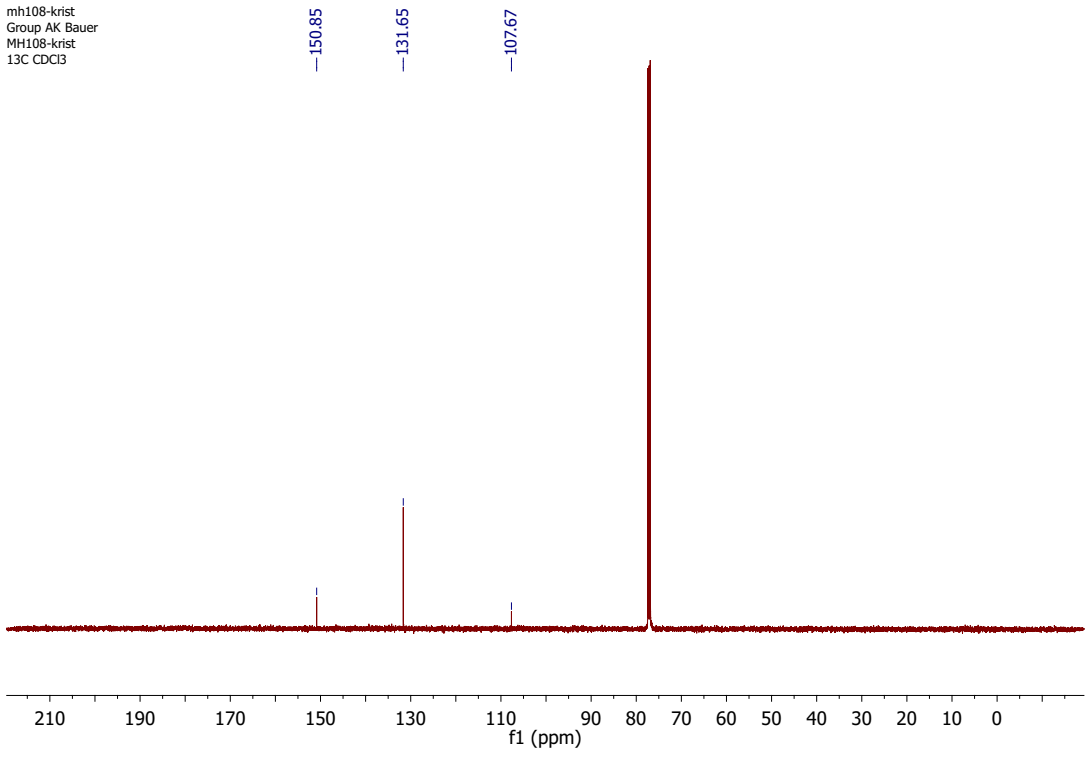

^{13}C NMR of **7**-Cl in $CDCl_3$.

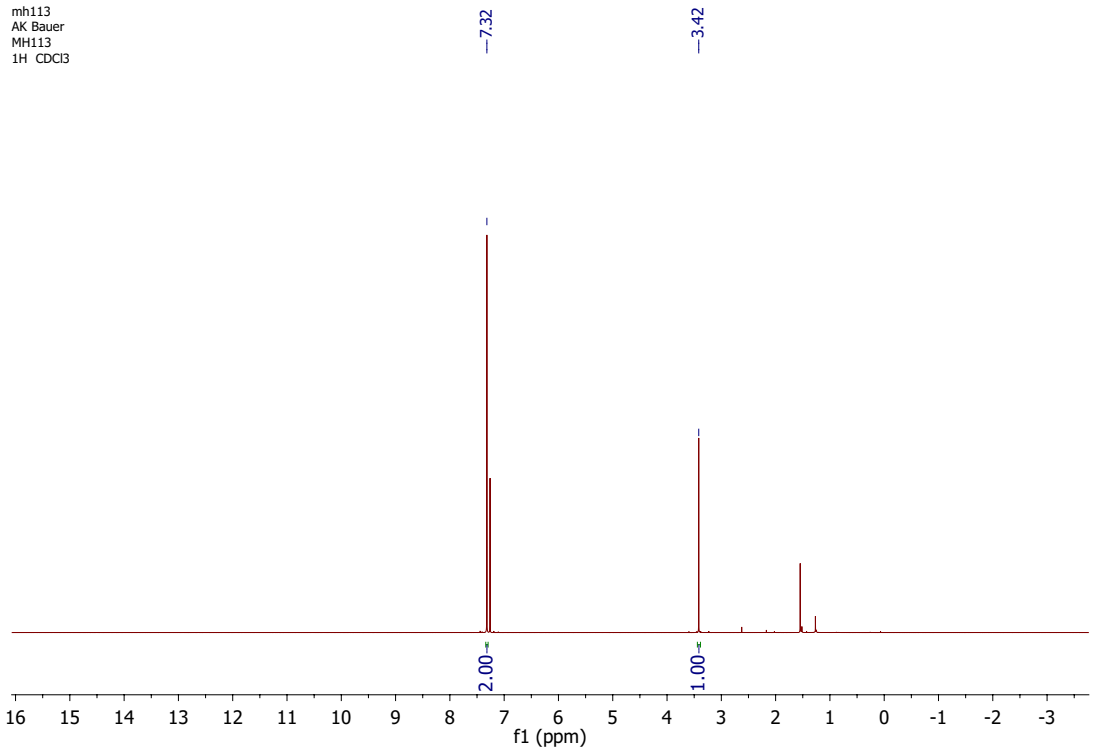

^{1}H NMR of **8**-Cl in $CDCl_3$.

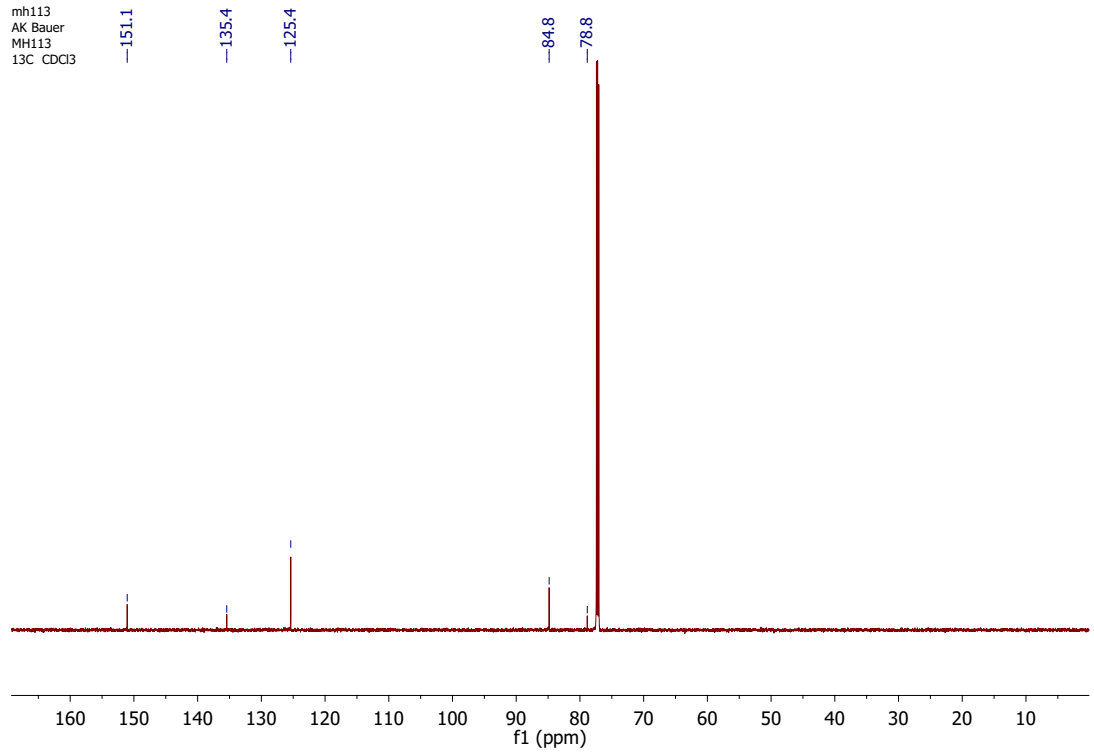

^{13}C NMR of **8**-Cl in $CDCl_3$.

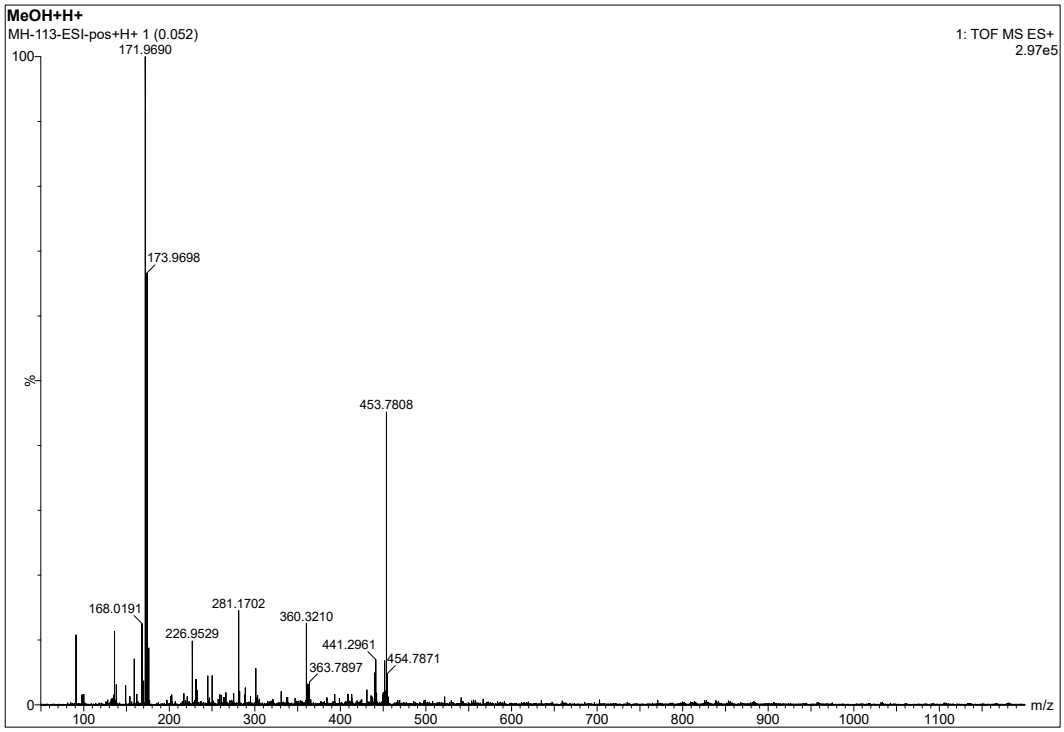

ESI-MS of **8**-Cl.

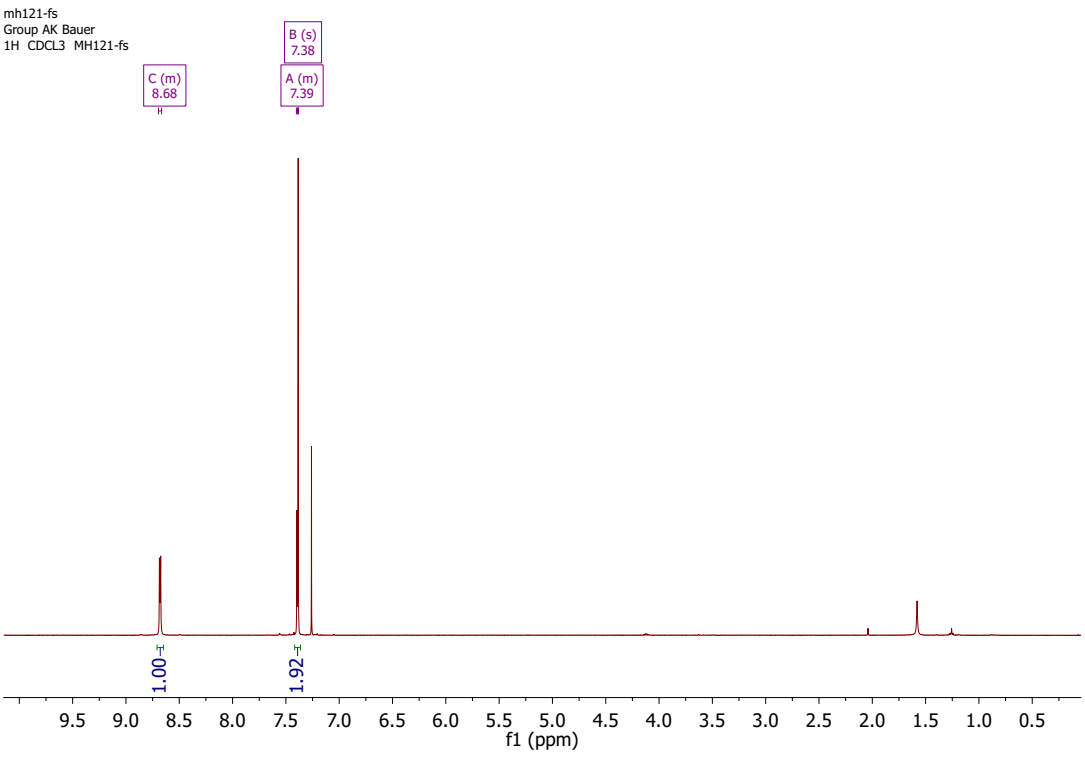

^{1}H NMR of **9**-Cl in $CDCl_3$.

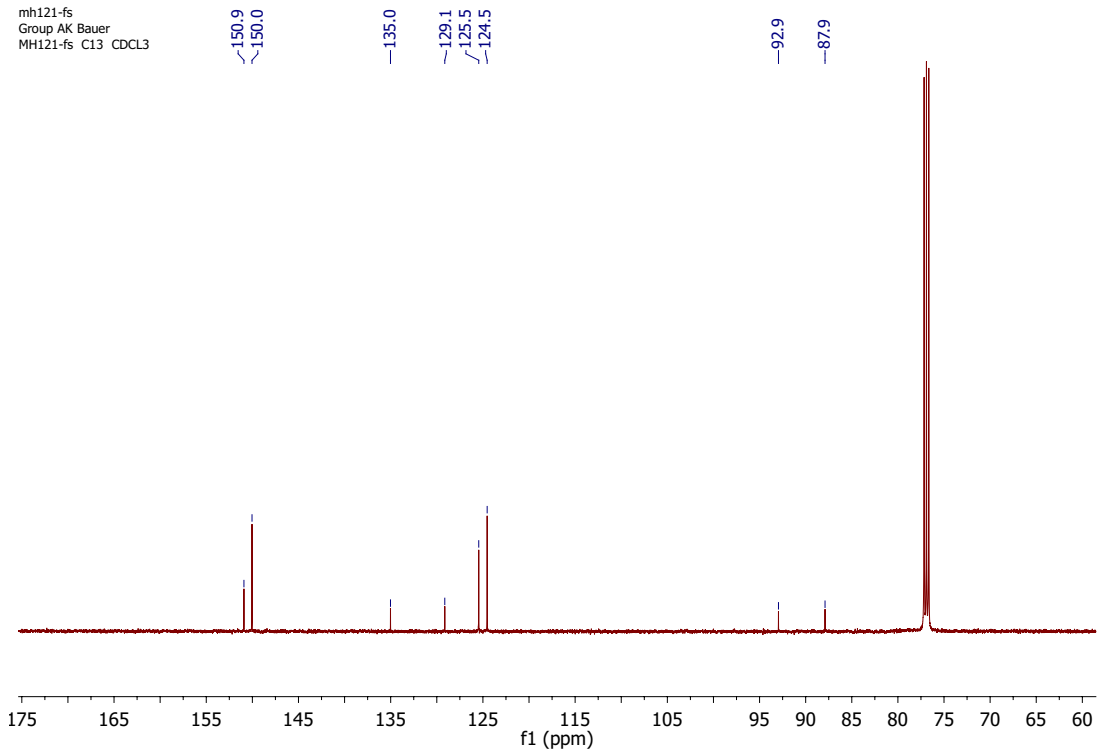

^{13}C NMR of **9**-Cl in $CDCl_3$.

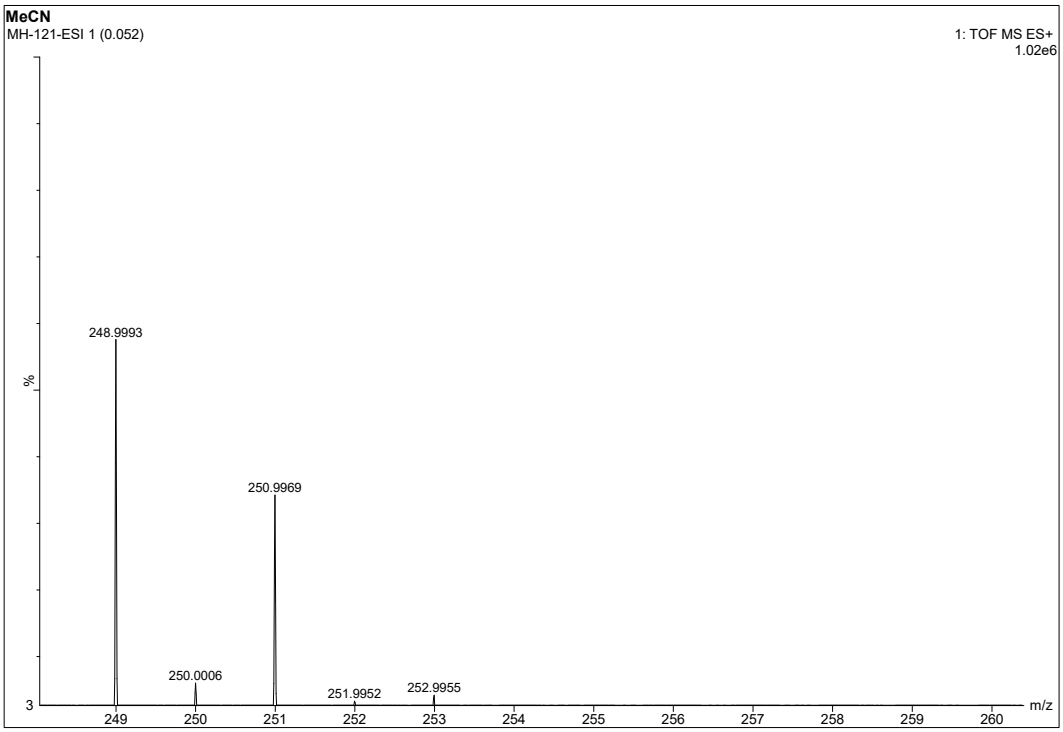

ESI-MS of **9**-Cl.

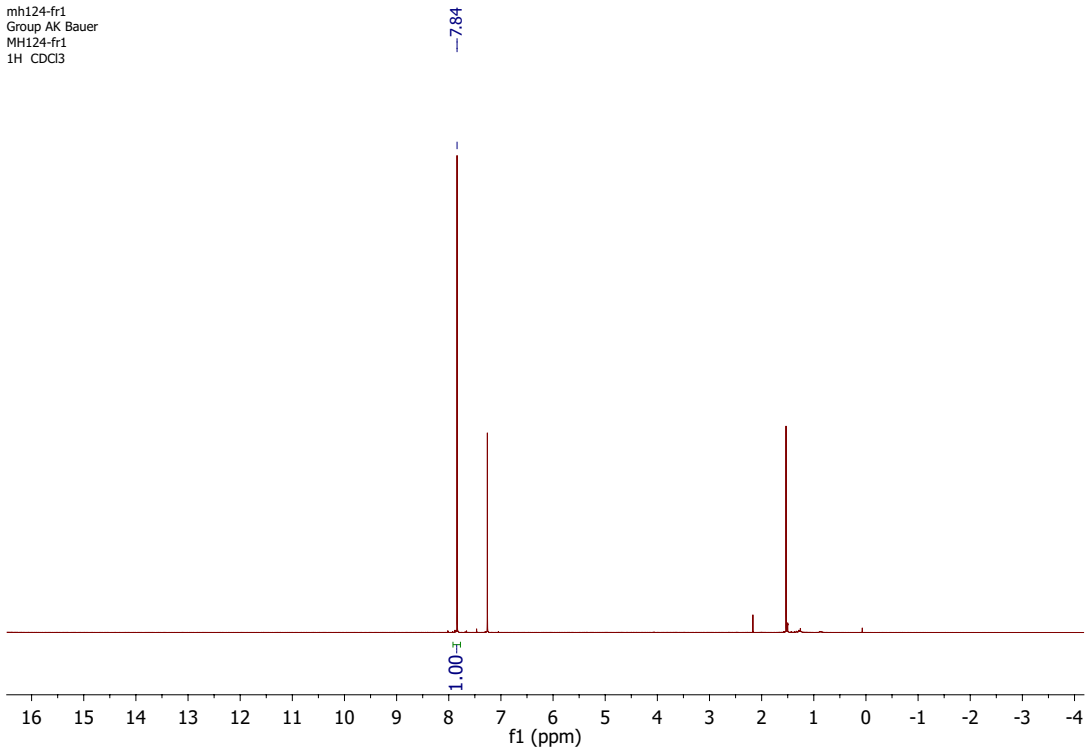

^{1}H NMR of **7**-Br in $CDCl_3$.

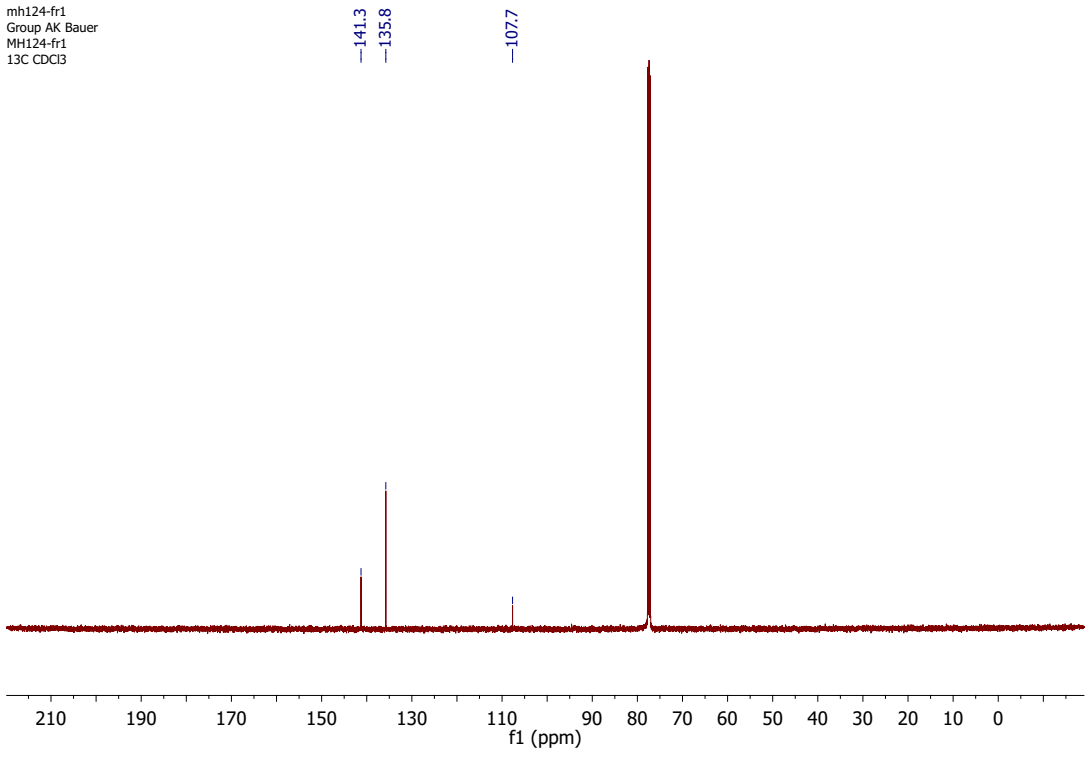

^{13}C NMR of **7**-Br in $CDCl_3$.

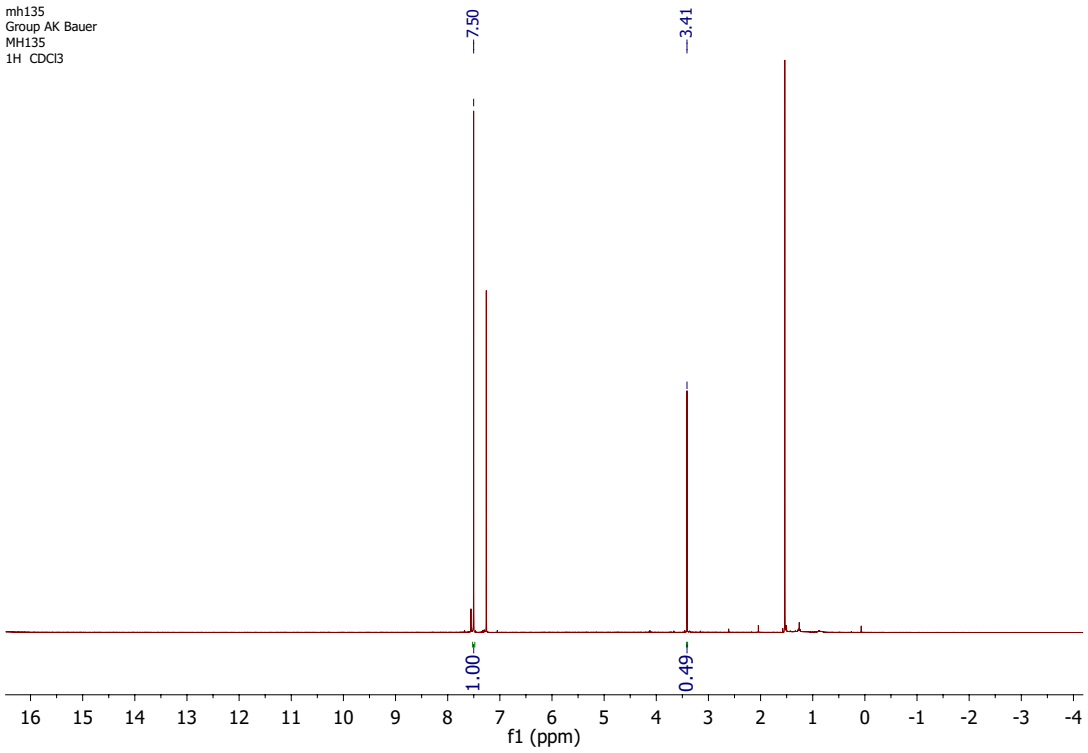

^{1}H NMR of **8**-Br in $CDCl_3$.

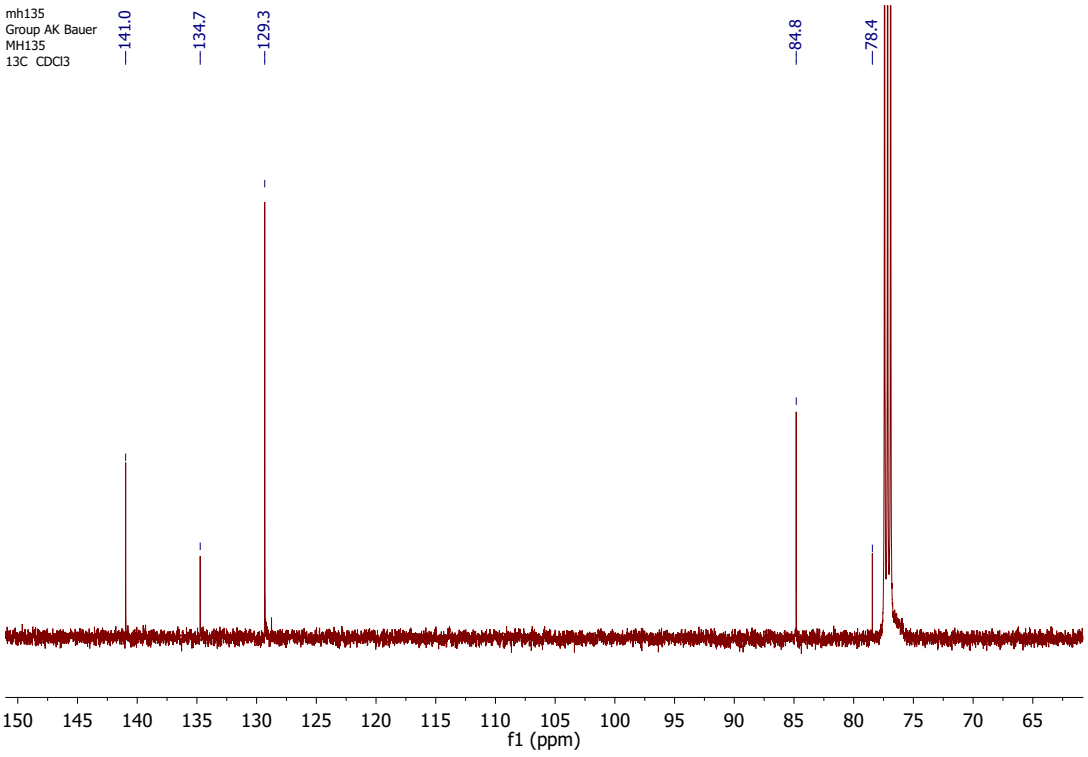

^{13}C NMR of **8**-Br in $CDCl_3$.

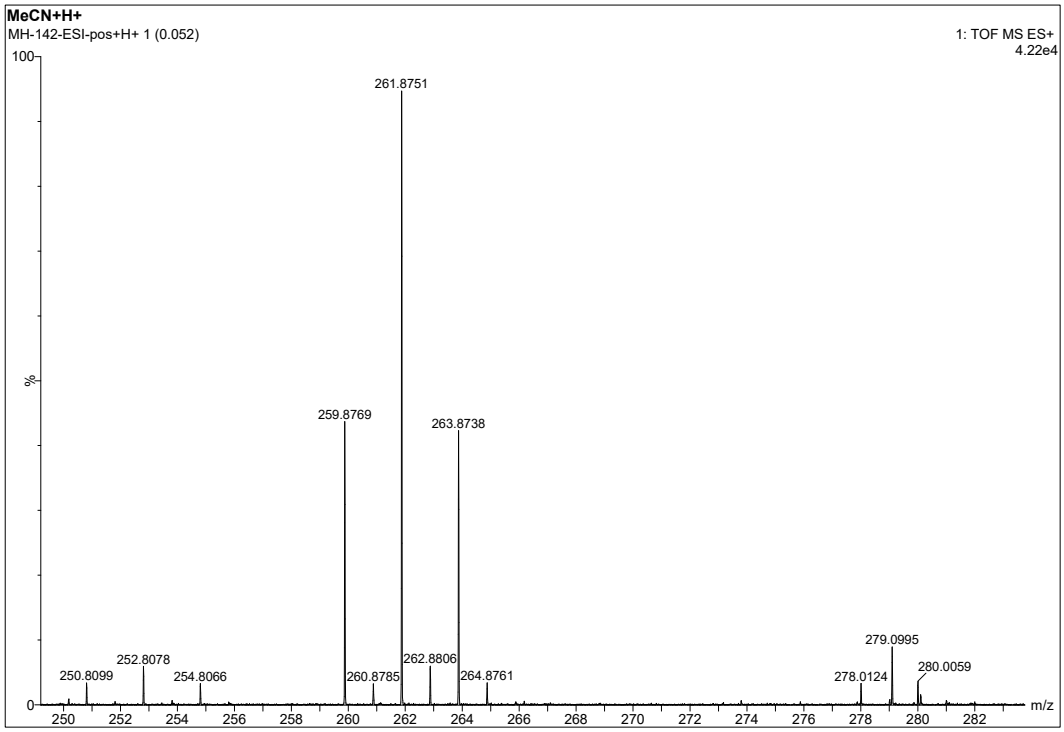

ESI-MS of **8**-Br.

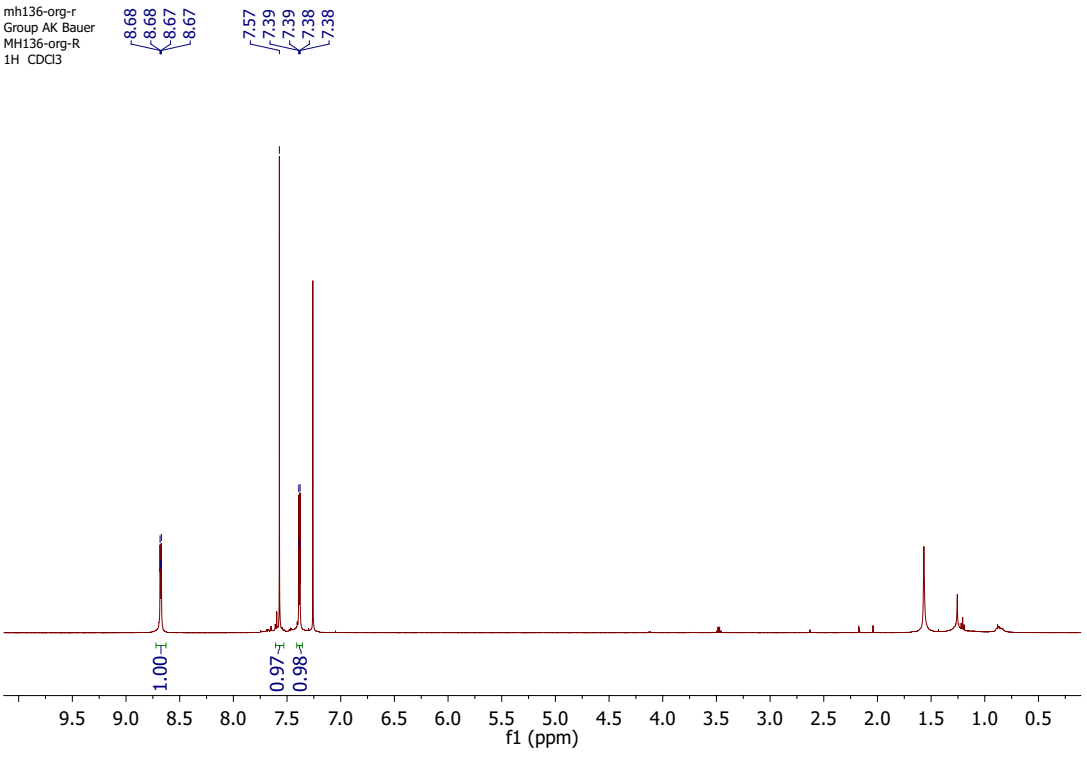

^{1}H NMR of **9**-Br in $CDCl_3$.

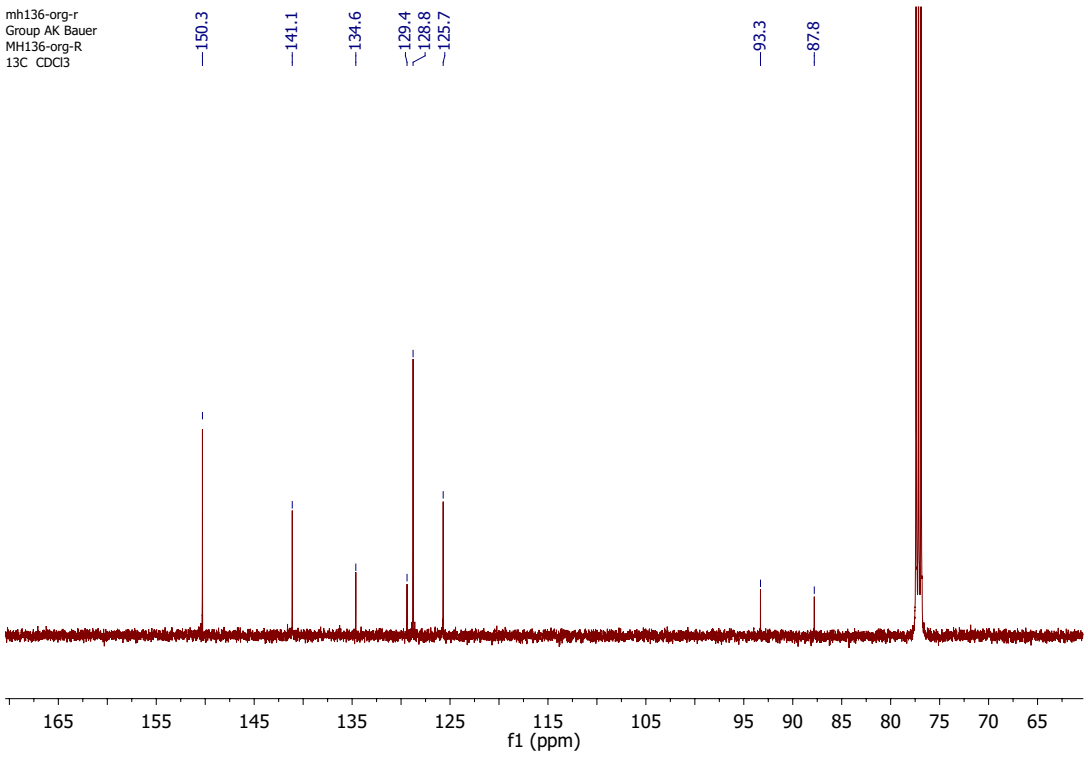

^{13}C NMR of **9**-Br in $CDCl_3$.

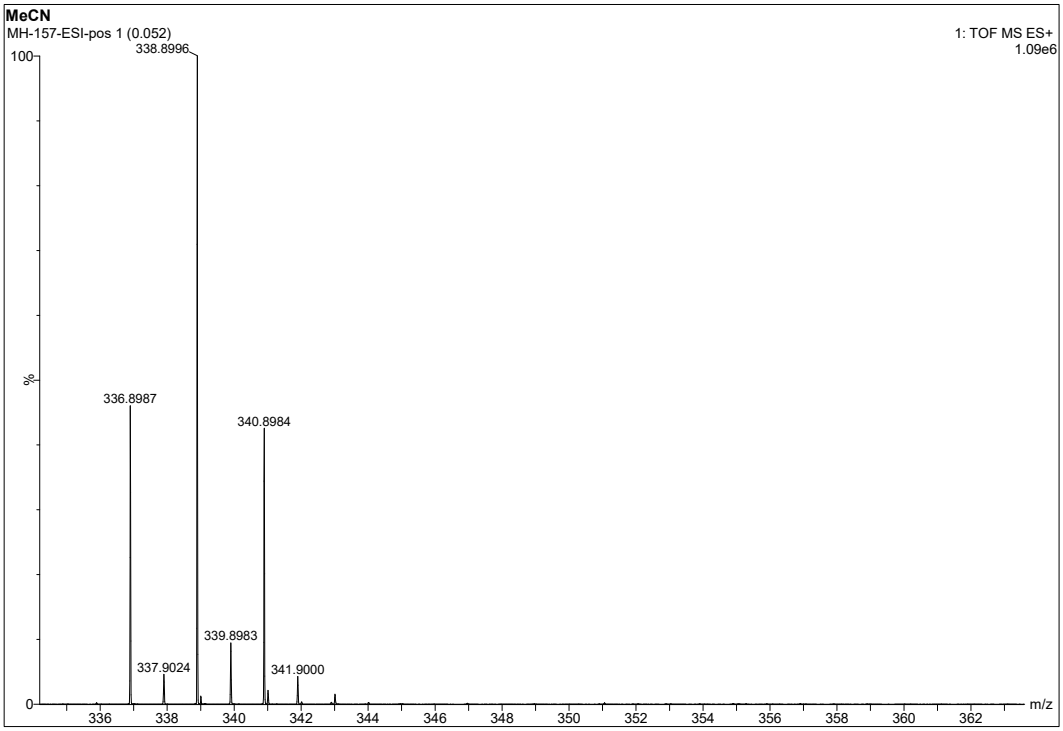

ESI-MS of **9**-Br.

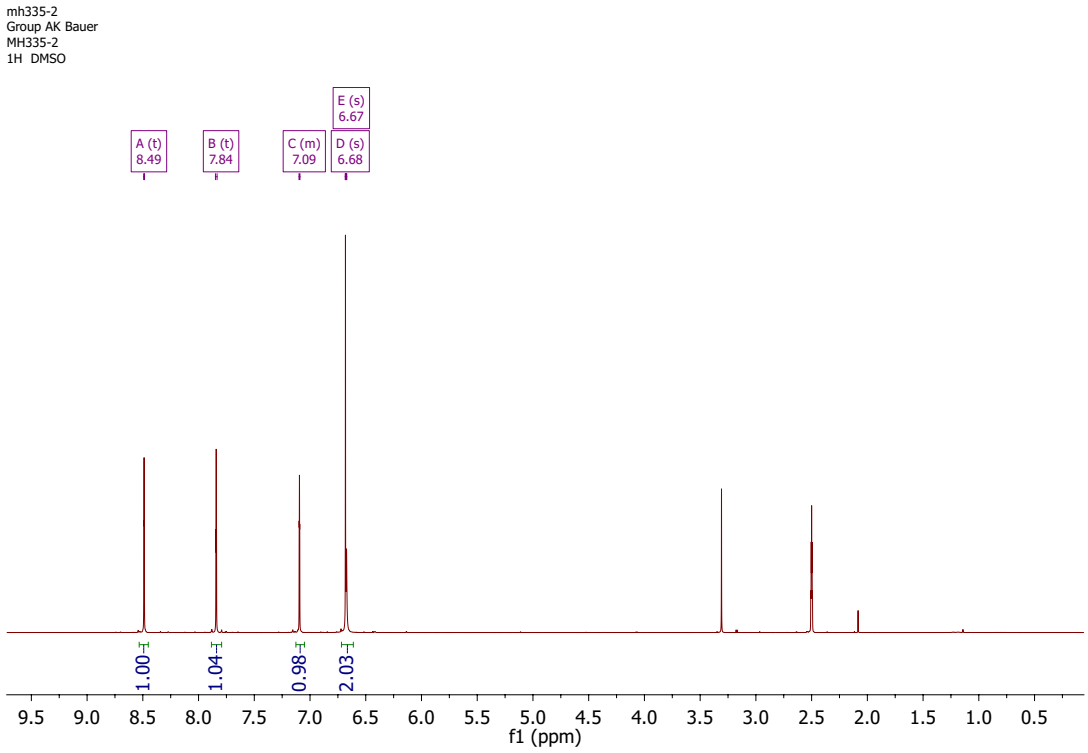

^{1}H NMR of **13** in DMSO-d$_6$.

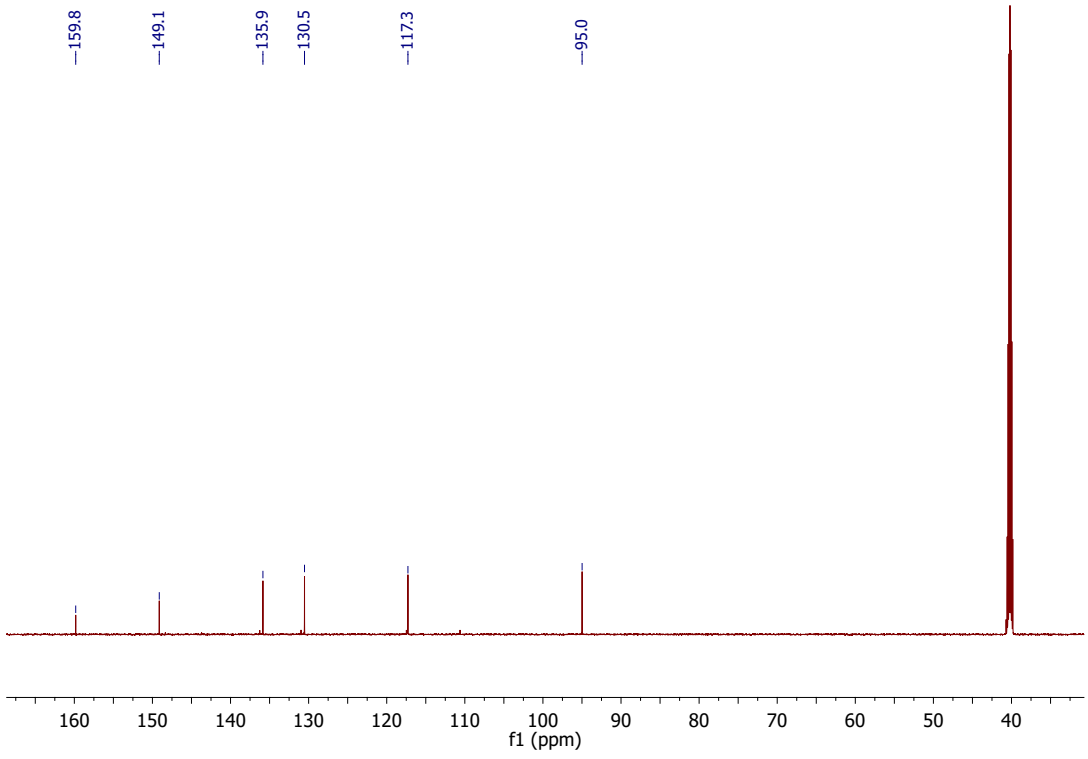

^{13}C NMR of **13** in DMSO-d$_6$.

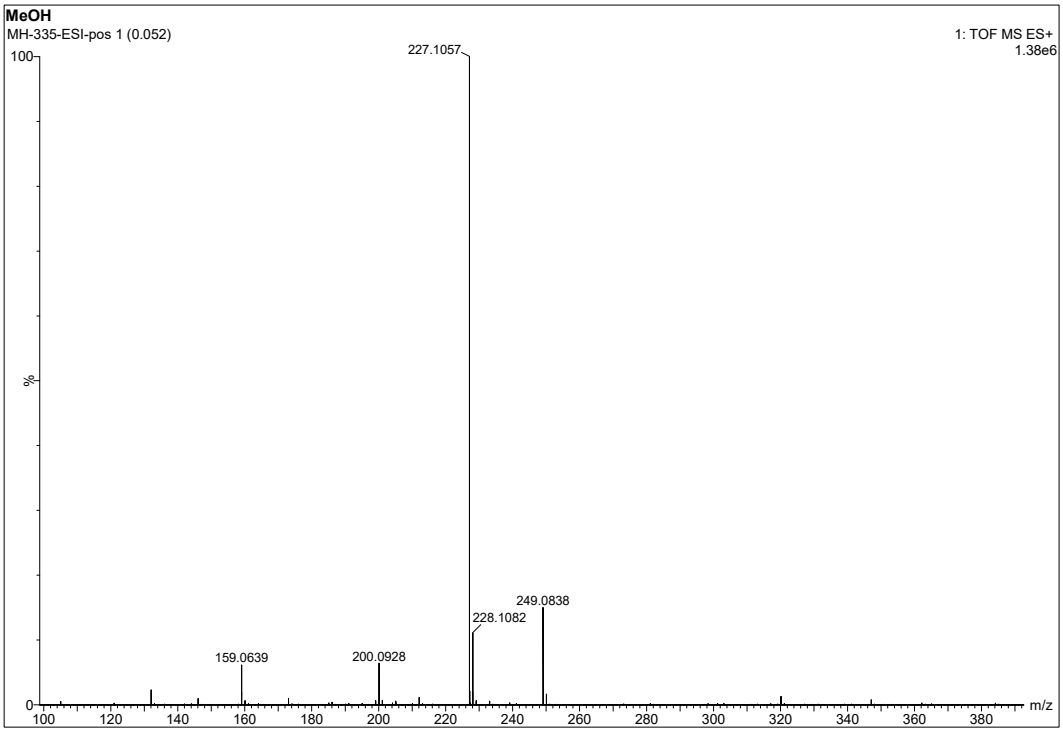

ESI-MS of **13**.

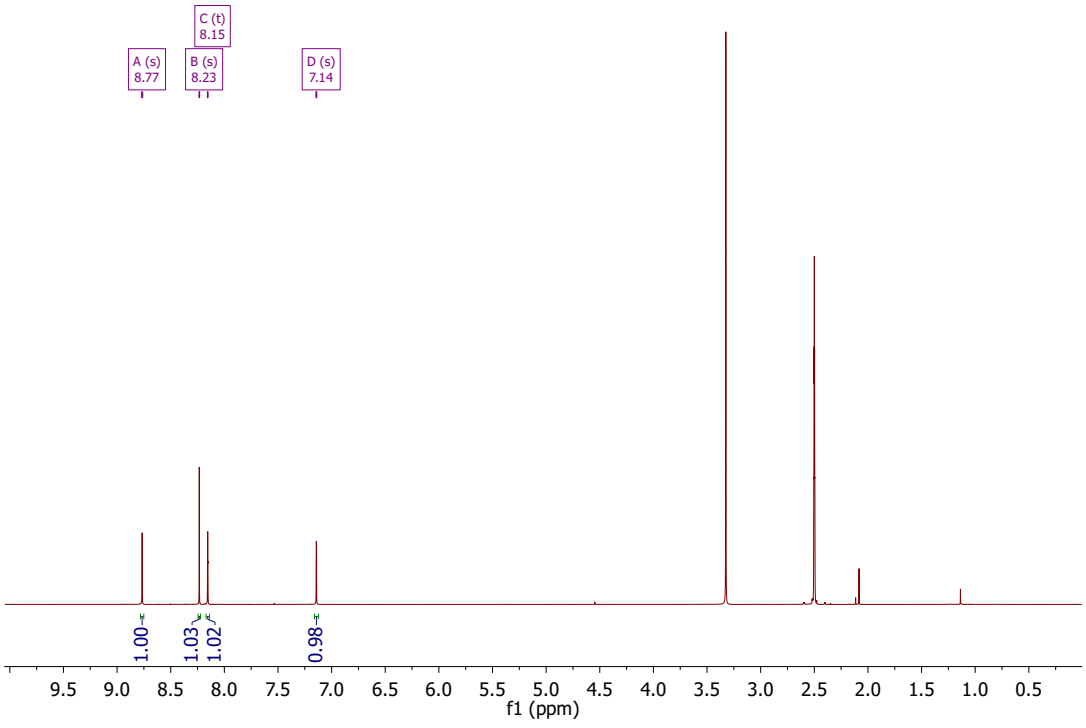

^{1}H NMR of **14** in DMSO-d_6.

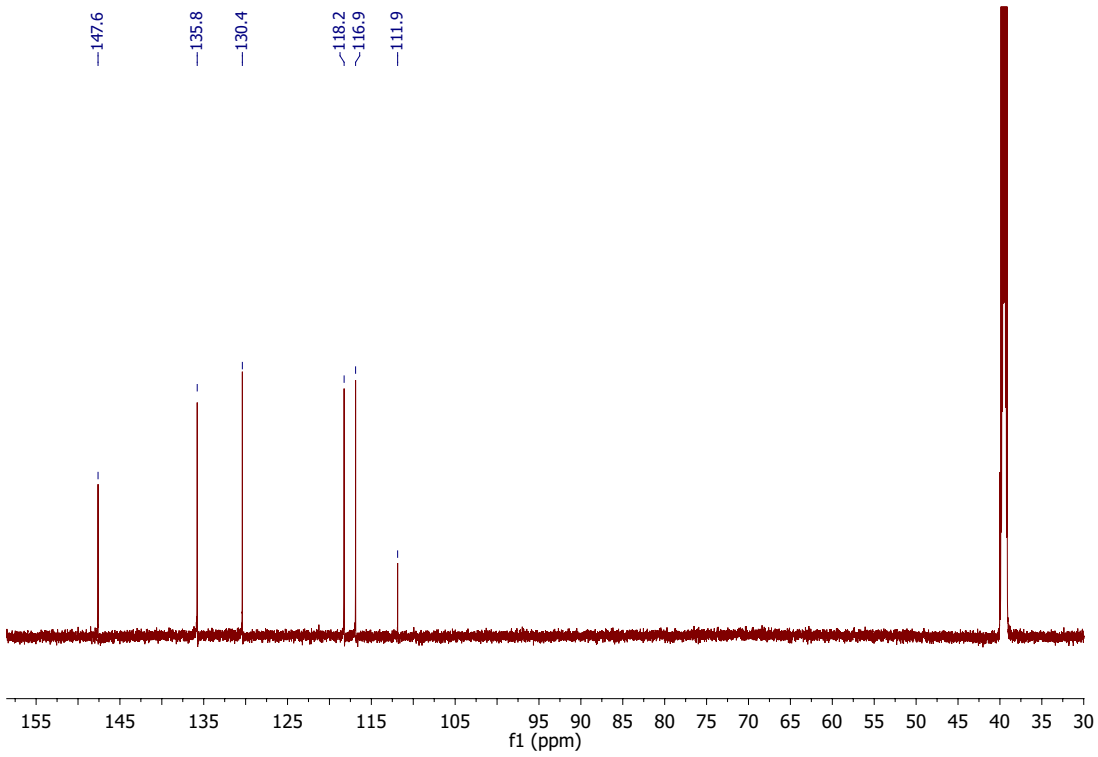

^{13}C NMR of **14** in DMSO-d_6.

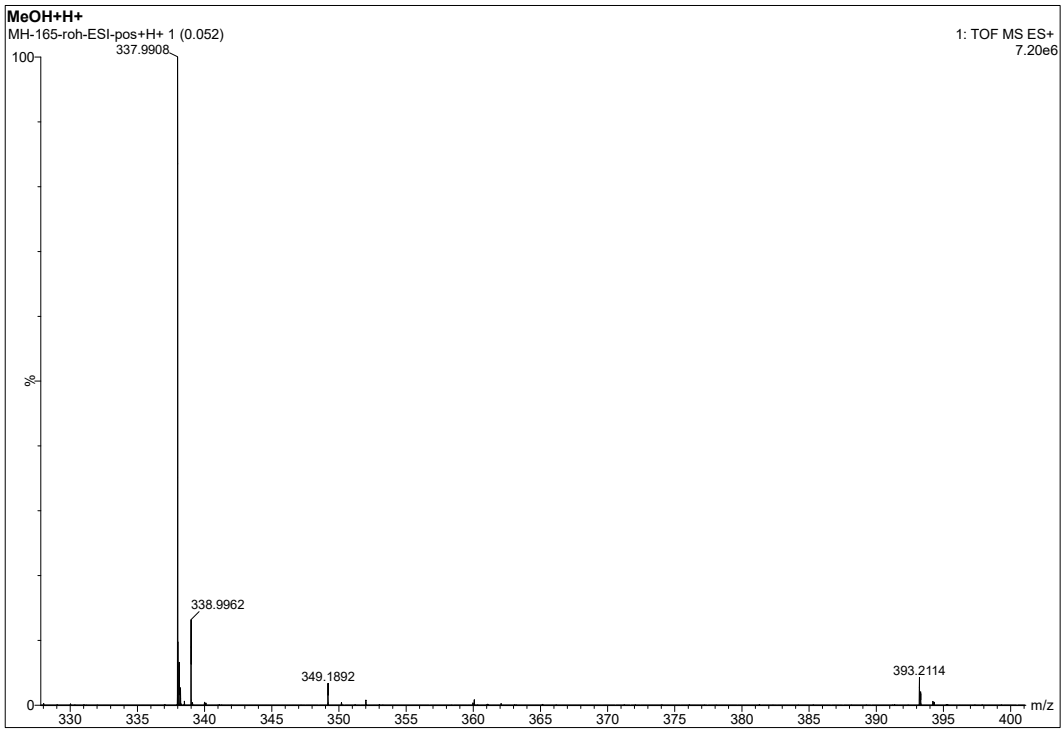

ESI-MS of **14**.

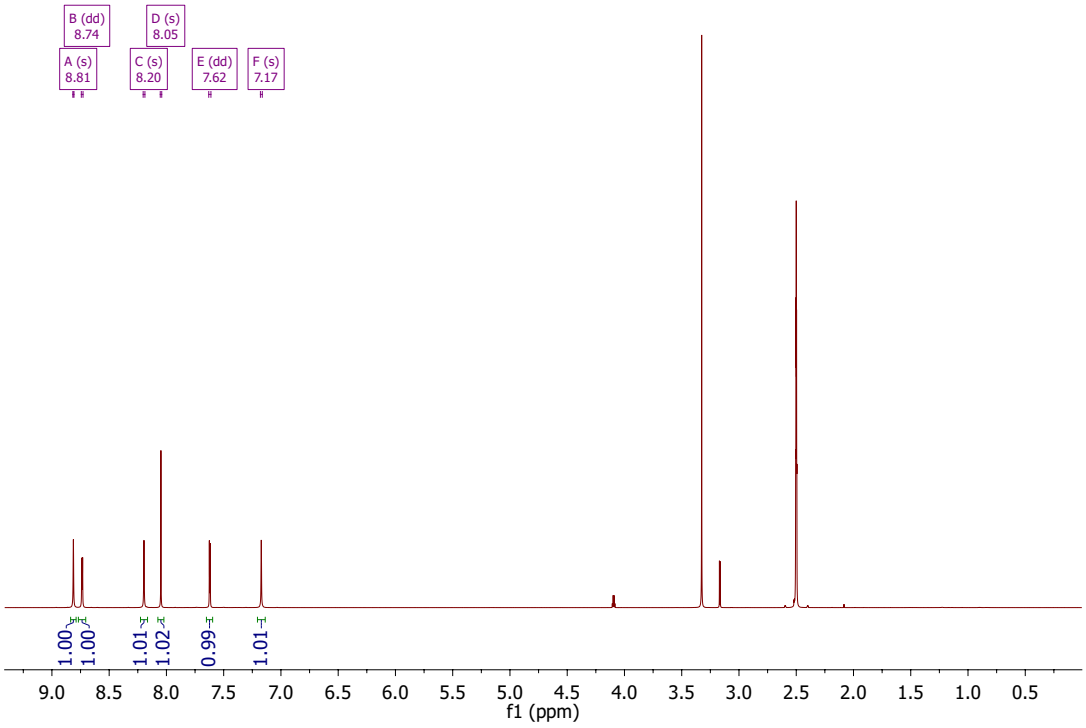

^{1}H NMR of **11** in DMSO-d$_6$.

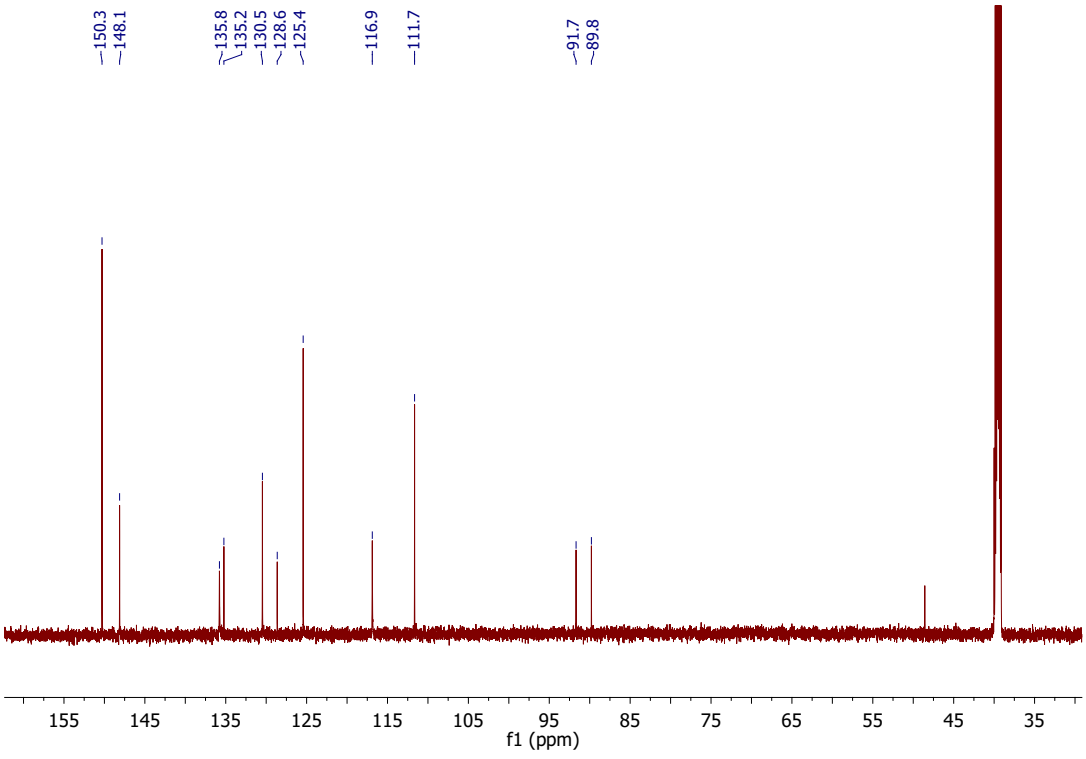

^{13}C NMR of **11** in DMSO-d$_6$.

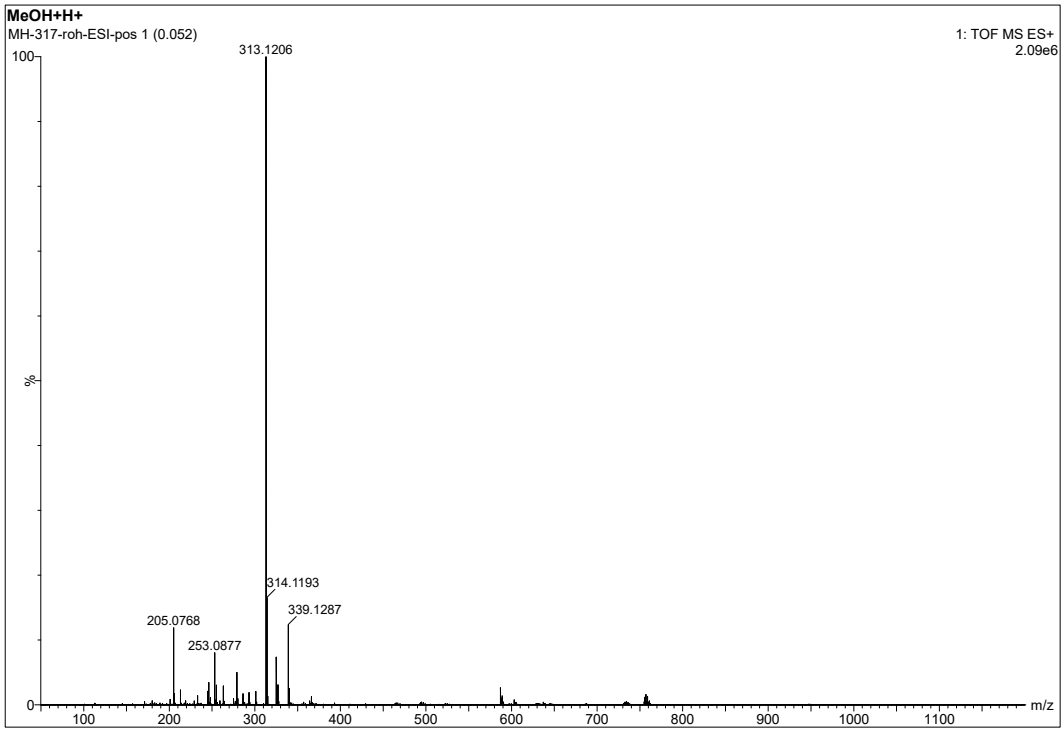

ESI-MS of **11**.

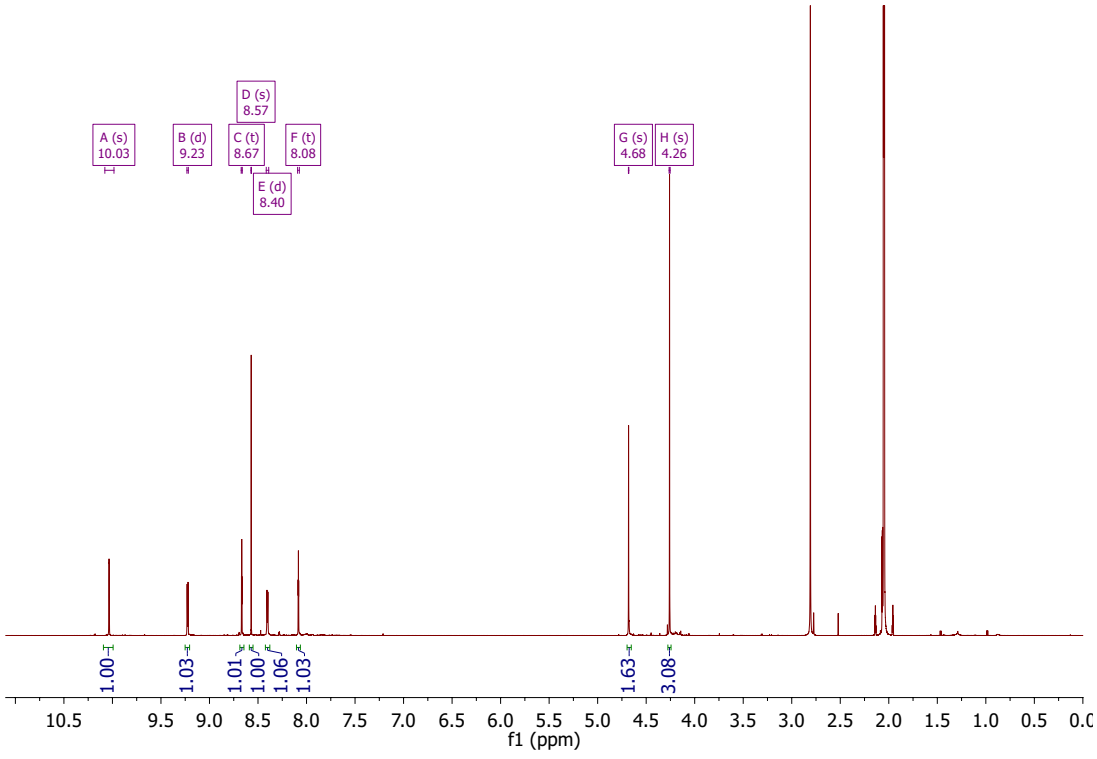

^{1}H NMR of **L5** in acetone-d_6.

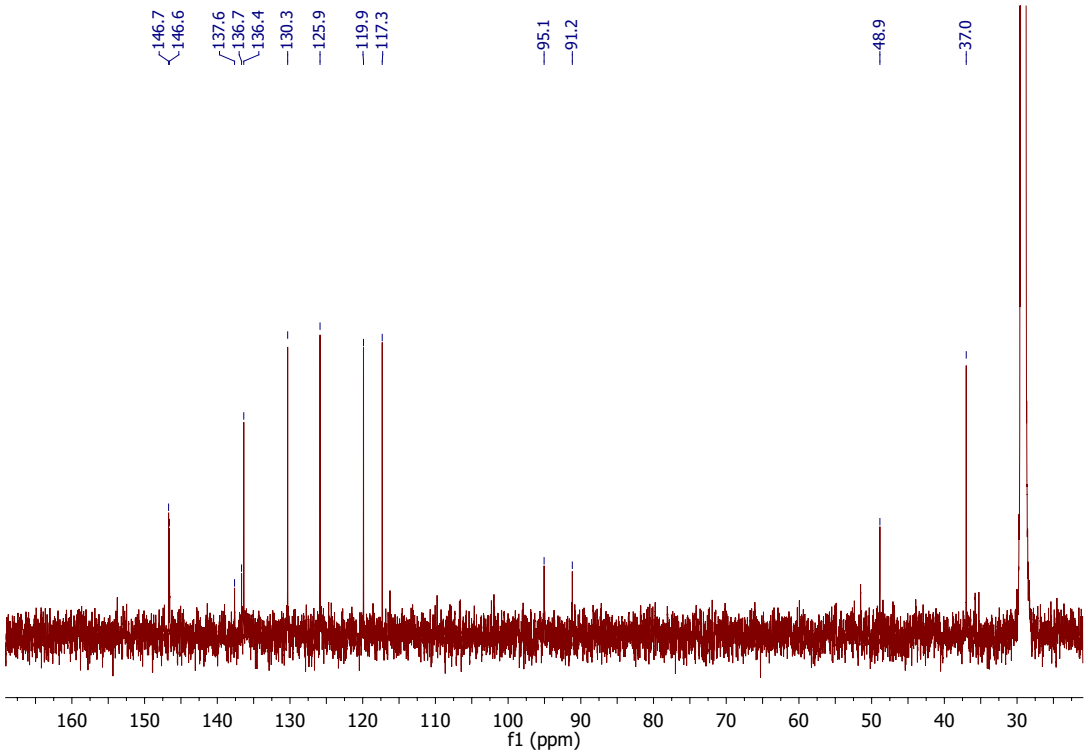

^{13}C NMR of **L5** in acetone-d$_6$.

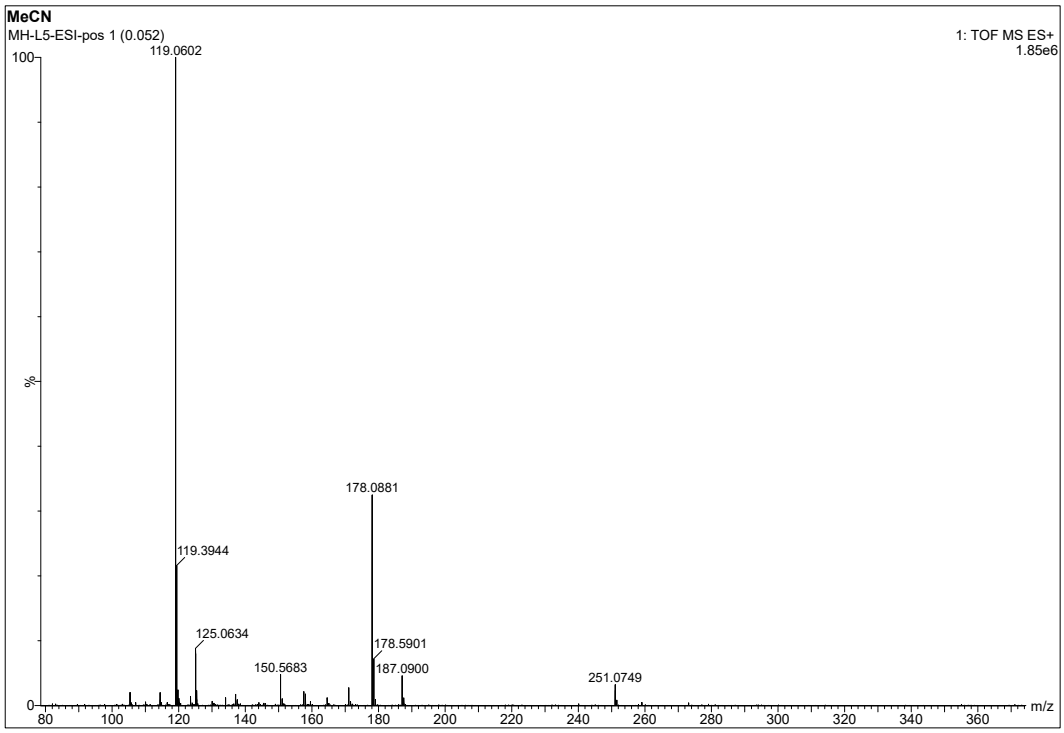
MeCN
MH-L5-ESI-pos 1 (0.052)
1: TOF MS ES+
1.85e6
100
%
0
119.0602
178.0881
119.3944
125.0634
178.5901
150.5683
187.0900
251.0749
m/z
80
100
120
140
160
180
200
220
240
260
280
300
320
340
360

ESI-MS of **L5**.

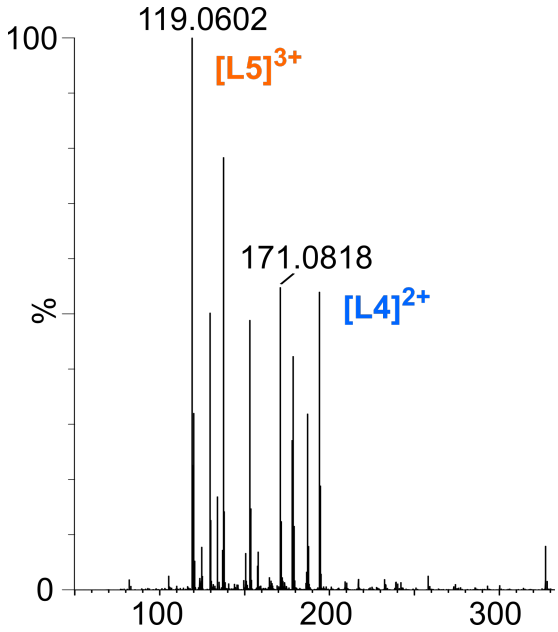

ESI mass spectrum of **L5** obtained after methylation of **L4**.

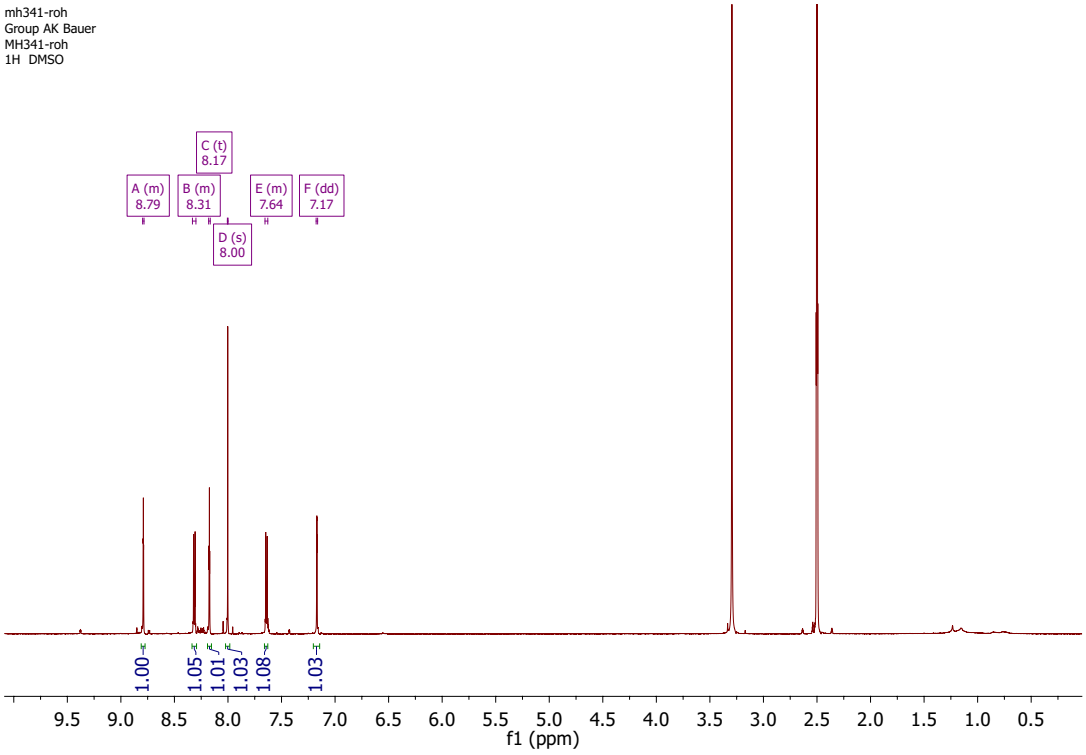

^{1}H NMR of **15** in DMSO-d_6.

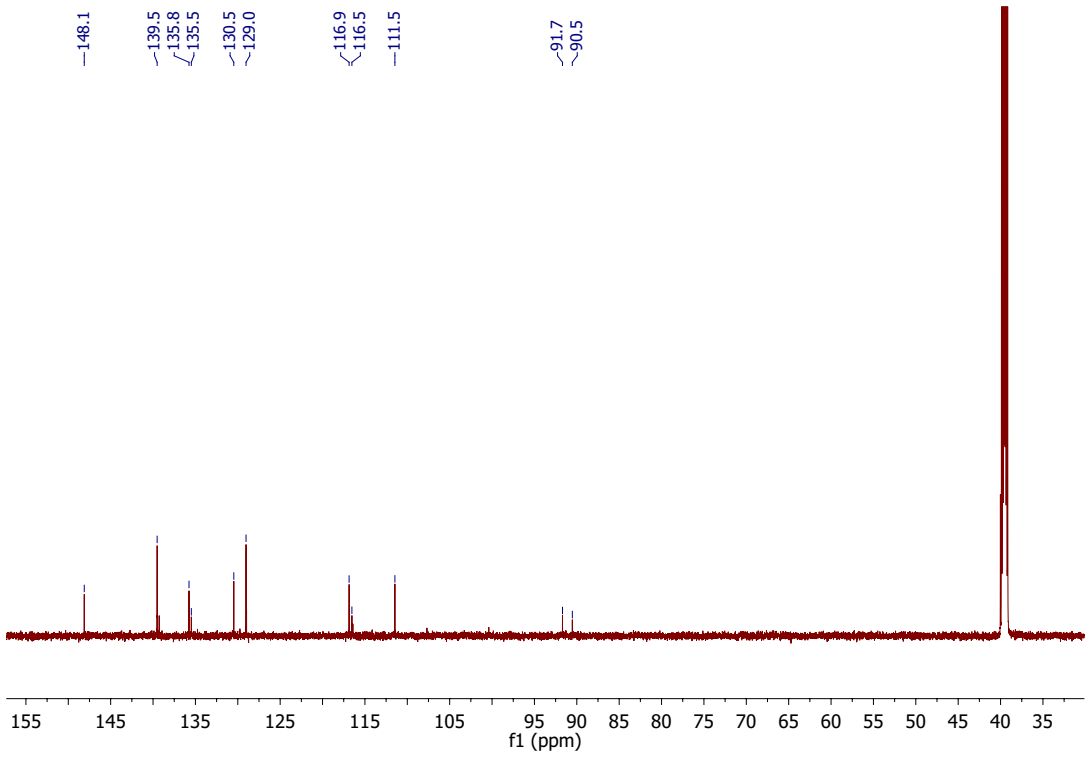

^{13}C NMR of **15** in DMSO-d_6.

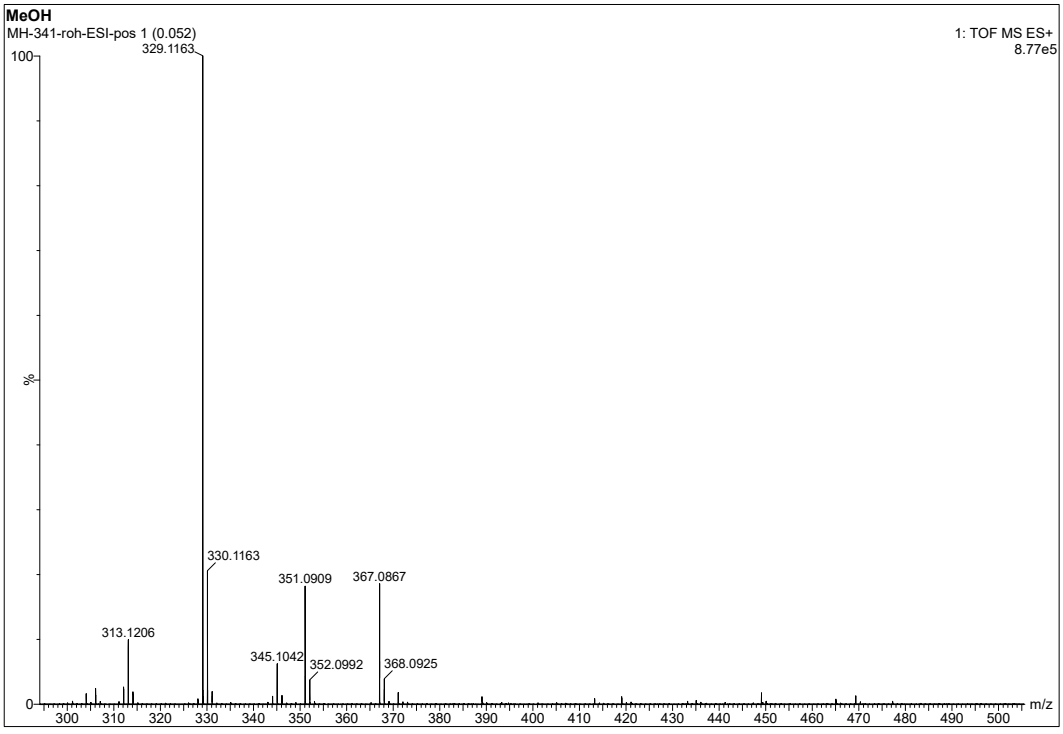

ESI-MS of **15**.

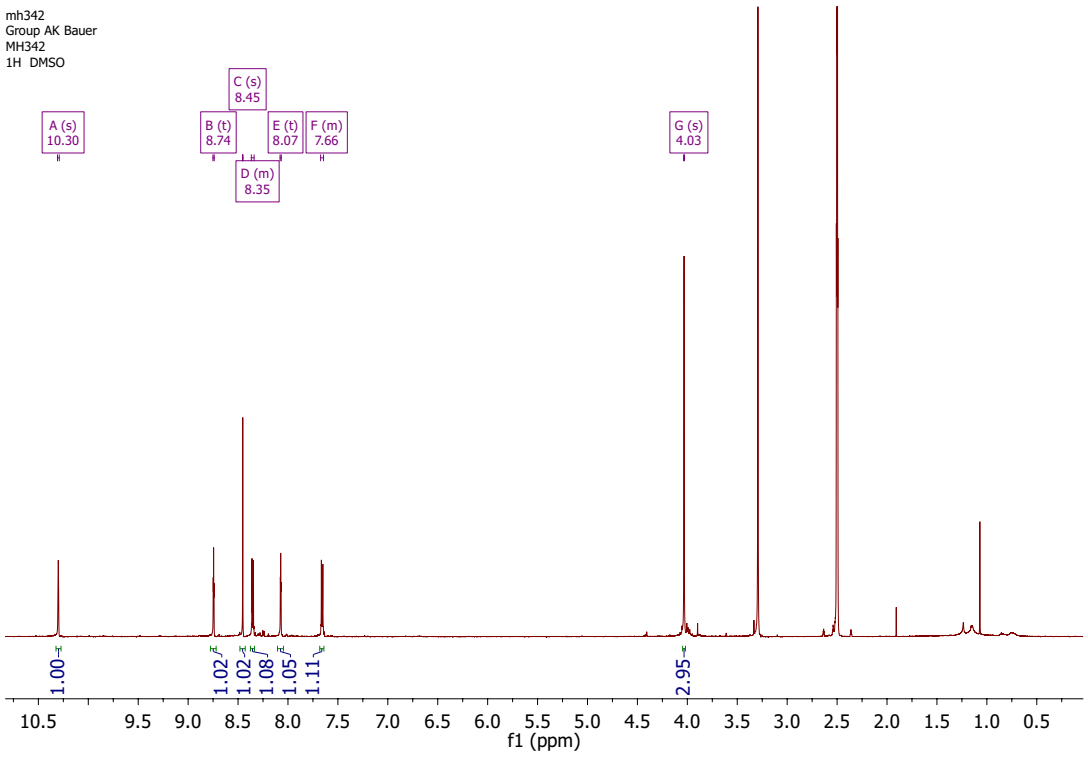

^{1}H NMR of **16** in DMSO-d$_6$.

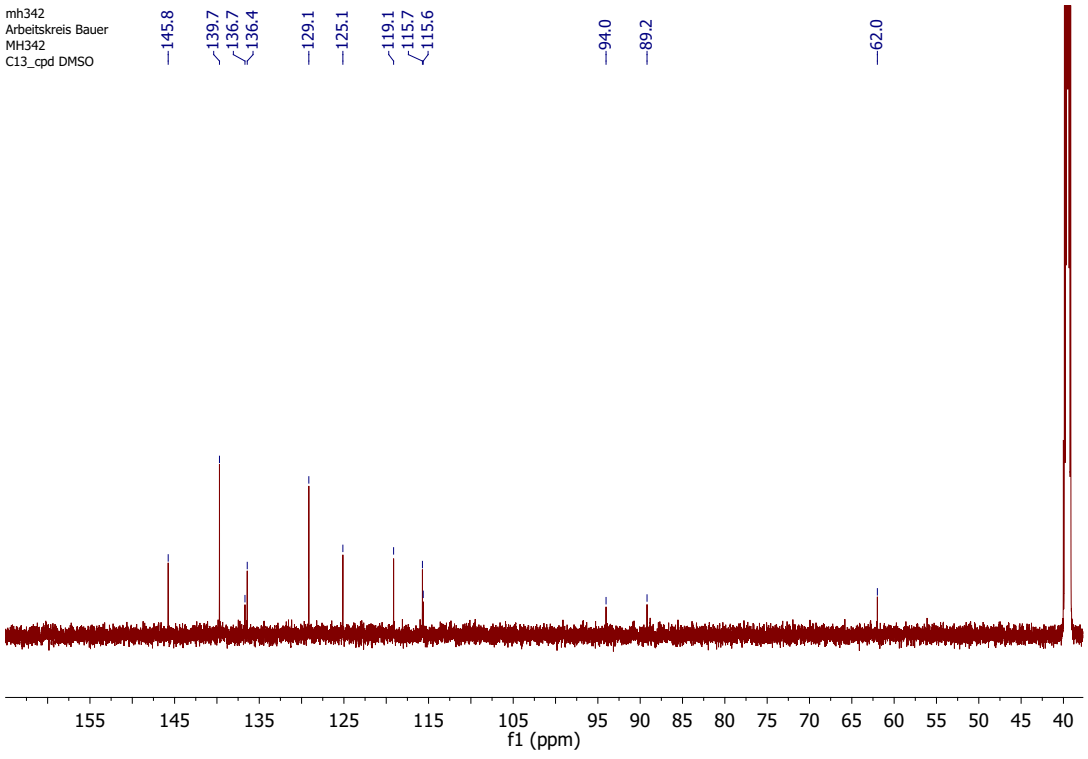

^{13}C NMR of **16** in DMSO-d$_6$.

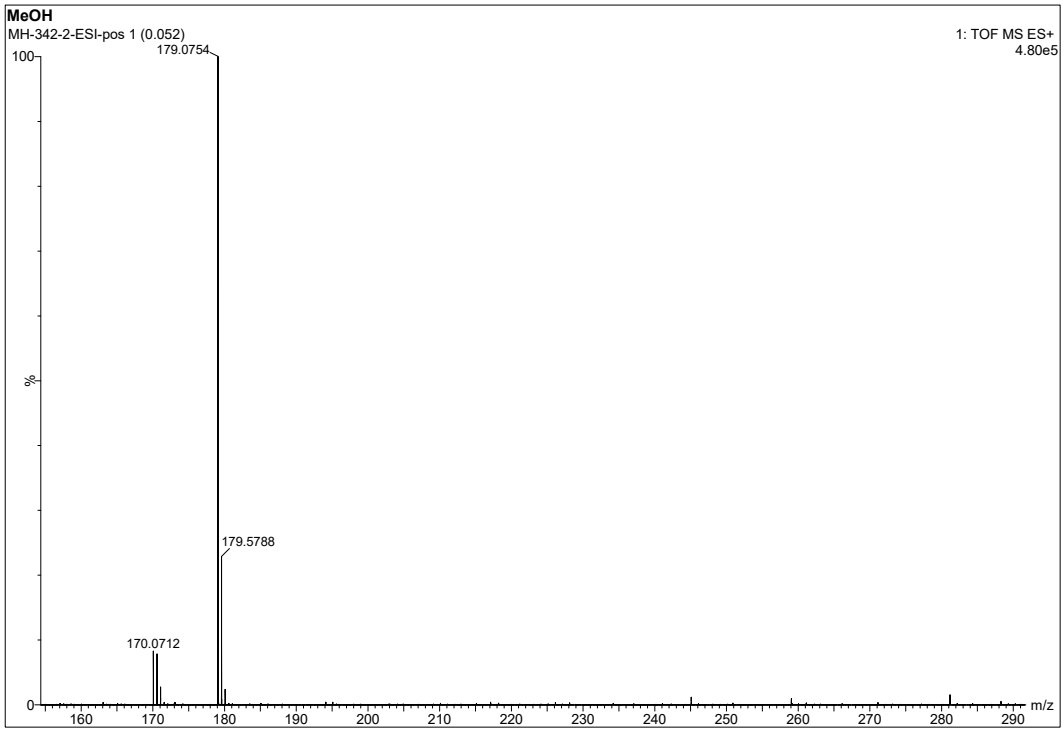

ESI-MS of **16**.

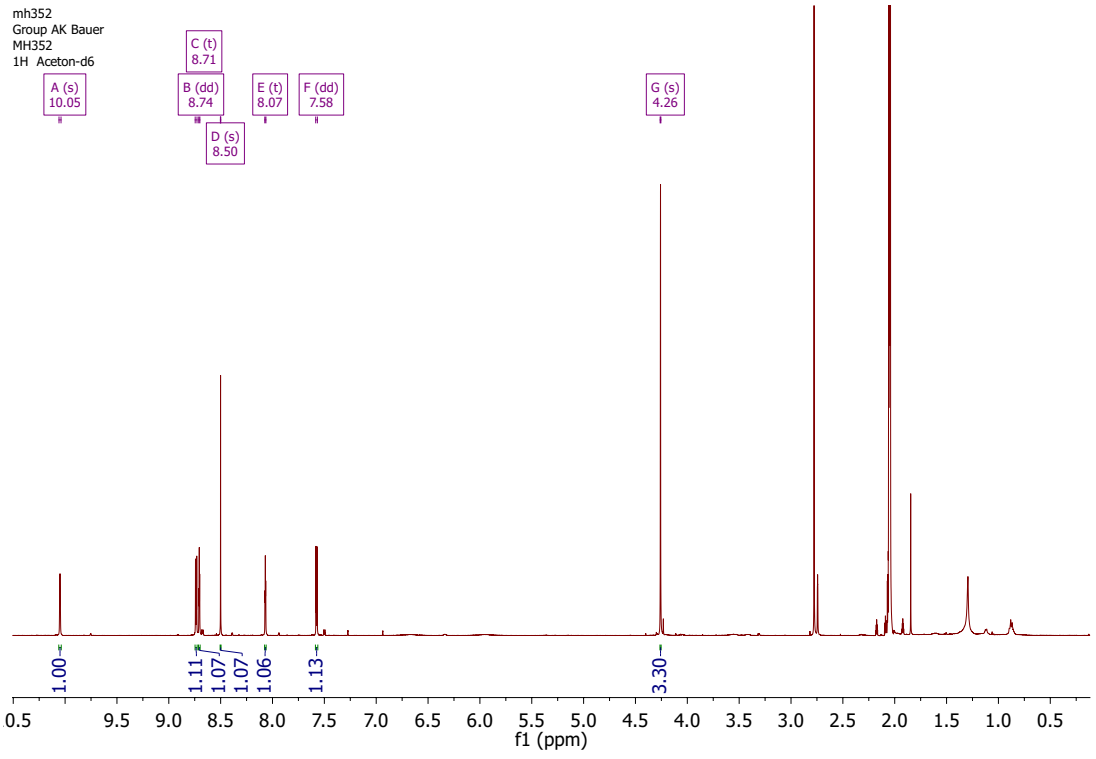

^{1}H NMR of **L4** in acetone-d_6.

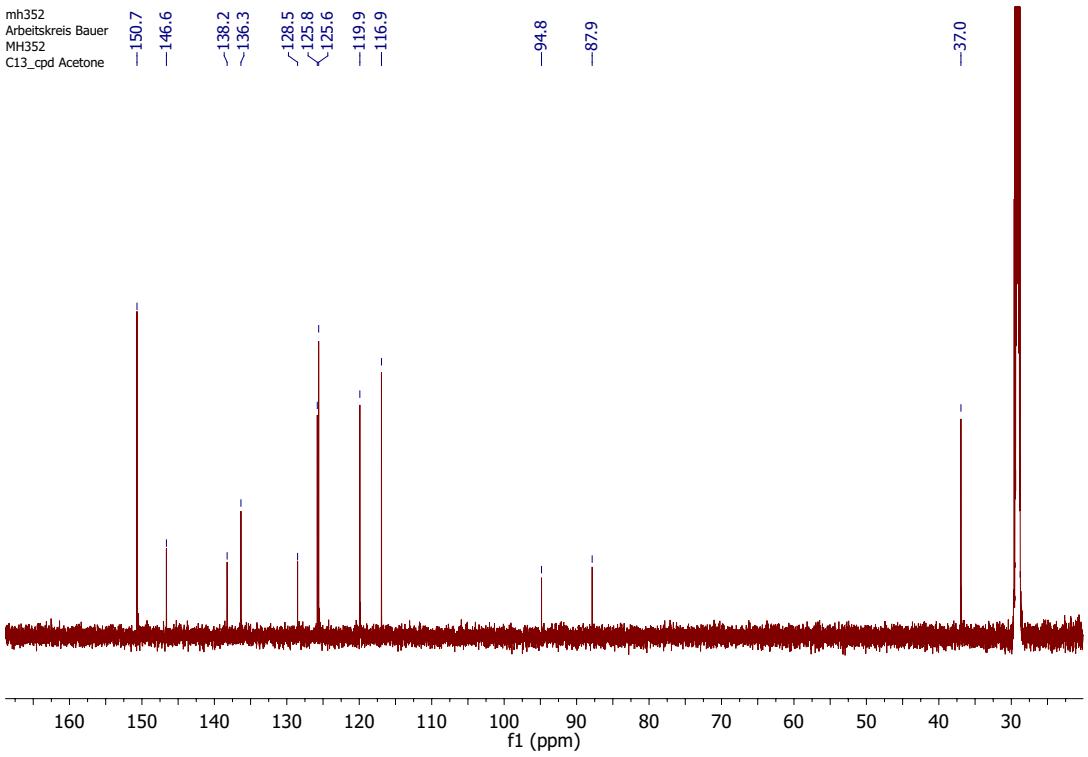

^{13}C NMR of **L4** in acetone-d$_6$.

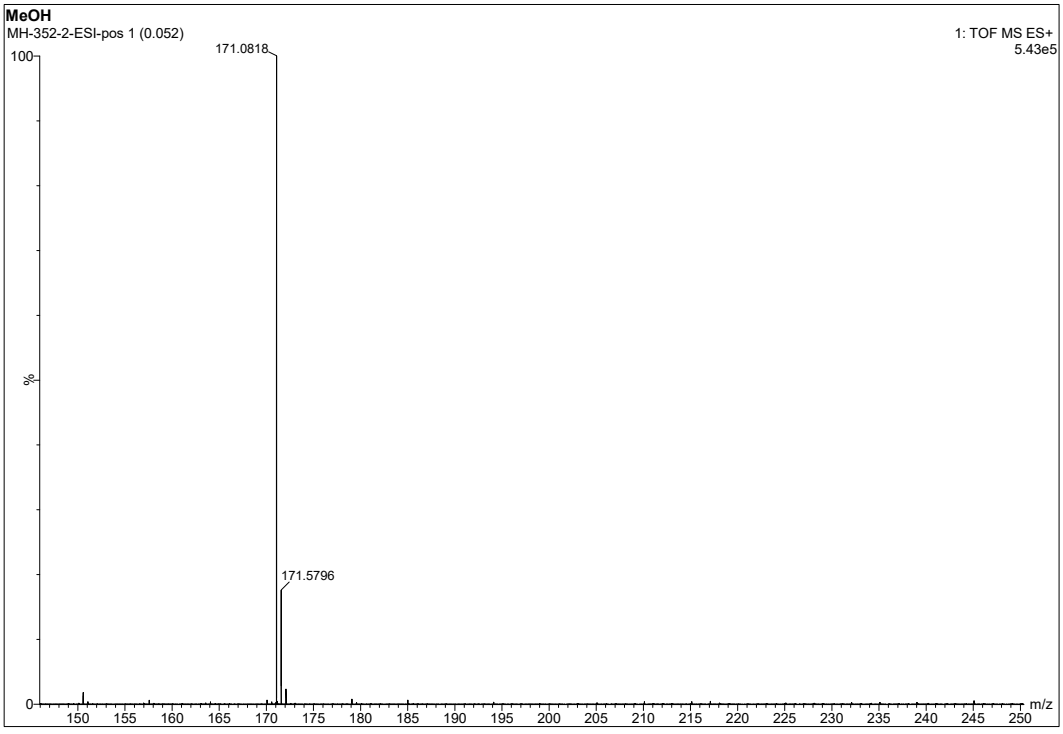

ESI-MS of **L4**.

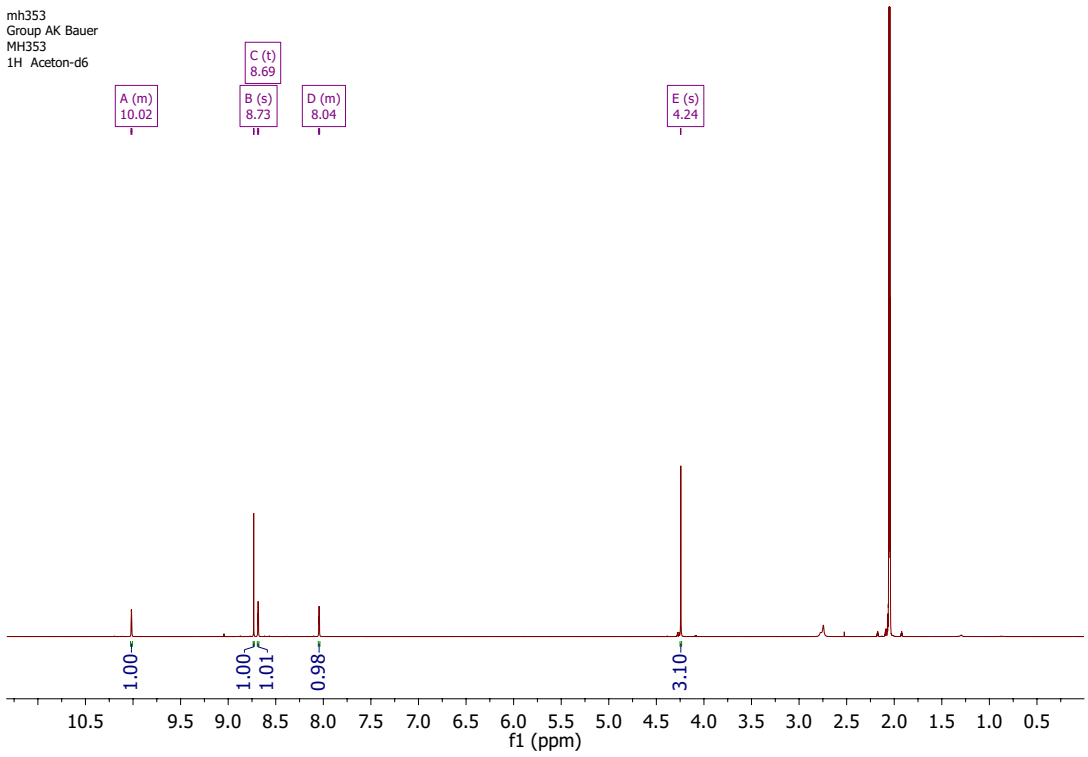

^{1}H NMR of **L6** in acetone-d_6.

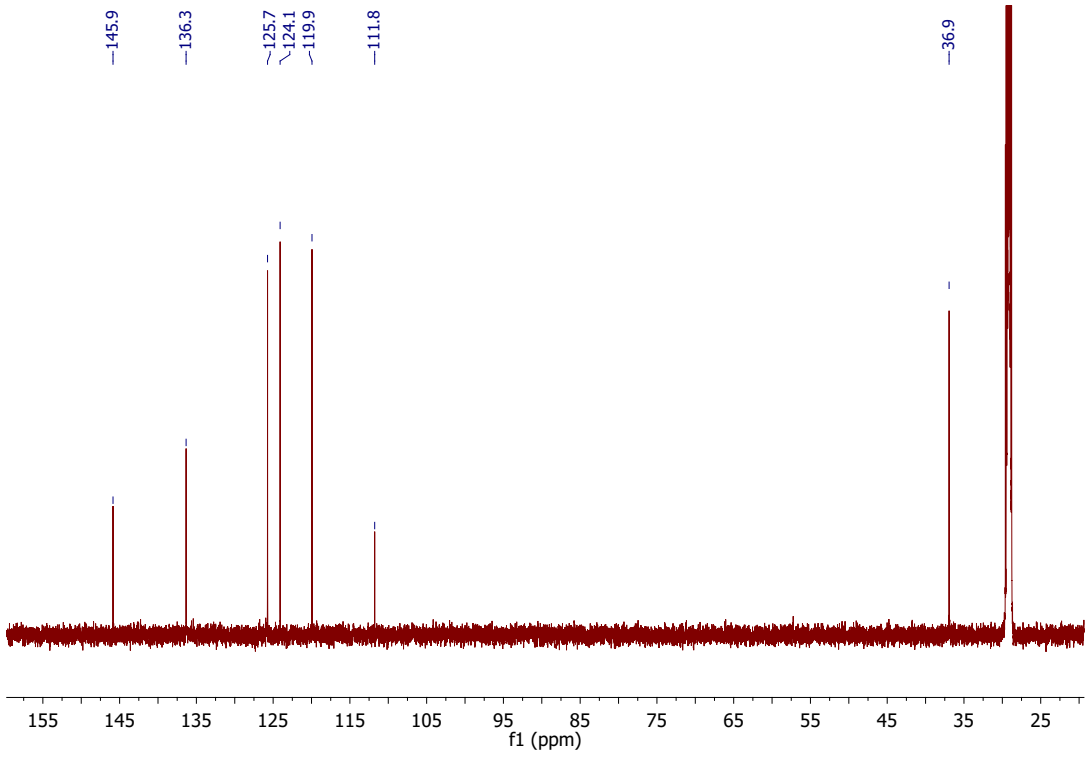

^{13}C NMR of **L6** in acetone-d_6.

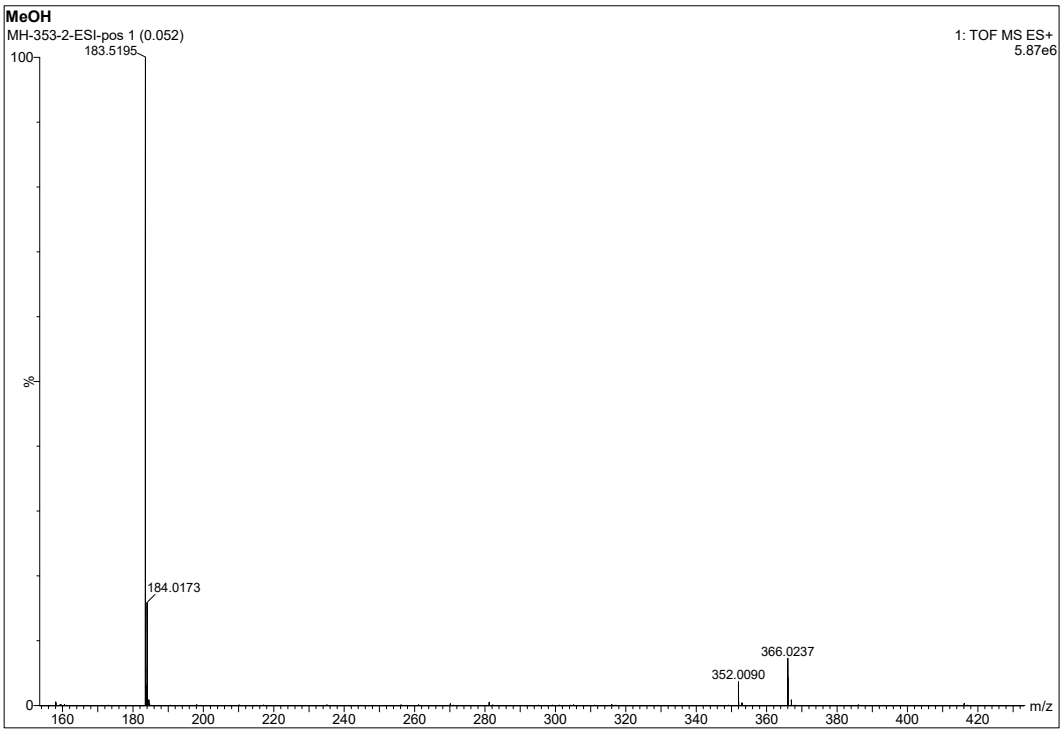
MeOH
MH-353-2-ESI-pos 1 (0.052)
1: TOF MS ES+
5.87e6
100
%
0
183.5195
184.0173
366.0237
352.0090
160
180
200
220
240
260
280
300
320
340
360
380
400
420
m/z

ESI-MS of **L6**.

9.2 Spectra of complexes

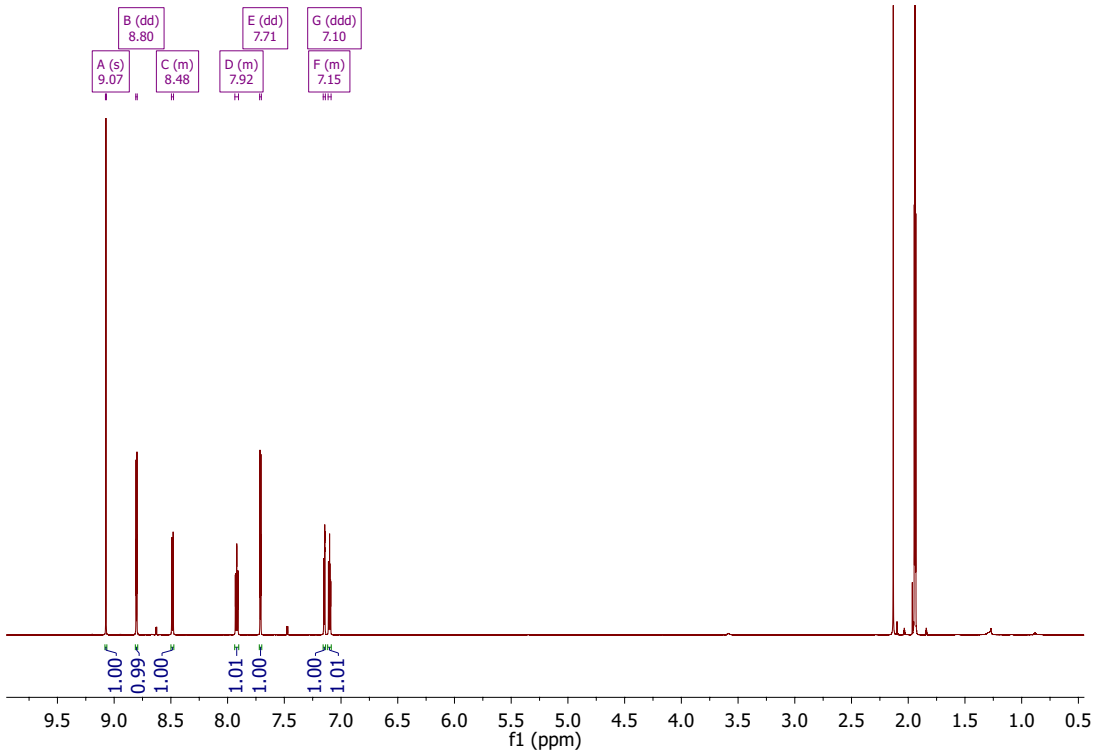

^{1}H NMR of $\mathbf{Fe1_{homo}}$ in CD_3CN.

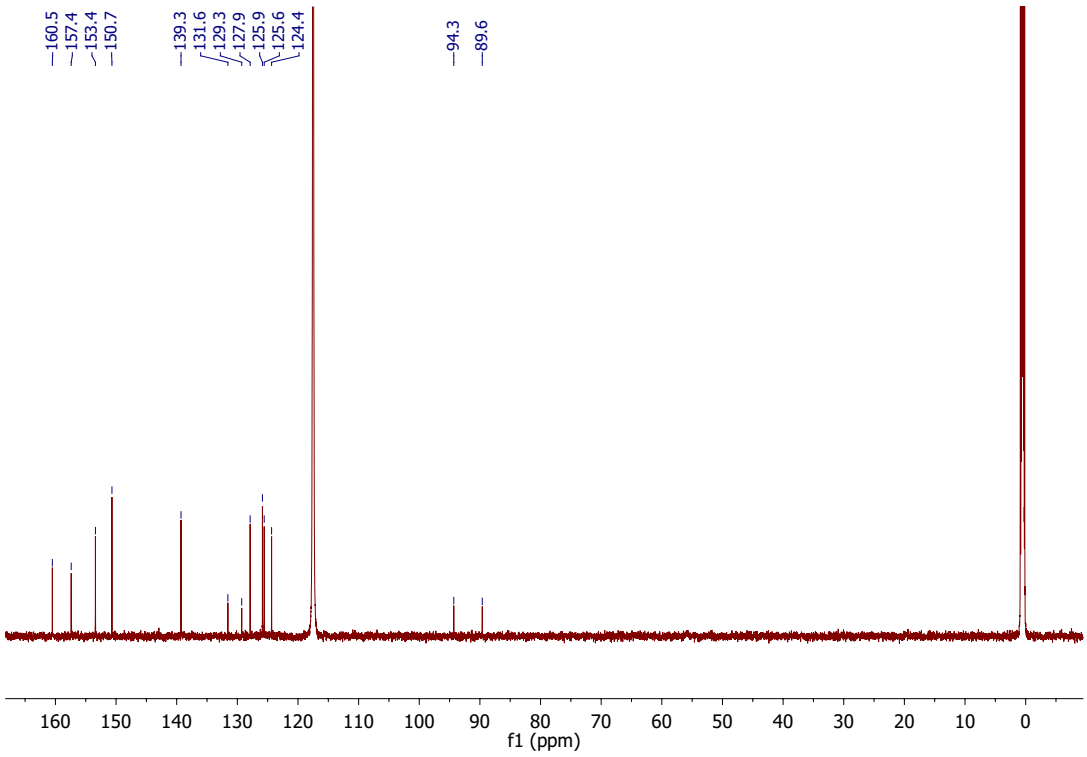

^{13}C NMR of $\mathbf{Fe1_{homo}}$ in CD_3CN.

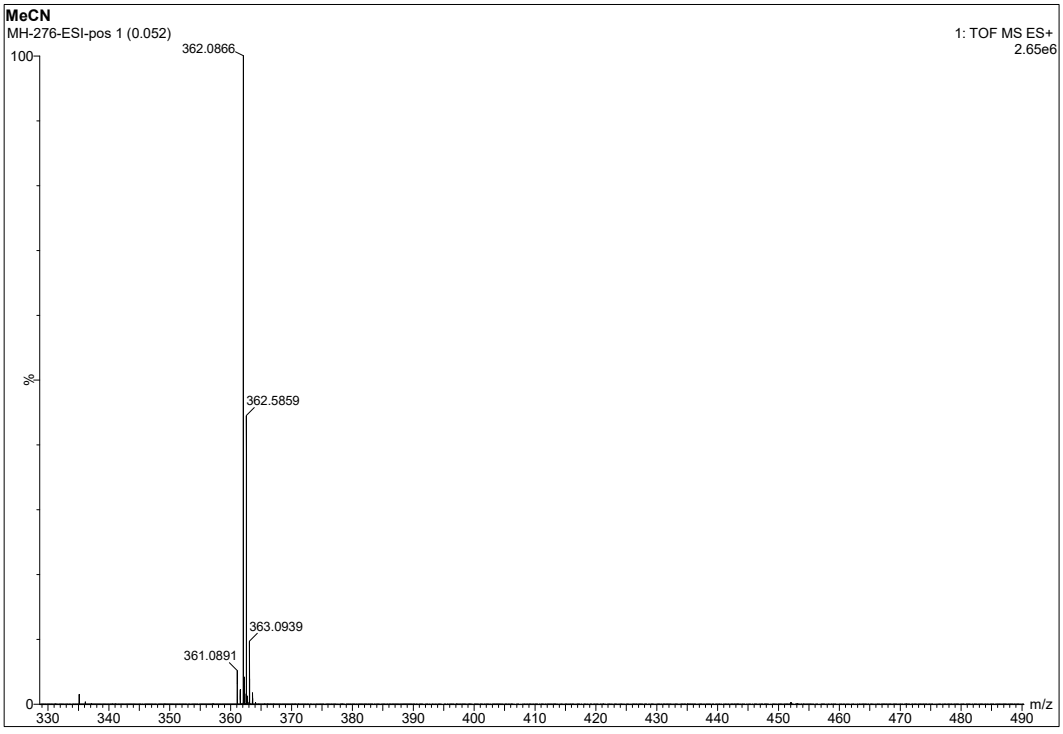

ESI-MS of $\mathbf{Fe1_{homo}}$.

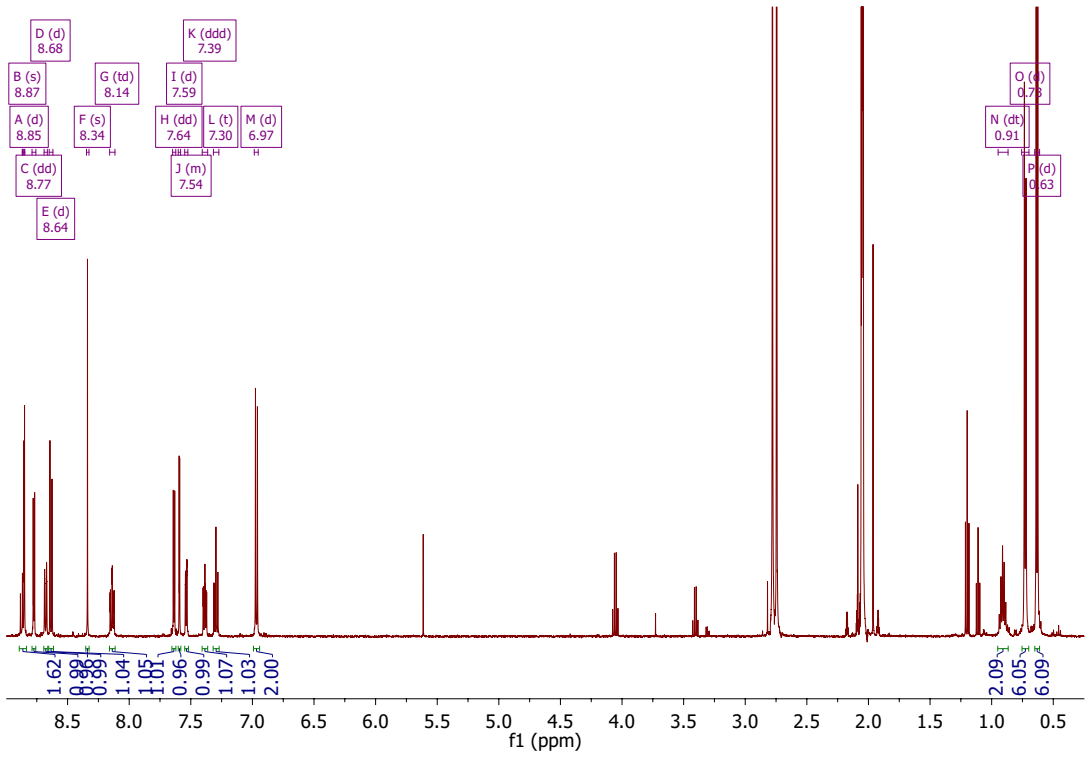

^{1}H NMR of **Fe1** in acetone-d$_6$.

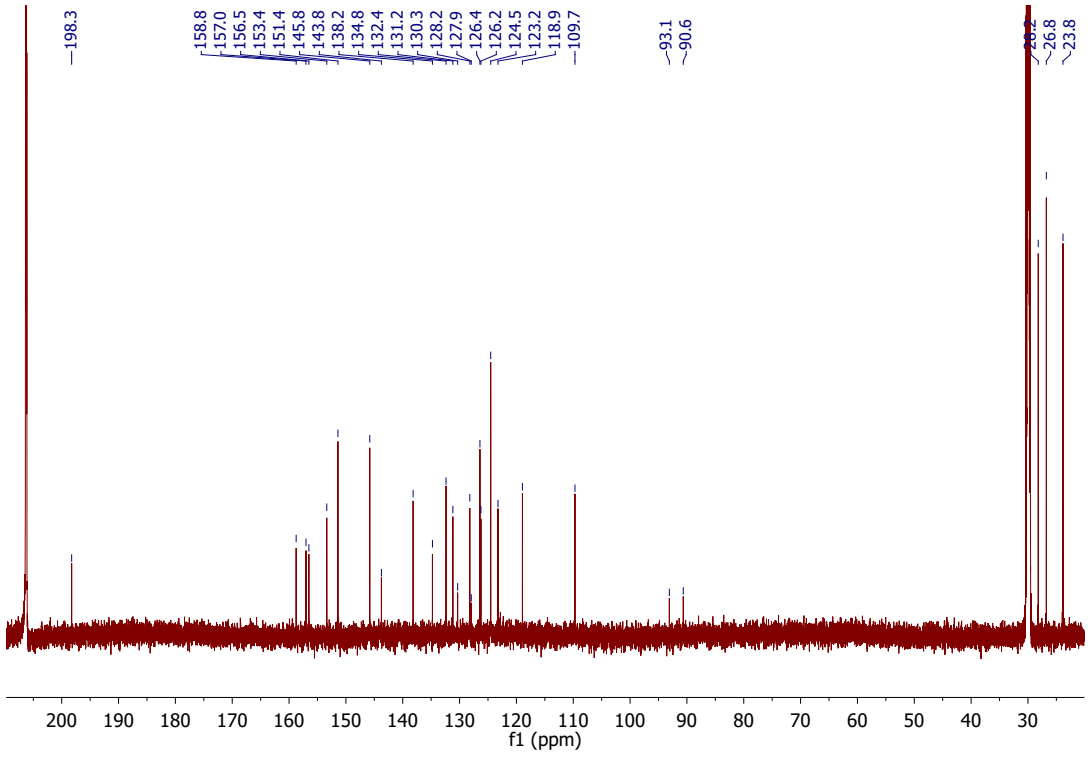

^{13}C NMR of **Fe1** in acetone-d$_6$.

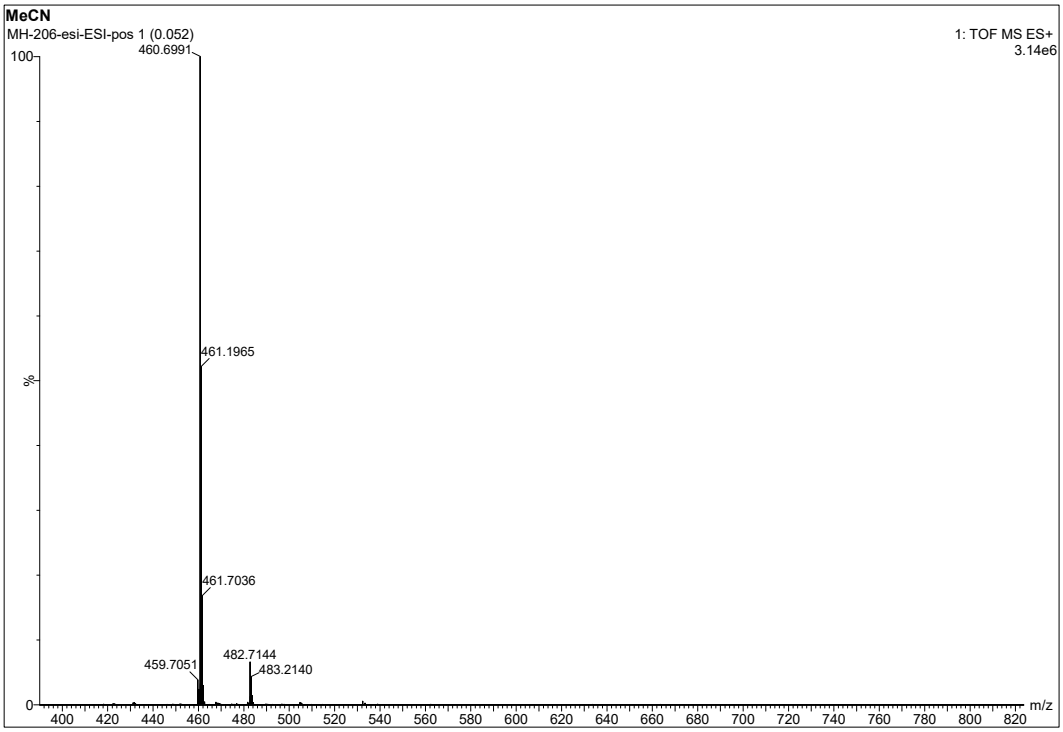

ESI-MS of **Fe1**.

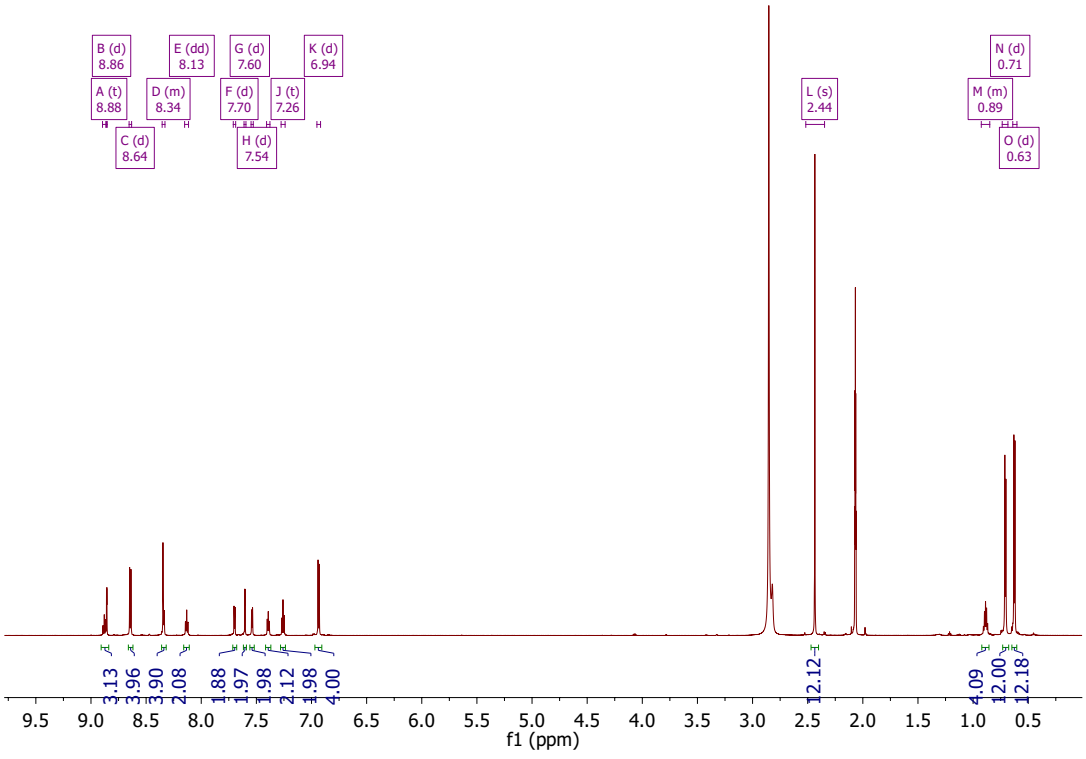

^{1}H NMR of **Dy1** in acetone-d_6.

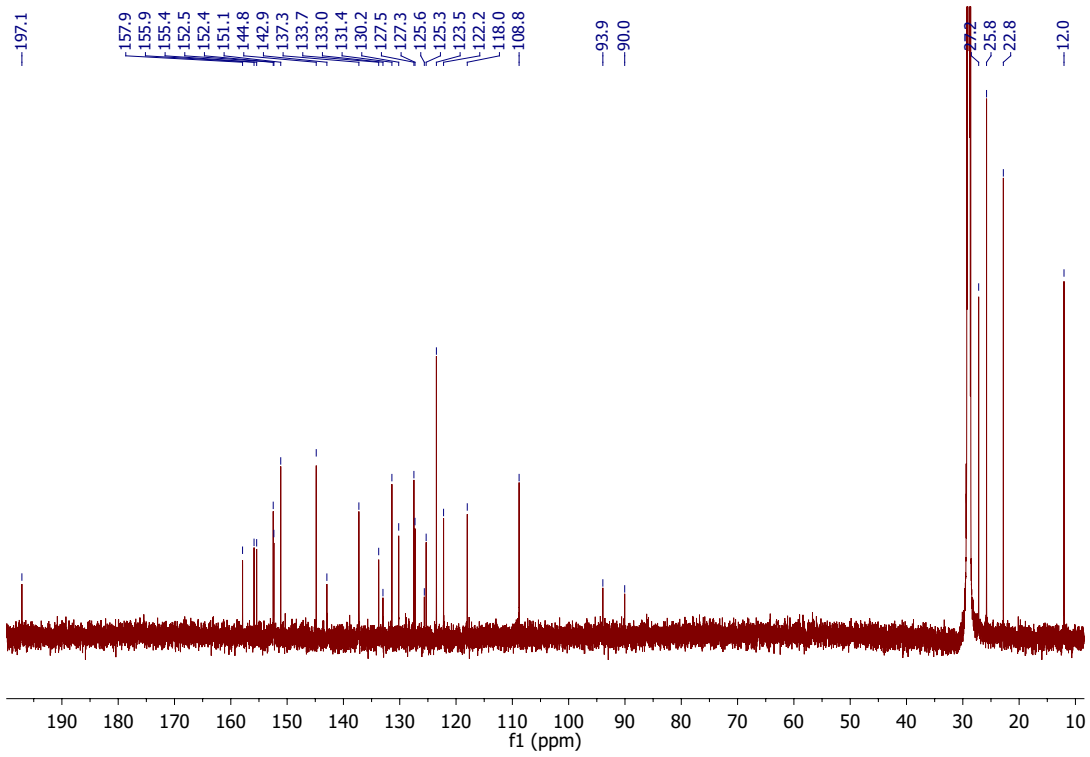

^{13}C NMR of **Dy1** in acetone-d$_6$.

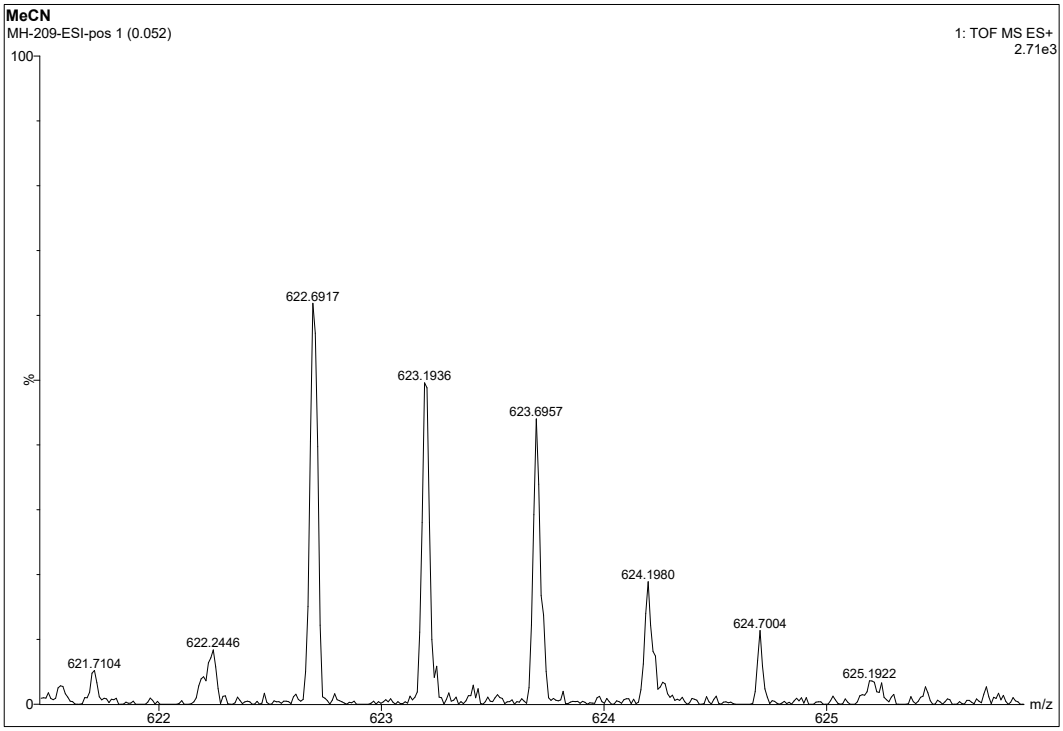

ESI-MS of **Dy1** showing $[M]^{2+}$. Signal intensity is very low due to dyad dissociation.

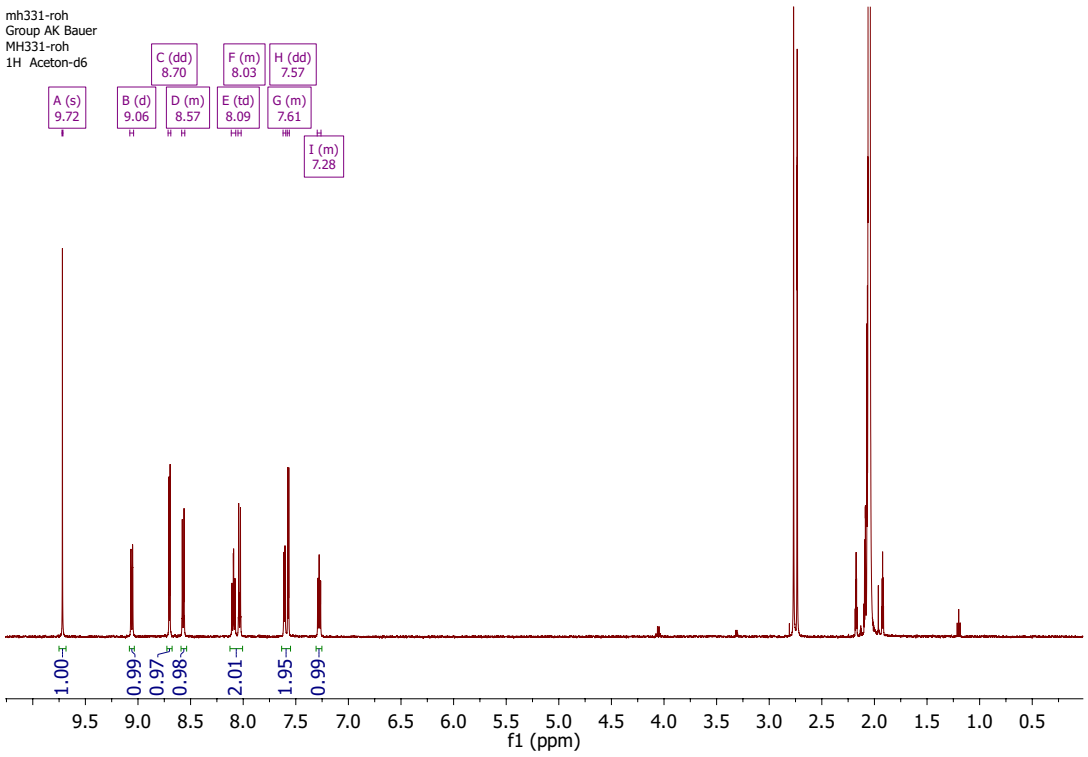

^{1}H NMR of **Fe2$_{\mathbf{homo}}$** in acetone-d$_6$.

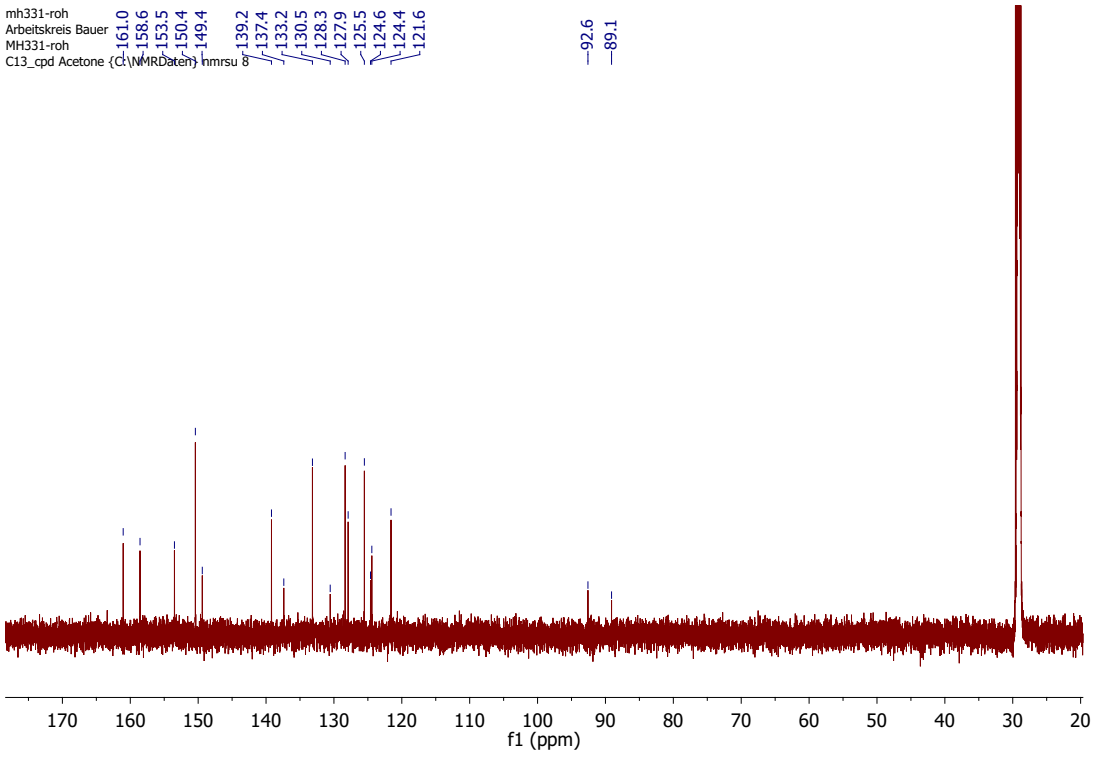

^{13}C NMR of **Fe2$_{\mathbf{homo}}$** in acetone-d$_6$.

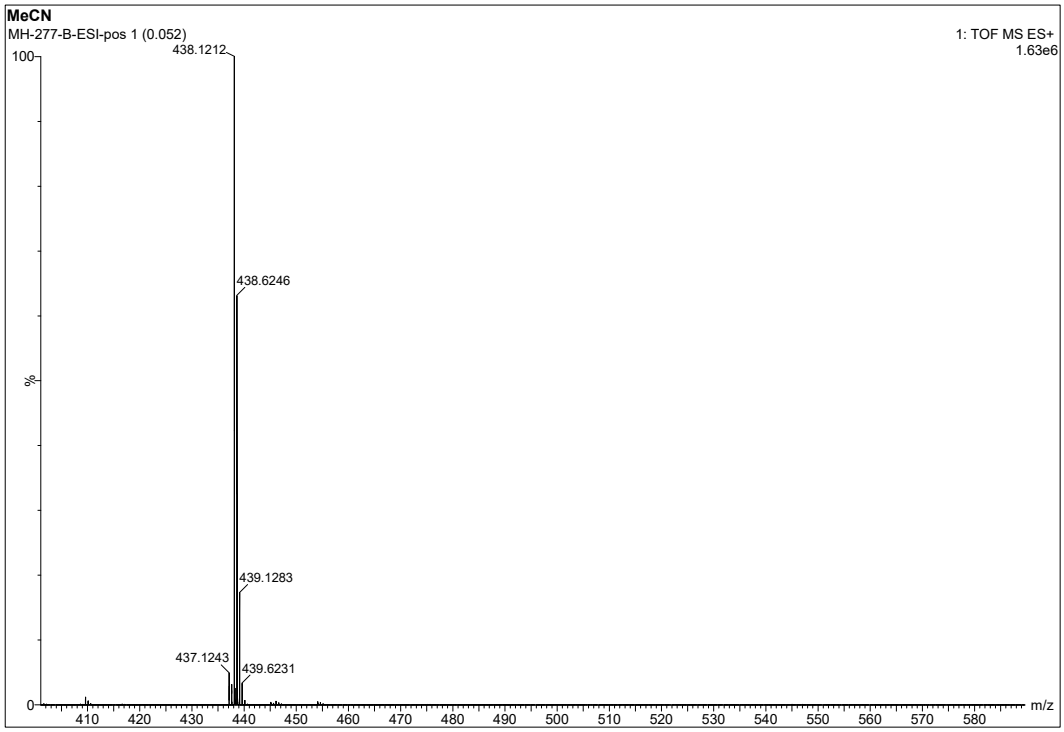

ESI-MS of $\mathbf{Fe2_{homo}}$.

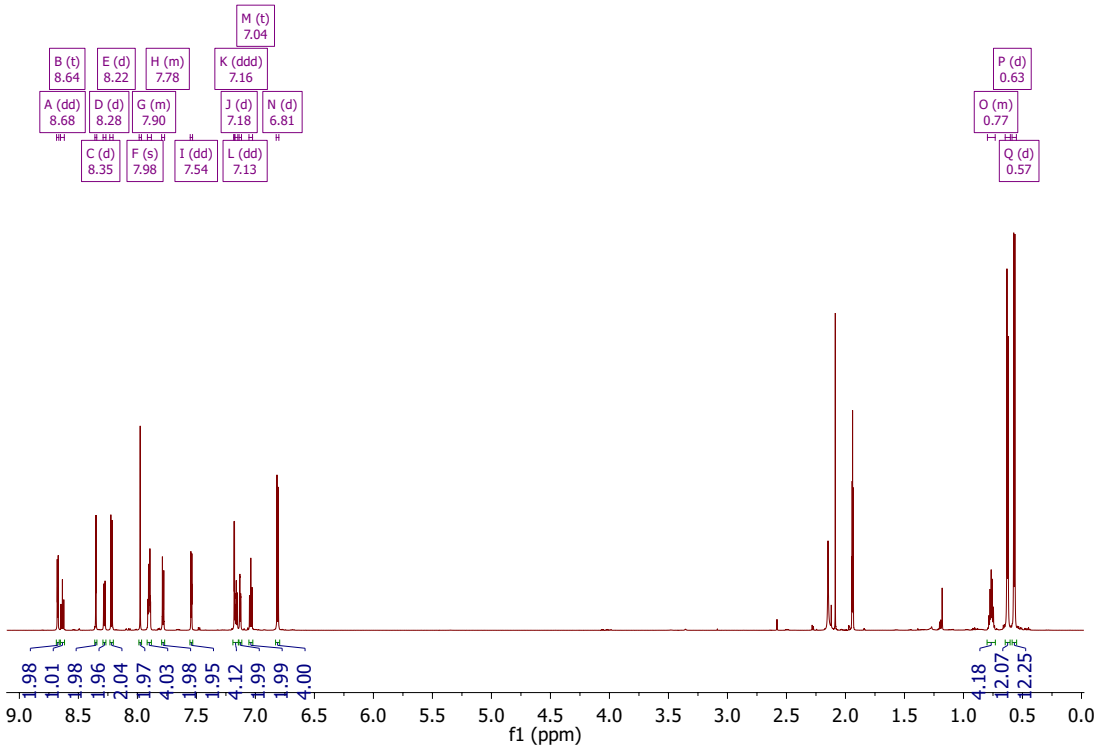

^{1}H NMR of **Fe2** in CD_3CN.

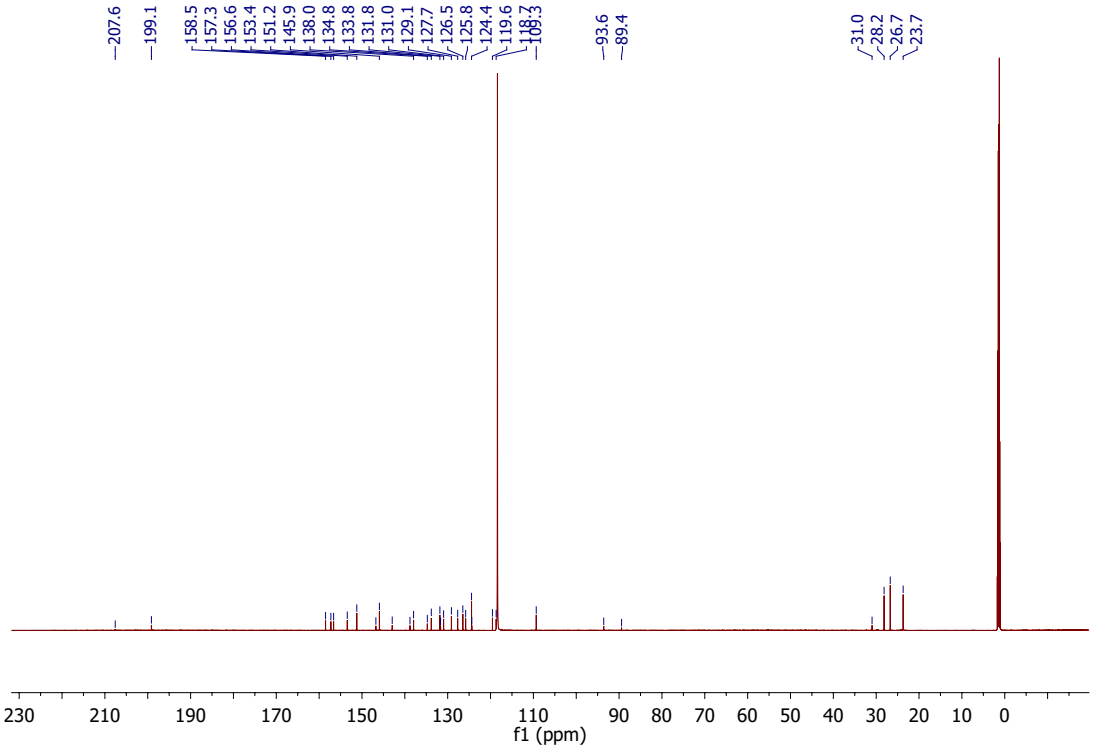

^{13}C NMR of **Fe2** in CD_3CN.

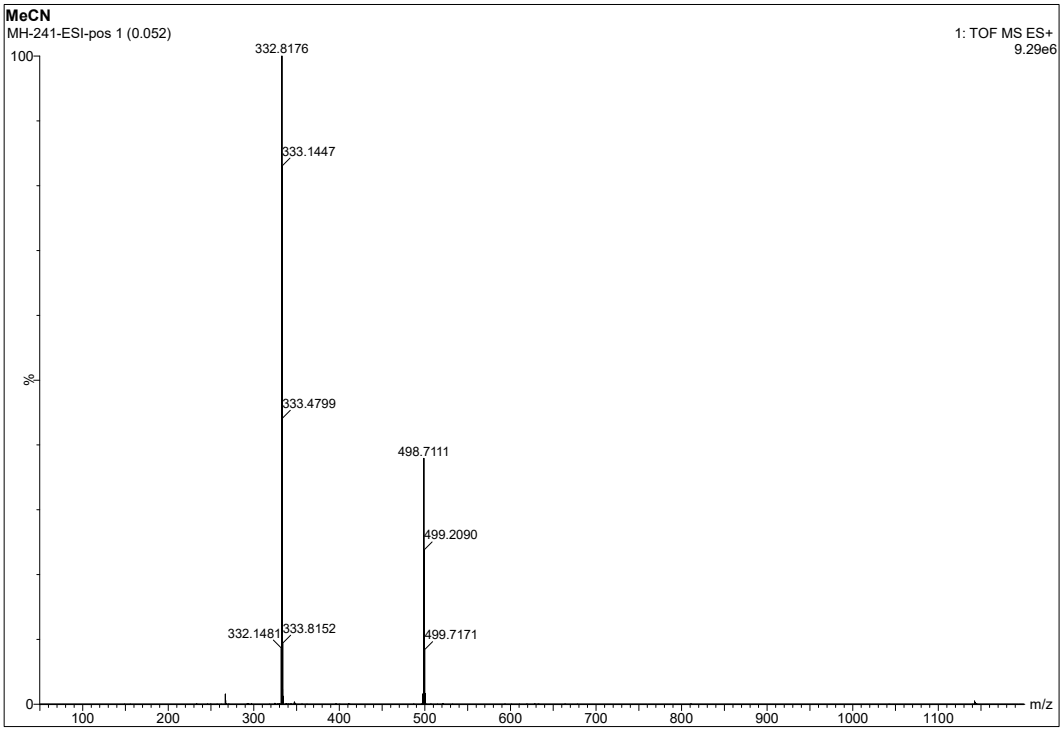

ESI-MS of **Fe2**.

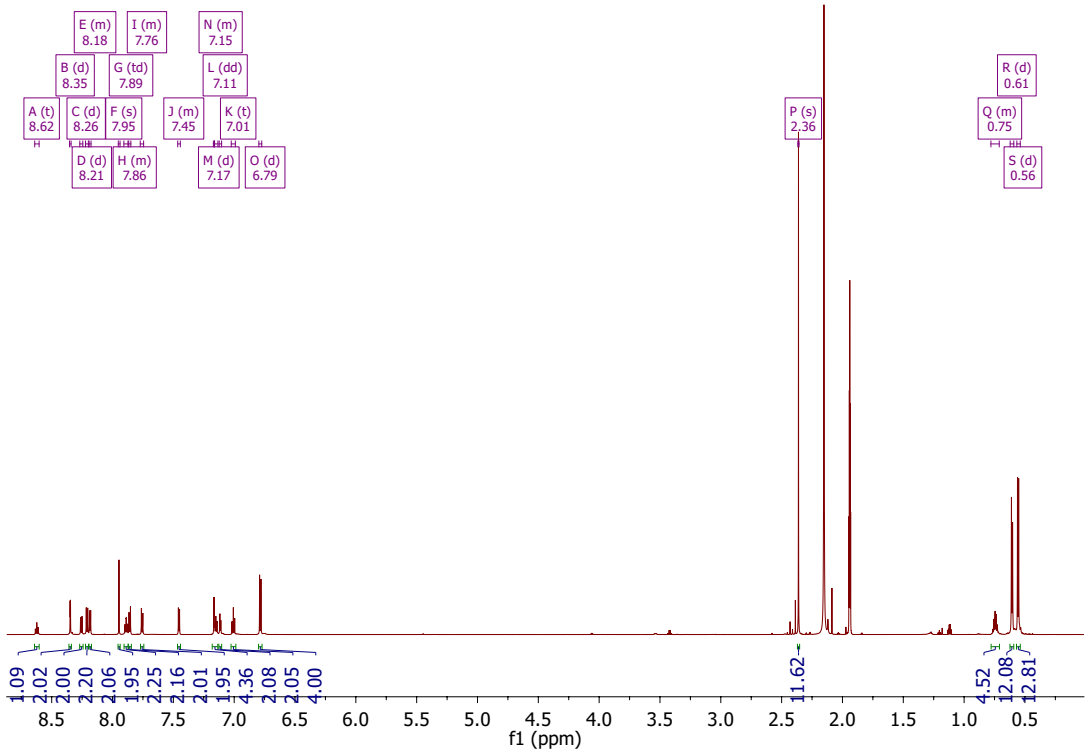

^{1}H NMR of **Dy2** in CD_3CN.

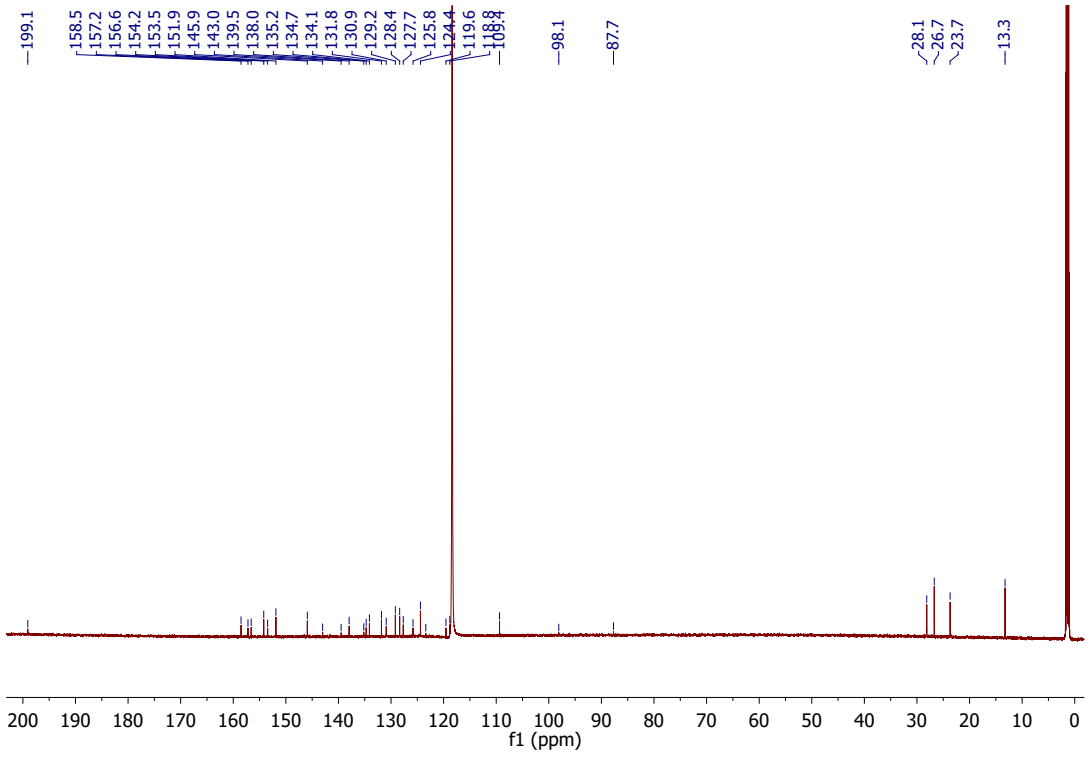

^{13}C NMR of **Dy2** in CD_3CN.

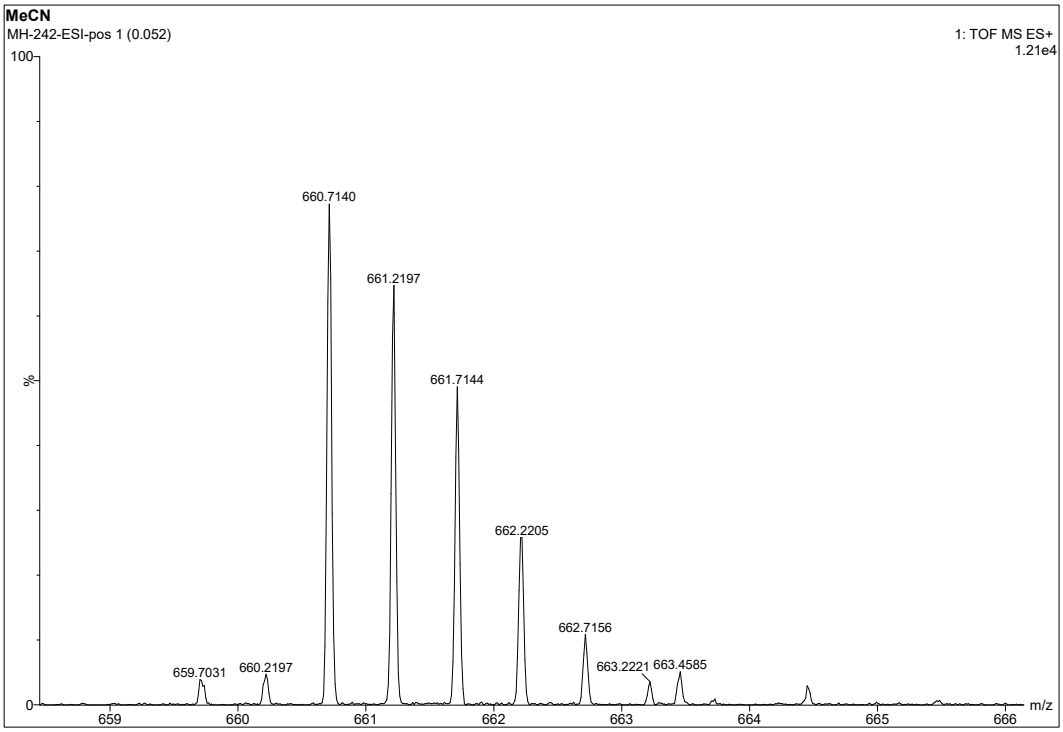

ESI-MS of **Dy2** showing $[M]^{2+}$. Signal intensity is very low due to dyad dissociation.

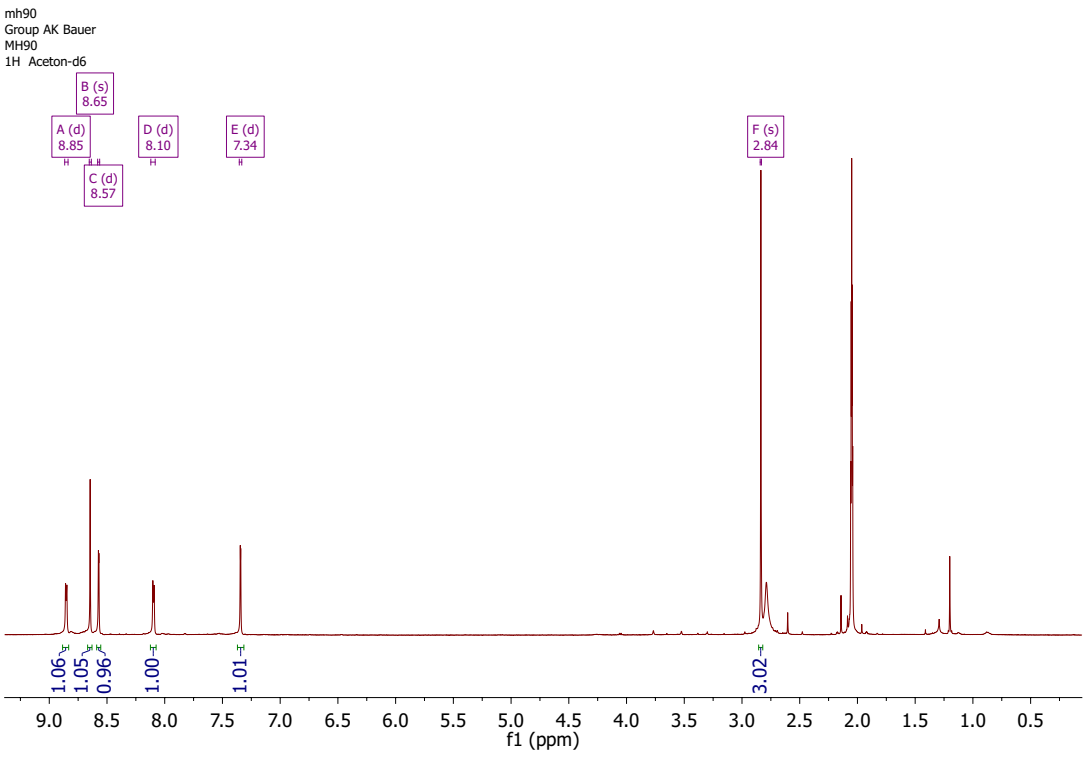

^{1}H NMR of $\mathbf{Fe3_{homo}}$ in acetone-d_6.

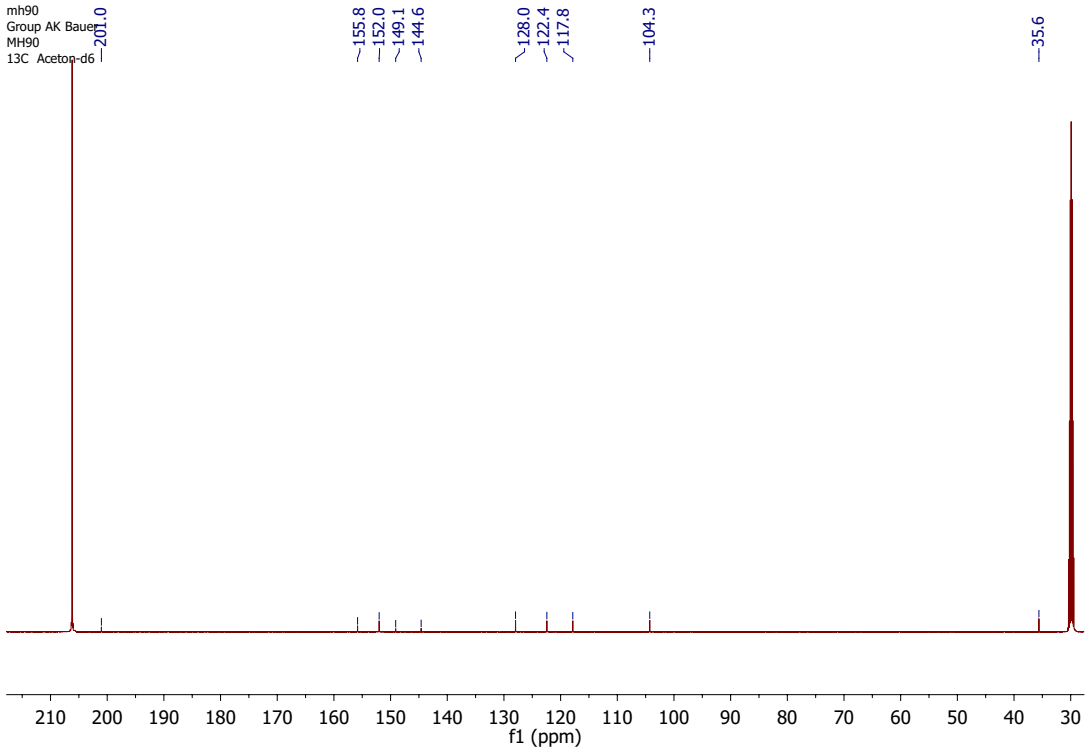

^{13}C NMR of **Fe3$_{\mathbf{homo}}$** in acetone-d$_6$.

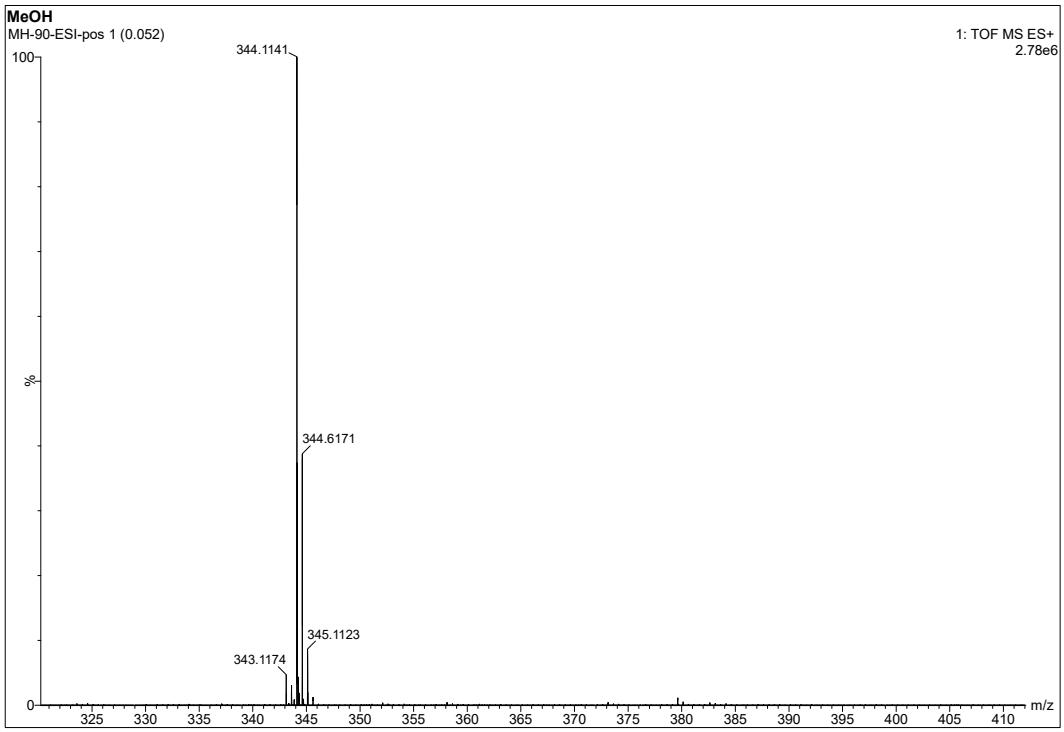

ESI-MS of **Fe3$_{\mathbf{homo}}$**.

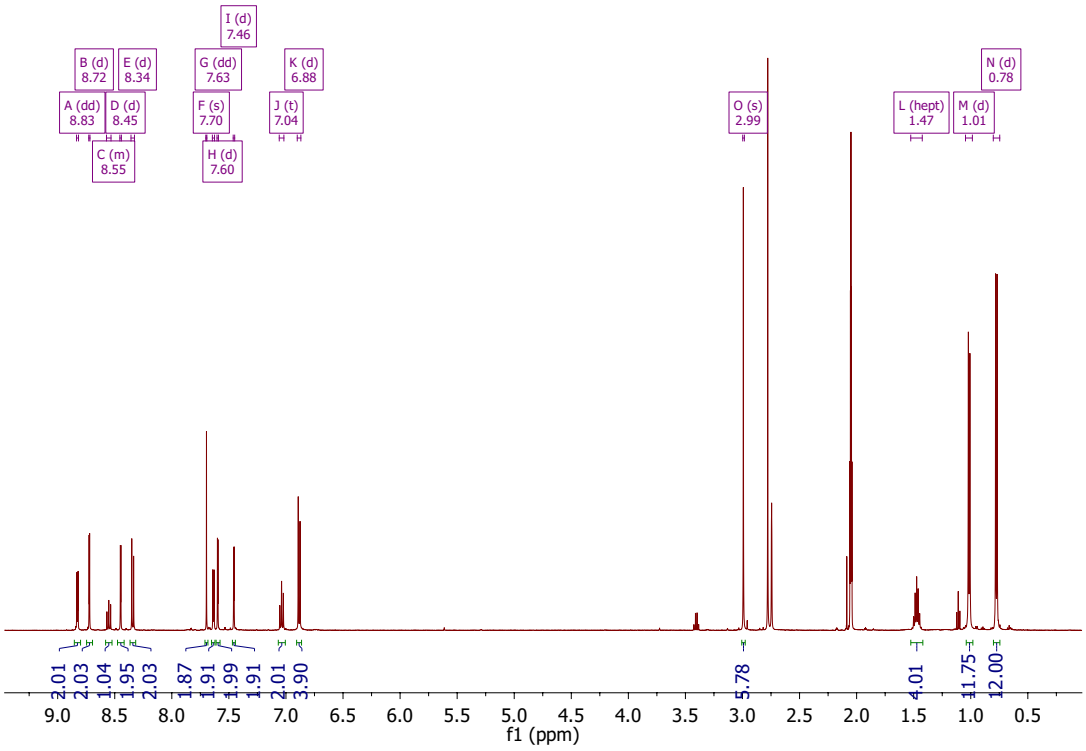

^{1}H NMR of **Fe3** in acetone-d$_6$.

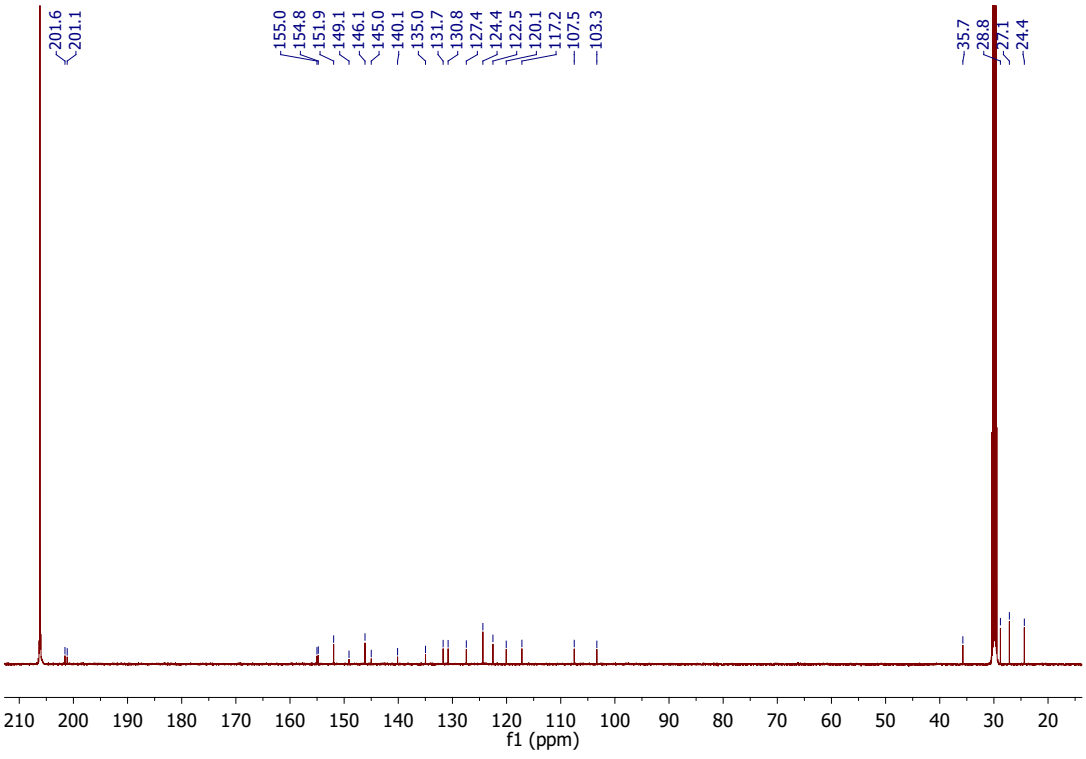

^{13}C NMR of **Fe3** in acetone-d$_6$.

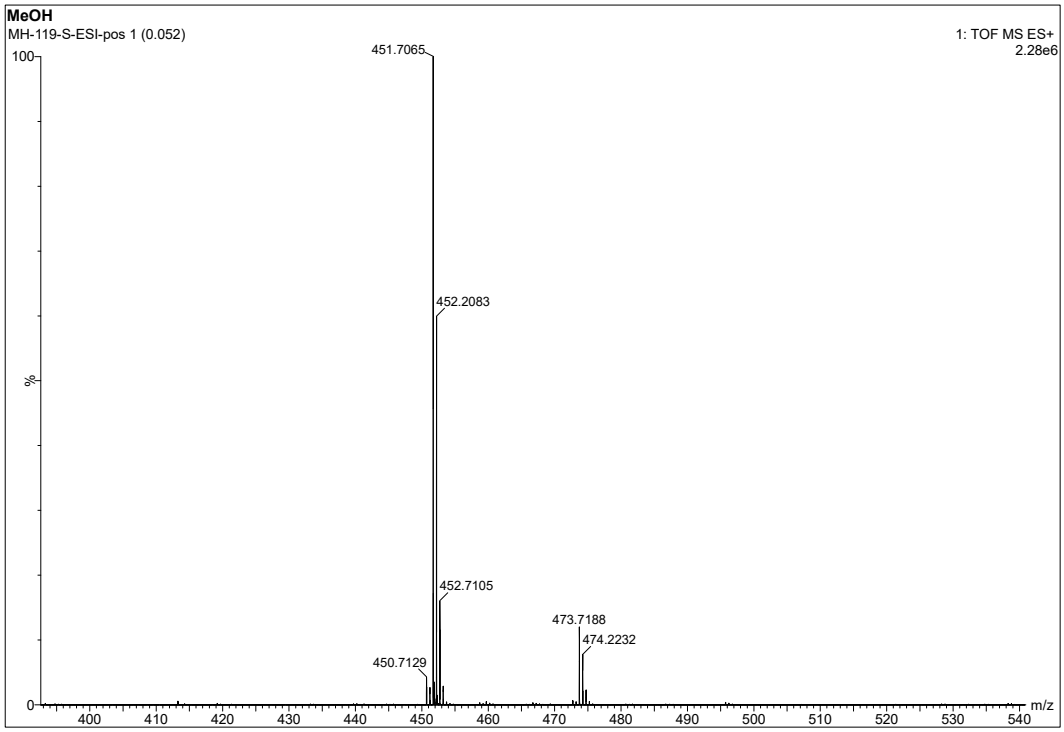

ESI-MS of **Fe3**.

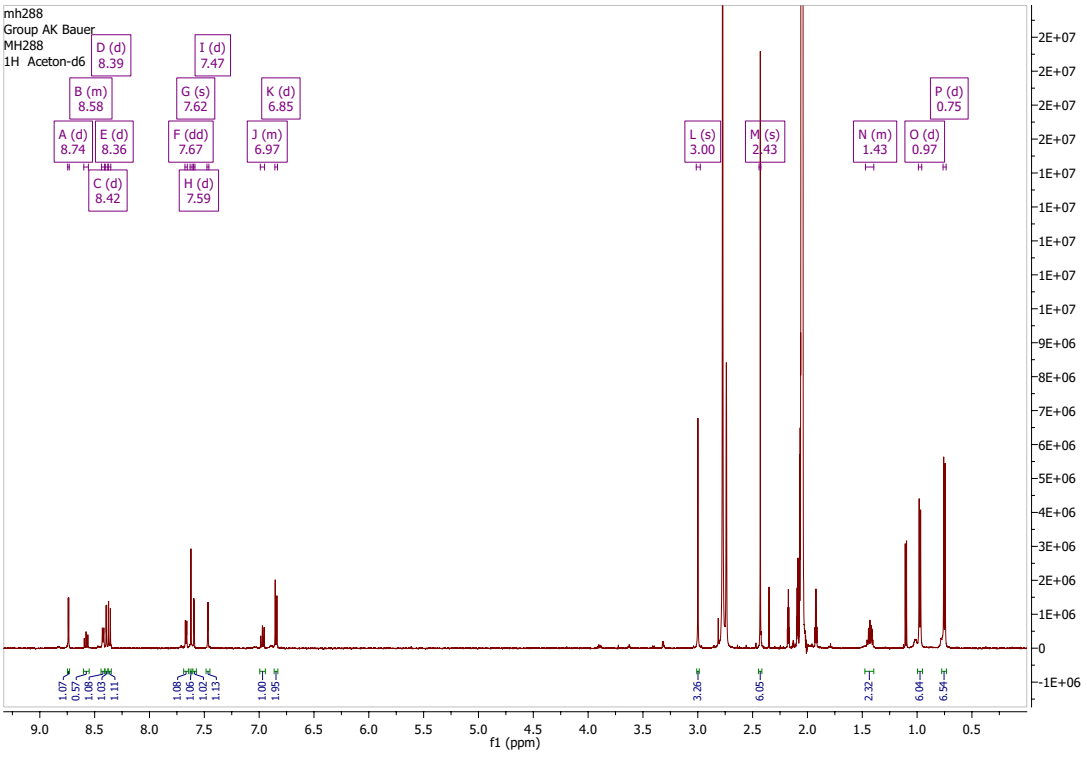

^{1}H NMR of **Fe3** in acetone-d_6.

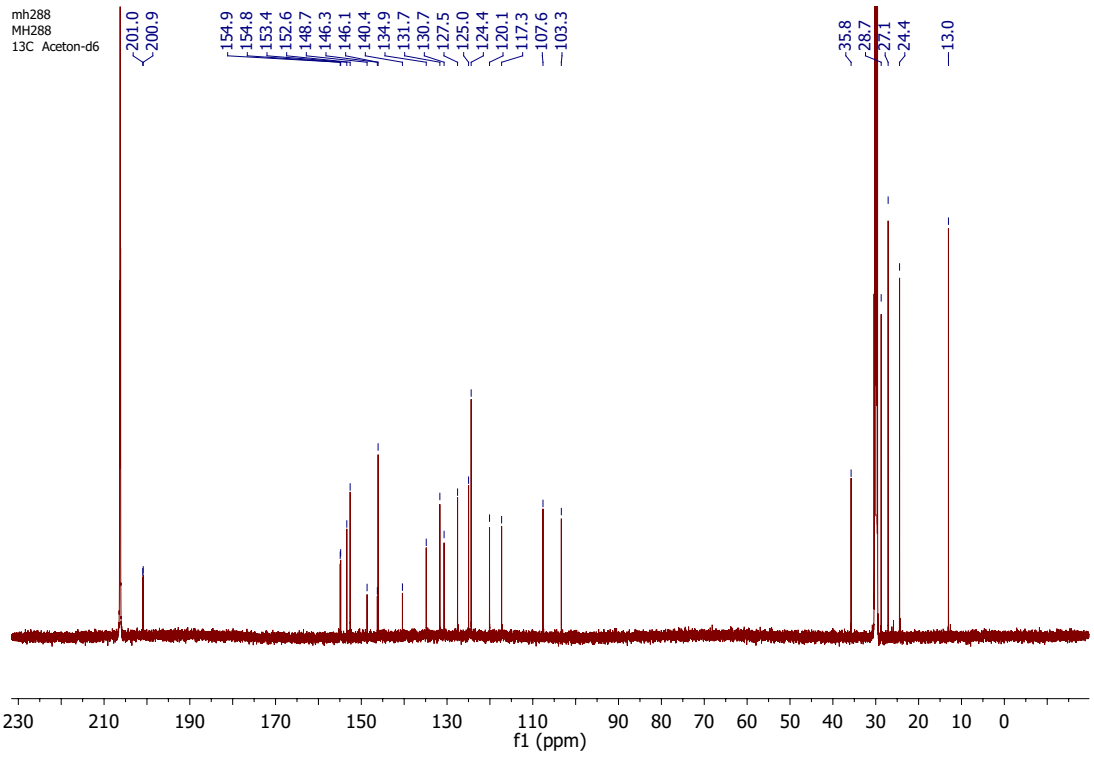

^{13}C NMR of **Fe3** in acetone-d$_6$.

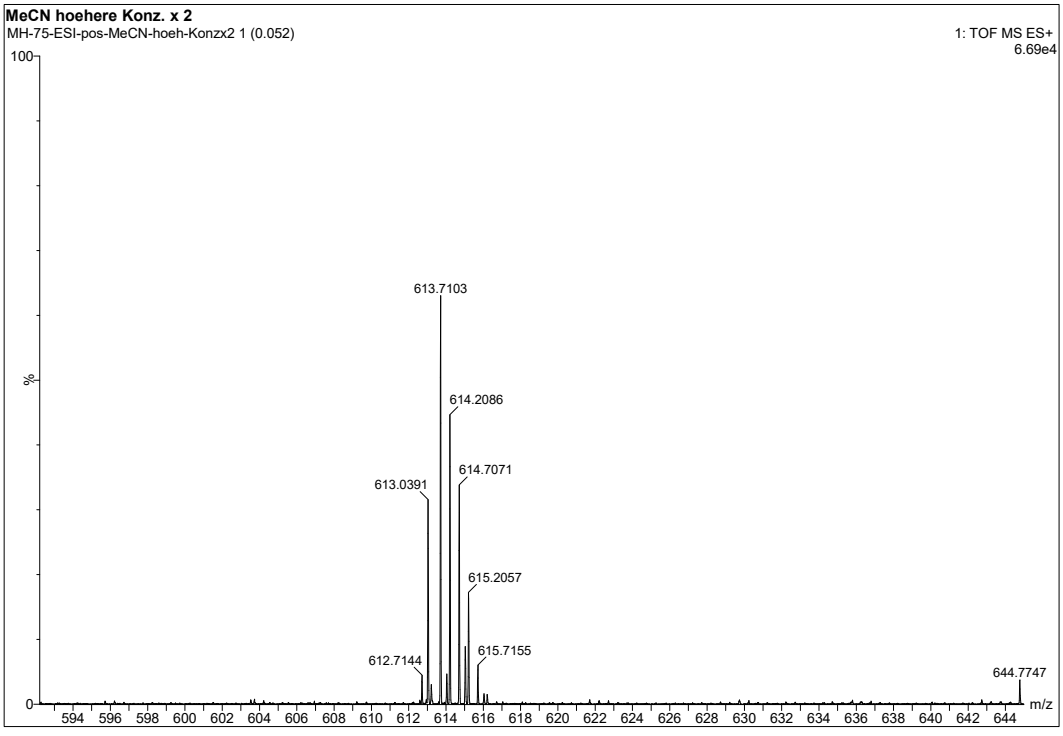

ESI-MS of **Dy3** showing $[M]^{2+}$. Signal intensity is very low due to dyad dissociation.

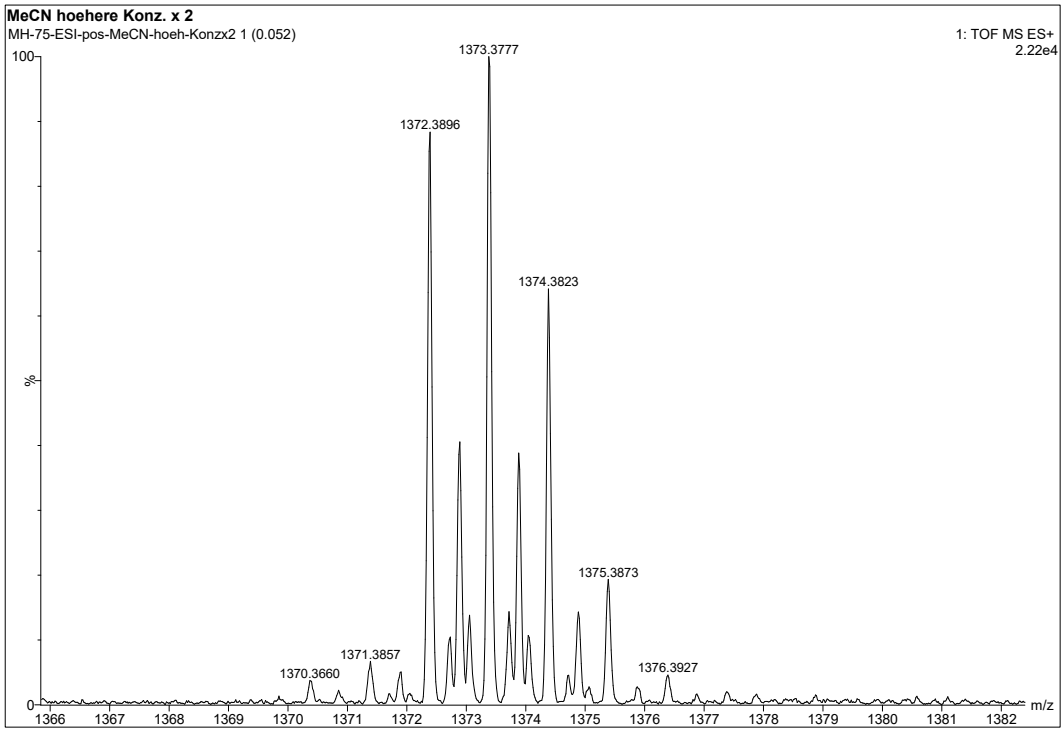

ESI-MS of **Dy3** showing $[M+PF_6]^+$. Signal intensity is very low due to dyad dissociation.

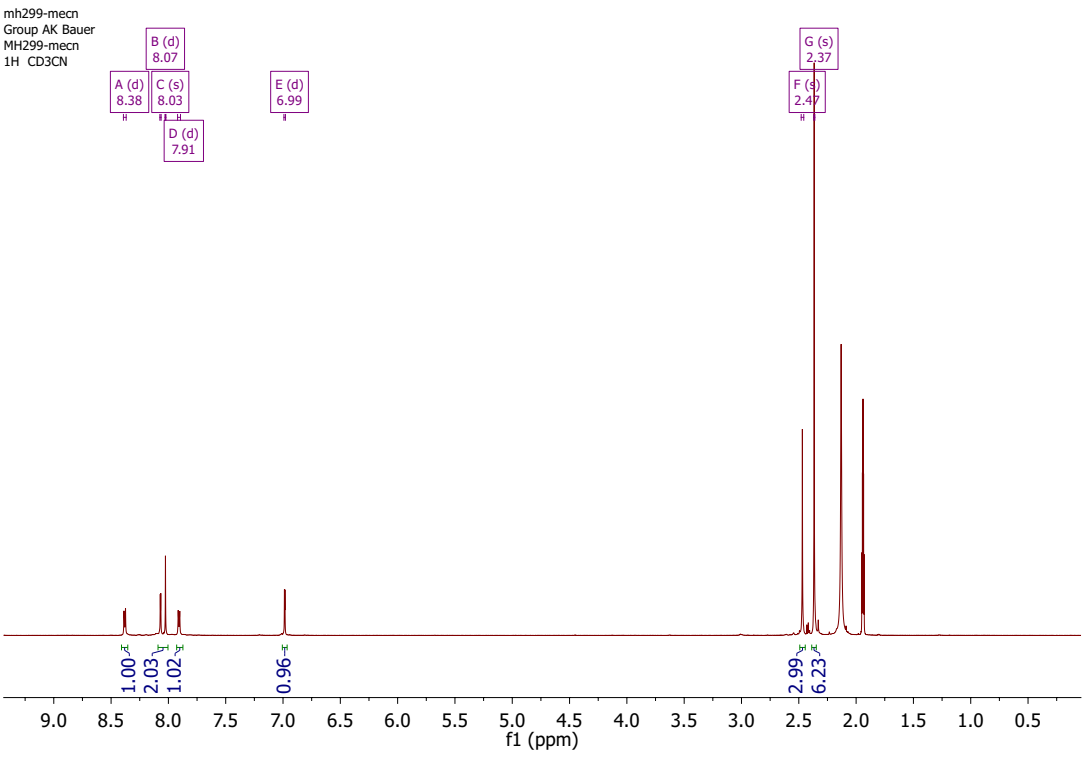

^{1}H NMR of **Tri3** in CD_3CN.

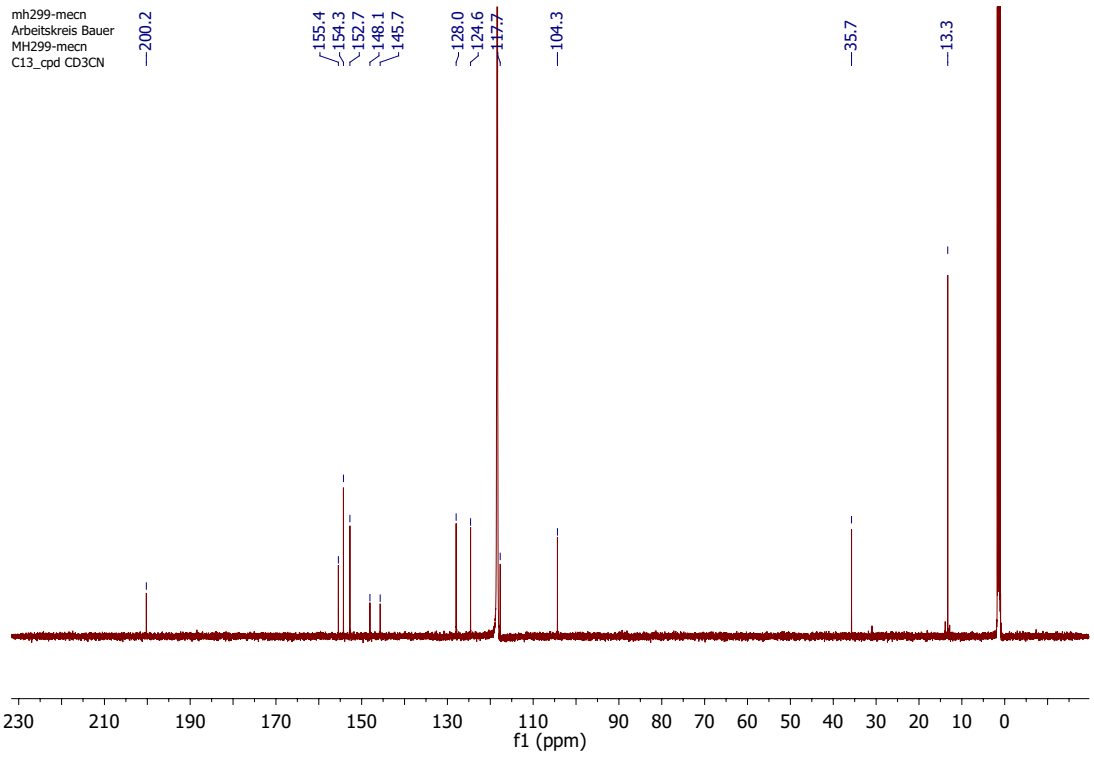

^{13}C NMR of **Tri3** in CD_3CN.

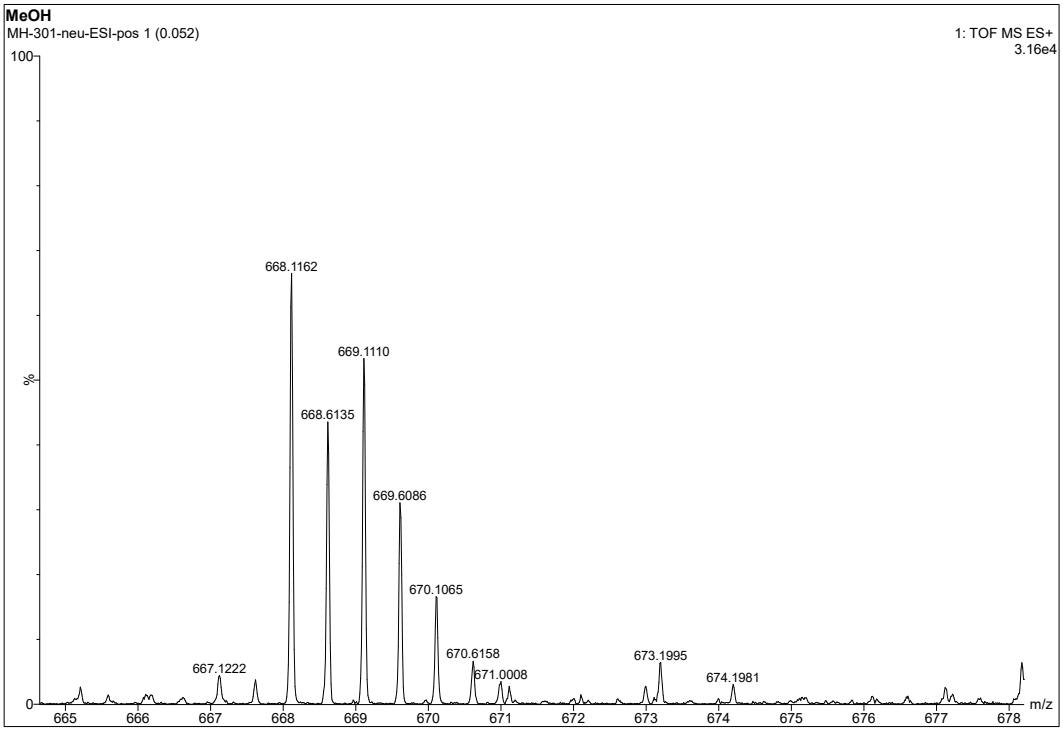

ESI-MS of **Tri3**. Signal intensity is very low due to triad dissociation.

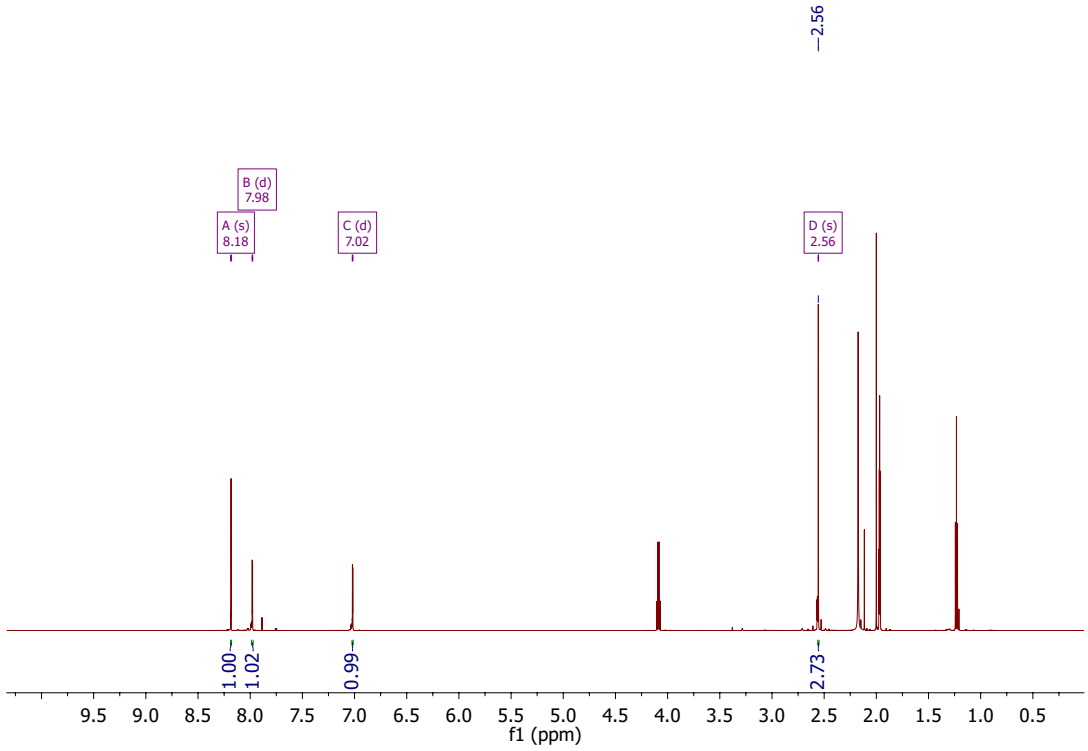

^{1}H NMR of **Fe6$_{\mathbf{homo}}$** in CD_3CN.

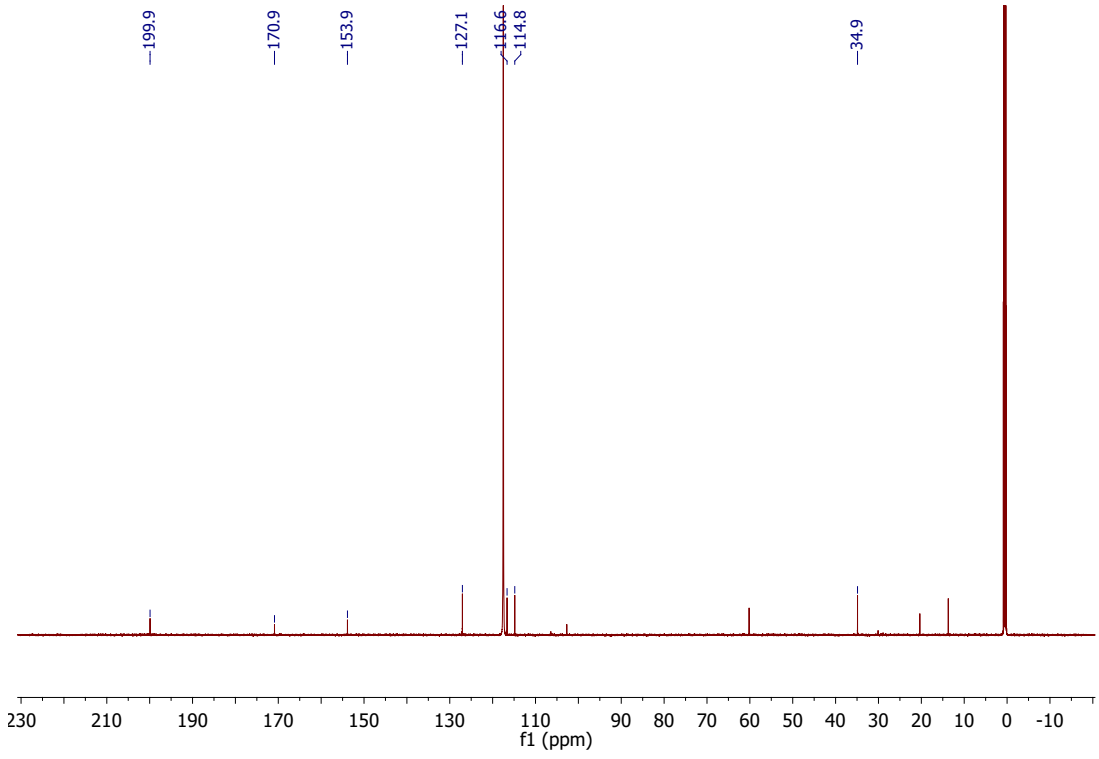

^{13}C NMR of **Fe6$_{\mathbf{homo}}$** in CD_3CN.

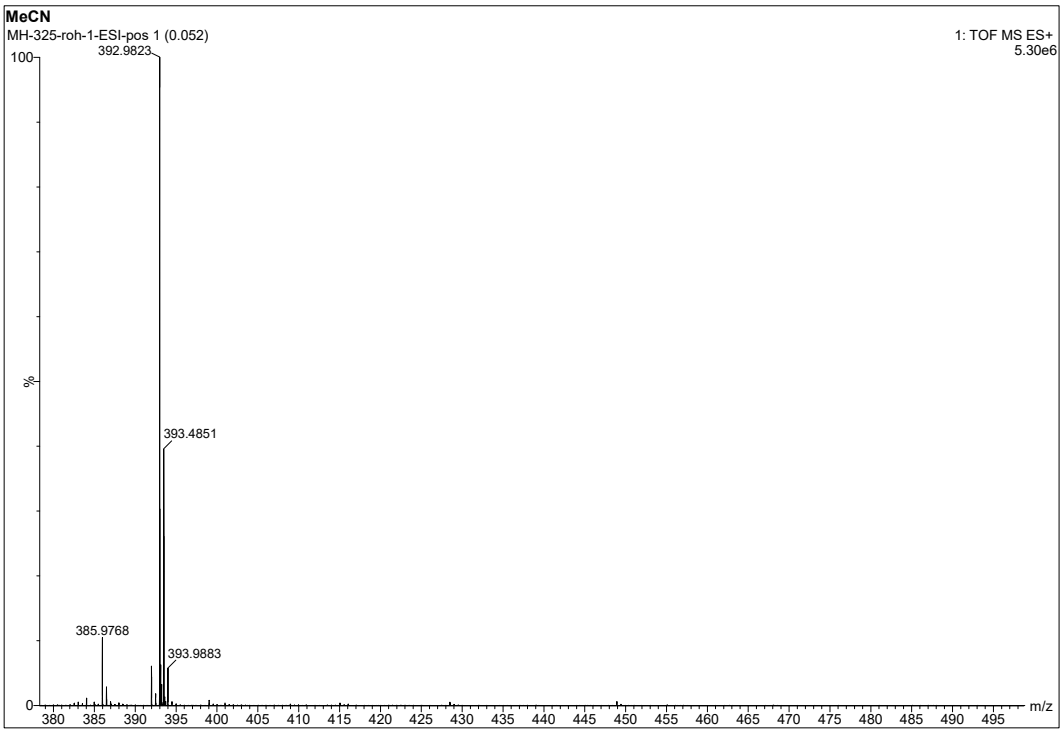

ESI-MS of $\mathbf{Fe6_{homo}}$.

Crystal data and refinement method of $Fe1_{homo}$.

Identification code	MH_0129n_0ma_a	
Empirical formula	C50 H40 F12 Fe N8 O2 P2	
Formula weight	1130.69	
Temperature	120(2) K	
Wavelength	0.71073 Å	
Crystal system	Orthorhombic	
Space group	$Pna2_1$	
Unit cell dimensions	a = 8.4361(9) Å	α= 90°.
	b = 31.651(3) Å	β= 90°.
	c = 18.3528(18) Å	γ = 90°.
Volume	4900.4(9) $Å^3$	
Z	4	
Density (calculated)	1.533 Mg/m^3	
Absorption coefficient	0.469 mm^{-1}	
F(000)	2304	
Crystal size	0.280 x 0.140 x 0.100 mm^3	
Theta range for data collection	2.219 to 28.311°.	
Index ranges	-11<=h<=11, -42<=k<=42, -24<=l<=24	
Reflections collected	140217	
Independent reflections	12177 [R(int) = 0.0544]	
Completeness to theta = 25.242°	99.8 %	
Absorption correction	Semi-empirical from equivalents	
Refinement method	Full-matrix least-squares on F^2	
Data / restraints / parameters	12177 / 22 / 710	
Goodness-of-fit on F^2	1.040	
Final R indices [I>2sigma(I)]	R1 = 0.0598, wR2 = 0.1486	
R indices (all data)	R1 = 0.0705, wR2 = 0.1571	
Absolute structure parameter	0.44(3)	
Extinction coefficient	n/a	
Largest diff. peak and hole	1.253 and -0.568 e.$Å^{-3}$	

Crystal data and refinement method of $Fe2_{homo}$.

Identification code	MH_0128n_0m_a	
Empirical formula	C56 H36 F12 Fe N8 P2	
Formula weight	1166.72	
Temperature	120(2) K	
Wavelength	0.71073 Å	
Crystal system	Orthorhombic	
Space group	Pbca	
Unit cell dimensions	a = 14.5962(8) Å	α= 90°.
	b = 17.7446(10) Å	β= 90°.
	c = 38.765(2) Å	γ = 90°.
Volume	10040.3(10) $Å^3$	
Z	8	
Density (calculated)	1.544 Mg/m^3	
Absorption coefficient	0.458 mm^{-1}	
F(000)	4736	
Crystal size	0.210 x 0.180 x 0.160 mm^3	
Theta range for data collection	2.090 to 28.308°.	
Index ranges	-19<=h<=19, -23<=k<=23, -51<=l<=51	
Reflections collected	300454	
Independent reflections	12471 [R(int) = 0.0546]	
Completeness to theta = 25.242°	99.9 %	
Absorption correction	Semi-empirical from equivalents	
Refinement method	Full-matrix least-squares on F^2	
Data / restraints / parameters	12471 / 0 / 767	
Goodness-of-fit on F^2	1.082	
Final R indices [I>2sigma(I)]	R1 = 0.0410, wR2 = 0.1061	
R indices (all data)	R1 = 0.0559, wR2 = 0.1217	
Extinction coefficient	n/a	
Largest diff. peak and hole	0.599 and -0.519 $e.Å^{-3}$	

Crystal data and refinement method of $Fe3_{homo}$.

Identification code	mo_mh_00152n_0m_a_sq	
Empirical formula	C39 H38 F12 Fe N12 O P2	
Formula weight	1036.60	
Temperature	120(2) K	
Wavelength	0.71073 Å	
Crystal system	Triclinic	
Space group	P-1	
Unit cell dimensions	a = 14.3669(9) Å	α= 96.830(2)°.
	b = 14.4037(9) Å	β= 101.957(2)°.
	c = 15.2503(10) Å	γ = 118.218(2)°.
Volume	2632.9(3) $Å^3$	
Z	2	
Density (calculated)	1.308 Mg/m^3	
Absorption coefficient	0.431 mm^{-1}	
F(000)	1056	
Crystal size	0.300 x 0.120 x 0.080 mm^3	
Theta range for data collection	2.113 to 31.511°.	
Index ranges	-21<=h<=21, -21<=k<=21, -22<=l<=22	
Reflections collected	176570	
Independent reflections	17524 [R(int) = 0.0683]	
Completeness to theta = 25.242°	99.9 %	
Absorption correction	Semi-empirical from equivalents	
Refinement method	Full-matrix least-squares on F^2	
Data / restraints / parameters	17524 / 0 / 656	
Goodness-of-fit on F^2	1.049	
Final R indices [I>2sigma(I)]	R1 = 0.0746, wR2 = 0.1908	
R indices (all data)	R1 = 0.1151, wR2 = 0.2269	
Extinction coefficient	n/a	
Largest diff. peak and hole	1.978 and -2.072 $e.Å^{-3}$	

Crystal data and refinement method of Fe1.

CCDC number	2195867
Empirical formula	C62 H65.50 F12 Fe N9 O1.50 P2
Moiety formula	C57 H55 N9 Fe, 2(P F6), C3 H6 O, C2 H4.5 O0.5
Formula weight	1306.52 Da
Color	violet
Shape	plate
Temperature	120(2) K
Wavelength	0.71073 Å
Crystal system	Monoclinic
Space group	$P2_1/c$
Unit cell dimensions	a = 26.9301(14) Å
	b = 11.0745(5) Å
	c = 21.3571(11) Å
	α= 90°
	β= 90.815(2)°
	γ = 90°
Volume	6368.8(5) $Å^3$
Z	4
Density (calculated)	1.363 mg/m^3
Absorption coefficient	0.371 mm^{-1}
F(000)	2706
Crystal size	0.26 x 0.20 x 0.16 mm^3
Theta range for data collection	1.988 to 26.389°
Index ranges	-33≤h≤33, -13≤k≤13, -26≤l≤26
Reflections collected	237684
Independent reflections	13001 [R(int) = 0.0377]
Completeness to theta = 25.242°	99.6 %
Absorption correction	Semi-empirical from equivalents
Refinement method	Full-matrix least-squares on F^2
Data / restraints / parameters	13001 / 0 / 790
Goodness-of-fit on F^2	1.020
Final R indices [I>2σ(I)]	R1 = 0.0625, wR2 = 0.1684
R indices (all data)	R1 = 0.0682, wR2 = 0.1745
Largest diff. peak and hole	1.80 e/$Å^3$ (0.83 Å from O1) and -1.50 e/$Å^3$ (0.60 Å from O1)

Crystal data and refinement method of Dy1.

CCDC number	2195869
Empirical formula	C62 H65.50 F12 Fe N9 O1.50 P2
Moiety formula	C65 H69 N13 Fe Co Cl O4, 2(P F6), C3 H6 O, C H Cl3
Formula weight	1713.94 Da
Color	red
Shape	block
Temperature	120(2) K
Wavelength	0.71073 Å
Crystal system	triclinic
Space group	P-1
Unit cell dimensions	a = 12.7510(5) Å
	b = 19.4461(10) Å
	c = 19.5383(9) Å
	α= 103.857(4)°
	β= 91.455(3)°
	γ = 96.679(4)°
Volume	4664.6(4) $Å^3$
Z	2
Density (calculated)	1.220 mg/m^3
Absorption coefficient	0.553 mm^{-1}
F(000)	1760
Crystal size	0.38 x 0.28 x 0.22 mm^3
Theta range for data collection	2.834 to 29.492°
Index ranges	-17≤h≤17, -19≤k≤26, -26≤l≤20
Reflections collected	55095
Independent reflections	22237 [R(int) = 0.0459]
Completeness to theta = 25.242°	99.8 %
Absorption correction	Semi-empirical from equivalents
Refinement method	Full-matrix least-squares on F^2
Data / restraints / parameters	22237 / 0 / 1037
Goodness-of-fit on F^2	1.025
Final R indices [I>2σ(I)]	R1 = 0.0739, wR2 = 0.1708
R indices (all data)	R1 = 0.1094, wR2 = 0.1909
Largest diff. peak and hole	0.93 e/$Å^3$ (1.59 Å from Cl73) and -0.86 e/$Å^3$ (0.78 Å from P1)

Crystal data and refinement method of Fe2.

CCDC number	2195868
Empirical formula	C66 H59 F12 Fe N9 O P2
Moiety formula	C63 H59 Fe N9, 2(P F6), C3 O
Formula weight	1340.01Da
Color	red
Shape	needle
Temperature	120(2) K
Wavelength	0.71073 Å
Crystal system	monoclinic
Space group	C2/c
Unit cell dimensions	a = 40.855(3) Å
	b = 13.7198(8) Å
	c = 23.3540(15) Å
	α= 90°
	β= 109.047(2)°
	γ = 90°
Volume	12373.6(13) $Å^3$
Z	8
Density (calculated)	1.439 mg/m^3
Absorption coefficient	0.384 mm^{-1}
F(000)	5520
Crystal size	0.30 x 0.10 x 0.08 mm^3
Theta range for data collection	2.146 to 30.531°
Index ranges	-58≤h≤58, -19≤k≤19, -33≤l≤33
Reflections collected	409074
Independent reflections	18910 [R(int) = 0.0998]
Completeness to theta = 25.242°	99.9 %
Absorption correction	Semi-empirical from equivalents
Refinement method	Full-matrix least-squares on F^2
Data / restraints / parameters	18910 / 0 / 855
Goodness-of-fit on F^2	1.067
Final R indices [I>2σ(I)]	R1 = 0.0595, wR2 = 0.1451
R indices (all data)	R1 = 0.0998, wR2 = 0.1794
Largest diff. peak and hole	1.85 e/$Å^3$ (1.49 Å from F25) and -1.58 e/$Å^3$ (0.63 Å from P2)

Crystal data and refinement method of Fe3.

CCDC code	2053792	
Empirical formula	C55 H60 F12 Fe N12 P2	
Formula weight	1234.94	
Temperature	100(2) K	
Wavelength	0.71073 Å	
Crystal system	Monoclinic	
Space group	C2/c	
Unit cell dimensions	a = 41.299(11) Å	α= 90°.
	b = 15.151(3) Å	β= 121.966(9)°.
	c = 22.208(7) Å	γ = 90°.
Volume	11789(5) $Å^3$	
Z	8	
Density (calculated)	1.392 Mg/m^3	
Absorption coefficient	0.396 mm^{-1}	
F(000)	5104	
Crystal size	0.274 x 0.239 x 0.196 mm^3	
Theta range for data collection	2.325 to 27.433°.	
Index ranges	-53<=h<=53, -19<=k<=19, -28<=l<=28	
Reflections collected	74175	
Independent reflections	13445 [R(int) = 0.0348]	
Completeness to theta = 25.242°	99.9 %	
Absorption correction	Semi-empirical from equivalents	
Refinement method	Full-matrix least-squares on F^2	
Data / restraints / parameters	13445 / 0 / 750	
Goodness-of-fit on F^2	1.020	
Final R indices [I>2sigma(I)]	R1 = 0.0382, wR2 = 0.0973	
R indices (all data)	R1 = 0.0468, wR2 = 0.1040	
Extinction coefficient	n/a	
Largest diff. peak and hole	0.570 and -0.657 $e.Å^{-3}$	

Crystal data and refinement method of Dy3.

CCDC code	2049533	
Empirical formula	C61 H71 Cl Co F12 Fe N15 O4 P2	
Formula weight	1518.49	
Temperature	100(2) K	
Wavelength	0.71073 Å	
Crystal system	Orthorhombic	
Space group	$P2_12_12_1$	
Unit cell dimensions	a = 14.673(2) Å	α= 90°.
	b = 19.008(3) Å	β= 90°.
	c = 29.325(3) Å	γ = 90°.
Volume	8178.9(19) $Å^3$	
Z	4	
Density (calculated)	1.233 Mg/m^3	
Absorption coefficient	0.527 mm^{-1}	
F(000)	3128	
Crystal size	0.724 x 0.334 x 0.316 mm^3	
Theta range for data collection	1.277 to 27.918°.	
Index ranges	-19<=h<=19, -24<=k<=24, -38<=l<=38	
Reflections collected	300927	
Independent reflections	19528 [R(int) = 0.0331]	
Completeness to theta = 25.242°	100.0 %	
Absorption correction	Semi-empirical from equivalents	
Max. and min. transmission	0.4308 and 0.3525	
Refinement method	Full-matrix least-squares on F^2	
Data / restraints / parameters	19528 / 508 / 960	
Goodness-of-fit on F^2	1.031	
Final R indices [I>2sigma(I)]	R1 = 0.0345, wR2 = 0.0872	
R indices (all data)	R1 = 0.0381, wR2 = 0.0897	
Absolute structure parameter	0.0153(19)	
Extinction coefficient	n/a	
Largest diff. peak and hole	0.528 and -0.419 $e.Å^{-3}$	

Optimized gas phase structure of Fe1 in cartesian coordinates (Angstroem):
122
Fe 21.17446539625873 2.96614523892719 8.72022263926293
N 22.84850382259722 0.93346587596815 6.87975684870498
N 23.85548846425781 2.37054050771886 8.07958190787154
N 22.77797619791331 3.88198363662181 9.33895902010150
N 21.33549685676019 5.14398927705133 10.50443211699540
N 19.22635838439082 4.91110504925038 10.37790621193070
N 21.10511466822955 1.59994088418335 10.19915904316169
N 19.62300992728927 2.02890976298743 8.18481659024984
N 20.73111220403626 4.01476414242048 7.07096027385455
N 11.73492490766459 -2.65981953848623 5.52260417630351
C 22.60270598066228 1.92504954907242 7.74404981674172
C 24.21102951975982 0.74635839462652 6.69225973410205
H 24.60080353416641 -0.01704337003573 6.04273008530885
C 24.85194707541093 1.65266167239036 7.44489363784690
H 25.90428349295636 1.83446590093329 7.57353022903106
C 23.96908154290422 3.44109135375892 8.95687637157303
C 25.14168921351151 4.01182698301964 9.41786004707559
H 26.11426213136849 3.66030300297037 9.10689299283637
C 25.01871376066602 5.06668585171831 10.31268776441184
H 25.91095660922505 5.54178614820107 10.69661861575665
C 23.77419185335675 5.51771488635038 10.73248228019802
H 23.68926163890941 6.33060761728199 11.43827684021755
C 22.66589658936907 4.87583540819440 10.20994302006119
C 20.80454316921017 6.10783635776143 11.34119273531136
H 21.39294378675162 6.80472855440243 11.91139198408241
C 19.47482705073153 5.95429730464394 11.25927931654933
H 18.68221028215190 6.49023126404729 11.75048223351381
C 20.36270022600877 4.38497520047289 9.90586844579683
C 21.85624838696398 0.17475522093745 6.16648186837487
C 21.34868555497976 -0.99153228554239 6.75259007709051
C 20.38696292176180 -1.69587148743021 6.03603020641088
H 19.96064532515678 -2.59893553177860 6.44891887643431
C 19.97458857981883 -1.27536276944197 4.78544692826950
H 19.23040477753042 -1.84443275451120 4.24453872570084
C 20.53120164622552 -0.14803167954551 4.21213155116853
H 20.21896373563229 0.14258848165596 3.21888974565520
C 21.49130286144933 0.60305673243985 4.88268275533761
C 21.86854787184118 -1.54257763264579 8.06649332986064
H 22.09477049653360 -0.70668544568417 8.73548961566200
C 20.86474490263612 -2.45000692538052 8.77486409524593
H 19.86816445426696 -2.01174277808161 8.82652999563977
H 21.20140488517424 -2.65341176722157 9.79097187821143
H 20.77207030275465 -3.41605600586514 8.27747662377383
C 23.16285980266999 -2.33463462252717 7.84495414910071
H 22.99566597979478 -3.15796534920774 7.14992324372011
H 23.51428158053908 -2.76035522690522 8.78541160850958
H 23.97183290437065 -1.72555912326589 7.44744607629422
C 22.14576387460524 1.77881822236690 4.18114169159027
H 22.41220667202584 2.53239285770467 4.92943908012638
C 23.42519427249877 1.33943499632930 3.45818241509910
H 23.20113439097687 0.56713932914040 2.72168288387669
H 24.18525604144661 0.94391497047585 4.12713025165351
H 23.87042206629558 2.18239223148473 2.92876444289838
C 21.23255683375810 2.44732758733517 3.15335290339343
H 21.14493656502274 1.85190131043804 2.24394429558401
H 21.64946959490268 3.40979064823613 2.85739689765199

H 20.22875510648721 2.61927233699546 3.53517218264492
C 17.89396044781851 4.51136702966644 10.01149126658099
C 17.26820758766816 3.49887355997524 10.74984984262973
C 15.97848002854551 3.14091565528615 10.37179916333734
H 15.45607368728503 2.36140572747691 10.90775108432860
C 15.33422041266109 3.77988575148784 9.32916194939325
H 14.32799325235832 3.48899718326636 9.05883592671460
C 15.96076472127033 4.80704742325895 8.64970370602200
H 15.42551271732866 5.31389096402339 7.85917512952120
C 17.25338397202183 5.20528530978032 8.97560228272656
C 17.90310351077450 2.86009656568952 11.97020861831366
H 18.97923852118573 2.76262016132250 11.79759141647096
C 17.35095642812923 1.46845574594225 12.27289372344829
H 17.31408847173945 0.83164028765709 11.38918048886769
H 16.34260364065759 1.51446302140352 12.68560790137326
H 17.97234083260842 0.97753262496860 13.02124936442476
C 17.69980832075200 3.74004429694029 13.20951503804090
H 18.17023800599425 4.71675660554675 13.11994594847093
H 18.12452342268795 3.25923106658345 14.09135393625358
H 16.63774669255454 3.89966842615660 13.39777947709089
C 17.87182220144195 6.39439985761723 8.26368506260322
H 18.95375154831563 6.24031337149242 8.19587343255963
C 17.33846978124011 6.58405813381277 6.84339401054491
H 17.97287294948494 7.28345486299232 6.29929509942300
H 16.33387707724941 7.00842476871171 6.84360978312037
H 17.30469076979448 5.65347148563578 6.28095527421688
C 17.61499797459328 7.69278336222062 9.03878934701922
H 18.02621362881132 8.54517775468146 8.49708055786738
H 18.06044884737459 7.69950646739812 10.03030010167025
H 16.54419288178910 7.86149370064326 9.15701021162704
C 21.94016851522706 1.45184772450217 11.22234206916214
H 22.76692138875395 2.14568294618189 11.28741242849370
C 21.78921617535594 0.46522076001966 12.18042586042025
H 22.49811247609469 0.38965746746677 12.99226146014213
C 20.72107068583757 -0.40763528558430 12.06950076864196
H 20.56805358495547 -1.19263698527631 12.79731383897403
C 19.84833003932541 -0.25817685656422 11.00704800571464
H 19.00810336303174 -0.92844913335211 10.90115310806912
C 20.06319371571041 0.75438384210733 10.08578967874400
C 19.20259410850588 1.00461565361296 8.92184205305202
C 18.06753683164117 0.30136392324008 8.56652367121549
H 17.70861224446419 -0.53219842990691 9.15269967376830
C 17.36690217825445 0.68292255820219 7.41787535431228
C 17.84002187590358 1.76349805895162 6.66760644109178
H 17.30637292401132 2.06615395809960 5.77882041594121
C 18.98217366966481 2.41841060069784 7.08727402857487
C 19.62685071916794 3.57010793787557 6.44092918983287
C 19.16358233601254 4.17291435347040 5.28427652639806
H 18.27630230697947 3.80258275555363 4.79009334583761
C 19.84702881719989 5.25786154295865 4.76274853003460
H 19.49778508990384 5.74048689202637 3.86035718776114
C 20.98016777660319 5.70822697406293 5.41521948402797
H 21.54696179470398 6.55074099666865 5.04590857646966
C 21.38492180627522 5.05428164800014 6.56643722045649
H 22.26717897233112 5.38148318810832 7.10007103775197
C 16.20105457290511 -0.01106202294548 7.02391637503261
C 15.20346463879533 -0.60212150152484 6.69017543295834
C 14.03044529689078 -1.29807977339035 6.29535458997461
C 13.32573524523136 -0.91934006367100 5.15333566018419
H 13.65490070773881 -0.08976114325849 4.54372520465976
C 12.18812200555383 -1.63511748294929 4.81687211561012

H 11.61720768487639 -1.36709179159127 3.93573666051022
C 13.55514631906669 -2.37681173025768 7.04015417658697
H 14.06681555397219 -2.70778906789297 7.93280917151875
C 12.40577702459466 -3.01774308092091 6.60672177302622
H 12.00970454568149 -3.85953106131689 7.16232636655648

Optimized gas phase structure of Fe2 in cartesian coordinates (Angstroem):
132
Fe 20.23088634034499 1.90669714343351 12.92781943784373
N 22.78395732391120 -0.01545014187417 13.20395748626087
N 20.85126584251466 -0.84295974439316 12.88547437974065
N 18.99257888353401 0.41017993301295 12.81352132669161
N 17.42101035686057 2.00949813819834 12.74191677271932
N 17.87910867218103 4.08573981493043 12.70555550344633
N 20.26385855094348 2.18531631401413 14.91836098471970
N 21.41612749521012 3.37747437760954 13.00418357180674
N 20.59654735175831 2.11992978341060 10.96054116010730
N 29.29120825709060 14.75277316125004 13.45834670718408
C 21.50637025005770 0.35052180435861 13.04906534456284
C 22.93360598309623 -1.39264784016028 13.12157612124369
H 23.89099450090034 -1.87367725016858 13.21160522738242
C 21.71646865212372 -1.92090464275580 12.92331162640553
H 21.41132320677856 -2.94587233058067 12.80743677675461
C 19.46588887578170 -0.82860026124188 12.78249302616218
C 18.63150829034059 -1.92602720009012 12.67137265282135
H 19.01017738889172 -2.93705283262993 12.64584098447327
C 17.26763202753939 -1.67414130255192 12.59689832771731
H 16.58022159846025 -2.50451201384714 12.51248501206981
C 16.76805178825725 -0.37865777434137 12.62401592370346
H 15.70621966747730 -0.19345924490392 12.55797792735748
C 17.69062250969226 0.64672865686237 12.72940294834768
C 16.20207923942112 2.65771171130153 12.66908919104310
H 15.25089849599885 2.15618361236260 12.64145291562534
C 16.49689009962775 3.96573032439633 12.64849908339211
H 15.84922286768010 4.82305192772275 12.59869330479668
C 18.47368129904093 2.88823718572756 12.77196928805676
C 23.84964415025463 0.87809332778794 13.56976484960329
C 24.15989136970200 0.99729080393055 14.93040602648457
C 25.14845869061635 1.91175296079751 15.28017841102753
H 25.41901784739671 2.03866135087893 16.31944436888126
C 25.80685755332800 2.65265489146610 14.31767876290946
H 26.56999742959191 3.36139222885784 14.61038008523807
C 25.52311521892007 2.46257593307565 12.97682756281923
H 26.08633783468548 3.01995993669957 12.24199006977009
C 24.55094467497884 1.55717463928533 12.56632015298772
C 23.54993920983927 0.10711169790567 15.99585255260761
H 22.55321202707762 -0.20720342722535 15.67135282489415
C 23.38947538366465 0.79859777618169 17.34800667759298
H 22.91191868684067 1.77045475315524 17.25762125846277
H 24.34688286494240 0.94141948547853 17.84995446639328
H 22.77892031861944 0.18402750852570 18.00946611715150
C 24.41633146191582 -1.14362029390716 16.18968751079005
H 24.55739643741363 -1.71536521866117 15.27474206963313
H 23.96788470774078 -1.80980623421591 16.92728574701122
H 25.40762974102227 -0.86767757425247 16.55117225834419
C 24.35219888531600 1.25763040026245 11.09346407336493
H 23.28399322933441 1.11829782984374 10.90296067724929
C 25.07105127355091 -0.04261796410708 10.71310674983113
H 24.95804177104715 -0.24283525917102 9.64715526665683
H 24.68590877173443 -0.91083366509692 11.24383804372457
H 26.13781112538578 0.03018117062571 10.92650650040835
C 24.85231229905068 2.37067400356914 10.17667686722753
H 24.53201788491477 2.17933343448377 9.15299363668353
H 25.94177055304063 2.41963292044193 10.15911218409048
H 24.48318547433755 3.35343550792086 10.47135708358859
C 18.54351866627979 5.35983448625658 12.62468464779304
C 18.80915007793113 6.06116647424238 13.80765946890915

C 19.43437566946664 7.29805645415013 13.68604239921524
H 19.65739278515874 7.87754889132640 14.57069799061496
C 19.76048446708003 7.81959883990548 12.44863583111914
H 20.24361766604280 8.78509938744052 12.38013202188760
C 19.44895776599067 7.12174254499758 11.29755776265935
H 19.68639478159066 7.56204209596499 10.33952001278033
C 18.82588472616358 5.87927762767273 11.35324318267747
C 18.37929205021281 5.56562976999231 15.17539291275708
H 18.48654403997348 4.47683349941671 15.20462167802263
C 19.21866983588849 6.14943273585594 16.31062327614453
H 20.28894835760929 6.09076708498105 16.11281133387693
H 19.01542903944080 5.61308279512045 17.23685130143216
H 18.97442159056325 7.19608059825823 16.49589073145427
C 16.90843297155352 5.90590730711697 15.44335367906954
H 16.22560303273888 5.41997275684831 14.75042507244112
H 16.74340734809956 6.98146692475850 15.37368719082881
H 16.62243311058542 5.59087104709303 16.44740102374533
C 18.42071916511529 5.18772185622336 10.06460415971090
H 18.49742764831104 4.10495752152525 10.20675090829817
C 16.97103162682933 5.52416643896787 9.69398307068637
H 16.70412876587113 5.05698943287214 8.74550290878832
H 16.84603309026840 6.60125137689387 9.57895737717414
H 16.24857164771818 5.18501196465548 10.43209763418198
C 19.30910132790526 5.56545746437334 8.87921817894196
H 19.13829254297439 4.87548792911097 8.05327580068706
H 20.36893475303328 5.53959284355085 9.12483908157342
H 19.08020038642434 6.56417397307959 8.50592817892226
C 19.58716458060320 1.51995314103136 15.84782430915187
H 18.96342149429196 0.70415205333515 15.50791817290145
C 19.64981614991517 1.83614999291221 17.19375327019826
H 19.06971364857728 1.27045426075657 17.90842656122418
C 20.46777400533526 2.87922814692265 17.59047215566181
H 20.55208306695828 3.15172529648068 18.63356744811265
C 21.19105755069764 3.56227580265922 16.62855899621674
H 21.84708836853833 4.37091724015653 16.91679804084680
C 21.06019847127298 3.20357028913758 15.29686087476210
C 21.71776017592749 3.90450713008597 14.18579491021264
C 22.53456606356037 5.01649797998175 14.27225492711086
H 22.81312730814649 5.42845969869148 15.23208337362498
C 23.01987105596607 5.60438043751100 13.10288784343899
C 22.67538227169645 5.02121621638975 11.88244113516112
H 23.00428129370869 5.47974990474046 10.96016239796033
C 21.87703475570731 3.89265609348554 11.86951076233194
C 21.42797290471675 3.14389170210888 10.68825834474307
C 21.83005910574713 3.42372386892485 9.39225522474388
H 22.50517616397183 4.24323292445662 9.19252985900136
C 21.36594307780048 2.63960519787682 8.35148293512287
H 21.67126036350576 2.84363108463190 7.33438486620886
C 20.50440628133418 1.59531220119442 8.63796722678443
H 20.11359980488684 0.95607568887187 7.85951680861089
C 20.14791913416974 1.37426192639643 9.95664417074388
H 19.47724552434064 0.56412487930756 10.20866983278628
C 23.85584425510356 6.80786886347494 13.15340449501370
C 23.57277633230618 7.83053666118111 14.05961051878710
H 22.71311330168035 7.75237851077953 14.71412143107912
C 24.34989994708538 8.97011644682471 14.10426941105898
H 24.11287471255686 9.76248058856531 14.80051949174583
C 25.44509598969142 9.11660096969041 13.24632501062078
C 25.73277118291901 8.08911256358591 12.34172426090142
H 26.58361492109414 8.18671895989536 11.68198103150980
C 24.94527081550713 6.95670091783351 12.29453399571285

H 25.20496872010191 6.16385426535252 11.60341110924241
C 26.24647892803827 10.28304415364964 13.29221669694263
C 26.92550251129785 11.27946954659040 13.32631387664632
C 27.72548770831234 12.45233641507495 13.37116504349521
C 27.44999531293123 13.47317923400410 14.28022003494156
H 26.62262412807433 13.39373587489833 14.97119692648770
C 28.26296071820042 14.59463956251056 14.27799981878246
H 28.07287926280829 15.40413200198406 14.97320576576787
C 29.55112006139049 13.78147552273075 12.59629402248311
H 30.39781220086789 13.93654823475656 11.93774725035024
C 28.80761439946304 12.61614811998680 12.50731758628255
H 29.06256034059040 11.85374307234216 11.78483309022601

Optimized gas phase structure of Fe3 in cartesian coordinates can be found here.[99]

Optimized gas phase structure of Dy1 in cartesian coordinates (Angstroem):
154
Fe 1.87083097985194 10.43476175169173 18.91767523280098
Co 2.02443399955718 1.98263349182497 8.46145883143278
Cl 2.02281841126951 0.62444005008439 6.74244423541477
O 3.48167627519555 0.13745857715441 9.97314880217199
O 3.07384089464319 4.02035710993499 6.71196906032627
O 0.56668780176796 3.87982466682079 7.01608698718895
O 0.97554356522625 -0.18920037228507 10.04158056197422
N 4.89317122789912 11.16562378662705 18.10683385690319
N 3.92270796376436 12.21197817196565 19.68230094295663
N 1.83514367760168 11.74569719531330 20.35808317711809
N -0.26687242986263 11.02372803372801 20.66056194399514
N -1.10836604049928 9.41792801254648 19.55040131199723
N 2.57272322480893 8.81631599565393 19.86939941994298
N 1.88440015400491 9.22395587205152 17.46643207554255
N 1.16929740976010 11.65901187368549 17.47985173014343
N 2.02449703687401 3.22821396528876 10.03710576082547
N 3.57479485468193 1.09583796510411 9.13195201422959
N 3.33441839280634 3.03657977300594 7.56949667157469
N 0.47375101402636 2.84059738453425 7.75519905092259
N 0.71474530165028 0.87193433151927 9.28221693646962
C 3.72776159095119 11.21385711939443 18.76260212837285
C 5.78731822196177 12.11356101327244 18.58592368016610
H 6.77282935007415 12.23214047176091 18.17161627035110
C 5.18104210839402 12.77559692902213 19.58212483771134
H 5.53664822034106 13.57664451913202 20.20579167874277
C 5.23528169991322 10.24945705712778 17.05177556174582
C 4.96806689515038 10.62213497019114 15.72816919903820
C 5.32795134607396 9.72352066736081 14.72930268212052
H 5.14035632285829 9.96597214005938 13.69302521765944
C 5.94536459518105 8.52505251485860 15.03281255197118
H 6.22422903426189 7.84619693621257 14.23807490640664
C 6.23193140280028 8.20333757152254 16.34579805440503
H 6.74221423119231 7.27410609558788 16.55604930897664
C 5.89193942601624 9.05784327021362 17.38979147498080
C 6.30105490874752 8.70651329177420 18.80859573697934
H 5.53502240338887 9.07849544088603 19.49695920884778
C 7.63906702409299 9.36037400210589 19.17556025081264
H 7.60447452677973 10.44671027819410 19.16944487437450
H 8.41998361004819 9.04940655447905 18.48096263195126
H 7.94694611665704 9.05638460977358 20.17651889279170
C 6.43981775862396 7.20075741186156 19.03378399225056
H 5.60423193767215 6.63605119938726 18.62499818333860
H 6.49875971161289 6.98963949180831 20.10124866767501
H 7.35460663313063 6.80950163094226 18.58720784996231
C 4.39097988293901 11.97401843963096 15.35365688232042
H 3.67044069071760 12.27423994709699 16.12063211819287
C 3.66358122198184 11.96164953972603 14.01041401105769
H 2.97448117412047 11.12263821899779 13.91569477175478
H 4.36030757579885 11.90959511978240 13.17316244595733
H 3.09656708140105 12.88382710171264 13.88696727645207
C 5.49334460946242 13.03819850848687 15.29562881090312
H 5.98451287342073 13.19452960330075 16.25341970229334
H 5.07912210978130 13.99861934998530 14.98712096068978
H 6.25951699206707 12.75956415921605 14.57158122987408
C 2.89022631881260 12.52414421950549 20.55709744491098
C 2.89508035024043 13.51556044890668 21.52166622297183
H 3.75285130889956 14.14913315953382 21.69189123253465
C 1.73536653785661 13.67181026706186 22.26942200823058
H 1.69752102652841 14.43538804154182 23.03411335183841

C 0.61955041135041 12.87492772965892 22.04866741937225
H -0.28213703464169 13.01262396297355 22.62676981571913
C 0.72241324363623 11.91269980327837 21.06053761569711
C 0.01430243084168 10.13874000736990 19.65197619681962
C -1.54682509273403 10.85945093245613 21.15648158019551
H -1.97108183501047 11.45503705314623 21.94538841005302
C -2.07353442173715 9.84808550832423 20.45033777043023
H -3.04874103413068 9.39827911623164 20.50508343198135
C -1.29109521536446 8.27842185488189 18.69208964003024
C -1.04948041346712 7.00552726098140 19.22632172109658
C -1.21253788627330 5.91768253160195 18.37430684038166
H -1.03839592084361 4.91629842386320 18.74271110312944
C -1.61280090735563 6.08993967745788 17.06311687335327
H -1.73497299033143 5.22956001574915 16.41880030336252
C -1.89241916895867 7.35539615880172 16.58065478716267
H -2.24071434932038 7.45970885016861 15.56304063933918
C -1.75487692989259 8.48068989089872 17.38623788722466
C -2.18989777540822 9.84070793872756 16.87499109006393
H -1.51007958261328 10.60082751123795 17.27180821321743
C -3.60550174060057 10.17069905320327 17.36363907555820
H -3.67865234356941 10.23010374468173 18.44736089811103
H -4.31503000196559 9.41553239359561 17.02432565981860
H -3.93044258484523 11.13324373309972 16.96730283527783
C -2.17148019181394 9.94514777873640 15.35170260194427
H -1.24038411497231 9.58067037094665 14.91776650126663
H -2.30597724863752 10.98331269292969 15.04956503250952
H -2.98668384047752 9.38041523475485 14.89806753883058
C -0.71541326358540 6.76843936691633 20.68709784682624
H -0.14597670538578 7.62413504602036 21.06402267213001
C 0.12829181494336 5.51467642720584 20.91604949985064
H 0.96512278218378 5.44421402110619 20.22545477153800
H -0.46407918651350 4.60466210671857 20.81579067640627
H 0.52818245457865 5.51623906369652 21.92990130425198
C -1.99840562806000 6.63376977986076 21.51690963048312
H -2.63088905338958 7.51720867086884 21.48023807023861
H -1.75677678571917 6.45215463361566 22.56455633442057
H -2.59397982551311 5.79140761549463 21.16356821658170
C 2.91639723843824 8.70750460412270 21.14713807124125
H 2.79759598039324 9.59000066860005 21.76135019045014
C 3.40931088166335 7.53493726900845 21.69426767313940
H 3.67834020045316 7.49923430457562 22.74012533134589
C 3.54447843480625 6.42874423707309 20.87552746077367
H 3.92328300211970 5.49364583825751 21.26453047812517
C 3.18036636617285 6.53557888416902 19.54411012354759
H 3.27159225460112 5.68176329461660 18.88748311834509
C 2.70106308886451 7.74285749653218 19.06597376718793
C 2.30368252079966 7.97930332792319 17.67113030626733
C 2.34401953991943 7.06943178870854 16.63085549745956
H 2.67920130587831 6.05343444441231 16.77812872680101
C 1.94453867852674 7.48440863169323 15.35822385519062
C 1.51347362017606 8.80172846383213 15.17903495072838
H 1.20748416662442 9.13065162942621 14.19651414875424
C 1.49186107160352 9.65075743919235 16.26930404500674
C 1.06615105237676 11.05652725196136 16.28005099347248
C 0.58817259415939 11.73164583492238 15.16838801945336
H 0.50783151596749 11.23286106473456 14.21380201229548
C 0.21034247930549 13.05682503012429 15.28819736707972
H -0.16487473208883 13.59870725339731 14.43091651984739
C 0.32283892731502 13.67117226545982 16.52301766715559
H 0.04159453353901 14.70436449178376 16.66710152721535
C 0.80635483842444 12.93278566829219 17.58858483942502

H 0.90208313134815 13.39040257913884 18.56350651438549
C 1.70133257513379 4.51293262645899 9.88187663560545
H 1.43430809134637 4.84642546749283 8.88755894958170
C 1.68065124882611 5.40239690048423 10.93776840033217
H 1.41007472036526 6.43291886521860 10.76050690219488
C 2.00732043414593 4.94859276147235 12.21283895266179
C 2.34538293672599 3.60651726129982 12.36364445647800
H 2.60948348939169 3.19850176077063 13.32822010538701
C 2.34156399430806 2.78395646874373 11.25409908072961
H 2.61506066438541 1.74134727990410 11.35134831350069
C 6.02356791484287 0.96106936651147 9.03273348962323
H 6.69118981581629 1.70269232255905 9.47514734970455
H 6.52160582388337 0.56025410428215 8.14809488739193
H 5.89821781245121 0.14721274103604 9.74127924137650
C 4.70140611302492 1.54817494752175 8.68026150394303
C 4.54771518736915 2.66315665183195 7.74769753806370
C 5.68665298833518 3.28087059760646 7.01427188457229
H 5.62777238678905 3.02249276147775 5.95535781086600
H 6.64429600223859 2.93536293438376 7.39322133194410
H 5.65794392406859 4.36802628807469 7.07769864683755
C -1.97500204556532 2.77567976566556 7.60246472754104
H -1.84997408640799 3.65473426648074 6.97655587595730
H -2.64347409597426 3.03206191580325 8.42637529293309
H -2.47189347411819 2.00869205921838 7.00567868070570
C -0.65275644931067 2.29706489371717 8.09198233117017
C -0.49878347999270 1.13223090434779 8.96142634382859
C -1.63753978338595 0.27661190378784 9.39485558269745
H -1.57829187145224 -0.69517081532910 8.90125576561899
H -2.59533902817389 0.72415616348742 9.14509678818135
H -1.60883238651708 0.08974549593080 10.46772834442614
H 2.05447524854930 4.04405237699110 6.66980591220613
H 1.99521182759722 -0.23600494230306 10.05405782910585
C 1.97415971560888 6.58820273906295 14.26373758095243
C 1.99246848492505 5.83214249512509 13.32471483896618

Optimized gas phase structure of Dy2 in cartesian coordinates (Angstroem):
164
Fe 20.34863674282454 2.09667934579946 12.92261229655693
N 22.88851932929359 0.30031448769455 13.71357375718716
N 21.03400431676739 -0.62123193741762 13.23024239705387
N 19.16901787515660 0.55138288875259 12.80830137634380
N 17.57577534825588 2.07930826585341 12.41028865452098
N 18.00241576819768 4.14581601011459 12.14695695720837
N 20.09478997491240 2.55271711685970 14.86749712542619
N 21.49463660374377 3.59841196706065 13.03270305244455
N 20.99151820894741 2.14985354423483 11.01488572857695
N 29.85861166995707 14.60789624288641 13.76069152724068
C 21.63365745094270 0.60464227119841 13.36214555656714
C 23.08027105002965 -1.07264671911514 13.78115945084409
H 24.02864329030413 -1.50966015871144 14.03753593513548
C 21.91216377503180 -1.65961282879125 13.48024491059522
H 21.64915152817432 -2.70109185261789 13.42300657543038
C 19.67041129077060 -0.66618453136780 12.96702437617086
C 18.87865137679929 -1.79760307005549 12.88928133398555
H 19.28083271454533 -2.79182332635978 13.01581645621414
C 17.52495681772303 -1.60267554732092 12.64750938638291
H 16.87004274422307 -2.46071315290140 12.58359277008265
C 16.99444296668059 -0.32937730356746 12.48576787608364
H 15.94082296780575 -0.18871870145350 12.29518155787735
C 17.87667708923352 0.73239364092996 12.57143208884856
C 16.36196137739203 2.67699902077151 12.12515125687937
H 15.42695439272436 2.14850380465213 12.06514178166938
C 16.63671119383549 3.97999465456990 11.96323810214454
H 15.98282355414292 4.80201813501801 11.73337617083787
C 18.60382921278992 2.98611071490130 12.43703497755964
C 23.87203167054786 1.26149401358815 14.13480277296346
C 23.97696878494046 1.52512531478368 15.50693185214145
C 24.88451304093233 2.50400763655693 15.89930317595761
H 24.99709885844636 2.74263734848340 16.94797176536682
C 25.66331520330226 3.16767777581973 14.97078285255215
H 26.36132202311081 3.92770031993431 15.29574732090239
C 25.58469739576871 2.83472575475243 13.63027510131963
H 26.24147493209881 3.33299685271761 12.93147543282710
C 24.70079205127195 1.86067528169728 13.17879374834658
C 23.23640934460414 0.72234308232436 16.55927588286280
H 22.29638062011068 0.35742348558974 16.13437102763890
C 22.88756470862245 1.52828099922849 17.80869257507348
H 22.42057715150730 2.47969542974548 17.56863154652990
H 23.76627420892956 1.73170645493766 18.42137239825054
H 22.19603619489382 0.96325833691774 18.43347852967687
C 24.08017490058895 -0.48619048040510 16.98402131653795
H 24.33989400053559 -1.14245939570449 16.15621610873350
H 23.54550490884585 -1.08546208907839 17.72146655345523
H 25.01505646935316 -0.15718051242097 17.43897936050389
C 24.72862520240952 1.40968959165960 11.73119874423187
H 23.70342097918790 1.21660410574928 11.40114811290078
C 25.52103205331839 0.10359554394430 11.59480699860102
H 25.57312032700520 -0.20275213286746 10.54956697393649
H 25.07757509948236 -0.72177567980654 12.14744971042420
H 26.54211027464820 0.23313297393891 11.95454293997760
C 25.34030112638186 2.44138887026889 10.78715536518095
H 25.17738505963366 2.14002763217723 9.75289228223523
H 26.41955018578562 2.52196908484440 10.92266749908562
H 24.91587621762084 3.43663216265249 10.92181025484184
C 18.69325869919492 5.38079767980959 11.88992272893446
C 18.97778125124706 6.24319216506949 12.95537593088413

C 19.70756944031866 7.39013244442900 12.66238646427747
H 19.95955998020966 8.08524729923515 13.45056302141169
C 20.10168534969943 7.67986566278999 11.36827816278759
H 20.66674487247752 8.58030158012199 11.16735519519015
C 19.74044310125405 6.84560054144661 10.32779757288962
H 20.01418993462141 7.11541295489909 9.31706164853127
C 19.01664570079399 5.68022614520024 10.55991444365820
C 18.43424151086360 6.01469016797106 14.35253038086812
H 18.50034549355427 4.94808678009895 14.58743268075972
C 19.19469691064528 6.78203198401257 15.43081147158245
H 20.27419954879882 6.64664340387096 15.35921998159645
H 18.87552456122236 6.44888072227410 16.41781105458433
H 18.99253888203919 7.85273126736307 15.38220886087022
C 16.95722192022926 6.42170494790650 14.42363062962050
H 16.32210551657672 5.83191201340305 13.76629652850415
H 16.83299075748312 7.47030756103278 14.15199297096259
H 16.57534171047961 6.29328765330797 15.43692971813482
C 18.52141137382836 4.85772181949290 9.38578557536616
H 18.39199557039182 3.81944592954550 9.70608648592908
C 17.16562936524881 5.39257195061646 8.90769986809134
H 16.78764558754750 4.79129331842916 8.08040120412168
H 17.26479698020686 6.41909162084682 8.55322558946497
H 16.40451063478169 5.39386064231428 9.68494060612563
C 19.48121388544225 4.85061226778376 8.19780010359859
H 19.17078091372328 4.09680570718867 7.47444748448499
H 20.50283941524970 4.62897837791830 8.49450282466087
H 19.48521342990089 5.80526549569892 7.67098598537783
C 19.28151632543720 1.97424874313065 15.74439837764609
H 18.71627016183388 1.11966937445095 15.39780654280219
C 19.13471768336002 2.42446095581288 17.04481687765454
H 18.44999246974658 1.92440891356043 17.71444377703828
C 19.87798966193683 3.51722300675383 17.45465770464920
H 19.79439496152648 3.89761941591018 18.46345190769888
C 20.74414999480310 4.10963866242999 16.55257845953192
H 21.34187361071649 4.95792916417563 16.85312552925273
C 20.82716491942493 3.61209036397701 15.26199339198758
C 21.65354974010404 4.20631717819125 14.20327160412759
C 22.50296683103143 5.29101905616173 14.32321433969270
H 22.68389536023591 5.75121751758772 15.28455137459078
C 23.15503355464243 5.77889019849984 13.19084225913054
C 22.94019431410184 5.12817354710866 11.97602499621231
H 23.40019086469901 5.51049027632137 11.07552665583904
C 22.11767241715401 4.01733001290471 11.93671210315818
C 21.84209048361264 3.16568379300356 10.77250608026986
C 22.43409369535254 3.33402676851390 9.53101531776127
H 23.11123118842091 4.15685704980204 9.35305698504640
C 22.15965086748158 2.43065243114166 8.51935946074952
H 22.61902977625308 2.54216134323964 7.54679232373096
C 21.27857377225281 1.39436218459742 8.77304144504487
H 21.02798839362592 0.66791502509410 8.01357959236016
C 20.71467897350506 1.29850214615742 10.03326736702562
H 20.01957532468411 0.50099824096250 10.25853632059995
C 24.04221264884983 6.94514331570902 13.27402051065781
C 23.70518385511568 8.03982898877098 14.07032867286365
H 22.76809298374516 8.04850661689573 14.61374433765488
C 24.53416282694474 9.14129676400545 14.14449656159763
H 24.25620292522436 9.99023485950030 14.75346677925591
C 25.73367072357396 9.17343847028703 13.42708050890752
C 26.07588872214454 8.07478540378671 12.63305316464049
H 27.00661918913944 8.08586520550065 12.08312905437824
C 25.23798413017137 6.98043459594396 12.55635780756639

H 25.53612032183759 6.13011324916555 11.95505348696148
C 26.58873415004641 10.30145592300812 13.50163286340560
C 27.31652731530165 11.26060886427724 13.56193995228233
C 28.17411200326523 12.38938833463930 13.63026845560893
C 27.88938861806611 13.46355352912138 14.46836016052199
H 27.00676273175364 13.46882557333089 15.09063933289303
C 28.75209593233781 14.53991358931076 14.50085587244479
H 28.53145956779850 15.37696640989838 15.14482951239131
C 30.13447159604980 13.58112068730175 12.95667295495993
H 31.03501448501604 13.63940287382121 12.36537672132475
C 29.33127119750823 12.46342644872701 12.86027264588914
H 29.60999699277454 11.66278546050339 12.19126306219319
H 29.99225505734489 16.54039108547950 18.27876634994300
C 30.06296862540809 17.44502105944697 17.67548191330880
H 30.97193850384660 17.96324128412363 17.98625610537162
H 29.21441019658502 18.08390874387354 17.90342608032037
O 31.81322696225630 15.65277899833305 16.58154253886118
C 30.14100815580846 17.12671934052944 16.22294736822705
H 32.44926093466427 15.15138736850109 15.95831505125277
H 27.50135177612781 18.36865386244203 16.22491562201724
N 30.98552407295139 16.28113553397105 15.75346089132598
H 28.68424314661644 19.65397693242235 16.01581832198475
C 28.25153736770383 18.77118418335628 15.54141506413078
C 29.30535177385482 17.77090152523299 15.21251734523026
O 33.15376077501296 14.57024405816746 14.73528394379650
H 27.74675031150607 19.09501755934628 14.63536894955051
Cl 32.41134551497526 17.97549699725845 13.95427636716120
Co 31.08414531816311 16.22442431914456 13.85369208684532
N 29.59598493129210 17.41381193522134 13.99512462083203
N 32.63914573923512 15.12335004590742 13.71748632774342
O 28.98037373124558 17.83378402440908 12.96972997627709
H 34.80074897846611 13.85669509068990 13.10296602000969
C 33.12822860371782 15.02817769388140 12.51509419718350
C 34.39421840989149 14.30803728290827 12.20206435306185
N 31.27021334387283 16.28333566246212 11.96043494543837
H 35.14529409670672 14.99232468593854 11.80316741068054
C 32.33744578890506 15.73132816115041 11.50782710973004
H 29.79804950271748 17.40223652248925 11.75571346824460
H 34.24669805011212 13.51883251106441 11.46208405276646
O 30.48722726007068 16.97125992656101 11.13621262882733
C 32.74543154556186 15.84526564686830 10.08031445075890
H 33.04100198611837 16.87385586515557 9.86527238298328
H 33.58571844729668 15.19693524447624 9.84813755532839
H 31.92136690621166 15.60542546846312 9.40927647659940

Optimized gas phase structure of Dy3 in cartesian coordinates can be found here.[99]

Loewdin %Fe 3d and % Co 3d character of dπ, dπ* and dσ* orbitals of Fe1 and Dy1.

	Fe1		Dy1			
	state	%Fe 3d character	state	%Fe 3d character	state	%Co 3d character
dπ	HOMO-2	81.0	HOMO-4	80.9	HOMO-15	36.5
	HOMO-1	68.8	HOMO-1	65.7	HOMO-9	41.2
	HOMO	68.1	HOMO	68.2	HOMO-8	38.2
dπ averaged		**72.6**		**71.6**		**38.6**
dπ*	LUMO	7.2	LUMO	6.5		
	LUMO+2	6.3	LUMO+4	6.2	LUMO+8	6.2
	LUMO+4	4.6	LUMO+6	4.6	LUMO+11	6.8
dπ* averaged		**6.0**		**5.8**		
dσ*	LUMO+7	68.5	LUMO+12	68.4	LUMO+2	59.8
	LUMO+14	60.2	LUMO+18	59.6	LUMO+7	51.2
dσ* averaged		**64.4**		**64.0**		**55.5**
HOMO-LUMO gap	-2.47 eV, 501.7 nm		-2.33 eV, 531.2 nm			
dπ-dσ* gap	-4.35 eV, 285.3 nm		-4.35 eV, 285.3 nm			
average dπ(Av)-dσ*(av) gap	-4.67 eV, 265.6 nm		-4.67 eV, 265.4 nm			

Loewdin %Fe 3d and % Co 3d character of dπ, dπ* and dσ* orbitals of Fe2 and Dy2.

	Fe2		Dy2			
	state	%Fe 3d character	state	%Fe 3d character	state	%Co 3d character
dπ	HOMO-2	80.9	HOMO-4	80.9	HOMO-16	35.7
	HOMO-1	68.3	HOMO-1	65.7	HOMO-12	37.2
	HOMO	69.0	HOMO	68.2	HOMO-9	30.8
dπ averaged		**72.7**		**71.6**		**34.6**
dπ*	LUMO	5.8	LUMO	6.5		
	LUMO+2	3.9	LUMO+4	6.2		
	LUMO+4	4.5	LUMO+6	4.6	LUMO+7	6.0
dπ* averaged		**4.7**		**5.8**		
dσ*	LUMO+9	67.3	LUMO+14	68.4	LUMO+2	59.5
	LUMO+15	60.9	LUMO+19	59.6	LUMO+7	54.2
dσ* averaged		**64.1**		**64.0**		**56.9**
HOMO-LUMO gap	-2.62 eV, 473.3 nm		-2.51 eV, 493.1 nm			
dπ-dσ* gap	-4.38 eV, 283.2 nm		-4.36 eV, 284.2 nm			
average dπ(Av)-dσ*(av) gap	-4.69 eV, 264.4 nm		-4.68 eV, 265.1 nm			

Loewdin %Fe 3d and % Co 3d character of dπ, dπ* and dσ* orbitals of Fe3 and Dy3 are published elsewhere.[99]

Computed dominant vertical excitation of Fe1. Donor and acceptor orbitals are visualized. Contribution to and character of the transition is specified.

transition (nm)	donor	acceptor	contribution	character
558.8	241 - HOMO 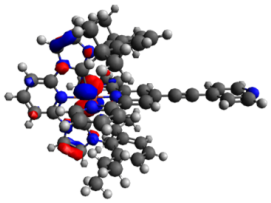	243 – LUMO+1 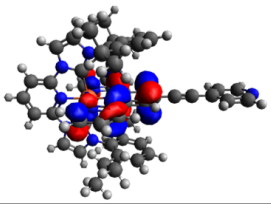	0.63	MLCT
	240 – HOMO-1 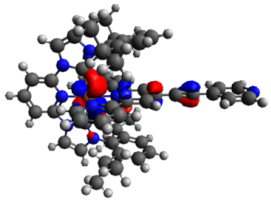	242 – LUMO 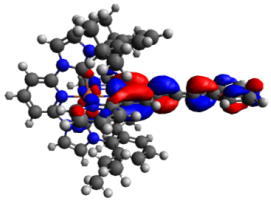	0.31	MLCT
482.8	240 – HOMO-1 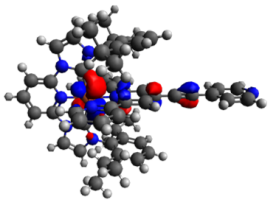	242 – LUMO 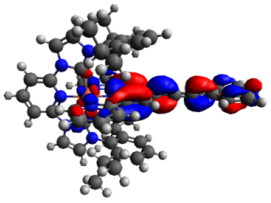	0.42	MLCT
	241 - HOMO 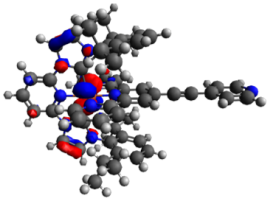	243 – LUMO+1 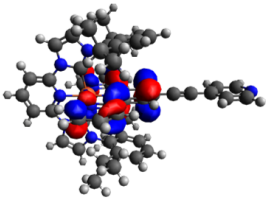	0.24	MLCT
400.2	240 – HOMO-1 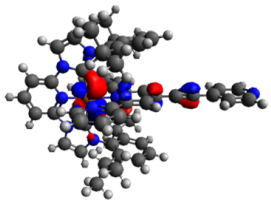	245 – LUMO+3 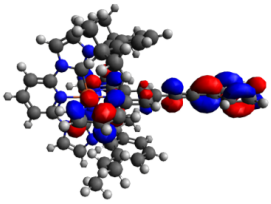	0.55	MLCT
	240 – HOMO-1 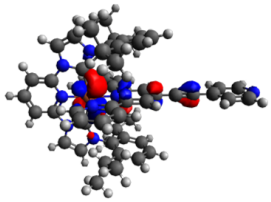	246 – LUMO+4 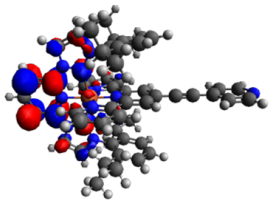	0.37	MLCT

399.7	240 – HOMO-1 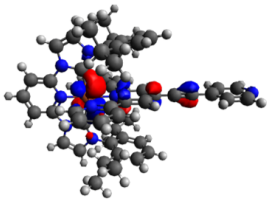	246 – LUMO+4 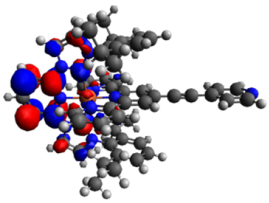	0.54	MLCT
	240 – HOMO-1 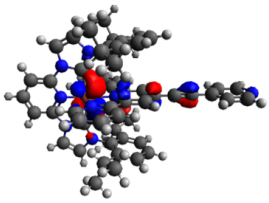	245 – LUMO+3 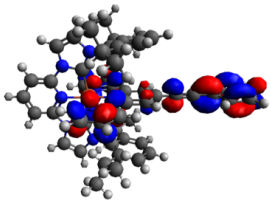	0.39	MLCT
371.6	241 - HOMO 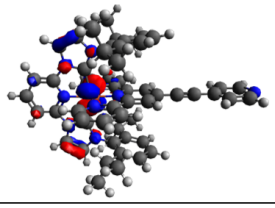	247 – LUMO+5 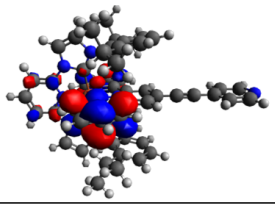	0.8	MLCT
328.6	231 – HOMO-10 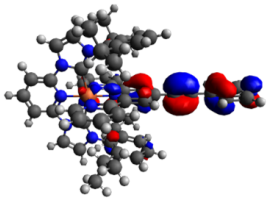	242 – LUMO 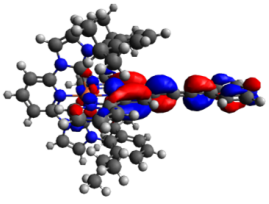	0.59	π-π*
323.8	235 – HOMO-6 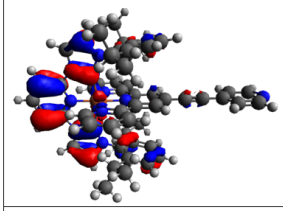	243 – LUMO+1 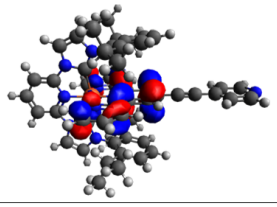	0.41	π-π*
	232 – HOMO-9 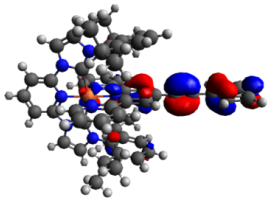	242 – LUMO 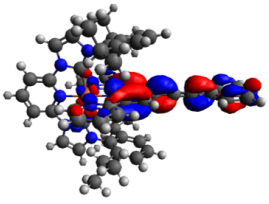	0.34	π-π*

317.1	232 – HOMO-9 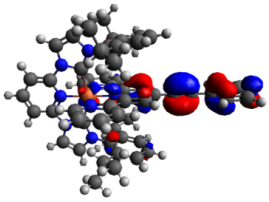	242 – LUMO 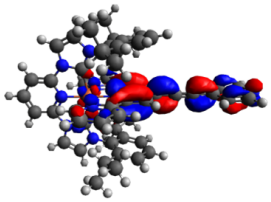	0.4	π-π*
	235 – HOMO-6 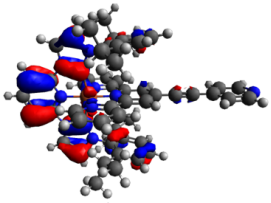	243 – LUMO+1 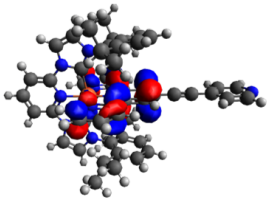	0.25	π-π*
268.0	232 – HOMO-9 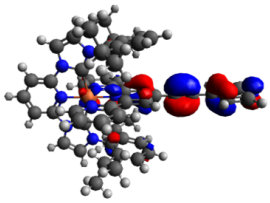	245 – LUMO+3 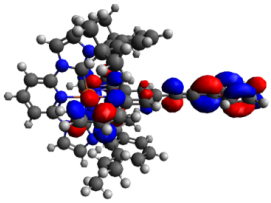	0.33	π-π*
	225 – HOMO-16 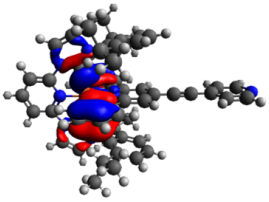	242 – LUMO 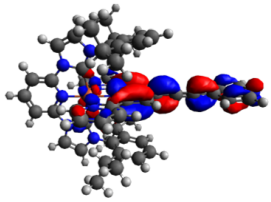	0.27	π-π*

Computed dominant vertical excitation of Dy1. Donor and acceptor orbitals are visualized. Contribution to and character of the transition is specified.

transition (nm)	donor	acceptor	contribution	character
570.6	324 – HOMO 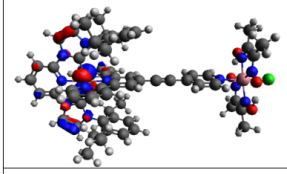	326 – LUMO+1 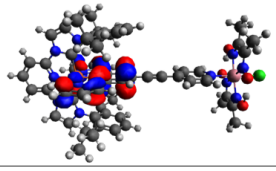	0.51	MLCT
	323 – HOMO-1 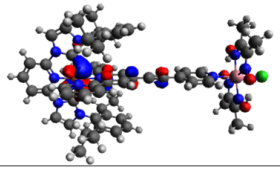	325 – LUMO 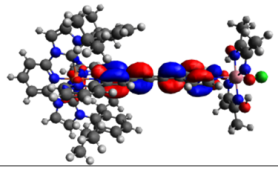	0.40	MLCT
513.3	323 – HOMO-1 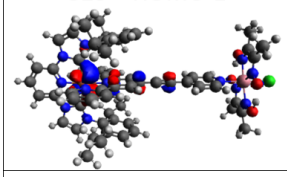	326 – LUMO+1 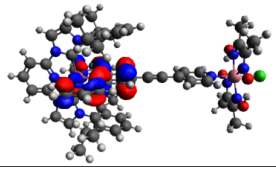	0.73	MLCT
	324 – HOMO 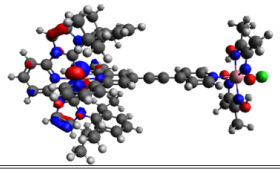	326 – LUMO+1 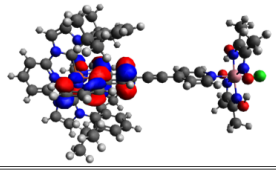	0.13	MLCT
505.2	323 – HOMO-1 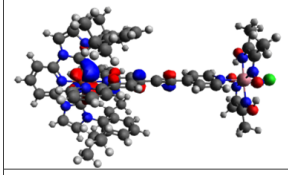	325 – LUMO 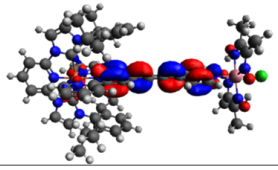	0.32	MLCT
	324 – HOMO 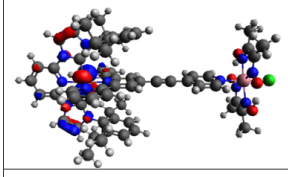	326 – LUMO+1 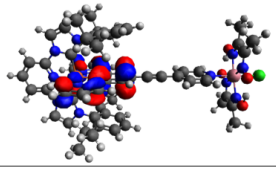	0.31	MLCT
	323 – HOMO-1 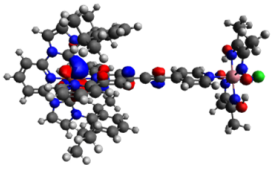	326 – LUMO+1 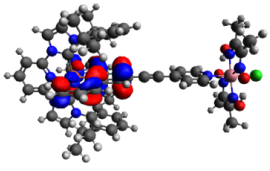	0.16	MLCT

402.3	315 – HOMO-9 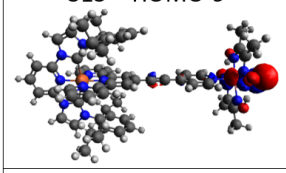	325 – LUMO 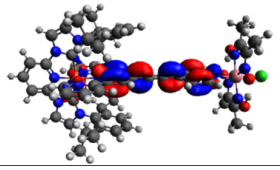	0.46	MLCT/ π-π*
	321 – HOMO-3 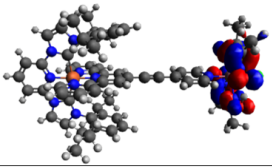	332 – LUMO+7 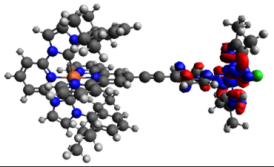	0.23	LMCT/ π-π*
	316 – HOMO-8 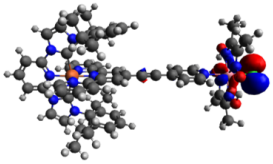	325 – LUMO 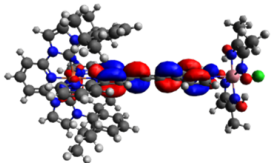	0.20	MLCT/ π-π*
345.0	310 – HOMO-14 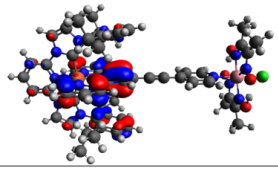	325 – LUMO 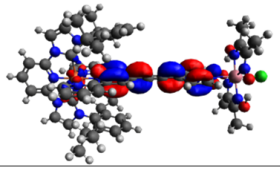	0.62	π-π*
307.9	307 – HOMO-17 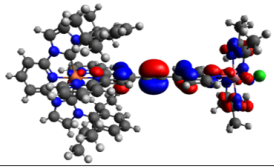	325 – LUMO 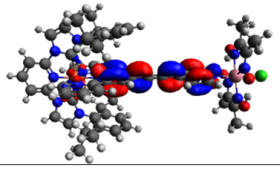	0.41	π-π*
	324 – HOMO 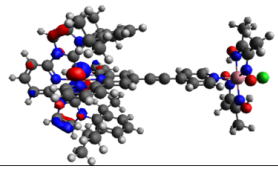	338 – LUMO+13 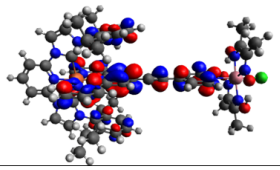	0.23	MLCT

Computed dominant vertical excitation of Fe2. Donor and acceptor orbitals are visualized. Contribution to and character of the transition is specified.

transition	donor	acceptor	contribution	character
548.7	261 – HOMO 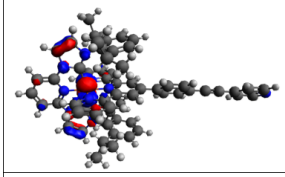	263 – LUMO+1 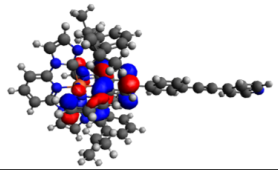	0.66	MLCT
	260 – HOMO-1 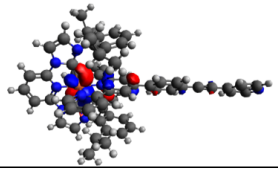	262 – LUMO 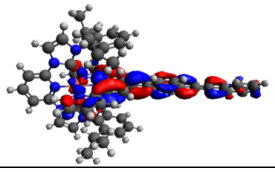	0.30	MLCT
514.2	260 – HOMO-1 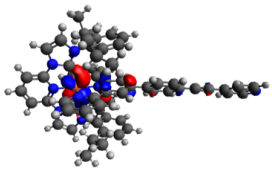	263 – LUMO+1 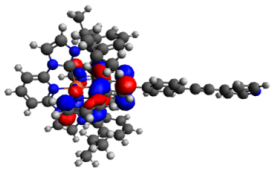	0.93	MLCT
478.6	260 – HOMO-1 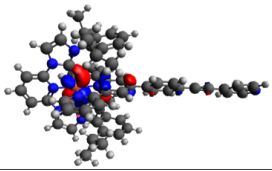	264 – LUMO+2 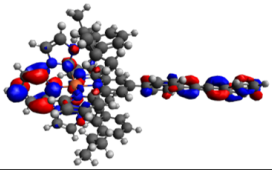	0.34	MLCT
	260 – HOMO-1 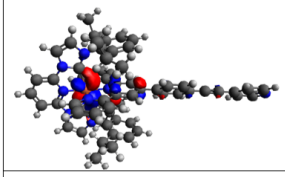	265 – LUMO+3 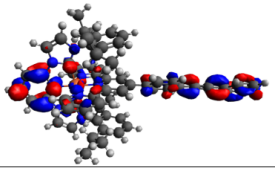	0.30	MLCT
	260 – HOMO-1 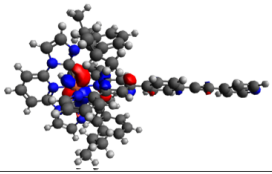	262 – LUMO 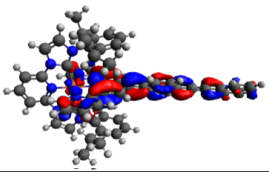	0.16	MLCT
474.9	260 – HOMO-1 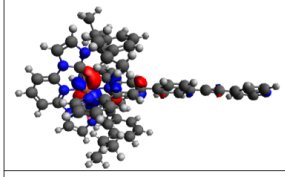	265 – LUMO+3 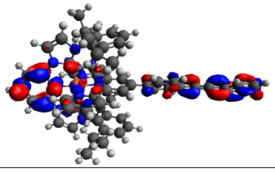	0.51	MLCT
	260 – HOMO-1 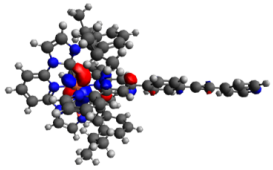	264 – LUMO+2 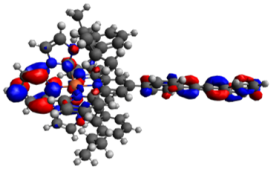	0.40	MLCT

470.6	260 – HOMO-1 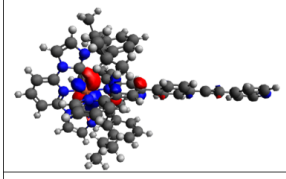	262 – LUMO 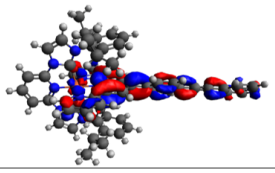	0.36	MLCT
	261 – HOMO 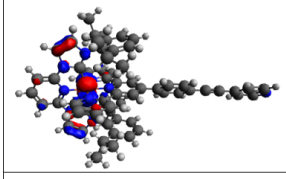	263 – LUMO+1 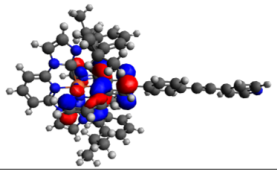	0.20	MLCT
	260 – HOMO-1 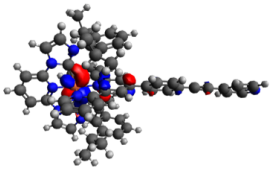	264 – LUMO+2 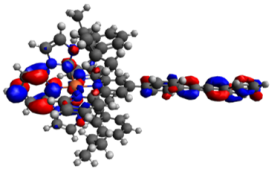	0.15	MLCT
376.8	261 – HOMO 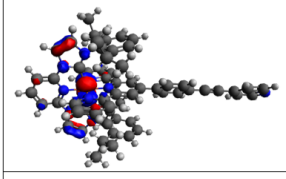	267 – LUMO+5 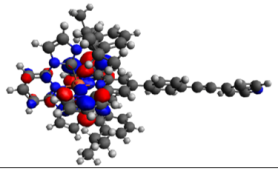	0.51	MLCT
	258 – HOMO-3 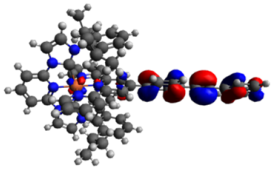	262 – LUMO 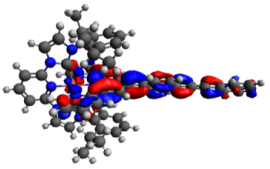	0.35	π-π*
313.6	260 – HOMO-1 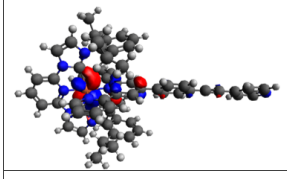	269 – LUMO+7 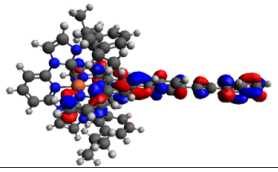	0.31	MLCT
	250 – HOMO-11 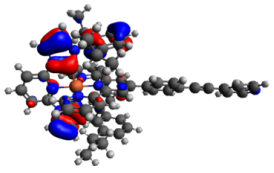	263 – LUMO+1 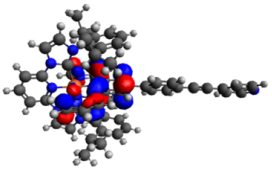	0.10	π-π*

307.5	256 – HOMO-5 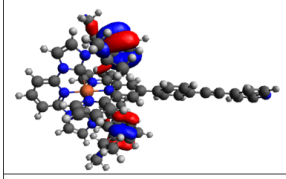	265 – LUMO+3 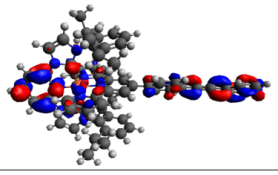	0.30	π-π*
	258 – HOMO-3 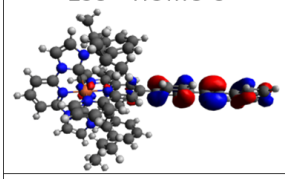	265 – LUMO+3 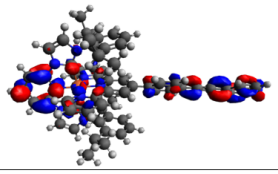	0.12	π-π*
	256 – HOMO-5 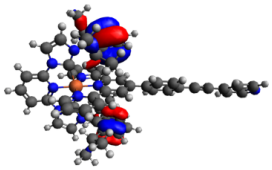	264 – LUMO+2 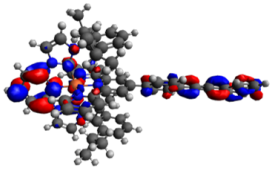	0.11	π-π*
305.8	256 – HOMO-5 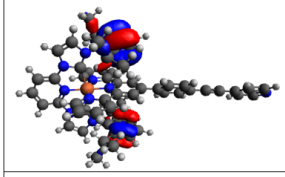	265 – LUMO+3 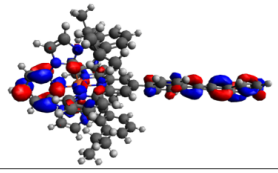	0.29	π-π*
	258 – HOMO-3 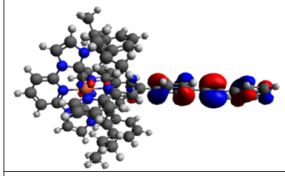	265 – LUMO+3 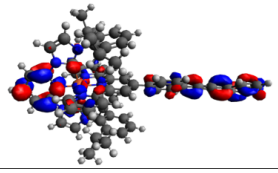	0.19	π-π*
	258 – HOMO-3 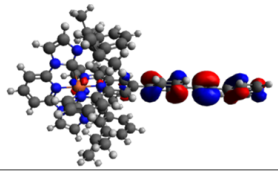	264 – LUMO+2 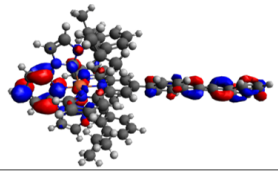	0.14	π-π*

Computed dominant vertical excitation of Dy2. Donor and acceptor orbitals are visualized. Contribution to and character of the transition is specified.

transition	donor	acceptor	contribution	character
555.5	344 – HOMO 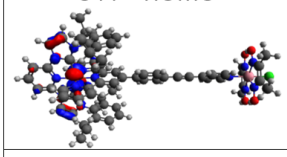	346 – LUMO+1 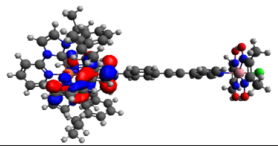	0.54	MLCT
	343 – HOMO-1 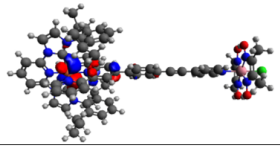	345 – LUMO 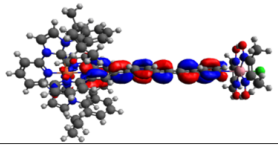	0.40	MLCT
541.7	343 – HOMO-1 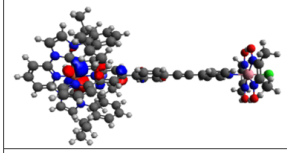	345 – LUMO 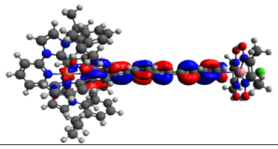	0.49	MLCT
	344 – HOMO 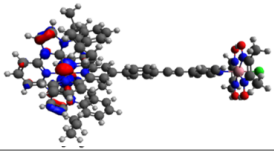	346 – LUMO+1 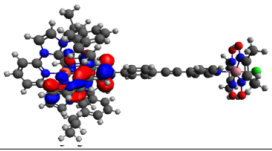	0.34	MLCT
395.3	339 – HOMO-5 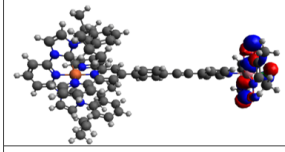	348 – LUMO+3 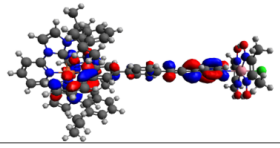	0.41	π-π*
	338 – HOMO-6 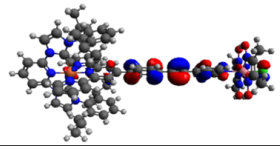	345 – LUMO 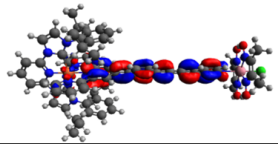	0.26	π-π*
368.0	344 – HOMO 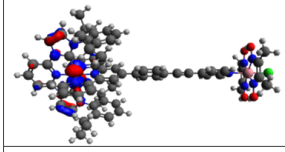	354 – LUMO+9 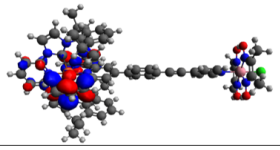	0.44	MLCT
	338 – HOMO-6 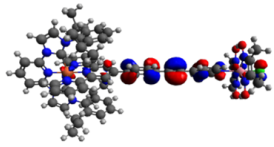	345 – LUMO 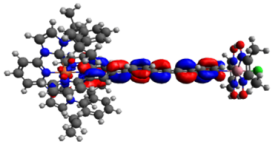	0.30	π-π*

326.8	336 – HOMO-8 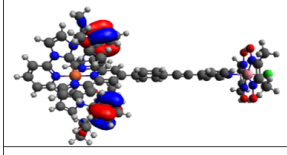	347 – LUMO+2 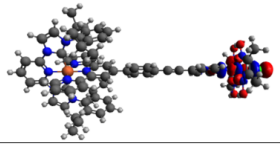	0.25	LMCT
	338 – HOMO-6 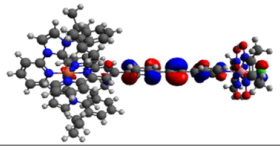	348 – LUMO+3 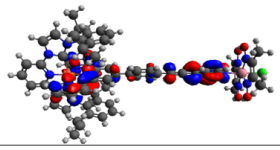	0.17	π-π*

Computed dominant vertical excitation of Fe3. Donor and acceptor orbitals are visualized. Contribution to and character of the transition is specified. Adapted from[99]

Transition (state)	Donor	Acceptor	Contribution	Character
a (8) 395.9 nm	HOMO (237) 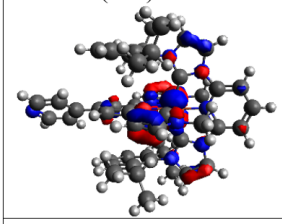	LUMO+3 (241) 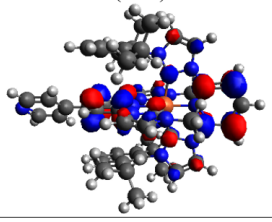	0.73	MLCT
	HOMO-2 (235) 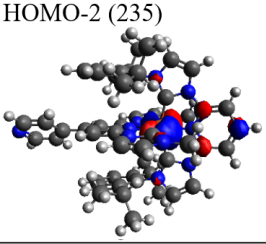	LUMO+1 (239) 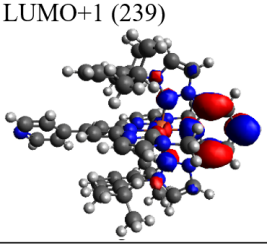	0.10	MLCT
b (6) 415.2nm	HOMO-2 (235) 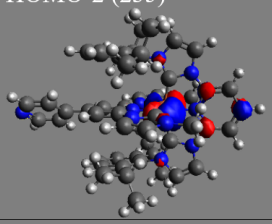	LUMO+1 (239) 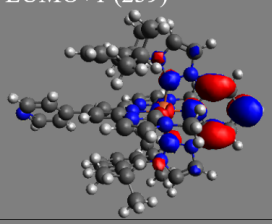	0.37	MLCT
	HOMO (237) 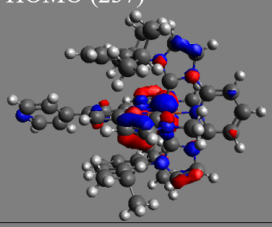	LUMO+2 (240) 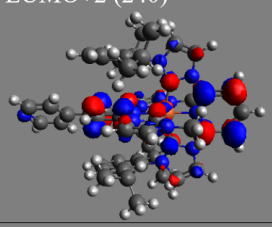	0.36	MLCT
	HOMO (237) 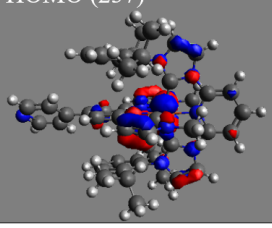	LUMO+3 (241) 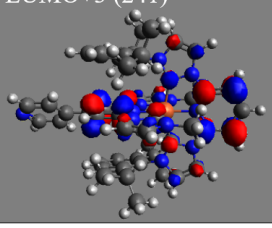	0.22	MLCT
c (4) 446.0 nm	HOMO-1 (236) 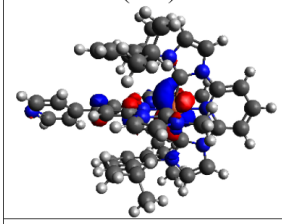	LUMO (238) 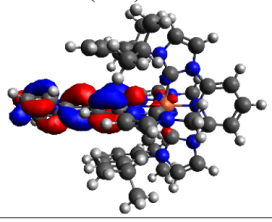	0.64	MLCT
	HOMO (237) 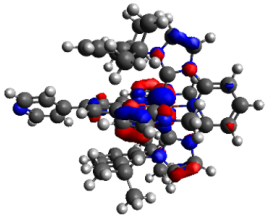	LUMO+2 (240) 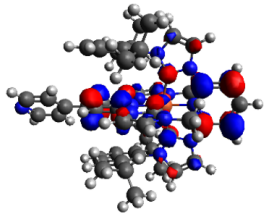	0.20	MLCT

	HOMO-2 (235) 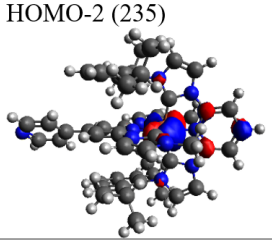	LUMO (238) 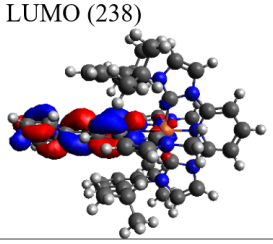	0.09	MLCT

Computed dominant vertical excitation of Dy3. Donor and acceptor orbitals are visualized. Contribution to and character of the transition is specified.Adapted from[99]

Transition (state)	Donor	Acceptor	Contri-bution	Character
a (17) 401.9 nm	HOMO (320) 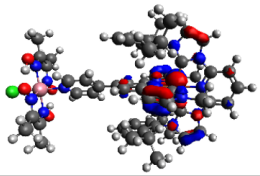	LUMO+7 (328) 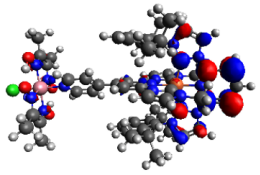	0.37	MLCT
	HOMO (320) 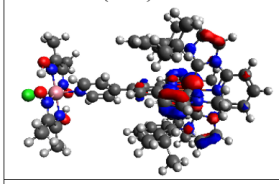	LUMO+4 (325) 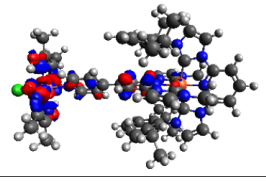	0.29	MLCT/ MMCT
	HOMO (320) 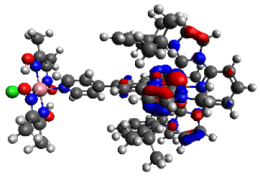	LUMO+5 (326) 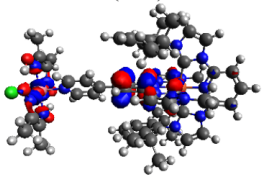	0.21	MLCT/ MMCT
b (15) 413.1 nm	HOMO (320) 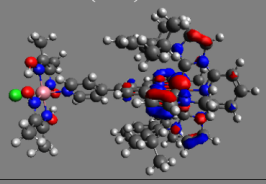	LUMO+7 (328) 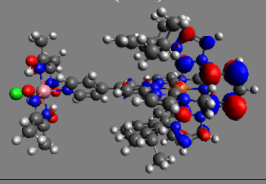	0.38	MLCT
	HOMO-2 (318) 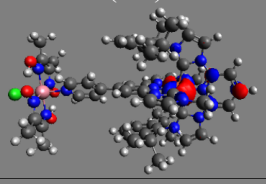	LUMO+3 (324) 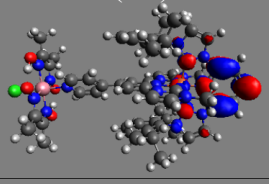	0.37	MLCT
	HOMO (320) 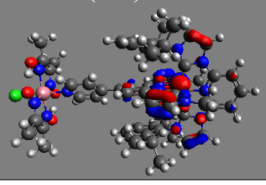	LUMO+5 (326) 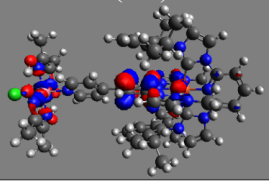	0.14	MLCT/ MMCT

c (8) 480.6 nm	HOMO-1 (319) 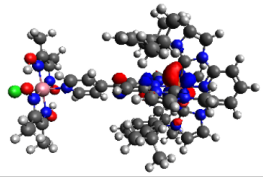	LUMO (321) 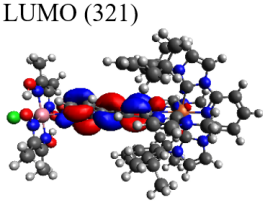	0.78	MLCT
	HOMO (320) 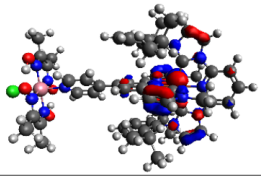	LUMO+5 (326) 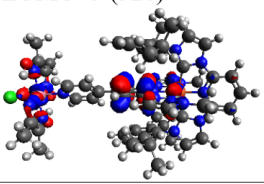	0.08	MLCT/ MMCT

Homoleptic iron complexes

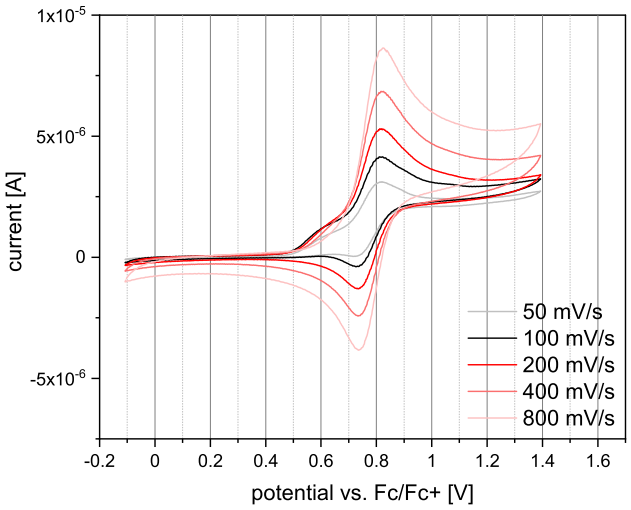

Cyclic voltammogram of **Fe1$_{\mathbf{homo}}$** vs. Fc/Fc^+ in MeCN with 50-800 mV/s scan rate - reversible Fe(II/III) oxidation.

Electrochemical data for oxidation/reduction in $Fe1_{homo}$.

v [mV/s]	50	100	200	400	800
E_{pa} [V]	0.81	0.81	0.81	0.81	0.82
E_{pc} [V]	0.74	0.75	0.74	0.74	0.74
$E_{1/2}$ [V]	0.78	0.78	0.77	0.78	0.78
ΔE [mV]	71	66	76	71	78
I_{pa} [10^{-6} A]	2.02	2.81	3.91	5.09	6.32
I_{pc} [10^{-6} A]	-0.99	-1.54	-2.85	-4.07	-5.58
I_{pa}/I_{pc}	2.04	1.83	1.37	1.25	1.13
$I_{pa}/\sqrt{v}$	0.29	0.28	0.28	0.25	0.22
$I_{pc}/\sqrt{v}$	-0.14	-0.15	-0.20	-0.20	-0.20

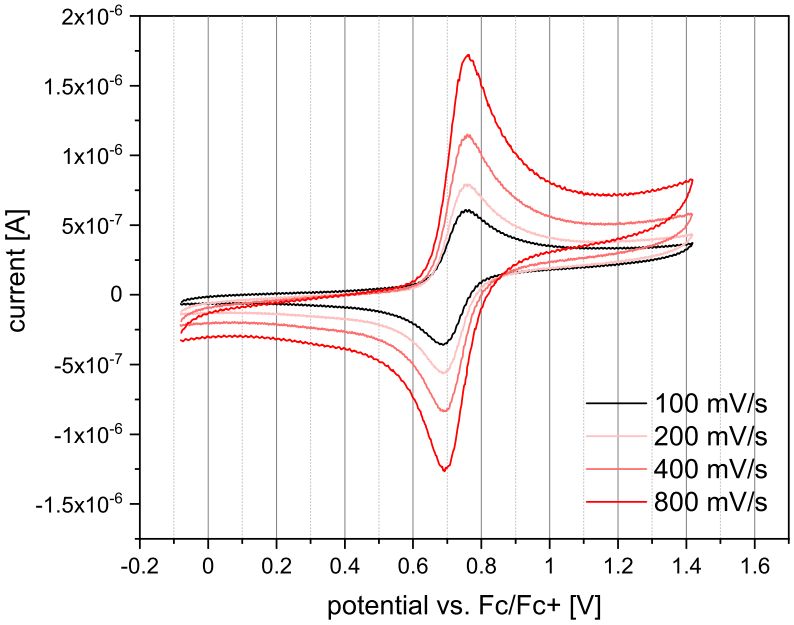

Cyclic voltammogram of **Fe2$_{\mathbf{homo}}$** vs. Fc/Fc^+ in MeCN with 50-800 mV/s scan rate - reversible Fe(II)/III) oxidation.

Electrochemical data for oxidation/reduction in $Fe2_{homo}$.

v [mV/s]	100	200	400	800
E_{pa} [V]	0.75	0.75	0.76	0.76
E_{pc} [V]	0.69	0.69	0.69	0.70
$E_{1/2}$ [V]	0.72	0.72	0.73	0.73
ΔE [mV]	68	66	66	61
I_{pa} [10^{-6} A]	0.44	0.64	0.96	1.45
I_{pc} [10^{-6} A]	-0.47	-0.64	-0.94	-1.45
I_{pa}/I_{pc}	0.92	0.99	1.02	1.00
$I_{pa}/\sqrt{v}$	0.04	0.05	0.05	0.05
$I_{pc}/\sqrt{v}$	-0.05	-0.05	-0.05	-0.05

v [mV/s]	100	200	400	800
E_{pa} [V]	-1.51	-1.50	-1.50	-1.51
E_{pc} [V]	-1.56	-1.56	-1.56	-1.56
$E_{1/2}$ [V]	-1.53	-1.53	-1.53	-1.54
ΔE [mV]	51	54	54	44

v [mV/s]	100	200	400	800
E_{pa} [V]	-1.64	-1.65	-1.64	-1.64
E_{pc} [V]	-1.69	-1.69	-1.68	-1.69
$E_{1/2}$ [V]	-1.67	-1.67	-1.66	-1.66
ΔE [mV]	49	42	49	46

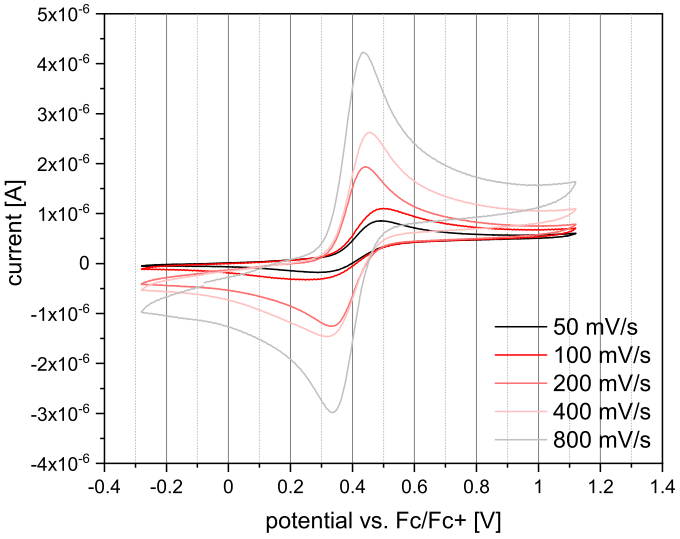

Cyclic voltammogram of $\mathbf{Fe3_{homo}}$ vs. Fc/Fc^{+} in MeCN with 50 - 800 mV/s scan rate - reversible Fe(II/III) oxidation.

Electrochemical data for oxidation/reduction in $Fe3_{homo}$.

v [mV/s]	50	100	200	400	800
E_{pa} [V]	0.49	0.47	0.43	0.45	0.44
E_{pc} [V]	0.31	0.29	0.34	0.33	0.34
$E_{1/2}$ [V]	0.40	0.38	0.39	0.39	0.39
ΔE [mV]	173	181	90	120	100
I_{pa} [10^{-6} A]	0.61	0.92	1.91	2.44	3.52
I_{pc} [10^{-6} A]	-0.44	-0.54	-1.67	-1.81	-2.99
I_{pa}/I_{pc}	1.37	1.71	1.15	1.35	1.18
$I_{pa}/\sqrt{v}$	0.09	0.09	0.14	0.12	0.12
$I_{pc}/\sqrt{v}$	-0.06	-0.05	-0.12	-0.09	-0.11

v [mV/s]	50	100	200	400	800
E_{pa} [V]	-1.81	-1.80	-1.81	-1.81	-1.81
E_{pc} [V]	-1.87	-1.87	-1.86	-1.87	-1.86
$E_{1/2}$ [V]	-1.84	-1.83	-1.83	-1.84	-1.83
ΔE [mV]	54	61	56	61	56
I_{pa} [10^{-6} A]	0.76	1.03	1.50	2.14	3.08
I_{pc} [10^{-6} A]	-0.54	-0.74	-1.03	-1.49	-2.15
I_{pa}/I_{pc}	1.42	1.38	1.45	1.44	1.44
$I_{pa}/\sqrt{v}$	0.11	0.10	0.11	0.11	0.11
$I_{pc}/\sqrt{v}$	-0.08	-0.07	-0.07	-0.07	-0.08

v [mV/s]	50	100	200	400	800
E_{pa} [V]	-2.00	-1.99	-1.99	-1.99	-2.00
E_{pc} [V]	-2.04	-2.04	-2.04	-2.05	-2.05
$E_{1/2}$ [V]	-2.02	-2.02	-2.02	-2.02	-2.03
ΔE [mV]	44	51	46	56	51

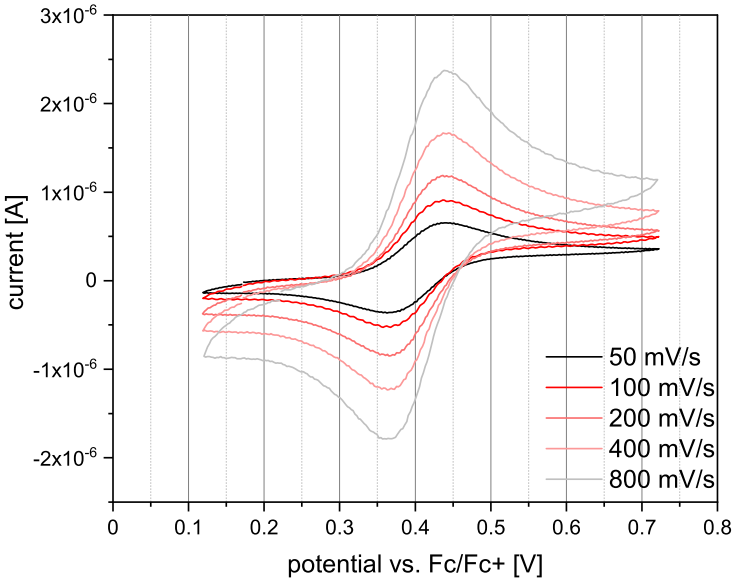

Cyclic voltammogram of **Fe6$_{\mathbf{homo}}$** vs. Fc/Fc^+ in MeCN with 50-800 mV/s scan rate - reversible Fe(II/III) oxidation.

Electrochemical data for oxidation/reduction in $Fe6_{homo}$.

v [mV/s]	50	100	200	400	800
E_{pa} [V]	0.43	0.44	0.43	0.44	0.44
E_{pc} [V]	0.36	0.37	0.37	0.37	0.37
$E_{1/2}$ [V]	0.40	0.40	0.40	0.40	0.40
ΔE [mV]	68	68	66	63	71
I_{pa} [10^{-6} A]	0.48	0.65	0.90	1.39	1.95
I_{pc} [10^{-6} A]	-0.48	-0.66	-0.91	-1.32	-1.86
I_{pa}/I_{pc}	1.01	0.98	0.98	1.06	1.05
$I_{pa}/\sqrt{v}$	0.07	0.07	0.06	0.07	0.07
$I_{pc}/\sqrt{v}$	-0.07	-0.07	-0.06	-0.07	-0.07

Heteroleptic iron complexes

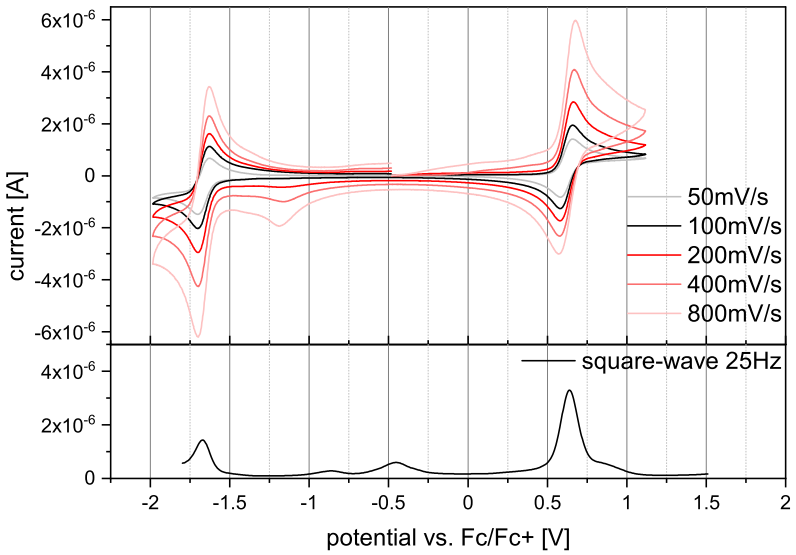

Cyclic voltammogram of **Fe1** vs. Fc/Fc^+ in MeCN with 50-800 mV/s scan rate.

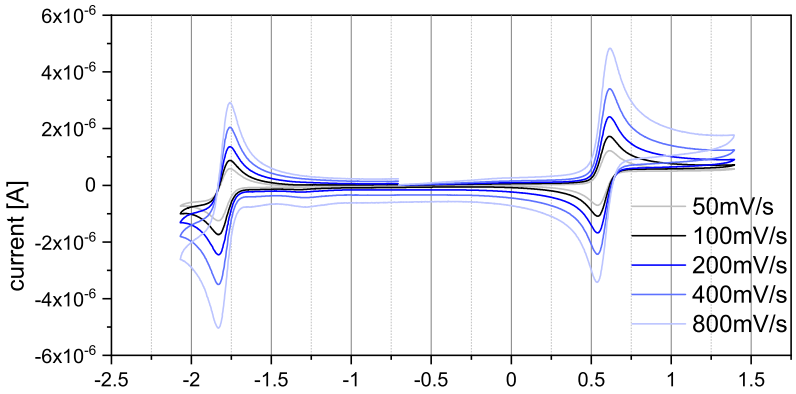

Cyclic voltammogram of **Fe2** vs. Fc/Fc^+ in MeCN with 50-800 mV/s scan rate.

Electrochemical data for oxidation/reduction in Fe1.

v [mV/s]	50	100	200	400	800
E_{pa} [V]	0.66	0.66	0.66	0.67	0.68
E_{pc} [V]	0.58	0.58	0.58	0.58	0.57
$E_{1/2}$ [V]	0.62	0.62	0.62	0.62	0.63
ΔE [mV]	76	73	83	88	100
I_{pa} [10^{-6} A]	1.18	1.64	2.34	3.24	4.53
I_{pc} [10^{-6} A]	-1.25	-1.79	-2.39	-3.15	-3.94
I_{pa}/I_{pc}	0.95	0.92	0.98	1.03	1.15
$I_{pa}/\sqrt{v}$	0.17	0.16	0.17	0.16	0.16
$I_{pc}/\sqrt{v}$	-0.18	-0.18	-0.17	-0.16	-0.14

v [mV/s]	50	100	200	400	800
E_{pa} [V]	-1.63	-1.63	-1.63	-1.63	-1.63
E_{pc} [V]	-1.70	-1.70	-1.70	-1.70	-1.70
$E_{1/2}$ [V]	-1.67	-1.67	-1.67	-1.67	-1.67
ΔE [mV]	71	63	66	66	66
I_{pa} [10^{-6} A]	1.18	1.74	2.34	3.49	5.10
I_{pc} [10^{-6} A]	-1.06	-1.49	-2.08	-2.90	-4.10
I_{pa}/I_{pc}	1.11	1.17	1.13	1.20	1.24
$I_{pa}/\sqrt{v}$	0.17	0.17	0.17	0.17	0.18
$I_{pc}/\sqrt{v}$	-0.15	-0.15	-0.15	-0.14	-0.14

Electrochemical data for oxidation/reduction in Fe2.

v [mV/s]	50	100	200	400	800
E_{pa} [V]	0.61	0.61	0.61	0.61	0.62
E_{pc} [V]	0.54	0.54	0.54	0.54	0.54
$E_{1/2}$ [V]	0.58	0.58	0.58	0.58	0.58
ΔE [mV]	73	71	71	71	78
I_{pa} [10^{-6} A]	1.07	1.50	2.10	2.94	4.10
I_{pc} [10^{-6} A]	-1.10	-1.55	-2.16	-2.94	-4.08
I_{pa}/I_{pc}	0.97	0.97	0.97	1.00	1.00
$I_{pa}/\sqrt{v}$	0.15	0.15	0.15	0.15	0.14
$I_{pc}/\sqrt{v}$	-0.16	-0.15	-0.15	-0.15	-0.14

v [mV/s]	50	100	200	400	800
E_{pa} [V]	-1.76	-1.76	-1.76	-1.76	-1.76
E_{pc} [V]	-1.83	-1.83	-1.83	-1.83	-1.83
$E_{1/2}$ [V]	-1.79	-1.79	-1.80	-1.79	-1.80
ΔE [mV]	68	63	66	66	71
I_{pa} [10^{-6} A]	1.01	1.39	2.15	3.14	4.34
I_{pc} [10^{-6} A]	-0.91	-1.24	-1.79	-2.55	-3.56
I_{pa}/I_{pc}	1.11	1.12	1.20	1.23	1.22
$I_{pa}/\sqrt{v}$	0.14	0.14	0.15	0.16	0.15
$I_{pc}/\sqrt{v}$	-0.13	-0.12	-0.13	-0.13	-0.13

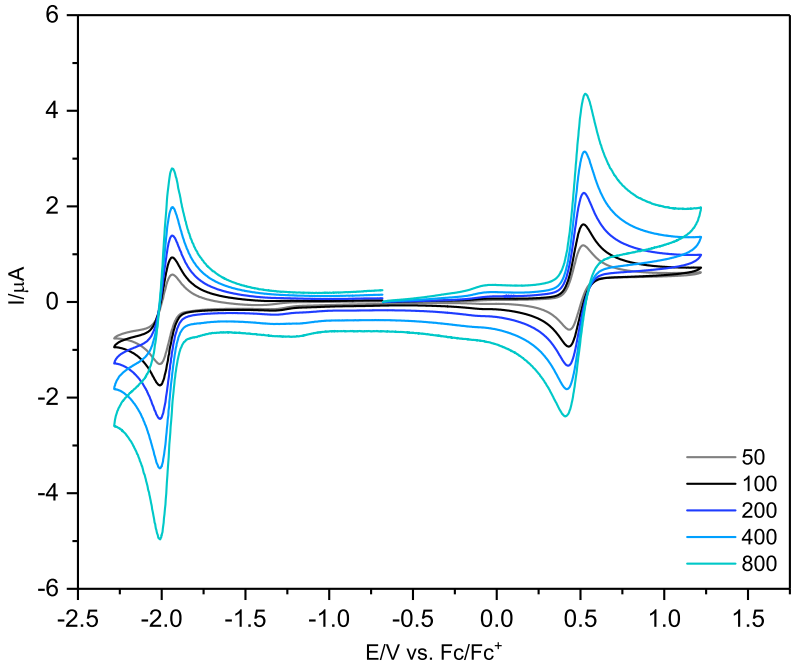

Cyclic voltammogram of **Fe3** vs. Fc/Fc^+ in MeCN with 50-800 mV/s scan rate.

Electrochemical data for reversible reduction in Fe3.

v [mV/s]	50	100	200	400	800
E_{pa} [V]	0.51	0.52	0.52	0.52	0.53
E_{pc} [V]	0.44	0.43	0.43	0.42	0.41
$E_{1/2}$ [V]	0.475	0.473	0.471	0.471	0.470
ΔE [mV]	76	85	93	98	115
I_{pa} [10^{-6} A]	0.99	1.39	1.92	2.63	3.56
I_{pc} [10^{-6} A]	-0.91	-1.34	-1.82	-2.14	-3.05
I_{pa}/I_{pc}	1.09	1.03	1.06	1.23	1.17
$I_{pa}/\sqrt{v}$	0.14	0.14	0.14	0.13	0.13
$I_{pc}/\sqrt{v}$	-0.13	-0.13	-0.13	-0.11	-0.11

v [mV/s]	50	100	200	400	800
E_{pc} [V]	-2.01	-2.01	-2.01	-2.01	-2.01
E_{pa} [V]	-1.94	-1.94	-1.94	-1.94	-1.94
$E_{1/2}$ [V]	-1.97	-1.97	-1.97	-1.97	-1.97
ΔE [mV]	66	68	66	68	68
I_{pc} [10^{-6} A]	-0.89	-1.26	-1.78	-2.51	-3.52
I_{pa} [10^{-6} A]	1.03	1.49	2.17	3.01	4.31
I_{pa}/I_{pc}	1.15	1.18	1.22	1.20	1.22
$I_{pc}/\sqrt{v}$	-0.13	-0.13	-0.13	-0.13	-0.12
$I_{pa}/\sqrt{v}$	0.15	0.15	0.15	0.15	0.15

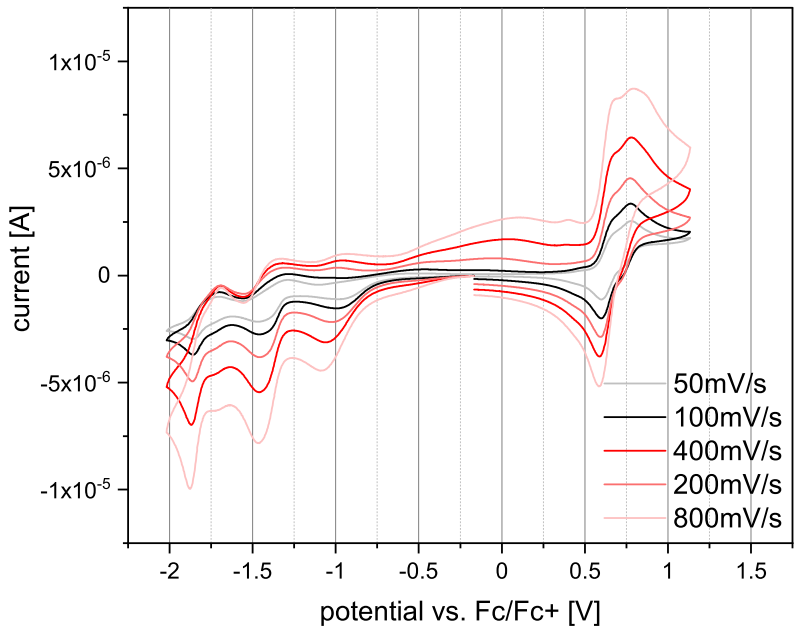

Cyclic voltammogram of **Dy1** vs. Fc/Fc^{+} in MeCN with 50-800 mV/s scan rate.

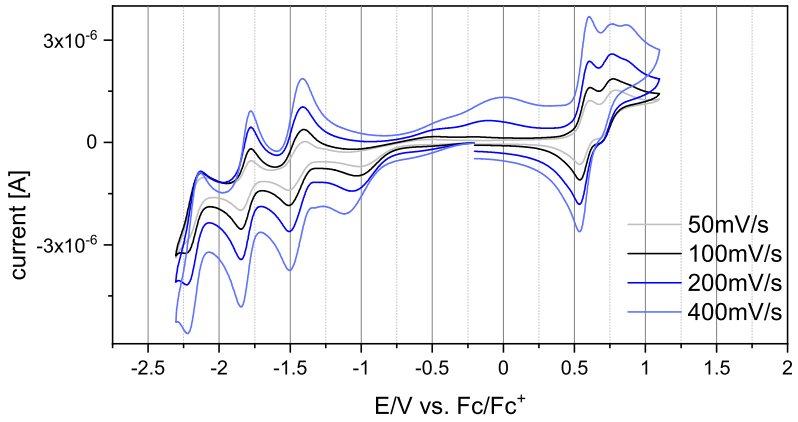

Cyclic voltammogram of **Dy2** vs. Fc/Fc^{+} in MeCN with 50-800 mV/s scan rate.

Electrochemical data for oxidation/reduction in Dy1.

v [mV/s]	50	100	200	400
E_{pa} [V]	0.79	0.77	0.77	0.77
E_{pc} [V]	0.74	0.74	0.74	0.74
$E_{1/2}$ [V]	0.77	0.75	0.75	0.76
ΔE [mV]	44	29	32	37

v [mV/s]	50	100	200	400
E_{pa} [V]	0.66	0.65	0.65	0.66
E_{pc} [V]	0.60	0.60	0.60	0.60
$E_{1/2}$ [V]	0.63	0.63	0.62	0.63
ΔE [mV]	54	51	51	59

v [mV/s]	50	100	200	400
E_{pa} [V]	-0.67	-0.54	-0.10	-0.03
E_{pc} [V]	-0.94	-0.96	-0.99	-1.03
$E_{1/2}$ [V]	-0.81	-0.75	-0.54	-0.53
ΔE [mV]	266	425	896	1001

v [mV/s]	50	100	200	400
E_{pa} [V]	-1.31	-1.32	-1.35	-1.37
E_{pc} [V]	-1.42	-1.43	-1.43	-1.44
$E_{1/2}$ [V]	-1.37	-1.37	-1.39	-1.40
ΔE [mV]	115	107	88	76
I_{pa} [10^{-6} A]	0.59	0.66	0.72	-0.94
I_{pc} [10^{-6} A]	-0.73	-1.01	-1.46	-2.08
I_{pa}/I_{pc}	0.80	0.65	0.49	-0.45
$I_{pa}/\sqrt{v}$	0.08	0.07	0.05	-0.05
$I_{pc}/\sqrt{v}$	-0.10	-0.10	-0.10	-0.10

v [mV/s]	50	100	200	400
E_{pa} [V]	-1.73	-1.73	-1.72	-1.72
E_{pc} [V]	-1.85	-1.85	-1.86	-1.86
$E_{1/2}$ [V]	-1.79	-1.79	-1.79	-1.79
ΔE [mV]	117	125	137	149
I_{pa} [10^{-6} A]	0.68	0.94	1.35	1.86
I_{pc} [10^{-6} A]	-0.66	-0.97	-1.45	-2.06
I_{pa}/I_{pc}	1.02	0.97	0.93	0.90
$I_{pa}/\sqrt{v}$	0.10	0.09	0.10	0.09
$I_{pc}/\sqrt{v}$	-0.09	-0.10	-0.10	-0.10

Electrochemical data for oxidation/reduction in Dy2.

v [mV/s]	50	100	200	400
E_{pa} [V]	0.78	0.77	0.77	0.75
E_{pc} [V]	0.71	0.71	0.71	0.70
$E_{1/2}$ [V]	0.75	0.74	0.74	0.73
ΔE [mV]	76	66	56	51

v [mV/s]	50	100	200	400
E_{pa} [V]	0.60	0.61	0.60	0.60
E_{pc} [V]	0.54	0.54	0.54	0.54
$E_{1/2}$ [V]	0.57	0.57	0.57	0.57
ΔE [mV]	61	66	59	63
I_{pa} [10^{-6} A]	0.78	1.05	1.55	2.18
I_{pc} [10^{-6} A]	-1.34	-1.86	-2.56	-3.55
I_{pa}/I_{pc}	0.58	0.56	0.60	0.61
$I_{pa}/\sqrt{v}$	0.11	0.11	0.11	0.11
$I_{pc}/\sqrt{v}$	-0.19	-0.19	-0.18	-0.18

v [mV/s]	50	100	200	400
E_{pa} [V]	-0.59	-0.55	-0.49	-0.04
E_{pc} [V]	-0.99	-1.01	-1.03	-1.09
$E_{1/2}$ [V]	-0.79	-0.78	-0.76	-0.57
ΔE [mV]	398	461	542	1050

v [mV/s]	50	100	200	400
E_{pa} [V]	-1.40	-1.41	-1.41	-1.41
E_{pc} [V]	-1.50	-1.50	-1.50	-1.50
$E_{1/2}$ [V]	-1.45	-1.46	-1.46	-1.46
ΔE [mV]	98	90	83	85
I_{pa} [10^{-6} A]	0.64	0.94	1.34	2.02
I_{pc} [10^{-6} A]	-0.56	-0.79	-1.13	-1.53
I_{pa}/I_{pc}	1.13	1.19	1.18	1.32
$I_{pa}/\sqrt{v}$	0.09	0.09	0.09	0.10
$I_{pc}/\sqrt{v}$	-0.08	-0.08	-0.08	-0.08

v [mV/s]	50	100	200	400
E_{pa} [V]	-1.78	-1.78	-1.78	-1.78
E_{pc} [V]	-1.84	-1.84	-1.84	-1.84
$E_{1/2}$ [V]	-1.81	-1.81	-1.81	-1.81
ΔE [mV]	61	63	59	63
I_{pa} [10^{-6} A]	0.49	0.80	1.25	1.83
I_{pc} [10^{-6} A]	-0.66	-0.95	-1.38	-1.98
I_{pa}/I_{pc}	0.74	0.84	0.90	0.93
$I_{pa}/\sqrt{v}$	0.07	0.08	0.09	0.09
$I_{pc}/\sqrt{v}$	-0.09	-0.10	-0.10	-0.10

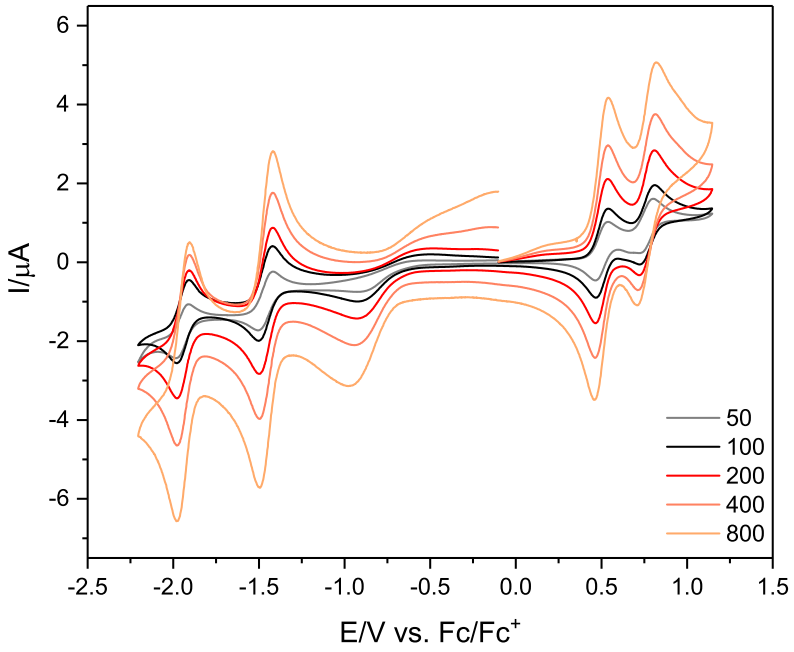

Cyclic voltammogram of **Dy3** vs. Fc/Fc^+ in MeCN with 50-800 mV/s scan rate.

Electrochemical data for oxidation/reduction in Dy3.

v [mV/s]	50	100	200	400	800
E_{pa} [V]	0.80	0.81	0.81	0.81	0.80
E_{pc} [V]	0.74	0.74	0.73	0.73	0.72
$E_{1/2}$ [V]	0.768	0.771	0.769	0.769	0.761
ΔE [mV]	59	71	76	85	79
I_{pa} [10^{-6} A]	0.68	0.86	1.27	1.60	1.99
I_{pc} [10^{-6} A]	-0.45	-0.59	-0.87	-1.15	-1.48
I_{pa}/I_{pc}	1.52	1.44	1.45	1.39	1.34
$I_{pa}/\sqrt{v}$	0.10	0.09	0.09	0.08	0.07
$I_{pc}/\sqrt{v}$	-0.06	-0.06	-0.06	-0.06	-0.05

v [mV/s]	50	100	200	400	800
E_{pa} [V]	0.53	0.53	0.53	0.53	0.53
E_{pc} [V]	0.46	0.46	0.46	0.46	0.46
$E_{1/2}$ [V]	0.497	0.498	0.494	0.495	0.493
ΔE [mV]	63	66	63	66	71
I_{pa} [10^{-6} A]	0.58	0.82	1.25	1.76	2.43
I_{pc} [10^{-6} A]	-0.71	-0.96	-1.42	-2.05	-2.86
I_{pa}/I_{pc}	0.81	0.85	0.88	0.86	0.85
$I_{pa}/\sqrt{v}$	0.08	0.08	0.09	0.09	0.09
$I_{pc}/\sqrt{v}$	-0.10	-0.10	-0.10	-0.10	-0.10

v [mV/s]	50	100	200	400	800
E_{pc} [V]	-1.50	-1.50	-1.50	-1.49	-1.49
E_{pa} [V]	-1.43	-1.42	-1.42	-1.42	-1.42
$E_{1/2}$ [V]	-1.46	-1.46	-1.46	-1.46	-1.46
ΔE [mV]	71	76	71	71	73
I_{pc} [10^{-6} A]	-0.72	-1.02	-1.53	-2.17	-3.00
I_{pa} [10^{-6} A]	0.82	1.24	1.76	2.57	3.72
I_{pa}/I_{pc}	1.13	1.22	1.16	1.18	1.24
$I_{pc}/\sqrt{v}$	-0.10	-0.10	-0.11	-0.11	-0.11
$I_{pa}/\sqrt{v}$	0.12	0.12	0.12	0.13	0.13

v [mV/s]	50	100	200	400	800
E_{pc} [V]	-1.97	-1.98	-1.97	-1.97	-1.97
E_{pa} [V]	-1.92	-1.92	-1.91	-1.91	-1.92
$E_{1/2}$ [V]	-1.94	-1.95	-1.94	-1.94	-1.94
ΔE [mV]	59	61	66	61	59
I_{pc} [10^{-6} A]	-0.56	-0.87	-1.31	-1.94	-2.77
I_{pa} [10^{-6} A]	0.68	1.05	1.59	2.25	3.21
I_{pa}/I_{pc}	1.21	1.21	1.22	1.16	1.16
$I_{pc}/\sqrt{v}$	-0.08	-0.09	-0.09	-0.10	-0.10
$I_{pa}/\sqrt{v}$	0.10	0.11	0.11	0.11	0.11

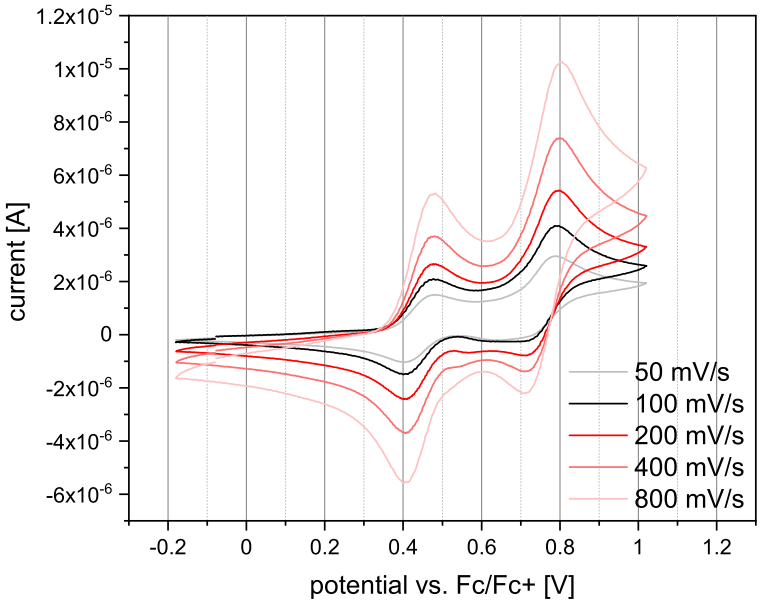

Cyclic voltammogram of **Tri3** vs. Fc/Fc^+ in MeCN with 50-800 mV/s scan rate - anodic side.

Electrochemical data for oxidation/reduction in Tri3.

v [mV/s]	50	100	200	400	800
E_{pa} [V]	0.79	0.79	0.79	0.80	0.80
E_{pc} [V]	0.72	0.73	0.73	0.73	0.73
$E_{1/2}$ [V]	0.75	0.76	0.76	0.76	0.77
ΔE [mV]	66	56	63	68	73
I_{pa} [10^{-6} A]	1.42	2.06	3.06	4.12	5.76
I_{pc} [10^{-6} A]	-0.87	-1.33	-1.69	-2.75	-3.78
I_{pa}/I_{pc}	1.63	1.55	1.81	1.50	1.52
$I_{pa}/\sqrt{v}$	0.20	0.21	0.22	0.21	0.20
$I_{pc}/\sqrt{v}$	-0.12	-0.13	-0.12	-0.14	-0.13

v [mV/s]	50	100	200	400	800
E_{pa} [V]	0.47	0.47	0.46	0.47	0.47
E_{pc} [V]	0.40	0.40	0.40	0.41	0.41
$E_{1/2}$ [V]	0.43	0.43	0.43	0.44	0.44
ΔE [mV]	66	66	63	61	61
I_{pa} [10^{-6} A]	0.86	1.17	1.81	2.49	3.71
I_{pc} [10^{-6} A]	-0.97	-1.38	-1.90	-2.60	-4.13
I_{pa}/I_{pc}	0.88	0.85	0.95	0.96	0.90
$I_{pa}/\sqrt{v}$	0.12	0.12	0.13	0.12	0.13
$I_{pc}/\sqrt{v}$	-0.14	-0.14	-0.13	-0.13	-0.15

List of Figures

2.1 Global temperature change relative to pre-industrial levels from 1850-1900. The 1.5°C global warming prediction is indicated till 2100. Adapted from[1]. . . . 3

2.2 Conventional and renewable processes for hydrogen production.[3] Depending on the used technology the produced hydrogen is labelled as blue, turquoise, grey or green. . . . 4

2.3 Comparison of AW electrolysis, SOEC and PEM electrolysis. Used membranes transmit hydroxide ions OH^-, oxygen ions O^{2-} or protons H^+. . . . 7

2.4 Redox catalytic cycle a) oxidative quenching mechanism, b) reductive quenching mechanism. . . . 10

2.5 Diffusive electron transfer in multi-component system and directional transfer in a dyad. . . . 11

2.6 Schematic potential energy surface diagram for $Ru(bpy)_3^{2+}$ (left) and $Fe(bpy)_3^{2+}$ (right), dashed arrows indicate non-radiative decays, phosph.= phosphorescent relaxation. . . . 13

2.7 Molecular structure and excited state lifetimes of $\mathbf{Fe(tpy)_2^{2+}}$[43], **C1**[44] and **C2**[45]. . . . 14

2.8 Molecular structure and excited state lifetimes of **C3**, **C3-COOH**, $\mathbf{C3\text{-}NMe_2}$ and **C4**, **C4-COOH**, $\mathbf{C4\text{-}NMe_2}$.[40,47]. . . . 15

2.9 Molecular structure of **C5**[51] and **C6**[52].Excited state lifetimes of **C6**. 16

2.10 Molecular structure and excited state lifetimes of **C7** and **C7-Co**.[53] 17

2.11 Molecular structure and excited state lifetimes of **C8** and **C9**.[55,56] . 17

2.12 Molecular structures of cobalt catalysts. . . . 19

2.13 Molecular structures of cobaloxime catalysts. . . . 20

2.14 Axial modification of cobaloxime complexes.[75] . . . 20

2.15 Homolytic and heterolytic mechanisms for hydrogen evolution catalyzed by cobalt catalyst.[76] . . . 21

2.16 Molecular structure of Ru-Co dyads. . . . 22

2.17 Molecular structure of Ir-Co dyads. . . . 23

2.18 Molecular structure of noble metal-free cobaloxime dyads.[53,83,84] . . 24

2.19 Variation of carbene count. . . . 26

2.20 Tuning of the bridging ligands by introducing acetylene and phenylacetylene spacers. . . . 26

2.21 Schematic structure of multimetal complexes - dyad and triad. . . . 27

3.1 Synthesis of pyridylethinylterpyridine **L1**. . . . 29

3.2 Synthesis of pyridylethinylphenylterpyridine **L2**, a) NH_3, NaOH, EtOH, RT b) $Pd(PPh_3)_2Cl_2$, CuI, PPh_3, TEA, 80°C, 3d. 30
3.3 Synthesis of bipyridyl-bis-imidazolium **L3**. a) $Pd(OAc)_2$, PPh_3, K_2CO_3, 1,4-dioxane/H_2O, 110°C, 2d; b) N-methylimidazole, 150°C, 5d. 31
3.4 Synthesis route 1 of **L4** - part 1. a) 1) trimethylsilyl acetylene, $Pd(PPh_3)_2Cl_2$, PPh_3, CuI, NEt_3, RT, 1d, 2) KOH, MeCN; b) $Pd(PPh_3)_2Cl_2$, PPh_3, CuI, THF/NEt_3, RT, 1d; c) N-methylimidazole, 150°C or 50°C. 31
3.5 ESI mass spectrum - twofold acetylation of **7-Br**. 32
3.6 Synthesis route 1 of **L4** - part 2. a) TMPMgCl·LiCl, I_2, THF, -40°C to RT, 14h; b) 1) $Pd(PPh_3)_2Cl_2$, PPh_3, NEt_3/THF (1:1), 0°C to RT, 1d, 2) KOH, MeCN; c) 4-iodopyridine, $Pd(PPh_3)_2Cl_2$, PPh_3, DIPA/THF (4:5); d) imidazole, CuO, K_2CO_3, DMF, 100°C, 1d or imidazole, NaH, DMF, 0°C to RT, 3d. 33
3.7 Synthesis route 2 of **L4** - part 1. a) imidazole, CuO, K_2CO_3, DMF, 150°C, 6d; b) KI, $NaNO_2$, HCl/H_2O (1:10) or H_2SO_4/H_2O (1:7); c) 4-ethinylpyridine hydrochloride, $Pd(PPh_3)_4$, CuI, DIPA/DMSO (1:1), RT, 2 weeks. 33
3.8 Aromatic region of ^{1}H NMR spectrum of a Sandmeyer-type reaction with concentrated hydrochloric acid. Iodo:chloro ratio is 1:2 in **14**. . 34
3.9 ESI mass spectrum of a Sandmeyer-type reaction with concentrated hydrochloric acid. Mass peaks of chloro and iodo derivatives $[M_{Cl}+H]^+$ and $[M_I+H]^+$ are detected. 35
3.10 Synthesis route 2 of **L4** - part 2. Isolation of **L5** instead. 35
3.11 ^{1}H NMR spectrum of **L5** in DMSO-d_6. 36
3.12 Synthesis route 2 of **L4** - part 3. a) MCPBA, $NaHCO_3$, DCM/H_2O, 40°C, 12h; b) MeI, MeCN, 80°C, 20h; c) 1) PBr_3, DCM, 50°C, 24h, 2) KPF_6, H_2O. 37
3.13 Synthesis of **L6**. a) MeI, MeCN, 70°C, 1d; b) 1) methyltriflate, DCM, -78°C, 2) KPF_6, H_2O. 38

4.1 Synthesis of $\mathbf{Fe1_{homo}}$ and $\mathbf{Fe2_{homo}}$. 40
4.2 Synthesis of $\mathbf{Fe3_{homo}}$ and $\mathbf{Fe4_{homo}}$. 40
4.3 Synthesis of $\mathbf{Fe5_{homo}}$. 41
4.4 Synthesis of $\mathbf{Fe6_{homo}}$. 41
4.5 Synthesis of $\mathbf{Fe(SP)Br_2}$. 42
4.6 Synthesis of **Fe1** and **Fe2** in THF. Anion exchange is performed with KPF_6 in H_2O. 43
4.7 Synthesis of **Fe3**. 43

4.8 Single crystal structure of **Fe1$_{homo}$** (top), **Fe2$_{homo}$** (middle) and **Fe3$_{homo}$** (bottom). Anisotropic displacement ellipsoids are drawn at the 50% probability level and hydrogens are omitted for clarity as well as counter ion PF_6^-. 45
4.9 Single crystal structure of **Fe1** (top), **Fe2** (middle) and **Fe3** (bottom). Anisotropic displacement ellipsoids are drawn at the 50% probability level and hydrogens are omitted for clarity as well as counter ion PF_6^-. 47
4.10 Absorption spectrum of **Fe1$_{homo}$** (black), **Fe2$_{homo}$** (blue), **Fe3$_{homo}$** (orange) and **Fe6$_{homo}$** (green). 49
4.11 Absorption spectrum of **Fe1** (black), **Fe2** (blue) and **Fe3** (orange). . 50
4.12 Molecular orbitals of **Fe1**, **Fe2** and **Fe3**; TPSSh, def2-TZVP(P), SMD (MeCN). HOMO-LUMO gaps are indicated (eV/nm). The average Fe 3d character is included for dπ, dπ* and dσ* orbitals in %. 51
4.13 Experimental and computational spectra of **Fe1** (red), **Fe2** (blue) and **Fe3** (orange); TPSSh, def2-TZVP, SMD(MeCN) or CPCM(MeCN). 53
4.14 Absorption changes upon protonation of homoleptic terpyridine iron complexes **Fe(tpy)$_2^{2+}$**, **Fe1$_{homo}$** and **Fe2$_{homo}$**. 55
4.15 Absorption changes upon protonation of iron complexes **Fe1**, **Fe2** and **Fe6$_{homo}$**. 56
4.16 Absorption changes upon protonation of tetra-carbene iron complexes **Fe3**, **Fe3$_{homo}$** and **C3**. 57
4.17 Cyclic voltammograms of homoleptic complexes **Fe1$_{homo}$**-**Fe6$_{homo}$** in MeCN ((nBu$_4$N)(PF$_6$), 100 mV/s, 1·10^{-3} mol/L). Artifacts are marked with an asteriks. 58
4.18 Cyclic voltammograms of heteroleptic complexes **Fe1** - **Fe3** in MeCN ((nBu$_4$N)(PF$_6$), 100 mV/s, 1·10^{-3} mol/L). 59
4.19 Changes in the UV-Vis spectrum of **Fe1** (1·10^{-4} mol/L) upon oxidation ($A_{gs} \rightarrow A_{ox}$ at +2.2 V (top), re-reduction at +0.53 V $A_{re\text{-}red}$ (middle), ligand-based reduction A_{red} at -2.3 V (bottom). 62
4.20 Changes in the UV-Vis spectrum of **Fe2** (1·10^{-4} mol/L) upon oxidation ($A_{gs} \rightarrow A_{ox}$ at +1.3 V and re-reduction at +0.53 V $A_{re\text{-}red}$ (top). Ligand-based reduction A_{red} occurs at -2.2 V (bottom). 63
4.21 Changes in the UV-Vis spectrum of **Fe3** (1·10^{-4} mol/L) upon oxidation ($A_{gs} \rightarrow A_{ox}$ at +0.75 V, re-reduction at +0.5 V $A_{re\text{-}red}$ and ligand-based reduction A_{red} at -2.5 V. Adapted from ref.[99] 64

5.1 Synthesis of **Dy1** and **Dy2**. a) 1) $CoCl_2$·6 H_2O, dimethylglyoxime, 95% EtOH, 70°C, 2) O_2, 30min. 65
5.2 Synthesis of **Dy3**. a) 1) $CoCl_2$·6 H_2O, dimethylglyoxime, 95% EtOH, 70°C, 2) O_2, 60min. 66

5.3 Synthesis of **Tri3**. 66
5.4 Single crystal structure of **Dy1** and **Dy3**. Anisotropic displacement ellipsoids are drawn at the 50% probability level. Hydrogens are omitted for clarity as well as counter ion PF_6^-. 67
5.5 Mole fraction of **Dy1** and **Dy2** calculated from proton integral ratio following equation: $f_{dyad} = I_{dyad}/(I_{dyad}+I_{PS})$. $I_{dyad}+I_{PS}$ is proportional to the total amount of species in solution. Inset shows evolution of **Fe2** proton signal (δ = 6.80 ppm) and decrease of dyad **Dy2** signal (δ = 6.78 ppm) in diluted dyad solution. 70
5.6 Insight into aromatic region of ^{1}H NMR of **Dy3** (concentrated=red, diluted=black) and **Fe3** (blue) in MeCN-d_3. Proton signals in diluted dyad solution originating from **Fe3** are marked with asterisks. Adapted from ref.[99]. 71
5.7 Mole fraction of dyad **Dy3** calculated from proton integral ratio (marked with squares in previous figure) following equation: $f_{dyad} = I_{dyad}/(I_{dyad}+I_{PS})$. Total amount of species in solution is proportional to $I_{dyad}+I_{PS}$. Adapted from ref.[99]. 72
5.8 Left) Insight into aromatic region of ^{1}H NMR spectra of **Tri3** (concentrated=orange, diluted=red, blue) and **Fe3$_{homo}$** (black) in MeCN-d_3. Right) Schematic structures of compounds present in solution upon triad dissociation: triad, asymmetric dyad and photosensitizer. . . . 72
5.9 Mole fraction of the compounds **Tri3**, asymmetric dyad and **Fe3$_{homo}$** present in solution upon triad dissociation. 73
5.10 Absorption spectra of **Fe1-2** and **Dy1-2** in MeCN at $1{\cdot}10^{-5}$ mol/L. . 75
5.11 Absorption spectra of **Fe3**, **Fe3$_{homo}$** and **Dy3**, **Tri3** in MeCN at $1{\cdot}10^{-5}$ mol/L. 76
5.12 Absorption spectra of **Dy1-3** in MeCN at $2.5{\cdot}10^{-4}$ mol/L till $3.2{\cdot}10^{-5}$ mol/L or $1.6{\cdot}10^{-5}$ mol/L. 78
5.13 Difference absorption spectra of **Dy3** in MeCN at $2.5{\cdot}10^{-4}$ mol/L till $3.2{\cdot}10^{-5}$ mol/L simulated by calculating $\Delta\epsilon = \epsilon_{Dy3}\text{-}f_n \cdot \epsilon_{Fe3}$. 79
5.14 Absorption changes of **Dy1-2** (top) and **Dy3**, **Tri3** (bottom) in MeCN upon protonation with TFA. 80
5.15 Molecular orbitals of **Fe1-3** and **Dy1-3** extracted from single point energy calculations; TPSSh, def2-TZVP(P), CPCM/SMD (MeCN). HOMO-LUMO gaps are indicated (eV/nm). The average Fe 3d and Co 3d character is included for dπ, dπ* and dσ* orbitals in %. . . . 82
5.16 Experimental and computational spectra of **Dy1** (red), **Dy2** (blue) and **Dy3** (orange); TPSSh, def2-TZVP, SMD(MeCN) or CPCM(MeCN). 84
5.17 Cyclic voltammograms of multimetal complexes **Dy1** - **Dy3** and **Tri3** in MeCN ($(n\text{Bu}_4\text{N})(PF_6)$, 100 mV/s, $1{\cdot}10^{-3}$ mol/L). 86

5.18 Changes in the UV-Vis spectrum of **Dy1**($1 \cdot 10^{-4}$ mol/L) upon oxidation ($A_{gs} \rightarrow A_{ox}$ at +0.9 V (top), re-reduction at +0.65 V $A_{re\text{-}red}$ and ligand-based reduction A_{red} at -1.43 V (bottom). 89

5.19 Changes in the UV-Vis spectrum of **Dy2** ($1 \cdot 10^{-4}$ mol/L) upon oxidation ($A_{gs} \rightarrow A_{ox}$ at +0.9 V and re-reduction at +0 V $A_{re\text{-}red}$ (top). Ligand-based reduction A_{red} occurs at -1.86 V (A_{red1}) and at -2.2 V (A_{red2}) (bottom). 90

5.20 Changes in the UV-Vis spectrum of **Dy3** ($1 \cdot 10^{-4}$ mol/L) upon oxidation ($A_{gs} \rightarrow A_{ox}$ at +0.78 V, re-reduction at +0.5 V $A_{re\text{-}red}$ and ligand-based reduction A_{red} at - 2.0 V. Adapted from ref.[99] 91

5.21 2D colormaps of transient absorption data for **Fe1**, **Fe2**, **Dy1** and **Dy2** in MeCN. Negative signals (bleach, stimulated emission) are shown in blue whereas positive ones (excited-state, photoproduct absorption) are in red. Contour lines are drawn at 20 % intervals with respect to the strongest (abs. value) signal. Delay x-axis becomes logarithmic for delays longer than 0.3 ps. The 550 nm gap corresponds to the spectral range of pump scattering. Additional pump scattering occurs at 405 nm. 94

5.22 Picosecond dynamics in transient absorption spectra of **Fe1**, **Fe2**, **Dy1** and **Dy2** in MeCN. Transient signal around the pump wavelength (550 nm) was omitted due to scattering artefacts. Residual pump scattering is also present around 405 nm. 95

5.23 Optical TA spectra of **Fe3** (a) and **Dy3** (b) excited at 515 nm in MeCN. First 5 ps of the evolution of kinetics at selected wavelengths for **Fe3** (c) and **Dy3** (d). Adapted from ref.[99] 98

6.1 Selected aromatic regions of proton NMR spectra of **Dy3**. Before irradiation (red), after 2.5 h (orange) and 22 h of irradiation in MeCN-d_3 at $2.5 \cdot 10^{-3}$ mol/L. Adapted from ref.[99] 102

6.2 Hydrogen evolution of **Dy3** (red) and the multi-component systems **Fe3**+**C14** (blue) and **[Ir]**+**C14** (black). Reaction conditions: 0.25 mM PS/cat/dyad in MeCN/water (1:1, 20 mL, 5% TEOA) under argon. Due to temperature correction and small volume production a negative slope of the blue curve originates after a longer time period. Adapted from ref.[99] 103

6.3 UV-Vis spectra of **Fe3**, **Dy3** and **C14** (= $Co(dmgH)_2pyCl$) combined with TA results at selected delay times.[119] 105

6.4 Relative intensities of $K\alpha_{1,2}$ and $K\beta'/K\beta_{1,3}$ emission lines and corresponding transitions assigned in an energy level diagram.[130] . . . 106

6.5 Schematic representation of the transient Kα XES signals of Fe and Co of **Dy3**. Grey area marks the region of interest (ROI) which is used to analyse the integrated areas at different delay times τ.[119] . . 107
6.6 Kα_1 emission line kinetics from -5 ps to 15 ps of iron and cobalt of **Dy3**.[119] 108
6.7 Kinetics of the cobalt Kα emission in **Dy3** and **C14** with corresponding fits. Differential signal is obtained by [C14]- [Dy3] and marked as blue lines (data+fit). Filled areas represent uncertainties.[119] 109
6.8 Schematic representation of holes (red) and electrons (blue) upon Fe $\rightarrow$ Co charge transfer in **Dy3**.[119] 110
6.9 Potential energy surface of ground and excited states of **Dy3** along the Fe-N distance (low x-axis) and the Fe-N bite angle (top x-axis).[119] 111

7.1 Proposed multimetal complex combing strategies deduced from this work. 116

List of Tables

3.1 Deoxygenation of **16**. 38

4.1 Crystallographic data of $\mathbf{Fe1_{homo}}$, $\mathbf{Fe2_{homo}}$ and $\mathbf{Fe3_{homo}}$. 44
4.2 Crystallographic data of **Fe1**, **Fe2** and **Fe3**. 46
4.3 Absorption properties of homoleptic and heteroleptic iron photosensitizers. 51
4.4 Redox potentials of homoleptic and heteroleptic iron photosensitizers.[a] 60

5.1 Crystallographic data of **Fe1**, **Dy1**, **Fe3** and **Dy3**. 68
5.2 Absorption properties of iron photosensitizers **Fe1-3**, $\mathbf{Fe3_{homo}}$ and multimetal complexes **Dy1-3** and **Tri3**. 77
5.3 Red-shift $\Delta\lambda$ of selected complexes upon protonation. 81
5.4 Redox potentials of iron-cobalt dyads **Dy1-3** and triad **Tri3**. Corresponding photosensitizer redox potentials in square brackets.[a] . . 87
5.5 Relaxation lifetimes τ_2 and τ_3 for **Fe1-2** and **Dy1-2**. 96
5.6 Kinetic data of transient spectra of **Fe1-2** and **Dy1-2**.[99] 98

6.1 Photocatalytic proton reduction of one-component system and multicomponent systems with Ir/Fe as photosensitizer and Co as catalyst. 104